Experimental study of void space, permeability and elastic anisotropy in crustal rock under ambient and hydrostatic pressure.

Philip Michael Benson

A thesis submitted to the University of London
for the degree of Doctor of Philosophy

Department of Earth Sciences
University College London

September, 2004

ProQuest LLC
789 East Eisenhower Parkway
P.O. Box 1346
Ann Arbor, MI 48106-1346

ABSTRACT

Anisotropy in the physical and transport properties of crustal rocks is a key influence on crustal evolution and energy resource management. Data from deep seismic soundings, borehole logging and laboratory measurement all show that the physical properties of the earth are anisotropic. Such anisotropy generally results from the superposition of fabric development during diagenesis and/or petrogenesis, and the application of anisotropic tectonic stresses. This leads to an aligned crack and pore fabric in crustal rocks that, in turn, leads to seismic velocity anisotropy and permeability anisotropy.

This thesis describes an experimental study which aims to investigate the relationships between pressure, pore fabric geometry and seismic and permeability anisotropy under hydrostatic pressures from room pressure to ~4km depth equivalence within the Earth's crust. Firstly, pore fabric analyses of three representative crustal rock types is presented. These rock types represent a range of crack and pore fabrics. The average void space shape and orientation is determined 3-D using the methods of anisotropy of magnetic susceptibility and velocity anisotropy. Scanning electron microscopy and fluorescent-dye crack imaging techniques further aid in the void space characterisation. Secondly, the development and application of an apparatus capable of contemporaneously measuring elastic wave velocity, porosity and permeability at effective pressures of up to 100 MPa is described. Results are analysed in terms of applied effective pressure and the rock pore fabric type and orientation.

Finally, the laboratory data are used to test models that attempt to predict geophysical parameters such as permeability and elastic wave velocity from microstructural attributes. This multi-facetted analysis allows a number of conclusions to be drawn, expanding the state-of-the-art in how the pore fabric microstructure of crustal rock is represented by the methods of elastic wave velocity and porosity, with reference to the hydrostatic confining pressure and hence the burial conditions of the rock.

CONTENTS

FIGURE LIST

TABLE LIST

ACKNOWLEDGEMENTS

During my time at the Department of Earth Sciences, University College London, I have been privileged to meet and work with many talented individuals. It is the nature of experimental work that the process of obtaining high quality, repeatable data is by no means a simple, quick or trivial exercise; and I will not admit how often a curse has passed my lips! Very little of the work presented in this thesis could have been undertaken if it were not for the support and seemingly endless energy of a large number of colleagues and friends who have helped and advised me in countless ways. Laboratory work is very much a team effort, even though only one name is on the cover of this one.

I would like to thank past and present laboratory members, Oswald Clint, Peter Sammonds, David Dobson, Melody Tribeck, and Dan Hatton for sharing their insights and thoughts with me; the technical staff, Sean Houlding, Richard Rabe, Danny Howard and Jim Davy for their help in everything from setting up data acquisition computing facilities to the preparation and analysis of thin sections, and scanning electron microscopy instruction. Most of all, however, I owe huge thanks to the engineering expertise of Neil Hughes, John Bowles, and Steve Boon, for their aid in developing the experimental equipment with me, and their instruction on the advanced engineering principles of its operation.

I gratefully acknowledge the support of the Department: David Price, John Platt, and Tony Hurford for taking the time to read and support a number of funding proposals; and Ron Dudman, Celine Ahmed, and Belinda Hewitt for so quickly answering questions and ordering components, supplies and other laboratory items, often at the last minute and involving some 'creative' accounting. During my time at UCL, I have been lucky to have been involved with projects, research and discussion with many groups outside London; and I have particularly enjoyed working with my collaborators: Patrick Baud (Strasbourg), Sergio Vinciguerra and Cettina Trovato (Naples), Aya Kameda (Stamford), and especially Alex Schubnel (Toronto), for the use of his Kachanov model code, applied in this investigation. Thanks also to Fabrice Surma (Strasbourg) for mercury porosimetry, Erik Spangenberg (Potsdam) for the specialist thin section preparation and analysis, and Ute Trautwein (Potsdam). Finally, for fascinating discussion and advice I thank Christian David and Laurent Louis. I also acknowledge the UCL graduate School for providing support to attend conferences and the Natural Environment Research Council for my studentship.

I am indebted to my three closest colleagues, who have guided my research over the last three years: Roy White for his long experience in the field of seismics and modeling, and Ellen Platzman for her infectious drive and her knowledge of geology and rock magnetism. But most of all, I thank Philip Meredith for his endless enthusiasm, and who has provided me with so much more than an insight into Rock Physics; by taking the time and effort to support and read a large number of external funding proposals, fellowship applications and conference attendance grants; for introducing me to a great many respected experts in the field of Rock Physics at international meetings; and for always having the time to share his knowledge and ideas over a well-earned beer.

1 INTRODUCTION

Anisotropy

Data from deep seismic soundings, borehole logging and laboratory measurement all show that the physical properties of the earth are anisotropic. This observation is fundamental to our understanding of crustal evolution and energy resource management, for example the efficient recovery of hydrocarbon and water resources, and the safe disposal of hazardous waste. Anisotropy may be defined as the variation in a property of a given system with the direction of measurement (e.g. Dullien, 1979, Winterstein, 1990). For example, the properties of a piece of wood may be regarded as anisotropic, the material being easier to work along the direction of the grain than across it. Likewise, when dealing with natural rock, the mechanical, physical and transport properties may vary with orientation. Such differences are primarily due to different structures or fabric when the material is examined in different directions, and such anisotropy may be visualised from the crustal scale to the grain scale. At the lower limit, such detail as physical void alignments (porosity) within the rock is involved. A common measurement used to asses anisotropy is elastic wave velocity, this property being highly sensitive to the void spaces within porous rock, especially for dry samples where the velocity contrast between the rock grain minerals and air filled void space is very large. Rock permeability also shows anisotropy, this property being closely related to the bulk porosity and pore space connectivity. Finally, potential field methods, including magnetic susceptibility and electrical conductivity, also exhibit anisotropy due to embedded components within the rock matrix such as magnetic and conductive grains and minerals.

Although the generating mechanisms that produce anisotropy are diverse, they may be grouped broadly into two areas. *Intrinsic* anisotropy arises due to fabric development during diagenesis and/or petrogenesis and may be regarded, in general, as the microscopic component of the overall anisotropy. This intrinsic anisotropy may be considerably enhanced by *extrinsic* anisotropy caused by the application of external factors such as anisotropic tectonic stresses, which may lead to a mechanically aligned secondary crack and pore fabric. Thus, the overall anisotropy forms as a result of the highly complex superposition through time of these fabric elements. In addition, extrinsic anisotropy may not necessarily be aligned with the intrinsic anisotropy produced during rock formation, and may instead act to produce a second alignment at an angle to the intrinsic fabric. Anisotropy, therefore, may appear on virtually any scale from the microscopic scale of grain/mineral alignment and microscopic fracturing to larger scale faulting processes in the Earth's crust, such as collision of subducting continental margins, orogenesis and strike-slip faulting (as in the San Andreas fault). Crucially, the anisotropy due to these processes can be measured at all of the scales involved – from laboratory to global.

The separation of intrinsic from extrinsic anisotropy is an important but non-trivial problem. Both types of anisotropy affect seismic velocities, as the mechanical properties of rock are governed by the stiffness of elements that make up both the microscopic and macroscopic rock fabric.

However, the permeability of a porous medium is dependent upon the connectivity of porosity within rock, and not simply the volume of pore space alone. This is important, as fluid storage and movement are key to understanding the evolution and dynamics of the crust, but is more difficult to measure and quantify remotely than are seismic velocities. For these important reasons, the inter-relation between the pore fabric in natural rocks and its velocity, permeability and porosity is crucial to the application and interpretation of field scale data in terms of rock physical properties, and to the application and use of petrophysical models. Visual guidance of pore fabric such as laminations or bedding/crossbedding is a common and simple first order guidance to experimental work. However, the response of the different fabrics as a function of burial depth and therefore pressure is still poorly understood in terms of the actual, quantitative, physical average pore space shape and alignment. The investigation of these interrelations may thus lead to a greater understanding of the causes and effects of anisotropy in terms of their dependent physical properties.

It should also be stressed that velocity and velocity anisotropy can be routinely measured in both the field on the reservoir scale, and in the laboratory on the microscopic scale. However, permeability anisotropy is much more difficult to measure, especially on the reservoir scale. Often, the permeability of rock is the parameter that is the most highly sought after due to its significance in the oil and water industries and to crustal fluid movement generally. Thus, knowledge of the permeability anisotropy within a rock body based upon pore fabric and seismic anisotropy will have wide ranging implications for the assessment of fluid flow, especially in rocks which are compartmentalised in some way.

1.1 Intrinsic and Extrinsic Anisotropy

Intrinsic anisotropy commonly includes the smaller scale microscopic effects (Winterstein, 1990; Wendt et al., 2003), such as clay particle alignment, preferential grain fabric orientations, mineralogical layering, and the inherent anisotropy of the material itself, right down to the atomic crystal lattice of the rock fabric. For example, the mineral olivine has a specific symmetry and orientation to its crystal lattice. This in turn yields physical properties which change with direction of measurement with respect to the lattice orientation. For example, the elastic stiffness of the crystal (Christensen, 1965; Kern, 1992). The preferred crystallographic orientation of crystals and grains is a key factor in anisotropy and has been widely studied (Thomsen, 1986; Lo et al., 1986; Winterstein, 1990; Wendt et al., 2003). Lamination of organic matter also contributes to this anisotropic effect (Vernik, 1993).

Extrinsic anisotropy is often defined to be broadly the opposite of intrinsic anisotropy (Winterstein, 1990) in terms of the processes acting during its formation, as it refers to anisotropy induced through the action of external forces and processes not fundamentally linked to the formation of the rock. Such processes do not include diagenesis and rock burial, but do include such mechanisms as deformation and uplift occurring after initial rock formation, the application of

anisotropic stress fields, and application of temperature differentials. Two of the key forms of extrinsic anisotropy are; (a) anisotropic stresses leading to aligned micro-cracks forming in the rock (Hudson, 1990; Hudson et al., 2001), and (b); the formation and subsequent alteration of the porosity and pore space of the rock fabric.

Layered sediments are also a key factor in producing anisotropy, most notably in rocks such as shale, where values of seismic anisotropy of up to 35% have been determined (Vernik and Nur, 1992; Johnston and Christensen, 1995; Hornby, 1998). In such instances, the figure refers to the maximum percent difference in seismic velocity observed with respect to the measurement directions, which in these cases are approximately co-axial with the shale layering. The small visual scale of this layering often leads to its mis-interpretation as extrinsic anisotropy, whereas via the definition above it is correctly described as intrinsic anisotropy due to its primary development occurring during the rock fabric formation itself. The problem whereby the seismic signal does not reveal such subtleties is linked to the wavelength of the measuring signal itself (Backus, 1962). In such cases, a medium composed of fine isotropic layers may appear anisotropic if the seismic wavelength is longer than the layer thickness. The solution is simply to use seismic signals which have a sufficiently small wavelength in order to fully recover the information; a difficult task on field scale as seismic wavelengths must be suitably long in order to achieve sufficient power and penetration (Sheriff and Geldart, 1995), and to keep dispersion and attenuation at manageable levels. Hence, the widespread use of laboratory based ultrasonic velocity measurement in order to investigate velocity anisotropy.

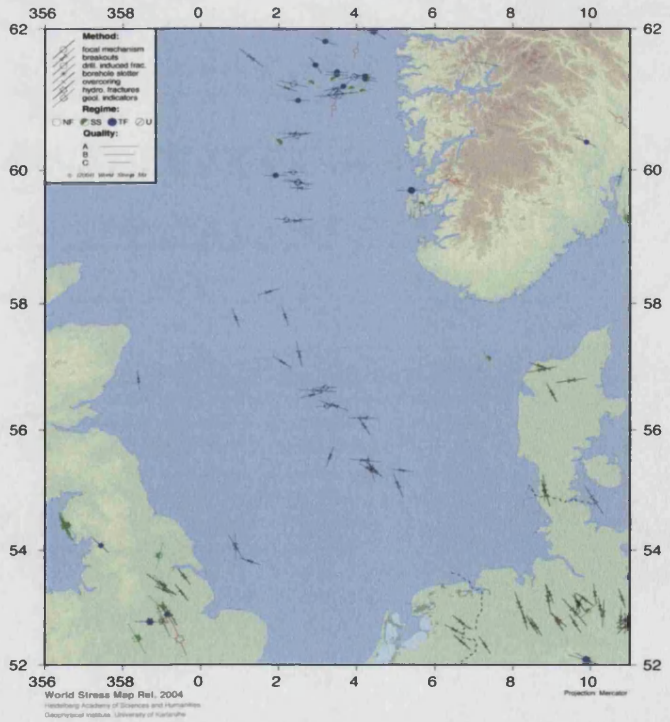

Figure 1-1. Tectonic stresses present in the North Sea area. From the world stress map project (Reinecker et al., 2004 – www.world-stress-map.org). Good alignments on land are seen due to the NW-SE movement of the mid Atlantic ridge, and the N-S movement of the African plate and Alps. Stress directions are significantly more random at sea (taken from oil well drilling data) due to faults and induced stresses, and through the stress field being refracted

What are the causes?

Having established that anisotropy is an important issue, and that its creation is, in part, due to anisotropic stresses, the question may therefore be raised as to where such stresses may be seen and quantified. Information regarding large scale crustal stresses have been compiled into a resource known as the world stress map project (Reinecker et al., 2004 – www.world-stress-map.org). This extensive dataset brings together information from earthquake focal mechanisms, well bore breakouts and drilling induced fractures, *in-situ* stress measurements (over coring, hydraulic fracturing, borehole slotter), and young geologic data (fault slip analysis and volcanic vent alignments). Figure 1-1 shows an example from the North Sea. Here, the stress orientations show two distinct alignments which can be related to known tectonic movements. These are from the African plate to the south and the mid-ocean ridge to the West. Whilst important, the use of such stress maps is not always applicable as they depend entirely on the *in-situ* stresses. These stresses cannot be controlled or modified in order to investigate the interrelation of stress upon other rock properties, and thus applied to other active areas of investigation in which the anisotropy is poorly understood. However, this problem may be partly solved though use of experimental testing machines which apply controlled deviatoric forces to instigate deformation, fracturing, and ultimately failure (figure 1-2).

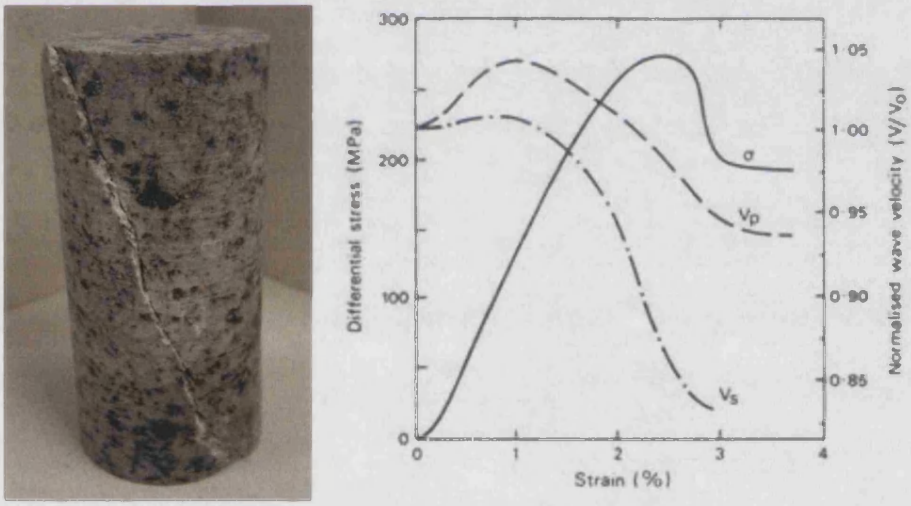

Figure 1-2. Left - example of an experimentally fractured test sample (granite), under deviatoric stress. Right – example of the changing physical properties of sample during the deformation leading up to and beyond failure, from another sample (after Meredith et al., 1990). As stress builds up, cracks perpendicular to σ_1 close, resulting in the increasing P-wave and S-wave velocity. As increasing stresses start to damage the rock, microcracks start to form, lowering the P-wave and S-wave velocity. At failure (approximately 3% strain), S-wave velocity is more heavily reduced than P-wave, and the cracks forming parallel to σ_1 coalesce to form the 30° fault seen in the sample

Establishing a link between laboratory and field measurement is fundamental in order to have confidence in such laboratory work. Fortunately, despite the wide variation in scales, many processes on the larger scale are observed in the laboratory. For example, theory predicts that under anisotropic stress regimes, shear fractures at approximately 30° to the maximum principal stress (Griffith, 1924) will form, as seen in figure 1-2 above.

At larger scales, figure 1-3 shows a 4m diameter horizontal tunnel, drilled for research purposes by using many small bores rather than by blasting one large shaft in order to prevent blasting damage. Tunnel damage can be clearly seen in the upper left and lower right corners of this figure. More specifically, these borehole 'breakouts' form wedge shaped holes in the tunnel walls, which are aligned with the minimum stress orientation measured in the local environment, as predicted from theory and observed from experimental rock mechanics (Paterson, 1978). Therefore, large scale anisotropy may be reproduced at laboratory scale with a certain degree of confidence, as the effects of large scale tectonic action and stresses produce aligned fracturing within crustal rock which appears to be mirrored in the laboratory environment.

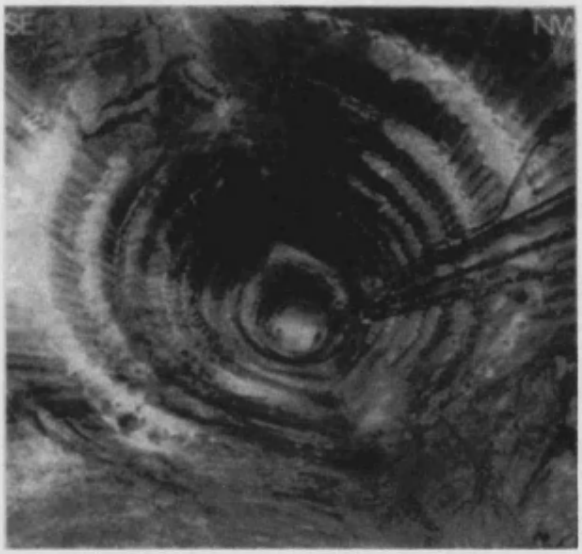

Figure 1-3. Borehole 'breakouts'. The missing 'wedge' shapes in the tunnel at the top left and bottom right of this image are approximately aligned with the minimum stress direction in the area

1.2 VOID SPACE ANISOTROPY

The terms 'pore fabric' and 'void space anisotropy' have been used many times up to this point, and require a rigorous definition before proceeding. The concept of assigning an equivalent geometrical shape to an average pore fabric is not new (Dullien, 1979), and may be defined in general terms by using a cross-section through a cartoon rock as in figure 1-4. In this simple (2D) example, the average porosity in the rock is assigned an equivalent void space in the shape of an ellipse. Obviously, real pore fabric possesses a three dimensional shape, and would be represented by an ellipsoid.

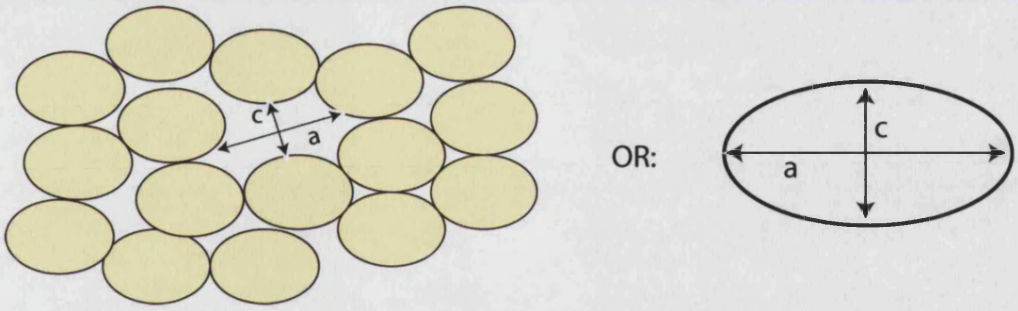

Figure 1-4. Pore space anisotropy is defined as the physical deviation of the average porosity shape from a sphere, in this 2-D example 'a' is the long axis and 'c' is the short axis giving a pore fabric anisotropy of 'a/c'

Although an ellipse is used here to represent the overall shape of the porosity, this is obviously an average and therefore a simplification (Zimmerman, 1991). The compressibility of different pore shapes as a function of their physical geometry varies widely, from the compressibility of simple spherical pores (Walsh et al., 1965), to highly complicated relations which compute compressibility in terms of a generalised pore shape (Sokolnikoff, 1956; Zimmerman, 1986). However, such a complicated approach is beyond the scope and need of this study, and an ellipsoidal representation is used here for ease of presentation, anisotropy determination, and the interpretation of results. The use of a relatively simple depiction also allows some key principles and parameters to be easily visualised.

Pore space anisotropy is defined as the relative physical shape and orientation of the average void space in the rock. Based on this definition, I now introduce a key parameter, the **bulk pore fabric anisotropy,** P_ϕ. This is defined as the fractional length ratio between the shortest and the longest principal ellipsoid axes, equivalent to the ratio 'a/c' in figure 1-4 above, and is often used in magnetic susceptibility and structural geology work. This is slightly different to bulk anisotropy commonly used with ultrasonic anisotropy '**A**', defined as: **A** = [velocity difference / velocity mean]. Both anisotropy definitions are used in this work. These, and other, parameters based on this representation of pore fabric geometry and alignment will be the topic of Chapters 4, 5 and 7. These Chapters also discuss the relative merits of these two definitions and their application. Before then, it should be stressed that, in general, no linear relationship exists between the physical pore fabric of the rock, and measured geophysical signals (such as elastic velocity, magnetic susceptibility, etc). This is addressed through adopting comparative methods, and through the application of the equivalent pore geometry (Hrouda et al., 2000), which will discussed thoroughly in Chapters 2 and 7. Note also that the average void space fabric could either be composed of a single shape, size and orientation in 3-D, or the superposition of many different sized and shaped pore spaces, which when added together effectively become equivalent to the single pore. Therefore, bulk pore fabric anisotropy data obtained from methods that quantify pore fabric must be interpreted with a degree of caution.

1.3 RATIONALE AND SCOPE OF WORK

Porosity is a ubiquitous feature of sedimentary rock. However, the processes responsible for porosity formation are diverse, ranging from depositional processes such as sorting and grain alignment, through diagenetic processes such as compaction and cementation, to deformational processes such as microcracking. The porosity that evolves from the superposition of these processes over time may therefore have a complex geometry or fabric. In particular, many of these processes, such as grain sorting, compaction and microcracking, have an inherent directionality which may lead to anisotropy of the void space and all been shown to play important roles in influencing the petrophysical properties of rock (Lo et al., 1986; Jones and Meredith, 1998; Rasolofosaon and Zinszner, 2002). This is important, since the void space geometry in porous rock is one of the key controls on other mechanical and physical properties. Clearly, therefore, the traditional measurement of porosity as a volume-averaged, scalar quantity is not capable of providing information about the shape and geometry of the void spaces which constitute that porosity.

Elastic wave velocity measurement is a commonly used tool with which to estimate void space shape and orientation (Bourbie and Zinszner 1985; Klimentos, 1991). Wave velocities provide a reasonable proxy for porosity since they are very sensitive to the presence of void space within a solid matrix (Wyllie et al., 1958). In addition, if done in multiple orientations they can be used to estimate pore space anisotropy. Pore space geometry may be inferred from such azimuthal velocity measurements by assuming that elastic velocity is related to the amount of void space crossed by the wave (Berge et al., 1992). However, the assumption that all void spaces affect velocity equally may not be valid, especially for cracked media. It is widely accepted that low and high aspect ratio porosity (such as thin cracks and equant pores respectively) can exert disproportionate influences on wave velocities (Bourbie and Zinszner 1985; Klimentos, 1991; Benson et al., 2003), and upon their anisotropy. Also, many factors other than the void space geometry may affect velocity anisotropy. For example, the rock matrix may exhibit anisotropy through an aligned grain fabric or from a crystallographically preferred orientation within the grains themselves. In situations where the anisotropy is evident, the elastic anisotropy parameters are often calculated using three orthogonal cores (Hornby, 1998), with a fourth core prepared at an angle to these (most commonly at 45°, for mathematical simplicity). An alternative method is to make multiple radial measurements around the circumference of each core of a three orthogonal core set. This allows an approximate velocity ellipsoid to be calculated (Louis et al., 2003; Benson et al., 2003), from which the principal anisotropy axes can be determined regardless of the orientation of the core set relative to the larger scale rock sampling co-ordinate frame.

Alternatively, void space geometry can be determined using the method of anisotropy of magnetic susceptibility (AMS). AMS has traditionally been used to measure the magnetic anisotropy of a dry rock matrix (Tarling and Hrouda, 1993). Used in this manner it has become a commonly used tool for measuring sedimentary grain fabrics and hence for inferring depositional process and palaeocurrent directions. In this work I denote the dry matrix AMS measurement as **mAMS**.

However, this tells us nothing about the void space. To determine void space anisotropy using this technique, I saturate the pore space with a highly susceptible magnetic ferrofluid, thus providing it with an artificial magnetic susceptibility. When the total AMS is now measured, termed **tAMS**, the pore fabric AMS (**pAMS**) is included in this total signal, such that tAMS = mAMS + pAMS. However, for many rock types, including two of the three used in this work, mAMS << tAMS, and we can assume pAMS = tAMS, reflecting the bulk pore space volume, shape and alignment (Benson et al., 2003; Pfleiderer and Halls, 1990, 1994).

While both the pAMS and velocity anisotropy methods have their respective merits, I consider that, since they measure different but complementary properties, they are more powerful when used together. Consequently, these methods have been combined in order to address some key questions regarding the interplay between the physical pore fabric of crustal rock and its connected porosity, and the effect of these properties upon the rock permeability, seismic wave velocity and velocity/permeability anisotropy. By using the pAMS method in the first instance, I am able to asses the 3-D pore fabric shape, alignment, and its degree of bulk anisotropy without any external frame of reference to guide the measurement. For instance, when measuring elastic wave velocity anisotropy, a layered shale may indicate the likely directions of minimum and maximum velocity though the obvious layering which is usually present (Vernik, 1997; Hornby, 1998).

However, the hypothesis that the pore fabric is approximately aligned with this visible indicator is a potential assumption in such work. Furthermore, if no visible fabric is available the elastic wave velocity may not be wholly representative of the maximum anisotropy. Through the use of an advanced interpretive process (Louis et al., 2003; Benson et al., 2003), a 3-D velocity anisotropy may be derived to quantitatively asses the maximum elastic anisotropy by using azimuthal velocities as a proxy to the pore fabric crossed by the elastic wave. This information is then directly compared with the pAMS data, known to reflect the actual pore fabric size, shape and alignment. The issues raised through such assumptions and comparisons will be the focus of discussion in Chapter 7.

Even though the influence of pore fabric upon other rock properties has been well documented (Yale, 1985), many aspects remain poorly understood. In particular, experimental data is still (in general) a rare commodity, especially for permeability measurement due to the relatively difficult technical aspects involved. In addition, combined porosity evaluation with permeability and seismic wave velocity measurement has rarely been carried out simultaneously upon natural rock samples. Therefore, any links between the rock components previously described which influence these parameters and their measured values may not be fully understood. To investigate this, I use the method of anisotropy of magnetic susceptibility to characterise and quantify the solid matrix AMS (mAMS) and the ferrofluid-saturated pore space AMS (tAMS and pAMS) of three representative crustal rock types. These are a high porosity sandstone (Bentheim), a mature low porosity sandstone (Crab Orchard), and a low porosity fractured granite (Takidani). With reference

to the principal anisotropy directions identified by pAMS and 3-D velocity anisotropy, an integrated and detailed high-pressure experimental programme is then conducted in which P-wave and S-wave seismic velocity, steady-state fluid flow permeability, and porosity are measured contemporaneously at effective pressures up to 90MPa; recreating pressure conditions at approximately 4km depth in the crust.

This interdisciplinary approach allows a number of questions to be addressed, such as: is there a relationship between permeability anisotropy and seismic velocity anisotropy? If this link exists, to what extent does it depend upon the physical pore fabric anisotropy? And how can the numerous models available aid in interpreting experimental data? By measuring and analysing the concomitant changes in porosity, velocity and permeability (and their anisotropy) as a function of simulated burial conditions, this experimental project aims to expand the picture of how different pore fabrics respond to the hydrostatic pressure acting in the crust. Furthermore, these interdisciplinary approaches will allow relationships to be defined between the size and shape of the void space geometry (geology), and the anisotropy of elastic velocity and fluid permeability (geophysics); allowing rock physical results to be discussed in terms of the sedimentary microstructure and its ability to elucidate petrophysical properties of the rock.

1.4 PREVIOUS WORK

Methods

The technique of anisotropy of magnetic susceptibility has been used in palaeomagnetic work for many years. The earliest work by Graham (1953), subsequently followed up by others such as Stacey (1960) and Uyeda et al. (1963), notes that flow in partially solidified magma and during rock deformation leads to an alignment of magnetic grains, and this visible foliation and lineation appears to correlate with the directional dependence of magnetic susceptibility measurement. Later work, using more advanced and sensitive instrumentation, expanded these ideas to sedimentary fabrics (Potter and Pettijohn, 1963; Rees, 1966), and to other geological structures generally (Bhathal, 1971; Hrouda, 1982; Collinson, 1983). The newest advance, involving the use of magnetic ferrofluid to impregnate the pore space of a porous rock, is much more recent. This method was championed by Pfleiderer and Halls (1990, 1993, 1994), and used recently as part of a pilot study by Gilrane (2000). This technique gives the porosity of the rock an artificial magnetic fabric, with a geometry and alignment related to the average pore geometry and shape. Previous work using petrographic image analysis and image autocorrelations have provided a high level of confidence in the match between the physical average pore space geometry, and the porosity observed in thin section analysis and tunnelling electron microscopy (Heilbronner, 1992).

This new technique has been exploited in applications as diverse as the manufacture and deformation of ceramics (Hrouda et al., 2000) and the analysis of pore fabric variations across folded

rock structures (Pfleiderer and Kissel, 1994). In general, as long as the natural susceptibility of the rock under investigation is low compared to the saturated rock sample, then the ferrofluid saturated tAMS measurement can accurately infer geological rock properties which are dependent upon the pore space fabric and connectivity (Pfleiderer and Halls, 1994). Hydraulic permeability, for instance, may be evaluated much more quickly than through conventional means, but only in terms of anisotropy, not magnitude. In a qualitative pilot study, Gilrane (2000) compared two apparently very different rock types, Crab Orchard sandstone (4.5% porosity) and Bentheim sandstone (23% porosity), and made preliminary studies of tAMS and elastic velocity anisotropy in order to compare their pore fabrics. For Bentheim sandstone, no visible rock fabric of any kind is obvious and yet a clear tAMS fabric is evident. This illustrates the usefulness of the method, as many rock types do not contain a visual indication of their principal anisotropy.

Seismic velocity anisotropy is probably the most common method of measuring anisotropy reported in the literature. The scale of investigation varies widely from deep level marine seismic (Sheriff and Geldart, 1995), to shallow reflection and refraction surveys (Palmer, 1986). However, on the very small scale of laboratory experimental investigation (of the order of cm) seismic pulses of far higher frequency have to be used than in the field. The advantage of this is that a higher resolution is achieved due to the smaller wavelength. This is the opposite situation to the field scale scenario, where a low frequency is required in order to achieve sufficient penetration and power into the target geology. In the laboratory, the pulse transmission technique (Birch, 1960; King, 1966) is by far the most common experimental method, which uses a *transducer* to convert an electrical signal into a mechanical pulse. Wave velocity may then be calculated from the time-of-flight of the received signals, and the sample dimensions (Benson et al., 2003; 2004; Wendt et al., 2003). This procedure will be briefly reviewed in Chapters 2 and 3. Classically, velocity anisotropy has often been studied in 2-D, using cylindrical core samples (Jones and Meredith, 1998; Louis et al., 2003). More recently, 3-D approaches have become possible through the complex procedure of machining spherical samples (Durrast et al., 2002) which helps to further minimise the issues associated with heterogeneity. Due to the difficulty in preparing such samples, the work presented in this thesis uses cylindrical cores together with a method of 'velocity levelling' between different samples prepared in an orthogonal arrangement. After this treatment, the velocities may be regarded as being made on a single sample (Louis et al, 2003; Benson et al., 2003). This procedure is detailed in Chapter 3.

Permeability is a key petrophysical parameter, and is influenced by a wide number of factors such as the material bulk porosity, the number and distribution of microcracks embedded within it, and the void space geometry and connectivity. Permeability is also important economically, as hydrocarbon reservoirs and aquifers require at least some permeability in order to be viable, even if the bulk porosity is high overall. This issue is becoming very important in mature hydrocarbon fields such as the Northern North Sea, in which previously uneconomic compartmentalised oil pockets exist. In addition, permeability anisotropy is important, especially within rock exhibiting a high degree of bedding or fabric alignment, such as in shales. A rock with a high level of permeability

anisotropy means that the permeability varies greatly depending upon the measurement (flow) direction. A considerable number of methods exist for permeability measurement. Ideally, a measurement technique which mimics the steady flow through rock should be employed, as this scenario is the most likely to occur in nature. However, such a method is inherently difficult in practice due to the engineering control issues involved. Therefore, early techniques used a number of analytical and interpretive methods in order to avoid these technological difficulties. These methods are summarised in Chapter 2.

Electrical resistivity of fluid saturated rock is another commonly made rock physical measurement, especially in borehole logging work due to its ease of measurement as drilling progresses. Electrical resistivity is useful as it provides a bulk measure of the insulating properties of the saturated rock, which are indicative of the conductivity contrast between pore fluid and the matrix. Often, rock matrix possesses a very high resistivity, with pore fluid possessing a far lower resistivity (Clint, 1999). Hence the overall measurement of the resistivity is related to the degree of connectivity, porosity, and tortuosity in the rock. Tortuosity is related to the degree of connectivity between pore space, and how tortuous the conduction path is around the solid matrix of the rock. Obviously, porosity is a key parameter sought in many applications, thus a relation between the porosity and electrical conductivity is highly desirable and has been determined empirically (Archie, 1942). However, electrical conductivity can be influenced by other factors found in rock, such as interference between clean sands and lithologies that possess a natural charge, including clay minerals and conducting minerals (Glover et al., 1994; 1996).

Previous rock types studied

Sedimentary rocks (sandstone and limestone)

Of all rock types, sandstone has had arguably the most investigation, due to its widespread abundance and the economic importance of this rock type in the hydrocarbon and water industries. Early work included investigations using Indiana limestone (Gupta, 1973), Bedford limestone and Boise sandstone (Toksoz et al., 1976). Later, the latter author investigated the Berea, Navajo, and Boise sandstones and also Spergen limestone (Toksoz et al., 1979). Berea and Boise sandstones in particular have been thoroughly investigated by many investigators including King (1966), Tosaya and Nur (1982), Christensen and Wang (1985), Prasad et al. (1997), and the much cited work of Lo et al. (1986). Other sandstones studied include the famous Fontainebleau sandstone (Bourbie and Zinszner, 1985) and Michigan sandstone (Prasad et al., 1997). Many of these authors concentrated on the (then recent) method of elastic wave velocity variation with confining pressure, stress or porosity (Bourbie and Zinszner, 1985), and it was not until later that anisotropy was specifically investigated. Anisotropy work often concentrated on rock with obvious layering such as shale (see later). However, a small number of important studies on sandstones and limestones have also been conducted. These include research on Berea sandstone (Lo et al., 1986; Sayers et al., 1990), and the study by Sammonds et al. (1989), who investigated the effect of deviatoric stresses upon the anisotropy of Darley Dale sandstone. More recently, studies using Bentheim sandstone and Crab

Orchard sandstone (Jones and Meredith, 1998; Benson et al., 2003; Louis et al., 2003) have shown that anisotropic fabrics may exist in rocks even if no obvious visible fabric is evident, such as that seen in shale. Solnhofen limestone (Baud et al., 2000) has also been studied due to its interesting properties, notably a very low porosity of just 3%, in experimental studies on deformation and mechanical anisotropy. In summary, these workers noted ultrasonic P-wave anisotropies in the range from 0% (i.e. isotropic) to as high as 20%, and that increasing hydrostatic confining pressure leads to an increase in the P-wave and S-wave velocity of the rock. In addition, the trend of this velocity increase is highly dependent upon the type of porosity present in the sample (e.g. equant pore or thin microcracks).

In an attempt to address this issue, Rathore et al. (1995) investigated a synthetic sandstone constructed from fused glass beads. Numerous foil discs were embedded within this matrix in order to simulate 'penny-shaped' cracks of known dimensions. The metal inclusions were then chemically leached from the glass beads using acid, leaving 'penny-shaped' voids. This synthetic sandstone was then used to make numerous P-wave and S-wave velocity measurements, which could them be used to verify and test models which use velocity information to predict crack density, alignment, and dimensions; these parameters being precisely known in this work. Obviously, this is not normally the case.

Sedimentary rocks (shale)

This rock type has also been thoroughly investigated due to its economic importance and widespread abundance, as it is estimated that approximately 75% of sedimentary rock is composed of shale. However, a major problem often encountered with shale is that, due to its friable nature, the sample is best retrieved and kept at pressure. Failure to do this may result in the core separating and becoming unrepresentative of the true situation in the Earth (Vernik and Liu, 1997; Jones and Meredith, 1998). Despite this, shale has been intensively studied with early work being carried out by Haskell (1941); subsequently continued by McDonal et al. (1958) and Bless and Ahrens (1977) who investigated the Pierre shale. More recent studies have dealt with cores cut at depth from boreholes, such as Hornby (1998), who describes experiments made upon the Kimmeridge clay shale from the North Sea, and Vernik and Nur (1992) who describe the anisotropy of mature hydrocarbon source rocks (Mississippian-Devonian shale) from producing reservoirs. Most authors agree that the intrinsic anisotropy of shale is due to the aligned clay minerals that constitute a high proportion of the rock (Vernik, 1997; Lo et al., 1986). These aligned clay minerals may produce seismic anisotropy in excess of 38%, which was observed in Chattanooga shale by Johnston and Christensen (1995). Clay particle alignment has been further verified by using X-ray diffraction techniques to constrain the preferred orientation of these clay minerals (Johnston and Christensen, 1995). Modeling the anisotropy response has also been a key focus of previous research (Sayers, 1994; 1999; Hornby et al., 1994). In all of these investigations, the shale anisotropy is noticeably higher than for sandstones, with a typical minimum of 20%, and maximum values as high as 38%. This is attributed both to the alignment of the clay platelets, and also the sedimentary layering itself.

When investigating the dependence of velocity with pressure, a similar trend is seen as for sandstone with velocity increasing with pressure. However, for this rock type, the velocity anisotropy decreases rapidly to 0% at confining pressures of ~100 MPa and above (Lo et al., 1986; Jones and Meredith, 1998).

Metamorphic rocks

Compared with sedimentary and igneous types, fewer studies are available for metamorphic rock anisotropy. In cases where such work has been done, the focus has more often been the lattice preferred anisotropy dependence upon pressure and temperature (Christensen, 1965; Kern, 1992), rather than its permeability. Carrara marble is a notable exception (Paterson, 1978; Peacock et al., 1994), having been used extensively over the years due to its easily deformable nature. In the early history of experimental rock physics this was an important consideration, as the systems of the time lacked the hydraulic and mechanical power necessary for the deformation and shear of 'hard' rocks. In general, metamorphic rock types contain a wider variety and concentration of minerals than, say, sandstones and therefore past studies often deal with the investigation of mineral orientation and composition (Christensen, 1965) and its effect on velocity anisotropy. Due to the makeup of the rocks, these studies are valuable, especially when made on single crystals as the resulting anisotropy is likely to be dominated by intrinsic related effects such as lattice preferred orientation and crystal lattice anisotropy. A small number of more recent studies have looked once again at this important rock category, such as the studies of Four mile Gneiss by Gottschalk et al. (1990) and Rawling et al. (2002), who investigated the mechanical properties of the rock at high stress using tri-axial ($\sigma_1=\sigma_2>\sigma_3$) deformation. In general, metamorphic rocks also exhibit high values of seismic anisotropy, of up to 32% in the case of amphibole (Christensen, 1965). Similar anisotropy values were obtained in the other studies, with the general trend of increasing ultrasonic velocity with pressure again seen.

Igneous rocks

Many types of igneous rock have been studied in the past, in particular Basalt and Granite. Although less important economically, granite has application in the geothermal power industry, and understanding the seismic anisotropy of basalt is a key factor to the application of field seismic data in monitoring activity on volcanic edifices. Many investigations deal with the determination of the elastic anisotropy measured from ultrasonic velocities, such as work on Chelmsford Granite from the Fletcher quarry in the USA (Lo et al., 1986; Sano et al., 1992). Other granites studied include Oshima and Barre granites (Sano et al., 1992) and Troy granite (Toksoz et al., 1976). Temperature effects upon mechanical strength and shear fracture have also been investigated (Odedra et al., 2001) who used Tsukuba granite from Japan. Takidani granite, also from Japan, exhibits velocity anisotropy of ~10% and is particularly interesting in that the larger scale jointed structure of this rock is reflected in the microscopic P-wave anisotropy variation (Kano and Tsuchiya, 2002). Westerly granite has also been widely used, especially to the investigation of permeability measurement (Brace et al., 1968). Early work on basalt includes a hornblende basalt from Chaffee

County, Colorado, San Marcos Gabbro and Bytownite Gabbro (Hughes and Maurette, 1957). More recent applications are highly interdisciplinary, investigating the relationship between thermal stress effects in the field and the associated seismic and permeability changes (Vinciguerra et al., 2004); this is fundamental in mitigating volcanic hazard, as water often plays a substantial part in the eruptive cycle of volcanoes. In the case of the granites studied, high values of anisotropy were common, ranging from 10% to 20% (P-wave), with significant velocity dependence upon pressure as a result of the highly micro-cracked rock microstructure. In contrast, many of the basalts studied exhibit lower anisotropy due to a more random alignment of their embedded microcracks (Vinciguerra et al., 2004).

Models and relations for geophysical data estimation

A large number of models has been proposed as aids to the interpretation and prediction of geophysical data. Such relations can be particularly useful when some 'parameter' of the rock may be easily measured but is ultimately not the final measurement sought. In such cases, a model may be used to estimate the desired quantity from the parameter measured. Two classic examples are the inference of permeability from porosity, or of porosity from electrical conductivity. Thus, models are potentially an extremely useful tool in modern geophysics and rock physics. However, in this study I focus on the experimental aspects of rock physics and geophysics, investigating many inter-related geophysical parameters during contemporaneous measurement and evaluation. Applying some of the models to the systematic and comprehensive datasets in this study will thus permit the test and verification of some models, as I have experimentally measured both the model input (such as pressure, porosity, and density), and the model output (such as velocity and permeability).

However, not all of the numerous geophysical models now available are appropriate to this study, and what follows is a brief summary of some selected models. In cases where the model is inappropriate, some key reasons are given. For this exercise, it is helpful to 'group' models into families, depending upon their type and operation. In the list below, the following convention is used. A 'tick' beside the model name is used if the model is eventually used in this work, and a 'cross' is used if the model is not, for example: ✓*Used,* ✗*Not-Used.* For those models which are used, a more detailed description of their theory and operation is given in Chapter 6.

Empirical/heuristic velocity models and simplified velocity anisotropy (phenomenological) models

✓***Eberhart-Phillips:*** This model was developed using the extremely large dataset of Han et al. (1986), which contains data from 80 well-consolidated sandstones from the Gulf of Mexico. These samples have accurately known porosities from 3 to 30%, clay contents from 0 to 55%, and elastic wave velocities (P-wave and S-wave). Eberhart-Phillips et al. (1989) used a multivariate analysis to derive an expression which relates the pressure dependence, porosity and clay content of the seismic wave velocity for the rocks in Hans' dataset. In the work presented here, clay content is not a variable. However, this model is still very useful as its constants may be grouped to form a more

basic type of the model. This is then used to fit the laboratory data, including pressure dependence (see Chapter 6).

*'**Thomsen's weak elastic anisotropy***: Thomsen's weak anisotropy model (Thomsen, 1986) is a simplification of full elastic anisotropy (see Chapter 2 and Chapter 6). Briefly, by fitting the azimuthal velocity data to this model it is possible to evaluate the degree of transverse isotropy in the sample (Mavko et al., 1998). In addition, the model allows a simple form of the bulk anisotropy parameters to be visualised for both P-wave and S-wave.

*'**Critical porosity models***: These models (Raymer et al., 1980; Nur et al., 1991; 1995; Mavko et al., 1998) all hypothesise that at some critical porosity, a rock no longer possesses the mechanical strength to remain consolidated. This porosity marks the boundary between the rock being supported by mechanical effects, and that of a suspension of rock grains 'supported' in a fluid. However, as this occurs only for rocks of very high porosity (approximately 40% for sandstones, and approximately 6% for 'cracked' 'hard' rocks), then this class of model is not appropriate to this work as the rocks in this study all possess far lower porosities in their respective classes than their critical value. A similar model related to this class is that of Krief et al. (1990), which models the V_p (or Biot co-efficient) for use as a lithology indicator, and likewise investigates high porosity rock up to 40%.

*'**Tosaya***: This model, introduced by Tosaya and Nur (1982), fits an empirical relation to a set of shaley sandstones, expressing velocity (P-wave and S-wave) in terms of porosity and clay content. This model is not used in this study, as the clay content of the rocks in this work is not precisely known and, more importantly, the model is limited to effective pressures of less than 40MPa (Mavko et al., 1998), far lower than the maximum pressure reached in this study (90MPa).

*'**Wyllie time average***: This heuristic relation was introduced by Wyllie et al. (1956, 1958), as a result of measurements upon a number of rock types and minerals, including anhydrite, calcite, dolomite, quartz, and slate. It expresses the slowness (=1/velocity) through the rock as a whole in terms of the volume weighted slownesses of the propagating wave through the individual components of the rock, including the pore space itself. However, this model suffers from a number of known deficiencies and assumptions (Mavko et al., 1998). These are that the rock is: (1) isotropic, (2), is a clean sandstone, and (3), the effect of intergranular cracks is not important. Therefore a minimum pressure of ~30MPa is required in order to ensure that the majority of crack-like pore spaces are closed. For these reasons, this model is not used in this study.

Effective medium (inclusion) velocity models

The general principle of these models is that an initial framework is taken with a known bulk modulus and shear modulus (a solid rock matrix of quartz, say). Porosity 'inclusions' are then added, which may be of any shape desired, until the porosity required has been achieved. In terms of the elastic moduli, the inclusions alter the overall properties of the solid in a mathematically predictable way, which is then used to build up the new 'effective' medium properties, including velocity. Each of the three groups of models listed below does the mathematics in a slightly different way.

'Hudson's model and the 'Kuster-Toksoz model: These models are similar in their operation, and both are used in this study (see Chapter 6 for detail). Hudson's model (Hudson, 1980, 1981; Peacock et al., 1994; Hudson et al., 2001) uses second order wave scattering theory of a mean wave field in order to compute the 1st order and 2nd order corrections due to 'cracks', as compared to an initial, uncracked isotropic elastic matrix. These cracks may be aligned or randomly orientated. The model is thus able to predict the influence of an aligned crack set upon azimuthal elastic velocity measurements, such as those made in this study. The Kuster and Toksoz (1974) model considers an elastic wave as it approaches and is scattered by an assemblage of pores in an initial unmodified host matrix of moduli (K_m, μ_m). In principle, by comparing the amplitude of the resultant scattered wave with the amplitude of a wave scattered as a result of encountering a single, spherical, inclusion with an effective modulus (K^*_{KT} and μ^*_{KT}) then permits the derivation of expressions which relate the effective moduli to the inclusion density.

'Kachanovs' model, the *Self-Consistent model and the 'Differential Effective Medium model: These three models build up a modified or effective rock modulus due to the inclusion of porosity into an initial, unmodified, host medium with known elastic properties. To do this, the models assume that an existing, dilute concentration of inclusions is already present. This concentration is then extended in order to obtain the required properties (i.e. porosity). A good review and explanation of the way in which these models work can be found in Zimmerman (1991) and Kachanov (1994). The Kachanov model (Kachanov, 1980; Sayers and Kachanov, 1995) introduces a crack density tensor due to an aligned crack set, and calculates the associated compliances using a continuum or boundary element method. These compliances are then inverted in order to evaluate the elastic wave velocities. This theory has been used in past work to predict the changing crack density with effective pressure (Schubnel and Guéguen, 2003), and the method is adopted in this work in a similar fashion. The self-consistent approach of Hill (1965) and Budiansky (1965) works through the introduction of a finite volume of porosity $\Delta\phi$ into an initial host material. The material is treated in such way so that the medium effectively has the pore embedded already. Zimmerman (1991) combines strain-energy, crack geometry and crack density relations to derive expressions which describe the evolution of the modified elastic modulus with crack density. The differential effective medium is similar to the self-consistent method in some respects. However, unlike the self-consistent method, the increments in porosity are injected as infinitesimal porosity additions. A pair of differential equations are produced (Zimmerman, 1991), which again describe the evolution of the modified elastic modulus with crack density.

Mixing models – *Voight-Reuss-Hill and *Hashin-Shtrikman bounds: The models of Voight-Reuss-Hill (Reuss, 1929; Hill, 1952) and Hashin-Shtrikman (Hashin and Shtrikman, 1963) are based upon the application of upper and lower 'bounds' to the data. Both models essentially 'mix' the moduli of the constituent mineral phases in the rock in proportion to their abundance in order to derive the maximum and minimum extent of the overall rock moduli (the bounds). As such, one of their more common uses is in application to very high pressure, deep level, mineral mixing problems where the rock composition changes. Neither of these models is used in this study. This is chiefly

because in the work described in this thesis, I am not dealing with rocks in which a mixture of different minerals is being considered as the first order effect upon elastic wave velocity.

Permeability models

All three of the following models are used in this study, and are fully explained in Chapter 2 and Chapter 6. Because permeability is so dependent upon the pore fabric connectivity, which is highly complex, it is very important to match the specific rock type with a specific model. Briefly, highly porous rocks favour the lattice Boltzmann gas model, and highly cracked rocks work well with the statistical approach of Guéguen and Dienes (1989). However, as most rocks contains pore fabrics which are essentially either a mixture of these two extremes, the percolation (or hydraulic radius approach) seems to work well in many cases (Guéguen and Palciauskas, 1994; Mavko et al., 1998).

- ***Statistical – Lattice Boltzmann gas***: This model approximates the pore fluid as a 'gas' of imaginary particles. These particles obey well defined collision rules (equivalent to the Navier-Stokes equation) whenever they encounter the solid matrix representing the rock fabric (Keehm et al., 2001). These models are best suited to high porosity rock due to collision assumptions surrounding the Navier-Stokes equations, and the finite particle size. In this study, the model is applied to the high porosity sandstone.
- ***Capillary/percolation – Guéguen and Dienes***: The statistical approach of Guéguen and Dienes (1989) uses a network of 'penny-shaped' cracks embedded in an impermeable host medium. Using statistical physics together with a connectivity probability factor, the model then calculates the equivalent effective area (and hence permeability), based upon the fluid movement through the network of linked cracks. In this study, the model is applied to the low porosity, cracked granite.
- ***Hydraulic radius – Kozeny-Carman***: This was the first permeability model which attempted to theoretically derive an expression linking bulk porosity to permeability. The Kozeny-Carman relation (Carman, 1961; Scheidegger, 1974; Guéguen and Palciauskas, 1994) estimates the permeability based upon the simplified key parameters of bulk porosity, internal surface area (which is represented by a sphere), and an idealised pore/crack fabric geometry representing cylindrical pipes or 'penny-shaped' cracks (Brace et al., 1968). In this study, the model is applied to a low porosity, cemented sandstone, as this rock is the most likely to have such a network of pipes due to its burial history and abundant cement, as compared to the other two rocks investigated. In addition, I include the critical porosity modification of Mavko and Nur (1997) which introduces a porosity below which no fluid flow is possible.

Electrical conductivity models

Electrical conductivity is another commonly measured property during geophysical surveying, in particular shallow seismic and borehole logging. It has also been investigated in the laboratory (Clint, 1999). Due to the constrains of time, electrical conductivity was not measured in this study. The key model and reference for electrical conductivity is Archie's law.

Archie's law (Empirical): This simple law uses the formation factor of the rock, which is given by $F=R/R_w$; where R is the resistivity of the fully saturated rock, and R_w is the resistivity of the pore fluid. Archie (1942) then related the formation factor 'F' to porosity 'ϕ' by the empirical relation: $F=a\phi^{-m}$, where a is a constant and 'm' is sometimes called the cementation exponent (Mavko et al., 1998), which varies with different rock types.

1.5 THESIS OUTLINE

This thesis describes a detailed experimental study investigating the complex relationships between porosity, void space anisotropy, elastic wave velocity anisotropy, and permeability anisotropy in porous rock, and their dependencies upon simulated burial conditions to 4km equivalent depth in the Earth's crust. The comprehensive experimental dataset is used to test a number of models which attempt to predict the parameters measured experimentally from other measured petrophysical data.

The thesis is divided into three broad sections, (1) introductory and background material, (2) experimental equipment and methods, and (3) acquisition and discussion of experimental data and modelling. These three general areas are split into a total of nine chapters. Chapter one introduces the problem and outlines the need for experimental work. In Chapter 2, I outline some basic theory and general techniques used in modern experimental geophysics, and referred to several times in the thesis. Chapter 3 describes, in detail, the development of the experimental equipment and the methods. Chapter 4 details the acquisition of experimental data at room pressure conditions. Chapter 5 expands the experimental investigation, taking into account the results from Chapter 4, to elevated hydrostatic pressure conditions, in which the rock porosity, permeability, and elastic wave velocity are measured contemporaneously to 90 MPa effective pressure. Chapter 6 uses this well constrained data in application to a number of models, including the Eberhart-Phillips relation, Thomsen and Hudson models, the Kachanov model, and the Lattice-Boltzmann and Kozeny-Carman methods. Chapter 7 discusses the experimental data and modeling results, and Chapter 8 draws a number of conclusions. Finally, Chapter 9 investigates a number of future avenues for research based on the findings of this study.

2 THEORY AND TECHNIQUES IN EXPERIMENTAL GEOPHYSICS

2.1 POROUS MEDIA AND POROSITY

2.1.1 PORE FABRIC EVOLUTION

At the simple end of the spectrum, a basic sedimentary rock, and its pore structure, can be visualised as forming when individual grains of material fall and settle under gravity, either within air (aeolian) or water (fluvial) environments to eventually form a layer of sediment (Leeder, 1982; Guéguen and Palciauskas, 1994). Contact between the grains forms the initial matrix, with the intergranular space forming the initial porosity. In addition, the direction of fluid flow (air or water) influences the deposition of the grains, with the long axis of the grains tending to align along the flow direction. This has direct consequence to the shape and alignment of the evolving pore fabric (figure 2-1). At this stage, the friction between grains balances the gravitational force, until deeper burial conditions act to reduce the initial porosity through compaction and diagenesis.

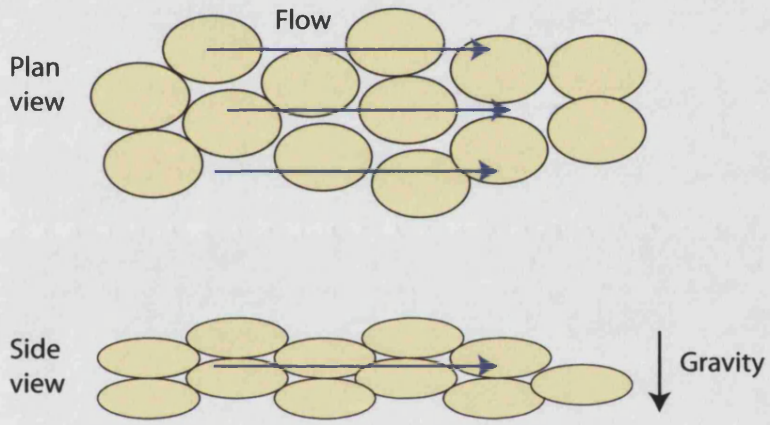

Figure 2-1. Schematic illustration of void space for grains of principle dimensions a≈b<c. Top figure illustrates the plan view of the grains in a fluvial environment, and the low illustration shows the side view.

Other, more complex, types of pore fabric may be generated through the larger scale physical aspects of the Earth environment, such as magma solidification, anisotropic stress fields and thermal stressing. These processes may result in the formation of a type of pore fabric referred to as 'crack' porosity, and may occur both at grain or mineral crystal boundaries, or as a fracture propagating through the grains themselves. To take the example of an aligned stress field, it has been shown experimentally (Paterson, 1978) that anisotropic stresses will generate 'penny-shaped' cracks, where the crack dimensions obey the general relationship a≈b>>c. Such cracks form with their long axes sub-parallel to the maximum principal stress direction, σ_1, and with crack normals aligned parallel to σ_3, where $\sigma_1>\sigma_2>\sigma_3$.

2.1.2 QUANTIFYING PORE FABRIC: MERCURY INJECTION POROSIMETRY

Porosity and connected porosity may be regarded, certainly in this investigation, as one of the most important components of a porous medium. A number of methods have been developed to investigate porosity, not only in terms of its bulk magnitude but also the relation between fractional porosity filled as a function of pore throat diameter (figure 2-2). By far the most common method is mercury injection porosimetry, which has an extensive literature. Good reviews can be found in Dullien (1979) and Modry et al. (1972). The basic principle is as follows. A small rock sample is placed in a bath of mercury, which is then pressurised, forcing the liquid into the void space through the pore necks of radius 'R'. As mercury is a 'non-wetting' fluid (Dullien, 1979), no liquid will enter the pore space until the capillary pressure, governed by the radius 'R' is exceeded. By monitoring the intruded volume of the mercury as a function of the applied pressure, and applying this to capillary pressure theory, the proportion of porosity as a function of pore throat radius can be determined (Guéguen and Palciauskas, 1994).

Figure 2-2. Pore throat diameter in relation to rock grains and void spaces

For a capillary of radius 'R', the capillary pressure required for a fluid of surface tension γ and contact angle θ (which is a constant for any given fluid) to enter is given by:

$$P_{cap} = \frac{2\gamma\cos\theta}{R} \qquad \textit{Equation 2-1}$$

where: P_{cap} is the capillary pressure.

The volume fraction of mercury entering the pore space is defined as the saturation $dS=d\psi_p/\psi_p$, where ψ_p is the pore volume. If this expression is equated to some, as yet unknown, function of pore volume fraction F(R)dR containing entry radii in the range R→R+dR:

$$dS = \frac{d\psi_p}{\psi_p} = -F(R)dR$$

From equation 2-1, it is seen that P_{cap} is inversely proportional to R, so that $dP_{cap}/P_{cap} = -dR/R$ (Guéguen and Palciauskas, 1994). Re-arranging for dR and substituting the resulting expression into the equation above thus gives a relationship for the saturation dS in terms of the pore volume fraction function F(R) and capillary pressure P_{cap}: $dS = F(R)R\frac{dP_{cap}}{P_{cap}}$. Finally, substituting equation 2-1 directly for P_{cap} and re-arranging for F(R) gives:

$$dS = \frac{F(R)R^2}{2\gamma\cos\theta} dP_{cap} \quad \Rightarrow$$

$$F(R) = \frac{dS}{dP_{cap}} \frac{2\gamma\cos\theta}{R^2} \qquad \textit{Equation 2-2}$$

This allows the fractional pore space to be evaluated as a function of the applied pore pressure using an imbibing liquid, assuming that it is both 'non-wetting' and incompressible. The definition of a non-wetting fluid (Guéguen and Palciauskas, 1994) is that of a liquid which has a contact angle greater than 90°, a condition which is satisfied for mercury for which γ=140° (in air). This condition means that the liquid does not imbibe spontaneously, and therefore no mercury will enter the void space of a porous object when place in a bath of the liquid. As mercury is essentially incompressible, any pressure applied to the mercury will be transferred through the liquid and can be directly equated to the capillary pressure of the pore necks which that fraction of mercury is being forced into (equation 2-2); thus permitting pore neck size distribution as a function of injected mercury volume to be investigated.

An example from the literature is shown in figure 2-3 below. This example is of a relatively pure sandstone (Nugget) of total porosity 17%. As the mercury is pressurised, the liquid is forced into more of the rock porosity (shown as a fraction of the total). The effective radius invaded decreases as the pressure increases, as a higher pressure is required to imbibe smaller pore throat radii as the experiment progresses. In this example, the largest pore throats possess a diameter of ~50 μm, with little change occurring below radii of ~0.1 μm. The break in slope of the relationship indicates that a peak pore throat population at about ~10 μm radius exists in this rock.

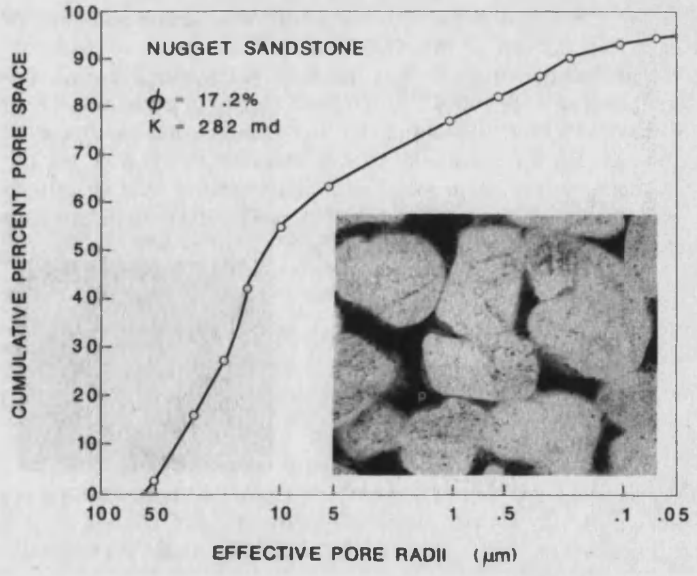

Figure 2-3. Mercury porosimetry curve for Nugget sandstone showing the increase in cumulative porosity with effective pore radius, which is related to the injection pressure as discussed in the text. Taken from Guéguen and Palciauskas (1994) from an original publication by Pittman (1984)

2.2 SOME FUNDAMENTALS OF ROCK PHYSICS

2.2.1 ANISOTROPIC STRESSES

Hooke's law is defined via: $\sigma = C\varepsilon$, where σ is stress, C is the elastic constant and ε is strain. Developing this relation further it can be seen that these fundamental parameters act in 3-D, giving rise to most rocks being anisotropic, with a purely isotropic material is a special case of anisotropy rather than vice-versa (e.g. Guéguen and Palciauskas, 1994; Mavko et al., 1998). Hooke's law in three dimensions can be written as:

$$\sigma_{ij} = C_{ijkl}\varepsilon_{kl} \qquad \textit{Equation 2-3}$$

Where the parameter C_{ijkl} is the elastic stiffness tensor. However, due to the symmetry of the stresses and strains, this equation may be simplified considerably, as noted by Mavko et al. (1998):

$$C_{ijkl} = C_{jikl} = C_{ijlk} = C_{jilk} \quad \text{and} \quad C_{ijkl} = C_{klij}$$

Another simplification may also be utilised, in which some of the repeated indices are replaced with a single subscript through the following convention; C_{ijkl} becomes $C_{I(J)}$ with the following values used for I(J) (Guéguen and Palciauskas, 1994; Mavko et al., 1998):

ij(kl)	I(J)
11	1
22	2
33	3
23, 32	4
13, 31	5
12, 21	6

Likewise, the strain tensor can be re-written using the same notation. In this case a factor of two is introduced for the off-diagonal terms due to symmetry:

$$\varepsilon_1 = \varepsilon_{11},\ \varepsilon_2 = \varepsilon_{22},\ \varepsilon_3 = \varepsilon_{33},\ \varepsilon_4 = 2\varepsilon_{23},\ \varepsilon_5 = 2\varepsilon_{31},\ \varepsilon_6 = 2\varepsilon_{12}$$

Finally giving the full anisotropic form of Hooke's law, with 21 independent elastic constants, is:

$$\begin{bmatrix}\sigma_{11}\\ \sigma_{22}\\ \sigma_{33}\\ \sigma_{44}\\ \sigma_{55}\\ \sigma_{66}\end{bmatrix} = \begin{bmatrix}C_{11} & C_{12} & C_{13} & C_{14} & C_{15} & C_{16}\\ & C_{22} & C_{23} & C_{24} & C_{25} & C_{26}\\ & & C_{33} & C_{34} & C_{35} & C_{36}\\ & & & C_{44} & C_{45} & C_{46}\\ & & & & C_{55} & C_{56}\\ & & & & & C_{66}\end{bmatrix}\begin{bmatrix}\varepsilon_{11}\\ \varepsilon_{22}\\ \varepsilon_{33}\\ 2\varepsilon_{23}\\ 2\varepsilon_{31}\\ 2\varepsilon_{12}\end{bmatrix}$$

Different forms of anisotropic behaviour can be described using this general form of Hooke's law, together with simplifications. Such simplifications depend upon the symmetry of the anisotropy desired. For example, for the special case of an isotropic rock, the full stiffness tensor above is simplified to give two independent elastic constants, which are related to the bulk modulus K and shear modulus μ via:

$$[1] \quad - \quad C_{11} = C_{22} = C_{33} = K+4/3\mu$$

$$[2] \quad - \quad C_{44} = C_{55} = C_{66} = \mu$$

Where: $C_{12} = C_{13} = C_{23} = C_{11}-2C_{44}$. *All other stiffness components are zero.*

The simplest form of anisotropy is planar transverse isotropy, which will be discussed at some length in Chapters 5, 6 and 7. This type of anisotropy occurs when a material is isotropic in one plane only, showing different physical properties only when they are measured at some angle to this plane. This situation is also the most intuitive, as many sedimentary rocks form due to depositional layering as outlined in section 2.1.1. Such sedimentary layering often *appears* transversely isotropic. A good example of such a rock is shale (Hornby et al., 1994; Johnston and Christensen, 1995; Hornby, 1998), as noted in section 1.4 previously. By adopting appropriate symmetry simplifications (Mavko et al., 1998), planar transverse isotropy will theoretically reduce the 21 independent elastic constants to five:

$$[1] \quad - \quad C_{11}=C_{22},$$

$$[2] \quad - \quad C_{33},$$

$$[3] \quad - \quad C_{44}=C_{55},$$

$$[4] \quad - \quad C_{66},$$

$$[5] \quad - \quad C_{13}=C_{23},$$

Where: $C_{12}=C_{11}-2C_{66}$. *All other stiffness matrix components are zero.*

2.2.2 HYDROSTATIC CONFINING PRESSURE AND 'EFFECTIVE' PRESSURE

Hydrostatic confining pressure is defined as when the stresses normal to a surface are equal ($\sigma_{xx}=\sigma_{yy}=\sigma_{zz}$), and therefore no shear stresses are present. However, when dealing with saturated porous media this is not the only stress (or pressure) which has to be considered. Within the pore fabric of the rock itself another stress field exists, which is commonly provided by the existence of pressurised pore fluids. Strictly, therefore, when dealing with experimental and modelling studies which involve saturated porous media, two pressures have to be defined in all cases and conditions. These are the hydrostatic confining pressure P_c acting over the rock externally, and the internal pore fluid pressure P_p, which acts in the opposite manner internally (figure 2-4).

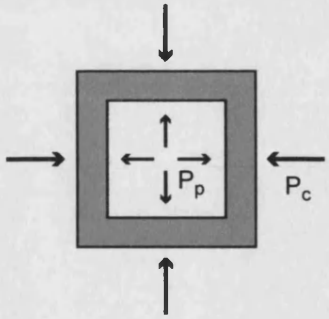

Figure 2-4. The principle of effective pressure. P_p denotes the pore pressure, and P_c denotes the hydrostatic confining pressure

Given the situation described, it is intuitive to visualise the situation whereby the pressure inside the rock frame acts so as to counteract the external confining pressure, yielding an 'effective' pressure which the rock fabric experiences. The concept of such an 'effective' pressure, P_e, was first introduced by Terzaghi (1936) who noted that such an approach often leads to an oversimplification of the stresses involved if the basic form of the approach was used (differential pressure), $P_d = P_c - P_c$. In this case, the effective pressure does note take into account forces such as the stresses between rock grains, which also provide resistance to the pore pressure in addition to the confining pressure. To account for these additional forces, Terzaghi (1936) introduced the constant α_p, and defined the effective stress as:

$$P_e = P_c - \alpha_p P_p \qquad \textit{Equation 2-4}$$

Where P_e is the effective pressure, P_c is the hydrostatic confining pressure and P_p is the pore pressure (Bernabe, 1987). The constant α_p accounts for other forces generally by reducing the contribution of the pore fluid in counteracting the confining pressure, as the mechanical strength of the rock matrix itself will act in addition to the pore pressure. However, as this is difficult to measure, the constant α_p often simply provides an experimental (heuristic) solution. It should also be noted that α_p is not the same for every rock type when considering different measurements; permeability and P-wave velocity, for example.

Alternatively, Zimmerman (1991) provides the expression: $\alpha_p = 1 - K_{bulk}/K_{grain}$, where K_{bulk} is the bulk modulus of the rock sample and K_{grain} is the modulus of the matrix mineral grains. Using these concepts it can be seen that for the 'perfect' rock in which the matrix provides no resistance to pressure, that α_p=1. This is known as 'simple effective pressure', and is often used in experimental studies without verification. However, numerous authors have shown in both experimental and modelling work that simple effective pressure (with α_p=1) is often incorrect, and have demonstrated values of α_p less than 1 (Boitnott and Scholz, 1990), to values as high as 5 (Al-Wardy and Zimmerman, 2004) for rocks containing high proportions of clay minerals. Deviations from α_p=1 are

principally due to factors such as partial saturation of the pore fabric, compressibility of the pore fluid, and the mechanical strength of the matrix noted earlier. Despite these limitations, simple effective pressure (with α_p=1) is used throughout this work. However, this will be experimentally justified in Chapter 5. In addition, as this study only seeks to compare the **change** in measured data with **changes** in effective pressure, and that P_e is increased by changing the confining pressure only, then these measured data should still be valid whether α_p=1 or not.

2.3 ANISOTROPY OF MAGNETIC SUSCEPTIBILITY (AMS)

2.3.1 OVERVIEW: MAGNETISM

Considering the three key forms of magnetism (diamagnetism, paramagnetism and ferromagnetism), a better understanding of how materials respond when exposed to an external magnetising field may be visualised with reference to figure 2-5 below. For an external magnetising field 'H', a solid takes on an internal magnetisation 'J'. However, this relationship is highly dependent upon the type of magnetic behaviour exhibited by the solid in question. For diamagnetic materials (fig. 2-5[A]), the induced magnetisation linearly opposes the applied field, and disappears completely on removal of the H field. The slope of the line defines the susceptibility of the material, and in essence describes the degree to which the material is magnetised in the presence on the external field. Paramagnetic materials (fig. 2-5[B]) show a similar behaviour. However, this time the induced magnetisation is aligned in the same direction as the magnetising field. Finally, for ferromagnetic materials (fig. 2-5[C]), we see that the susceptibility is not a constant, and that for these materials, magnetisation does not reduce to zero on removal of the external field. In such materials, the adjacent magnetic moments interact strongly (as previously noted) and the induced magnetisation can be orders of magnitude stronger that for diamagnetism of paramagnetism. The induced magnetisation saturates (J_s) at high external field strengths, and the solid retains a magnetism on removal of the field.

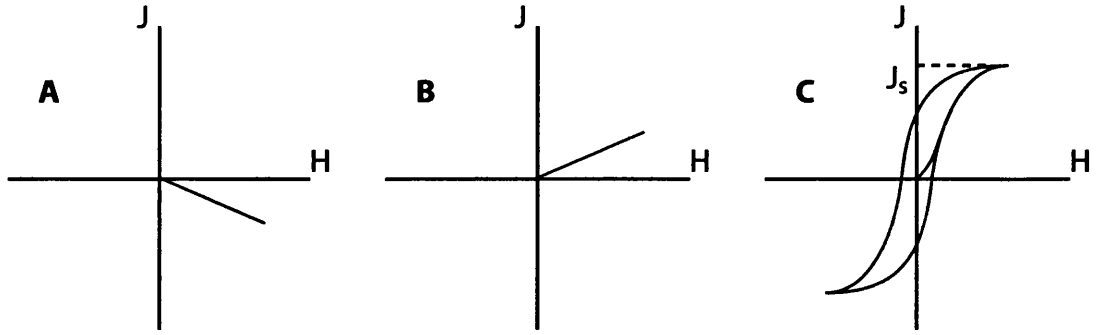

Figure 2-5. Quantitative illustration of how the magnetisation J varies with a magnetising field H for (A) a diamagnetic material, (B) paramagnetic material and (C) a ferromagnetic material. Js denotes the saturation magnetisation

Superparamagnetism may also be defined. Materials with such properties are described as magnetically 'soft', because they rapidly gain and loose their magnetism as external fields are applied or removed. Consider a solid particle of material of volume V. The bond energy of the internal coupled magnetic moments is equal to k_BV, where k_B is the Boltzman constant. However, with decreasing particle size k_BV will also decrease until the thermal energy k_BT exceeds the magnetic moment energy barrier, and break the bond. When this occurs, the internal moments align independently of the particle to any applied magnetising fields. If a field is now applied to the material, it will therefore tend to align the large (super)moment of the particle as a whole. However, the k_BT energy will seek to oppose this, as it does in the phenomenon of paramagnetism, hence the term superparamagnetism. Such materials are commonly colloidal suspensions of sub-micron sized magnetically permeable particles. As these particles are free to rotate within the larger body of the suspension, then they leave no net magnetisation. However, on the application of even quite a small magnetic field the atomic magnetic moments will rapidly align, thus giving rise to high values of susceptibility for the suspension as a whole, even though the individual moment of a particle is small by comparison.

2.3.2 ANISOTROPY OF MAGNETIC SUSCEPTIBILTY

In section 2.3.1, the term magnetic susceptibility was introduced. This is now formally defined in the following relations (Tarling and Hrouda, 1993):

$$M_i = K_\chi H_i, \quad and: \quad J_i = \chi H_i \qquad \textit{Equation 2-5}$$

Where M_i is the magnetization per unit volume, K_χ is volume susceptibility, χ is mass susceptibility, H_i is the magnetising field, and J_i is the magnetisation per unit mass. Susceptibility is a measure of the ability of a material to acquire a magnetisation in the presence of an H field.

However, when dealing with induced magnetisations and susceptibility, an important effect needs to be introduced at this point, known as the **demagnetisation factor**. The demagnetising effect occurs on application of the initial H field. The initial magnetising field induces magnetic moments in the sample which have the effect of opposing the applied field as a function of the magnetisation, M. Mathematically, the opposing field is given by Collinson (1983) as:

$$H_j^{opp} = H - NM$$
$$H_j^{opp} = H - NK_\chi H_j \qquad j=x,y,z$$

where: H_j^{opp} is the opposing field

H_j is the applied field

M is magnetisation

N is the demagnetising factor

On the sample level, this effect will therefore act to reduce the value of susceptibility measured. However, this phenomenon can be minimised through using small H fields, and by using specific sample geometries. Theoretically, the perfect sample shape is a sphere, which has a demagnetizing factor, N, of 1/3 (Parasnis, 1997). As spherical samples are extremely difficult to prepare in the laboratory, cylindrical core samples are still generally used in practice. However, by using the specific dimensions of sample length to diameter ratio of ~0.84, the demagnetisation factor is effectively the same as a sphere (Porath et al., 1966; Tarling and Hrouda, 1993).

Following on from the definition of susceptibility, I now define the anisotropy of magnetic susceptibility (AMS) as the variation of magnetic susceptibility with direction of measurement. Like other forms of anisotropy, it can arise in many different ways (Bhathal, 1971). The two chief mechanisms are (a), the inherent anisotropy residing in the mineral itself; and (b), an aligned rock fabric or grain matrix, such as the alignment of platy grains during rock deposition and formation as noted in section 2.1.1. Equation 2-5 can thus be re-written as functions describing the relation between magnetism and the applied field in each of three orthogonal axes: x, y and z:

$$M_x = K_{xx}H_x + K_{xy}H_y + K_{xz}H_z$$
$$M_y = K_{yx}H_x + K_{yy}H_y + K_{yz}H_z$$
$$M_z = K_{zx}H_x + K_{zy}H_y + K_{zz}H_z$$

OR:

$$\underline{\underline{M}} = K_{ij}\underline{\underline{H}}_j \qquad \textit{Equation 2-6}$$

Where K_{ij} is the susceptibility tensor of the sample. Equation 2-6 can be simplified by considering the equivalent relations $K_{xy}=K_{yx}$, $K_{yz}=K_{zy}$ and $K_{zx}=K_{xz}$ (Collinson, 1983), which reduces K_{ij} to a symmetrical tensor containing six independent constants. A convenient and constructive way to describe this tensor is by considering the susceptibility as an ellipsoid with principal axes x_1, x_2 and x_3, and with susceptibility along these axes of K_1, K_2, K_3 respectively, representing the maximum, intermediate and minimum values (figure 2-6):

$$\frac{x_1^2}{K_1^2} + \frac{x_2^2}{K_2^2} + \frac{x_3^2}{K_3^2} = 1$$

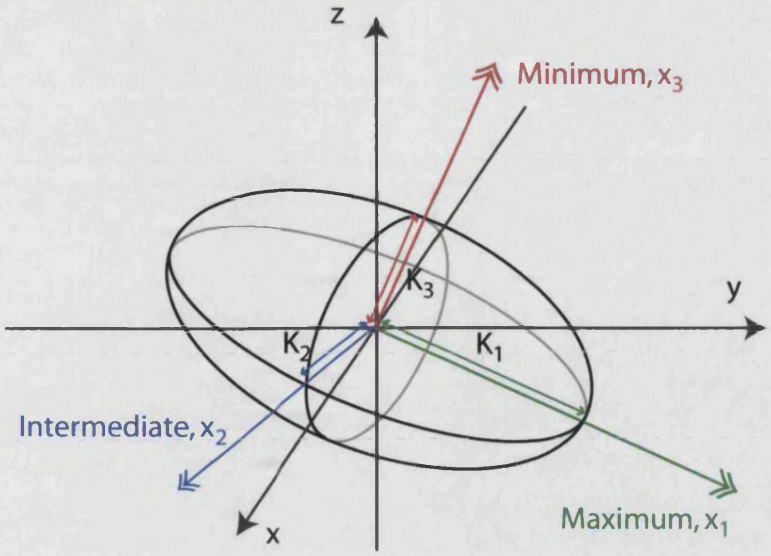

Figure 2-6. Graphical representation of a susceptibility ellipsoid of principal susceptibility axis lengths $K_1>K_2>K_3$, and principal direction axes X_1, X_2 and X_3, relative to a general co-ordinate frame Oxyz. After Tarling and Hrouda, 1993

The ellipsoid in figure 2-6 above can be used to define and visualise anisotropy parameters which together describe the relative size and shape of the susceptibility ellipsoid (Hrouda, 1981, 1982; Tarling and Hrouda, 1993). In equation 2-7 below, lineation is defined as the fractional ratio between the maximum and intermediate susceptibility values, and foliation represents the fractional ratio between the intermediate and minimum susceptibility values. Comparison of these two ratios allows the 'oblateness' or 'prolateness' of the ellipsoid to be evaluated (Flinn, 1962). The bulk anisotropy factor describes the maximum deviation of the ellipsoid from a sphere, using the ratio between maximum and minimum susceptibility values:

$$P_1 = K_{max}/K_{int} = Lineation, L$$
$$P_2 = K_{max}/K_{min} = Anisotropy, P \qquad \textit{Equation 2-7}$$
$$P_3 = K_{int}/K_{min} = Foliation, F$$

Note, however, that this definition of anisotropy is not the same as that introduced for elastic wave velocities (see Chapter 4), which is defined as the ratio of the velocity difference to the velocity mean, rather than the ratio of maximum to minimum susceptibility values, as above. This is a historical difference.

2.3.3 Determining AMS in practice

Standard methods of measuring AMS have been reported in the literature (e.g. Collinson, 1983; Tarling and Hrouda, 1993). The specific instrumentation and method used in this study is discussed in Chapter 3, however, it is useful before then to introduce some key principles. Two standard sample size and shapes are commonly used in the field of AMS work, either a cube of side

~2.1cm or a cylinder of 2.5cm diameter and approximately 2.2cm length. The latter shape is used in this study (figure 2-7). Ideally, as noted previously, a spherical sample would be best due to the internal demagnetising effect. However, as these cylinder dimensions closely approximate the demagnetising coefficient of a sphere (i.e. with a length to diameter ratio of ~0.84), they have become a common sample shape used in palaeomagnetic work. In addition, this sample shape is easy to prepare both in the field and in the laboratory.

To evaluate AMS, measurements of susceptibility in least six different orientations are required in 3-D, as an ellipsoidal surface possess six degrees of freedom. However, in this study 15 directional susceptibility measurements are made, the additional data allowing statistical checks on the data quality to be made. An ellipsoid is fitted to the data using a least squares method, from which the direction and length of the principal axes can be extracted (Jelinek, 1977; 1978).

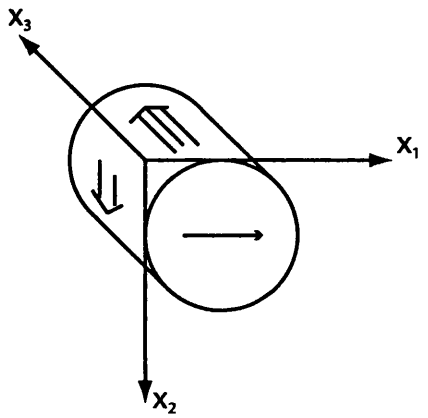

Figure 2-7. The standard AMS sample co-ordinate frame used in this study

AMS has traditionally been used to measure the magnetic anisotropy of a dry rock matrix (Tarling and Hrouda, 1993). Used in this manner it can be used to measure sedimentary grain fabrics, and hence infer the associated depositional processes and palaeocurrent directions (Stacey, 1960; Uyeda et al., 1963; Bhathal, 1971). Other directional rock fabrics associated with mechanisms as diverse as lava solidification, intrusions, and strained/deformed rock structures may also be easily and quickly measured with the AMS technique. However, as this study is interested in the void space anisotropy, another approach must be taken.

2.3.3.1 VOID SPACE AMS MEASUREMENT USING A MAGNETIC FERRO-FLUID

Magnetic ferrofluid is a suspension of magnetically permeable particles (commonly magnetite) in a carrier fluid. This carrier fluid can be any liquid, but often a light mineral oil is employed. These types of fluids are very different to other types of magnetic fluids such as 'clutch fluid', which solidifies in the presence of a magnetic field; a colloidal ferrofluid is able to retain its flowing properties even in very intense magnetic fields. Modern commercial ferrofluid (figure 2-8) contains up to 10^{23} particles per litre (i.e. a 1 molar concentration) of ~10nm diameter, and possesses

a very high susceptibility of ~1.9 SI. Although the particles are small enough that thermal agitation (Brownian motion) keeps them in suspension, over a long period of time gravitational and magnetic forces can cause ferrofluids to settle out. It is possible to put a quantitative value on these suspension stability requirements by considering the energy required per particle, revealing that gravity is more of a threat to a stored bottle of ferrofluid than is the Earth's magnetic field (Rosensweig, 1985). An even greater threat to the stability of the fluid is from agglomeration due to electrostatic Van-der-Waals forces between particles. Coating the particles in a thin antistatic monolayer to keep the magnetite particles apart essentially eliminates this problem. These innovations allow modern ferrofluids to possess a shelf-life of up to 10 years in some cases (George Thompson, Ferrotec (UK) Ltd., per. Comm., 2003).

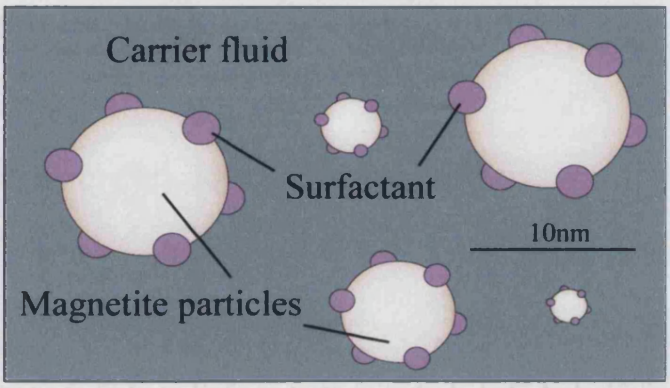

Figure 2-8. Schematic view of a ferrofluid, with magnetically permeability particles of magnetite in this example.

Magnetite particles used in magnetic ferrofluids are generally prepared in one of two ways, either through the grinding of micron sized particles over a long time period (approximately 1000 hours) or through direct chemical precipitation. Both methods produce particles with a mean size of ~10nm. Two types of superparamagnetism exist that are applicable to ferrofluids. If an applied H field is changed, the induced magnetisation of the ferrofluid 'relaxes' to take on a new value. It is this time, termed the relaxation time, which defines the two distinct types of superparamagnetism observed. The first mechanism occurs by physical particle rotation within the ferrofluid and is termed the Brownian rotational diffusion time, τ_B. This has its origin in thermodynamics and, for a particle volume V and fluid viscosity η_0, is given by Rosensweig (1985) as:

$$\tau_B = \frac{3V\eta_0}{k_b T}$$

where: τ_B is the Brownian rotational diffusion time

k_b is Boltzman's constant

T is the absolute temperature

The second type of relaxation occurs by the rotation of the magnetic vector within the particle itself and is termed the Neel mechanism. In each magnetic particle, two possible orientations for the magnetic moment exist, which are 180° apart along the 'easy' axis of magnetisation (Collinson, 1983). Changing the spin vector from one orientation to the other requires that an energy barrier 'αV' must be overcome, where α is the anisotropy constant. For $\alpha V<k_bT$, the thermal energy is sufficient for this process to occur and the Neel relaxation time is given by (Rosensweig, 1985):

$$\tau_N = \frac{1}{f_0}\exp\left(\frac{\alpha V}{k_b T}\right)$$

If $\tau_N<\tau_B$ then the relaxation occurs by the Neel mechanism, and the material possesses intrinsic superparamagnetism. However, if $\tau_B<\tau_N$, the relaxation occurs by thermal (Brownian) motion and the ferrofluid possesses extrinsic superparamagnetism. Values for τ_B can be easily calculated by considering a ferrofluid that is allowed to dry so that the particles are no longer free to rotate, leaving only the Neel mechanism effective (intrinsic paramagnetism). For 10nm magnetite particles at 25°C a typical value for τ_B is $7.6\text{x}10^{-7}$s, larger than τ_N which is approximately $1\text{x}10^{-7}$s (Rosensweig, 1985). We are therefore dealing predominantly with intrinsic superparamagnetism for this fluid. This is important as, if the smaller of the two time constants is small compared to the experiment duration, then the ferrofluid can be regarded as paramagnetic. For the experiments in this study, the frequency of investigation used was 875Hz, giving a period of $1.14\text{x}10^{-3}$s, and so this condition is easily satisfied for this particular fluid.

If we now saturate the pore space of rock with this ferrofluid, the pore volume will acquire an 'artificial' susceptibility (figure 2-9). Measurement of the total AMS, which I term tAMS, represents the superposition of the AMS signal from the rock matrix (mAMS) and the ferrofluid filled pore fabric AMS (pAMS), so that tAMS = pAMS + mAMS. For many porous rocks mAMS is several orders of magnitude lower than tAMS, and it can therefore be neglected (Pfleiderer and Halls, 1990, 1994; Benson et al., 2003). This will be discussed in detail in Chapters 4 and 7. In general, however, the ferrofluid AMS technique has several advantages over other methods used to investigate void space anisotropy (such as elastic anisotropy). The greatest advantage is that the full, 3D pore space anisotropy ellipsoid can be quickly and fully determined from measurements on a single core, together with error statistics. In addition, this ellipsoid can be derived with no prior knowledge of the principal anisotropy axes of the rock under test. Note, however, that pAMS measures the anisotropy of the connected pore space that is accessible to the ferrofluid rather than the total porosity. For this reason, past work (Pfleiderer and Halls, 1994; Benson et al. 2003) has concentrated on demonstrating the strong correlation between pAMS and permeability anisotropy, since there is no direct, general relation between permeability and scalar porosity (Rasolofosaon and Zinszner, 2002) but permeability anisotropy is likely to be governed by the geometry and connectivity of the elements that make up the pore space which is well described by pAMS.

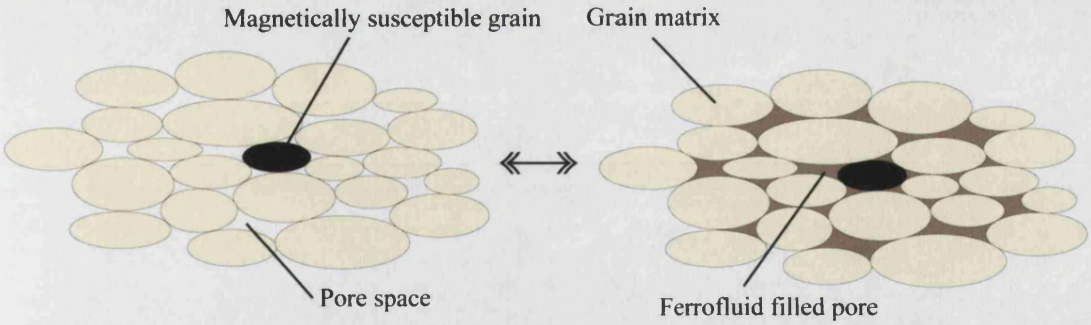

Figure 2-9. Schematic visualisation of a rock pore fabric before and after ferrofluid saturation

2.3.4 EQUIVALENT PORE CONCEPT

The AMS, including the lineation and foliation factors, does not directly measure the physical pore fabric. However, by considering the theoretical demagnetisation of the general ellipsoid, it is possible to relate how a physical pore fabric may relate to the magnetic measurement of lineation, foliation and the magnetic bulk anisotropy. This is done by evaluating the demagnetisation factors associated with the general ellipsoid in terms of their **physical** principal dimensions (Osborn, 1945), thus allowing a comparison between the average physical pore space geometry, and the resulting magnetic data which can be measured using the AMS method. Dealing with ellipsoids is mathematically complex, but still easier than the alternatives due to the ease with which the ellipsoid can be used to picture the tensor mentioned earlier. This analysis leads to what is known as the *equivalent pore concept* (Hrouda et al., 2000), in which an average physical pore space shape and alignment is modelled which will produce the same magnetic properties as in the measured specimen. This allows an estimation of the physical pore shape anisotropy to be derived.

The reason for this desire is as follows. The anisotropy factors described up to this point (L, F and P – equation 2-7), are simply the ratios of principal susceptibilities. This, however, is not exactly the same as the actual physical pore fabric dimensions, but is merely the magnetic response to a magnetically susceptible pore fabric. The equivalent pore concept attempts to link the physical void space to the lineation and foliation quantitatively in order to calculate the actual physical dimensions which would produce the measured values of lineation and foliation. Naturally, it might be intuitively expected that the tAMS and the physical pore geometry are a very close match (at least qualitatively), but to argue that the ratios of L & F match the physical ellipsoidal axes of a/b and b/c exactly (where a>b>c) may be premature at this stage.

To do this, consider the shape AMS of an intrinsically isotropic grain or pore (Uyeda 1963; Hrouda et al., 2000):

$$L = \frac{K_1}{K_2} = \frac{(1 + k_i N_2)}{(1 + k_i N_1)}, \quad F = \frac{K_2}{K_3} = \frac{(1 + k_i N_3)}{(1 + k_i N_2)}, \quad P = \frac{K_1}{K_3} = \frac{(1 + k_i N_3)}{(1 + k_i N_1)} \qquad \textit{Equation 2-8}$$

where: subscripts 1, 2 and 3 refer to the principal axes shown in figure 2-6,

$K_1>K_2>K_3$ are the principal susceptibilities,

$N_1>N_2>N_3$ are the demagnetising factors along those axes.

k_i denotes the intrinsic susceptibility, which is defined by $k_i = \kappa_m/(1+N\kappa_m)$, where,

κ_m is the measured ferrofluid susceptibility,

N=1/3 (demagnetising factor of a sphere).

Physically, the intrinsic susceptibility can be visualised as the susceptibility value that would be obtained from measuring a ring of material, i.e. with no demagnetisation factor acting internally to reduce the measured susceptibility as a result of the magnetic dipoles which are set up at the edges of the sample (Collinson, 1983). For ellipsoidal geometries, the demagnetisation factors can be derived exactly as a function the physical principal length axes (a > b > c), and are given by Osborn (1945) as:

$$N_1 = \frac{\cos\varphi\cos\vartheta}{\sin^3\vartheta\sin^2\alpha}\left[F(n,\vartheta) - E(n,\vartheta)\right] \qquad \textit{Equation 2-9}$$

$$N_2 = \frac{\cos\varphi\cos\vartheta}{\sin^3\vartheta\sin^2\alpha\cos^2\alpha}\left[E(n,\vartheta) - \cos^2\alpha F(n,\vartheta) - \frac{\sin^2\alpha\sin\vartheta\cos\vartheta}{\cos\varphi}\right] \qquad \textit{Equation 2-10}$$

$$N_3 = \frac{\cos\varphi\cos\vartheta}{\sin^3\vartheta\cos^2\alpha}\left[\frac{\sin\vartheta\cos\varphi}{\cos\vartheta} - E(n,\vartheta)\right] \qquad \textit{Equation 2-11}$$

where:

$$\cos\vartheta = c/a \qquad (0\le\theta\le\pi/2)$$

$$\cos\varphi = b/a \qquad (0\le\varphi\le\pi/2)$$

$$\sin\alpha = \left\{\frac{1-(b/a)^2}{1-(c/a)^2}\right\}^{\frac{1}{2}} = \frac{\sin\varphi}{\sin\vartheta} = n \qquad (0\le\alpha\le\pi/2)$$

F(n, θ) and E(n, θ) are elliptic integrals of the first and second kind respectively, n is the integral modulus, and θ is the integral amplitude. Unfortunately the elliptical integrals in these expressions mean that they cannot easily be re-arranged for direct substitution into equation 2-8. To address this issue, the approach of Hrouda et al. (2000) is used, in which the values of lineation and foliation are calculated for set, fixed, values of the ratio of physical principal axes (a/b) and (b/c), and used as a 'lookup' chart (figure 2-10) in order to read off approximate values of a/b and b/c of any given set of (L,F).

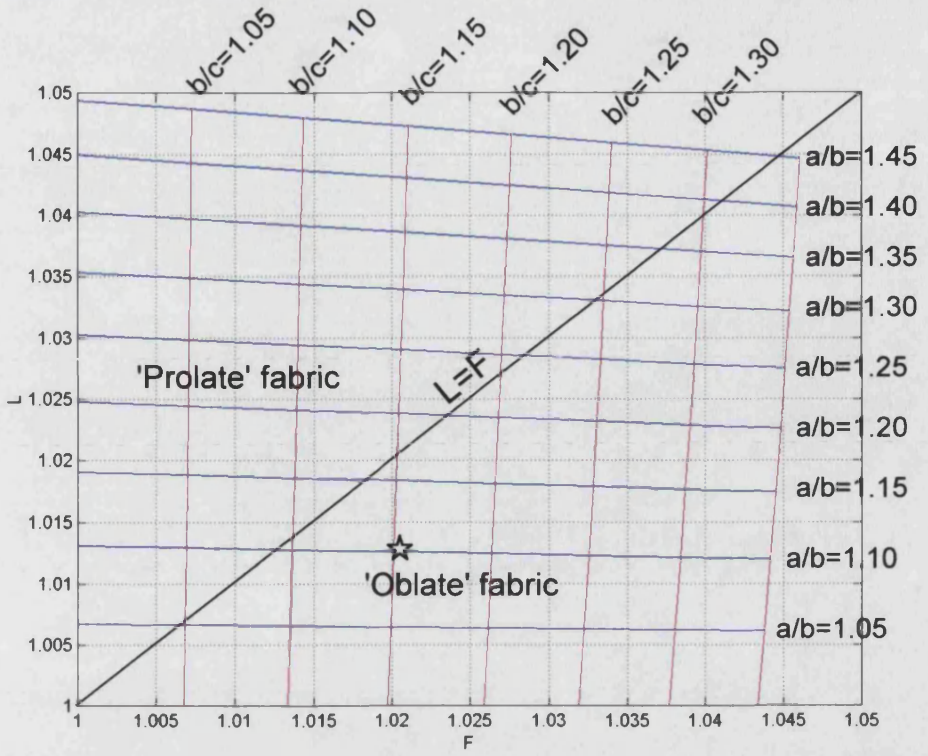

Figure 2-10. Relation between Lineation (L), Foliation (F) and the physical average void space shape defined by principal axes of length a>b>c. In this example, intrinsic susceptibility, K_i = 3.34

By plotting the measured magnetic lineation and foliation from laboratory experiments on the chart above, values for the equivalent average physical pore ellipsoid can be estimated by simply 'reading off' the appropriate figures, and interpolating as necessary. For example, a specimen (marked with a ★) with a value of L,F = (1.013,1.02) has a physical pore space with principal ellipsoid length axis ratios of a/b = 1.1 and b/c = 1.15. The chart is easily re-calculated for any desired range of a/b and b/c in order to obtain the required precision for lineation and foliation.

2.4 ELASTIC VELOCITY

2.4.1 MECHANICAL PULSE GENERATION AND THE PULSE TRANSMISSION TECHNIQUE

In order to measure the elastic wave velocity of a material, a mechanically generated wave is propagated through the material and the time-of-flight over a known distance 'd' is measured. The velocity can then be very simply calculated: velocity=distance/time. Any mechanical means will achieve this aim, and the magnitude of such an event varies enormously; from small scale 'hammer and plate' methods during a seismic refraction survey, to blasting caps and "vibroseis" for land-based seismic reflection surveys, to large airgun arrays for marine seismic methods (e.g. Sheriff and Geldart, 1995). For laboratory measurements, however, the scale of investigation is far smaller, and thus the method for mechanical pulse generation is very different, in terms of both frequency and amplitude.

The standard method for generating mechanical pulses in this context is through the use of a piezoelectric material. These are a unique class of solids which deform rapidly in a predictable manner in response to an applied electric field (figures 2-11 and 2-12). By accurately controlling the input voltage pulse (excitation), the output mechanical pulse can also be precisely controlled (timing, amplitude and frequency). Conversely, by accurately monitoring the charge over the solid with time, the onset of input mechanical signals can be measured, together with analysis of their frequency and amplitude. Piezoelectric materials are therefore ideally suited to the application of input elastic signal generation in laboratory P-wave and S-wave measurement, amongst many other uses such as ultrasonic weld testing and medical imaging.

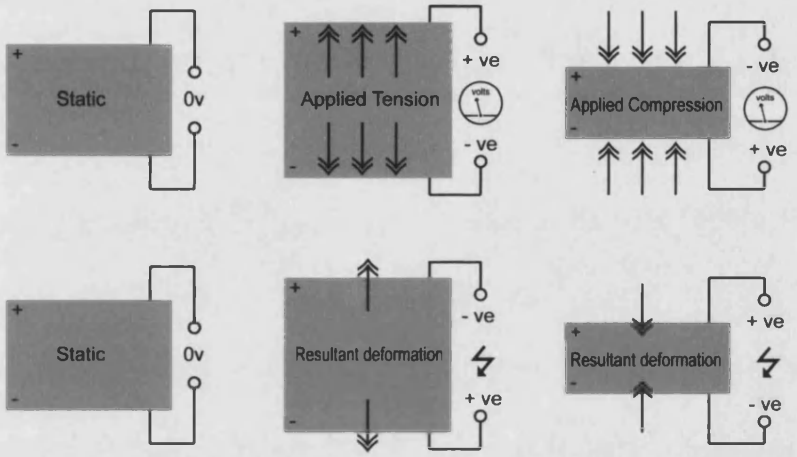

Figure 2-11. The piezoelectric effect for compression (P-wave). When the crystal is mechanically strained (top row), a charge develops over the opposing crystal surfaces – this is the direct piezoelectic effect. The converse piezoelectric effect occurs when charges are directly applied to the crystal sufaces, resulting in mechanical strain (bottom row)

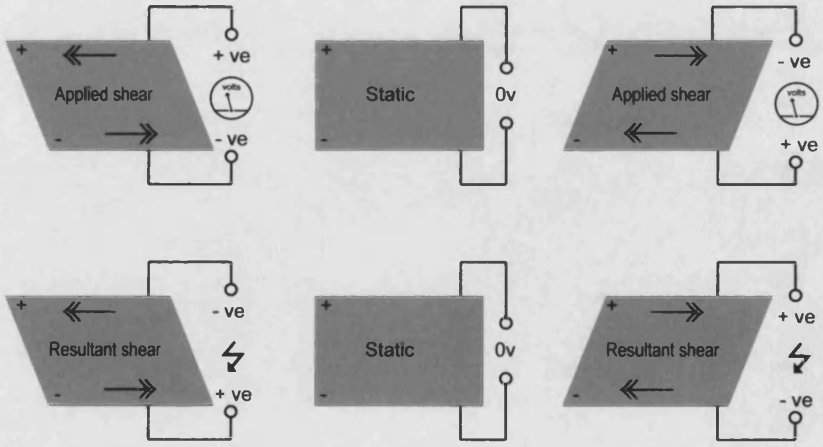

Figure 2-12. The piezoelectric effect for shear mode (S-wave). This time, the direct (top row) and converse (lower row) piezoelectric effect produce a different crystal deformation mode, due to the make-up of the material. Here, the crystal deformation acts to produce a net mechanical moment, as illustrated, resulting in a shearing motion.

A common piezoelectric material is PZT (Lead-Zirconate-Titanate), a synthetic piezoelectric ceramic which is especially useful as it can be formed into many different sizes and shapes. The most commonly used shape is that of a disk (figure 2-13), which is usually plated with gold contacts on each side to act as electrodes. This crystal element is usually bundled into a convenient case in order to protect the delicate crystal element and to make handling more convenient. Such a package is called a transducer (figure 2-14), and additionally includes a number of backing components aimed at damping any uncontrolled oscillations which often result in a 'ringing' appearance to the recorded signal, due to interference and reflections between the crystal faces, and off the packaging itself.

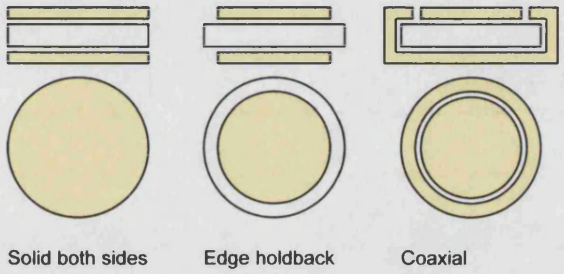

Figure 2-13. Some typical PZT crystal element electrode coatings

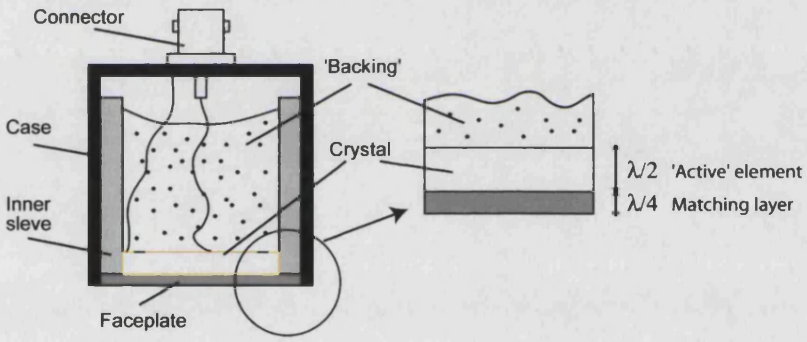

Figure 2-14. Cross section through a typical commercial transducer

Regardless of exactly where the velocity measurement is taking place (whether inside a pressure vessel, on the laboratory bench or in a water tank, for instance), the schematic setup shown in figure 2-15 illustrates the principle of the time-of-flight technique (Birch, 1960). A pulse generator is used to produce electrical pulses of known amplitude and frequency, which are input to the crystal or transducer. The resultant mechanical pulse traverses the sample under test, and is received by a second transducer, which converts the transmitted mechanical pulse back into an electrical signal after a time delay. These signals are first pre-amplified before being displayed and recorded using a digital storage oscilloscope, which also has a direct feed from the signal generator in order to trigger the pulse timing. Low-loss coaxial cable connects the transducers. Finally, a calibration (t_0) measurement is made, by placing the transducers in direct contact (i.e. with no sample present). This allows the measurement of the bare electrical and transducer system, which is then subtracted from the total time with the sample present (equation 2-12).

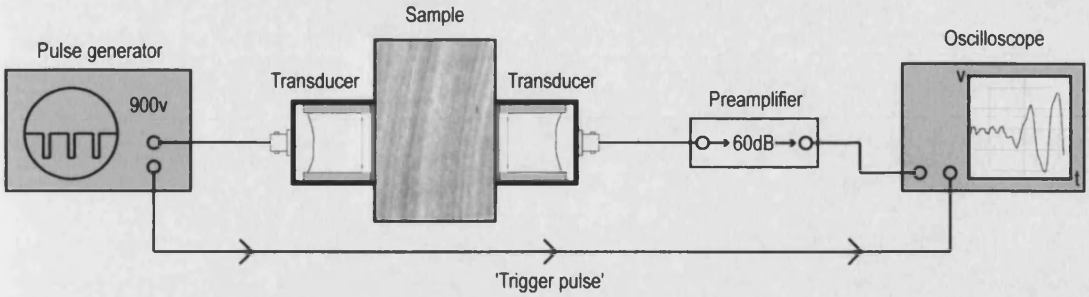

Figure 2-15. *Experimental set-up schematic for the pulse transmission technique.*

$$V = d/(t - t_0) \quad \textit{Equation 2-12}$$

where d is sample diameter

t is the time taken for the 'time of flight' – the recorded pulse via the oscilloscope

t_0 is the time of flight with no sample present

V is the elastic wave velocity.

2.4.2 VELOCITY ANISOTROPY

Velocity anisotropy is determined by measuring the elastic wave velocity (V_p or V_s) as a function of radial azimuth around a core in 2D. This can be extended to 3D by fitting the azimuthal velocity measurements to an ellipsoid in much the same way as introduced for AMS. However, as velocity is closely linked to elasticity, then the use of an ellipsoid to define such anisotropy parameters is strictly an approximation. This is because, in general terms, elastic anisotropy can only be fully described by a fourth rank tensor (equation 2-3); whilst an ellipsoid describes a second rank tensor. The method of applying such an ellipsoidal approximation, and its limitations, will be fully discussed in Chapter 5 and Chapter 7.

2.5 PERMEABILITY

Permeability describes the ability or ease with which fluid can pass through a cracked or porous solid. Numerous methods exist for the measurement of permeability. Ideally, a measurement technique which utilises steady-state-flow should be used, as this is likely to represent the situation found in nature. However, as already noted in Chapter 1, such an approach is inherently difficult due to the engineering control issues which must be addressed in order to make this technique work. Therefore a number of alternative methods have been used in the past in an effort to try and avoid these technological difficulties.

Rather than using a pore liquid, Klinkenberg (1941), used an inert gas as the fluid, which flows through the rock sample pore space under known pressure conditions. However, as gas is

compressible, an extrapolation of the inverse pressure to zero is required in order to simulate an incompressible fluid. In addition, this method is dependent upon a capillary model, and this may produce different results depending on the model chosen.

For very low permeabilities, the pulse decay method of Brace et al. (1968) was developed. Here, permeability is determined by measuring the change in pressure through time at one end of a sample due to the introduction a sharp pressure step or 'pulse' into the other end (Hsieh et al., 1981; Trimmer, 1981). The disadvantage of this method lies in the interpretation of the exponential pressure-decay / time curve which is produced, which requires processing after stable experimental conditions have been achieved. This occurs only after temperature fluctuations have ceased. As such conditions occur only after a number of minutes, this method therefore relies on processing the lowest quality segment of the data.

Alternatively, permeability may be evaluated by introducing a well-controlled 'sinusoidal' pressure fluctuation into one end of the sample under test (Kranz et al., 1990; Fischer, 1992). Here, permeability is calculated from the phase shift in the output pressure sinusoid as a result of encountering the sample, which in essence acts as a filter. The output amplitude data also allows percolation to be evaluated.

The falling head permeameter (e.g. Bear, 1988), uses water to provide a pressure 'head' of an initial, known, height above one end of the sample. Measuring the decrease of the head through time as the water flows through the sample is then used to calculate the permeability. The issue with this method is the non-linear pressure differential – the pressure created by the water head decreases with time.

High performance liquid chromatography (HPLC) pumps have also been used to evaluate permeability (Main et al., 1994), which are specialist devices operating at high pressure and constant flow rate. These pumps are used to force pore water through a rock sample. Measuring the resulting pressure gradient across the sample then allows the evaluation of permeability using Darcy's law. Recently, more complex methods have been developed which measure permeability in 3-D using X-ray tomography (Rasolofosaon and Zinszner, 2002). This method captures X-ray image 'slices' of a saline liquid invasion front as the fluid moves under a pressure gradient through the sample under test.

However, all of these methods suffer from interpretive and processing issues ranging from the compressibility of gas to non-steady state effects, as well as the need for various curve-fitting methods and analysis. Such analytical methods are prone to error but are technologically simple. However, in this work the opposite method is employed (steady-state-flow), which is more technologically challenging but which does not require such a lengthy interpretation to arrive at a result. Importantly, I consider the steady-state-flow method to be more representative of the true

situation in the Earth, in which crustal fluid movement is more likely to be due to a constant (and relatively low) pressure gradient, rather than as a result of pressure pulses or 'forced' fluid movement, except perhaps during rapid tectonic event such as active faulting.

2.5.1 STEADY STATE FLOW METHOD

The theoretical basis for the steady-state-flow method is that of Darcy's law. This can be visualised by considering the fluid volume which crosses perpendicular to a cross-sectional area 'S' per unit area per unit time (figure 2-16). Or, alternatively, a porous material posses a permeability of 1 Darcy if a pressure gradient of 1 atmosphere per cm will produce a flow rate of 1 ml^3/second for a fluid of 0.01 Poise viscosity through a cube having a side length of 1cm (Dullien, 1979; Guéguen and Palciauskas, 1994). A dimensional analysis easily shows that the dimension of permeability is L^2, with the unit of Darcy equal to $0.97x10^{-12}m^2$. A number of limitations must be considered when dealing with Darcy's law, the most important of which is the volume flow rate (flow velocity), which must be low for Darcy's law to be valid. At high volume flow rates the law breaks down, typically for velocities greater than 1 m/s (Guéguen and Palciauskas, 1994). In this regime the flow becomes turbulent (high Reynolds numbers) and ceases to describe a Newtonian fluid.

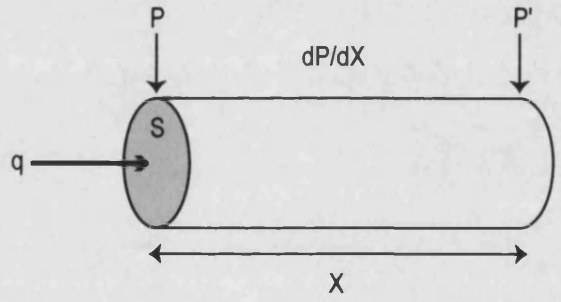

Figure 2-16. Schematic of Darcy's law: elemental sample length X, and area S

Mathematically, the Darcy's law states that (for horizontal flow):

$$q = -\frac{k}{\eta}\frac{dP}{dx} \qquad \textit{Equation 2-13}$$

where: q is the 'Darcy velocity' (volume/(time × area)) of the fluid,
k is the permeability,
η is fluid viscosity (which is constant at a given temperature),
dP/dx is the pressure gradient over the sample length.

To apply this in a laboratory setting as used in this study, a pressure gradient (differential pressure) is measured and controlled over a sample length (Jones and Meredith, 1998). The resulting fluid flow is accurately measured as a function of time, allowing computation of the flow rate (figure 2-17). Importantly, (and unlike other methods) this technique does not rely on curve fitting.

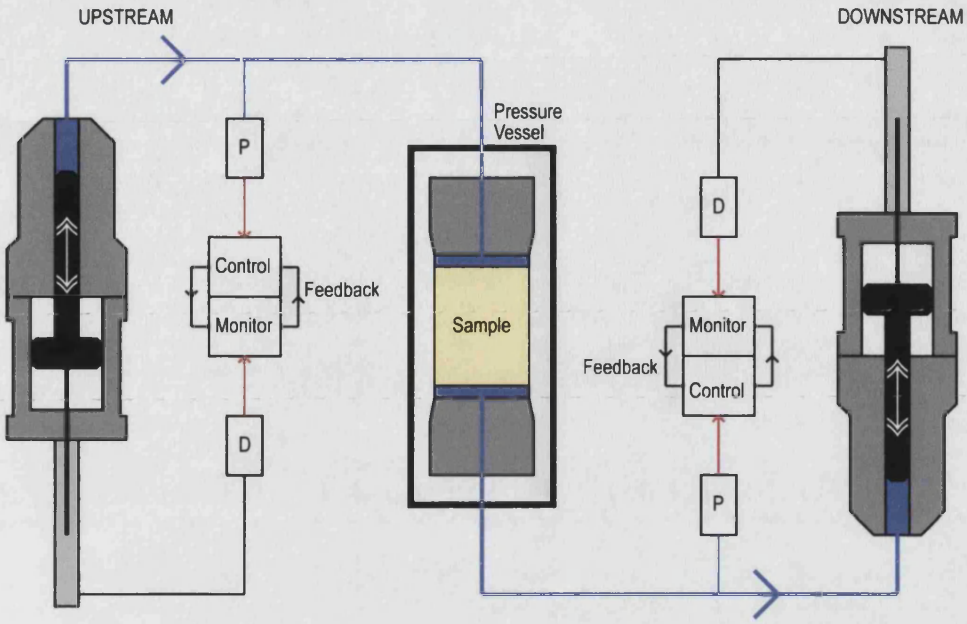

Figure 2-17. Principle of steady state flow, after Jones and Meredith (1998). A sample is held under elevated hydrostatic pressure. Two servo-controlled high pressure fluid intensifiers then apply a controlled, constant pore pressure differential to each end of the sample (P). The resulting fluid flow volume from each intensifier is then measured via the displacement transducers 'D'

Re-arranging equation 2-13 for permeability, k, and substituting (P-P') for the differential pressure, where P is the pressure at one end of the sample, and P' the pressure at the other end, together with sample length X (figure 2-15), we obtain:

$$k = \frac{q\eta}{dP/dX} \approx \frac{q\eta X}{(P - P')}$$

The Darcy fluid velocity, q, is defined as the fluid volume which passes through the section S over time t: $q = \frac{V}{S}$, where V is the volume flow rate (m^3/second). For the (vertical) experimental set-up shown in figure 2-16, a cylindrical sample of length X and diameter d is used, so that the area 'S' can be written as: $S = \pi \frac{d^2}{4}$, giving:

$$k = \frac{V}{(P - P') \pm \rho g h} \frac{4\eta X}{\pi d^2} \qquad \textit{Equation } 2\text{-}14$$

Where 'h' is the height of the sample setup. The gravity term 'ρgh' can be neglected for the permeability values determined is this study.

Finally, this equation can be simplified by using some of the particular experimental conditions and parameters used in this study, in which pressure is measured in MPa, sample dimensions in are expressed in cm, and volume flow rate 'V' is measured in ml/second. The constant for the viscosity of water, η, is 10^{-2} Pa/s. This value is dependent upon temperature. However, as the work is carried out in a temperature controlled laboratory, this is unlikely to have any effect upon the measurements. Integrating these constants into equation 2-14 above gives the following expression for Darcy permeability in m^2:

$$k = \frac{1}{10^6}\frac{dD}{dt}\frac{1}{10^6(P-P')}\frac{4.10^{-2}X}{10^{-2}\pi d^2}$$

$$k = \frac{4}{10^{12}}\frac{X}{\pi d^2}\frac{dD/dt}{(P-P')} \qquad \textit{Equation 2-15}$$

where dD/dt is the measured volume flow rate in cm^3/second, (P-P') is the pressure difference between sample ends in MPa, 'X' and 'd' are the sample length and diameter respectively, in cm.

2.5.2 PERMEABILITY ANISOTROPY

In a manner similar to elastic wave anisotropy, permeability anisotropy may also be defined by considering the individual components of fluid flow. Darcy's law, if separated into three principal components (Rice, 1970; Dullien, 1979; Bernabe, 1992; Rasolofosaon and Zinszner, 2002) and written as a tensor equation, is then:

$$v_i = -\frac{1}{\eta}\left(k_{i1}\frac{\partial P}{\partial x_1} + k_{i2}\frac{\partial P}{\partial x_2} + k_{i3}\frac{\partial P}{\partial x_3}\right) \quad (i=1,2,3)$$

where the indices 1, 2, and 3 represent the x, y and z axes, and the constant k_{ij} forms the elements of the second order permeability tensor, which can also be written:

$$v = -\left(\overline{\overline{k}}/\eta\right)\nabla P,$$

where: $\overline{\overline{k}} = \begin{pmatrix} k_{11} & k_{12} & k_{13} \\ k_{12} & k_{22} & k_{23} \\ k_{13} & k_{23} & k_{33} \end{pmatrix}$

As already introduced, in this investigation the permeability in three orthogonal directions X, Y, Z is directly measured. These data are then used with a simplified permeability anisotropy defined by: $(k_{max}-k_{min})/k_{mean}$, where k_{max} and k_{min} are the experimentally measured maximum and minimum values. Together with the aid of the complimentary and powerful methods of mAMS, pAMS and elastic velocity anisotropy, the difficult and time consuming step of determining the permeability tensor may be neglected. These ideas will be more fully discussed in Chapters 5, 6 and 7.

3 EXPERIMENTAL MATERIALS, METHODS AND EQUIPMENT

In this chapter I describe the materials, specialist experimental equipment, and the methods and techniques used during the course of this study. Although some of the equipment used is commercial, a number of specialist components were designed and developed for the specific use of this project, requiring significant development and testing phases. The largest of these was the development of a steady-state-flow permeameter fitted with integral elastic transducers, allowing the apparatus to measure fluid flow permeability, elastic wave velocity and porosity change contemporaneously to effective pressures of up to 275MPa. A number of important calibrations are also presented, as well as details of experimental accuracy.

3.1 SAMPLE MATERIALS

In order to compare a wide range of differing natural pore fabrics, three different rock types were chosen for the investigation which possess widely contrasting properties in terms of void space. Bentheim sandstone (figure 3-1), Crab Orchard sandstone (figure 3-2), and Takidani granite (figure 3-3) represent virtually the full range of porosity seen in nature. These range from a high porosity, pure quartz sandstone (Bentheim); to a low porosity sandstone (Crab Orchard), containing a visible crossbedding; to a low porosity, fractured, crystalline rock (Takidani). Table 3-1 summarises the key properties and mineralogical components of each of the rock types chosen. These three rock types provide the basis of comparison between the different pore fabric anisotropy techniques described in Chapter 2 of pAMS and elastic wave anisotropy. These different, well characterised pore fabrics will then provide insight into the factors influencing the permeability anisotropy and porosity measurements made at elevated pressures.

3.1.1 BENTHEIM SANDSTONE

Bentheim sandstone (BHS) from the Lower Saxony Basin, north-west Germany, is an off-white sandstone with a porosity of 23.7±0.7% (Klein et al., 2001). Mineralogically, it is a fairly pure quartzite, dominated by predominantly sub-rounded quartz grains approximately 0.25mm in diameter, and cemented by siliceous cement (table 3-1, figure 3-4[A]). The quartz is colourless in plain-polarized light (PPL) and shows low 1st order grey interference colours in cross-polarized light (XPL). Some grains showing undulose extinction. Only minor amounts of "accessory" minerals are present, including variably altered orthoclase feldspars, sparse grains of plagioclase (exhibiting multiple twinning) and microcline (which exhibits cross-hatched twinning). Where present, most of the feldspars have been altered to clay minerals, where they possess a dirty appearance, although some feldspar may be seen which appears colourless in PPL. In XPL, low 1st order grey interference colours are seen, with muscovite mica occurring as elongated flakes which is colourless in PPL but showing high upper 2nd order to 3rd order interference colours in XPL. Zircon is present as very small sub-rounded to rounded grains, appearing colourless with very high relief in PPL and high

birefringence in XPL. Occasional lithic fragments are present, which consist mostly of pure fine sandstones and siltstones. Overall, there is little variation in grain size (other than the tiny Zircons), and grains generally sub-rounded and roughly equigrannular with no preferential alignment discernible in thin-section, with an apparently random orientation of grains.

Figure 3-1. Bentheim sandstone shown in outcrop (taken from Kemper, 1976)

3.1.2 CRAB ORCHARD SANDSTONE

Crab Orchard sandstone (COS) comes from the Cumberland plateau, Tennessee, USA. It is a red, fine-grained, crossbedded fluvial sandstone (figure 3-2). Grains are generally subhedral to sub-rounded, exhibit no preferred alignment (Benson et al., 2003), and have a mean size of approximately 0.25 mm (table 3-1, figure 3-4[B]). Porosity is 4.5%±0.5%. Compositionally the rock is 85% quartz with significant feldspar and some lithics (Benson et al., 2003). A cement of sericitic clay and mica is abundant, and this appears to have destroyed much of the original porosity. Cementation is thought to have occurred early on in diagenesis, as nearly all grains show triple junctions, with few point contacts. The rock is compositionally and texturally mature, with a reasonable degree of compaction. In hand specimen, an obvious millimetre scale bedding is visible to the naked eye. However, the lowest magnification setting of the microscope (x4) is to high for this crossbedding to be clear in thin section analysis. There is definite alignment of mica flakes along this axis (i.e. parallel to the bedding). Some micas also show kinking along the same axis, i.e. they have aligned preferentially with their long axes parallel to the bedding and have then been deformed along that axis, as a likely result of compaction, flow or flocculation (Stearns, 1954).

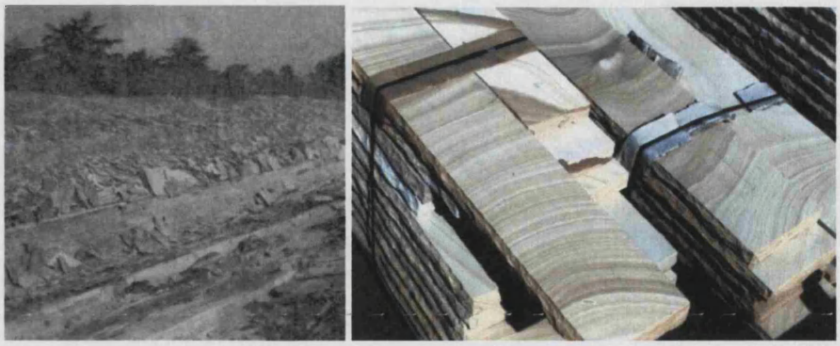

Figure 3-2. Tennessee Crab Orchard sandstone in outcrop (left), and (right) slabs (4.5 inches thick, approx 18 inches wide. (Outcrop photograph taken from Stearns (1954); quarried block image courtesy of Goliath Stone company: http://www.goliathstone.com/Tennessee.htm)

3.1.3 TAKIDANI GRANITE

Takidani granite (TDG) is a coarse grained granodiorite from the Japanese Alps, and comes from what is reportedly one of the youngest exposed plutons in the world at 1.2Ma (Kano and Tsuchiya, 2002). Rock composition is of anhedral, roughly equigrannular, quartz crystals in the range 0.5mm-1mm (Kano and Tsuchiya, 2002; Daniel Howard, per. comm., 2004) (table 3-1, figure 3-4[C]). Some crystals also contain fluid inclusions. As well as plagioclase and orthoclase, both perthites (orthoclase host crystal exsolving blebs or lamellae of plagioclase) and antiperthites (plagioclase host crystal exsolving blebs or lamellae of orthoclase) are present. Plagioclase feldspars show complex zoning (concentric, oscillatory), which is combined with multiple twinning. There is also some evidence of magma mixing. The feldspar crystals are subhedral to euhedral and impart a seriate texture to the rock (i.e. the crystals show a complete range of sizes from <<1mm to ~3mm).

In PPL the hornblende present shows pleochroism from green to brown, with twinning common and visible in both PPL (distinguishable by different rates of pleochroism between the twins) and XPL (distinguishable by different birefringence of the twins). Basal sections show a characteristic 120° intersecting cleavage, and prismatic sections (sections along long axis of the crystal) shows one good cleavage parallel to the long axis. In XPL the crystals show moderate birefringence but this is masked to some extent by the strong body colour. Biotite usually occurs as crystal laths intergrown with crystals of hornblende, forming hornblende-biotite glomerocrysts, typically pale/medium brown in colour – dark brown pleochroism in PPL, and high to very high birefringence in XPL; but as with the hornblende this is masked by the very strong body colour of the biotite. Chlorite occurs primarily as an alteration product of biotites though also as an alteration product of the hornblende. Generally this is colourless in PPL but distinguishable in XPL by anomalous deep "Berlin Blue" colour. Any opaques are generally small and occur as intergranular masses as well as inclusions within the larger crystals of the main minerals. Rutiles are generally small, with a deep red brown colour in PPL – this strong body colour again masks the birefringence in XPL. Apatites occur as small acicular crystals, often within the larger crystals of the main

constituent minerals. In PPL they are colourless but are distinguishable by their high relief, and in XPL they show low birefringence greys, similar to the quartz and feldspars. Zircons generally also occur, as small, colourless, subhedral crystals distinguishable by their very high relief. In XPL they show very high birefringence colours. No preferred orientation of mineral grains (crystals) is visible in thin section, and no porosity is visible of any kind.

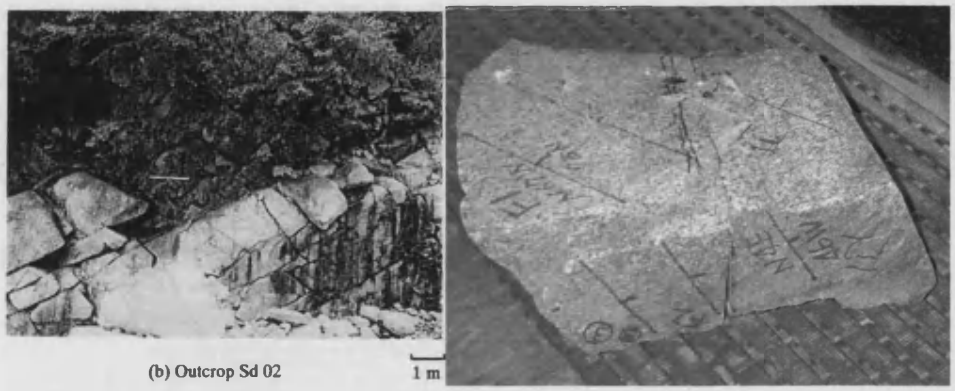

Figure 3-3. Takidani granite shown in outcrop (left). Right - the 'Lozenge' shaped block of Takidani granite used in this study. Field photo taken from Kano and Tsuchiya, 2001

Rock Type	Main mineralogy	Other minerals present	Summary
Bentheim sandstone	Quartz, ~95%	Feldpar~1-2%, mostly orthoclase, but also minor amounts of plagioclase (composition indeterminate) and microcline. Clay minerals (indeterminate), ~1-2% (including altered feldspars), Muscovite mica<<1%, Zircon<<1%, Lithic fragments <1%.	A well-sorted, compositionally and texturally mature, fairly pure quartz-arenite (quartzite)
Crab Orchard sandstone	Quartz, 75-80%	Orthoclase feldspar, variably altered to sericite 10-12%. Lithic grains and polycrystalline quartz, ~1-2%. Clay minerals (Predominantly iron rich clays, also sericite and a small amount of chlorite), ~5%. Muscovite mica ~1-2%, also some phengite mica, overall similar to muscovite but in PPL displays a slight green colour and is slightly but definitely pleochroic. Calcite occurs occasionally as a cement, usually in conjunction with clays~2-3%. Accessories include Zircon.	A fairly mature, compact sub-arkose.
Takidani granite	Quartz, ~30% Feldspar, ~55% Amphibole, ~10% Biotite, ~5-8%	Chlorite (alteration product of Biotite) Opaques (probably Pyrite), Rutile, Apatite, Zircon	A granodiorite

Table 3-1 Summary of rock petrography used in this study

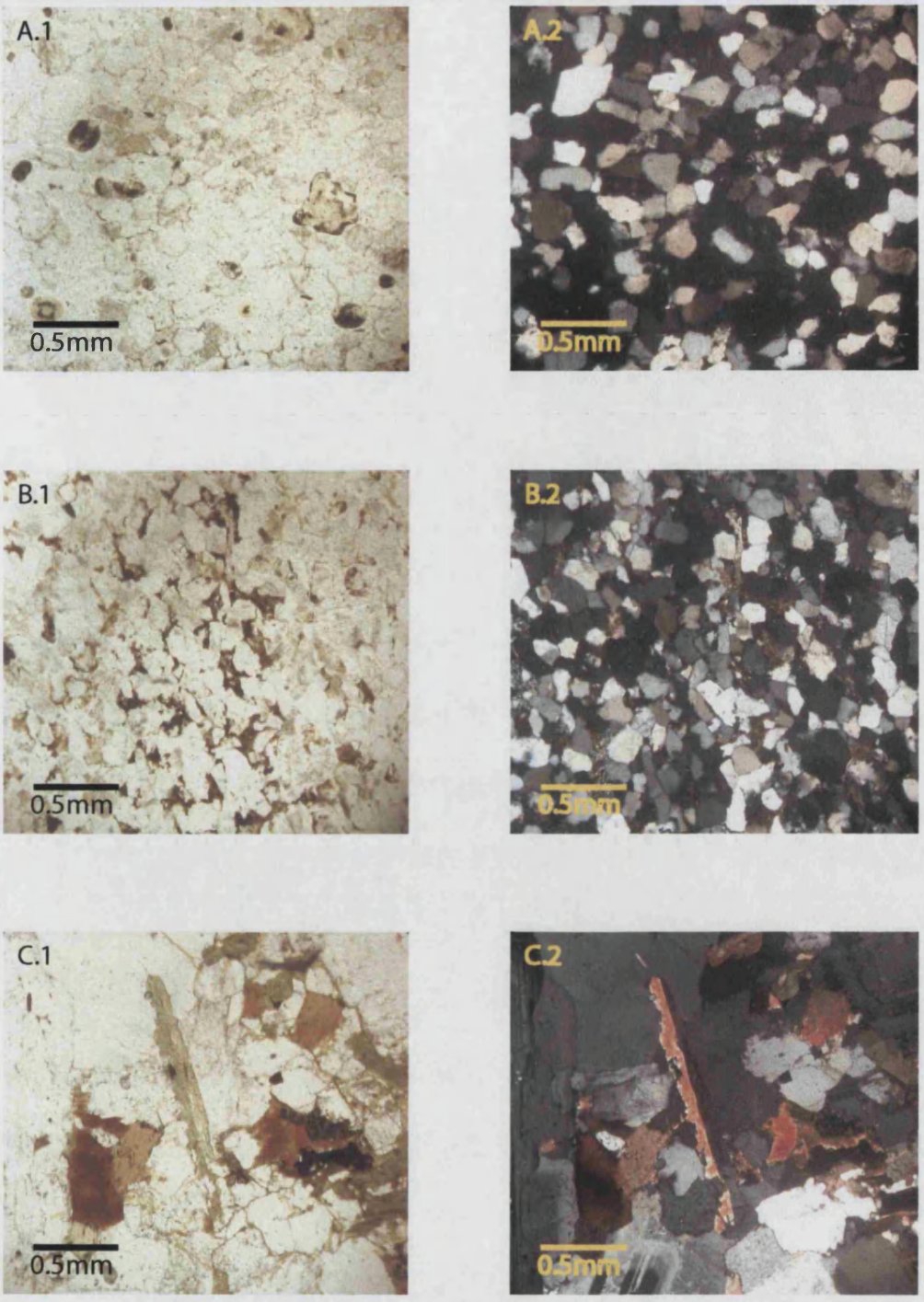

Figure 3-4. Photomicrographs of (A) Bentheim sandstone, (B) Crab Orchard sandstone, and (C) Takidani granite, taken under (1) plain-polarised light and (2) cross-polarised light.

3.1.4 IMAGES OF ROCK MICROSTRUCTURE

A number of independent imaging methods for quantifying pore fabric geometry have been undertaken in order to visually see any obvious pore fabric geometry in a qualitative manner. A range of imaging techniques is available to for this task, ranging from the thin section images seen in figure 3-4 previously, to scanning electron microscopy (SEM) photomicrographs. In the case of thin section analysis, where porosity is often difficult to distinguish, the void space is saturated with blue

epoxy resin to make the void space stand out prominently. However, neither of these methods is able to image large scale microcrack networks easily. To address this issue, a novel method was used, which utilises standard thin sections saturated with an dye that fluoresces under ultraviolet (UV) light. Under a reflected UV light source, any cracks or pore fabric then show up clearly.

3.1.4.1 BENTHEIM SANDSTONE

The two figures below (3-5 and 3-6) show the open and highly porous structure of Bentheim sandstone. In all images, the pore fabric looks identical even with the image taken in different planes relative to a common co-ordinate frame (see section 3.2.1), as indicated. Scanning electron micrographs of freshly broken rock surfaces shows a small amount of clay cement. In thin section, the blue epoxy staining emphasises the porosity, including a small number of intergranular 'cracks'. UV fluorescence sections were not necessary for this rock type.

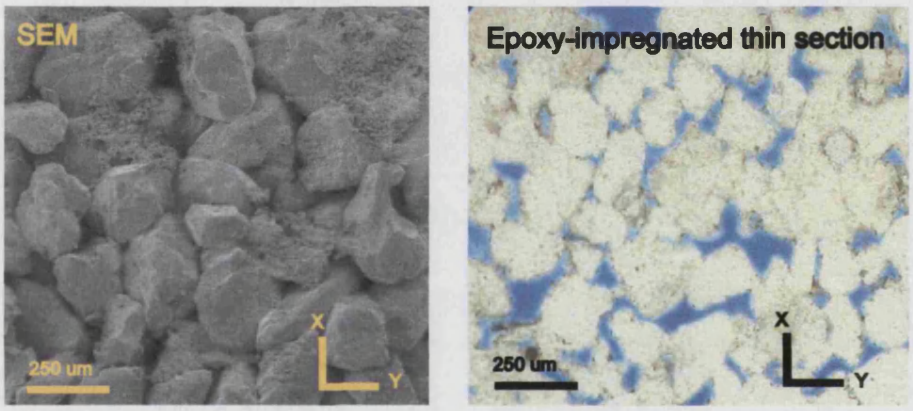

Figure 3-5. Bentheim sandstone matrix detail using scanning electron microscopy (left) and a blue-epoxy stained thin section (right). Both images prominently show the rock's open pore space structure. Image plane parallel to bedding plane.

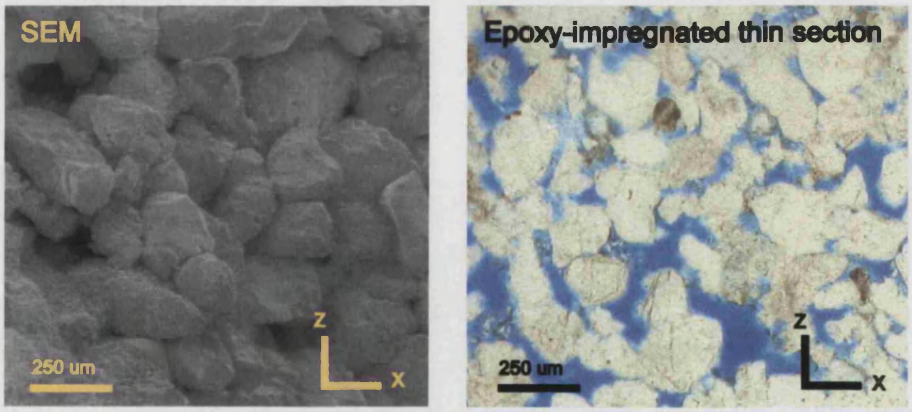

Figure 3-6. Bentheim sandstone matrix detail using scanning electron microscopy (left) and a blue-epoxy stained thin section (right). Image plane normal to bedding plane.

3.1.4.2 CRAB ORCHARD SANDSTONE

The more complex structure of Crab Orchard sandstone is seen to contain both an 'equant' pore fabric element, and a 'cracked' element. Figures 3-7 and 3-8 show scanning electron micrographs and blue epoxy stained thin sections for Crab Orchard sandstone for two orthogonal orientations relative to the common co-ordinate frame. The lower porosity and compact structure of COS as compared to BHS are both obvious from these images, in particular the blue-stained thin sections where few areas of porosity are visible. Both pores and cracks can be clearly seen, with the cracks present obvious in the SEM images. However, any orientation of the general pore space is unclear from this qualitative imaging method. Again, UV florescence sections were not necessary for this rock type.

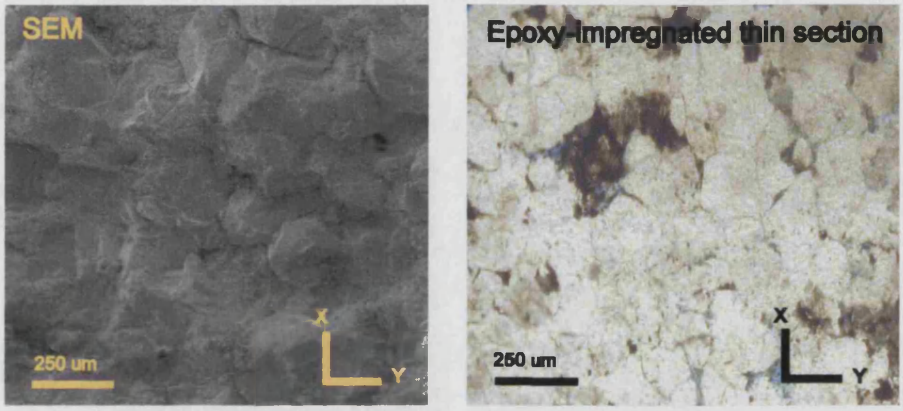

Figure 3-7. Crab Orchard sandstone matrix detail using scanning electron microscopy (left), and a blue-epoxy stained thin section (right). A complex structure of both pores and cracks is visible. Image plane parallel to bedding plane

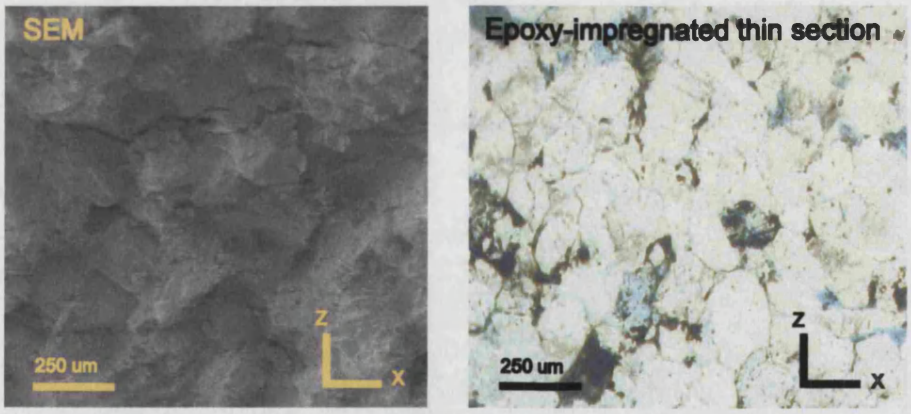

Figure 3-8. Crab Orchard sandstone matrix detail using scanning electron microscopy (left), and blue-epoxy stained thin section (right). Image plane normal to bedding plane

3.1.4.3 TAKIDANI GRANITE

Due to its low porosity, blue-stained thin sections do not adequately saturate for Takidani granite, and also possess insufficient contrast for porosity discrimination. Therefore, they are not presented here. Instead, the UV fluorescence technique is used in its place. In general, the low porosity Takidani granite shows a significant cracked element in the SEM and UV fluorescence images below (figures 3-9 and 3-10), with no obvious areas of 'equant porosity' in the sense of the BHS and COS rocks seen earlier. In addition, a clear crack fabric orientation is observed, approximately aligned with the XZ plane.

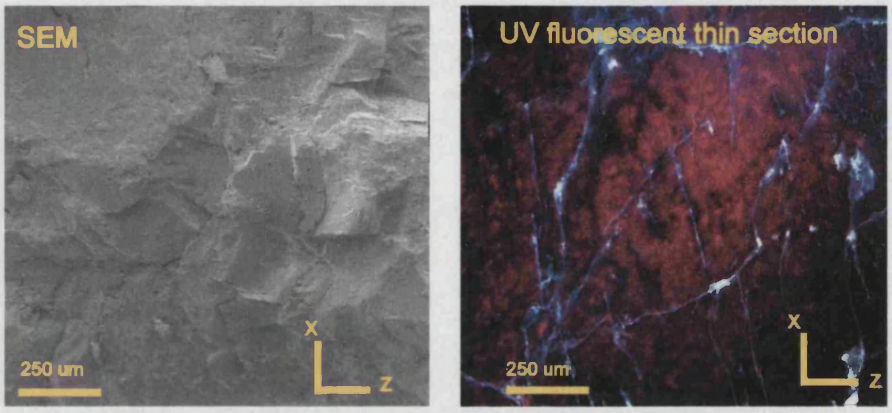

Figure 3-9. Takidani granite matrix detail using scanning electron microscopy (left), and UV dye impregnated thin section (right). A highly cracked structure is seen. Image plane parallel to XZ plane

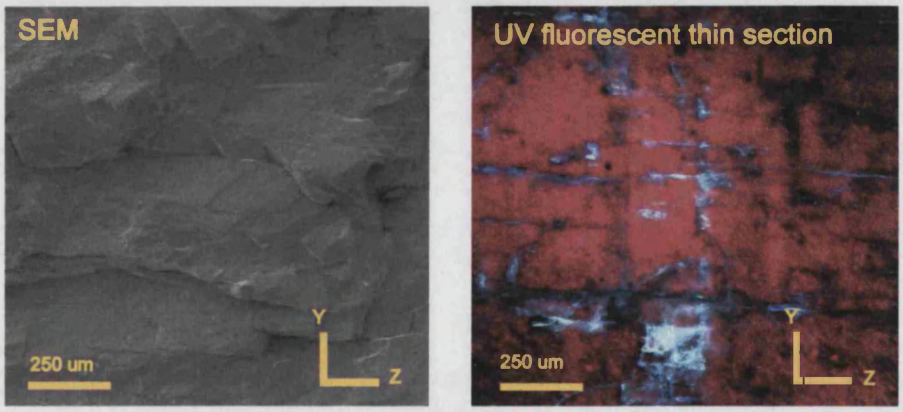

Figure 3-10. Takidani granite matrix detail using scanning electron microscopy (left), and UV dye impregnated thin section (right). A highly cracked structure is seen, which also exhibits a highly aligned nature. Image plane parallel to YZ plane

3.2 CHARACTERISATION MEASUREMENTS AT ROOM PRESSURE CONDITIONS

3.2.1 SAMPLE PREPARATION

The preparation of samples is slightly different depending on the measurement being undertaken; either AMS or velocity/permeability. Common to both measurement types is the preparation of a right-cylindrical core by drilling a sample of material with a hollow coring drill of either 25mm diameter (for AMS cores) or 38.1mm (for the preparation of elastic wave velocity and permeability cores). Cores are drilled along three orthogonal directions, as illustrated in Figure 3-11. For COS, the 'Z' axis is taken as normal to the observed macroscopic bedding. For BHS, where there is no visible fabric in hand specimen, the 'Z' axis is taken as normal to the large scale bedding observed in the quarry. For TDG, the 'Z' axis is taken as normal to the largest 'plane' of the block as received from Japan (co-incident to the vertical axis in figure 3-3). The common co-ordinate system illustrated in figure 3-11 is employed for preparing all samples, and for describing and interpreting the results. This ensures that directional measurements across differing techniques can be compared easily.

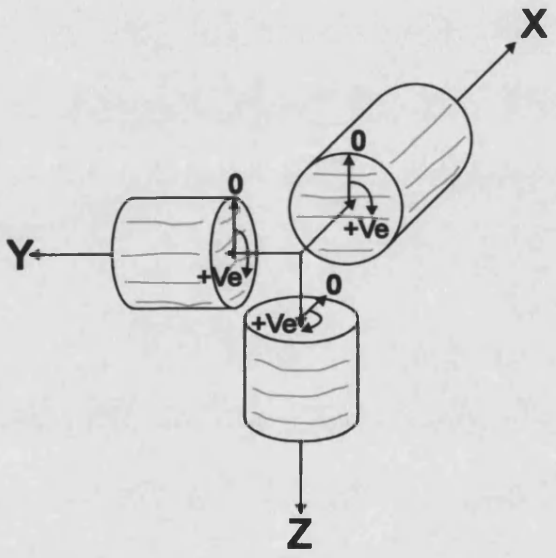

Figure 3-11. Coring direction common co-ordinate frame of reference. The grey 'stripes' on the cores illustrate the example when using the clearly cross-bedded Crab Orchard sandstone. The orthogonal X, Y and Z axes define the common co-ordinate reference system used throughout this study, with the 0° angle marked upon each of the three example cores used as a point of reference for 2-D velocity anisotropy measurement (Chapter 4)

3.2.1.1 VELOCITY AND PERMEABILITY MEASUREMENT

The right circular cores for elastic wave velocity anisotropy and hydrostatic velocity/permeability are ground to 40mm lengths using a diamond impregnated grinding wheel. This process achieves a length accuracy of 0.01mm, with sample end faces parallel to within 0.01mm. The combination of grain and sample size typically ensures that a minimum of at least 10 grain diameters per wavelength is present, and that at least 10 wavelengths are present across a

sample diameter or length as encountered by the propagating elastic wave. This is important as to ensure that the wavefront 'sees' the rock as a single homogeneous medium, rather than a collection of individual rock grains, and to help minimise scattering effects often encountered if grain size is of the same order of size (i.e. diameter) as the wavelength of the elastic signal. Typical wavelengths are 4.5mm for P-waves and 3mm for S-waves (for granite, representing a 'worst' case scenario).

3.2.1.2 AMS SAMPLE PREPARATION

AMS samples are prepared from the 25mm diameter cores by slicing them into ~22mm lengths using a dual diamond coated cutting disk arrangement. The resulting AMS cores are thus 25.4mm in diameter and ~22mm in length, corresponding to a length/diameter ratio of ~0.88. To evaluate tAMS, samples were saturated with EMG-905 ferrofluid (Ferrotec, UK Ltd.) diluted by a factor of 5 (for COS) or 20 (for BHS) with additional carrier fluid (Multipar 'H', from Multisol Ltd). This produces fluid susceptibilities of 0.35 SI for COS saturation fluid, and 0.095 SI for BHS saturation fluid. Diluting the ferrofluid keeps the bulk susceptibility of the saturated rock samples within measurable range and minimises demagnetization effects. For TDG, the natural AMS of the rock itself creates special issues, which will be discussed in Chapter 4. In this case undiluted ferrofluid is used, which has a susceptibility of 1.6 SI. All samples were saturated by vacuum immersion for 12 hours. After saturation each sample is dried of excess fluid and wrapped in 'cling-film' food wrapping, with the end faces capped using two circular pieces of thin plastic (shim). This entire package is then permanently sealed using a small length of 25mm diameter 'heat shrink' tubing which contracts permanently on the application of heat to encase and seal the sample from ferrofluid leaks (figure 3-12). A number of samples were sliced open at the end of their experimental run to confirm visually that the samples had saturated throughout (figure 3-12).

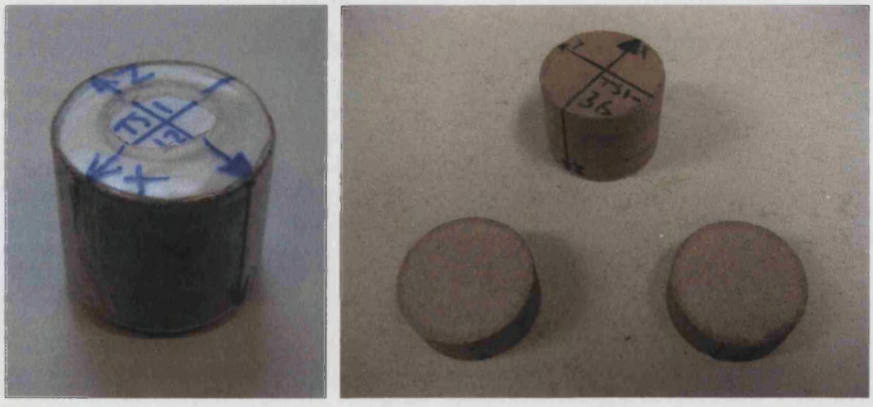

Figure 3-12. Left - a prepared, ferrofluid saturated AMS sample ready for measurement, and (right) a sample post measurement, sliced open to reveal the dark staining of the ferrofluid.

3.2.2 POROSITY

Porosity is determined using the standard ISRM water saturation porosity (gravimetric) technique, using the difference in weight of dry and saturated samples. Samples were oven dried for 72 hours before being weighed. Standard vacuum immersion was then used to saturate samples with water, with the immersed samples held under vacuum for between 24 hours (BHS and COS) and 7 days (Takidani granite) to achieve full saturation. The porosity of every sample used in this study was measured individually, so that prior to each test run under elevated hydrostatic pressure conditions an accurate room pressure porosity could be used with measured porosity changes in order to permit the determination of bulk sample porosity with increasing hydrostatic pressure.

In addition, other checks upon porosity were utilised. Firstly, mercury porosimetry. This method is useful in two ways, both as to provide independent confirmation of the gravimetric porosity, and also to provide information relating to the pore throat diameter of the rock. This is potentially useful when interpreting and discussing the elevated pressure permeability data, as a rock matrix must possess a threshold of connected porosity (percolation threshold) to possess a non-zero permeability. Secondly, the bulk susceptibility of each (ferro-fluid saturated) sample may be used to determine porosity, as the bulk ferrofluid susceptibility per unit volume is accurately known. The 'susceptibility porosity' may then be calculated by considering the susceptibility of rock before and after ferrofluid saturation. The difference between these two values is due to the volume of ferrofluid in the sample. Using the susceptibility of unit ferrofluid volume, porosity is then calculated based on the ratio of sample ferrofluid volume uptake to bulk sample volume, assuming full saturation. Alternatively, if the 'susceptibility porosity' is compared to porosity as measured using the standard gravimetric method, then the level of ferrofluid saturation in the sample may be estimated.

3.2.3 ANISOTROPY OF MAGNETIC SUSCEPTIBILITY

Magnetic susceptibility was measured using a KLY-2 'Kappabridge' susceptibility bridge (AGICO Instruments, see http://www.agico.com for details). This is a 'semi-automatic' instrument used for the measurement of magnetic susceptibility to high precision, and is made up of three components. Firstly, a pick-up unit containing the magnetic field coils; secondly, the electronic control and measurement unit; and finally, a PC computer for control and data logging (figure 3-13). The high instrument sensitivity of $4x10^{-8}$ SI allows accurate determination of susceptibility anisotropy even in rocks and materials of low bulk susceptibility. However, for the purpose of this study, any potential problems associated with the accurate measurement of low bulk susceptibilities were avoided due to the high overall susceptibilities created due to the ferrofluid impregnation of the porous rock samples.

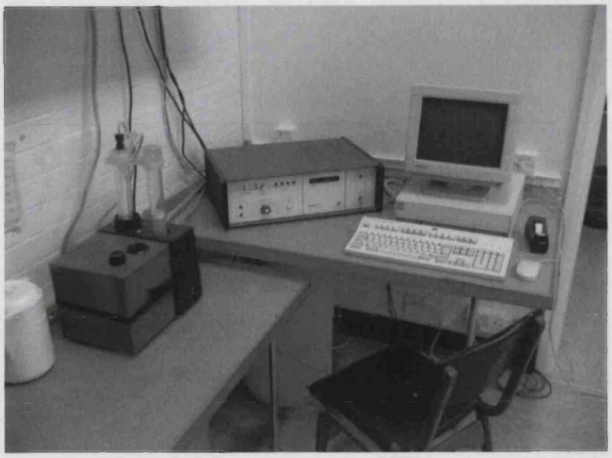

Figure 3-13. AMS equipment in the laboratory, with KLY-2 pickup unit (left), electronic bridge/measurement unit (centre) and data logging PC (right) .

Briefly, the instrument operates much in the same way as a Wheatstone bridge does in electronics (Jelinek, 1973, Jelinek and Pokorny, 1997). To measure susceptibility, the instrument is fitted with highly accurate 6^{th}-order compensated solenoids, which produce and measure the 'H' field using an inductivity bridge principle.

To determine AMS, sample susceptibility is calculated in 15 specific orientations in 3-D, which is done by rotating the sample manually (hence the term used earlier of a 'semi-automatic' instrument) into each of five different positions. These five orientated measurements are in turn repeated for each of the three planes, or faces, shown below in figure 3-14. In practice, an operator keeps one of the three key markings facing him/her, and then rotates the arrow shown through the five key directions, before manipulating the sample to move the next marking into view, and continuing the process. This gives 15 specific orientations in total. Positions 1-5 rotate the X_1X_2 sample plane through the five directions, positions 6-10 rotate face X_2X_3 through the same five directions, and finally, positions 11-15 rotates the X_1X_3 plane through five directions. These 15 directional susceptibility readings are then fitted to an ellipsoid using a least squares method (Jelinek, 1978), in order to calculate the six independent components of the susceptibility tensor, and the principal directions of the ellipsoid axes. It can also be seen that a number of positions are the same in 3-D space. These repeated susceptibility measurements allow for statistical checks on the quality of data, such as derivation of standard deviation. All AMS measurements (i.e. the ellipsoid fitted to the 15 individual readings) used in this study have a standard deviation equal to or better than a 2.5σ variation. Any measurements with standard deviations higher than this were repeated in full.

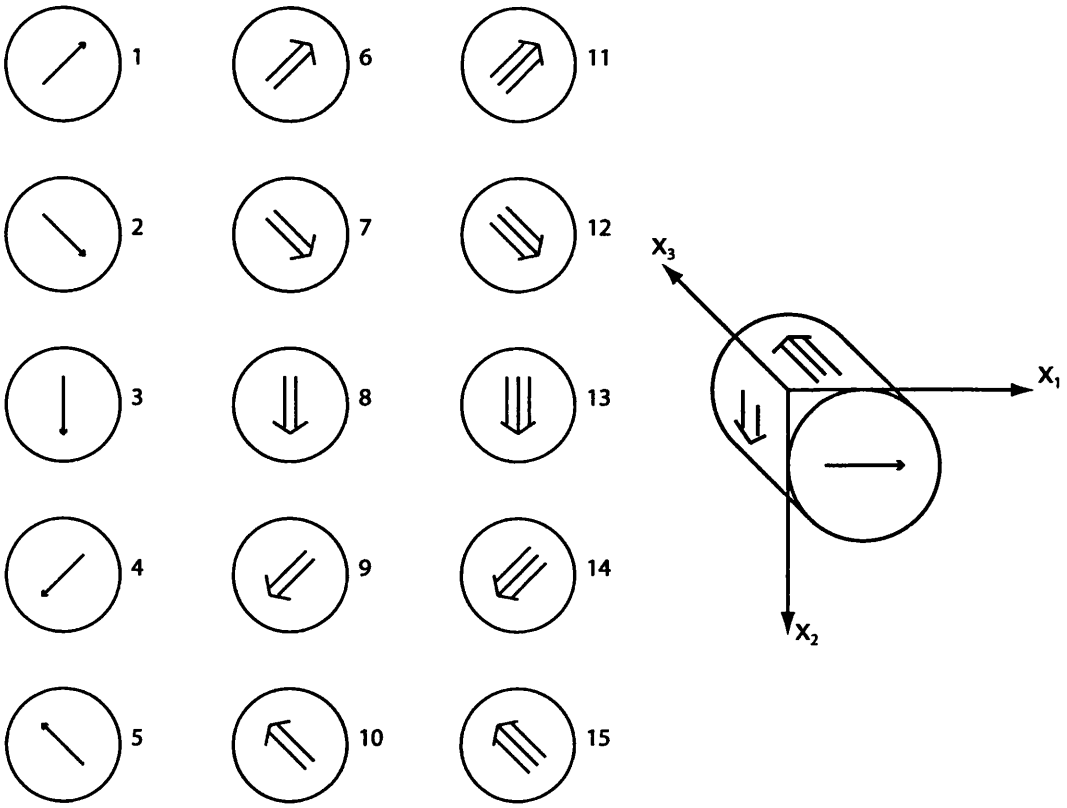

Figure 3-14. Left - summary of the 15 orientations used for susceptibility measurement. The 15 susceptibility measurements are fitted to an ellipsoidal surface, describing the AMS principal directions in length and orientation. The arrows correspond to those shown in the sample co-ordinate frame (right). In essence, each of the three sample 'faces' is rotated through the 5 separate directions. The AMS principal directions may not, of course, be aligned with the sample co-ordinate frame may not, hence the use of the general sample frame x_1,x_2,x_3. The alignment of the AMS is therefore determined relative to the sample, and hence the general co-ordinate frame (figure 3-11)

3.2.4 ELASTIC WAVE VELOCITY CHARACTERISATION

Ambient conditions elastic velocity measurement was performed using Panametrics A303S-SU P-wave transducers and V153-RB S-wave transducers, both of 1MHz central frequency (PZT-5A). Transducers are excited with a 900 volt pulser/receiver (DPR300, JSR Ultrasonics), with resulting waveforms displayed, measured and stored using a HP Agilent Infiniium oscilloscope. A simple jig was used to hold the sample and transducers, and also permit the rotation of the sample about its central axis for measurement of elastic wave velocity anisotropy (figure 3-15).

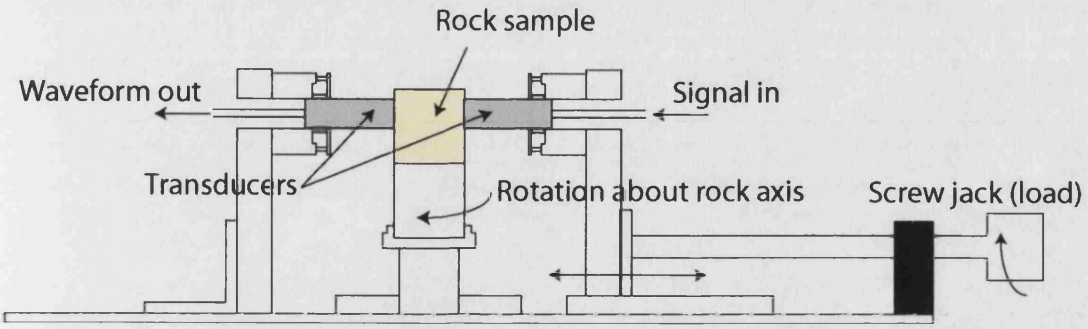

Figure 3-15. Velocity measurement jig. The sample is rotated in 10° increments about its axis, allowing elastic wave velocity to be calculated at each azimuth. The orientation of each sample is accurately known with respect to the general co-ordinate frame (fig. 3-11)

P-wave and S-wave time-of-flight measurements were made across the diameter of the 38.1mm x 40mm cores in 10° radial increments. The time-of-flight data is recorded directly from the digital storage oscilloscope allowing velocity to be trivially calculated from the core diameter ($v = diameter / time$). The 'picking' of the time-of-flight 'onset' from the received waveform requires a certain degree of experience. This is discussed in section 3.4. To allow for statistical analysis and to help reduce any apparent sample variability, three cores along each of the orthogonal 'X', 'Y' and 'Z' axes (figure 3-11) were characterised using this method, and for each rock type. Particular care was taken with the S-wave polarisation, which has two distinct experimental set-ups. I define the S_A polarisation as the S-wave measurements in which both the direction of propagation and polarisation plane are in the XY plane (refer to figure 3-16). The S_B polarisation is defined as those S-wave velocity measurements for which the direction of propagation is in the XY plane, but with a polarisation plane perpendicular to the XY plane.

However, the situation is further complicated when dealing with the changing orientation of the cores. For example, for the visible (planar) anisotropy illustrated in the core-set for figure 3-16 it is clear that at the 0° and 180° locations on the 'X' and 'Y' axis cores, the S-wave polarisation for S_A and S_B measurements is essentially the same. Therefore in this particular example the polarisation has no meaning in these locations. Alternatively, the only locations on X and Y axis cores where the S_A and S_B polarisations have a definitive meaning are at the 90° and 270° locations, therefore some caution must be exercised in interpreting azimuthal S-wave data when measuring anisotropic materials. For measurements around the 'Z' axis cores, however, the two polarisations are always distinct as the rotation axis is normal to the visible anisotropy plane.

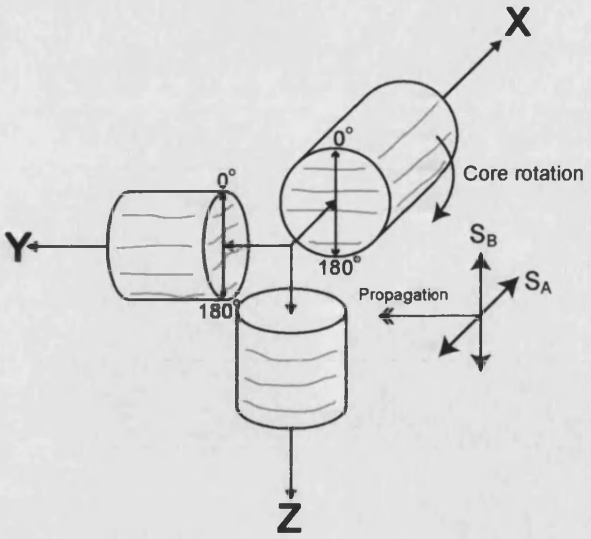

Figure 3-16. Coring axis shown with comparison between S-wave polarisation and the cross-bedding on Crab Orchard sandstone. For Z axis cores, S_A and S_B modes are consistent and unchanging with azimuth; however, this is not the case for X and Y axis cores. See text for detail

3.2.5 MERCURY POROSIMETRY

It has often been quoted that no rigorous relation exists between porosity and permeability (Guéguen and Palciauskas, 1994), as permeability depends upon pore space connectivity rather than simply the bulk pore volume. In addition, a minimum connectivity must be present in order to establish permeability (percolation), as noted previously. Furthermore, the level of connectivity is greatly influenced by any 'minimum common denominator' or constriction, which is not necessarily the bulk pore space. Such a controlling influence is more likely to be as a result of the geometry and diameter of the pore throats that lead to the void space, rather than those pore spaces themselves. The method of mercury porosimetry is capable of evaluating these pore throat diameters as a function of the fractional void space invasion (i.e. the fraction of mercury filled void space volume to total void space volume). The method also provides a second check upon bulk porosity. In contrast to the gravimetric porosity technique, the mercury injection pore throat distribution allows the presence of multiple pore sizes to be identified, whereas the water saturation method measures a 'bulk' property only. In this work, mercury porosimetry was made upon two samples of each rock type.

Standard commercial equipment was used for mercury porosimetry measurement. In the case of Tennessee and Bentheim sandstone, which possess a relatively high porosity (over 5%), a Micromeritics PoreSizer 9320 porosimeter was used. However, for Takidani granite, which possesses a much lower porosity (less than 1%), a Fisons Macropore 120 interfaced with a Fisons 2000WS micro-porosimeter was used. For both instruments, the principle of operation is as follows. Samples of ~16mm diameter by approximately 20mm length are oven dried in vacuum for a minimum of 12 hours and weighed. They are then inserted into a sample holder within the equipment, where the vacuum is reintroduced. The sample holder (complete with sample) is filled

with mercury, and, once full, atmospheric pressure is allowed back into the sample holder. This first step has the effect of forcing mercury into the larger pores (if any), and, in effect, 'pressurises' the (initially evacuated) sample from 0 MPa to 0.1 MPa (1 atmosphere) through the use of the vacuum. The sample holder is then transferred to a small pressure vessel where the sample is pressurised up to 200MPa in order to force mercury into the remainder of the porosity. Mercury inbibation is measured through the changing capacitance of the sample holder.

3.3 MEASUREMENT AT ELEVATED PRESSURE

To evaluate the relation between elastic wave velocities and pore structure / fabric and permeability, ideally we would want to measure them all simultaneously on the same sample under the same elevated pressure conditions. I have therefore developed and built an apparatus to achieve this as the major prerequisite to this experimental study.

3.3.1 EQUIPMENT DESCRIPTION

The servo-controlled measurement cell was developed from an existing apparatus designed to carry out measurements of steady-state fluid flow permeability upon 'tight' crustal rock down to nano-Darcy range (10^{-21} m^2) (Jones & Meredith, 1998; Phillips, 2002). It comprises a 275 MPa hydrostatic pressure vessel equipped with dual 70 MPa servo-controlled pore fluid intensifiers (Figure 3-17). Confining pressure up to 100 MPa is generated using a small gas powered pump, with higher pressures achieved through connection to an external hydraulic power-pack. The following sub-sections describe this apparatus, and the engineering design and development required to add the simultaneous measurement of axial P-wave and S-wave velocity with permeability and porosity.

Figure 3-17 Hydrostatic pressure equipment housed in a temperature controlled laboratory. From left to right – data logging PC, electronics rack, and, most importantly, the servo-controlled measurement cell itself

3.3.1.1 GENERAL DESCRIPTION AND OPERATION

In order to add a simultaneous elastic wave velocity measurement capability to the existing apparatus, it was necessary to design a new sample sub-assembly internal to the pressure vessel consisting of pore pipework, rubber jacketing, internal pressure housings for the elastic-wave transducer crystals, and high pressure electrical connections. Other parts of the apparatus were upgraded with the same electronic ancillary equipment (pulser/receiver and oscilloscope) as used for the ambient conditions elastic wave velocity measurement, to ensure compatibility and ease of use. The measurement cell is shown in schematic form below (figure 3-18) showing its three key systems. Firstly, a 300MPa hydrostatic pressure vessel fitted with a confining pressure generation system using silicone oil; secondly, the servo-controlled dual pore pressure system, with one high-pressure intensifier connected to the top of the sample, and an identical intensifier connected to the bottom of the sample; thirdly, the electrical circuit, for excitation of the internal transducers and waveform measurement. To minimise any temperature-induced pressure fluctuations, the equipment is located within a temperature-controlled laboratory. An internal thermocouple is used to continuously monitor the temperature inside the pressure vessel next to the sample assembly during each experiment.

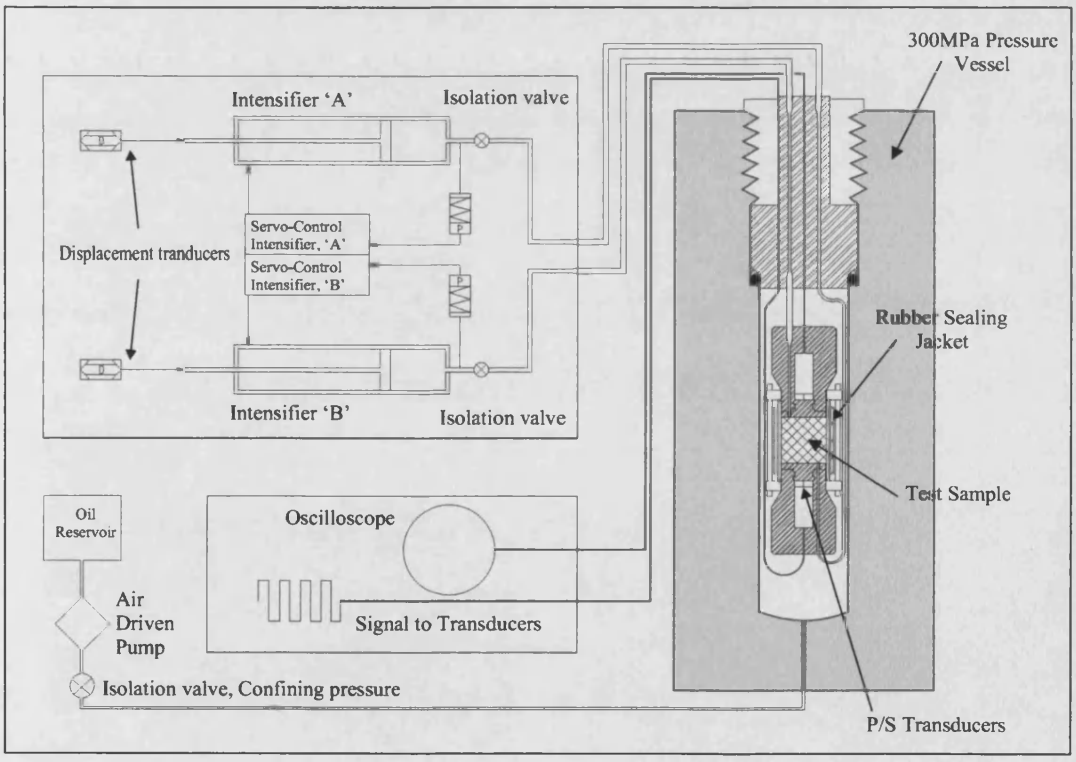

Figure 3-18. Servo-controlled measurement cell schematic. Three basic subsystems can be identified, (red) the 'push-pull' dual volumometer system which is essentially the same equipment as described in figure 2-16, (green) the hydrostatic confining cell, and (blue) the pulse transmission velocity measurement system

3.3.1.2 SERVO-CONTROL SYSTEM

The servo-control system consists of two identical hydraulic intensifiers, which provide high pressure pore fluid (distilled water) to each end of the test sample set-up, and are essentially the same as previously described by Jones and Meredith (1998) in figure 2-16. Each intensifier has a maximum internal volume of 45cc, and is servo-controlled using analogue electrical feedback from an external pressure transducer in order to maintain any pressure from 1.5 MPa to 70 MPa to an accuracy of ±5kPa (0.005 MPa). The intensifiers are fitted with integral displacement transducers which monitor the position of the high-pressure pistons, thus enabling the intensifiers also to be used as volumometers. For permeability measurements, the upstream and downstream intensifiers were set to slightly different control pressures in order to maintain a small, constant, differential pressure across the sample. In practice, the differential pressure used depends upon the rock being tested. For the Bentheim sandstone, a differential pressure of 0.2 was applied, whilst for the lower permeability Crab Orchard sandstone and Takidani granite, a slightly higher differential pressure of 0.5 MPa was used. In all experiments, a mean pore fluid pressure of 2.5 MPa was set, with increasing confining pressure used to increase the effective pressure to the desired level. Once steady-state flow is established, permeability can be determined from the rate of fluid flow in ml/s, the pressure gradient in MPa/cm, and the sample dimensions (cm) via direct application of Darcy's law as shown in Chapter 2 (equation 2-15).

3.3.1.3 A NEW DESIGN FOR SIMULTANEOUS VELOCITY AND PERMEABILITY MEASUREMENT

Although the measurement of permeability and elastic wave velocity has been performed independently for many years, the servo-controlled measurement cell can, for the first time, measure both of these properties contemporaneously. As already noted, the original servo-controlled measurement cell ('Permeameter'), was designed to measure steady state flow permeability only, and was therefore only equipped with a pore fluid hydraulic circuit. The new equipment additionally incorporates internal P-wave and S-wave piezoelectric transducers, fitted into new 'end-caps' which feature internal cavities to isolate the delicate transducer crystals from the high pressure confining oil. A schematic of the sample arrangement between two identical 'end-caps' is shown below in figure 3-19. Each 'end-cap' also contains a pore fluid connection to an intensifier, in order to allow the introduction of pore fluid to one end of the sample, and to be received at the other. These new 'end-caps' allow a full suite of P-wave, S-wave, permeability and also porosity change (discussed later in section 3.3.2.2) to be measured contemporaneously with effective pressure.

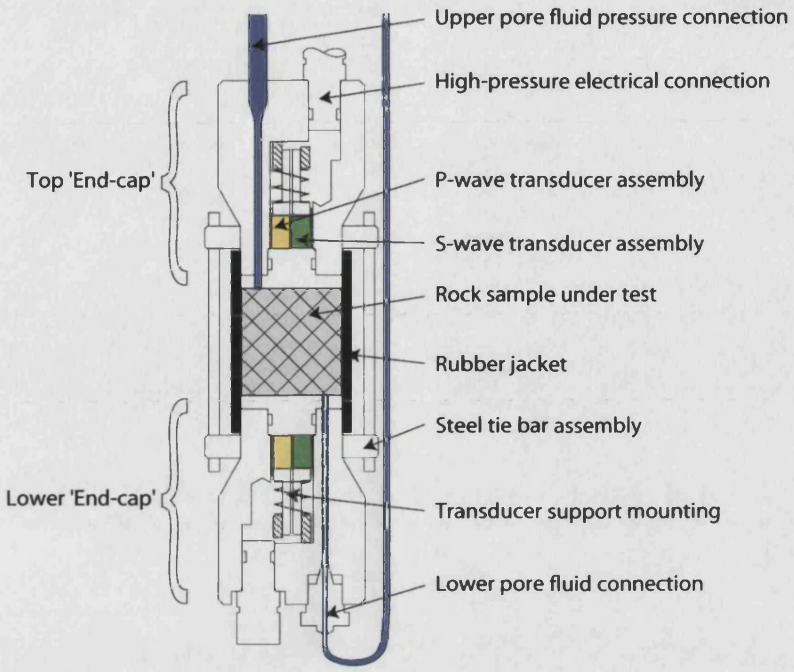

Figure 3-19. Schematic of sample arrangement within hydrostatic pressure vessel showing key components (labelled)

3.3.1.4 PORE FLUID HYDRAULIC CIRCUIT OPERATION

Detail of an 'end-cap' is illustrated in figure 3-20. To give the end-cap sufficient strength and low overall size, all components are manufactured from high strength FV-520-B hardened stainless steel. Two ports at the rear end of the end-cap are used for pore fluid connection and electrical connection. For pore fluid connection, standard $1/8^{th}$ inch high pressure stainless steel pipework is used (in common with the rest of the servo-controlled measurement cell pipework), with the exception of the lower end-cap, where a short length of $1/16^{th}$ inch pipe is used to connect the end-cap to the top seal of the pressure vessel. This gives greater flexibility when assembling the set-up. The high pressure electrical connectors use an existing design (Clint, 1999), which permits a low-noise electrical connection whilst preserving a high integrity pressure seal up to 400MPa. The piezo-electric transducer assembly is housed inside the internal cavity of each end-cap and connected to the rear of the electrical 'lead-throughs' using 'miniature' co-axial cable. Finally, the top of each end-cap consists of a 'spreader plate' which receives the high pressure water from the intensifier and distributes it over each face of the sample using a concentric ring etching. The entire assembly is sealed using a number of 'O' ring and PTFE seals between the individual mechanical components.

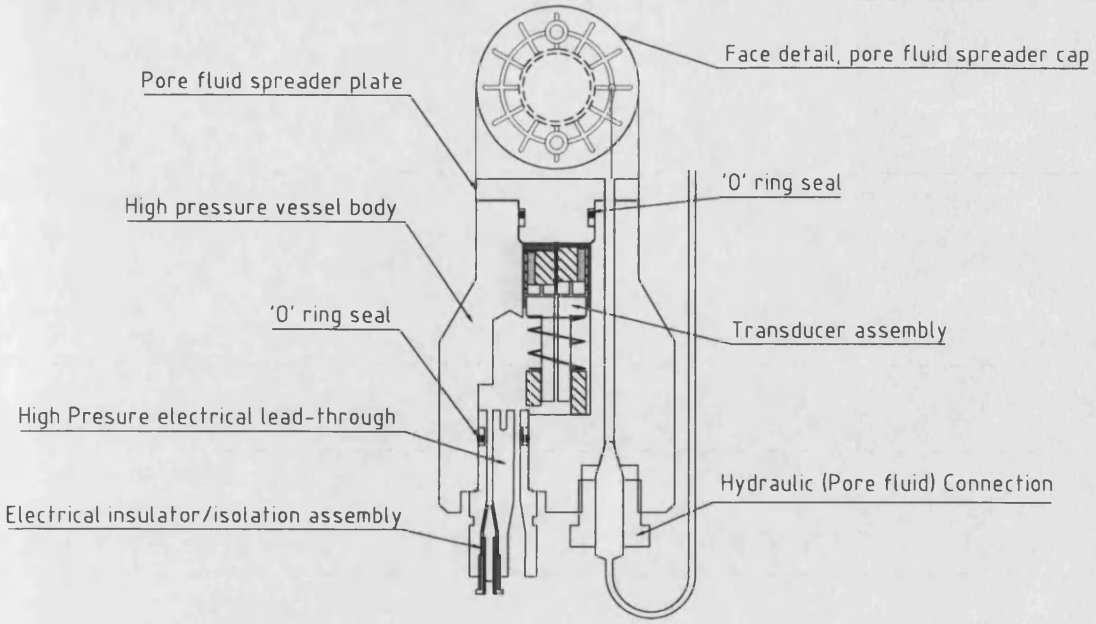

Figure 3-20. Detail of an 'Endcap', as seen in figure 3-19. Engineering drawing courtesy Steve Boon

3.3.1.5 Elastic velocity electrical circuit operation

One of the most technologically challenging aspects of the equipment, and of the project as a whole, was developing the system to house, mount and operate the P-wave and S-wave PZT-5A transducer crystals inside each end-caps. Due to the space constrains within each end-cap, insufficient room is available to use commercial (damped) transducers, so that only the bare PZT crystals are employed, which produce noticeable 'ringing' due to their un-damped nature. The need to isolate the delicate crystals from the high pressure externally results in the transducer elements not being in direct contact with the rock sample under test. Loss and degradation of signal were chief concerns during development, as the generated mechanical pulse first has to propagate through 15mm of hardened steel before encountering the rock sample. The design is further complicated by the necessity to electrically connect the transducers to the pulser/receiver though many connectors and sill maintain a high quality, low-loss signal. The solution designed is illustrated in figure 3-21.

Each end-cap includes a cylindrical internal compartment of 16mm diameter and 40mm length, which houses the transducer assembly. Each assembly mounts two PZT crystals of 1 MHz central frequency, one compressional (P) mode and one shear (S) mode. As supplied, each crystal is nominally 15mm in diameter and 1-2mm in thickness; however, to maximise the area used at the rear of the pore fluid spreader plate (figure 3-20) for which to bond the PZT crystals, they are each cut in half along a diameter and mounted to a 'backing' to form transducer 'elements'. In this way, a 'complete' transducer assembly gives the appearance of a single, circular, transducer disk; one half consisting of the P-mode crystal, and the other half the S-mode crystal. The backing consists of two co-axial electrical connectors which match up and connect to similar co-axial gold contacts on the PZT crystals. This backing is constructed using 15mm copper tubing with a 10mm brass rod mounted axially. The space between these two conductors is filled with a rubber compound to act as

an insulator. This support is then cut in half (axially) and used to mount the semi-circular PZT transducer elements, the metal components of this support being used as electrical connections to the transducer. The entire assembly is bonded to the rear of each pore spreader plate using an electrically conductive, silver loaded epoxy, and compressed onto the rear of the spreader plate using a custom made rubber and spring mounting system. P-wave and S-wave transducer halves are electrically isolated from each other using two small pieces of plastic shim, and from the end cap itself using a thin piece of plastic tubing.

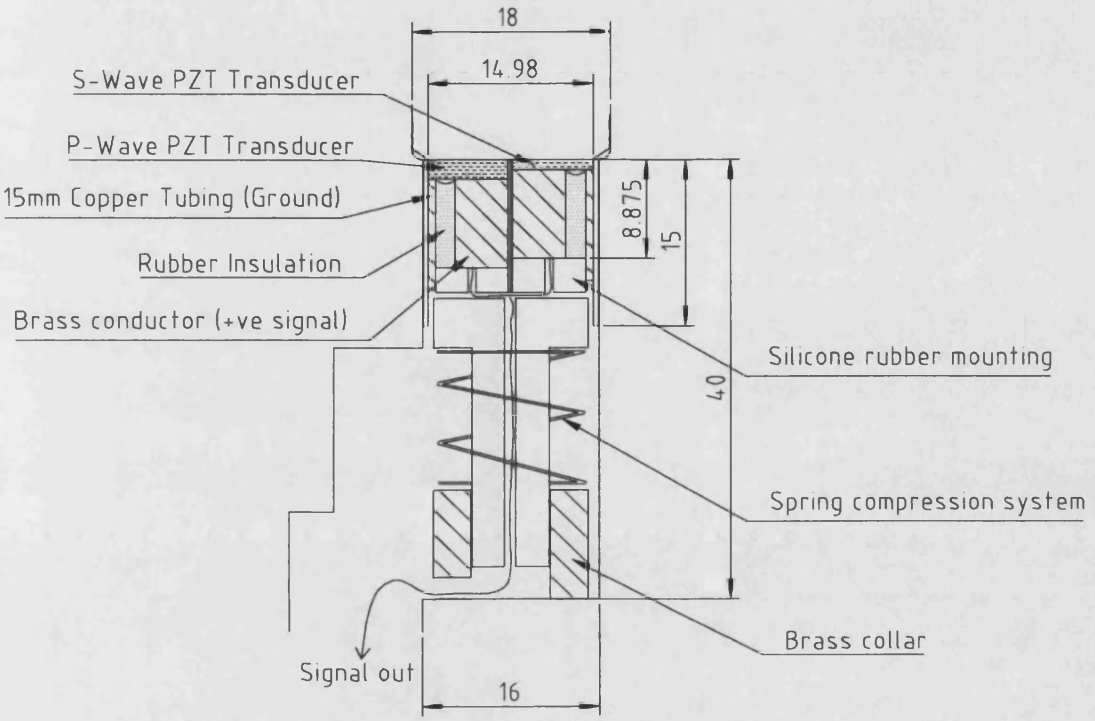

Figure 3-21. Detail of the transducer assembly housed inside each endcap for velocity measurement at elevated hydrostatic pressures. Dimensions in mm.

3.3.2 MEASUREMENT METHODS AND PROTOCOLS

Hydrostatic measurement cell data was logged as a function of time using a National Instruments AT-MIO-16XE-50 data acquisition (DAQ) card running on a PC equipped with 'LabView 6.1' data acquisition software and running 'Precision Data acquisition and Control 7.13' virtual instrument (Masizame Technologies). Calibration data is entered directly into the software, which then converts each transducer output in volts directly into the appropriate physical quantity (e.g. transducer pressure in MPa, volumometer volume in ml), allowing 'real-time' measurement of permeability with time using the method introduced in Chapter 2. This has the added advantage of being able to easily diagnose any leaks or problems within the apparatus, as the displacement of a volumometer is shown in real time, and in cm^3. If a leak develops, then the displacement change with time will be different for each volumometer, which is more easily identified as compared to monitoring voltage with time, for example. Using this equipment it is possible to record up to 3200 samples per second per channel, with six channels of data recorded during the experiments (pressure

and volume of intensifier 'A', pressure and volume of intensifier 'B', confining pressure and internal vessel temperature). In practice, 'blocks' of 1600 samples were averaged (i.e. every 0.5 seconds) in order to improve the signal to noise ratio and reduce random error. As permeability/porosity changes over time represent relatively slow events, no information was lost due to the use of this method.

Hydrostatic pressure experiments were conducted at a constant average pore pressure of approximately 2.5 MPa, and with confining pressures ranging from 7.5 to 92.5 MPa, to yield the desired effective pressures of between 5 and 90 MPa, corresponding to a maximum depth of approximately 3.5km within the crust. Contemporaneous measurements of permeability, porosity and elastic wave velocities (P-wave and S-wave) were made in increments of 5 MPa for effective pressures of 5-20 MPa, and 10 MPa increments for effective pressures of 30-90 MPa in order to better observe and resolve any rapid changes at lower effective pressures. The use of a differential pressure of 0.15 MPa between the sample ends for Bentheim sandstone, and of 0.5 MPa for Crab Orchard sandstone and Takidani granite (noted earlier) ensures that the differential pressure accounts for no more that 10% of the effective pressure, shown in past work to be a source of uncertainty, due to the 'effective pressure gradient' otherwise created.

3.3.2.1 PERMEABILITY: PROTOCOL

Permeability is calculated in real-time using a 'rolling window' to calculate the gradient of the displacement change with time to give the fluid flow volume rate. This window typically consists of the last 10 to 600 measurements at any given point in time (1 measurement now defined as a 1/2 second average of 1600 samples described earlier). The number of measurements used for the window width depends upon the permeability of the rock under test. For Bentheim sandstone, 10 measurements is sufficient, whereas at the other extreme, Takidani granite requires 600. The slope of the windowed linear regression is directly related to the permeability of the sample though the sample dimensions and the pressure gradient over the sample, as derived in section 2.5.1. The sample dimensions are entered into the logging software at the start of each experimental run, with the pressure gradient also calculated directly from the logging equipment and software. This procedure has numerous advantages over the alternative method involving 'off-line' data processing, such as the ability to quickly define the achievement of steady-state flow, and again to determine if any leaks are present – as permeability data from each intensifier should be 'equal and opposite' in sense (figures 3-22 and 3-23). Finally, experimental error in permeability is estimated using approximately 100 sequential permeability measurements over time in order to calculate a mean and standard deviation. This method gives an error of between 4% and 8%, depending on the rock type measured.

3.3.2.2 POROSITY CHANGE: EXPERIMENTAL METHOD AND PROTOCOL

Measurements of sample porosity change with increasing effective pressure were made (contemporaneously with permeability, V_p, and V_s) via the following method. Figure 3-22 below illustrates the data as it is logged during the procedure though the following steps:

1. Prior to any interruption, displacement change (permeability) is stable.
2. The downstream reservoir isolation valve (Figure 3-18 – intensifier 'A') is closed and the pressure in the upstream intensifier and sample allowed to equilibrate.
3. After equilibration, the effective pressure is increased.
4. The displacement of the upstream intensifier (B) piston due to the effective pressure increase (which is still connected, providing pore pressure to the sample) is monitored and logged. This displacement directly measures the volume of water expelled from the sample due to the closure of cracks and pores, i.e. the change in porosity due to the increase in effective pressure.
5. The downstream intensifier (A) is re-connected, allowing fluid flow to re-commence through the sample.
6. New steady-state flow is achieved, representing a new (usually lower) permeability.

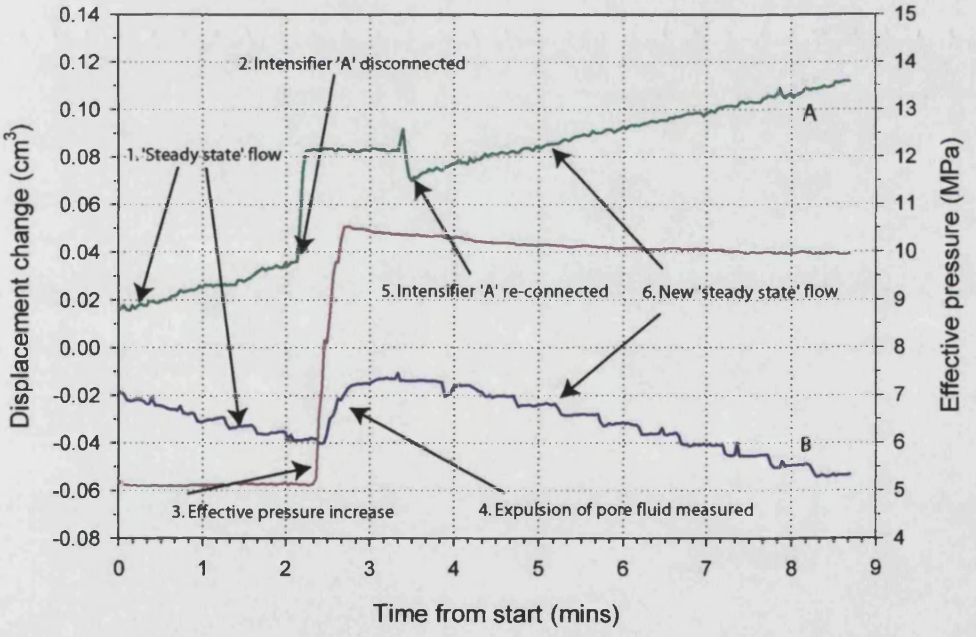

Figure 3-22. Example of volumometer displacement variation with time due to a small (constant) applied pressure differential across a sample of Crab Orchard sandstone. The green trace illustrates volume change for intensifier 'A' and blue trace for intensifier 'B'. The red trace shows the applied effective pressure. See text for full explanation of procedure.

The porosity at start of each experiment is measured gravimetrically so that the porosity change during each step measured can be used to calculate an overall 'bulk' sample porosity change with effective pressure. However, the first step from 0 to 5 MPa cannot be monitored as no pore

pressure exists and therefore no pore fluid expulsion can be observed. This step is corrected for using the following process. Initially, the porosity at 5 MPa is taken as equal to the initial gravimetric porosity, and the porosity variation is calculated using the method described above. This porosity curve is then analysed using commercial curve-fitting software (Sigma-plot software, using an exponential decay with linear component), and the fitted curve extrapolated to 0 MPa pressure. The mismatch between predicted 'zero MPa' porosity and the actual, gravimetric, 'zero MPa' porosity is used to calculate a constant offset which is then applied to all the previously incorrect data. This process thus corrects porosity as a function of pressure, after which the 0MPa value is equal to the value measured gravimetrically, and where the 0 MPa to 5 MPa porosity change has, in essence, been interpolated from the known porosity change measured experimentally.

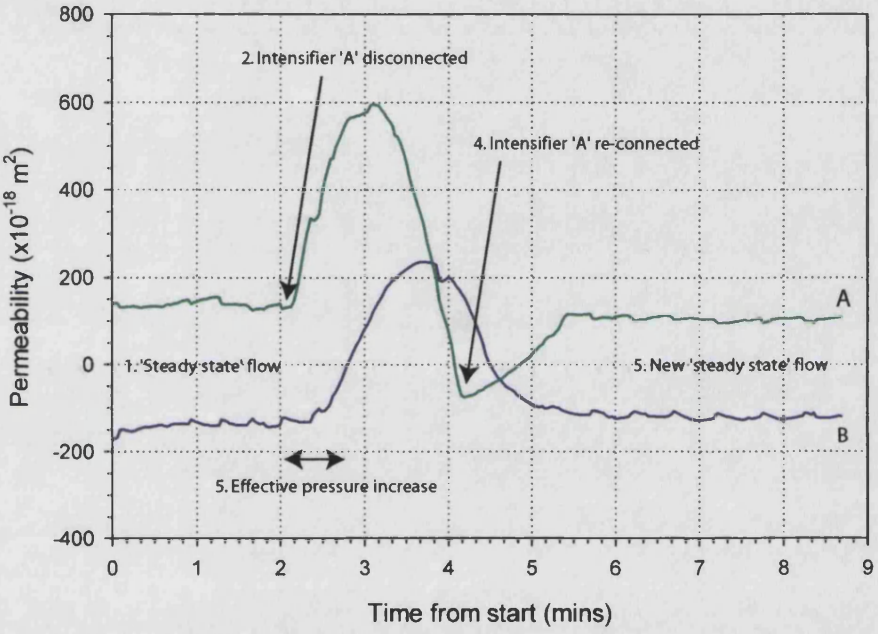

Figure 3-23. Permeability as calculated from the volume flow rate in figure 3-22 for each volumometer, showing the variation with time and applied effective pressure. During steady-state flow, small changes in permeability occur due to friction within the volumometer system, resulting in 'noise' of ~5%

3.4 CALIBRATIONS

The servo-controlled measurement cell is a complex piece of apparatus, containing two control pressure transducers, two displacement transducers for use in determining volumometer piston displacement, and a confining pressure monitor transducer. Before experimental measurements can be conducted using the servo-controlled measurement cell, a number of calibrations must be performed in order to accurately relate the various transducer outputs (in volts) to pressure, intensifier volume, and calibrated time-of-flight times. The control pressure transducers are the most important of these, as the differential pressure between the top and bottom of the sample must be accurately known and set. This is especially important for high permeability rocks in which a low differential pressure is crucial in order to achieve steady state flow before the internal

piston within each volumometer runs out of travel, and hence is unable to provide pressure, ending the experiment. In addition, P-wave and S-wave 'circuit' timings are also required, as each of the end-caps described in section 3.3.1.4 possess 15mm of steel in front of its transducer crystals, which must be accounted for when measuring time-of-flight times when a sample is present between them.

Pressure calibration is performed using a 'dead weight' pressure generation system, consisting of a number of accurately know weights which, when coupled with a simple hydraulic piston system, provides a highly accurate hydraulic pressure which can then be applied to any pressure measurement system which requires calibration. This allows transducer voltage output to be measured as a function of known pressure (figures 3-24, 3-25). The gradient and intercept of this calibration is entered directly into the logging software, so that all measurements are converted as they are recorded as described in section 3.3.2 earlier. Linear regression results (gradient and intercept) for figures 3-24 and 3-25 are summarised in table 3-2.

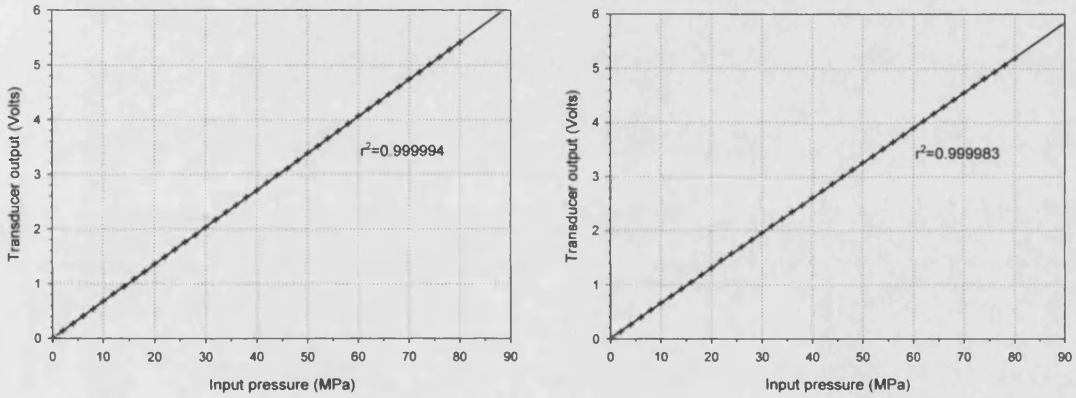

Figure 3-24. Servo-controlled measurement cell pressure transducer calibration: volumometer 'A' (left plot) and 'B' (right)

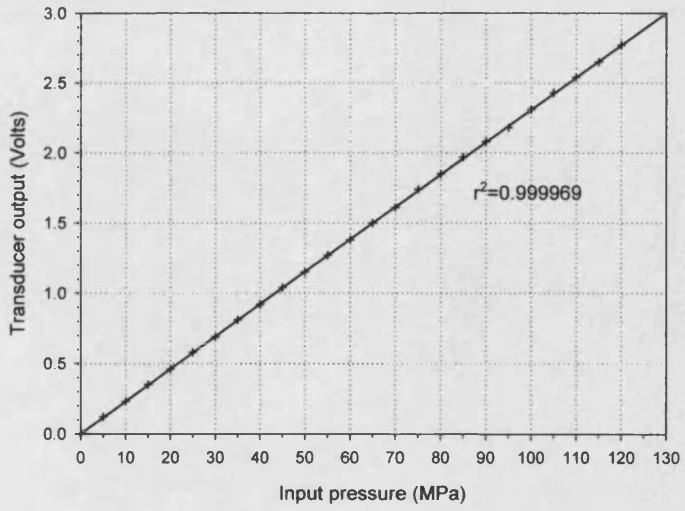

Figure 3-25. Servo-controlled measurement cell: confining pressure transducer calibration

Transducer	Gradient (Voltage output per 1MPa pressure increase)	Intercept
Control pressure, volumometer 'A'	0.0676	0.0033
Control pressure, volumometer 'B'	0.0648	0.0121
Confining pressure monitor	0.0231	0.0006

Table 3-2. Servo-controlled measurement cell pressure transducer calibration summary. The key value is the gradient, representing the voltage change per pressure change

Volumometer volume change was calibrated by measuring the physical volume of water expelled from each piston over its useable range and recording the change in voltage output as recorded from the internal LVDT. This then (trivially) gives a value for voltage/cm^3 volume change, which is entered into the logging software. For volumometer 'A' this value is 0.220119 V/cm^3; for volumometer 'B' a value of 0.250664 V/cm^3 was measured.

P-wave and S-wave velocity calibration is measured by placing the two end-caps in direct contact, and measuring the time-of-flight with no sample present. Calibration using the ambient conditions velocity anisotropy jig is performed in a similar way, by placing the two transducers in direct contact. An example P-mode waveform (figure 3-26) illustrates the signal recorded during the servo-controlled measurement cell calibration. These particular wave velocity calibrations are made more difficult than other types of velocity calibration due to the construction of the end-caps themselves, which use bare 'un-damped' transducers crystals due to the limited space available inside each endcap as noted earlier. This effect, added with the need for the wave to travel through a total of 30mm of steel, results in the waveform often taking on a 'ringing' appearance. This is reduced once the sample has been pressurised to a modest degree, the calibration shown is made at a confining pressure of 30MPa. However, no time-of-flight dependency upon pressure was seen during calibration, as expected.

A 'stacking' procedure is used with all measurements (whether under ambient or elevated hydrostatic pressure). This technique is common in the seismic exploration industry (e.g. Sheriff and Geldart, 1995), and in my experiments a total of 256 waveforms are stacked and averaged. This results in a far cleaner signal, which is relatively free from random noise. Picking the absolute time was done by eye, by measuring the '1st break' downwards from the 0 volts level, and recording the time at which the waveform had reached a fixed (negative) value. Typically the value chosen for this threshold was approximately 10% of the maximum negative peak, -0.004V in the example shown in figure 3-26. However, as this study is primarily concerned with anisotropy, the bulk velocity measurement is less important that the variation with pressure (in the servo controlled measurement cell, or with radial angle in the case of the azimuthal velocity measurements). Importantly, this variation can be measured to a much higher accuracy as a result of tracking the first break than the bulk velocity measurement itself. P and S calibrations are summarised in table 3-3.

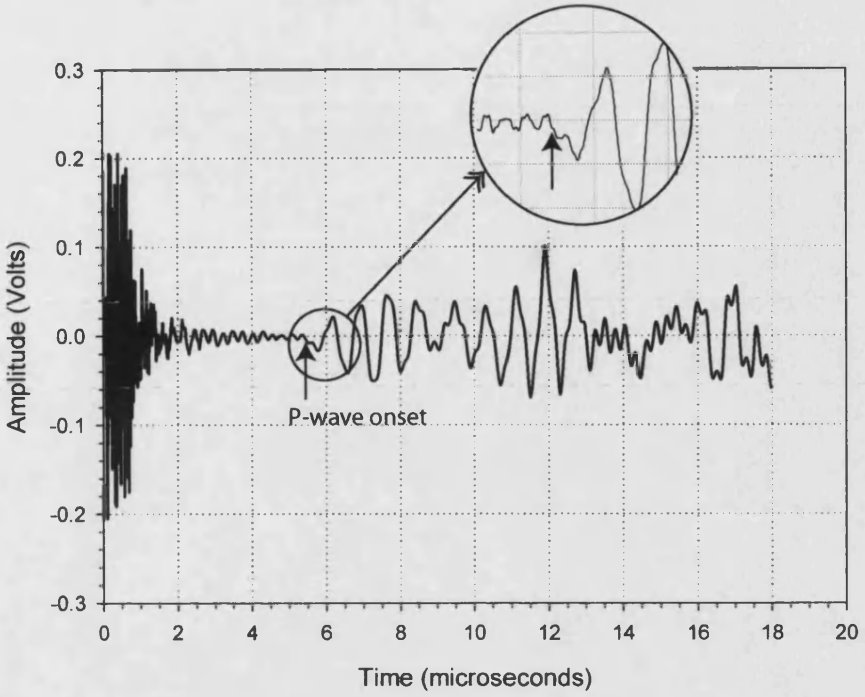

Figure 3-26. P-wave calibration signal. See text for details of onset time picking

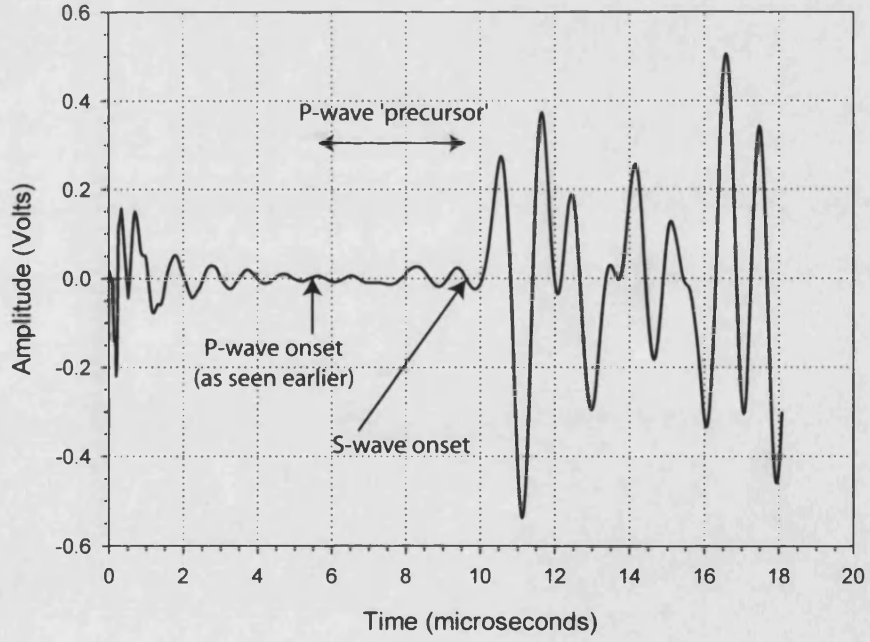

Figure 3-27. S-wave calibration signal. Separating the S-wave onset from the P-wave precursory signal is a non-trivial task. See text for details

S-wave calibration and measurement are more difficult due to the inherent P-wave component present in all shear mode crystals. The P-wave precursor can be seen in figure 3-27, with the actual P-wave onset indicated using the dedicated P-wave transducer signal as measured in figure 3-26.

Wave type and condition	Calibration (μs)
P-wave (ambient)	0.826
S-wave (ambient)	0.812
P-wave (hydrostatic)	5.451
S-wave (hydrostatic)	9.616

Table 3-3. 'No sample present' calibration times for the various wave types and sample conditions. Ambient refers to the elastic wave velocity measurements made under room pressure conditions, hydrostatic refers to measurements made under pressure in the servo controlled pressure cell

3.4.1 SOURCES OF EXPERIMENTAL ERROR

In general, sources of error fall into two categories. (1) physical experimental measurement error, which is unavoidable in experimental work, and (2) human errors involved in the interpretation of the physical results; the best example of this is the 'picking' of the P-wave or S-wave onset.

3.4.1.1 PHYSICAL ERRORS

Measurement error is minimised through the adoption of the standard best practices, such as averaging physical measurements and by performing accurate calibrations on a regular basis. Most of the procedural best practices have already been noted, such as averaging during the logging process. The use of the three-orthogonal arrangement helps to reduce the sample variability, as when considering a complete 3-core set, there are many directions in the common frame of reference whose physical measurements lie on more than one different core. This allows a 'levelling' or 'surveying' method to be adopted to interpreting the data, which is fully described in Chapter 5.

3.4.1.2 HUMAN ERROR

Human error occurs throughout all the measurements and experiments described, and is potentially the greater source overall. Estimating these errors are difficult, as many of the measurements rely in some part on interpretation of signals. In order to minimise this kind of uncertainty, various approaches were taken which, whilst the 'absolute' measurement itself is still an issue, the variation of the signal between successive measurements is of a high accuracy, and free from random errors as much as possible. To help achieve this aim, experiments were made together in a 'series' with the same operator, as this will allow more accurate determination of *anisotropy*, especially for the velocity anisotropy work. Table 3-4 lists the common experimental sources of error, with associated values.

Measurement type	Accuracy
Sample length	±0.01 mm
Sample mass	±0.001 g
Sample parallelism	±0.01 mm
Susceptibility	$\pm 2 \times 10^{-8}$ SI
Confining pressure	±0.1 MPa
Pore pressure(s)	±0.01 MPa
Volumometer displacement	±0.001 cm^3
P-wave velocity (absolute)	1%
S-wave velocity (absolute)	2%
P-wave velocity (relative)	0.5%
S-wave velocity (relative)	0.5%

Table 3-4. Summary of experimental error sources and values

4 RESULTS: ROOM PRESSURE MEASUREMENTS

In this Chapter, the results are presented of void space anisotropy measurements as determined using the techniques of anisotropy of magnetic susceptibility (AMS), and anisotropy of ultrasonic wave velocity (P-wave and S-wave), made under room pressure conditions. While each technique has its merits, I consider that, since they measure different but complementary properties, they are more powerful when used together. The principal anisotropy directions derived from AMS ellipsoids are directly compared to the principal anisotropy directions as determined from the elastic wave anisotropy ellipsoid, allowing independent verification of pore fabric shape and alignment regarding the pore fabric anisotropy often assumed when employing the frequently used method of velocity anisotropy. By investigating the three different rock types introduced in Chapter 3, which posses highly contrasting visual fabrics, this multidisciplinary work aims to further the scientific understanding of the causes of anisotropy in terms of void space geometry and alignment.

4.1 ANISOTROPY OF MAGNETIC SUSCEPTIBILITY

4.1.1 INTRODUCTION

Throughout this Chapter, and the remainder of this work, I will adopt the nomenclature for the different types of anisotropy of magnetic susceptibility (AMS) as first introduced in Chapters 1 and 2; referring to the dry rock matrix AMS as mAMS, total ferrofluid saturated AMS as tAMS, and the AMS of the saturated rock pore fabric only as pAMS. As previously noted, for ferrofluid saturated samples measurements of the total anisotropy of magnetic susceptibility (tAMS) overwhelmingly reflects the average void space alignment, if the matrix susceptibility (mAMS) is low in comparison. For Bentheim sandstone tAMS≈19600 and mAMS≈17, and for Crab Orchard sandstone tAMS≈12900 and mAMS≈46; thus for these sandstones the condition of tAMS>>mAMS is easily met, as the ferrofluid saturated bulk susceptibility of the samples exceeds the bulk matrix susceptibility by a factor of approximately 10^3 in both cases. However, for Takidani granite, this condition is not satisfied (tAMS≈23300, mAMS≈18200), and so the data must be processed before being interpreted. The procedure to address this issue will be the topic of section 4.1.2.3.

A useful graphical method of displaying directional data in three dimensions is through the use of lower hemisphere (equal area) stereographic projection, or **stereonet**. This method is adopted here in order to display the principal anisotropy directions as derived from mAMS, tAMS and pAMS data, with reference to the general X-Y-Z co-ordinate frame described in Chapter 3. This study is also concerned with bulk magnitude of the void space anisotropy, and to avoid confusion and conflict with other parameters, it is useful to introduce some terms from the outset. In AMS studies, the parameter 'P' is commonly used to describe the ratio of the lengths of the maximum principal susceptibility axis to the minimum principal susceptibility axis (i.e. K_{max}/K_{min}). However, as this study deals with three forms of AMS measurement (mAMS, tAMS and pAMS), I introduce three different forms of the general 'P' parameter. Here, P_m refers to the ratio above as determined

from mAMS data, P_t is defined using tAMS data, and P_ϕ is defined using the pAMS data, i.e. the *void space fabric* alone. Using the stereonet method together with P_t and P_ϕ magnitudes thus allows the principal anisotropy shape and orientation in three dimensions to be described.

4.1.2 PRINCIPAL PORE SPACE ANISOTROPY DIRECTIONS

To test for any possible sample coring direction dependency, for example as a result of heterogeneity, AMS samples were drilled with core axes in each of the three orthogonal axes shown in figure 3-16. For each sample, the resultant AMS principal directions were then rotated on the basis of the known core axis orientation back to the common frame of reference. After this procedure, AMS principal directions show no coring direction dependence (figure 4-1). In all stereonets, and all rock types, the same notation is used for the principal ellipsoid directions, with maximum directions denoted by squares, intermediate directions denoted by triangles, and minimum directions denoted by circles.

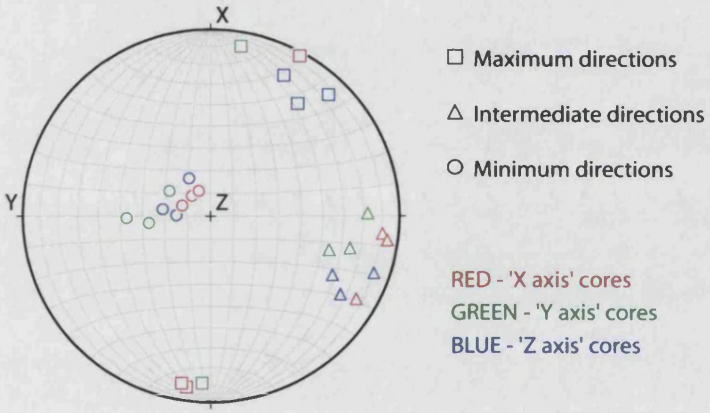

Figure 4-1. Example tAMS data illustrating principal orientations from samples cored in three orthogonal directions. After the vectors have been rotated for the known sample axis direction in space, tAMS orientations are in excellent agreement. Note that in this figure only, the colours denote the different core axis directions, for illustration purposes

Each measured AMS sample produces a representative magnetic ellipsoid (either mAMS or tAMS), with a shape and alignment defined by the length and direction of the three orthogonal principal axes. To allow for statistical analysis, multiple samples are measured and presented on each plot. The scatter in the principal directions is analysed using the statistical method of Bingham (1974), which is a commonly used technique in structural geology and palaeomagnetism. This method is used to calculate a 95% 'confidence ellipsoid'. The Bingham (1974) method has a distinct advantage over other methods, such as that of Fisher (1952), in that the technique is bimodal in operation. This means that the 95% confidence cone represents an *ellipse* upon the stereonet, with a maximum error direction and a minimum error direction. For axially symmetric distributions (such as that described by the minimum values in figure 4-1 above), these two errors will be approximately equal, and approximately equivalent to the Fisher (1952) confidence cone. However, for the determination of statistical variation distributed within a plane (such as the maximum and intermediate values seen in figure 4-1), these errors will not be the same. Therefore, the Bingham

statistical method is used as a more rigorous technique for calculating the errors throughout this work rather than the Fisher method.

4.1.2.1 BENTHEIM SANDSTONE

Figure 4-2 shows mAMS and tAMS principal directions obtained from measurements on Bentheim sandstone. For this rock type, pAMS is approximately equal to tAMS due to the high magnitude of ferrofluid saturated susceptibility signal as compared to the matrix susceptibility signal. For pAMS data, distinct populations of maximum and intermediate directions can be seen, which are approximately orthogonal to each other and also to the minimum direction; i.e. pAMS maximum and intermediate directions lie at 90° to each other, and within a plane which is at 90° to the third axis. The minimum direction is approximately aligned along the Z axis of the co-ordinate frame. Scatter in the data is, in general, lowest for the pAMS minimum directions, which are tightly clustered (table 4-1). The intermediate and maximum susceptibility directions are distributed along a great circle essentially sub-parallel to the XY plane, as demonstrated by the associated Bingham error ellipses (table 4-1, figure 4-3).

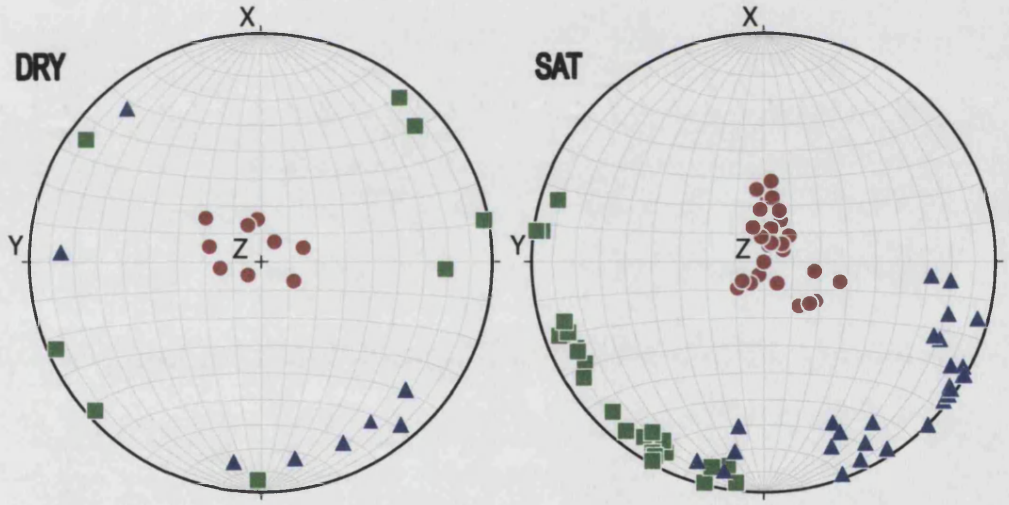

Figure 4-2. Stereographic projection (stereonet) of principal ellipsoid directions for Bentheim sandstone matrix mAMS (left) and pore fabric tAMS (~pAMS) (right). Maximum directions are denoted by green squares, intermediate directions denoted by blue triangles, and minimum directions denoted by red circles. The X-Y-Z co-ordinate frame is that described in figure 3-18

Bentheim Sandstone		Principal anisotropy axes: Bingham averages				
		Clustering Co-efficient	Trend (degrees)	Plunge (degrees)	95% confidence cones (degrees)	
					Maximum	Minimum
mAMS	Minimum	0.82	312	82	---	---
	Intermediate	0.68	147	10	---	---
	Maximum	0.71	61	4	---	---
tAMS	Minimum	0.93	38	83	6	4
	Intermediate	0.78	135	12	15	5
	Maximum	0.77	226	10	17	3

Table 4-1. Bentheim sandstone principal ellipsoid mAMS and tAMS directional data. The clustering co-efficient represents the degree to which the directions are orientated in space, with a clustering co-efficient of 1 representing perfect directional alignment. For mAMS data, insufficient clustering results in the Bingham statistical method being unable to determined a confidence ellipse, denoted '---'

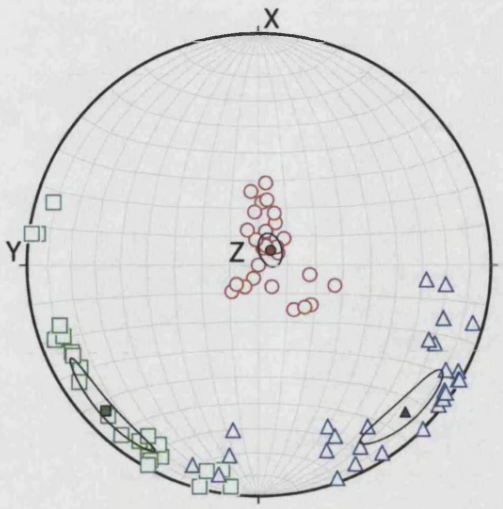

Figure 4-3. Bentheim sandstone final tAMS data: Maximum directions are denoted by open green squares, intermediate directions denoted by open blue triangles, and minimum directions denoted by open red circles. The Bingham averages in table 4-1 are plotted as solid symbols (red-minimum, blue-intermediate, green-maximum), with associated error ellipses.

4.1.2.2 CRAB ORCHARD SANDSTONE

Unlike Bentheim sandstone, Crab Orchard sandstone posseses a clearly visible crossbedded fabric in hand specimen. On a still larger scale, macro-scale (1-2m) bedding is observed in outcrop (Stearns, 1954). For convenience, the edges of the quarried blocks were cut as nearly co-incident with the larger scale bedding as possible. The block edges are then used as the X-Y-Z frame of reference (figure 3-16) for coring and displaying the directional data. As for BHS, pAMS is taken to approximate tAMS due to the high revel of ferrofluid saturated bulk susceptibility as compared to the matrix bulk susceptibility.

For COS, mAMS and pAMS results (figure 4-4), indicate a prominent minimum principal axis at approximately 280°-290° of azimuth and 60°-70° dip (table 4-2). In a similar fashion to the BHS principal axes, the two populations of pAMS maximum and intermediate directions are seen to be distinct, lying approximately at 90° to each other and within the same plane. Inspecting the pAMS maximum and intermediate directions together illustrates that this plane is very clearly defined, and lies at approximately 90° to the pAMS minimum direction. The small difference between the pAMS minimum direction and the Z axis (~15°), which is approximately normal to larger scale bedding as previously noted, is approximately equal to the crossbedding dip with respect to the XY plane as observed in hand specimen. This confirms that the pore-fabric geometry is primarily controlled by the macroscopic crossbedding visible in the sandstone (i.e. that the visible crossbedding fabric is also representative of the pore fabric).

Figure 4-5 shows the average directional results as estimated using Bingham statistics, with 95% error ellipses. Comparing this data to the prominent, visible fabric of COS, it can be seen that both the pAMS maximum and intermediate ellipsoid directions lie sub-parallel to the observed crossbedding plane of the sandstone. In addition, the pAMS maximum and intermediate directions lie approximately sub-parallel to the strike and dip of the cross-bedding, respectively. The scatter of the data in Figure 4-5, as reflected in the error angles (table 4-2), is attributed to the natural variability of the material. Scatter is lowest for the pAMS minimum directions, which are well defined, whilst the intermediate and maximum susceptibility values are less tightly clustered. Additionally, the pAMS maximum and intermediate directions show maximum Bingham error values within the plane of the crossbedding, which is consistent with the observations and dataset as a whole.

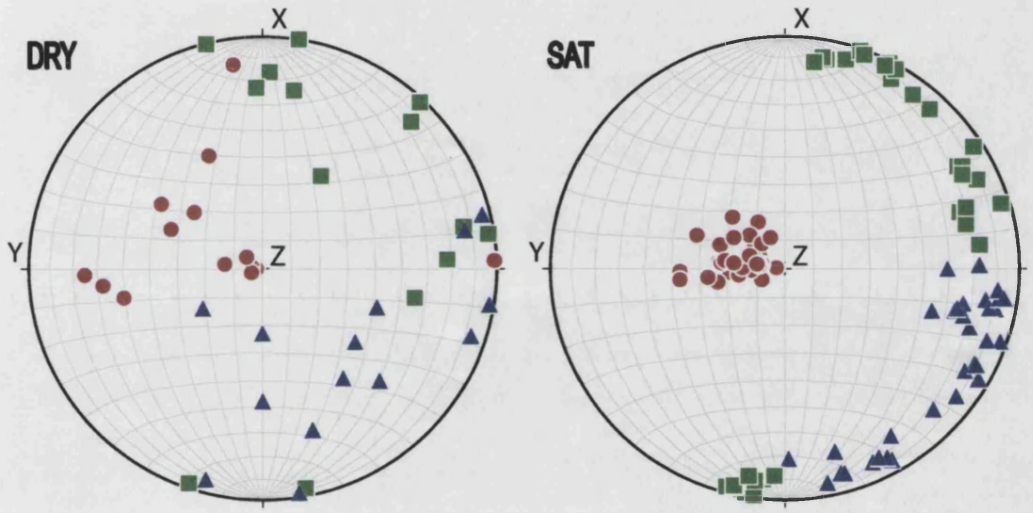

Figure 4-4. Stereographic projection (stereonet) of principal ellipsoid directions for Crab Orchard sandstone matrix mAMS (left) and pore fabric tAMS (~pAMS) (right). Maximum directions are denoted by green squares, intermediate directions denoted by blue triangles, and minimum directions denoted by red circles. The X-Y-Z co-ordinate frame is that described in figure 3-18

Crab Orchard Sandstone		Principal anisotropy axes: Bingham averages				
		Clustering Co-efficient	Trend (degrees)	Plunge (degrees)	95% confidence cones (degrees) Maximum	Minimum
mAMS	Minimum	0.73	290	61	---	---
	Intermediate	0.50	138	38	---	---
	Maximum	0.64	26	14	---	---
tAMS	Minimum	0.97	284	74	4	2
	Intermediate	0.80	121	16	13	4
	Maximum	0.81	29	5	13	3

Table 4-2. Crab Orchard sandstone principal ellipsoid mAMS and tAMS directional data. The clustering co-efficient represents the degree to which the directions are orientated in space, with a clustering co-efficient of 1 representing perfect directional alignment. For mAMS data, insufficient clustering results in the Bingham statistical method being unable to determined a confidence ellipse, denoted '---'

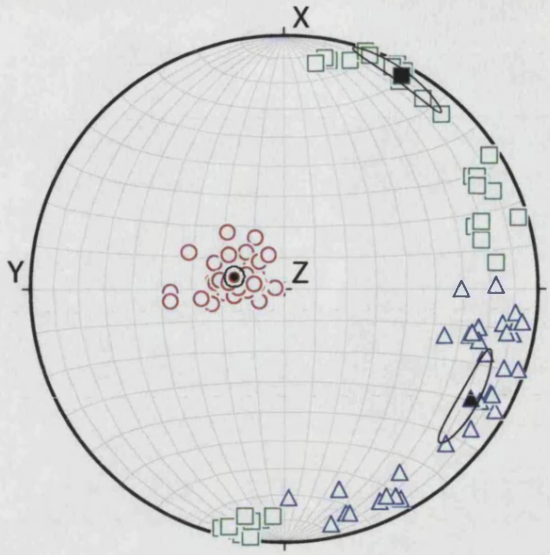

Figure 4-5. Crab Orchard sandstone final tAMS data: Maximum directions are denoted by open green squares, intermediate directions denoted by open blue triangles, and minimum directions denoted by open red circles. The Bingham averages in table 4-2 are plotted as solid symbols (red-minimum, blue-intermediate, green-maximum), with associated error ellipses.

4.1.2.3 TAKIDANI GRANITE

Takidani granite posseses a very high natural susceptibility of over 18000 $x10^{-6}$ SI, over three orders of magnitude higher than for the sandstones. In addition, Takidani granite has a low porosity of approximately 1%. With such a high natural susceptibility, the notion that previously held for the sandstone samples, namely that the bulk, saturated, susceptibility dominates over the natural bulk matrix susceptibility, may no longer be relied upon. In addition, simply achieving a high level of ferrofluid saturation is also difficult due to the low porosity. Achieving a high saturation is crucial, as this requirement must be met if the ferrofluid filled void space bulk susceptibility is to have any chance of dominating over the high natural mAMS value, so that pAMS may be determined.

In order to address the issue of saturation, a number of experimental methods were employed. Firstly, the traditional vacuum immersion was tried, with samples of Takidani granite being immersed in ferrofluid and held under vacuum and for a period of 2 weeks, followed by 72 hours under 6 bars of nitrogen gas pressure to force the ferrofluid into the evacuated void space. Secondly, the first method was combined with high pressure fluid intensifiers operating at pore (ferrofluid) pressures of 50MPa in the high pressure confining cell in an attempt to force the ferrofluid into the void space. Destructive examination of samples performed after these methods show that neither process has fully saturated the sample, with the ferrofluid appearing (visually) to enter no more than approximately $1/3^{rd}$ of the pore space (figure 4-6).

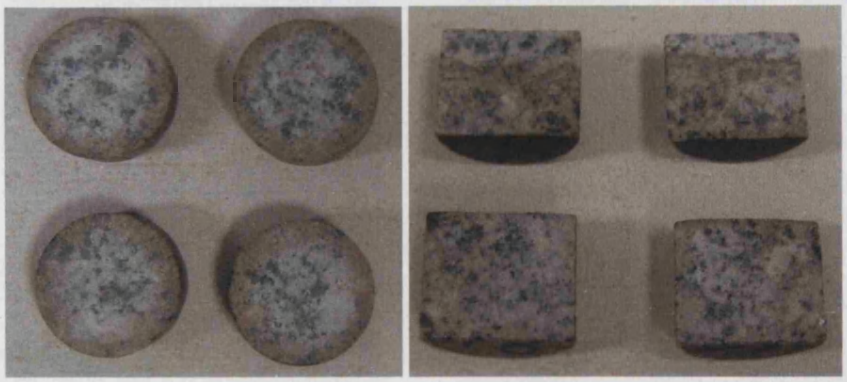

Figure 4-6. Attempting to saturate Takidani granite. Left – using standard vacuum immersion, followed by 6bar nitrogen gas pressure. Right – using high pressure intensifiers to force ferrofluid at 50MPa in to the rock (for confining pressure of between 52-55MPa)

With this limitation in mind, figure 4-7 shows the principal mAMS and tAMS directions for Takidani granite. Initial coring directions were based upon the block as obtained from outcrop, with the Z direction taken along the small dimension of the lozenge shaped block of rock (the vertical axis in figure 3-10). Both mAMS and tAMS indicate a minimum principal axis at approximately 56°-58° of azimuth and 28° dip (table 4-3). The mAMS minimum principal directions are well constrained, with maximum and intermediate directions approximately aligned within a plane with a normal coincident with the mAMS minimum direction. Like the sandstones, maximum and intermediate directions statistically lie approximately 90° to one another within this plane (table 4-3, figure 4-8). However, as the bulk susceptibility is only approximately 30% higher than the matrix bulk susceptibility, then it follows that tAMS principal ellipsoid directions (figure 4-7) will be dominated by the matrix susceptibility rather than being a good representation of the pore fabric (pAMS).

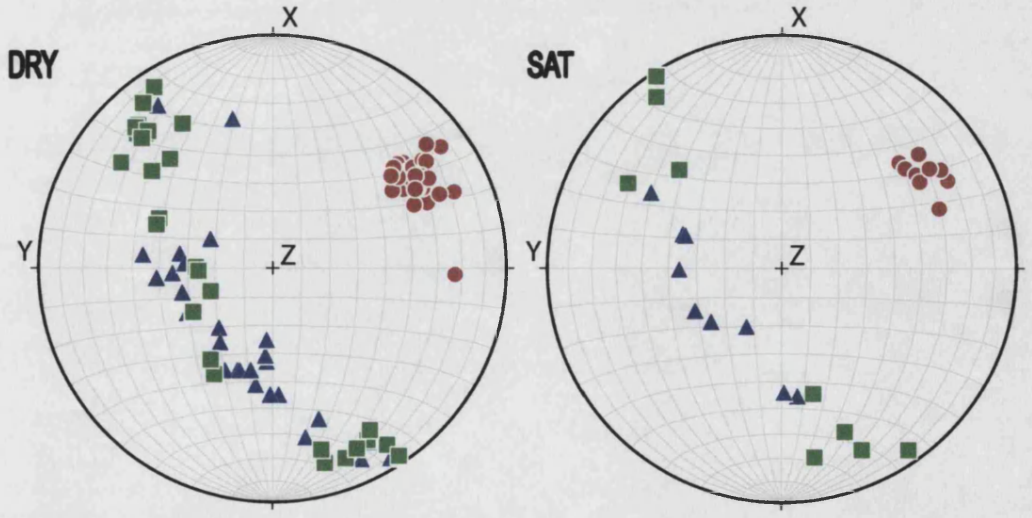

Figure 4-7. Stereographic projection (stereonet) of principal ellipsoid directions for Takidani granite matrix mAMS (left) and total sample tAMS (right). Maximum directions are denoted by green squares, intermediate directions denoted by blue triangles, and minimum directions denoted by red circles. The X-Y-Z co-ordinate frame is that described in figure 3-18

Takidani Granite		Principal anisotropy axes: Bingham averages				
		Clustering Co-efficient	Trend (degrees)	Plunge (degrees)	95% confidence cones (degrees)	
					Maximum	Minimum
mAMS	Minimum	0.98	59	28	3	3
	Intermediate	0.68	202	57	25	3
	Maximum	0.68	320	17	25	3
tAMS	Minimum	0.89	57	28	5	5
	Intermediate	0.70	249	62	---	---
	Maximum	0.79	150	5	---	---
pAMS	Minimum	0.66	44	17	---	---
	Intermediate	0.61	322	17	---	---
	Maximum	0.61	160	64	---	---

Table 4-3. Takidani granite principal ellipsoid mAMS, tAMS and pAMS directional data. The clustering co-efficient represents the degree to which the directions are orientated in space, with a clustering co-efficient of 1 representing perfect directional alignment. For tAMS and pAMS data, insufficient clustering results in the Bingham statistical method being unable to determined a confidence ellipse, denoted '---'

In an attempt to address the problem of matrix susceptibility dominating the measured tAMS signal, the matrix susceptibilities were subtracted from the tAMS susceptibilities in order to yield the influence of the ferrofluid filled pore fabric alone. This was done by subtracting each of the 15 directional matrix susceptibilities from the 15 directional ferrofluid saturated susceptibility measurements on a direction-by-direction and sample-by-sample basis (referring to the 15 measurement method in Chapter 3). The resulting 'difference' susceptibility matrix was then fit to the 3-D ellipsoidal surface in the usual way. In principle, this would allow the natural susceptibility to be removed, leaving only the effect of the ferrofluid filled void space anisotropy to contribute to the AMS size, shape and alignment, in essence giving pAMS, as desired. In practice, however, the results are poorly constrained (figure 4-8), showing large scatter in the data. This in turn results in a lack of confidence in the derived principal directions. However, despite this limitation a tentative pAMS minimum direction may be discerned (by eye) with an average azimuth and dip of 45° and 30° respectively. Given the extreme difficulty in obtaining this data, this is a reasonable comparison to the mAMS minimum direction alignment (figure 4-8).

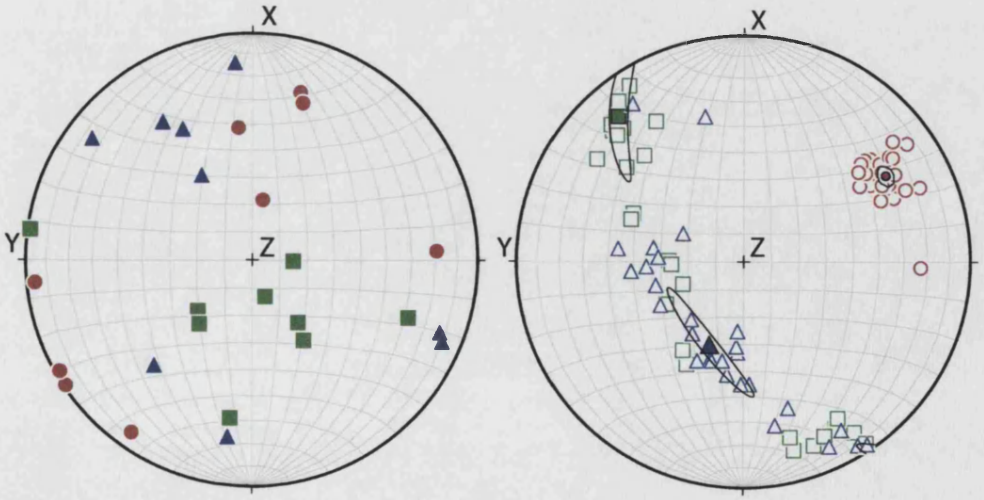

Figure 4-8. Takidani granite final pAMS data (left) with mAMS data (right), for comparison. Maximum directions are denoted by green squares, intermediate directions denoted by blue triangles, and minimum directions denoted by red circles. The Bingham averages in table 4-2 are plotted mAMS figure only) as solid symbols (red-minimum, blue- intermediate, green-maximum), with associated error ellipses.

4.1.3 FABRIC ANISOTROPY

As already introduced (Chapter 2), AMS ellipsoids have a shape defined through the length of three principal ellipsoid axes, denoted K_{min}, K_{int} and K_{max}, where K is the susceptibility in that principal direction. The bulk anisotropy parameters P_ϕ, P_m, and P_t have already been expressed in these terms (section 4.1.1). As well as these bulk measures of susceptibility anisotropy, two other useful pore fabric indicators are now defined. Lineation 'L' is defined as the length ratio of major to intermediate axes (K_{max}/K_{int}, representing linear fabric contribution), and foliation 'F' is defined as the length ratio of the intermediate to minor axes (K_{int}/K_{min}, representing planar fabric contribution). These expressions are effectively 'borrowed' from structural geology, and are useful in describing the relative shape of the ellipsoidal structures relative to the overall fabric size, shape and alignment. In essence, lineation and foliation measure the relative degree to which the rock fabric (mAMS data), or pore fabric (pAMS data) is oblate or prolate respectively. However, in this work these parameters are explicitly defined for each type of measurement, whether that is mAMS, tAMS or pAMS, giving L_m, L_t, L_ϕ, and F_m, F_t and F_ϕ for the different fabrics and measurements. These parameters are summarised in table 4-4.

Symbol	Parameter description
P_m	Bulk susceptibility anisotropy of matrix
P_t	Bulk susceptibility anisotropy of ferrofluid saturated sample
P_ϕ	Bulk susceptibility anisotropy of pore space
L_m	Lineation of matrix
L_t	Lineation of ferrofluid saturated sample
L_ϕ	Lineation of pore space
F_m	Foliation of matrix
F_t	Foliation of ferrofluid saturated sample
F_ϕ	Foliation of pore space

Table 4-4. Summary of susceptibility parameters and definitions

These definitions of bulk anisotropy are used because they have become standard practice in context of AMS work, and are therefore widely quoted in the literature. However, we define a second form of bulk anisotropy 'A', which is used parallel to the traditional P parameter from now on. 'A' is defined by the general relation A = 100% * ([max-min]/mean). This parameter is in standard use when quoting elastic wave anisotropy. For consistency, I also calculate AMS anisotropy using this form of relation (as well as the 'P' definition as well).

Bentheim sandstone

For Bentheim sandstone, a matrix anisotropy and pore anisotropy (P_m and P_ϕ) of 3.8% and 1.5% respectively is calculated (table 4-5 and 4-6). To further understand the pore fabric anisotropy the graphical method of Flinn (1962) is used, which plots lineation vs. foliation using a Flinn diagram. This allows the relative balance of lineation and foliation to be visualised, rather than simply the bulk pore fabric anisotropy as quoted above, and in turn allows the degree of 'oblateness' or 'prolateness' to be visualised. For BHS, a generally oblate fabric to the rock structure (figure 4-9) is clear, whether determined though mAMS or pAMS data. In addition, mAMS data gives a more oblate result than for pAMS. In general, however, it should be noted than an oblate fabric is usually expected for sedimentary rock due to the nature of the rock formation.

Bentheim Sandstone mAMS	Bulk Susceptibility (10^{-6} SI)	Principal axis length (normalised to bulk susceptibility)			Anisotropy parameters			
		Minimum	Intermediate	Maximum	L_m	F_m	P_m	A, %
Average (N=9)	17	0.978	1.007	1.015	1.008	1.022	1.038	3.7
Standard Deviation	9	0.013	0.007	0.007	0.003	0.002	1.022	2.0
Minimum	9	0.946	1.001	1.010	1.004	1.015	1.026	2.5
Maximum	36	0.987	1.023	1.031	1.014	1.033	1.090	8.6

Table 4-5. Bentheim sandstone mAMS magnitude data summary

Bentheim Sandstone tAMS (~pAMS)	Bulk Susceptibility (10^{-6} SI)	Principal axis length (normalised to bulk susceptibility)			Anisotropy parameters			
		Minimum	Intermediate	Maximum	L_t	F_t	P_t	A, %
Average (N=27)	19604	0.993	1.002	1.006	1.004	1.010	1.015	1.5
Standard Deviation	639	0.002	0.002	0.001	0.002	0.004	1.003	0.3
Minimum	18326	0.988	0.998	1.004	1.002	1.005	1.011	1.1
Maximum	20744	0.995	1.005	1.008	1.007	1.018	1.022	2.2

Table 4-6. Bentheim sandstone tAMS magnitude data summary

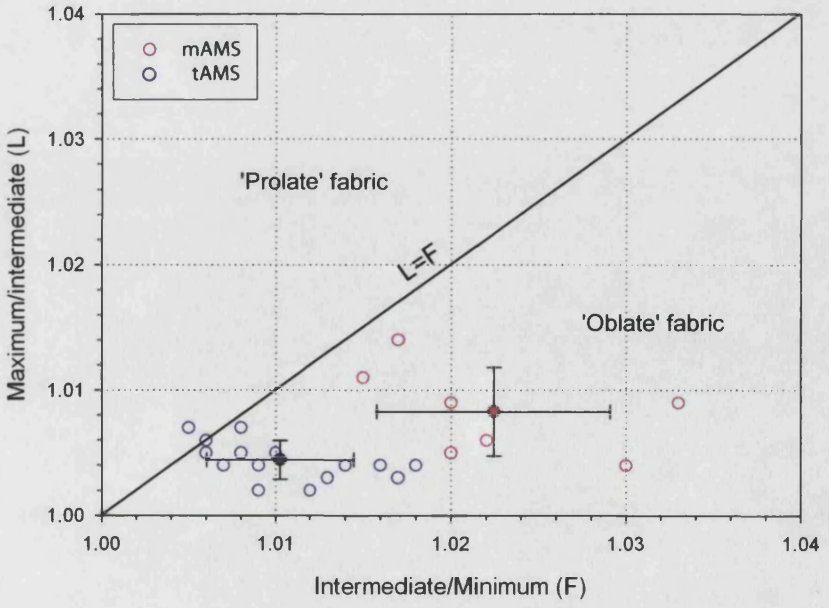

Figure 4-9. Bentheim sandstone plot of lineation vs. foliation for all AMS ellipsoids measured (open symbols). Solid symbols represent the average lineation and foliation, with associated error. mAMS data is shown in red, tAMS data in blue.

Crab Orchard sandstone

For Crab Orchard sandstone, a matrix and pore anisotropy (P_m and P_ϕ) of 4.6% and 3.8% respectively is calculated (table 4-7 and 4-8), a higher value of pore fabric anisotropy than as compared to BHS. From the Flinn diagram we see that COS has a highly oblate fabric to the rock structure (figure 4-10), for both mAMS and pAMS data. Again, like for BHS, mAMS data gives a more oblate result than for pAMS. However, the level of 'oblateness' is higher than as compared to BHS. Given the obviously crossbedded samples, the result that COS shows higher pore fabric anisotropy compared to BHS is almost intuitive.

Crab Orchard Sandstone mAMS	Bulk Susceptibility (10^{-6} SI)	Principal axis length (normalised to bulk susceptibility)			Anisotropy parameters			
		Minimum	Intermediate	Maximum	L_m	F_m	P_m	A, %
Average (N=14)	46	0.974	1.006	1.020	1.015	1.033	1.047	4.6
Standard Deviation	28	0.014	0.009	0.012	0.017	0.021	1.025	2.4
Minimum	20	0.950	0.981	1.008	1.002	1.005	1.015	1.5
Maximum	127	0.993	1.019	1.051	1.072	1.073	1.085	8.2

Table 4-7. Crab Orchard sandstone mAMS magnitude data summary

Crab Orchard Sandstone tAMS (~pAMS)	Bulk Susceptibility (10^{-6} SI)	Principal axis length (normalised to bulk susceptibility)			Anisotropy parameters			
		Minimum	Intermediate	Maximum	L_t	F_t	P_t	A, %
Average (N=31)	12879	0.979	1.005	1.017	1.012	1.027	1.039	3.8
Standard Deviation	2107	0.005	0.004	0.003	0.005	1.009	1.006	0.6
Minimum	9993	0.971	0.998	1.011	1.003	1.015	1.030	2.9
Maximum	17820	0.984	1.012	1.020	1.022	1.043	1.050	4.9

Table 4-8. Crab Orchard sandstone tAMS magnitude data summary

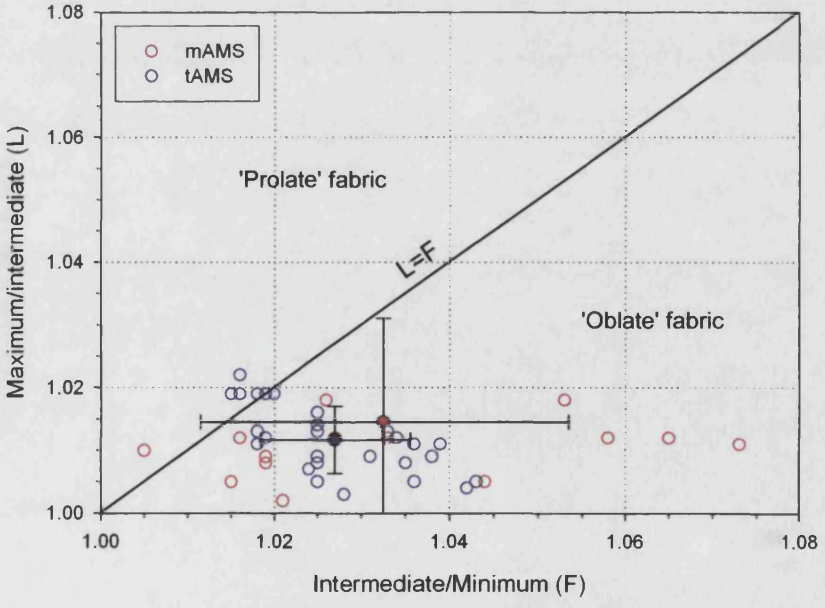

Figure 4-10. Crab Orchard sandstone plot of lineation vs. foliation for all AMS ellipsoids measured (open symbols). Solid symbols represent the average lineation and foliation, with associated error. mAMS data is shown in red, tAMS data in blue.

Takidani granite

For Takidani granite, a matrix and total anisotropy (P_m and P_t) of 9.4% and 8.2% respectively is calculated (table 4-9 and 4-10), a higher value of pore fabric anisotropy than for either of the sandstones. From the Flinn diagram it appears that TDG posseses a highly oblate structure (figure 4-11), and for both the mAMS and tAMS data the level of 'oblateness' is higher than BHS or COS. However, the Flinn diagram as plotted for Takidani pAMS data (L_ϕ, F_ϕ, P_ϕ) reveals an equant structure with a high level of uncertainty. This may simply be an artefact of the difficulty in subtracting the already high value of mAMS signal from the tAMS signal, and attempting to interpret small variations in the small resultant pAMS signal. Given that the average matrix bulk susceptibility is 18184, and the average ferrofluid saturated bulk susceptibility is 23257, then this gives an average 'pores only' susceptibility of 4429 which represents just 25% of the initial matrix value. Therefore, the classic problem of attempting to detect small variations over and above an already high background 'level' may exist with the TDG pAMS data generally. Therefore, significant caution must be exercised when interpreting the TDG pAMS data.

Takidani Granite mAMS	Bulk Susceptibility (10^{-6} SI)	Principal axis length (normalised to bulk susceptibility)			Anisotropy parameters			
		Minimum	Intermediate	Maximum	L_m	F_m	P_m	A, %
Average (N=31)	18184	0.945	1.018	1.037	1.019	1.078	1.098	9.4
Standard Deviation	7741	0.009	0.008	0.006	0.012	0.017	1.014	1.3
Minimum	6379	0.931	0.991	1.022	1.001	1.038	1.053	5.1
Maximum	28260	0.971	1.029	1.055	1.065	1.103	1.120	11.3

Table 4-9. Takidani granite mAMS magnitude data summary

Takidani Granite tAMS	Bulk Susceptibility (10^{-6} SI)	Principal axis length (normalised to bulk susceptibility)			Anisotropy parameters			
		Minimum	Intermediate	Maximum	L_t	F_t	P_t	A, %
Average (N=9)	23257	0.951	1.016	1.033	1.017	1.068	1.087	8.2
Standard Deviation	8127	0.008	0.006	0.008	0.012	0.013	1.015	1.4
Minimum	12320	0.941	0.999	1.022	1.004	1.046	1.057	5.5
Maximum	33060	0.967	1.025	1.048	1.048	1.085	1.109	10.2

Table 4-10. Takidani granite tAMS magnitude data summary

Takidani Granite pAMS	Bulk Susceptibility (10^{-6} SI)	Principal axis length (normalised to bulk susceptibility)			Anisotropy parameters			
		Minimum	Intermediate	Maximum	L_ϕ	F_ϕ	P_ϕ	A, %
Average (N=9)	4429	0.962	0.999	1.039	1.039	1.039	1.081	7.7
Standard Deviation	884	0.020	0.012	0.022	0.031	0.027	1.044	4.0
Minimum	2571	0.913	0.978	1.013	1.007	1.017	1.029	2.9
Maximum	5769	0.984	1.021	1.090	1.115	1.119	1.169	15.6

Table 4-11. Takidani granite pAMS magnitude data summary

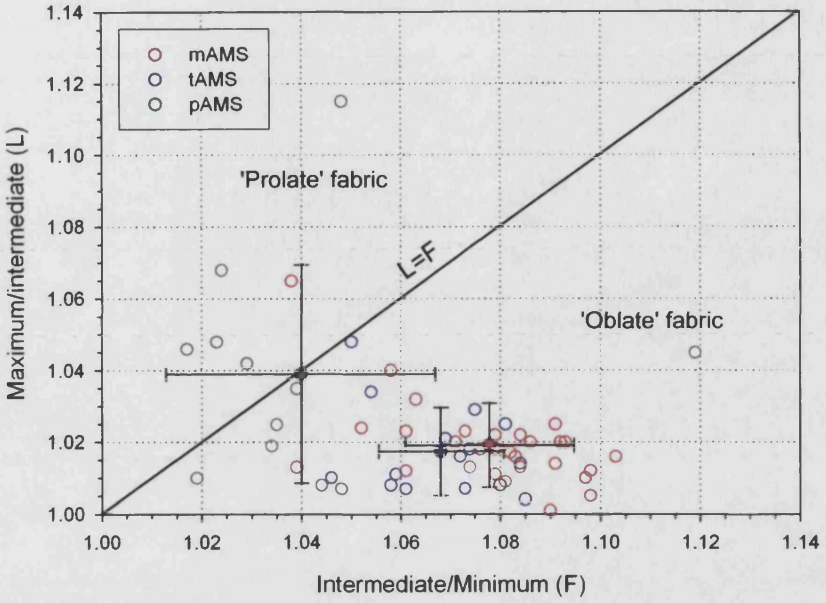

Figure 4-11. Takidani granite plot of lineation vs. foliation for all AMS ellipsoids measured (open symbols). Solid symbols represent the average lineation and foliation, with associated error. mAMS data is shown in red, tAMS data in blue and pAMS data in green.

4.1.4 FERROFLUID SATURATION ESTIMATION

For each sample, the magnitude of total susceptibility can be used to calculate the total volume of ferro-fluid in that sample, as the susceptibility of a unit volume of ferrofluid is accurately known. This allows the porosity to be calculated via $\phi = 100\%*\kappa_{sample}/(V*\kappa_{unit})$, where κ_{sample} is the susceptibility of the ferrofluid in the sample, κ_{unit} is the susceptibility of unit volume of ferrofluid and V is the volume of the sample. If the calculated porosity using this method matches the standard gravimetric porosity described earlier in Chapter 3, then it follows that the sample is fully saturated. The calculated 'susceptibility porosity' is presented in table 4-12 below for each rock type investigated together with the gravimetric porosity for comparison. In most cases, the susceptibility porosity and gravimetric porosity are in general agreement. However, a noticeable exception occurs for Takidani granite for which the susceptibility porosity calculated is approximately 1/4 to 1/3 of that obtained using gravimetric methods. This suggests that Takidani is only saturated by ferrofluid to this level, which is consistent with the visual confirmation seen in figure 4-6 earlier.

Rock type	Gravimetric Porosity (%)	'Susceptibility' Porosity (%)	Mercury injection Porosity (%)
Bentheim Sandstone	22.50±0.40	21.63±0.84	24.11±0.30
Crab Orchard Sandstone	4.95±0.15	4.23±0.37	5.43±0.33
Takidani Granite	0.95±0.04	0.33±0.09	1.16±0.04

Table 4-12. Porosity comparison between gravimetric and susceptibility methods in order to test for ferrofluid saturation level. Mercury injection porosity is included for completeness

4.2 ELASTIC WAVE VELOCITY

4.2.1 INTRODUCTION

Measurement of elastic wave velocities is a commonly used method for estimating the physical properties of rock, due to the sensitivity of elastic wave velocity upon rock microstructure and particularly void space. P-wave and S-wave velocities are, in general, highly sensitive to the void space of rock, as the stiffness of any pore fluid (gas or liquid) provides a marked contrast to that of the host rock matrix. In this way, the measurement of directional elastic wave velocities may be used as a proxy for measuring the void space geometry. Here, a suite of P-wave and S-wave velocity data is presented (both S_A and S_B mode, as defined in Chapter 3), made upon Bentheim sandstone, Crab Orchard sandstone and Takidani granite. Velocities are measured as a function of azimuth around each of the cylindrical core circumferences described in figure 3-18. The 'core-sets' described by figure 3-18 consist of three orthogonal cores, with cores axes at 90° to each other along the X, Y and Z directions. Velocity data are then presented either as a 2-D variation representing the velocity change with azimuth around a single core, or (via the data processing described later) a principal direction in 3-D by using the velocity data from the entire core-set.

For the purpose of describing velocity directions in 3-D, it is necessary to ensure that velocity data from all three orthogonal planes is treated in a comparable way. To do this, the assumption is made that a velocity measured in a particular direction in space should be the same, regardless of the core upon which it is made. This assumption is reasonable given that all the cores are prepared in close proximity to each other from the same block of material, which appears homogeneous on larger (block) scales. For example, a velocity measured along the X-axis direction in figure 3-18 may be determined through a velocity at an azimuth of 0° on the Z axis core (XY plane) or the 90° azimuth upon the Y axis core (XZ plane). However, even of these two measurements were to differ, it is not possible to stay which velocity is more appropriate, as each measurement was made upon a specific core, and therefore just as valid. However, to ensure a robust solution when using the velocities made upon three orthogonal cores, it is necessary to ensure that particular velocities made in those specific directions which coinside are equal in magnitude. To achieve this goal, a 'levelling' technique is used, in which a velocity direction is taken at an initial point, and assumed to be 'correct'. In this study, the point chosen for this purpose is taken as the 180° azimuth upon the Z axis core (in the XY plane). In addition, all velocities within the core-set are normalised to the maximum velocity encountered in the core-set as a whole (figure 4-12), before any levelling modifications are made. In the typical example shown in figure 4-12, the maximum velocity to which all the velocities are normalised to is that in the Y_{270} azimuth (i.e. the velocity at 270° upon the Y axis core, which is in the XY plane, or VY_{270}).

Referring to figure 4-12 throughout, the levelling method proceeds in the following manner. Starting from the Z_{180} point (on the XY plane), the relative mis-match between the Z_{180} and Y_{270} points is evaluated. This relative change (~1%) is then applied to all azimuthal data around the Y

axis core. Velocity data around the Y axis core is then traced around the core circumference (step 1, fig. 4-12), until the next co-incident location is encountered, which is the Y_{180} point, corresponding to the X_{180} point. The mis-match between these two normalised velocities is again evaluated, and the relative change applied to the X axis data equally to bring the Y_{180}/X_{180} point into agreement. Velocity data around the X axis core is now traced (step 2, fig. 4-12), until the final co-incident location is encountered, at X_{90}/Z_{90}. Again the mis-match is evaluated. This time, however, the relative correction cannot be made to the Z axis data, as this would influence the Z_{180} velocity point and lead to a continuous loop of correction. Instead, the final mis-match is divided equally between all data points encountered through steps 1, 2, and 3, which is the final trace back to the initial start/end point. The total mis-match is ~1.5%, which is then divided between 27 data points over the three steps. Due to the symmetry of the azimuthal velocity data (which will become obvious later in this section), it is only necessary to conduct this procedure upon a 90° segment of each azimuth, as velocities 180° away in azimuth undergo similar trends. In addition, points 90° away in azimuth will also undergo similar trends relative to the symmetry point (the Z-axis).

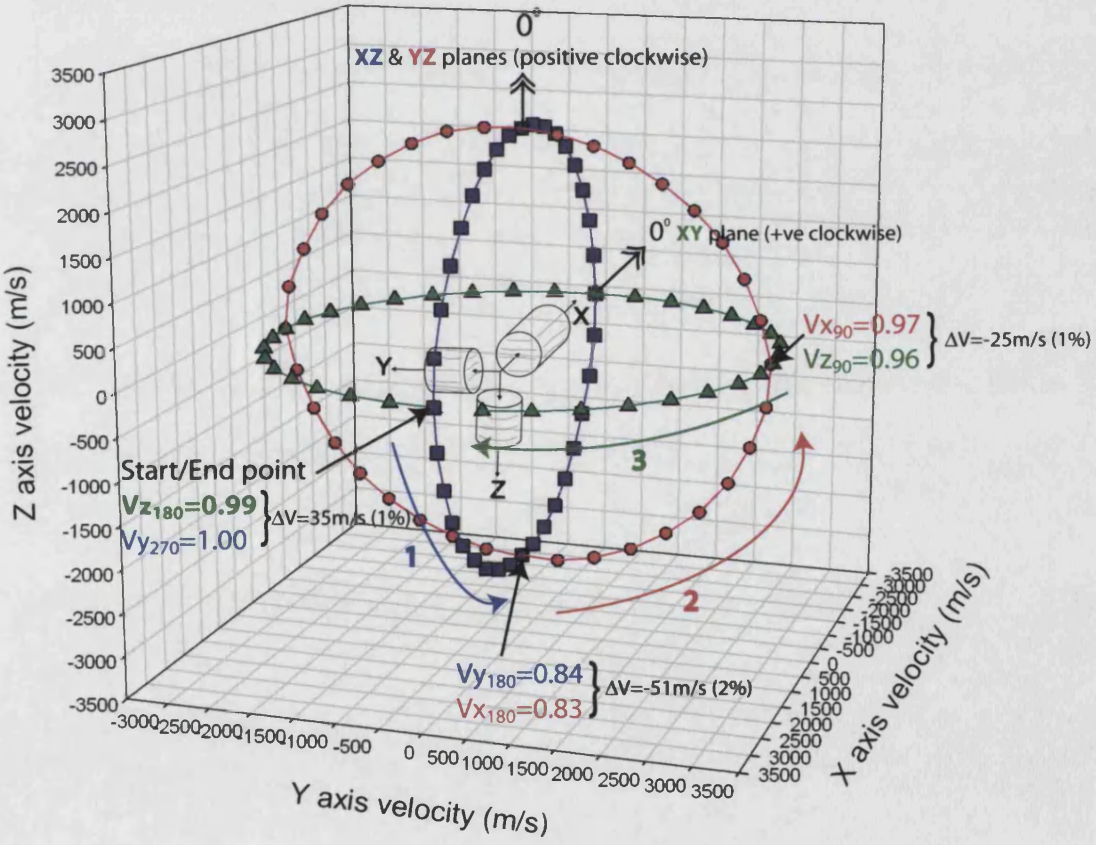

Figure 4-12. The levelling process showing a typical 3D core-set example in 3D location space. The distance from the origin to each data point gives the velocity of that point. The starting and finish point is the Z_{180} point (the 180° azimuth upon the Z axis core), shown in bold. Three specific locations are marked, where the velocity in 3-D is set to zero through a levelling method. In each case, the changes required are small, less that 2%. Velocity is normalised in this case to maximum V=3101 m/s located at point Y_{180}. The 0° point marks the 'zero' azimuth in each axis (as fig. 3-18)

It should be stressed that at no point does the velocity change exceed the measurement error of between 1 to 2%, and as such the 'changes' to the velocity data are very small indeed. The procedure, however, does allow a more rigorous and stable result for the later computation of the three dimensional principal elastic wave velocity directions, during which these velocity data are fitted to a constant ellipsoidal surface. Any 'step' changes (as a result of a slight miss-match between velocity made upon different cores), may therefore be avoided, allowing 3-dimensional velocity directions to be calculated with added confidence and accuracy.

Bentheim sandstone

Velocity data for Bentheim sandstone are presented in Figure 4-13 and 4-14 for dry and saturated samples respectively. For dry data, a clear P-wave variation with azimuth is seen, which is highest for velocity data within the YZ and XZ planes. P-wave velocity variation is lowest within the XY plane. For S-wave data, a similar overall trend exists compared to the P-wave data, with S-wave velocity variation highest in the XZ and YZ planes and lowest in the XY plane. For both P-wave and S-wave data, a velocity minimum is seen at ~0° and ~180°, and velocity maxima at ~90° and ~270°. Using the measured velocity variation, we can calculate the bulk experimental elastic anisotropy defined as $P_{exp} = 100\%*[(V_{max}-V_{min})/V_{mean}]$, where V is the experimentally measured velocity with azimuth. Note, again, that this definition of the bulk anisotropy (P) is slightly different to that as used for AMS. Evaluating the anisotropy confirms that both Vp and Vs anisotropy is highest in the XZ and YZ planes, at approximately 9% and 5% respectively (table 4-13).

On water saturation of the samples, a clear increase in average velocity is observed, from ~3054 m/s to ~3856 m/s (approximately a 26% rise), with maximum P-wave anisotropy decreasing from ~9% to ~5% (table 4-13). However, the S-wave velocity and velocity anisotropy does not change significantly during the saturation process. This is entirely consistent with theory as, for perfect fluid pressure communication, liquids do not support shear mode displacement, but do support compressional mode displacement.

Bentheim sandstone anisotropy		Velocity (m/s)		Anisotropy parameter, A_{exp} (%) $[100\%*(V_{max}/V_{min})/V_{mean}]$					
				YZ plane		XZ plane		XY plane	
		average	Std. dev.	average	Std. dev.	average	Std. dev.	average	Std. dev.
Dry	Vp	3055	235	5.9	0.3	9.2	1.6	3.2	0.4
	Vs_A	1888	489	4.8	0.5	4.8	1.7	2.7	1.2
	Vs_B	1882	486	4.7	0.8	5.4	0.7	2.7	1.2
Saturated	Vp	3846	32	2.8	0.4	5.0	0.4	2.6	0.6
	Vs_A	1941	35	5.8	0.9	5.0	0.8	3.0	0.6
	Vs_B	1951	31	4.0	0.8	4.0	0.3	2.3	0.8

Table 4-13. Bentheim sandstone elastic wave velocity anisotropy: laboratory data summary

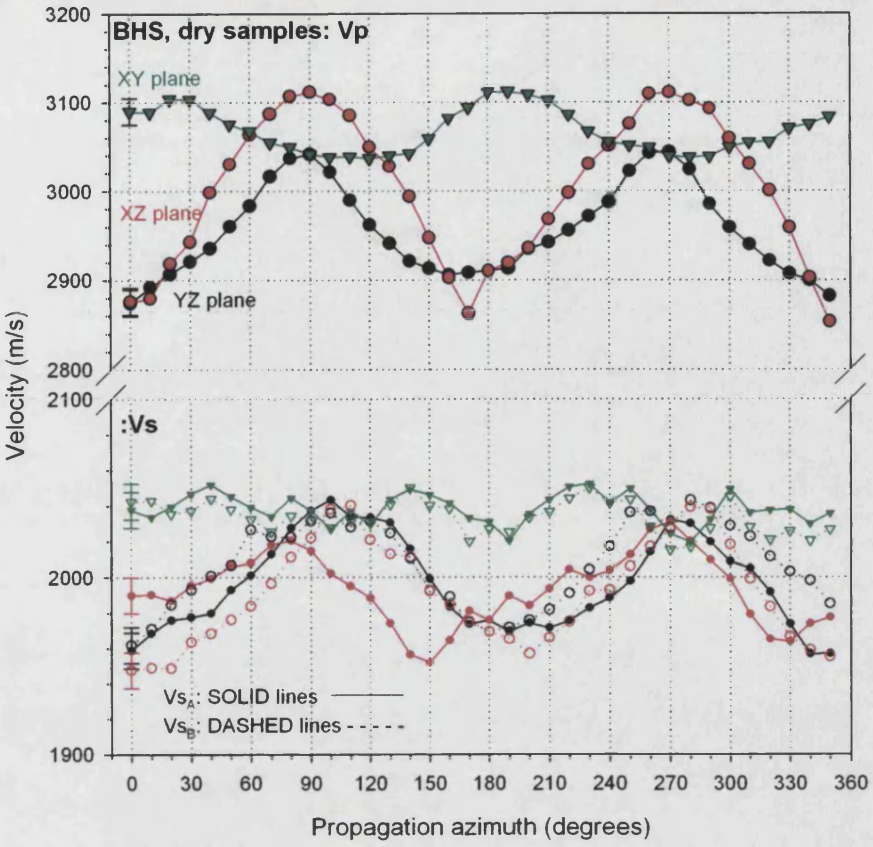

Figure 4-13. Bentheim sandstone elastic wave anisotropy (dry samples)

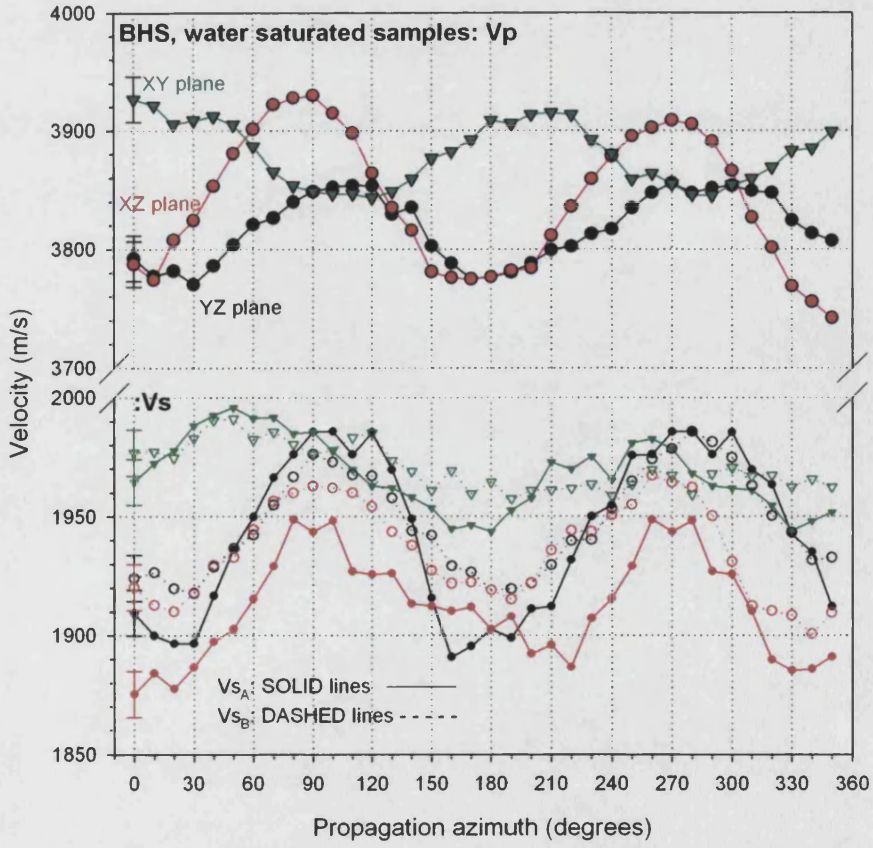

Figure 4-14. Bentheim sandstone elastic wave anisotropy (saturated samples)

Crab Orchard sandstone

Velocity data for Crab Orchard sandstone are presented in Figure 4-15 and 4-16 for dry and saturated samples respectively. Like the Bentheim sandstone data, for dry data a clear P-wave anisotropy is seen, which is highest within the XZ and YZ planes. S-wave data also shows this trend. However, in addition, the S_A velocity variation is of an overall higher magnitude as compared to S_B data by approximately 100 m/s. Although the maximum observed (dry) P-wave velocities are of approximately the same magnitude compared to the Bentheim sandstone data, the degree of velocity anisotropy is higher. For COS, a P-wave velocity anisotropy of ~19% is calculated in the XZ and YZ planes, with S_A and S_B wave velocity anisotropy approximately the same within statistical error, at ~8% and ~10% respectively. The lowest anisotropy again occurs within the XY plane, which is coincident to the visual alignment to the crossbedding in the rock.

Like the situation for BHS, a large increase in COS average velocity is observed upon sample saturation, with P-wave velocity increasing by ~54% from 2843 m/s to 4389 m/s (table 4-14). At the same time, P-wave anisotropy decreases markedly on saturation from ~19% to ~11%. Upon saturation, S-wave velocity is slightly higher, although the S-wave velocity anisotropy remains approximately the same at ~10%.

Crab Orchard sandstone anisotropy		Velocity (m/s)		Anisotropy parameter, A_{exp} (%) $[100\%*(V_{max}/V_{min})/V_{mean}]$					
				YZ plane		XZ plane		XY plane	
		average	Std. dev.	average	Std. dev.	average	Std. dev.	average	Std. dev.
Dry	Vp	2843	136	17.9	2.0	18.7	2.6	4.5	2.3
	Vs_A	1866	41	8.3	0.9	8.4	0.9	3.1	0.2
	Vs_B	1771	79	10.1	2.3	10.4	1.3	2.1	0.5
Saturated	Vp	4390	118	8.7	1.9	10.6	2.6	3.6	0.6
	Vs_A	2167	110	12.2	3.1	12.3	0.9	6.7	1.7
	Vs_B	2108	81	8.7	2.3	8.1	1.3	5.9	1.5

Table 4-14. Crab Orchard sandstone elastic wave velocity anisotropy: laboratory data summary

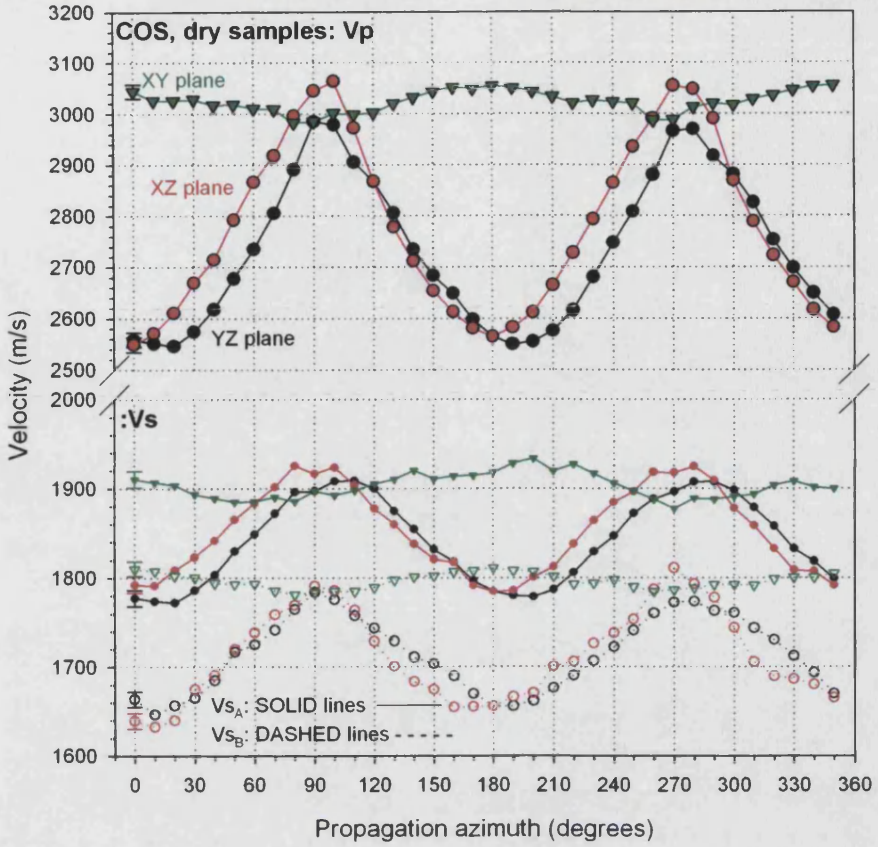

Figure 4-15. Crab Orchard sandstone elastic wave anisotropy (dry samples)

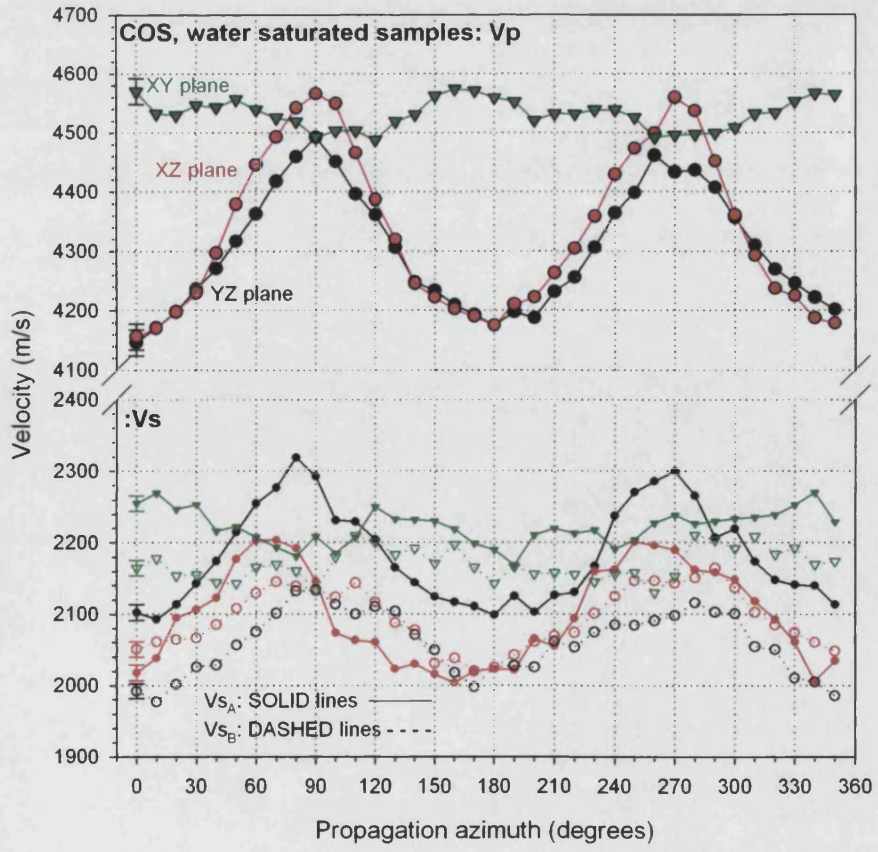

Figure 4-16. Crab Orchard sandstone elastic wave anisotropy (saturated samples)

Takidani granite

Finally, azimuthal velocity data is presented for Takidani granite (figures 4-17 and 4-18), for dry and saturated samples respectively. Measurement of elastic wave velocity for this rock type proved to be far more challenging than for the sandstone samples shown previously, leading to a higher level of error in the velocity data. In addition, it is not immediately evident from the data that any plane in particular shows a minimum anisotropy, unlike the situation for BHS and COS XY plane data. In general, the difficulty in measuring accurate P-wave and S-wave velocities for TDG is attributed to poor signal propagation through the rock, together with transducer/rock interface coupling. Despite these issues, dry P-wave velocity shows a clear and obvious anisotropy in all three measurement planes (YZ, XZ and XY). For P-wave velocity, the highest anisotropy is calculated from YZ plane data at ~11%, with XZ and XY anisotropy slightly lower (table 4-15). Dry S-wave anisotropy is statistically highest in the XY plane, at approximately 10%

Like the sandstones, Takidani granite velocity data shows a clear increase in average P-wave velocity upon saturation, from 4811 m/s to 5978 m/s (24% increase), and a large concomitant decrease in P-wave anisotropy from ~11% to ~3%. Like the Crab Orchard sandstone data, S-wave velocity is slightly higher upon saturation, although the S-wave velocity anisotropy remains approximately unchanged at 6-7%, which is consistent with theory as previously noted.

Takidani granite anisotropy		Velocity (m/s)		Anisotropy parameter, A_{exp}(%) [100%*(V_{max}/V_{min})/V_{mean}]					
				YZ plane		XZ plane		XY plane	
		average	Std. dev.	average	Std. dev.	average	Std. dev.	average	Std. dev.
Dry	Vp	4811	334	11.0	2.3	8.7	1.0	6.3	2.5
	Vs_A	3189	62	7.6	1.1	6.8	4.4	9.5	1.3
	Vs_B	3135	122	7.3	1.3	9.5	1.2	8.4	1.0
Saturated	Vp	5978	113	2.8	0.8	3.3	0.5	2.2	0.7
	Vs_A	3264	64	6.0	1.1	6.8	2.4	5.7	2.5
	Vs_B	3324	55	5.8	0.5	3.8	1.0	7.7	2.0

Table 4-15. Takidani granite elastic wave laboratory data summary

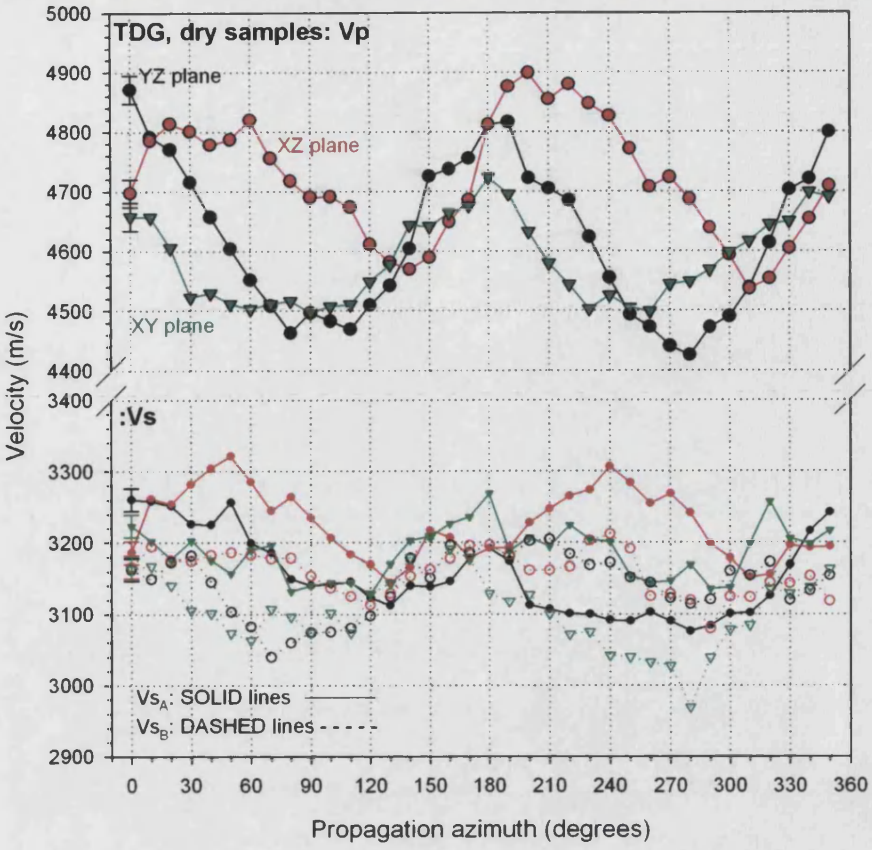

Figure 4-17. Takidani granite elastic wave anisotropy (dry samples)

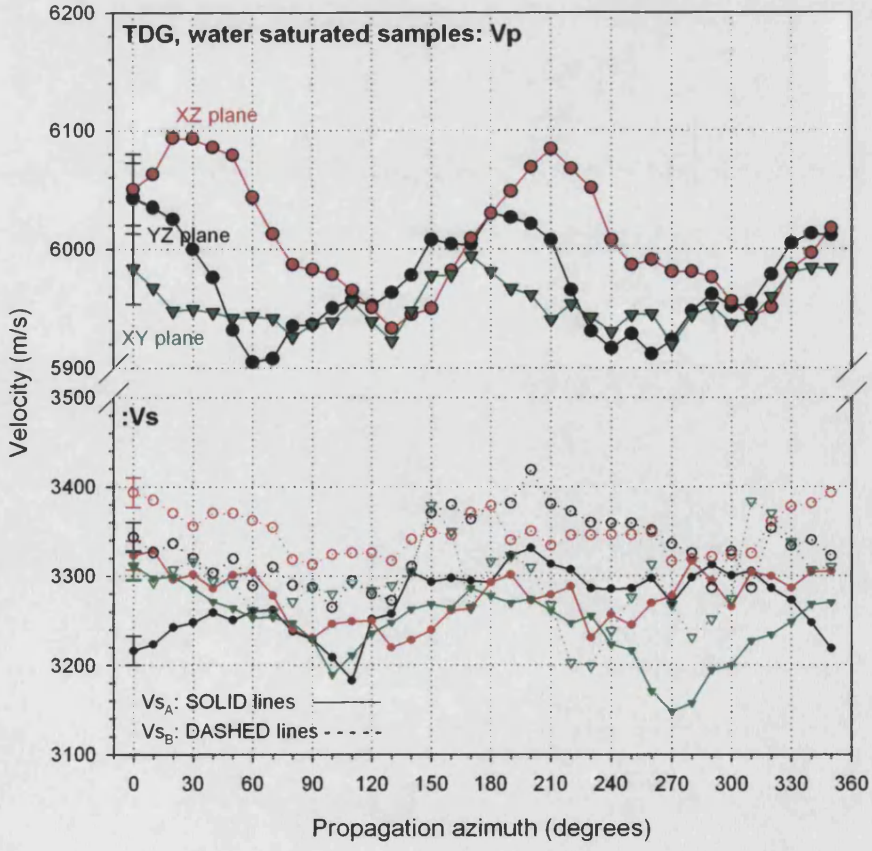

Figure 4-18. Takidani granite elastic wave anisotropy (saturated samples)

4.2.2 PRINCIPAL ANISOTROPY DIRECTIONS FROM VELOCITY DATA

In order to accurately determine the precise direction at which the elastic wave velocity is at minimum or maximum in 3-D, a technique is employed which fits the azimuthal velocity data as taken from a complete core-set (as in figure 3-16 and 4-12) to an ellipsoidal surface. As shown in figures 4-12, using a set of three cores with axes aligned with the orthogonal X, Y and Z directions together with velocity data from each plane (i.e. azimuthal velocities from the YZ plane, XZ plane and XY plane respectively) thus allows a point in cartesian co-ordinate space to be assigned to each of the 108 velocity measurements made on the core-set. These data are then fit to a 3-D ellipsoid using a least squares method. The limitations of this method will be more thoroughly analysed in Chapter 7. There are numerous advantages to using this approach, including the ability to visualise the P-wave and S-wave velocity principal directions using a stereonet in a manner exactly similar to the pAMS data. Importantly, it also allows the principal ellipsoid alignment in 3-D to be visualised even when the original core-set is not aligned with the anisotropy plane. Thus, prior knowledge of the principal anisotropy axes is not required. In addition, the use of a simple ellipsoidal approximation also allows the minimum, intermediate and maximum velocities to be calculated, and therefore the associated elastic anisotropy parameters of the ellipsoid.

The detailed procedure is as follows. In each analysis, the 108 velocity measurements (36 from each of three orthogonal cores) are used to determine velocity ellipsoids by applying the general equation for an ellipsoid to the slownesses calculated from the elastic velocities, using the method of Louis et al. (2003):

$$Ax^2 + By^2 + Cz^2 + Dxy + Exz + Fyz = 1 \qquad \text{- General equation of an ellipsoid}$$

Where: A, B, C, D, E, F are constants which define the length and direction of the principal axes
x, y and z are the cartesian co-ordinates of the ellipsoidal surface

This equation may be written in matrix form as:

$$(x \quad y \quad z) \bullet \begin{pmatrix} A & D/2 & E/2 \\ D/2 & B & F/2 \\ E/2 & F/2 & C \end{pmatrix} \bullet \begin{pmatrix} x \\ y \\ z \end{pmatrix} = 1$$

For a number of velocity measurements 'k', we now define the i^{th} velocity measurement V_i in each direction U_i, as given by the unit vector $U_i(l_i,m_i,n_i)$. This permits the above equation to be re-written in terms of a least squares system:

$$\begin{pmatrix} l_1^2 & m_1^2 & n_1^2 & l_1m_1 & l_1n_1 & m_1m_1 \\ . & . & . & . & . & . \\ l_k^2 & m_k^2 & n_k^2 & l_ky_k & l_kn_k & m_kn_k \end{pmatrix} \bullet \begin{pmatrix} A \\ B \\ C \\ D \\ E \\ F \end{pmatrix} = \begin{pmatrix} 1/v_1^2 \\ . \\ 1/v_k^2 \end{pmatrix}$$

Defining the system matrix as **Q**, the parameter vector as **P** and the inverse velocity (slowness) vector as **W**, we get the following least squares solution for the parameter matrix:

$$\overline{\overline{P}} = \left({}^t\overline{\overline{Q}}.\overline{\overline{Q}} \right)^{-1} . \left({}^t\overline{\overline{Q}}.\overline{\overline{W}} \right)$$

For the experiments described in this study, the total number of measurements 'k' is 108, thus yielding an over-determined inverse problem as the number of parameters sought (A to F) is only 6. Solving the parameter matrix **P** above for its eigenvectors and eigenvalues thus allows a unique solution to be determined which describes the length and direction of the principal axes in 3-D cartesian co-ordinates. Quality of fit is evaluated by solving the forward problem, yielding maximum residual errors in velocity of ~1.2%, ~1.4%, and ~1.9% for BHS, COS and TDG respectively, which is approximately equal to the velocity measurement accuracy. The concomitant accuracy in principal direction as a result of the velocity magnitude errors above is approximately ±2°. A typical forward solution is shown in figure 4-19, which displays the ellipsoidal model solution together with the measured laboratory data for both P-wave and S-wave elastic velocity. The velocity as calculated from the model lies within the experimental error in all planes of measurement and for both P-wave and S-wave velocity. Finally, to permit statistical analysis nine cores are used, three in each of the X, Y and Z directions. This gives 27 unique combinations of X, Y and Z; each of which yields an ellipsoid with three principal directions. Thus, when displaying the principal directions using this method, which I term the ellipsoidal velocity model (EVM), Bingham statistics may be employed on the 27 directions, thus allowing the degree of clustering etc. to be determined for direct comparison to the pAMS data.

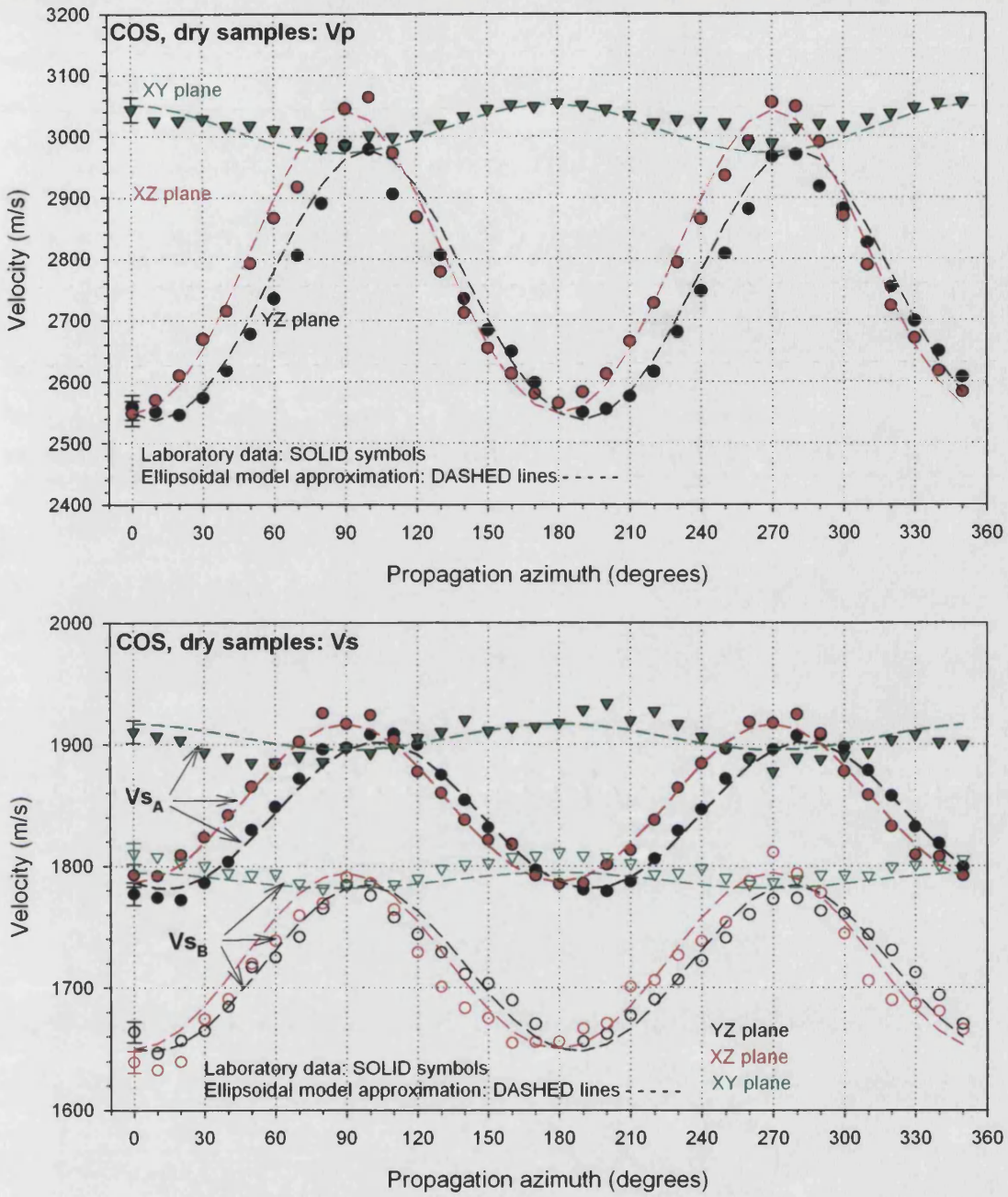

Figure 4-19. P-wave (top) and S-wave (bottom) anisotropy data example for Crab Orchard sandstone. The symbols show the laboratory data (in the case of Vs only, open symbols denote Vs_B, solid symbols denote Vs_A) and dashed lines denote the Ellipsoidal Velocity Model (EVM) approximation.

4.2.2.1 BENTHEIM SANDSTONE

Using the levelled data together with the method just introduced, 3-D principal velocity orientations are derived. In general, velocity data for Bentheim sandstone produces average ellipsoids (table 4-16 to 4-18; figure 4-20) with well clustered principal directions. The notable exception is for dry Vs_A data, which is poorly constrained. Overall, the direction of velocity minimum lies approximately coincident with the Z direction, with maximum and intermediate values distributed sub-parallel to the XY plane. Within the XY plane, the velocity maximum and intermediate directions lie approximately 90° apart. This general trend is noted for P-wave and S-

wave velocity (S_A and S_B polarisation), and for both dry samples and water saturated samples. For P-wave data, maximum principal directions are orientated approximately along the X axis, with intermediate directions approximately aligned along the azimuth of ~285° (close to the Y axis direction). However, for S-wave data these directions have seemingly been reversed, in particular for the S-wave saturated data, where the maximum principal direction is approximately aligned with the Y axis and the intermediate direction with the X axis.

In general, when comparing the principal velocity directions to the pAMS principal directions, a very strong correlation is observed. A particularly close correlation is seen between the velocity minimum directions and the pAMS minimum directions. However, only the dry P-wave velocity minimum agrees with the pAMS direction within Bingham statistical error. In addition, the maximum and intermediate velocity directions are similarly not aligned with the maximum and intermediate pAMS directions within the reported Bingham error ellipses. Despite this, the general XY plane described by maximum/intermediate velocity and pAMS values shows a high level of correlation (for example, between the pAMS and the P-wave stereonets).

Bentheim Sandstone Vp velocity		Principal anisotropy axes: Bingham averages					
						95% confidence cones (°)	
		Velocity (m/s)	Clustering Co-efficient	Trend (degrees)	Plunge (degrees)	Maximum	Minimum
Dry	Minimum	2888	0.99	42	86	3	1
	Intermediate	3023	0.95	282	6	7	2
	Maximum	3118	0.93	190	1	8	2
Saturated	Minimum	3767	0.93	304	73	3	1
	Intermediate	3852	0.95	104	8	8	4
	Maximum	3920	0.94	169	6	6	2

Table 4-16. Bentheim sandstone: P-wave velocity principal directions

Bentheim Sandstone Vs_A velocity		Principal anisotropy axes: Bingham averages					
						95% confidence cones (°)	
		Velocity (m/s)	Clustering Co-efficient	Trend (degrees)	Plunge (degrees)	Maximum	Minimum
Dry	Minimum	1956	0.85	331	70	11	5
	Intermediate	2016	0.55	142	25	58	16
	Maximum	2075	0.60	66	10	43	5
Saturated	Minimum	1888	0.93	236	88	6	4
	Intermediate	1941	0.95	343	3	6	3
	Maximum	1996	0.97	72	8	4	3

Table 4-17. Bentheim sandstone: S_A-wave velocity principal directions

Bentheim Sandstone Vs_B velocity		Principal anisotropy axes: Bingham averages					
						95% confidence cones (°)	
		Velocity (m/s)	Clustering Co-efficient	Trend (degrees)	Plunge (degrees)	Maximum	Minimum
Dry	Minimum	1963	0.95	248	81	7	2
	Intermediate	2031	0.74	328	6	18	5
	Maximum	2056	0.70	64	11	23	3
Saturated	Minimum	1912	0.90	267	86	8	3
	Intermediate	1952	0.70	173	13	8	7
	Maximum	1989	0.73	87	10	3	2

Table 4-18. Bentheim sandstone: S_B-wave velocity principal directions

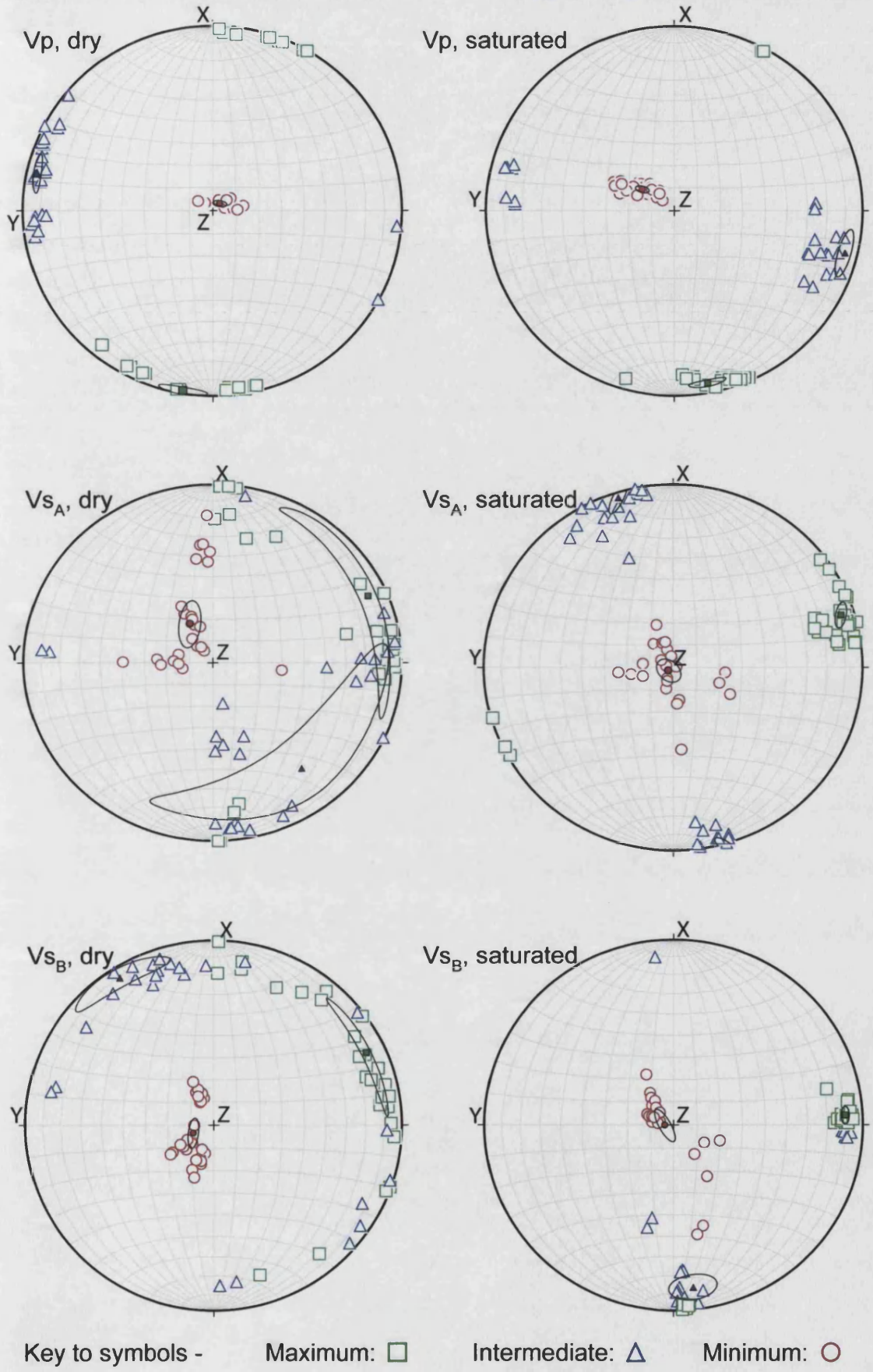

Figure 4-20. Bentheim sandstone ellipsoidal velocity model (EVM) principal directions for P-wave velocity (top figures), S_A-wave velocity (middle figures) and S_B wave velocity (lower figures); and for dry and water saturated samples (left hand and right hand figures respectively). Open symbols denote the principal directions with solid symbols denoting the averages, with Bingham error ellipses

4.2.2.2 CRAB ORCHARD SANDSTONE

Velocity data for Crab Orchard sandstone produces an average ellipsoid (Table 4-19 to 4-21, figure 4-21) with well clustered principal axes. Like the BHS data, the direction of velocity minimum lies approximately coincident with the 'Z' direction, with maximum and intermediate values distributed sub-parallel to the XY plane. Again, within the XY plane the maximum and intermediate directions lie approximately 90° apart. This general trend is observed for both P-wave and S-wave velocity (S_A and S_B polarisation), and for both dry and water saturated samples. Nearly all velocity directions are tightly clustered, with similar Bingham confidence ellipses as compared to the pAMS data. On comparison to the COS pAMS directions, a high degree of correlation between minimum principal directions is noted, although again not quite within the reported Bingham error ellipses. The maximum and intermediate pAMS directions closely match the maximum and intermediate dry velocity directions (although not quite within statistical error), but this close correlation is not as obvious for saturated data. However, the general plane formed by the pAMS maximum and intermediate values is in excellent agreement with the plane formed by the elastic velocity maximum and intermediate values.

Crab Orchard Sandstone Vp velocity		Principal anisotropy axes: Bingham averages					
		Velocity (m/s)	Clustering Co-efficient	Trend (degrees)	Plunge (degrees)	95% confidence cones (°) Maximum	Minimum
Dry	Minimum	2534	0.99	263	80	2	1
	Intermediate	2973	0.89	89	8	9	2
	Maximum	3051	0.90	6	2	9	2
Saturated	Minimum	4146	0.99	342	86	2	2
	Intermediate	4474	0.84	278	1	12	2
	Maximum	4555	0.85	180	2	11	2

Table 4-19. Crab Orchard sandstone: P-wave velocity principal directions

Crab Orchard Sandstone Vs_A velocity		Principal anisotropy axes: Bingham averages					
		Velocity (m/s)	Clustering Co-efficient	Trend (degrees)	Plunge (degrees)	95% confidence cones (°) Maximum	Minimum
Dry	Minimum	1778	0.97	269	76	4	2
	Intermediate	1901	0.72	95	11	14	4
	Maximum	1921	0.75	12	5	14	3
Saturated	Minimum	2034	0.93	11	72	8	2
	Intermediate	2173	0.52	335	6	---	---
	Maximum	2296	0.59	80	6	33	7

Table 4-20. Crab Orchard sandstone: S_A-wave velocity principal directions

Crab Orchard Sandstone Vs_B velocity		Principal anisotropy axes: Bingham averages					
		Velocity (m/s)	Clustering Co-efficient	Trend (degrees)	Plunge (degrees)	95% confidence cones (°) Maximum	Minimum
Dry	Minimum	1645	0.99	275	83	2	2
	Intermediate	1777	0.68	86	6	17	3
	Maximum	1803	0.75	22	3	18	2
Saturated	Minimum	2008	0.97	341	86	5	1
	Intermediate	2110	0.72	62	1	18	5
	Maximum	2201	0.68	24	2	25	1

Table 4-21. Crab Orchard sandstone: S_B-wave velocity principal directions

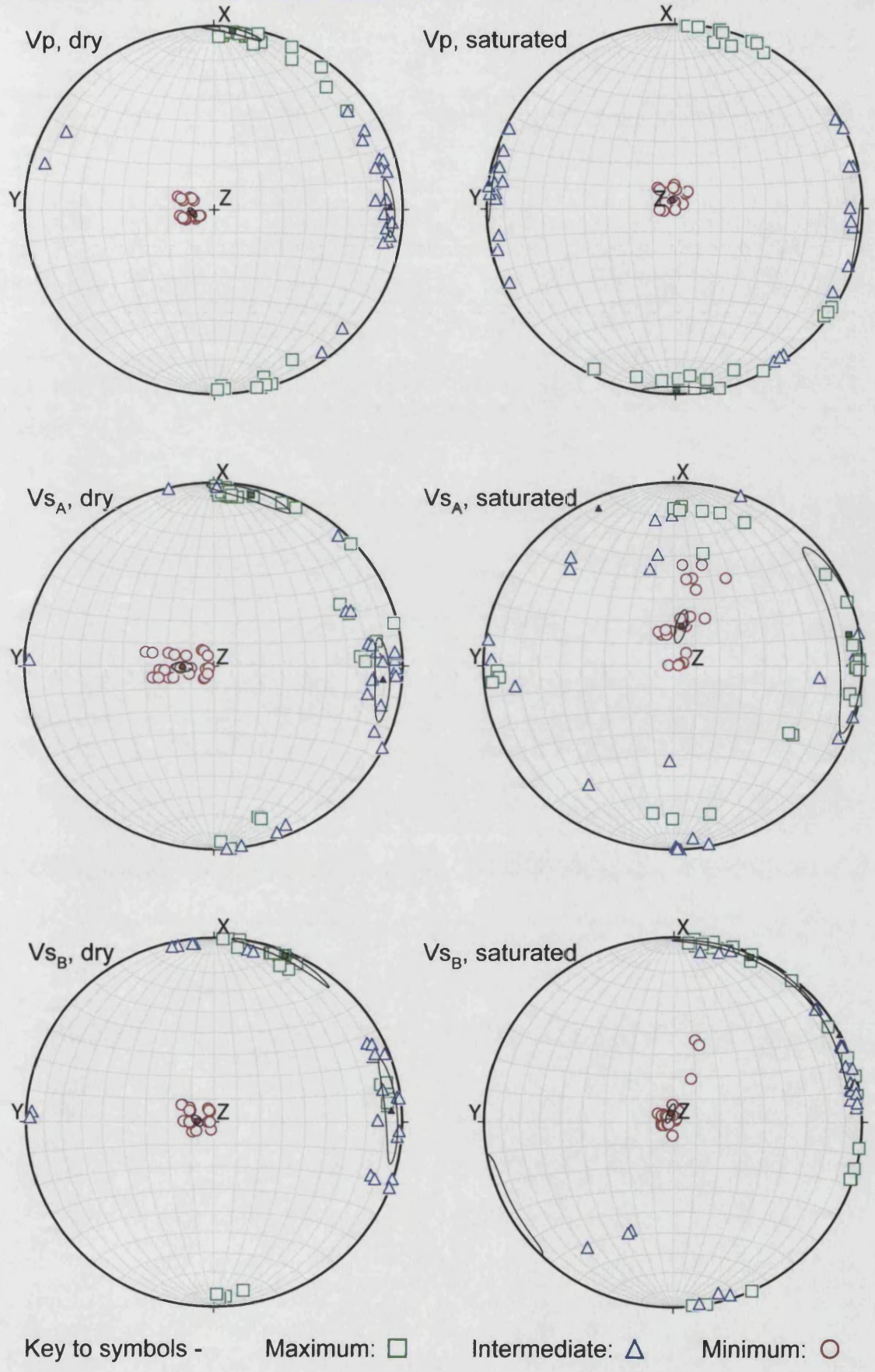

Figure 4-21. Crab Orchard sandstone ellipsoidal velocity model (EVM) principal directions for P-wave velocity (top figures), S_A-wave velocity (middle figures) and S_B wave velocity (lower figures); and for dry and water saturated samples (left hand and right hand figures respectively). Open symbols denote the principal directions with solid symbols denoting the averages, with Bingham error ellipses

4.2.2.3 TAKIDANI GRANITE

In general, the principal ellipsoid directions for Takidani granite are less well constrained than for the sandstone data, with larger Bingham error ellipses. For dry Takidani granite the directional data exhibits a minimum principal direction at approximately 50-75° azimuth and 12-26° of plunge (table 4-22 to 4-24; figure 4-22). Maximum and intermediate principal directions are aligned approximately orthogonal to this direction and to each other, a pattern familiar from the previous two rock types. However, for saturated samples the principal directions generally show poor correlation between each elastic wave type (Vp, Vs_A, Vs_B). When comparing these three velocity stereonets, only the alignment of the maximum velocity direction remains consistent throughout, and in agreement with the maximum principal velocity orientation as derived from the dry data. It should also be noted that the principal anisotropy directions do not fit as well to an ellipsoidal surface (as illustrated by the orthogonality between mean principal directions) as compared to the sandstone samples. This will be the subject of discussion in Chapter 7 and Chapter 8.

Despite the greater uncertainty in principal ellipsoid orientation, there is excellent agreement between the tAMS minimum principle orientation shown earlier (figure 4-8) and the dry elastic wave principal directions shown in figure 4-22. Interestingly, the tAMS maximum and intermediate directions appear to be the reversed when compared to the maximum and intermediate directions determined from dry elastic wave anisotropy. However, the general plane described by the dry elastic wave anisotropy ellipsoid maximum and intermediate directions is in good agreement with the plane described by tAMS maximum and intermediate directions. As already noted, water saturated TDG samples show poorly constrained principal directions, with only the Vs_B stereonet showing any correlation to the tAMS data, and for minimum principal directions only.

As previously discussed, the tAMS data does not specifically describe the pore fabric, as this signal is dominated by the matrix AMS. Although the principal directions are tenuous, and requires a cautious interpretation, the pAMS minimum direction (~45° azimuth, ~30° plunge) is in broad agreement with the dry elastic velocity minimum principal direction. It is likely that TDG possesses a cracked fabric; therefore the dry elastic wave velocity principal orientations will provide a good visualisation of any overall crack fabric alignment within this rock, as cracks greatly influence elastic wave velocity and velocity anisotropy. It is also conceivable that the same physical processes which produced the aligned crack fabric in TDG may also influence mAMS, resulting in the observed approximate correlation between principal anisotropy orientations.

Takidani Granite Vp velocity		Principal anisotropy axes: Bingham averages					
						95% confidence cones (°)	
		Velocity (m/s)	Clustering Co-efficient	Trend (degrees)	Plunge (degrees)	Maximum	Minimum
Dry	Minimum	4450	0.91	74	12	7	3
	Intermediate	4606	0.61	335	13	41	10
	Maximum	4876	0.78	176	59	7	4
Saturated	Minimum	5866	0.48	343	42	---	---
	Intermediate	5976	0.53	57	5	---	---
	Maximum	6093	0.62	129	78	35	6

Table 4-22. Takidani granite: P-wave velocity principal directions

Takidani Granite Vs_A velocity		Principal anisotropy axes: Bingham averages					
						95% confidence cones (°)	
		Velocity (m/s)	Clustering Co-efficient	Trend (degrees)	Plunge (degrees)	Maximum	Minimum
Dry	Minimum	3093	0.75	76	31	17	5
	Intermediate	3151	0.52	301	25	59	16
	Maximum	3279	0.83	181	31	11	3
Saturated	Minimum	3193	0.59	113	10	27	16
	Intermediate	3266	0.50	161	3	48	25
	Maximum	3334	0.59	159	72	31	12

Table 4-23. Takidani granite: S_A-wave velocity principal directions

Takidani Granite Vs_B velocity		Principal anisotropy axes: Bingham averages					
						95% confidence cones (°)	
		Velocity (m/s)	Clustering Co-efficient	Trend (degrees)	Plunge (degrees)	Maximum	Minimum
Dry	Minimum	2995	0.63	53	26	42	8
	Intermediate	3107	0.51	304	35	45	22
	Maximum	3238	0.47	165	55	---	---
Saturated	Minimum	3240	0.78	63	16	14	7
	Intermediate	3332	0.70	155	4	19	7
	Maximum	3391	0.76	144	71	14	7

Table 4-24. Takidani granite: S_B-wave velocity principal directions

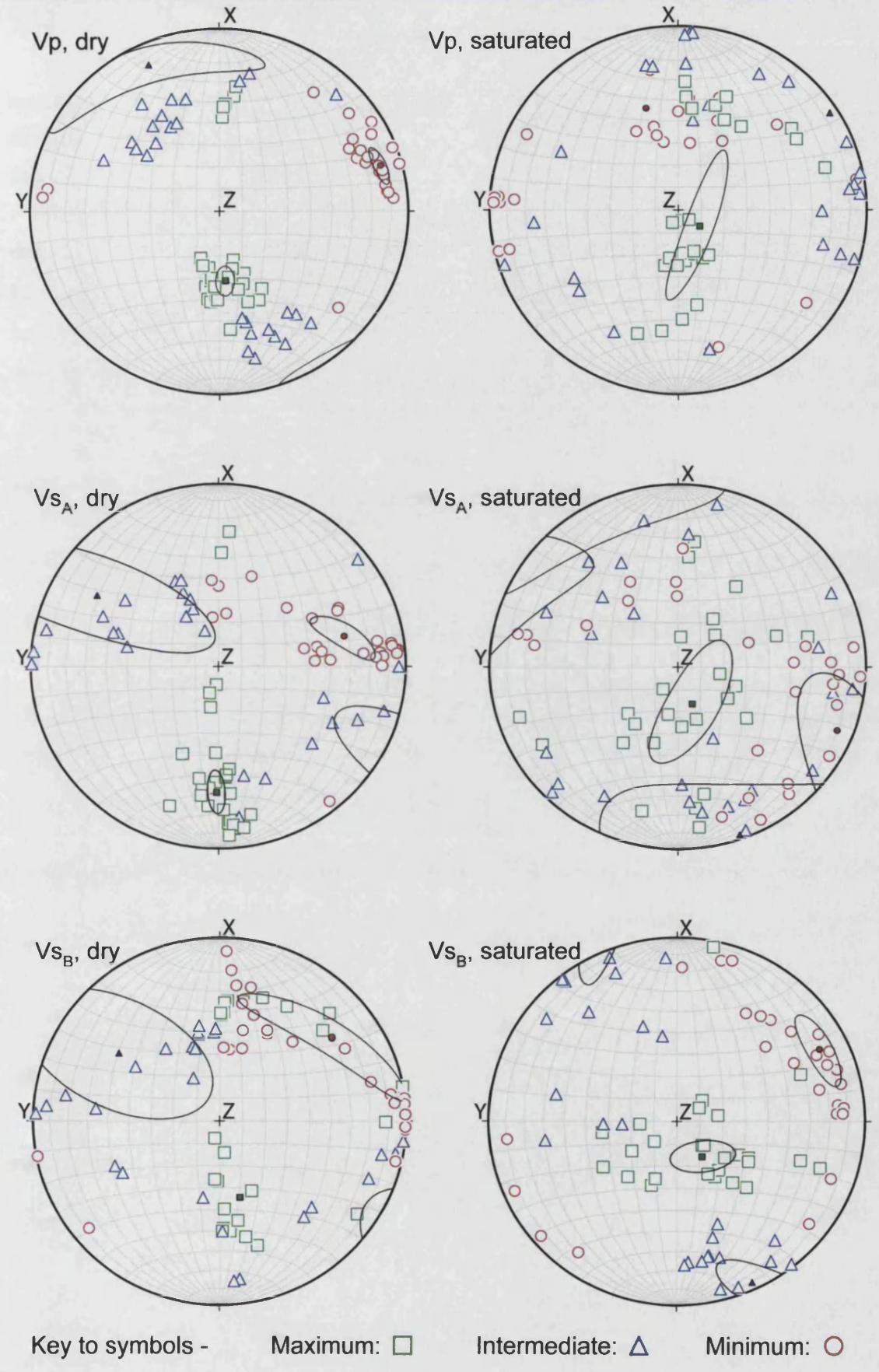

Figure 4-22. Takidani granite ellipsoidal velocity model (EVM) principal directions for P-wave velocity (top figures), S_A-wave velocity (middle figures) and S_B wave velocity (lower figures); and for dry and water saturated samples (left hand and right hand figures respectively). Open symbols denote the principal directions with solid symbols denoting the averages, with Bingham error ellipses

4.2.3 VELOCITY 'PSEUDO' FLINN DETERMINATION

As briefly noted, in addition to the minimum and maximum principal velocity magnitude and direction the EVM method allows the determination of an intermediate velocity magnitude and direction which experimental measurement is unable to accurately determine. This allows a range of parameters to be computed for each individual ellipsoid, analogous to the lineation and foliation parameters determined from the AMS data. Here, I use a similar approach with the velocity data, to define the EVM bulk 'A' anisotropy as $A_V = 100\%*[(V_{max}-V_{min})/V_{mean}]$, the 'velocity lineation' as $L_V = V_{max}/V_{intermediate}$, and 'velocity foliation' as $F_V = V_{intermediate}/V_{min}$. Where the maximum, intermediate and minimum velocities used in these calculations are those principal velocities as determined from the EVM method.

In the work presented here, three cores in each direction are measured, giving 27 unique combinations and thus ellipsoids. Anisotropy data calculated from the EVM principal directions in each of the 27 ellipsoids and for each rock type is summarised in tables 4-25, 4-26 and 4-27 below. Direct comparison between velocity anisotropy factors (L_V, F_V and A_V), mAMS anisotropy factors (A_m, P_m, L_m, F_m), tAMS anisotropy factors (A_t, P_t, L_t, F_t), and pAMS anisotropy factors (A_ϕ, P_ϕ, L_ϕ, F_ϕ) will be the subject of discussion in Chapter 7.

Bentheim Sandstone		Velocity (m/s)		Velocity ellipsoid principal axial ratios					
				Lineation, L_V ($=V_{max}/V_{int}$)		Foliation, F_V ($=V_{int}/V_{min}$)		Anisotropy, A_V (%) $[100*(V_{max}/V_{min})/V_{mean}]$	
		average	Std. dev.	average	Std. dev.	average	Std. dev.	average	Std. dev.
Dry	Vp	3010	18	1.032	0.014	1.047	0.012	7.6	0.8
	Vs_A	2016	35	1.030	0.020	1.031	0.020	5.9	2.1
	Vs_B	2016	33	1.012	0.017	1.034	0.008	4.6	1.7
Saturated	Vp	3846	10	1.018	0.005	1.023	0.005	4.0	0.6
	Vs_A	1941	14	1.028	0.078	1.028	0.017	5.6	1.6
	Vs_B	1951	15	1.019	0.068	1.021	0.011	3.9	0.9

Table 4-25. Bentheim sandstone: model velocity and velocity anisotropy

Crab Orchard Sandstone		Velocity (m/s)		Velocity ellipsoid principal axial ratios					
				Lineation, L_V ($=V_{max}/V_{int}$)		Foliation, F_V ($=V_{int}/V_{min}$)		Anisotropy, A_V (%) $[100*(V_{max}/V_{min})/V_{mean}]$	
		average	Std. dev.	average	Std. dev.	average	Std. dev.	average	Std. dev.
Dry	Vp	2853	17	1.026	0.011	1.173	0.014	18.1	1.2
	Vs_A	1866	17	1.011	0.008	1.069	0.019	7.7	1.6
	Vs_B	1742	12	1.015	0.009	1.080	0.013	9.1	1.3
Saturated	Vp	4392	26	1.018	0.007	1.079	0.017	9.3	1.3
	Vs_A	2168	52	1.057	0.040	1.069	0.027	12.1	3.0
	Vs_B	2106	35	1.043	0.014	1.052	0.028	9.2	3.0

Table 4-26. Crab Orchard sandstone: model velocity and velocity anisotropy

Takidani Granite		Velocity (m/s)		Velocity ellipsoid principal axial ratios					
				Lineation, L_V ($=V_{max}/V_{int}$)		Foliation, F_V ($=V_{int}/V_{min}$)		Anisotropy, A_V (%) $[100*(V_{max}/V_{min})/V_{mean}]$	
		average	Std. dev.	average	Std. dev.	average	Std. dev.	average	Std. dev.
Dry	Vp	4644	41	1.059	0.013	1.035	0.015	9.2	1.7
	Vs_A	3174	53	1.041	0.029	1.019	0.013	5.9	3.0
	Vs_B	3113	78	1.042	0.019	1.038	0.023	7.8	2.5
Saturated	Vp	5979	61	1.020	0.012	1.019	0.009	3.8	1.3
	Vs_A	3264	35	1.021	0.009	1.023	0.011	4.3	1.4
	Vs_B	3321	31	1.018	0.008	1.028	0.010	4.5	0.8

Table 4-27. Takidani granite: model velocity and velocity anisotropy

5 RESULTS: MEASUREMENTS AT ELEVATED PRESSURE

As the results from the last chapter help to demonstrate, the rock types studied in this investigation possess a range of pore fabrics; from those dominated by quasi-equant pores, through those with a mixture of pores and cracks, to those dominated by cracks. In order to determine the effect of these void space components upon the important rock physics properties of elastic velocity, porosity and permeability, a range of experiments was undertaken upon these well characterised materials at elevated hydrostatic effective pressures from 5 to 90 MPa. Although these parameters are vital in determining the nature (both transport and mechanical) of porous media, they have seldom been measured contemporaneously or with reference to the pore fabric characterisation presented in this investigation. The results presented here should therefore shed fresh insight into the nature of permeability and elastic anisotropy dependencies upon pore fabric type and geometry, and introduce how void space may be considered in a more meaningful way than the simple scalar quantity of porosity. This will be the subject of extensive discussion in Chapter 7.

A sub-set of the 38mm diameter samples as used for the ambient pressure velocity measurements was used for these elevated pressure tests. Permeability, porosity, and axial P-wave and S-wave elastic velocities were measured contemporaneously at each incremental increase in effective pressure on cores with axes in each of the X, Y and Z directions. In a similar fashion to that adopted in Chapter 4 (fig. 4-12), I refer to measurements made on a samples cored in a particular orientation with a suffix. Unlike the azimuthal velocity measurements, however, the velocity measurements are made axially, not radially, and a 'double suffix' is adopted. For example, the axial P-wave velocity in the Z direction made upon Z axis cores is written as Vp_{zz}. The use is again made of the acronyms BHS for Bentheim sandstone, COS for Crab Orchard sandstone, and TDG for Takidani granite, as introduced earlier. For all rocks, elastic wave velocity increases and the porosity decreases with increasing effective pressure, as expected. However, the magnitude of these variations (anisotropy) varies greatly with both rock type and applied effective pressure.

5.1 CALIBRATION MEASUREMENTS

Three key calibration studies were undertaken in the experimental programme in order to confirm the effects being measured were due to the applied effective pressure, and that valid comparisons could be made between data obtained from saturated samples at high hydrostatic confining pressures, and data from the characterisation methods and techniques used at room pressure. These steps are important, as the methodologies introduced in the next sub-section require pore fluid to be present for the porosity and permeability determination.

Dry sample measurements

Firstly, a small number of tests were made upon dry samples at elevated hydrostatic pressure. Figure 5-1 shows the results of these tests for Bentheim sandstone. Results for the dry

samples show the same overall trends with effective pressure as for water saturated samples. An increase in velocity is observed with increasing effective pressure, and the elastic velocity in the 'Z' direction is lower, while the velocity in the 'X' axis is higher (Vp_Z<Vp_X). These tests provide additional confirmation that the measured effects from the elevated pressure tests are due to the changing microstructure of the rock, rather than any pore fluid / rock matrix interaction, such as velocity changes due to chemical effects. In addition, it should be noted that velocity *differences* are highest at low effective pressures (since V_p is faster through water than through air), but this difference decreases at higher effective pressure when porosity (i.e. void space volume) decreases. This is exactly what would be expected intuitively. Thus, the direct comparison between dry EVM principal directions, saturated EVM data, pAMS information and saturated hydrostatic elastic wave measurement can be made with a high degree of confidence.

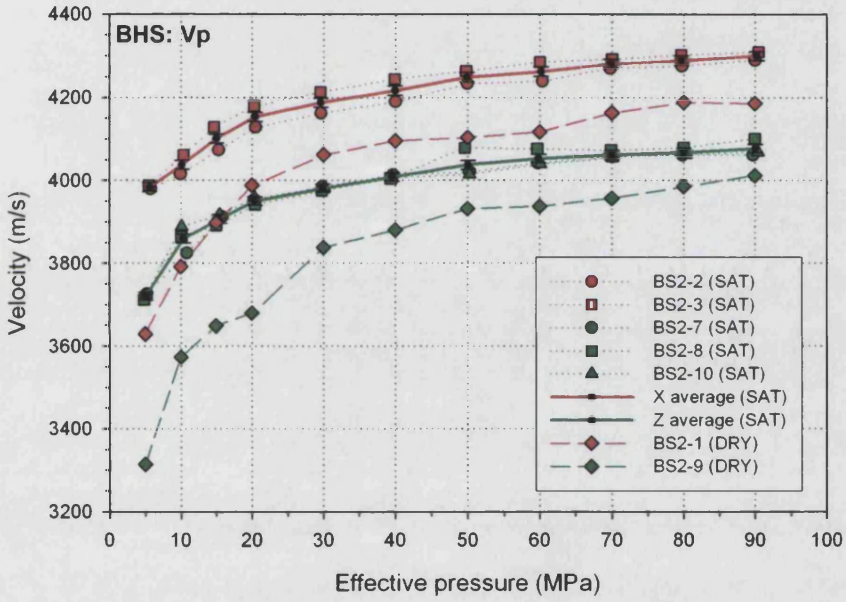

Figure 5-1. An example dataset for Bentheim sandstone showing the effect of water saturation upon velocity at elevated hydrostatic pressure. Red symbols/lines denote Vp_{xx} measurements and green symbols/lines denote Vp_{zz} measurements. Dotted lines illustrate the saturated sample measurements, with the dashed lines showing the dry sample velocity change. Solid lines denote average values for the saturated measurements made in those directions

Use of the 'simple' effective pressure law

Secondly, during the experimental programme the simple effective stress law with α_p=1 is assumed (refer to section 2.2.3). To test this assumption, a calibration experiment was conducted. Using a saturated sample of COS, the increase in confining pressure (P_c) was controlled simultaneously with the increase in mean pore pressure (P_p), in order to achieve a constant value of P_c-P_p = 9.5MPa (figure 5-2). At each confining and pore pressure increase, sample permeability and P-wave velocity was measured. Figure 5-2 shows that these two parameters remain essentially constant over the entire pressure range. It therefore follows that the simple effective pressure law, with α_p=1, is appropriate for permeability and elastic wave velocity as measured in this work, and

the use of a simple effective pressure law can thus be used with confidence. In addition, as this test was performed for the most 'complex' rock used (in terms of composition), then it is likely that the simple effective pressure law likewise holds for the highly porous BHS, and the simple (and extensive) crack fabric seen in TDG.

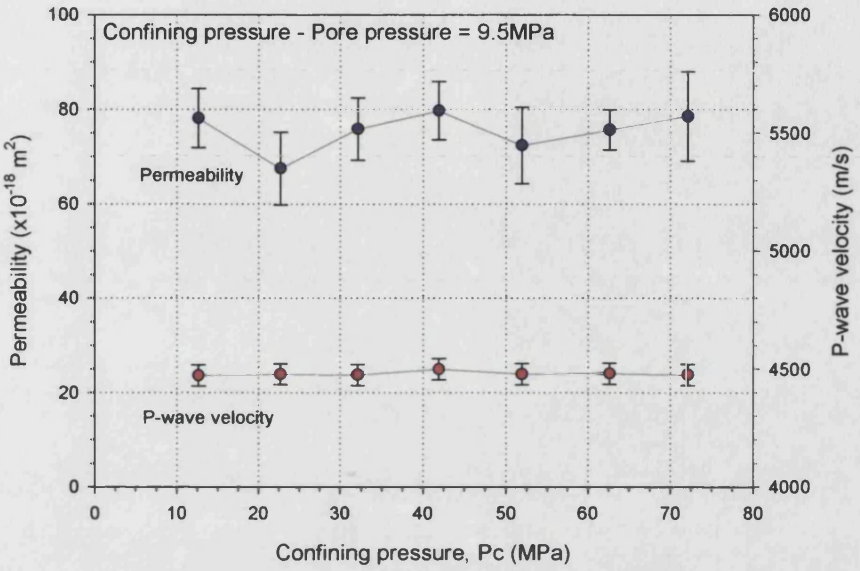

Figure 5-2. 'Simple' effective pressure law verification using a sample of water saturated COS

In addition, as all the parameters are recorded *contemporaneously* during each experiment (pore pressures, confining pressure, and intensifier volume displacements with time), then these data will still be valid relative to each other as all measurements are made upon the same sample and under the same pressure conditions. However, as a final, additional, precaution against any possible difficulty in comparing data across different samples and rock types, the same mean pore pressure of 2.5 MPa was used in all experiments, with confining pressure being varied in order to achieve the desired effective pressure. This would still allow direct comparison to be made, even if $\alpha_p \neq 1$. However, as the simple effective pressure law with $\alpha_p=1$ has been seen to hold, it is used throughout this study for describing experimental pressure conditions (i.e. essentially the same as the definition of 'differential pressure' as used by Zimmerman (1991), and others).

Sample shortening

The third calibration concerns the physical dimensions of the sample itself, as it is pressurised within the hydrostatic confining cell. Under increasing pressure, a small decrease in the physical sample length will occur, defined here as 'shortening'. The hydrostatic measurement cell is unable to measure this effect directly, but as any sample length change has implications for the calculation of velocity and permeability, then the shortening effect must be determined. This is done by directly measuring the change in sample length with increasing pressure using a triaxial deformation apparatus operated in hydrostatic mode, with the capability of directly measuring sample shortening (Sammonds et al., 1989). Water saturated samples of approximately 100mm

length by 40 mm diameter were used, maintained in a saturated state at 2.5 MPa pore pressure. A high precision displacement transducer capable of measuring length change to an accuracy of ±0.001mm was then used to measure the decrease in sample length with stepwise increase in hydrostatic pressure (figure 5-3). The length change vs. effective pressure data is then normalised by the pressure change and sample length to give a shortening 'coefficient' representing the change in length per MPa increase in pressure per mm of sample length, essentially equivalent to a compliance (MPa^{-1}). Table 5-1 summarises the calculated compliances.

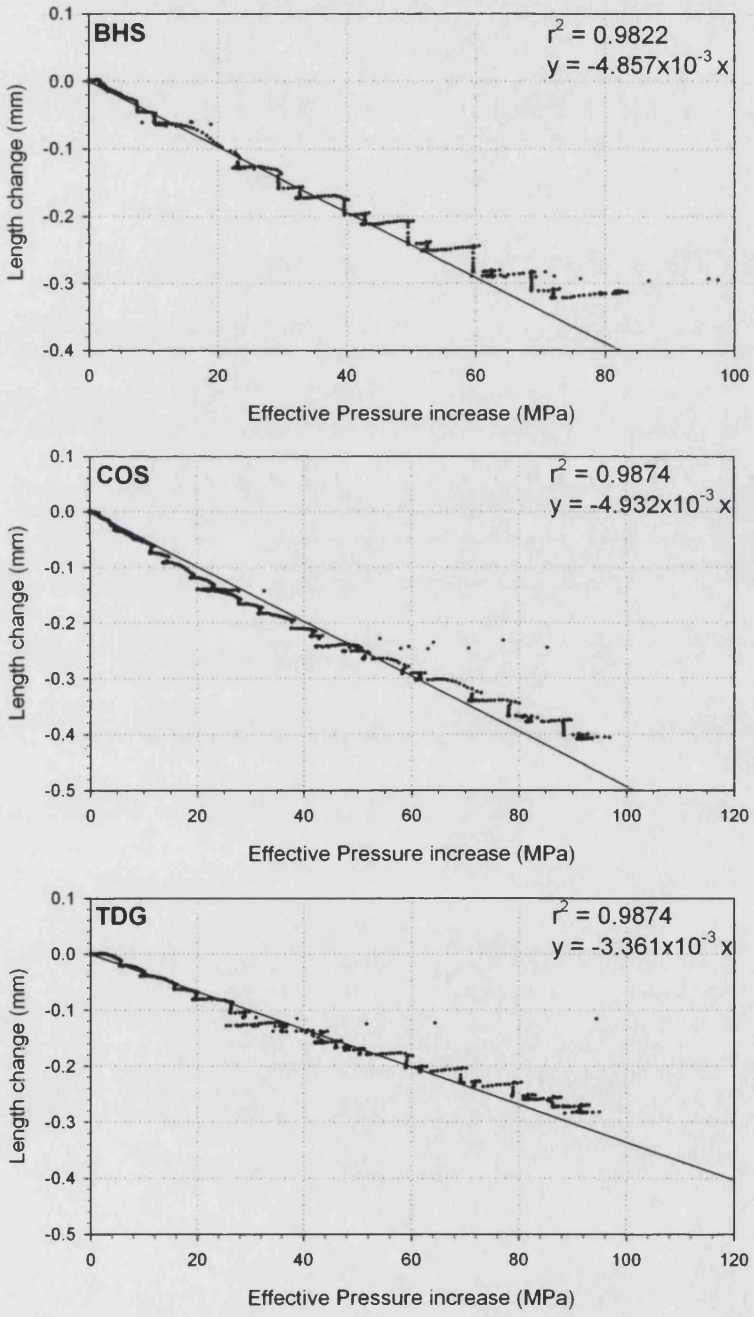

Figure 5-3. Hydrostatic shortening experiments for Bentheim sandstone (Top), Crab Orchard sandstone (Middle), and Takidani granite (bottom). In each plot, the linear trend in decreasing sample length change with increasing effective pressure is clear. Note also the 'steps' in pressure, created as the pressure is increased in steps; a small delay then occurs before the rock frame reacts, giving the decreasing length change for each pressure increment illustrated

These compliances are then used to correct the known initial sample length for experiments made in the servo-controlled measurement cell to the correct length values, according to the measured prevailing pressure conditions. Likewise, these corrected lengths are used to obtain correct elastic wave velocities, also as a function of effective pressure. All data presented in this Chapter has been corrected in this manner. An example for Bentheim sandstone is shown below (figure 5-4). Here, the sample shortening is of a similar overall magnitude to the velocity measurement accuracy, illustrating the importance of such a correction. However, for permeability such a small length correction has an insignificant effect upon permeability calculation compared with the permeability measurement accuracy and natural sample variability. For example, the length of BHS has changed by approximately 0.4% at 90MPa, but the permeability error lies in the range of approximately 4-8%.

Rock type	'Compliance' (MPa^{-1})
Bentheim sandstone	4.86E-5
Crab Orchard sandstone	4.93E-5
Takidani granite	3.36E-5

Table 5-1. Summary of compliances for Bentheim sandstone, Crab Orchard sandstone and Takidani granite. As these rocks are anisotropic, measurements were made both parallel and normal to bedding (microcracking in the case of TDG). Interestingly, no difference in the measured compliance was determined

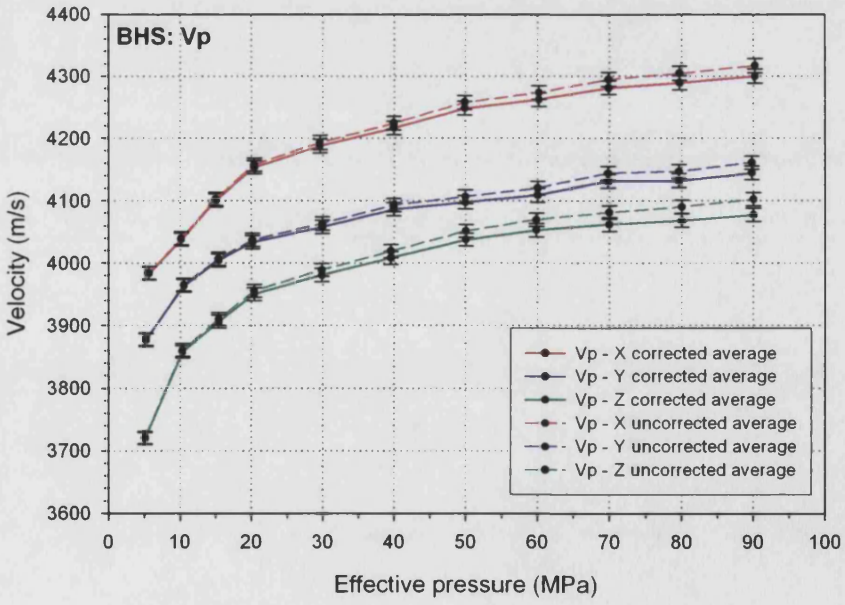

Figure 5-4. The effect of sample 'shortening' upon the apparent elastic velocity: change with pressure

5.2 ELASTIC WAVE VELOCITY

5.2.1 BENTHEIM SANDSTONE

For BHS, P-wave and S-wave velocity increases with effective pressure, as shown in figures 5-5 and 5-6 respectively. Note that in these figures, all laboratory data is shown individually, with two samples in each of the X and Y directions, and three in the Z direction. This allows the variability between the axial velocity of the individual samples, as well as the direction of velocity measurement, to be clearly seen. The average values for each direction are shown by bold solid lines, with 0.5% velocity error bars representing the accuracy that velocity changes may be determined within the measurement cell, as discussed in Chapter 3 (table 3-4); i.e. this is not the same calculating an error for velocity based upon an average sample direction at each stepwise increase in pressure. To do so would only reveal the variability the different samples measured at each pressure step, rather than as a true illustration of the accurate changes with pressure actually recorded.

Velocities measured in the Z direction (V_{zz} – along the pore fabric minimum principal axis), have the lowest values at each pressure step, with V_{xx} exhibiting the highest values. P-wave velocity increases rapidly at low effective pressures, with the rate of increase decreasing rapidly at higher pressures above approximately 20-30 MPa where a prominent 'knee' is clearly seen. Above a pressure of ~50 MPa, the velocity-pressure relationship is almost linear. For S-wave data, a similar general trend is obvious, with V_{xx} data showing the highest velocities and V_{zz} data showing the lowest velocities. The prominent 'knee' seen in the P-wave data at ~20-30 MPa is also visible, and again the velocity-pressure relationship becomes almost linear above ~50 MPa. Figure 5-7 plots a summary of P-wave and S-wave average data together.

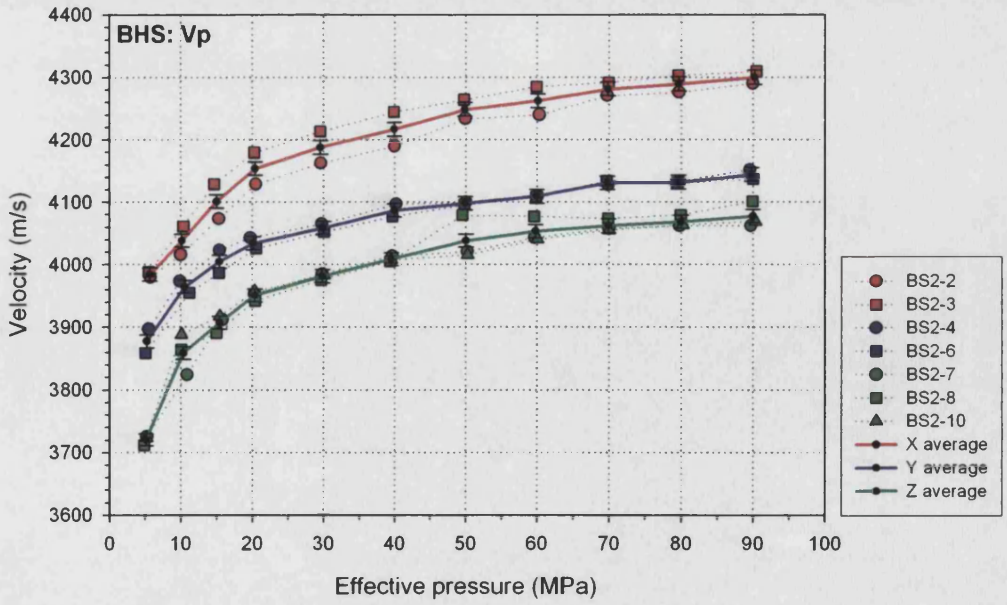

Figure 5-5. Bentheim sandstone P-wave velocity variation with effective pressure. Red colours denote V_{xx} data, blue denotes V_{yy} data and green V_{zz} data. Solid symbols show the experimental laboratory data, joined by dotted lines. Black symbols show the data averages at each pressure step for each direction, connected with a bold, solid line

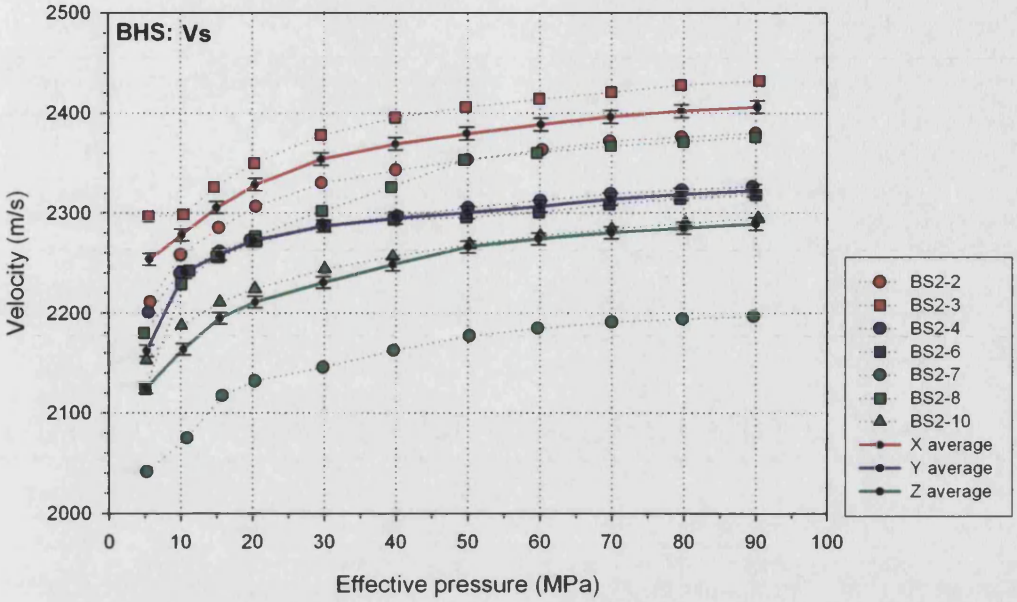

Figure 5-6. Bentheim sandstone S-wave velocity variation with effective pressure. Red colours denote V_{xx} data, blue denotes V_{yy} data and green V_{zz} data. Solid symbols show the experimental laboratory data, joined by dotted lines. Black symbols show the data averages at each pressure step for each direction, connected with a bold, solid line

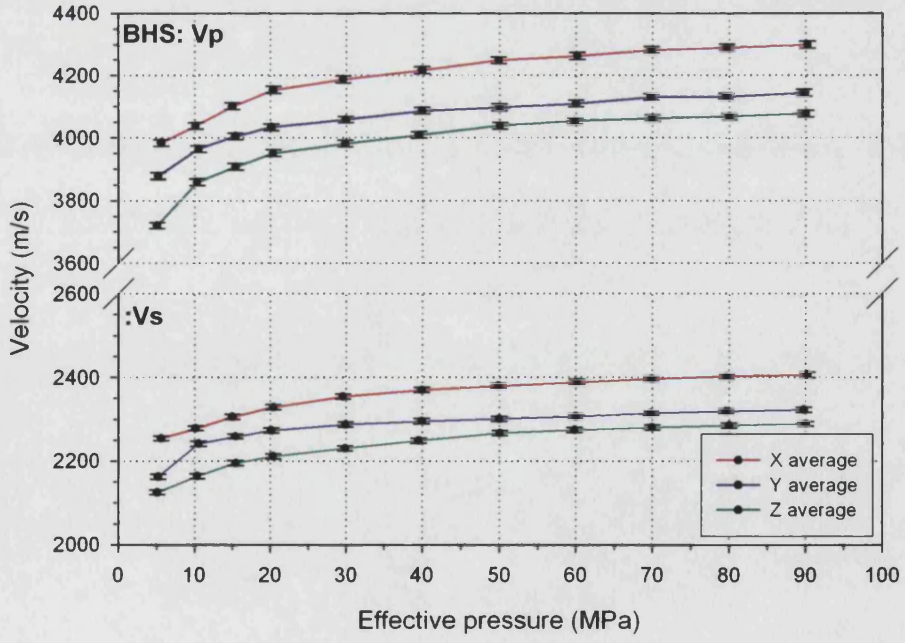

Figure 5-7. Bentheim sandstone P-wave (top plot) and S-wave (lower plot) velocity variation with effective pressure. Red colours denote V_{xx} data, blue denotes V_{yy} data and green V_{zz} data. Black symbols show the data averages at each pressure step for each direction, connected with a bold, solid line

5.2.2 CRAB ORCHARD SANDSTONE

For COS, P-wave and S-wave velocities also increase with effective pressure, as shown in figures 5-8 and 5-9 respectively. Nine samples were measured in total, with three samples for V_{xx}, two samples for V_{yy} and four samples for V_{zz}. Average values are again shown for each direction with bold lines, together with 0.5% errors.

For P-wave data, V_{xx} measurements with pressure shown the highest velocities at each pressure step, with V_{zz} data showing the lowest. In addition, V_{xx} and V_{yy} measurements are essentially the same within experimental error. However, in contrast to the BHS data, although the elastic velocity increases continuously with pressure, it does so at a continually decreasing rate. Unlike the BHS velocity data, the Crab Orchard sandstone P-wave velocity-pressure relationship does not show the prominent 'linear' segment observed in the BHS velocity data above 20-30 MPa. In addition, the velocities are higher for COS at each pressure step than for BHS.

For S-wave velocity, a similar trend is observed as compared to the COS P-wave data. V_{xx} data show the highest velocities and V_{zz} the lowest velocities. S-wave velocity increases with increasing effective pressure. However, up until ~30 MPa the individual velocity changes with measurement direction remain well separated, but after this point the velocities start to converge. At high effective pressures approaching 90 MPa, the velocities along the different directions cannot be distinguished within the 0.5% error. The convergence is more clearly seen in figure 5-10, which summarises both the P-wave and S-wave average data.

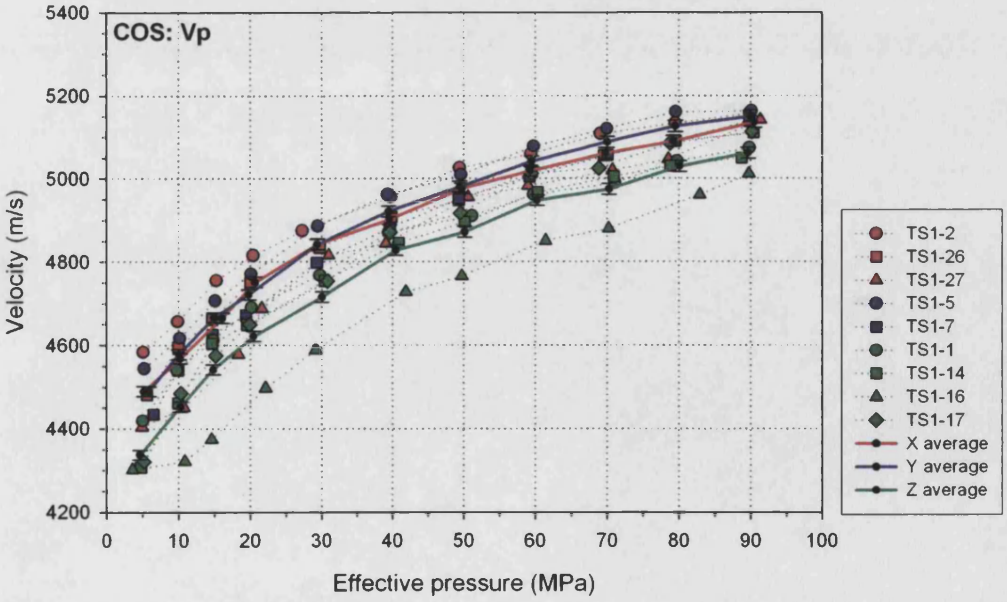

Figure 5-8. Crab Orchard sandstone P-wave velocity variation with effective pressure. Red colours denote V_{xx} data, blue denotes V_{yy} data and green V_{zz} data. Solid symbols show the experimental laboratory data, joined by dotted lines. Black symbols show the data averages at each pressure step for each direction, connected with a bold, solid line

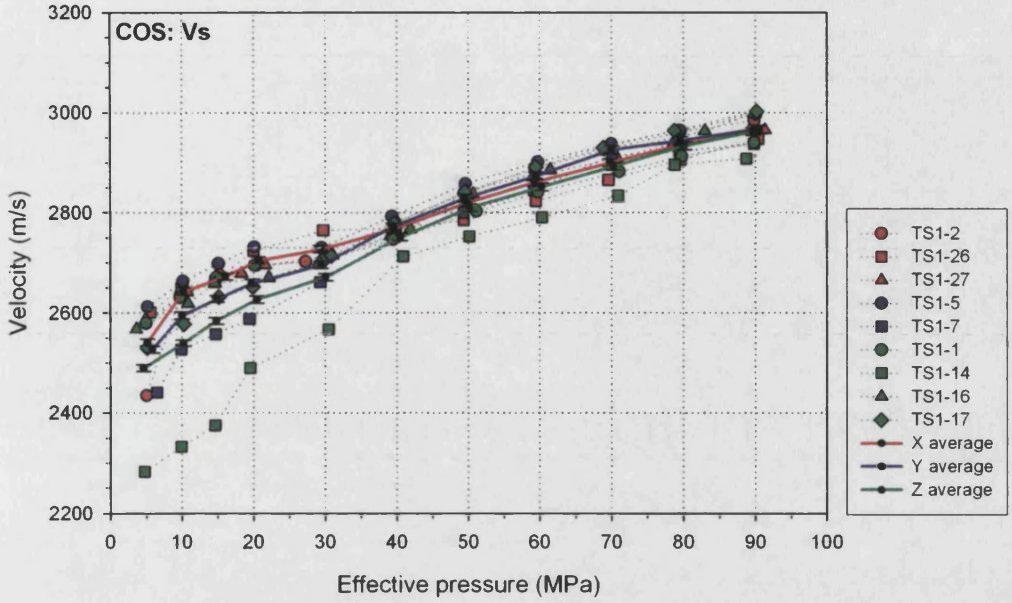

Figure 5-9. Crab Orchard sandstone S-wave velocity variation with effective pressure. Red colours denote V_{xx} data, blue denotes V_{yy} data and green V_{zz} data. Solid symbols show the experimental laboratory data, joined by dotted lines. Black symbols show the data averages at each pressure step for each direction, connected with a bold, solid line

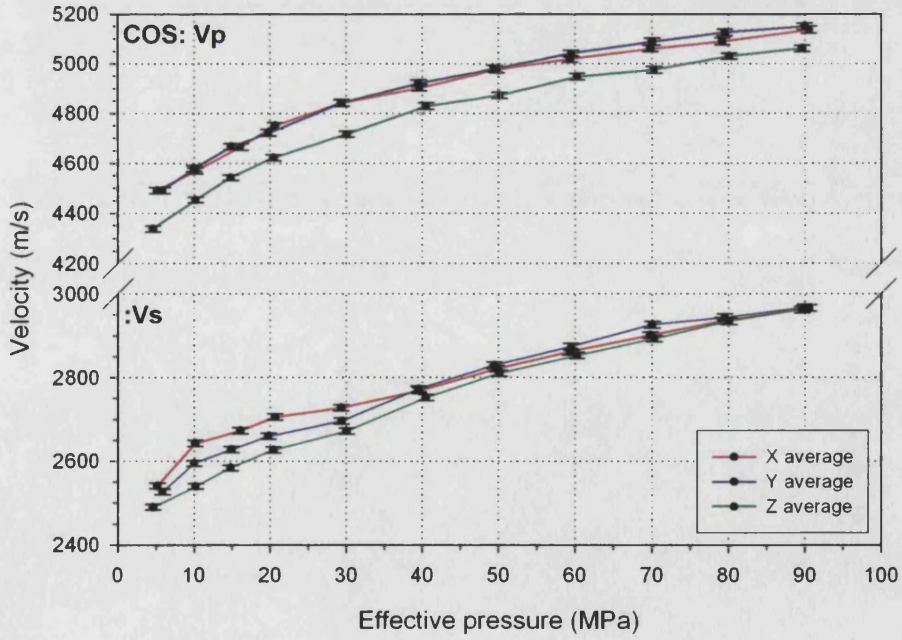

Figure 5-10. Crab Orchard sandstone P-wave (top plot) and S-wave (lower plot) velocity variation with effective pressure. Red colours denote V_{xx} data, blue denotes V_{yy} data and green V_{zz} data. Black symbols show the data averages at each pressure step for each direction, connected with a bold, solid line

5.2.3 TAKIDANI GRANITE

For Takidani granite, P-wave and S-wave velocities also increase with increasing effective pressure, as shown in figures 5-11 and 5-12 respectively. Eight samples were used in the laboratory experiments, with three samples used for V_{xx} and V_{yy} tests, and two for V_{zz}. Average velocity values are again shown in each direction by the bold lines with 0.5% error.

For P-wave data, V_{yy} measurements are lowest on average and V_{zz} measurements are the highest, although a wide variation is seen on a sample-by-sample basis. P-wave velocity increases with increasing effective pressure, and like the BHS data seen earlier, a prominent 'knee' is visible at ~20MPa, after which the velocity-pressure relation is almost linear.

For S-wave data, V_{yy} measurements have the lowest average velocities with V_{xx} the highest. Velocity increases with increasing effective pressure for all directional measurements and as for COS S-wave data, a velocity convergence is again seen. For TDG this occurs between the V_{yy} (slow data) and V_{zz} velocities, which become equal in value at 90 MPa within 0.5% error. Figure 5-13 illustrates both P-wave and S-wave average data for comparison. In general, elastic velocities are higher than for the sandstone velocity data, which is consistent with the room pressure elastic velocity data, and examples in the literature.

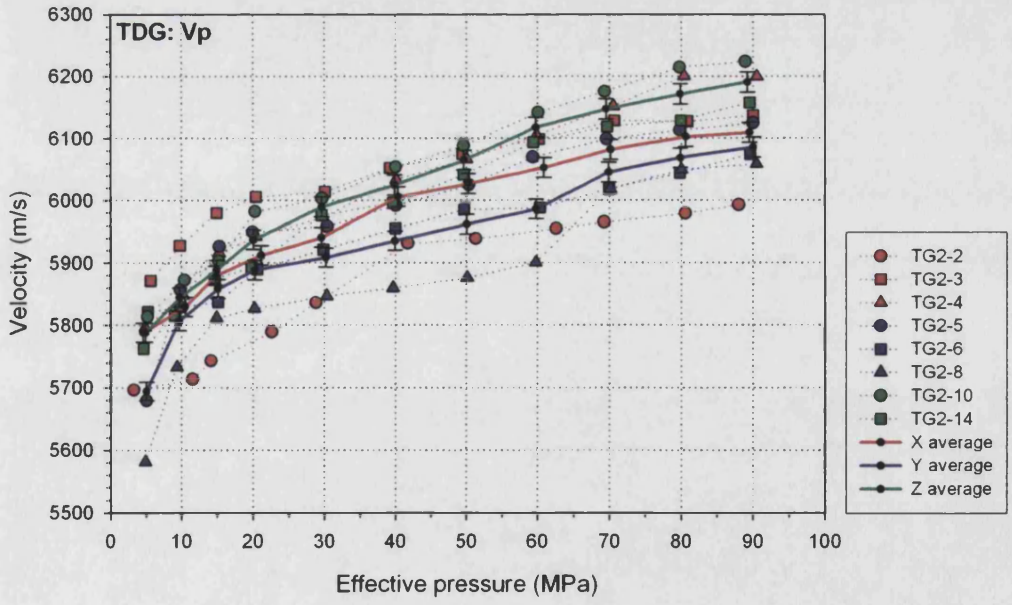

Figure 5-11. Takidani granite P-wave velocity variation with effective pressure. Red colours denote V_{xx} data, blue denotes V_{yy} data and green V_{zz} data. Solid symbols show the experimental laboratory data, joined by dotted lines. Black symbols show the data averages at each pressure step for each direction, connected with a bold, solid line

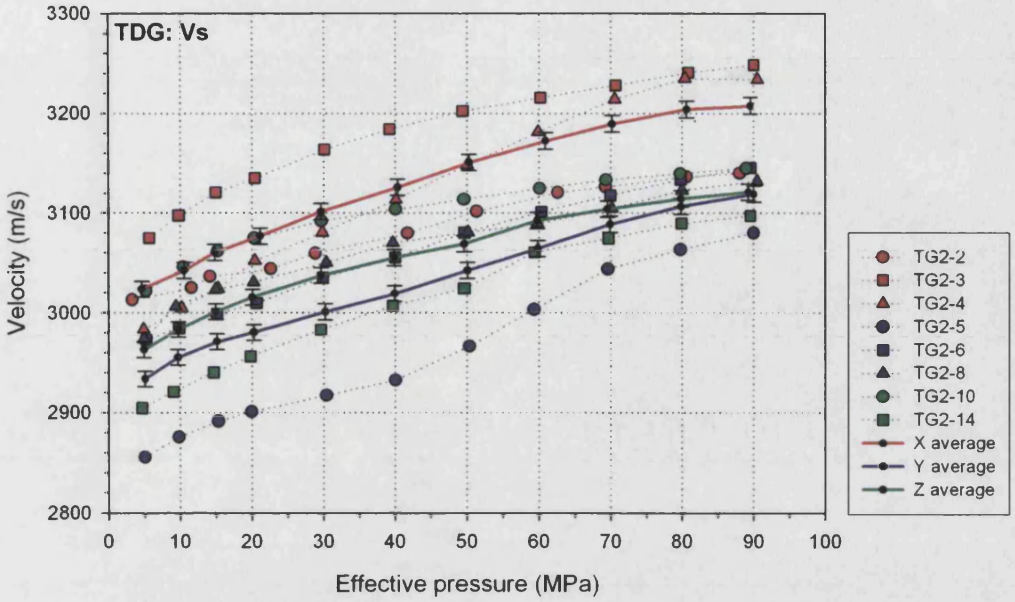

Figure 5-12. Takidani granite S-wave velocity variation with effective pressure. Red colours denote V_{xx} data, blue denotes V_{yy} data and green V_{zz} data. Solid symbols show the experimental laboratory data, joined by dotted lines. Black symbols show the data averages at each pressure step for each direction, connected with a bold, solid line

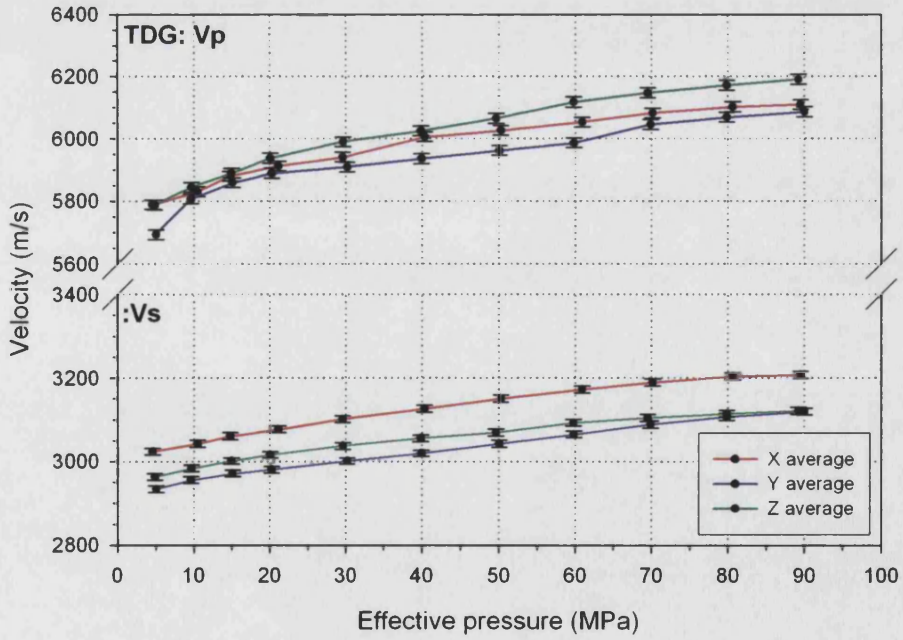

Figure 5-13. Takidani granite P-wave (top plot) and S-wave (lower plot) velocity variation with effective pressure. Red colours denote V_{xx} data, blue denotes V_{yy} data and green V_{zz} data. Black symbols show the data averages at each pressure step for each direction, connected with a bold, solid line

5.2.4 ELASTIC ANISOTROPY AS A FUNCTION OF EFFECTIVE PRESSURE

As can be seen in the previous sections, for each rock type we have both the velocity magnitude and its direction of measurement, guided by the room pressure characterisation methods of pAMS, mAMS and elastic velocity anisotropy. By comparing data from different cores (orientations), but at the same hydrostatic stress conditions, we are therefore able to calculate the anisotropy variation with effective pressure. Figures 5-14, 5-15 and 5-16 show typical data from Bentheim sandstone, Crab Orchard sandstone, and Takidani granite respectively. Percent anisotropy is calculated in the usual way (100%*[Max-Min]/Mean), but at each stepwise increase in pressure, using data from the maximum velocity directions (V_{xx} and V_{yy} for the sandstones; V_{xx} and V_{zz} for Takidani granite), and the minimum directions (V_{zz} for the sandstones, V_{yy} for Takidani granite), in each case. In general, for each rock type the anisotropy change with increasing effective pressure show similar overall trends, but with important differences.

Firstly, for BHS, we see an initial rapid decrease in Vp anisotropy, after which the P-wave anisotropy remains approximately constant at ~2% up until 90 MPa effective pressure. In contrast, Vs anisotropy shows small, continuous decrease in anisotropy with effective pressure from ~2.5% at 5 MPa to ~1.5% at 90 MPa.

Secondly, for COS a larger decrease in elastic anisotropy (both Vp and Vs), with increasing effective pressure is illustrated as compared to BHS. P-wave anisotropy decreases rapidly from ~3% at 5 MPa to ~0.5% at 15 MPa, after which the anisotropy remains constant within error, with the exception of the last 20 MPa where the anisotropy rises slightly. S-wave data exhibits a very large decrease in anisotropy, which decreases from ~7.5% at 5 MPa to ~1% at 90 MPa. For both P-wave and S-wave anisotropy data, little decrease with pressure occurs after a 30-40 MPa threshold.

Finally, TDG also shows a marked decrease in elastic anisotropy. P-wave anisotropy decreases from ~3% at 5 MPa to 1% at 10-15 MPa, after which the anisotropy remains approximately constant until a second threshold pressure is reached at ~50 MPa, at which point the P-wave anisotropy decreases again, reaching 0% at 90 MPa. S-wave anisotropy shows a similar trend, initially decreasing from ~1.5% at 5 MPa to ~1% at ~20 MPa, after which the anisotropy remains essentially constant within error until the second threshold pressure is reached at ~50 MPa, after which the S-wave velocity also decreases to 0% at 90 MPa. Note that, in principle, a negative anisotropy cannot occur (as seen in the TDG S-wave data point at 90 MPa). However, this is simply as a result of Vs_{yy} being higher that Vs_{xx} at this point, i.e. the velocities reversing as compared to the original definition whereby the V_{yy} measurements were taken as the lowest. In any case, the anisotropy measurement is still 0% within the error reported.

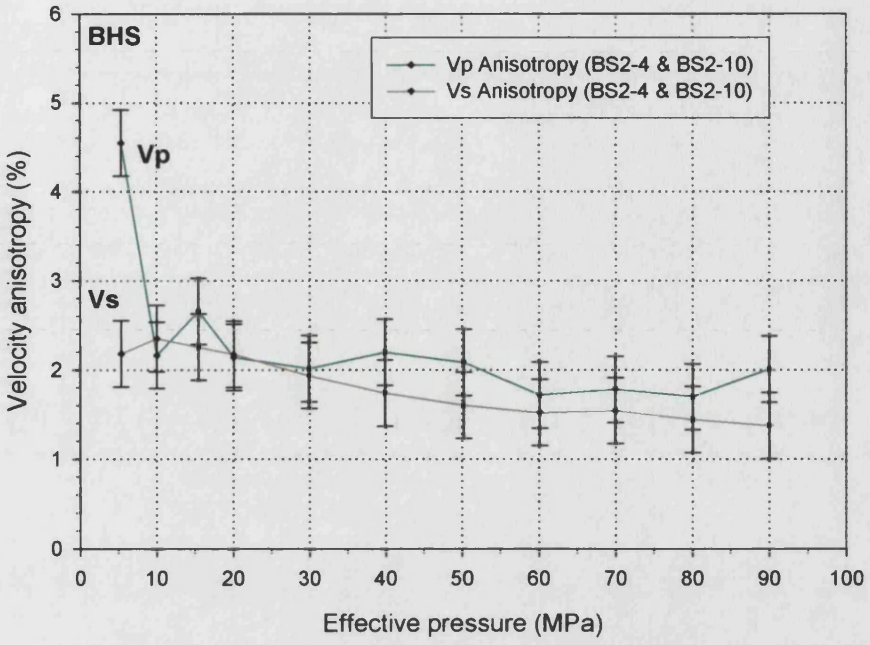

Figure 5-14. Bentheim sandstone velocity anisotropy variation with effective pressure

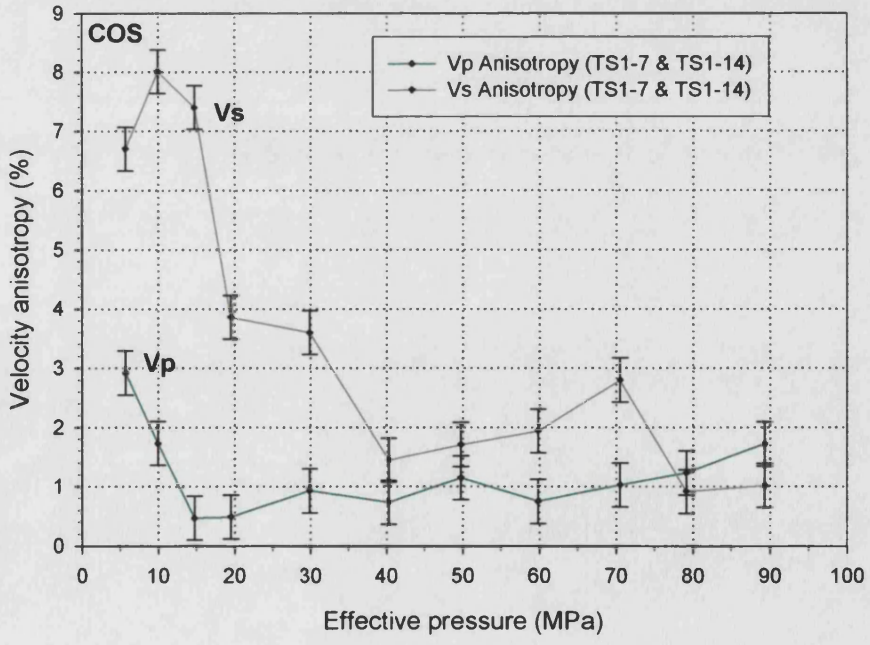

Figure 5-15. Crab Orchard sandstone velocity anisotropy variation with effective pressure.

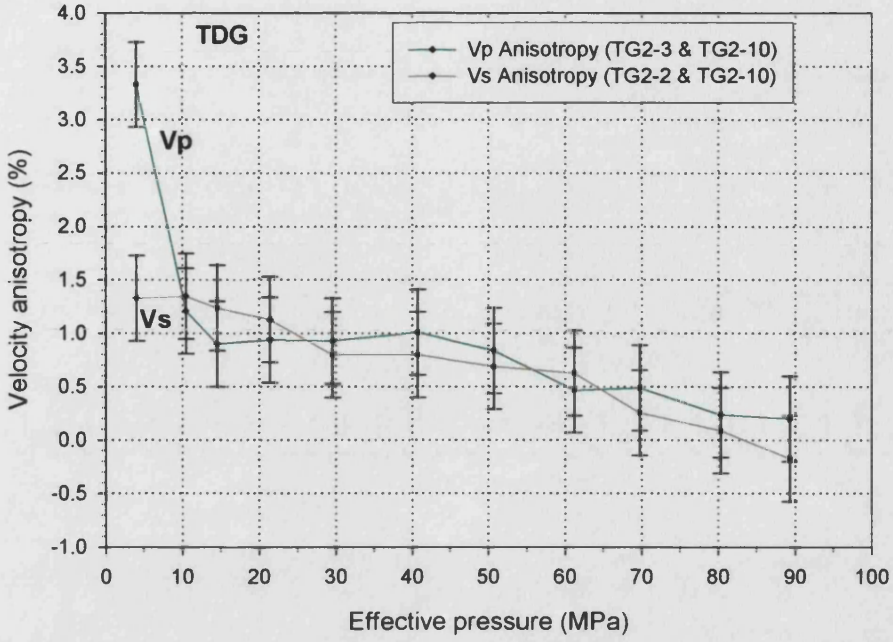

Figure 5-16. Takidani granite Bentheim velocity anisotropy variation with effective pressure.

5.3 PERMEABILITY AND POROSITY

5.3.1 INTRODUCTION

The servo-controlled measurement cell, as previously noted, has the ability to measure porosity and permeability contemporaneously with elastic wave velocity, via the protocols and methods detailed in Chapter 3. In this section, results are presented for porosity and permeability change with increasing effective pressure.

5.3.2 POROSITY AND PERMEABILITY AS A FUNCTION OF EFFECTIVE PRESSURE

Bentheim sandstone

The porosity of Bentheim sandstone decreases with increasing effective pressure, effectively mirroring the increase in elastic wave velocity seen earlier. Between 5 MPa and 90 MPa effective pressure the average porosity decreases by 0.77 percentage points (22.31% to 21.54%), which equates to a relative decrease of approximately 3.5% (figure 5-17). In addition, this figure illustrates the slightly different porosity-pressure trends between samples, which can be attributed to sample variability rather than measurement error. The error bars associated with average porosity are taken as the measurement error rather that the standard deviation using the normalised porosity at each step, to avoid this influence of sample variability.

Permeability of BHS at 5 MPa effective pressure is approximately 0.82 $x10^{-12}$ m^2 (figure 5-18), and essentially does not vary within sample variability with either increasing effective pressure or permeability measurement direction (either X, Y or Z). Figure 5-19 summarises porosity change together with the permeability change. From this illustration, it is clear that the decreasing porosity (22.31% to 21.54%) does not significantly influence the permeability (i.e. the connected porosity) of the rock as pressure is increased from 5 MPa to 90 MPa.

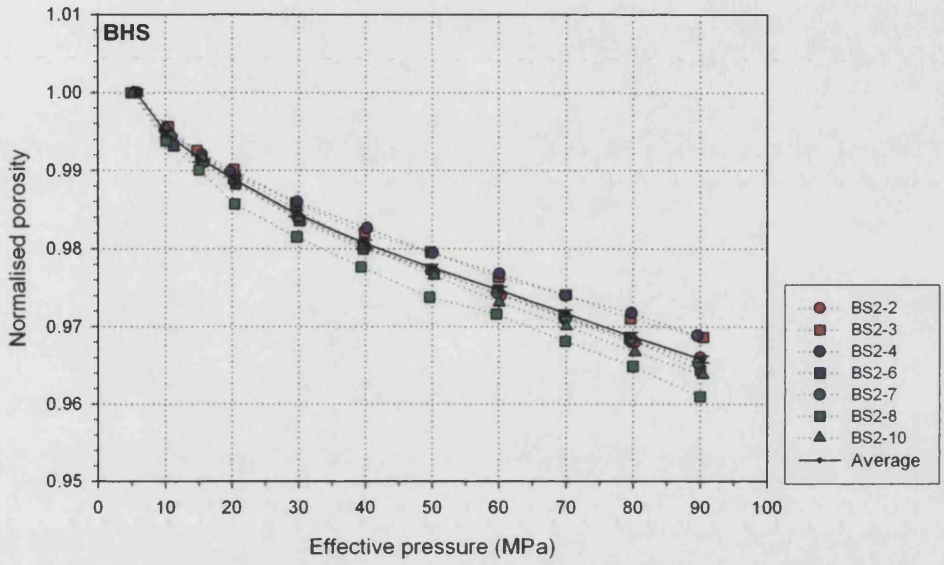

Figure 5-17. Bentheim sandstone normalised porosity variation with effective pressure. Solid symbols denote laboratory data, connected by dotted lines. Red denotes X core axis data, blue denotes Y core axis data, and green denotes Z axis cores. Black symbols/solid line denoted the average of all data. The normalised porosity at 5MPa corresponds to 22.3% (average data only)

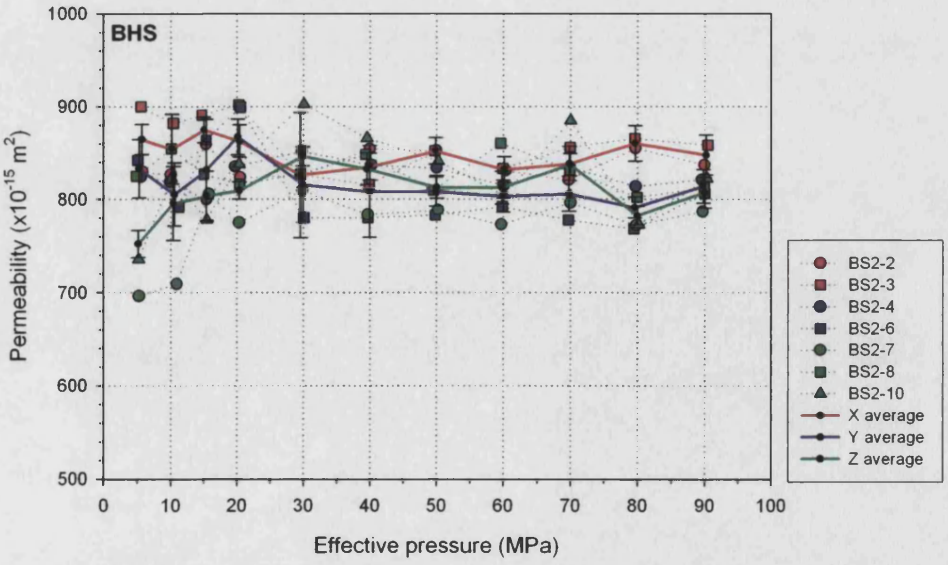

Figure 5-18. Bentheim sandstone permeability variation with effective pressure. Solid symbols denote laboratory data, connected by dotted lines. Red denotes X core axis data, blue denotes Y core axis data, and green denotes Z axis cores. Solid lines denote average values based upon core axis

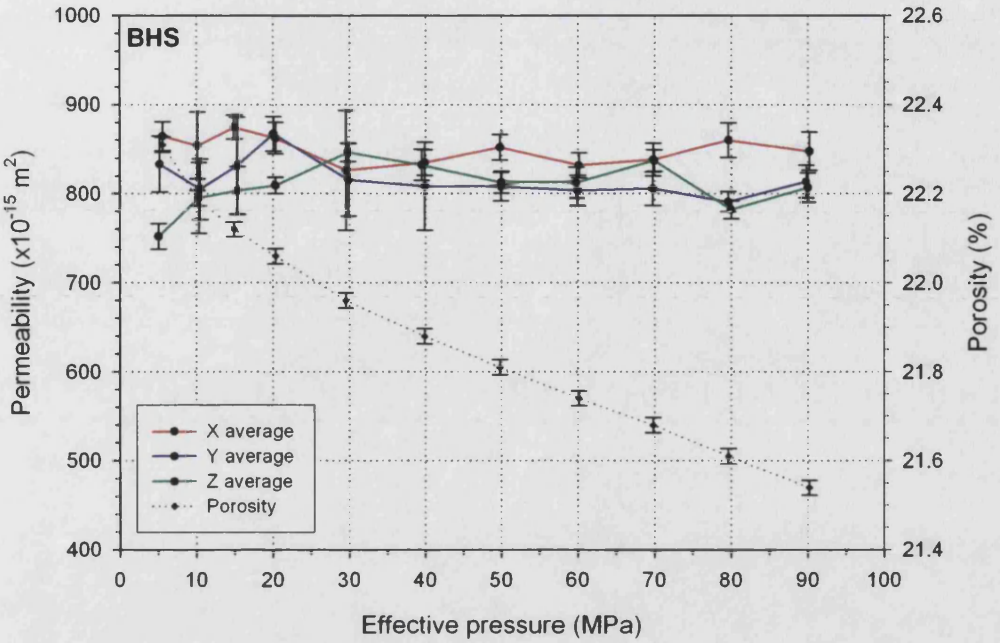

Figure 5-19. Bentheim sandstone average porosity and permeability variation with effective pressure

Crab Orchard sandstone

Normalised porosity for Crab Orchard sandstone decreases with increasing effective pressure (figure 5-20), again mirroring the increase in the observed elastic velocity earlier. Between 5 MPa and 90 MPa the average normalised porosity decreases by 0.47 percentage points (4.76% to 4.29%), which equates to a relative decrease of approximately 10%. In terms of normalised porosity change, this is a far higher decrease than as compared to the BHS normalised porosity decrease seen earlier. However, a higher sample variability is evident in the porosity for COS as compared to BHS, with sample TS1-7 exhibiting a particularly large decrease in normalised porosity over the effective pressure range displayed.

Permeability of COS at 5 MPa effective pressure is 130 x 10^{-18} m^2, 115 x 10^{-18} m^2, and 50 x 10^{-18} m^2 for permeabilities in the X, Y and Z directions respectively (figure 5-21). In addition, for the same pressure conditions the permeabilities measured in the X and Y directions are the same within reported experimental error (i.e. the crossbedding plane as indicated by pAMS and velocity anisotropy principal direction data). As effective pressure increases to 90 MPa, permeability decreases by over an order of magnitude, in stark contrast with BHS permeability data. Figure 5-22 summarises the porosity and average directional permeability increase with effective pressure increase. Unlike the equivalent plot for BHS, a clear link is seen between the porosity decrease (4.76% to 4.29%), and the decreasing permeability over the effective pressures increase from 5 to 90 MPa.

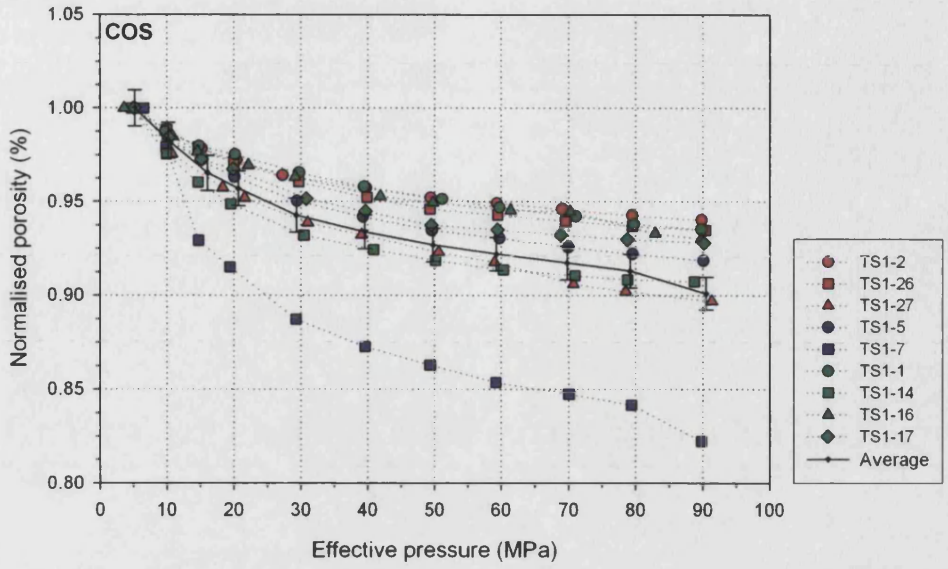

Figure 5-20. Crab Orchard sandstone normalised porosity variation with effective pressure. Solid symbols denote laboratory data, connected by dotted lines. Red denotes X core axis data, blue denotes Y core axis data, and green denotes Z axis cores. Black symbols/solid line denoted the average of all data. The normalised porosity at 5MPa corresponds to 4.8% (average data only)

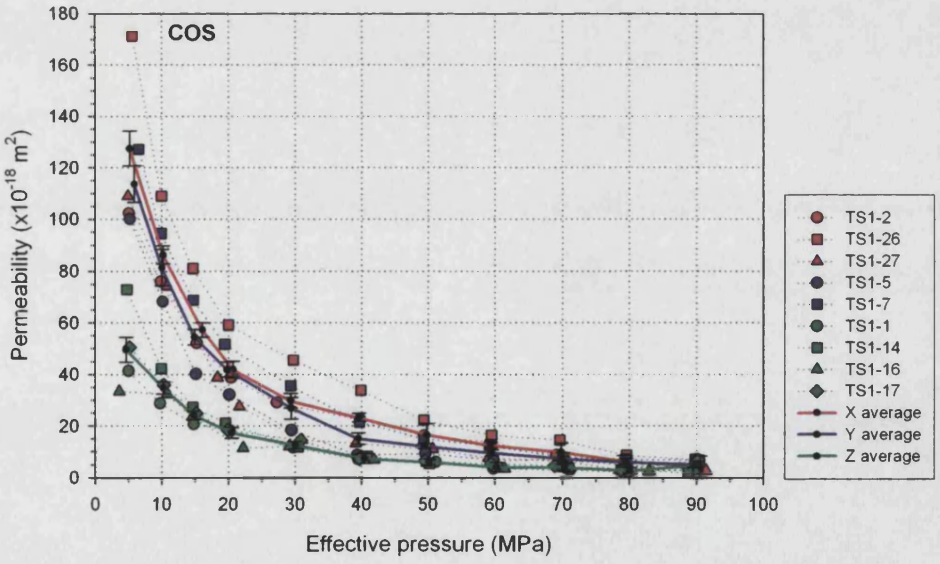

Figure 5-21. Crab Orchard sandstone permeability variation with effective pressure. Solid symbols denote laboratory data, connected by dotted lines. Red denotes X core axis data, blue denotes Y core axis data, and green denotes Z axis cores. Solid lines denote average values based upon core axis

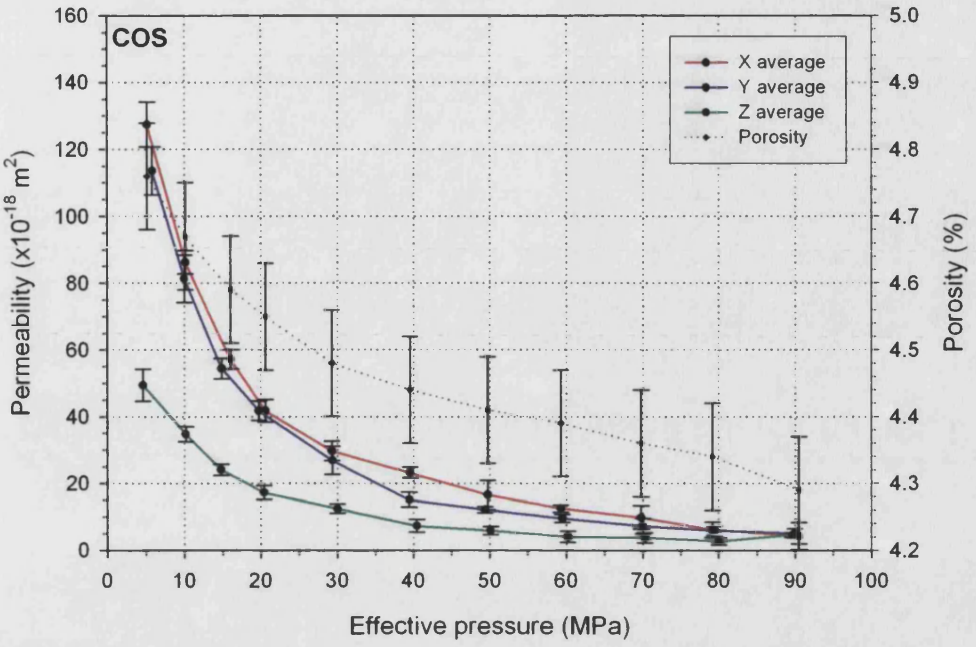

Figure 5-22. Crab Orchard sandstone average porosity and permeability variation with effective pressure

Takidani granite

Normalised porosity for Takidani granite is shown in figure 5-23. Between 5 MPa and 90 MPa effective pressure, the average normalised porosity decreases by 0.13 percentage points (0.92% to 0.79%), which equates to a relative porosity decrease of approximately 14%, the highest of any rock type investigated. However, a high sample variability is again evident with respect to TDG porosity as compared to BHS or COS.

Takidani granite permeability at 5 MPa effective pressure is approximately 21 x 10^{-18} m^2, 11 x 10^{-18} m^2, and 31 x 10^{-18} m^2 for X direction, Y direction and Z direction permeabilities respectively (figure 5-24). The permeability of TDG decreases significantly with increasing effective pressure, by approximately an order of magnitude over the pressure range from 5 MPa to 90 MPa. The direction of lowest permeability is well matched to the minimum elastic velocity principal direction derived in Chapter 4, and also (tenuously) to the tAMS and pAMS minimum principal direction. Figure 5-25 summarises the porosity decrease (0.92% to 0.79%) with permeability decrease over the increasing effective pressure from 5 to 90 MPa, illustrating a link between porosity and permeability decrease. Note that the average permeability in the X and Z directions are similar, although not quite within experimental error until ~15 MPa pressure is achieved.

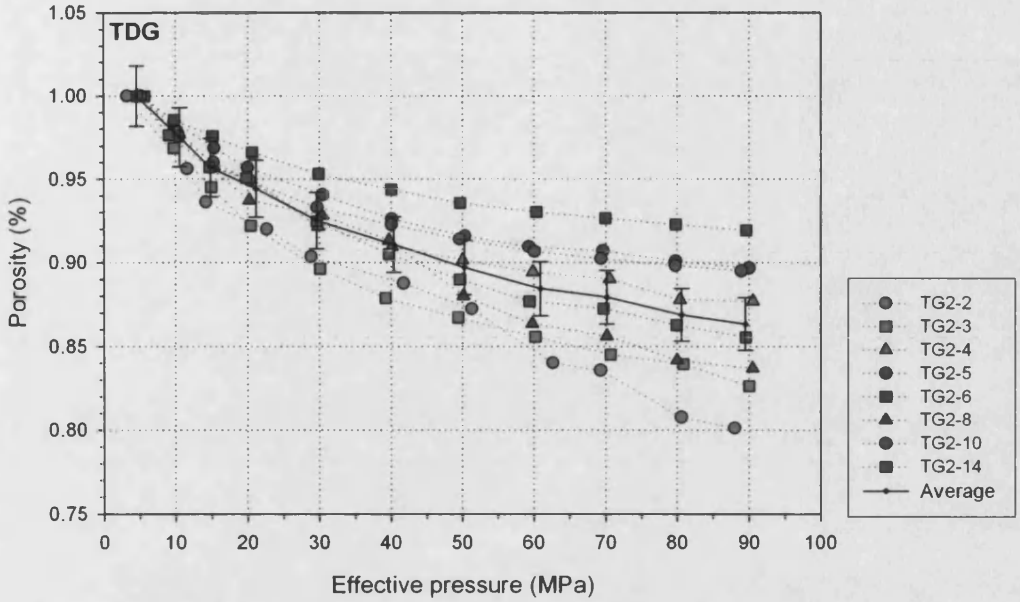

Figure 5-23. Takidani granite normalised porosity variation with effective pressure. Solid symbols denote laboratory data, connected by dotted lines. Red denotes X core axis data, blue denotes Y core axis data, and green denotes Z axis cores. Black symbols/solid line denoted the average of all data. The normalised porosity at 5MPa corresponds to 0.9% (average data only)

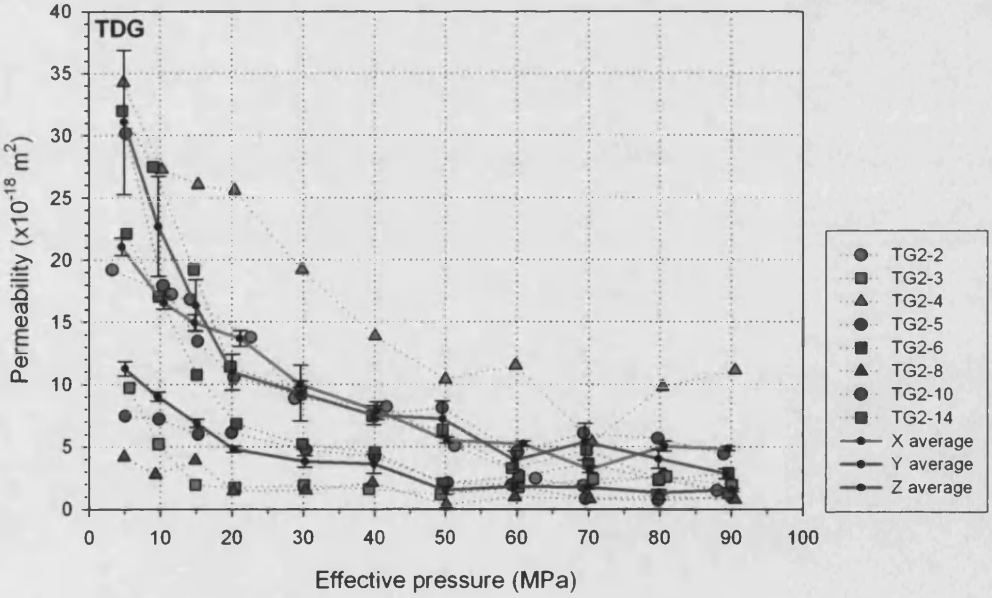

Figure 5-24. Takidani granite permeability variation with effective pressure. Solid symbols denote laboratory data, connected by dotted lines. Red denotes X core axis data, blue denotes Y core axis data, and green denotes Z axis cores. Solid lines denote average values based upon core axis

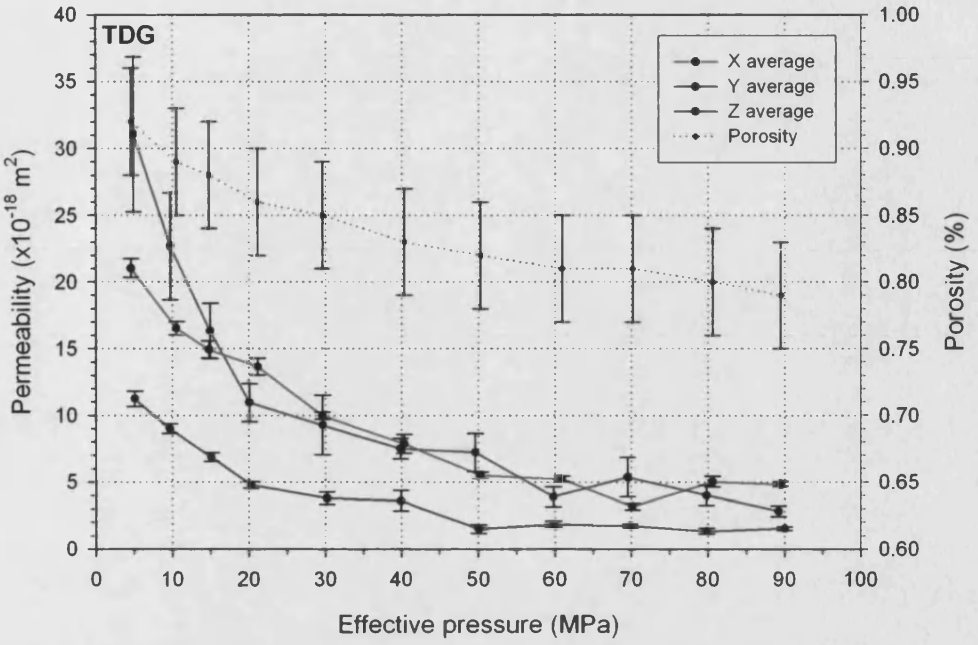

Figure 5-25. Takidani granite average porosity and permeability variation with effective pressure

5.3.3 PERMEABILITY ANISOTROPY

Permeability anisotropy is calculated using the general formula ($100\%*[k_{max}-k_{min}]/k_{mean}$), where k is the permeability. The anisotropy using this method is calculated at each stepwise increase in effective pressure, using average permeability values in each of the X, Y and Z directions. As the rocks in this work all possess a plane in which two permeability values are approximately the same (i.e. maximum, within the symmetry plane), then this gives rise to two anisotropy measurements for each rock through using data from each orthogonal 'maximum' direction (for BHS and COS, the X and Y axes; for TDG, the X and Z axes) together with data from the third, 'minimum', permeability direction (Z axis for BHS and COS, Y axis for TDG).

For Bentheim sandstone (figure 5-26), permeability anisotropy falls rapidly from 10-15% at 5 MPa to 0% after ~30 MPa as effective pressure increases. After ~30 MPa, no permeability anisotropy is obvious. Again, note that the reported anisotropy error bars reflect the measurement error rather than permeability anisotropy variability with pressure. This variability is likely to be due to the difficulty in experimentally determining relatively small changes in a large number (i.e. a small difference between X/Y and Z axis permeability, but with the overall permeability value being very high). In addition, areas of 'negative' anisotropy refer to the scenario whereby the permeability along the Z direction is higher than in the X and Y directions (which are taken as maximum for calculation purposes). The interpretation of such regions of negative anisotropy is that the permeability anisotropy in these areas is effectively zero.

For Crab Orchard sandstone (figure 5-27), a permeability anisotropy of ~60% to ~100% is calculated. The seemingly random variation over the pressure range from 5 MPa to 90 MPa is likely to be due to the statistics once again, and therefore an average permeability anisotropy may be calculated of ~80% throughout the pressure range. For Takidani granite (figure 5-28), a similar situation is seen, with permeability anisotropy of ~60% to ~130%. Again, taking the seemingly random variation of permeability with increasing effective pressure into account as a sample statistical effect, an average permeability anisotropy of ~80% may be determined.

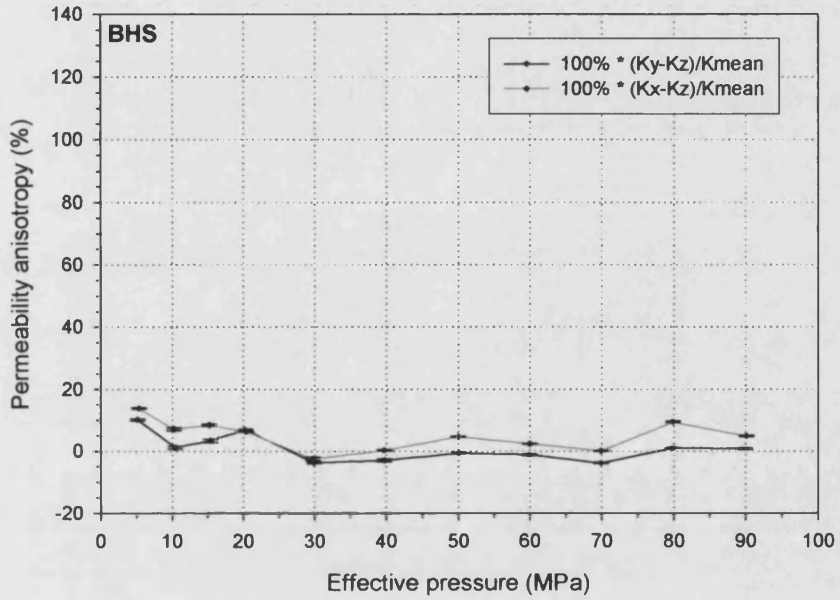

Figure 5-26. Bentheim sandstone average permeability anisotropy variation with effective pressure

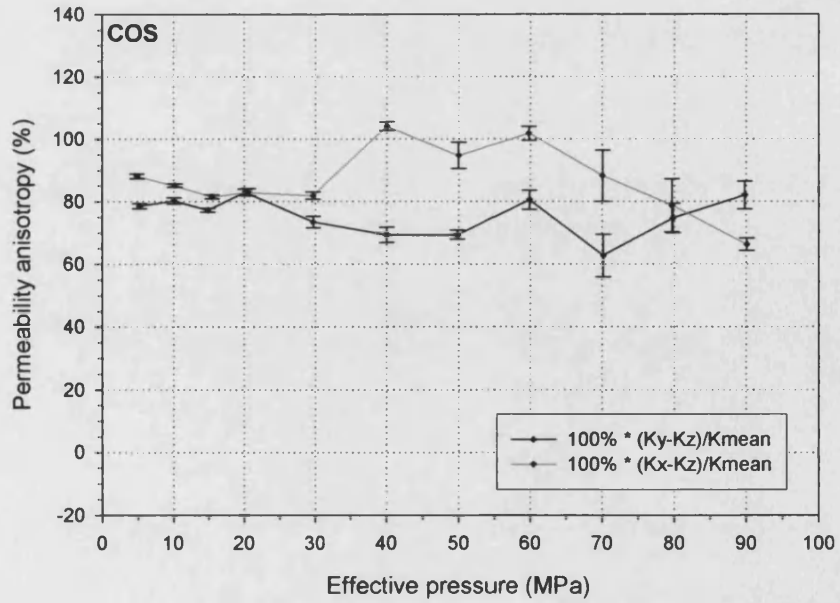

Figure 5-27. Crab Orchard sandstone average permeability anisotropy variation with effective pressure

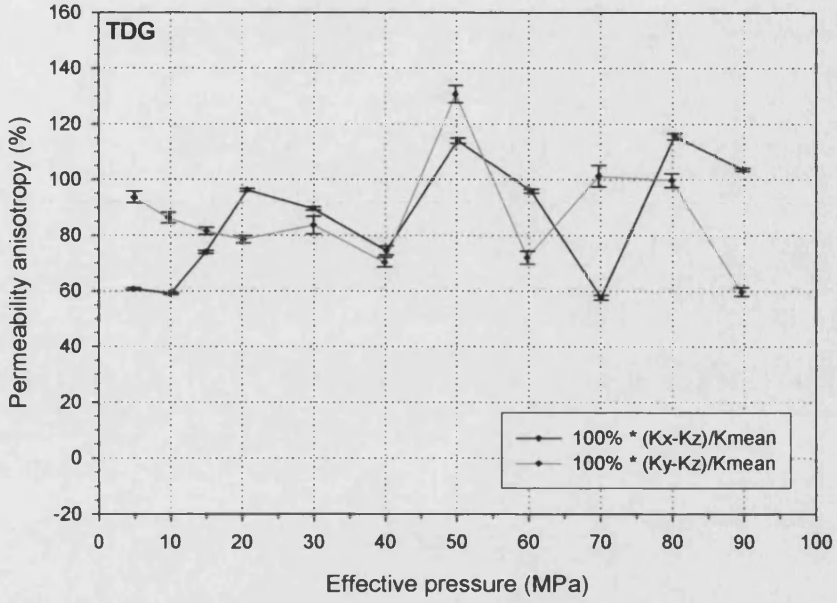

Figure 5-28. Takidani granite average permeability anisotropy variation with effective pressure

6 MODELING OF EXPERIMENTAL DATA

Experimental studies measuring rock physical properties such as elastic wave velocities and permeabilities are relatively easy in the laboratory at ambient conditions. Whilst this has application in itself, we would obviously like to know properties deeper in the Earth (at higher pressures). However, far fewer measurements have been conducted under such conditions due to the technical complexities involved. Even where they have, the focus has been to measure different parameters upon different samples. Such an approach often introduces other issues, such as the problems of reproducibility of physical conditions and also the natural heterogeneity of the rocks. This has resulted in the development of a large number of models aiming to predict properties of materials at depth from those made at lower pressure (for example). However, in order to have confidence in such models and relations, it is necessary to test their results by direct comparison to a 'control experiment' of some kind.

In this study, I have developed experimental equipment and techniques which can measure porosity, P-wave velocity, S-wave velocity and permeability contemporaneously under conditions simulating burial depths up to approximately 4km (100 MPa). These data, therefore, provide such a 'control' in the form of the large and unique dataset presented in this study, and are well suited to the application of objectively testing some of the models which attempt to predict seismic velocity and permeability based upon other rock fabric parameters, as both the model input data and the model output data have been measured independently. The application of a small number of models to the extensive data collected during the course of this investigation will therefore provide an a ideal opportunity to test and investigate some of these models, and is mutually advantageous to both the modelling and the experimental programme. However, this study has focussed more upon the experimental aspect of the rock physics problem outlined in Chapter 1, and does not seek explicitly to introduce any detailed mathematical advancements to the large number of applicable models available.

This chapter summarises the chosen models, the reasons for their selection, and compares the experimentally obtained data with their predicted output. The choice of model for this exercise is important, as such a large number of relations exist which attempt to predict elastic and transport properties from the general properties of porous media. The models chosen are taken from the larger list introduced in Chapter 1. These are the models of Thomsen (1986), Eberhart-Phillips (1989), with constants of proportionality derived through a least square fit to the experimental data, the model of Kuster and Toksoz (1974), Zimmerman's (1991) differential effective medium model, and the crack models of Hudson (1980, 1981), and Kachanov (1994).

In addition to elastic wave velocities, the laboratory programme also measured rock transport (permeability) properties. However, as the three rock types used in this work possess such contrasting pore fabrics and permeabilities, three different models are applied to the experimental

data depending upon the model strengths and weaknesses. These models are the Lattice-Boltzman gas approximation (Keehm, 1990); the Kozeny-Carman relation for fluid flow (Carman, 1961); and the percolation/statistical model of Guéguen and Dienes (1989). In this investigation, the Lattice Boltzmann gas model is applied to Bentheim sandstone, the Kozeny-Carman model is applied to Crab Orchard sandstone, and the model of Guéguen and Dienes is applied to the cracked Takidani granite.

6.1 EMPIRICAL AND PHENOMENOLOGICAL VELOCITY MODELS

6.1.1 INTRODUCTION

6.1.1.1 THOMSEN'S WEAK ANISOTROPY MODEL

Even in its most simple form, elastic anisotropy may be mathematically daunting, and the desire to interpret observed elastic anisotropy to the elastic stiffness matrix in simple and relatable terms has prompted a useful simplification known as Thomsen's weak anisotropy model (Thomsen, 1986). In principle, this simplification proceeds in the following manner. Recalling the general form of anisotropic elasticity introduced in Chapter 2, it is seen that 21 independent elastic constants exist in order to fully describe the rock frame stiffness. However, in the case of transverse isotropy, which may be found in many layered sedimentary rocks such as shales (Hornby, 1998; Johnston and Christensen, 1995; Vernik and Nur, 1992), we can reduce the number of truly independent elastic constants (C_{ij}) to five:

$$\begin{bmatrix} c_{11} & c_{12} & c_{13} & 0 & 0 & 0 \\ c_{12} & c_{11} & c_{13} & 0 & 0 & 0 \\ c_{13} & c_{13} & c_{33} & 0 & 0 & 0 \\ 0 & 0 & 0 & c_{44} & 0 & 0 \\ 0 & 0 & 0 & 0 & c_{44} & 0 \\ 0 & 0 & 0 & 0 & 0 & c_{66} \end{bmatrix}, \quad \text{where: } c_{66} = \frac{1}{2}(c_{11} - c_{12})$$

By taking only the P and S wave velocities propagating along the symmetry axes, denoted α and β respectively, and assuming that the anisotropy is 'weak', defined as lying between 0% and 10-20%, Thomsen (1986) derives the following simplified elastic constants:

$$\alpha = \sqrt{c_{33}/\rho}$$
$$\beta = \sqrt{c_{44}/\rho}$$
$$\varepsilon = \frac{c_{11} - c_{33}}{2c_{33}}$$
$$\gamma = \frac{c_{66} - c_{44}}{2c_{44}}$$
$$\delta = \frac{(c_{13} + c_{44})^2 - (c_{33} - c_{44})^2}{2c_{33}(c_{33} - c_{44})}$$

Where ρ is the average medium density, and c_{xx} are the elastic stiffness elements making up the matrix c_{ij}.

The parameters α and β are thus defined in term of the elastic constants in a similar way to the definition of P-wave and S-wave velocity using bulk P-wave modulus ($K+4\mu/3$) and shear moduli for isotropic media (Chapter 2). In addition, we have also defined the parameters ε and γ. These parameters are relatively easy to interpret as the maximum attainable fractional velocity differences along principal directions for V_p and V_s respectively. These parameters are useful, as they can characterise the shape of the anisotropy in a similar way to that in which the AMS can define the pore shape using the relative balance of foliation and lineation factors. For example, in this notation 'elliptical' anisotropy is described in instances where $\delta=\varepsilon$. For finely (isotropically) arranged layers, such as might be found in clays, the anisotropy is characterised by $\delta<\varepsilon$. Relative to a symmetry axis normal to the transverse isotropy, Thomsen (1986) then writes the azimuthally varying velocities in terms of these new parameters, (Mavko et al., 1998):

$$V_P(\theta) \approx \alpha\left(1 + \delta\sin^2\theta\cos^2\theta + \varepsilon\sin^4\theta\right)$$
$$V_{SV}(\theta) \approx \beta\left(1 + \frac{\alpha^2}{\beta^2}(\varepsilon - \alpha)\sin^2\theta\cos^2\theta\right) \qquad \textit{Equation 6-1}$$
$$V_{SH}(\theta) \approx \beta\left(1 + \gamma\sin^2\theta\right)$$

Where $V_x(\theta)$ is the velocity at an angle θ to the transversely isotropic (TI) symmetry axis.

These equations can be applied directly to the experimental velocities measured as a function of azimuth around the rock core circumference, as described in Chapter 3 earlier, with respect to a TI symmetry axis based upon the visible crossbedding and/or the pAMS and velocity ellipsoid principal axes allowing the constants α, β, ε and γ to be evaluated through a least squares fit to the laboratory data.

6.1.1.2 EBERHART-PHILLIPS RELATIONS

Eberhart-Phillips (1989) used the classic dataset of Han (1986), which contains a large number (80) of water saturated sandstone samples with porosities ranging from 3 to 30 percent, with a multivariate analysis in order to determine an empirical fit (equations 6-2 and 6-3) between effective pressure, porosity and clay content and their experimentally measured P-wave and S-wave ultrasonic velocities. Although the rocks studied in this investigation do not exhibit such a wide range of porosity, these relations are still a useful way in which to visualise how the experimental pressure conditions influence the measured velocity. Equation 6-4 shows a general form of the relation used in this work, in which the key constants have been replaced with the general parameters A, D, E and F. In this general relation, the constant 'A' has replaced the dependency of velocity upon porosity and clay content as seen in the equations of Eberhart-Phillips. Constants are evaluated though a least squares best-fit to the experimental data for both P-wave and S-wave data and for each rock type up to the maximum effective pressure of 90MPa.

$$V_p = 5.77 - 6.94\phi - 1.73\sqrt{C} + 0.446\left(P_{eff} - 1.0e^{-16.7P_{eff}}\right) \qquad \textit{Equation 6-2}$$

$$V_s = 3.70 - 4.94\phi - 1.57\sqrt{C} + 0.361\left(P_{eff} - 1.0e^{-16.7P_{eff}}\right) \qquad \textit{Equation 6-3}$$

$$V = A + DP_{eff} - Ee^{-FP_{eff}} \qquad \textit{Equation 6-4}$$

Where: ϕ is the sample porosity,

C is the sample clay content,

P_{eff} is the applied effective pressure,

V is the measured ultrasonic velocity,

A, D, E, and F are constants.

6.1.2 THOMSEN MODEL FITTING: COMPARISON WITH LAB DATA

Bentheim sandstone

The Thomsen model fit to Bentheim sandstone laboratory P-wave and S-wave data is, overall, very good, showing correlation co-efficients ranging from 0.79 to 0.99. Two planes of measurement are applicable to the planar transverse isotropy (PTI) variation, shown in figures 6-1 (YZ plane), and figure 6-2 (XZ plane). Figure 6-1 (YZ plane) does, however, illustrate some areas in which the model fit is outside the experimental velocity accuracy. In particular, the range 0°-60° for P-wave data, and numerous areas on the S-wave plot, 0°-70° and 140°-250°. However, it should be stressed that S-wave data is much more difficult to measure accurately than P-wave data, and that the absolute variation is also smaller. This means that when this smaller S-wave velocity change with azimuth is plotted with the same diagram dimensions, it acts to accentuate the velocity change, which (for S-wave data) changes by only 70 m/s over the entire scale, compared to the P-wave

velocity variation which covers a velocity range of 140 m/s. For the XZ plane data (figure 6-2), the P-wave model fit does not compare well to the experimentally measured data, even though the correlation co-efficient is high (0.99), with only the regions at 70°-110° and 240°-280° showing agreement within experimental error. The S-wave model fit is also poor, with the areas at 130°-150° and 260°-300° lying outside the experimental data error bounds. The Thomsen parameters, α, β, ε and γ (table 6-1) agree well with the 'A' values calculated using the measured laboratory data (summarised in table 6-2). However this is of little surprise, given that the data itself is used to generate these parameters.

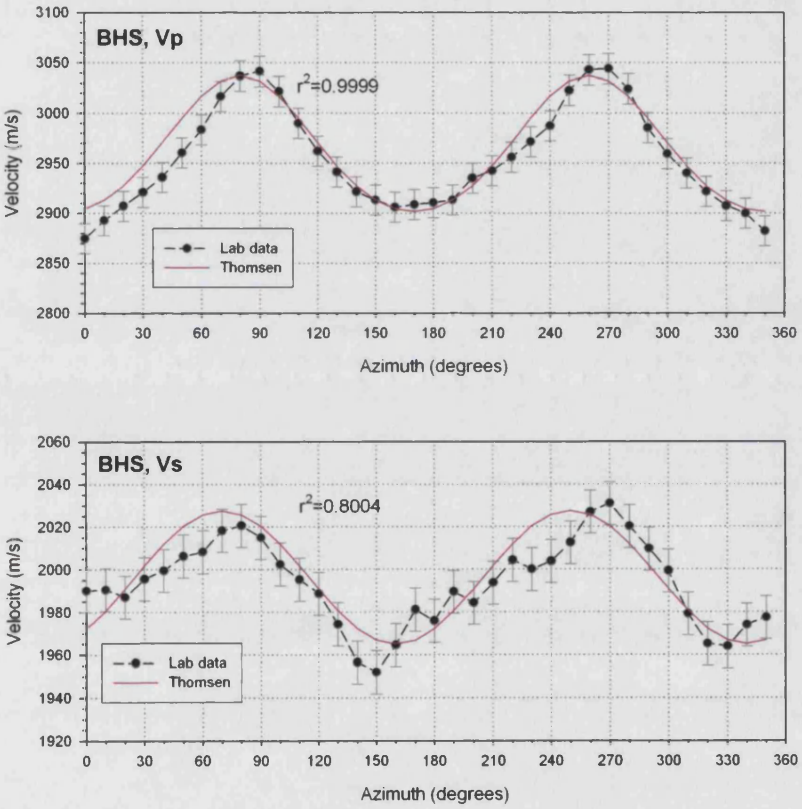

Figure 6-1. Least squares Thomsen model fit to Bentheim sandstone azimuthal data (X direction core axis, YZ plane), for P-wave (top) and S-wave (bottom)

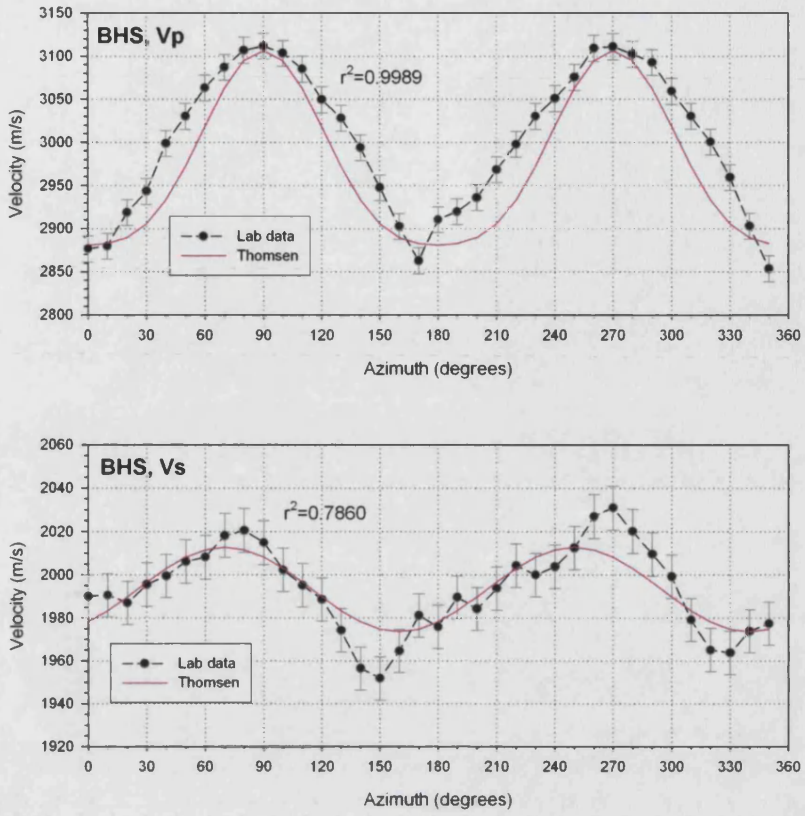

Figure 6-2. Least squares Thomsen model fit to Bentheim sandstone azimuthal data (Y direction core axis, XZ plane), for P-wave (top) and S-wave (bottom)

Crab Orchard sandstone

For Crab Orchard sandstone, the Thomsen model fit to laboratory P-wave and S-wave data is excellent, showing correlation co-efficients ranging from 0.79 to 0.99. The same two planes of measurement are applicable as for BHS, with figures 6-3 illustrating YZ plane variation, and figure 6-4 showing XZ plane data. A few areas of the modelled azimuthal velocity variation lie outside the experimental velocity error, such as 80°-100° and 260°-280° for YZ plane P-wave data and 100°/280°-290° for XZ plane P-wave data. However, virtually the entire model S-wave velocity variation lies within experimental velocity data error – perhaps surprising given the known difficulties in measuring S-wave velocity, noted earlier. Thomsen parameters (α, β, ε and γ – table 6-1) agree well with the anisotropy 'A' values calculated using the laboratory data (i.e. from the maximum, minimum, and mean velocity values measured azimuthally – summarised in table 6-2). Additionally, in the case of the XZ plane the modelled anisotropy values are within the standard deviation of the experimental anisotropy values.

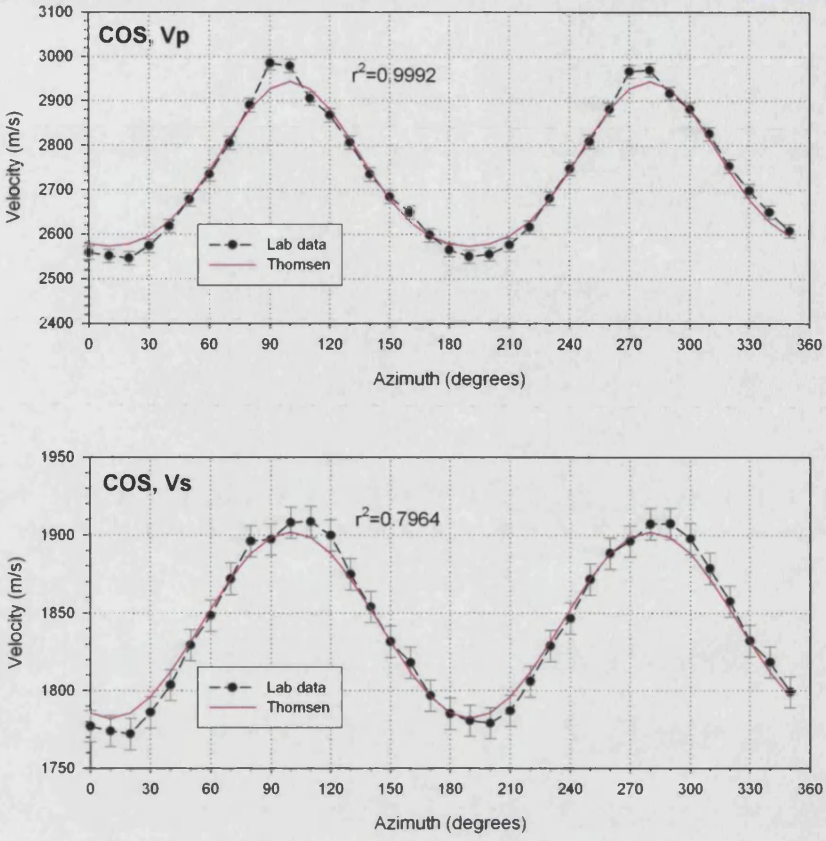

Figure 6-3. Least squares Thomsen model fit to Crab Orchard sandstone azimuthal data (X direction core axis, YZ plane), for P-wave (top) and S-wave (bottom)

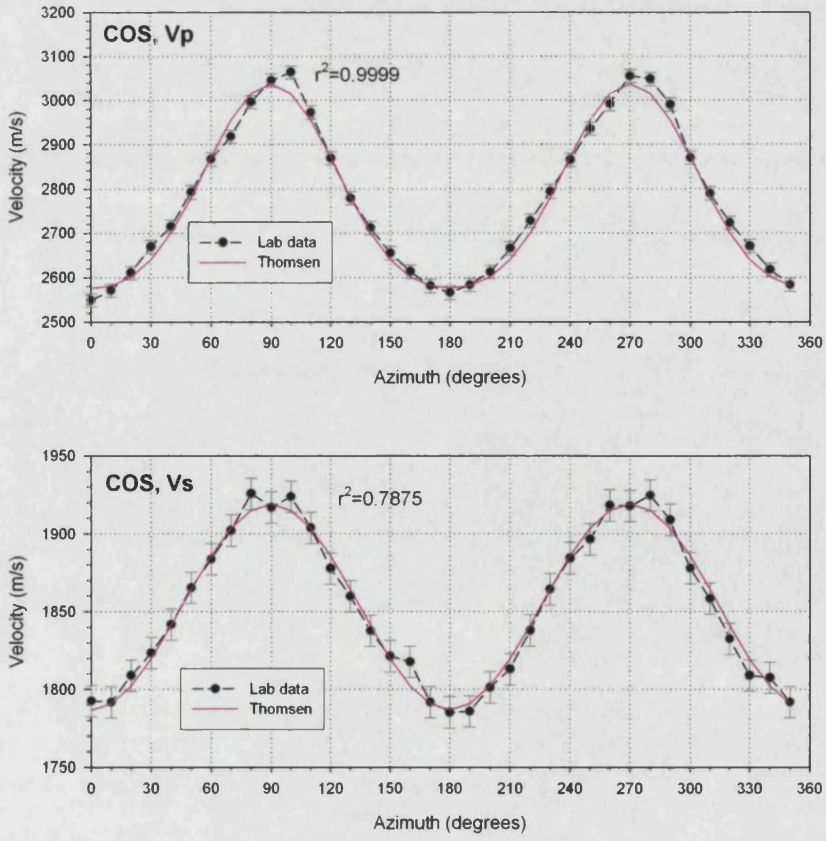

Figure 6-4. Least squares Thomsen model fit to Crab Orchard sandstone azimuthal data (Y direction core axis, XZ plane), for P-wave (top) and S-wave (bottom)

Takidani granite

Finally, figures 6-5 and 6-6 illustrate the Thomsen model fit to laboratory P-wave and S-wave data for Takidani granite. For this rock type, the correlation co-efficients are generally lower, ranging from 0.7 to 0.9. The applicable planes for azimuthal measurements (as determined by P-wave velocity ellipsoid principal directions) are the YZ plane (figure 6-5) and the XY plane (figure 6-6). In general, few areas of the modelled azimuthal velocity variation agree well within experimental velocity error, with only the P-wave data showing a good match. This may be due to a number of factors, such as the difficulty in measuring the P-wave and S-wave velocity for this rock type, but it is more likely to be due to Takidani granite displaying a more complex type of anisotropy than the PTI modelled by this Thomsen approach. However, given that problems were encountered when measuring accurate laboratory velocities for Takidani granite due to poor signal propagation (especially for S-wave), the *general trend* for the modelled azimuthal variation is still good, even for S-wave data (particularly figure 6-6). Unlike the sandstones, Thomsen anisotropy parameters (table 6-1), are all significantly lower than the anisotropy 'A' values calculated from laboratory data (table 6-2), in both YZ and XY planes.

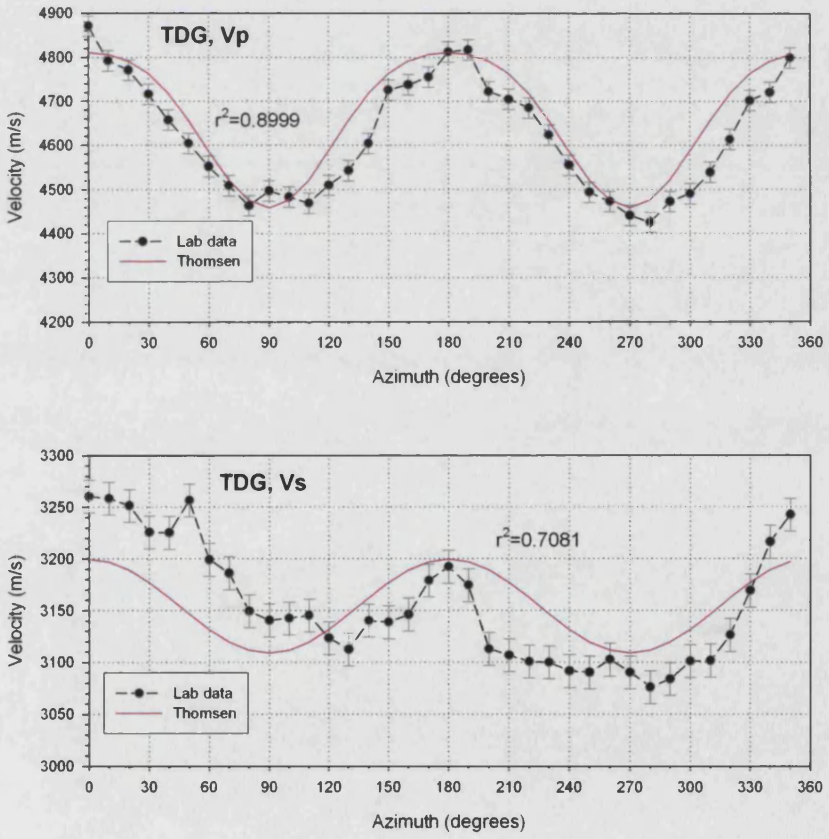

Figure 6-5. Least squares Thomsen model fit to Takidani granite azimuthal data (X direction core axis, YZ plane), for P-wave (top) and S-wave (bottom)

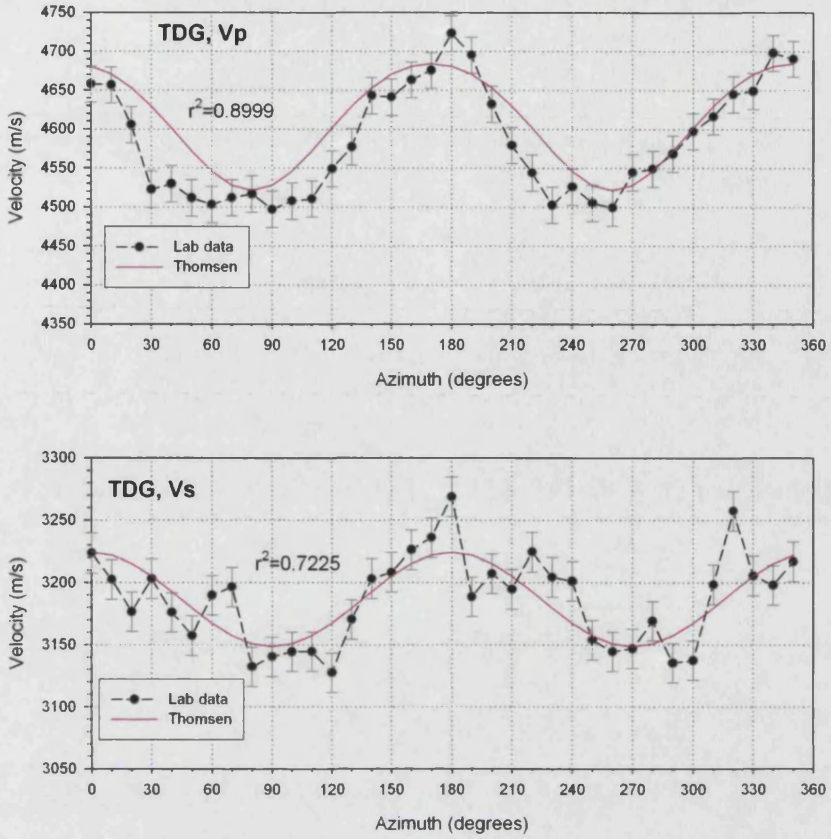

Figure 6-6. Least squares Thomsen model fit to Takidani granite azimuthal data (Z direction core axis, XY plane), for P-wave (top) and S-wave (bottom))

Rock type / direction	Thomsen weak elastic anisotropy parameters				
	Alpha (m/s)	Beta (m/s)	**Epsilon, %**	**Gamma, %**	Delta, %
BHS, X (YZ plane)	2902	1965	**4.7**	**3.2**	1.0
BHS, Y (XZ plane)	2881	1974	**7.8**	**2.0**	10.0
COS, X (YZ plane)	2573	1782	**14.4**	**6.7**	6.6
COS, Y (XZ plane)	2575	1787	**17.9**	**7.4**	9.6
TDG, X (YZ plane)	4811	3200	**7.3**	**2.8**	9.7
TDG, Z (XY plane)	4685	3224	**3.5**	**2.4**	6.6

Table 6-1. Thomsen weak anisotropy model fit to laboratory data: output parameters (fractional) for all rock types. Alpha and Beta are equivalent to average P-wave and S-wave velocity respectively, Epsilon is equivalent to the P-wave anisotropy, Gamma, S-wave anisotropy

LAB data Comparison		Velocity (m/s)		Anisotropy parameter, A (%)					
				Ox (YZ plane)		Oy (XZ plane)		Oz (XY plane)	
		average	Std. dev.	average	Std. dev.	average	Std. dev.	average	Std. dev.
BHS	Vp	3055	235	**5.9**	0.3	**9.2**	1.6	3.2	0.4
	Vs	1888	490	**4.8**	0.5	**4.8**	1.7	2.7	1.2
COS	Vp	2843	140	**17.9**	2.0	**18.7**	2.6	4.5	2.3
	Vs	1866	41	**8.3**	0.9	**8.4**	0.9	3.1	0.2
TDG	Vp	4811	334	**11.0**	2.3	8.7	1.0	**6.3**	2.5
	Vs	3189	62	**7.6**	1.1	6.8	4.4	**9.5**	1.3

Table 6-2. Thomsen weak anisotropy: Anisotropy 'A' values calculated from laboratory azimuthal velocity data for comparison to models, with the relevant P-wave and S-wave anisotropy figures shown in bold for comparison to the bold figures in table 6-1

6.1.3 EBERHART-PHILLIPS MODEL FITTING: COMPARISON WITH LAB DATA

The fit between the Eberhart-Phillips (E-P) empirical model and the experimental data is shown in figure 6-7 (Bentheim sandstone), figure 6-8 (Crab Orchard sandstone) and figure 6-9 (Takidani granite). Values for the constants A, D, E and F determined with the least squares fit are summarised in table 6-3 and 6-4 for P-wave and S-wave respectively.

Bentheim sandstone (figure 6-7) E-P model data shows an excellent fit to the experimentally measured velocity. Separate regressions were performed upon each of the X, Y and Z direction velocity measurements with pressure. A good model fit to the data is intuitively expected, given that it was designed for use upon sandstones for porosities in the range 3-30%, in which case Bentheim sandstone is well suited with a porosity of ~22%. From figure 6-7, it is clear that by the time 'higher' pressures of over 40-50 MPa are reached, the pressure dependence has fallen sharply (the factor $\exp^{\{-FPeff\}}$ in equation 6-4 is approximately 10^{-3} at 50 MPa, decreasing further with higher pressures). This results in a largely linear trend after this pressure, as already noted from the experimental data.

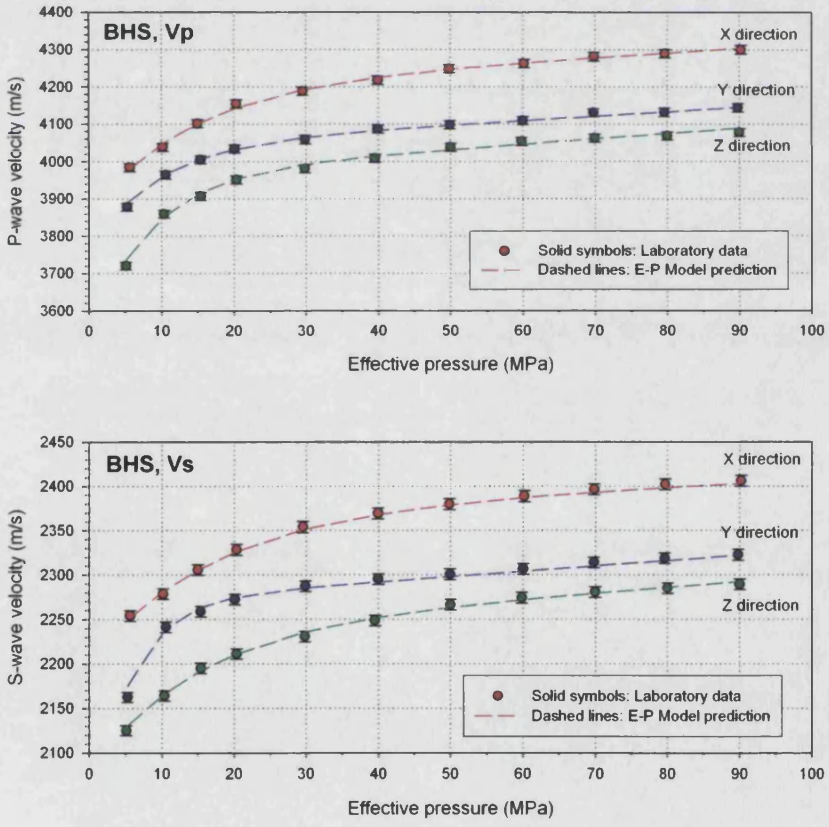

Figure 6-7. Eberhart-Phillips model fit (r^2=0.9999) to Bentheim sandstone velocity-effective pressure data (X direction core axis), for P-wave (top) and S-wave (bottom). Solid symbols show the laboratory data. Dashed lines shows the model fit. The colour code is as follows: Red-X direction, Blue-Y direction, Green-Z direction

Eberhart-Phillips model data also shows an excellent fit to the Crab Orchard sandstone experimental velocities (figure 6-8), and even models a sharp S-wave velocity change at approximately 10 MPa (X direction). The good fit to the experimental data is, again, not surprising, as the inverse problem allows a close solution to be determined. It is interesting to note that COS has a porosity (4%) at the low end of the porosity range used by Eberhart-Phillips (1989) when developing the model, and yet the model data is a good fit to the experimental velocity data. However, unlike the BHS case the model clearly illustrates that the velocity variation does not reach an obvious linear trend at higher effective pressure – the velocity **change** (not plotted) continues to decrease at even the highest pressure attained.

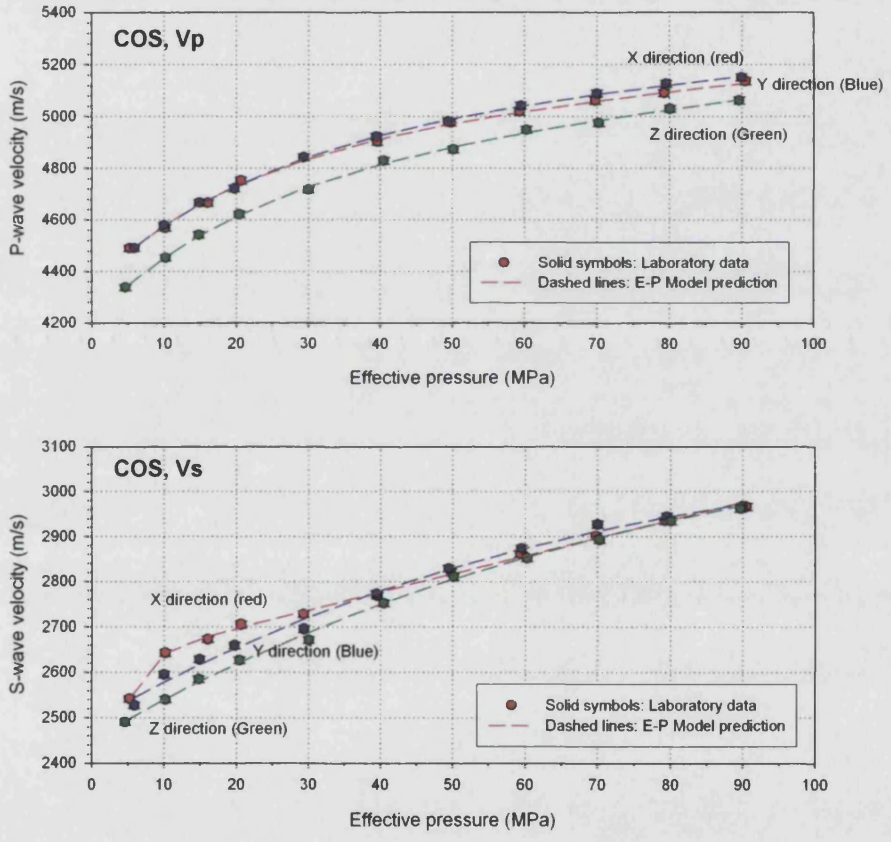

Figure 6-8. Eberhart-Phillips model fit (r^2=0.9999) to Crab Orchard sandstone velocity-effective pressure data (X direction core axis), for P-wave (top) and S-wave (bottom). Solid symbols show the laboratory data. Dashed lines shows the model fit. The colour code is as follows: Red-X direction, Blue-Y direction, Green-Z direction

Eberhart-Phillips model data for Takidani granite shows a good fit to the experimental values (figure 6-9), which is perhaps somewhat unexpected as TDG is not a sandstone, and has a porosity (1%) outside the porosity range used by Eberhart-Phillips (1989) when developing the model. However, any rock type should be well approximated by the Eberhart-Phillips approach (Mavko et al., 1998) as, strictly, the model simply assigns an empirical pressure dependence (with a constant vertical linear offset) to a set of experimental data. Like the BHS case, a clear velocity-pressure linear trend is seen at effective pressures over approximately 20 MPa for V_p data. However, a linear trend is not seen in the V_s model/laboratory data at any pressure.

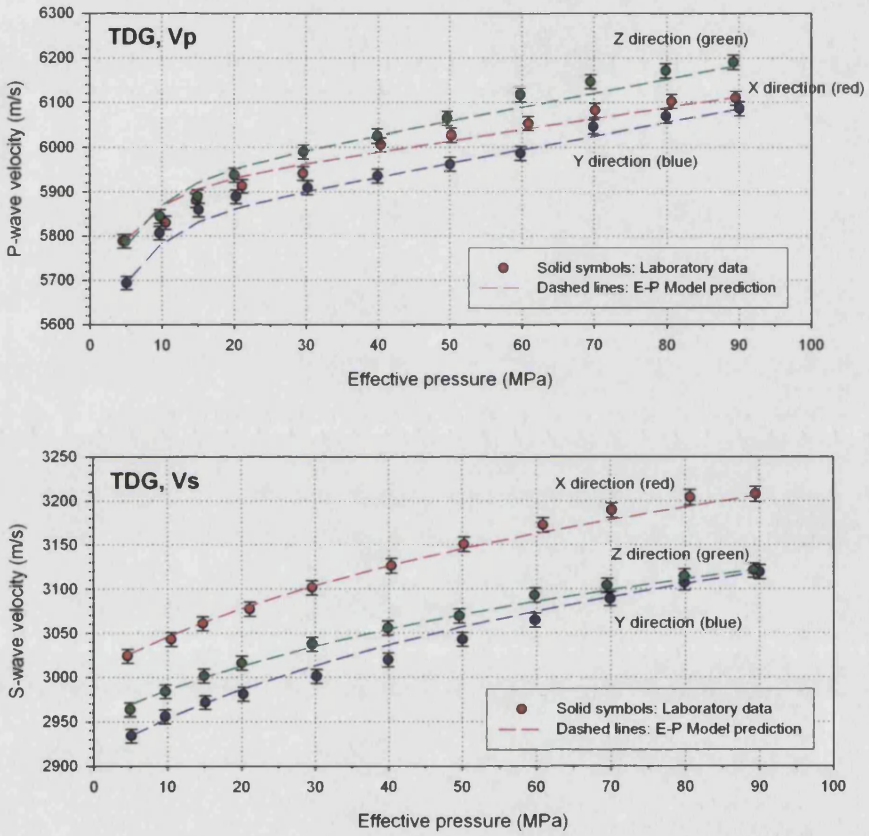

Figure 6-9. Eberhart-Phillips model fit (r^2=0.9999) to Takidani granite velocity-effective pressure data (X direction core axis), for P-wave (top) and S-wave (bottom). Solid symbols show the laboratory data. Dashed lines shows the model fit. The colour code is as follows: Red-X direction, Blue-Y direction, Green-Z direction

Rock type / direction	Eberhart-Philips relation: Vp Parameters			
	A	D	E	F
BHS, X	4195.7	1.2	333.5	0.072
BHS, Y	4036.8	1.2	279.9	0.114
BHS, Z	3962.4	1.4	427.8	0.119
COS, X	4873.6	2.9	526.1	0.048
COS, Y	4925.2	2.7	573.6	0.042
COS, Z	4768.6	3.4	550.7	0.045
TDG, X	6038.2	1.0	296.3	0.032
TDG, Y	5820.7	3.0	565.1	0.269
TDG, Z	5947.0	2.8	230.0	0.057

Table 6-3. Eberhart-Phillips least square fit parameters (P-wave)

Rock type / direction	Eberhart-Philips relation: Vs Parameters			
	A	D	E	F
BHS, X	2367.7	0.4	164.9	0.059
BHS, Y	2268.0	0.6	262.1	0.191
BHS, Z	2238.5	0.6	158.8	0.068
COS, X	2616.7	4.0	659.3	0.370
COS, Y	3456.8	-1.4	965.4	0.011
COS, Z	3150.3	0.4	700.6	0.013
TDG, X	3889.7	-2.1	881.9	0.0065
TDG, Y	2940.5	2.0	69.5	0.265
TDG, Z	3048.7	0.9	105.5	0.035

Table 6-4. Eberhart-Phillips least square fit parameters (S-wave)

6.2 INCLUSION (EFFECTIVE MEDIUM) MODELS

6.2.1 INTRODUCTION

Inclusion models are so-named due to the method in which they model porosity in the host rock matrix, by introducing successive generations of void space *inclusions* stepwise with the changing moduli and density of the rock frame. These inclusions may have any dimension required, such as spherical pores, needle-like pores, or (most commonly) 'penny-shaped' low aspect ratio void space, or **cracks** (figure 6-10). Three inclusion models are introduced in this Section, with the two most appropriate models used to evaluate P-wave and S-wave elastic velocity at elevated hydrostatic pressure from the modelled crack density evolution. Additional mathematical detail over that introduced here can be found in Zimmerman (1991) for randomly distributed cracks and Mavko et al., (1998) for crack distributions.

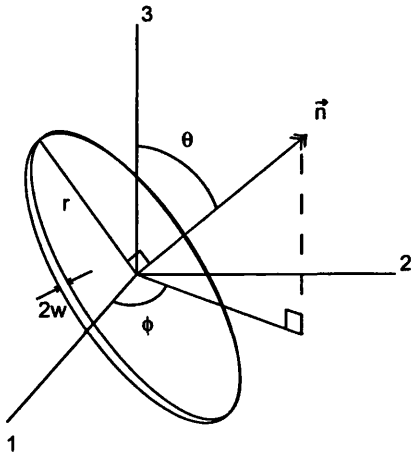

Figure 6-10. 'Penny-shaped' crack geometry. The aspect ratio α is given by w/r, which for a crack is typically <0.01

For the penny shaped crack shown in figure 6-10, we can define a number of important parameters which will be used throughout the following brief explanations of the models, and throughout this study. Crack dimensions are of average aperture or 'thickness' 2w, and semi-major axis length 'r'. This gives a crack **aspect ratio** defined as $\alpha=<w/r>$, and crack volume of $4\pi\alpha r^3/3$.

Obviously, most naturally fractured materials contain more than one crack, and we can therefore define the 'crack density parameter' $\Gamma=Nr^3/V_b$ (Zimmerman, 1991) where N is the number of cracks of radius r in the representative volume V_b; referred to hereafter simply as the **crack density.** The crack density is one of the key controls upon the medium moduli and hence the elastic wave velocities.

6.2.1.1 SELF-CONSISTENT EFFECTIVE MEDIUM APPROACH

The Self-Consistent (SC) approach was first introduced by Hill (1965) and Budiansky (1965), and works by considering the introduction of a finite volume of porosity $\Delta\phi$ into a host material of bulk and shear modulus K and μ, respectively. This is done by introducing new pores into a medium which effectively has the pore embedded already. In this way, the Self-Consistent model aims to account for simple crack and pore interactions without getting into the complex and protracted arguments surrounding many-body problems (Zimmerman, 1986, 1991). Zimmermann (1991) combines strain-energy, crack geometry and crack density relations to produce the expressions repeated below (for dry cracks), which describe the evolution of the modified bulk and shear modulus with crack density (Equations 6-5 and 6-6).

$$\frac{K^*_{SC}}{K_m} = 1 - \frac{16}{9}\frac{\left(1-\upsilon^{*2}_{SC}\right)}{\left(1-2\upsilon^*_{SC}\right)}\Gamma \qquad \textit{Equation 6-5}$$

$$\frac{\mu^*_{SC}}{\mu_m} = 1 - \frac{32}{45}\frac{\left(1-\upsilon^*_{SC}\right)\left(5-\upsilon^*_{SC}\right)}{\left(2-\upsilon^*_{SC}\right)}\Gamma \qquad \textit{Equation 6-6}$$

Where: K^*_{SC} is the effective, Self-Consistent Bulk modulus

K_m is the matrix bulk modulus

ν^*_{SC} is the effective, Self-Consistent Poisson's ratio

ν_m is the matrix material Poisson's ratio

μ^*_{SC} is the effective, Self-Consistent shear modulus

μ_m is the matrix shear modulus

Γ is the crack density, given by $\Gamma = \dfrac{45}{16}\dfrac{\left(\upsilon_m-\upsilon^*_{SC}\right)\left(2-\upsilon^*_{SC}\right)}{\left(1-\upsilon^{*2}_{SC}\right)\left(10\upsilon_m-3\upsilon^*_{SC}\upsilon_m-\upsilon^*_{SC}\right)}$

In addition, Zimmerman (1991), gives the approximation: $\upsilon^*_{SC} = \upsilon_m\left(1-\dfrac{16\Gamma}{9}\right)$, which simplifies the otherwise complicated dependence of the crack density Γ upon Poisson's ratio, ν.

6.2.1.2 DIFFERENTIAL EFFECTIVE MEDIUM APPROACH

The differential effective medium (DEM) approach is very similar to the self-consistent method. However, unlike the self-consistent method, the increments in porosity are injected as *infinitesimal* porosity additions. This time, using the limit of $d\phi \rightarrow 0$, a pair of differential equations are produced. These are again combined with strain-energy, crack geometry, and density relations (Zimmerman, 1991) to produce expressions which describe the evolution of the modified bulk and shear modulus with Poisson's ratio (Equations 6-7 and 6-8). For dry cracks, this gives:

$$-\frac{1}{K^*_{DEM}}\frac{d\ln K^*_{DEM}}{d\Gamma} = \frac{16\left(1-\upsilon^{*2}_{DEM}\right)}{9\left(1-2\upsilon^*_{DEM}\right)} \qquad \textit{Equation 6-7}$$

$$-\frac{1}{\mu^*_{DEM}}\frac{d\ln \mu^*_{DEM}}{d\Gamma} = \frac{32\left(1-\upsilon^*_{DEM}\right)\left(5-\upsilon^*_{DEM}\right)}{45\left(2-\upsilon^*_{DEM}\right)} \qquad \text{Equation 6-8}$$

Where: K^*_{DEM} is the effective, Differential Effective Medium Bulk modulus

μ^*_{DEM} is the effective, Differential Effective Medium Shear modulus

ν^*_{DEM} is the effective, Differential Effective Medium Poisson's ratio

and $\Gamma = \frac{5}{128}\ln\left(\frac{3-\upsilon^*_{DEM}}{3-\upsilon_m}\right) + 6\ln\left(\frac{1-\upsilon^*_{DEM}}{1-\upsilon_m}\right) + 9\ln\left(\frac{1+\upsilon^*_{DEM}}{1+\upsilon_m}\right) - 16\ln\left(\frac{\upsilon^*_{DEM}}{\upsilon_m}\right)$

Zimmerman (1991) gives the approximations: $\frac{K^*_{DEM}}{K_m} = \left(\frac{\upsilon^*_{DEM}}{\upsilon_m}\right)^{10/9}\left(\frac{3-\upsilon^*_{DEM}}{3-\upsilon_m}\right)^{-1/9}\left(\frac{1-2\upsilon^*_{DEM}}{1-2\upsilon_m}\right)^{-1}$,

and an initial estimate is then made for the ratio: $\frac{\upsilon^*_{DEM}}{\upsilon_m} = e^{-8\Gamma/5}$ which is used within an iterative loop to determine the effective Bulk modulus, K^*_{DEM}. The general relation, $\mu = 3K\frac{(1-2\upsilon)}{(2+2\upsilon)}$, relates bulk and shear modulus via the Poisson's ratio ν to obtain the shear modulus, μ.

6.2.1.3 KUSTER AND TOKSOZ MODEL

The model of Kuster and Toksoz (1974) is slightly different in operation to the methods introduced earlier (Self-Consistent, Differential Effective Medium), specifically in the way in which it estimates the effective elastic moduli. The Kuster-Toksoz (K-T) model considers an elastic wave as it approaches and is scattered by a dilute ($\phi/\Gamma \ll 1$) assemblage of pores which are embedded in a host matrix of moduli (K_m, μ_m). The amplitude of the resultant, scattered, wave is then compared to the amplitude of a wave scattered as a result of encountering a **single** spherical inclusion with an *effective* modulus (K^*_{KT} and μ^*_{KT}). Equating these two physical problems then allows expressions

comparing the two moduli, based on the host and effective matrix physical properties, to be derived. Kuster and Toksoz (1974) give these expressions as:

$$\left(K_{KT}^{*}-K_m\right)\frac{\left(K_m+\frac{4}{3}\mu_m\right)}{\left(K_{KT}^{*}+\frac{4}{3}\mu_m\right)}=\sum_{i=1}^{N}x_i\left(K_i-K_m\right)P^{mi}$$

$$\left(\mu_{KT}^{*}-\mu_m\right)\frac{\left(\mu_m+\frac{4}{3}\zeta_m\right)}{\left(\mu_{KT}^{*}+\frac{4}{3}\zeta_m\right)}=\sum_{i=1}^{N}x_i\left(\mu_i-\mu_m\right)Q^{mi}$$

Where: K^{*}_{KT} is the effective Kuster-Toksoz Bulk modulus

μ^{*}_{KT} is the effective Kuster-Toksoz Shear modulus

x_i is the inclusion material 'i' volume ratio

K_i is the Bulk modulus of inclusion material 'i'

μ_i is the Shear modulus of inclusion material 'i'

and the simplifying parameter ζ is defined as: $\zeta=\frac{\mu_m}{6}\frac{\left(9K_m+8\mu_m\right)}{\left(K_m+2\mu_m\right)}$

The quantities 'P^{mi}' and 'Q^{mi}' are geometrical factors which depend upon the size and shape of the inclusions being considered. For the 'penny shaped' crack introduced earlier, Mavko et al. (1998) states that:

$$P^{mi}=\frac{K_m+\frac{4}{3}\mu_i}{K_i+\frac{4}{3}\mu_i+\pi\alpha\beta_m},\qquad Q^{mi}=\frac{1}{5}\left(1+\frac{8\mu_m}{4\mu_i+\pi\alpha\left(\mu_m+2\beta_m\right)}+2\frac{K_i+\frac{2}{3}\left(\mu_i+\mu_m\right)}{K_i+\frac{4}{3}\mu_i+\pi\alpha\beta_m}\right)$$

where: $\beta=\mu\frac{\left(3K+\mu\right)}{\left(3K+4\mu\right)}$ and: $\gamma=\mu\frac{\left(3K+\mu\right)}{\left(3K+7\mu\right)}$

However, these complicated equations are more easily interpreted and implemented when expressed in terms of crack density. Zimmerman (1991) and White (2002, Per. Comm. To RZ) provide the following, less complicated expressions:

$$K_{KT}^{*}=K_m\frac{1-\left\{\frac{32}{27}\left(1+\upsilon_m\right)\right\}\Gamma}{1+\left\{\frac{16}{27}\frac{\left(1+\upsilon_m\right)^2}{\left(1-2\upsilon_m\right)}\right\}\Gamma}$$ *Equation 6-9*

$$\mu^{*}_{KT} = \mu_m \frac{1-\left\{\frac{32(5-\upsilon_m)(7-5\upsilon_m)}{675(2-\upsilon_m)}\right\}\Gamma}{1+\left\{\frac{64(5-\upsilon_m)(4-5\upsilon_m)}{675(2-\upsilon_m)}\right\}\Gamma} \qquad \textit{Equation 6-10}$$

where: $\upsilon_m = \frac{(3K_m - 2\mu_m)}{(6K_m + 2\mu_m)}$, and Γ is the crack density.

6.2.2 RANDOM CRACK INCLUSION MODEL FITTING: COMPARISON WITH LAB DATA

Using these three inclusion models (SC, DEM, K-T), relationships between crack density and normalised velocity change can now be evaluated. For model input, average matrix moduli values (K_m, μ_m), are calculated using volume average weighted rock compositions for Bentheim sandstone, Crab Orchard sandstone, and Takidani granite. The three rocks studied possess very similar average elastic properties, and so little change in the general crack density–velocity relations are seen (figures 6-11, 6-12 and 6-13). However, this exercise is important for confirmation purposes. The general trend of normalised velocity decrease with crack density increase is obvious, as might be expected intuitively. It should be noted, however, that the self-consistent approach over-estimates the decrease in normalised velocity with increasing crack density. This effect has been previously noted by other authors (Bruner, 1976), and occurs due to a shortcoming of the SC model, which effectively models the effect of the inclusions twice (Zimmerman, 1991). For this reason, the SC model is no longer considered in this work, and from this point onwards, only the DEM and K-T models are used.

The experimental velocity data cannot be interpreted in terms of crack density directly. As seen in Chapter 5, hydrostatic pressure increase is accompanied by a simultaneous rise in the elastic wave velocity of the rock. Notionally, this process may occur due to embedded microcracks progressively 'closing up' with increasing elevated pressure, thus decreasing the crack density and increasing the overall bulk moduli, and hence the observed elastic wave velocity. By making the initial assumption that the rocks under test possess zero crack density at the highest effective pressure attained (90 MPa), and that the grain matrix moduli do not change significantly with pressure, we can invert the normalised experimental velocity changes for the crack density using the DEM and K-T models. This is done using the normalised experimental velocity information V_x/V_0, for each rock type, where V_x is the velocity (Either P-wave or S-wave) at pressure x, and V_0 is the velocity at 90 MPa hydrostatic pressure. Performing this calculation at each stepwise change in experimental velocity with effective pressure will yield the concomitant evolution of crack density.

In order to do this accurately, a simple linear fit is made to the DEM and K-T model data in figures 6-11, 6-12 and 6-13 (individually, and for both P-wave and S-wave), so that the crack density can be expressed as an accurately known function of normalised velocity for each rock type. This allows the normalised experimental velocity data to be used to calculate the associated crack density at each pressure step at which the velocities are measured, yielding a plot of the decreasing crack density of each rock with increasing hydrostatic pressure.

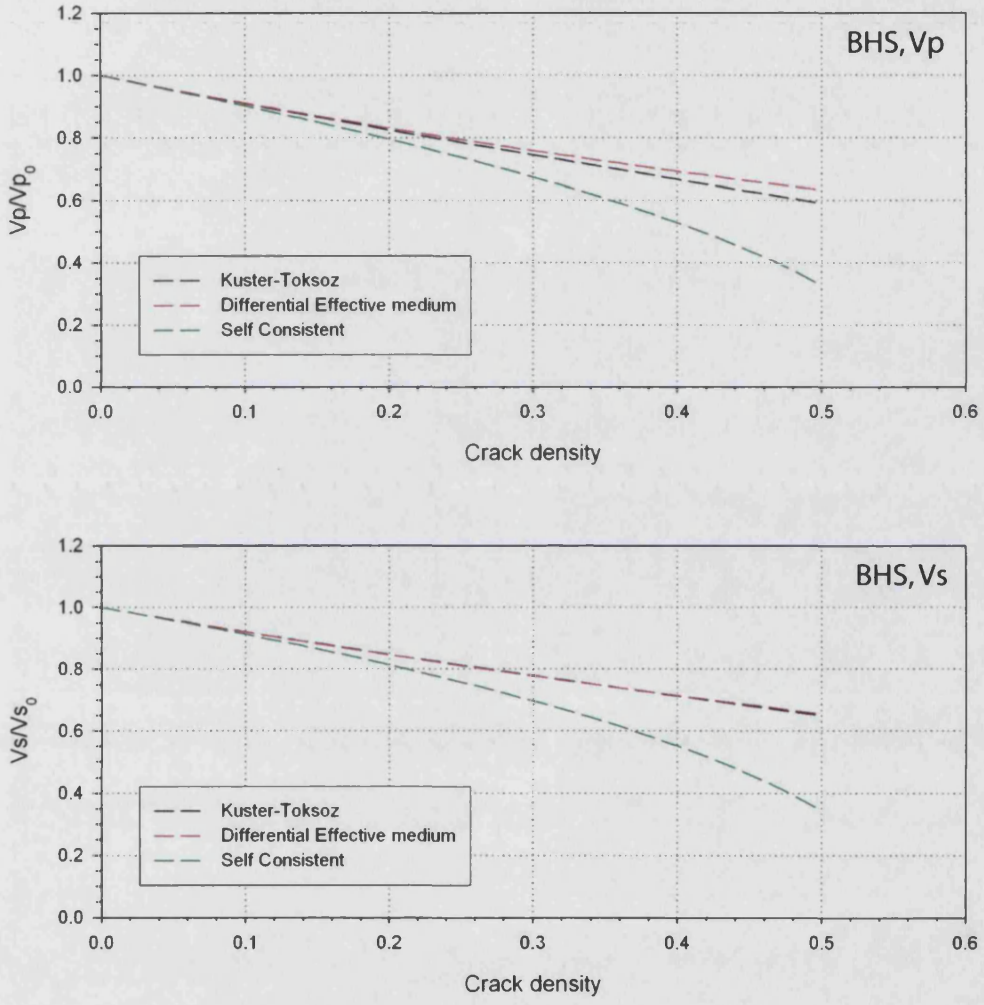

Figure 6-11. Kuster-Toksoz (K-T), Differential effective medium (DEM) and Self-consistent (SC) predictions for the effect of increasing crack density upon elastic wave velocity (normalised), for ***Bentheim sandstone****. Vp – top, and Vs – bottom. The Self-Consistent approach is not used in the final analysis, see text for details. The relationship between the crack density Γ and the normalised velocity change V/V_0 in each case is given by: $Vp/Vp_0=1-0.85\Gamma$ (K-T), $Vp/Vp_0=1-0.81\Gamma$ (DEM), $Vs/Vs_0=1-0.73\Gamma$ (K-T), and $Vs/Vs_0=1-0.74\Gamma$ (DEM).*

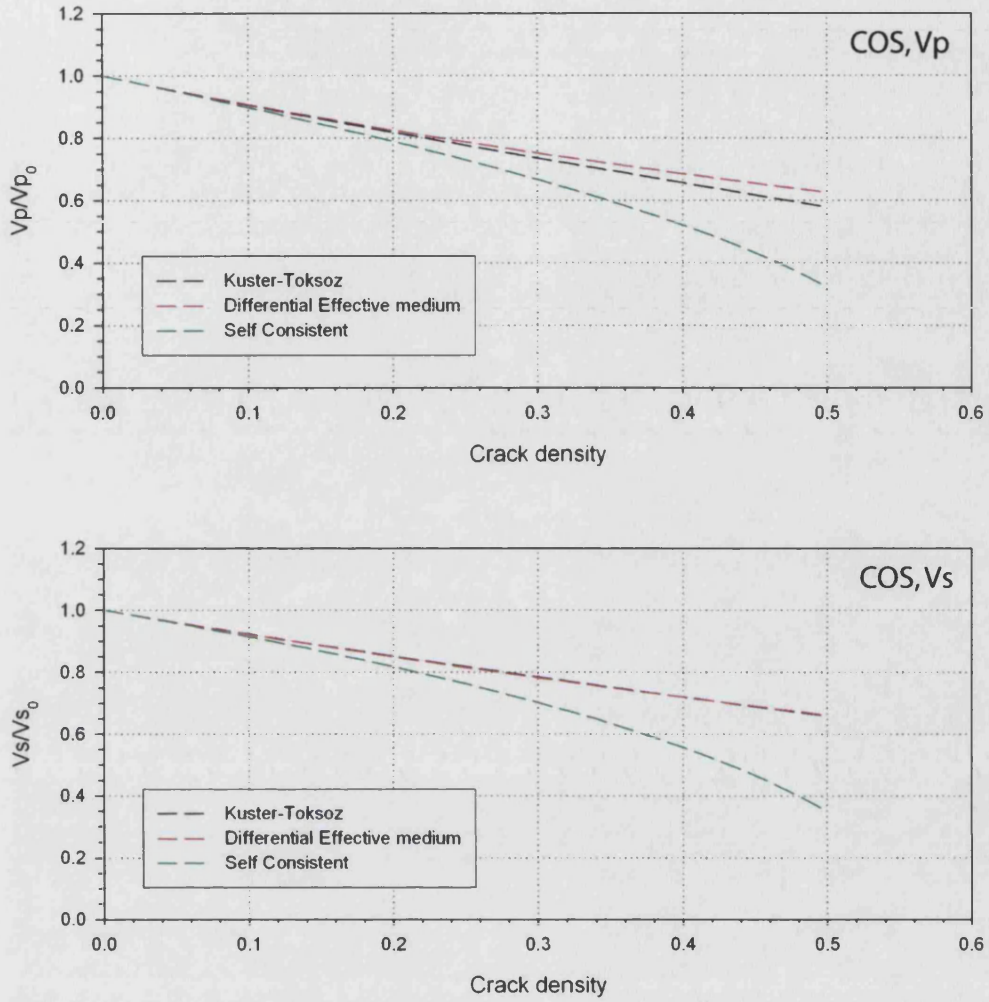

Figure 6-12. Kuster-Toksoz (K-T), Differential effective medium (DEM) and Self-consistent (SC) predictions for the effect of increasing crack density upon elastic wave velocity (normalised), for ***Crab Orchard sandstone****. Vp – top, and Vs – bottom. The Self-Consistent approach is not used in the final analysis, see text for details. The relationship between the crack density Γ and the normalised velocity change V/V_0 in each case is given by: $Vp/Vp_0=1-0.88\Gamma$ (K-T), $Vp/Vp_0=1-0.82\Gamma$ (DEM), $Vs/Vs_0=1-0.72\Gamma$ (K-T), and $Vs/Vs_0=1-0.73\Gamma$ (DEM).*

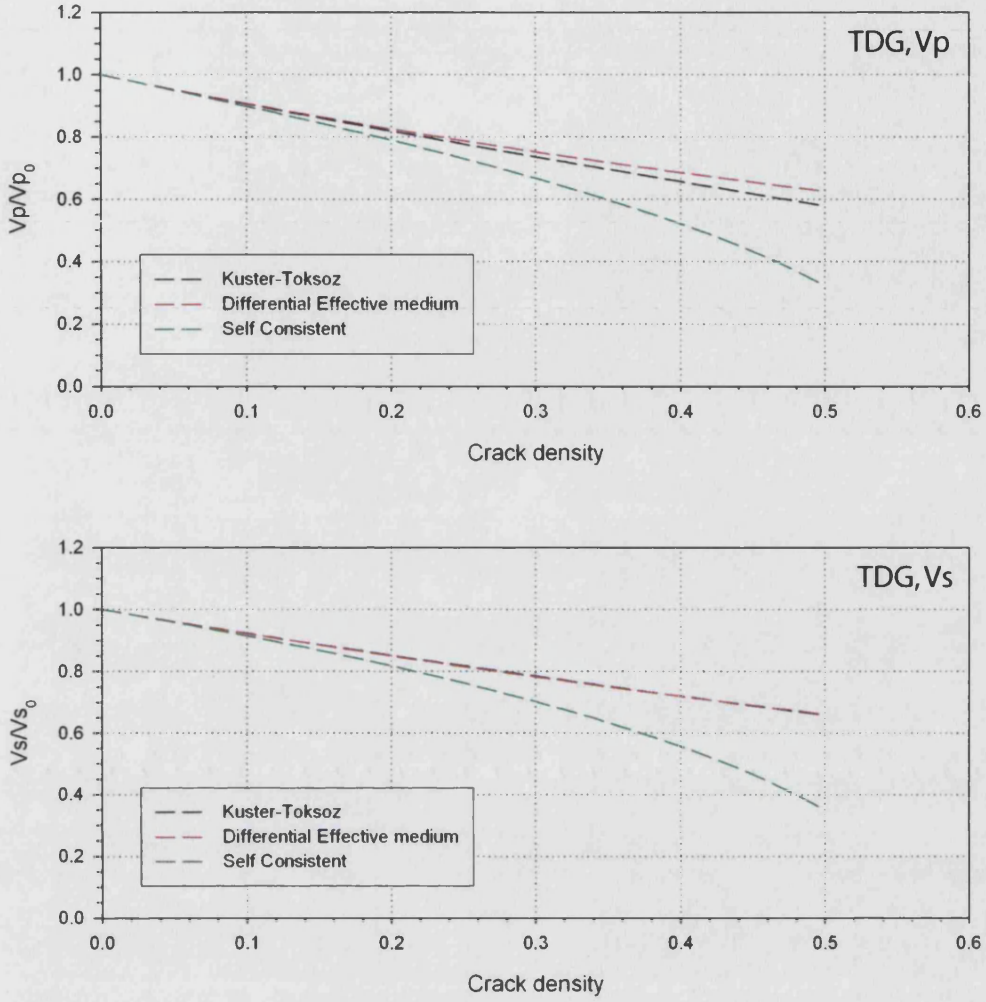

Figure 6-13. Kuster-Toksoz (K-T), Differential effective medium (DEM) and Self-consistent (SC) predictions for the effect of increasing crack density upon elastic wave velocity (normalised), for ***Takidani granite****. Vp – top, and Vs – bottom. The Self-Consistent approach is not used in the final analysis, see text for details. The relationship between the crack density Γ and the normalised velocity change V/V_0 in each case is given by: $Vp/Vp_0=1-0.88\Gamma$ (K-T), $Vp/Vp_0=1-0.82\Gamma$ (DEM), $Vs/Vs_0=1-0.72\Gamma$ (K-T), and $Vs/Vs_0=1-0.73\Gamma$ (DEM).*

Bentheim sandstone

Figure 6-14 (below) shows a normalised experimental velocity dataset for Bentheim sandstone. Displayed in this manner the velocity increases from ~92.5% and ~93.5% at 5 MPa to 100% (by definition) at 90 MPa, for P-wave and S-wave velocity respectively. Using the model crack density / velocity relations shown in figure 6-11, the experimental crack density evolution can now be determined as a function of pressure, and also porosity, which is also experimentally known at each pressure step.

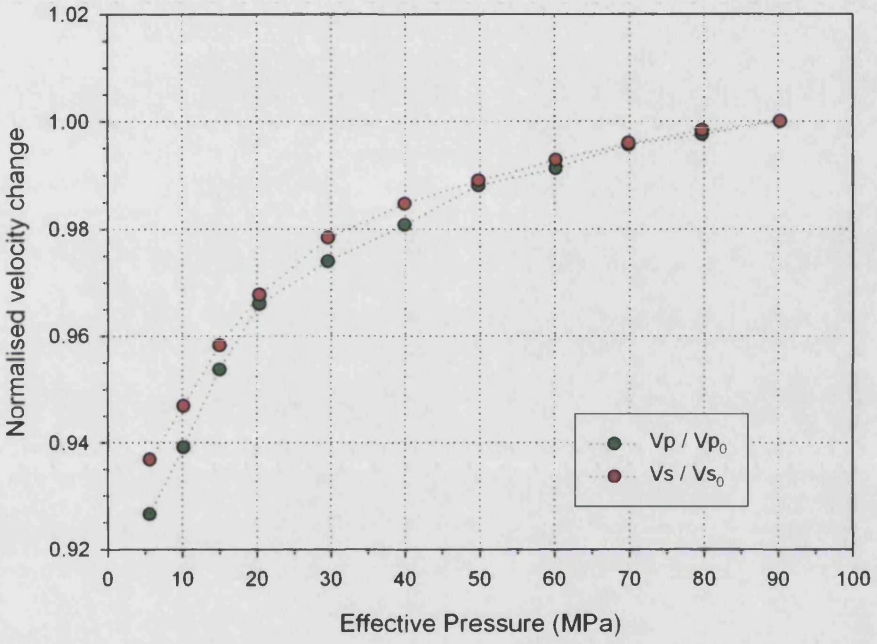

Figure 6-14. Laboratory elastic wave variation with effective pressure for ***Bentheim sandstone****, with velocity (P-wave and S-wave) normalised to 1 at 90 MPa. Plotted in this way, the initial velocities are 92.5% and 93.5% at 5MPa for Vp and Vs respectively*

As effective pressure increases (figure 6-15, top two figures), the inclusion model crack density decreases, with a prominent 'knee' at approximately 20-30 MPa. Kuster-Toksoz and the Differential Effective Medium models produce very similar results, with SC model data not plotted for the reason given earlier. Plotting the crack density variation with experimentally measured porosity rather than effective pressure (figure 6-15, middle figures), also shows this break in slope. If the change in porosity is considered to be mostly due to crack closure, then a crack porosity ϕ_c may be defined as $\phi_c = 4\pi\alpha\Gamma/3$. Therefore the gradient of the porosity-model crack density variation will equal $(4\pi\alpha/3)^{-1}$, allowing the crack aspect ratio α to be determined. Before the 'knee', $\alpha = 0.04$ and after, $\alpha = 0.01$, suggesting that BHS possesses two clear populations of crack aperture, and that larger cracks close up first with increasing effective pressure. Comparison with the experimental P-wave and S-wave velocity (figure 6-15, lower figures) also shows a noticeable change of slope at approximately 20-30 MPa pressure, and as the crack density is based upon this information, then this

result is entirely consistent as the non-linear Γ-P_{eff} relation will significantly influence the rock properties.

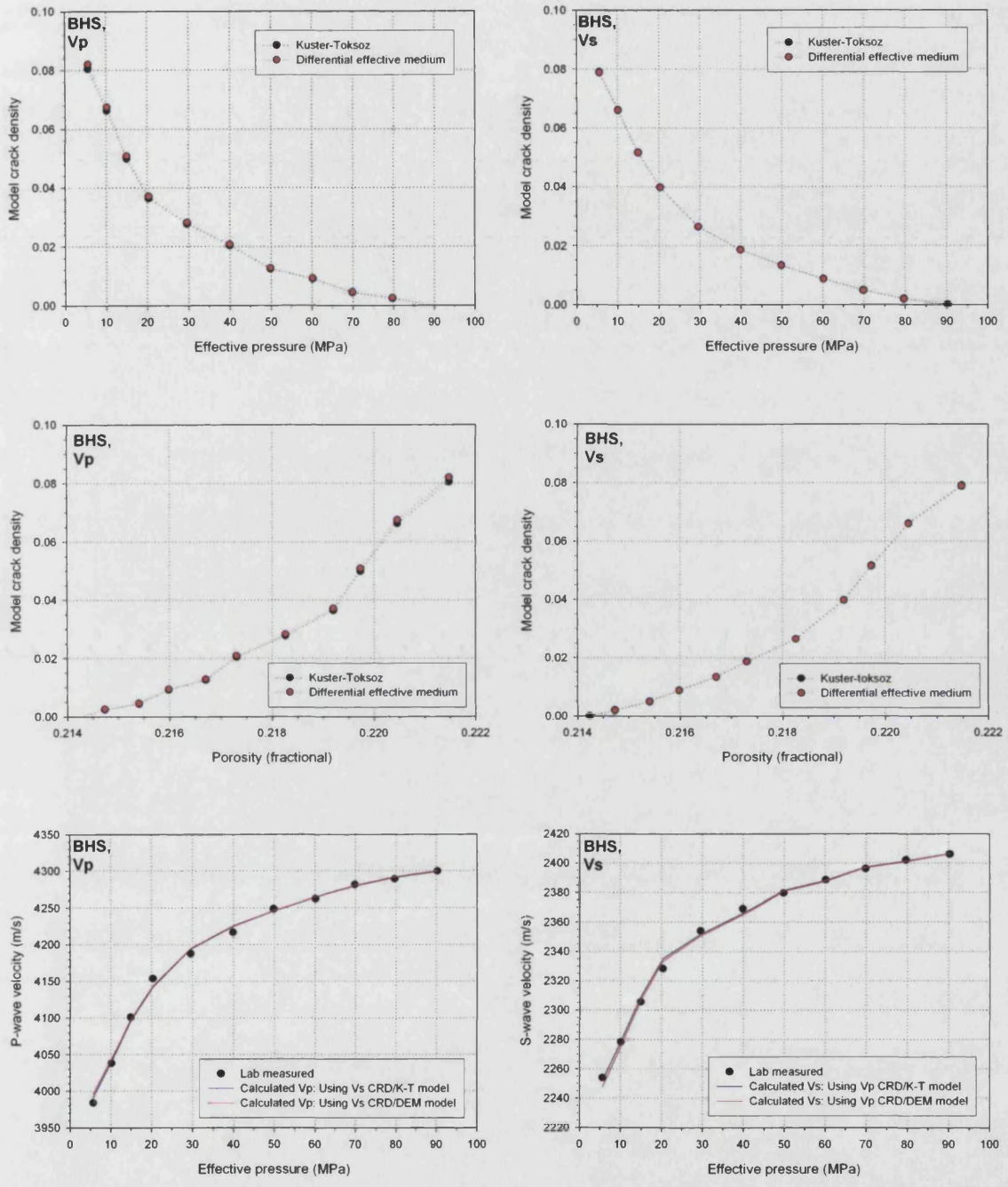

Figure 6-15. Inclusion model data for Bentheim sandstone. The top two figures show the model crack density variation with pressure step for P-wave and S-wave data. The middle two figures show the laboratory concomitant porosity values rather than the effective pressure values at each step, allowing a porosity-crack density evolution to be visualised which the model does not explicitly allow for. The lower two figures show a 'semi-inverse' solution, in which the S-wave crack density variation with pressure is used to calculate the theoretical P-wave velocity variation (bottom left); and vice versa (bottom right). These two lower figures also plot the laboratory measured P-wave and S-wave data for comparison.

Finally, it is possible to use the crack density evolution to predict velocity as a function of effective pressure by using the crack density as obtained though the normalised P-wave experimental

data to compute S-wave velocity data (figure 6-15, bottom figures), and vice-versa. This can then be directly compared to the experimentally obtained data. Again, as both the P-wave and S-wave velocity show very similar crack density variations, it is entirely logical that the predicted values are in close agreement with the experimental data. The danger with this method, of course, lies in the partially 'circular argument' nature of such an approach. However, as P-wave and S-wave velocity changes are relatively interchangeable and well matched through the application of the inclusion models, then the same general mechanism is likely to be acting equally for both P-wave and S-wave cases, and to the same degree.

Crab Orchard Sandstone

For Crab Orchard sandstone (figure 6-16 below), the situation is slightly more complicated. When comparing laboratory data to the equivalent BHS case (fig. 6-14), the most obvious difference is the greater degree of velocity change with pressure. For COS, normalised velocity increases from 85.5% and 87.5% at 5 MPa (P-wave and S-wave) to 100% at 90 MPa. This is a far larger velocity change over the same pressure range than for Bentheim sandstone, suggesting a higher crack density change.

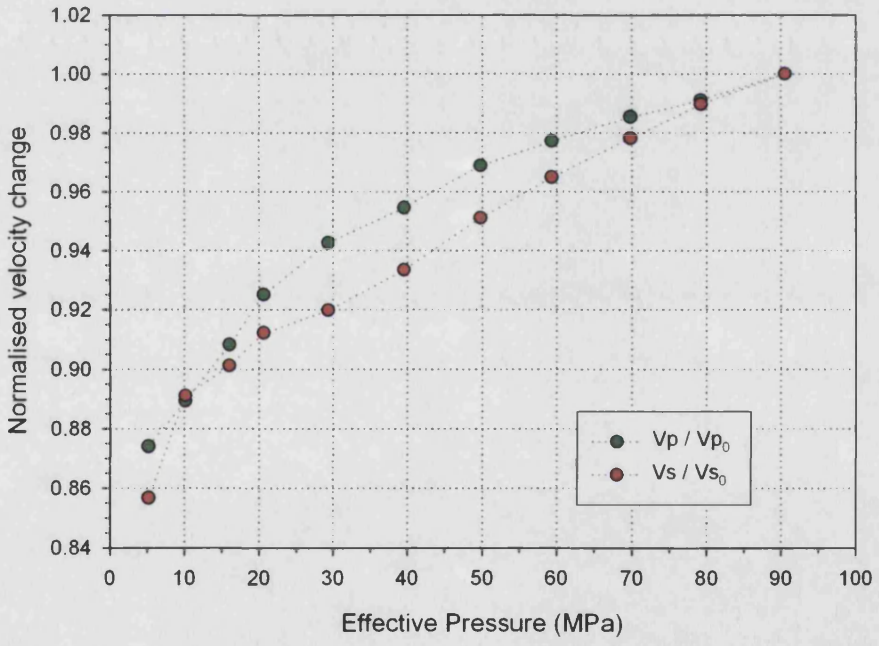

Figure 6-16. Laboratory elastic wave variation with effective pressure for ***Crab Orchard sandstone****, with velocity (P-wave and S-wave) normalised to 1 at 90 MPa. Plotted in this way, the initial velocities are 88% and 85.5% at 5MPa for Vp and Vs respectively, a larger velocity drop than compared to BHS*

Model data (figure 6-17, upper figures) supports this argument, predicting a higher crack density of approximately 0.14 and 0.19 for P-wave and S-wave respectively at 5 MPa effective pressure. Unlike the BHS data seen earlier, no obvious break of slope is seen in the crack density variation with either effective pressure or porosity. From the porosity-crack density relationship (middle figures), an average crack aspect ratio of approximately $\alpha = 0.006$ is determined, lower than

for BHS. Finally, when modeling P-wave and S-wave velocity data from the crack density information (figure 6-17, bottom) we no longer see a good match between model and experimental velocities, which may be partly explained due to the different crack density evolution between P-wave and S-wave data. However, the poor fit is also likely to be as a direct result of the known anisotropy of COS, whereas the theories used (DEM, K-T) assume random, and hence isotropic, crack orientations.

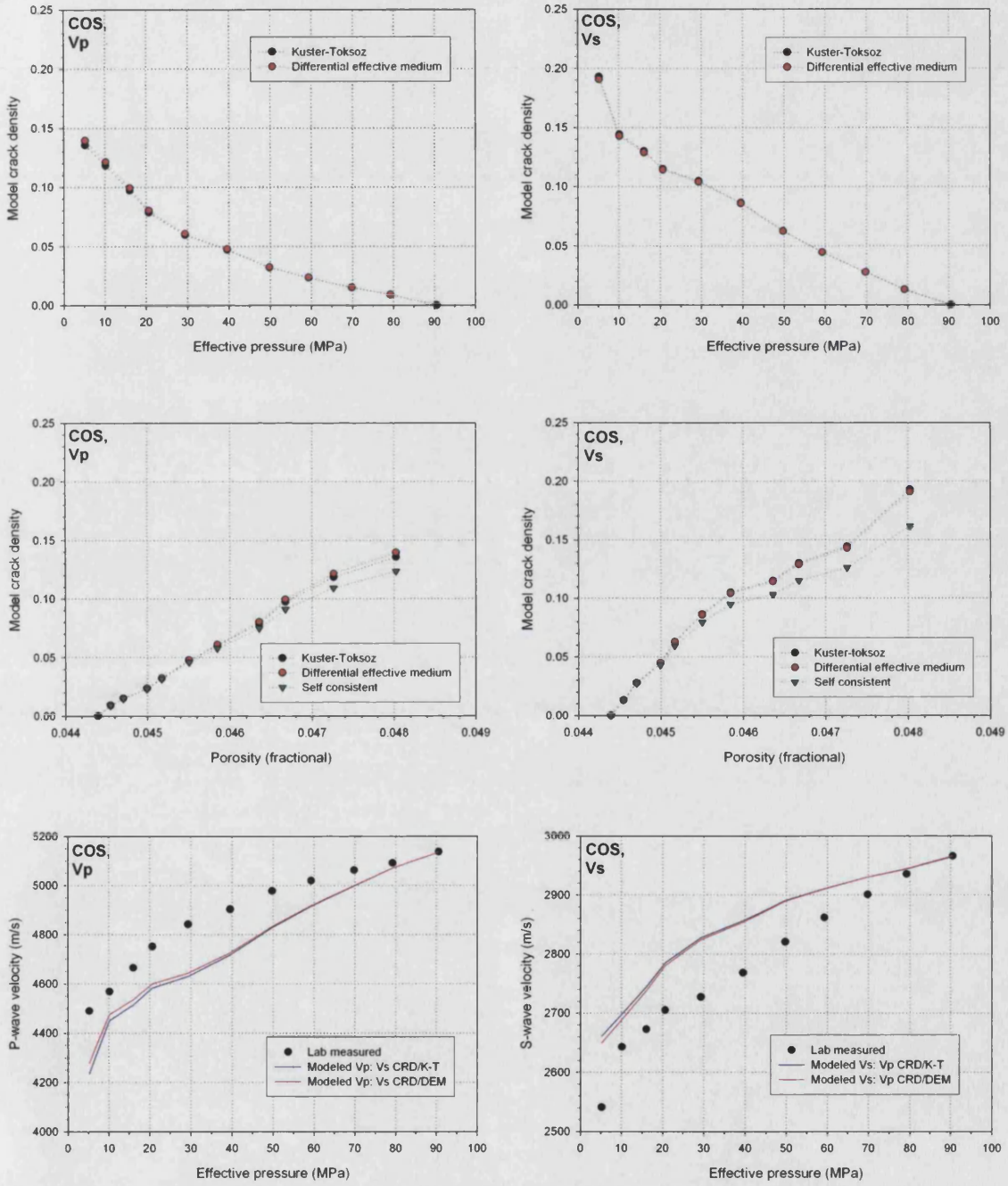

Figure 6-17. Inclusion model data for ***Crab Orchard*** *sandstone. The top two figures show the model crack density variation with pressure step for P-wave and S-wave data. The middle two figures show the laboratory concomitant porosity values rather than the effective pressure values at each step, allowing a porosity-crack density evolution to be visualised which the model does not explicitly allow for. The lower two figures show a 'semi-inverse' solution, in which the S-wave crack density variation with pressure is used to calculate the theoretical P-wave velocity variation (bottom left); and vice versa (bottom right). These two lower figures also plot the laboratory measured P-wave and S-wave data for comparison.*

Takidani granite

For Takidani granite (figure 6-18), the change in normalised velocity ranges from 93.5% and 95% at 5 MPa (P-wave and S-wave) to 100% at 90MPa, suggesting a crack density which is slightly lower than for BHS (for example). Given the low porosity of this rock type (less than 1%), and that a larger grain size (~2mm) may result in fewer intergranular cracks, then this result is entirely consistent with petrophysical knowledge of this rock type.

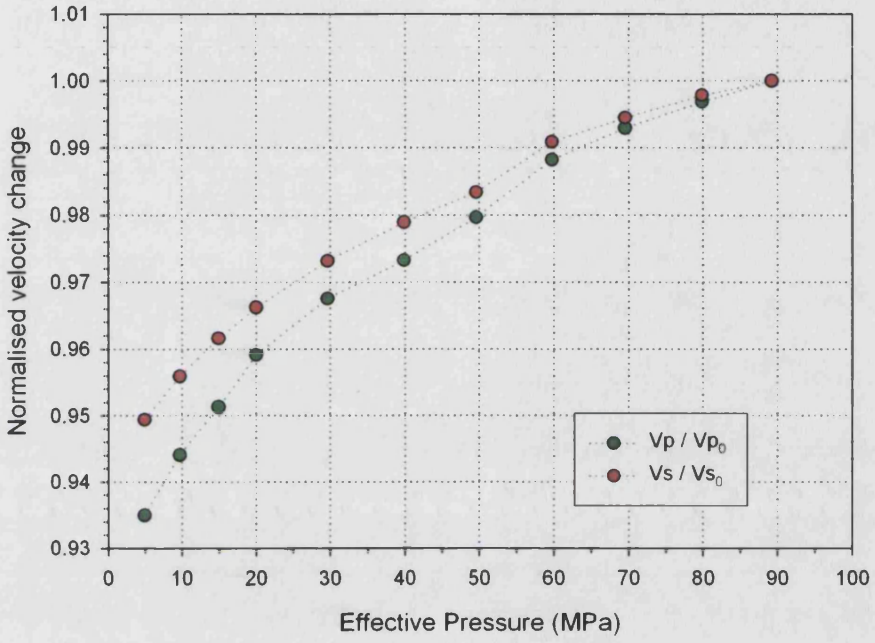

Figure 6-18. Laboratory elastic wave variation with effective pressure for ***Takidani granite****, with velocity (P-wave and S-wave) normalised to 1 at 90 MPa. Plotted in this way, the initial velocities are 93.5% and 95% at 5MPa for Vp and Vs respectively*

The model data supports this, predicting a crack density of approximately 0.055 and 0.070 for P-wave and S-wave respectively at 5 MPa effective pressure. Like the COS data, no obvious break of slope can be seen in the plots of crack density with effective pressure (figure 6-19, top) or crack density with porosity (figure 6-19, top). From this porosity-crack density relationship, an average crack aspect ratio of approximately $\alpha = 0.004$ is determined, lower than for either BHS or COS and consistent with the observation that TDG is a predominantly cracked rock. Also like the COS data, crack density as predicted from P-wave and S-wave data is slightly different. When modeling P-wave and S-wave velocities from this crack density information, a poor fit is seen when comparing modelled velocity data to laboratory values; however, a general agreement in the trend is still obvious. For this purely cracked rock type, therefore, inclusion models may be less suitable than for other relations such as the 'crack' models of Hudson (1980, 1981) and Kachanov (1994). These will be the focus of section 6.3.

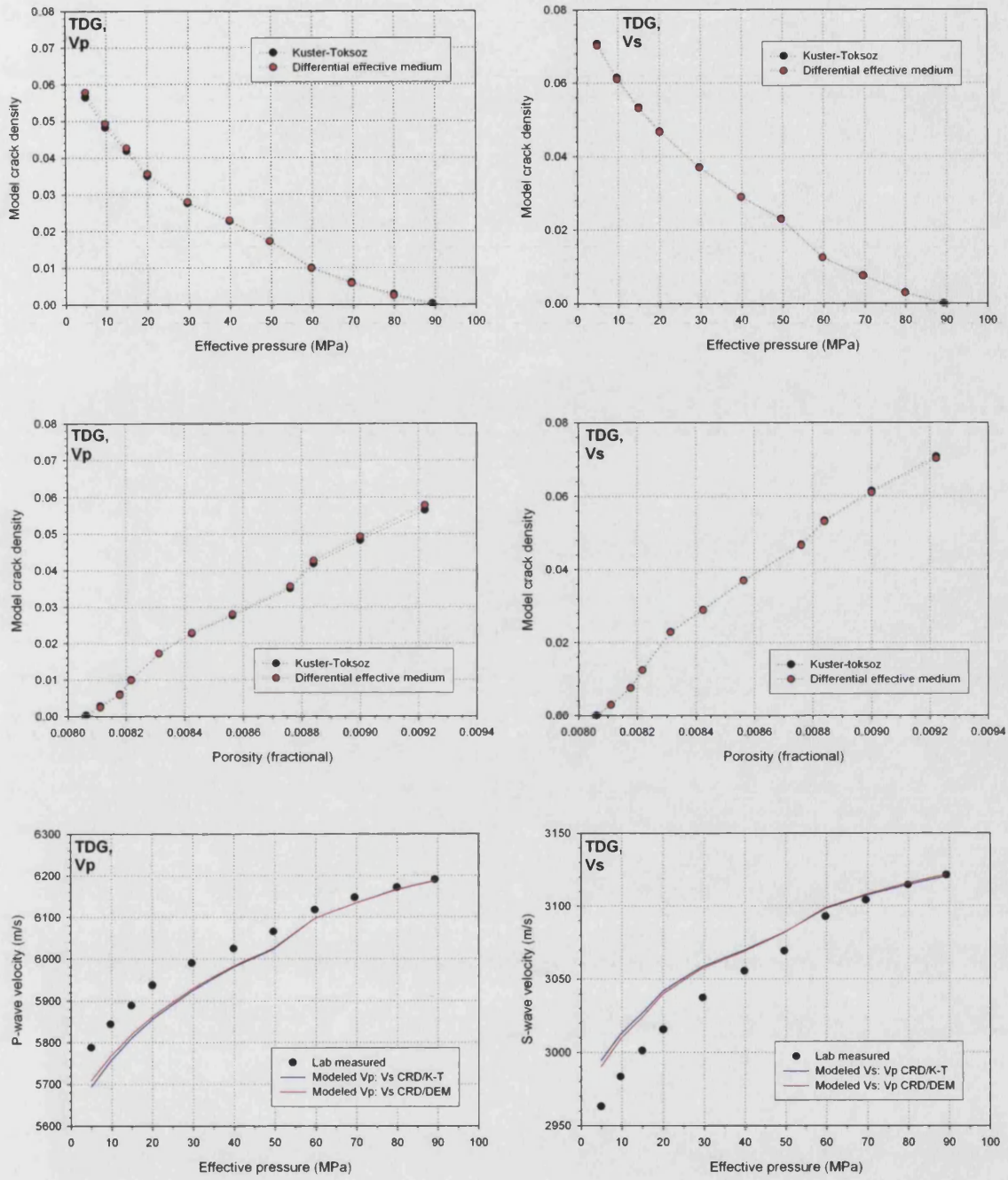

Figure 6-19. Inclusion model data for ***Takidani granite****. The top two figures show the model crack density variation with pressure step for P-wave and S-wave data. The middle two figures show the laboratory concomitant porosity values rather than the effective pressure values at each step, allowing a porosity-crack density evolution to be visualised which the model does not explicitly allow for. The lower two figures show a 'semi-inverse' solution, in which the S-wave crack density variation with pressure is used to calculate the theoretical P-wave velocity variation (bottom left); and vice versa (bottom right). These two lower figures also plot the laboratory measured P-wave and S-wave data for comparison.*

6.3 ALIGNED CRACK MODELS

6.3.1 INTRODUCTION

I now introduce two models which deal exclusively with low aspect ratio void space inclusions, or cracks. Strictly, these models are also inclusion models. However, as these particular models are almost always used to model an aligned 'crack' porosity, in this thesis I discuss them separately from the Differential Effective Medium, Kuster-Toksoz and Self Consistent models introduced previously, for simplicity. These models rely on scattering theory which treats the pore assemblage as a scattering medium which has a mathematically predictable effect upon the mean wave field, allowing the elastic moduli to be calculated. The model of Hudson (1980, 1981) models the variation of azimuthal elastic wave velocity relative to the influence of an aligned crack set; whereas the model of Kachanov (1980, 1994) calculates the changing crack compliance and hence crack density and velocity evolution with increasing effective pressure.

6.3.1.1 HUDSON'S THEORY

This theory is based upon second order scattering of the mean wave field (Hudson, 1980, 1981; Hudson et al., 2001), and invokes low aspect ratio, penny shaped ellipsoidal cracks as scattering bodies. The model assumes that crack radius and distance between cracks is large compared to that of a wavelength (approximately a ratio of 10:1 between crack radius and distance and the wavelength). In principle, the model works by the following method. C_{ij}^{0} is an isotropic background matrix, as given in section 2.2.1. The scattering due to the penny shaped cracks then gives rise to a first order correction stiffness matrix C_{ij}^{1} which can be theoretically derived based upon the crack geometry, symmetry and alignment. A second order correction, C_{ij}^{2}, may also be included (Mavko et al., 1998). The full effective modulus, C_{ij}^{eff} is then the supposition of the three stiffness matrices:

$$c_{ij}^{eff} = c_{ij}^{0} + c_{ij}^{1} + c_{ij}^{2} \qquad \textit{Equation 6-11}$$

However, the second order correction is usually not required, and is neglected in this work.

The model assumes a number of conditions. The most important of these is that the crack density consists of a single population of identical cracks, with no distribution in terms of aspect ratio and alignment. Thus, this theory will give a maximum possible anisotropy based upon an 'idealised' transversely isotropic rock. From the previous analysis using thin sections, UV florescent thin sections and scanning electron micrographs, this is likely not to be the case for the Takidani granite, for example. This is addressed by considering an appropriate crack orientation distribution. For planar transverse isotropy (PTI), Hudson (1990), and Mavko et al. (1998) give expressions for crack density Γ upon a rotationally symmetric distribution around a symmetry axis (Fisher distribution):

$$\Gamma(\theta) = \frac{\Gamma_t}{2\pi} \frac{e^{(\cos\theta)/\sigma^2}}{\sigma^2\left(e^{1/\sigma^2} - 1\right)} \qquad \textit{Equation 6-12}$$

where: Γ_t is the total crack density given by $\Gamma_t = 3\phi_c/4\pi\alpha$ (where ϕ_c is the crack porosity and α is the crack aspect ratio)

θ is the angle to the symmetry axis.

$\Gamma(\theta)$ is the crack density as seen along angle θ

σ is the standard deviation of θ.

In this work, a random distribution of cracks is used whose normals deviate from the symmetry axis by angle θ, and where this deviation is rotationally symmetric about the symmetry axis. Using equation 6-12 together with the generalised first order stiffness correction given by Hudson (1990), (see Appendix) the following expressions are produced for small σ:

$$C_{11}^1 = -\Gamma_t \frac{U_3}{\mu}\left(\lambda^2 + 4\lambda\mu\sigma^2 + 12\mu^2\sigma^4\right) - \Gamma_t U_1 \mu\left(4\sigma^2 - 12\sigma^4\right)$$

$$C_{12}^1 = -\Gamma_t \frac{U_3}{\mu}\left(\lambda^2 + 4\lambda\mu\sigma^2 + 4\mu^2\sigma^4\right) + \Gamma_t U_1 \mu\left(4\sigma^4\right)$$

$$C_{13}^1 = -\Gamma_t \frac{U_3}{\mu}\left[\lambda^2 + 2\lambda\mu\left(1-\sigma^2\right) + 4\mu^2\left(\sigma^2 - 4\sigma^4\right)\right] + 4\Gamma_t U_1 \mu\left(\sigma^2 - 4\sigma^4\right)$$

$$C_{33}^1 = -\Gamma_t \frac{U_3}{\mu}\left[\lambda^2 + 4\lambda\mu\left(1-\sigma^2\right) + 4\mu^2\left(\sigma^4 - 2\sigma^2 + 1\right)\right] - 4\Gamma_t U_1 \mu\left(\sigma^2 - \sigma^4\right)$$

$$C_{44}^1 = -\Gamma_t \frac{U_3}{\mu}\left[4\lambda^2\left(\sigma^2 - 4\sigma^4\right)\right] - \Gamma_t U_1 \mu\left[1 - \sigma^2 - 4\left(\sigma^2 - 4\sigma^4\right)\right]$$

$$C_{66}^1 = \left(C_{11}^1 - C_{12}^1\right)/2$$

Where, for dry cracks as used in this study, $U_1 = \frac{16(\lambda + 2\mu)}{3(3\lambda + 4\mu)}$, and $U_3 = \frac{4(\lambda + 2\mu)}{3(\lambda + \mu)}$

And: C^1_{xy} are the first order stiffness co-efficients

Γ_t is the total crack density

μ is the isotropic shear modulus

λ is the Lamé modulus, where $\lambda = K - 2\mu/3$ (K is the bulk modulus)

Using the maximum experimentally observed P-wave and S-wave velocity (from the experimental velocity variation with azimuth – figure 6-1 for example), the bulk and shear moduli of the background (isotropic) matrix are first calculated allowing C^0_{ij} to be determined. For calculation of the first order correction matrix (C^1_{ij}), a crack porosity of 0.005 and an aspect ratio of 0.01 are used for all rock types, so that the standard deviation σ may be easily compared between rocks. These corrections are then substituted into equation 6-11 to compute the effective stiffness matrix

C_{ij}^{eff}, which is then used to calculate the seismic wave velocity with propagation angle relative to the crack symmetry. By varying the maximum permissible angular distribution (σ), the model azimuthal velocity variation is heuristically matched to the experimental data, allowing the maximum angular spread of cracks to be estimated within each rock type.

6.3.1.2 KACHANOV'S MODEL

This is a first order perturbation model which uses the principles of stress and strain to consider an elastically inhomogeneous volume element containing cracks (Kachanov, 1980, 1994; Sayers and Kachanov, 1995). In their simplest form, perturbation theories compute the effective elastic modulus of a cracked solid as a linear function of crack density:

$$\frac{E_m}{E^*} = 1 + h\Gamma$$

Where E_m is the matrix Young's modulus, E^* is the effective medium Young's modulus, and Γ is the crack density. 'h' is a scaling parameter which depends on the matrix and fluid properties, together with the crack geometry and interactions.

For the simplest case of an isotropically cracked medium, Kachanov (1992, 1994) derives an expression which evaluates the effective frame moduli in terms of the matrix and fluid properties and the crack geometry and interactions (or lack thereof). The same crack geometry shown earlier in figure 6-4 is used, with the crack aspect ratio again defined as α=<w/r>. In addition, fluid transport properties are dependent upon a crack connectivity probability factor 'f' (percolation factor). Kachanov (1994) shows that the effective moduli in this case are described by the expressions:

$$\frac{E_m}{E^*} = 1 + \frac{\Gamma}{3h}\left(1 + \frac{3}{5}\left[\left(1 - \frac{\upsilon_m}{2}\right)\frac{\zeta}{1+\zeta} - 1\right]\right)$$

$$\frac{\mu_m}{\mu^*} = 1 + \frac{\Gamma}{3h}\left(1 + \frac{2}{5}\left[\left(1 - \frac{\upsilon_m}{2}\right)\frac{\zeta}{1+\zeta} - 1\right]\right)$$

Where, for non-interacting penny shaped cracks:

E^* is the effective Young's modulus

E_m is the matrix Young's modulus

μ^* is the effective shear modulus

μ_m is the matrix shear modulus

ν_m is the matrix Poisson's ratio

Γ (crack density) is given by: $\Gamma = \frac{1}{V}\sum_{0}^{N} c_i^3$, with c_i being the radius of the i^{th} crack, and N the total number of cracks embedded in the representative volume V.

h is given by Kachanov (1994) as: $h = \frac{3(1-\upsilon_m/2)}{16(1-\upsilon_m{}^2)}$ (penny-shaped cracks),

ζ is the saturation parameter, defined as: $\zeta = \chi^{-1}\frac{E_m\alpha}{K_f}$. This compares the fluid bulk modulus K_f to the crack bulk modulus $\chi^{-1}E_m\alpha$, assuming that crack volume is dependent on crack aperture.

χ is a non-dimensional geometrical factor defined by: $\chi = 16\frac{1-\upsilon_m{}^2}{3\pi}$

However, this is too simplistic for Takidani granite, in which the anisotropy is generated by an aligned crack fabric. For this (PTI) case the relationship between the effective medium elastic moduli and the crack density is more complicated, and is given by Sayers and Kachanov (1995) (see Appendix A.1). The resulting compliances in these expressions are then inverted to calculate the elastic stiffness matrix, and hence elastic wave velocity, using a code developed by Schubnel and Hazzard (Per. Comm., 2004).

6.3.2 HUDSON MODEL FITTING: COMPARISON WITH LAB DATA

Bentheim sandstone

In general, Hudson model azimuthal velocity data for Bentheim sandstone shows a close fit to the experimental values (figures 6-20 to 6-21). In addition, for P-wave velocities in particular, an excellent match to the Thomsen (TI) model data is noted. The fit between P-wave model and P-wave laboratory data in the YZ plane (fig. 6-20) is within experimental error, with a few small areas of exception, such as at approximately 0-80°. However, S-wave model velocity in this plane is within experimental error only in the azimuth range 260°-340° and is slightly out of step as compared to the Thomsen velocity data. However, the general S-wave model trend is still well matched to the laboratory data.

For XZ plane data (figure 6-21) a generally good match between the model velocities and laboratory measured velocities are also seen. For P-wave data, the Hudson model velocity lies within experimental error at approximately 0-30° and 150-200°; whereas the S-wave model prediction is within experimental error through much of the azimuth range. Finally, as noted, Hudson model velocity change with angle is calculated by using an appropriate crack density distribution with a wider angular distribution resulting in lower variation of elastic velocity over the angle range. For the BHS, an angular crack angle spread of 28.5° (average) is required to give the observed velocity azimuthal distribution.

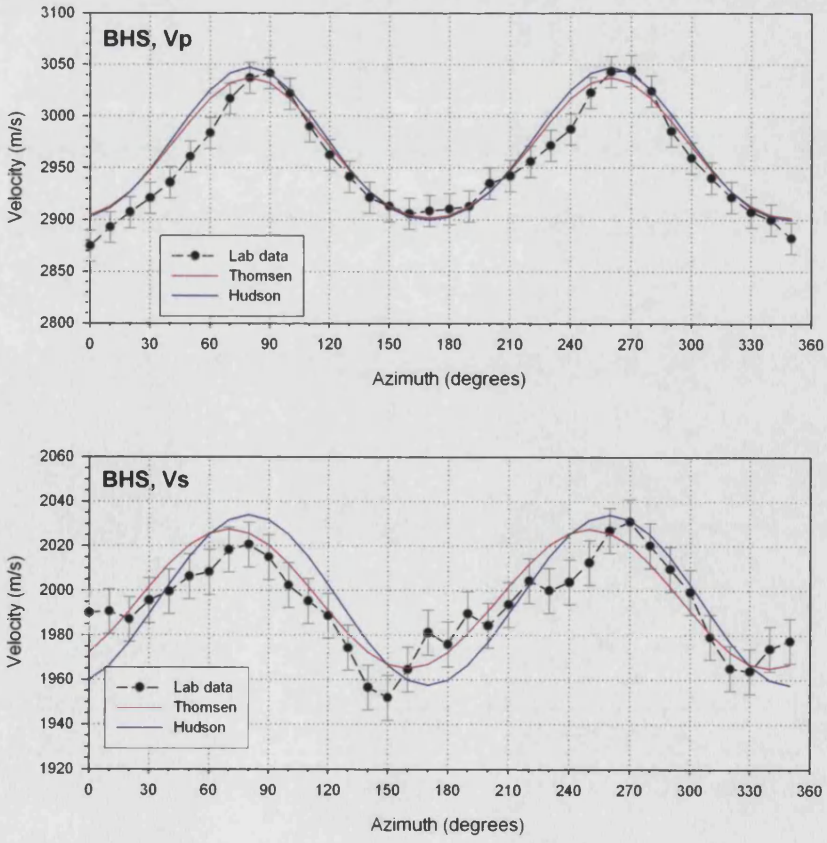

*Figure 6-20. Hudson model fit to Bentheim sandstone azimuthal data (**X direction core axis**, YZ plane), for P-wave (top) and S-wave (bottom), with the Thomsen model fit seen earlier for comparison*

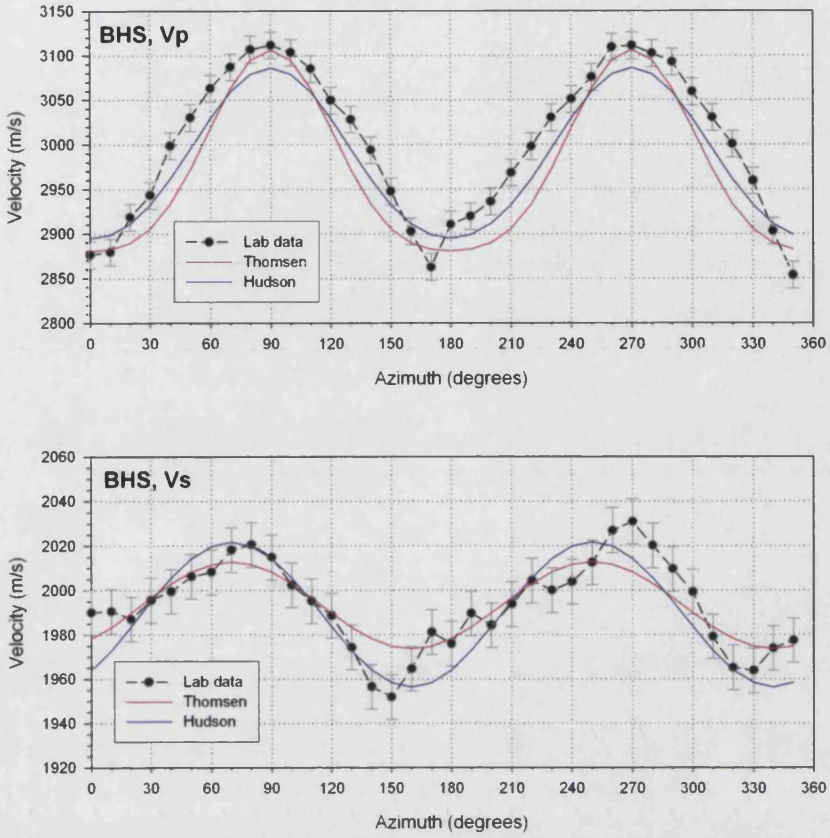

Figure 6-21. Hudson model fit to Bentheim sandstone azimuthal data ***(Y direction core axis****, XZ plane), for P-wave (top) and S-wave (bottom), with the Thomsen model fit seem earlier for comparison*

Crab Orchard sandstone

Overall, Hudson model azimuthal velocity data for Crab Orchard sandstone shows a close fit to the experimental values (figures 6-22 to 6-23), but with some obvious deviations. For P-wave data (both XZ and YZ planes), the model velocity prediction lies within experimental velocity error at azimuths of approximately 0°, 90°, 180° and 270° (both XZ and YZ planes). For S-wave data, a generally poorer fit is seen between the model and experimental velocities than for the P-wave model data. In addition, the S-wave velocity model variation (i.e. the peak to peak change) is lower than the velocity change (anisotropy) measured experimentally. However, when considering the velocity-azimuth models (i.e. Thomsen and Hudson) in comparison with the experimental data, it should be noted that these two models are testing different rock properties. The Thomsen model describes whether the data is PTI using a simplification to theory, whereas the Hudson model explains this variation in terms of the physical (micro) mechanical rock properties. For COS, the Thomsen model indicates that, in this case, the rock exhibits a strongly transversely isotropic nature. For COS, a Hudson angular crack angle spread (σ) of 26° is required to give the velocity azimuthal distribution, very similar to BHS.

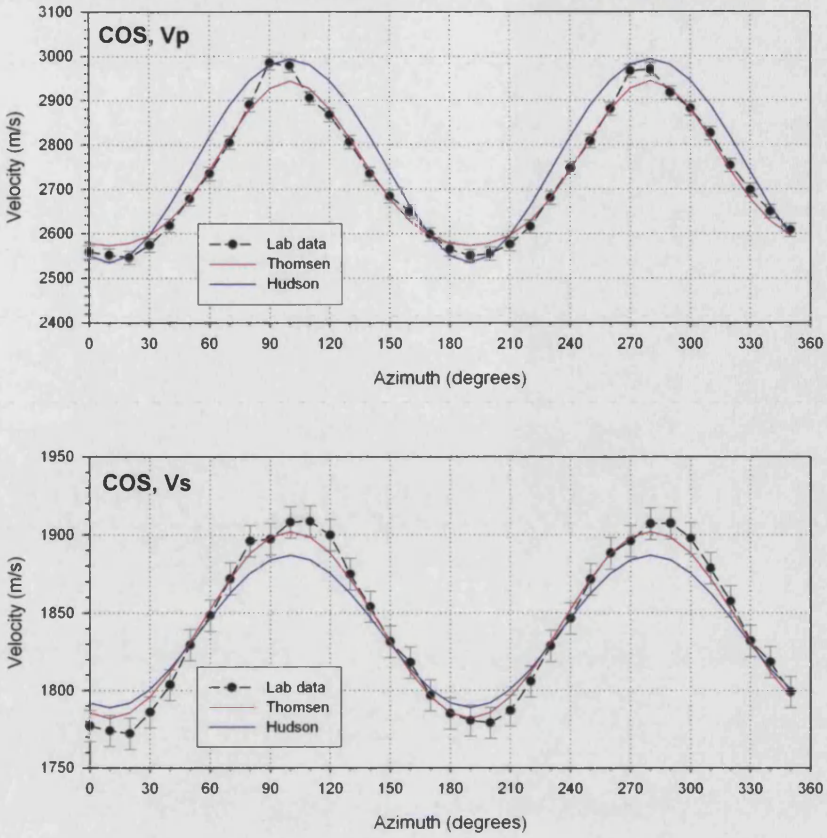

*Figure 6-22. Hudson model fit to Crab Orchard sandstone azimuthal data (**X direction core axis**, YZ plane), for P-wave (top) and S-wave (bottom), with the Thomsen model fit seem earlier for comparison*

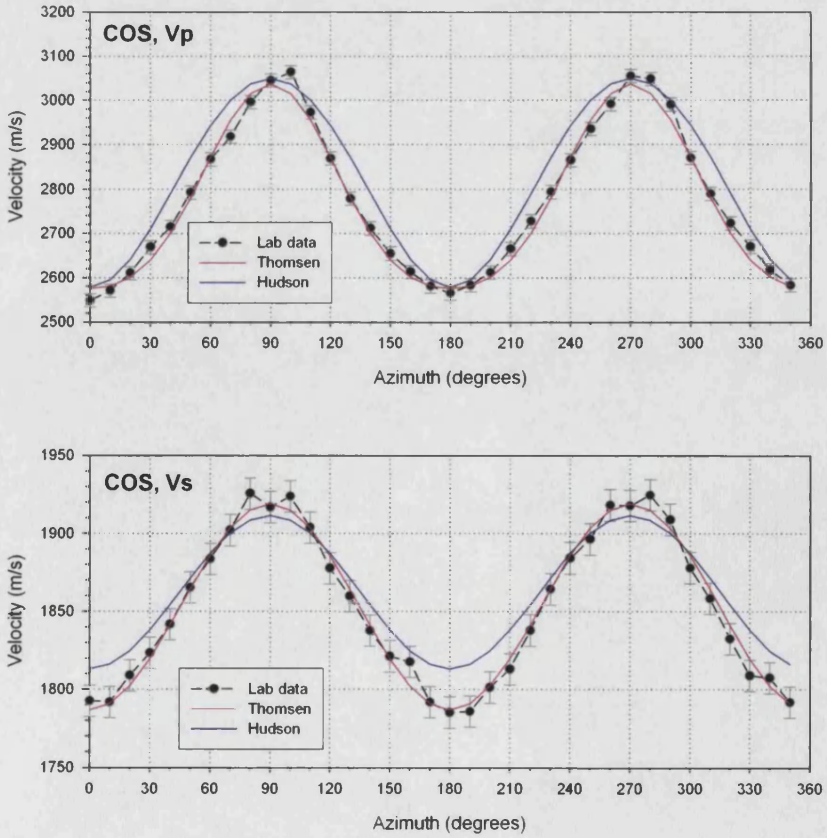

*Figure 6-23. Hudson model fit to Crab Orchard sandstone azimuthal data (**Y direction core axis**, XZ plane), for P-wave (top) and S-wave (bottom), with the Thomsen model fit seem earlier for comparison*

Takidani granite

Finally, Hudson model azimuthal velocity data for Takidani granite shows a reasonable fit with the experimental values (figures 6-24 and 6-25). For P-wave data (both XZ and YZ planes), the model velocity prediction is excellent, especially in the YZ plane where the model data approximately lies within experimental data error for the entire azimuth. For S-wave data, a generally poorer fit is seen between the Hudson model velocities and experimental velocities. S-wave data for the YZ plane is especially poor. However, this is likely to be due to the extreme difficulty encountered when measuring accurate laboratory S-wave velocities for Takidani granite rather than simply a model effect. In comparison to COS, P-wave Hudson model velocity data are a closer fit to the experimental velocities over a greater azimuth range than for the Thomsen model; supporting the notion that the Takidani may not be PTI, and that the rock is showing a higher degree of mechanical anisotropy as compared to the sandstones. This lends further support for the dominance of cylindrical transverse isotropy (CTI) in this rock rather than PTI. CTI is described when cracks align with their long axes in the same direction, but which have crack normals distributed in a plane at 90° to that first alignment, rather than in a single direction as in PTI. For TDG, a Hudson angular crack angle spread (σ) of 27.5° is required to give the experimentally observed velocity azimuthal distribution.

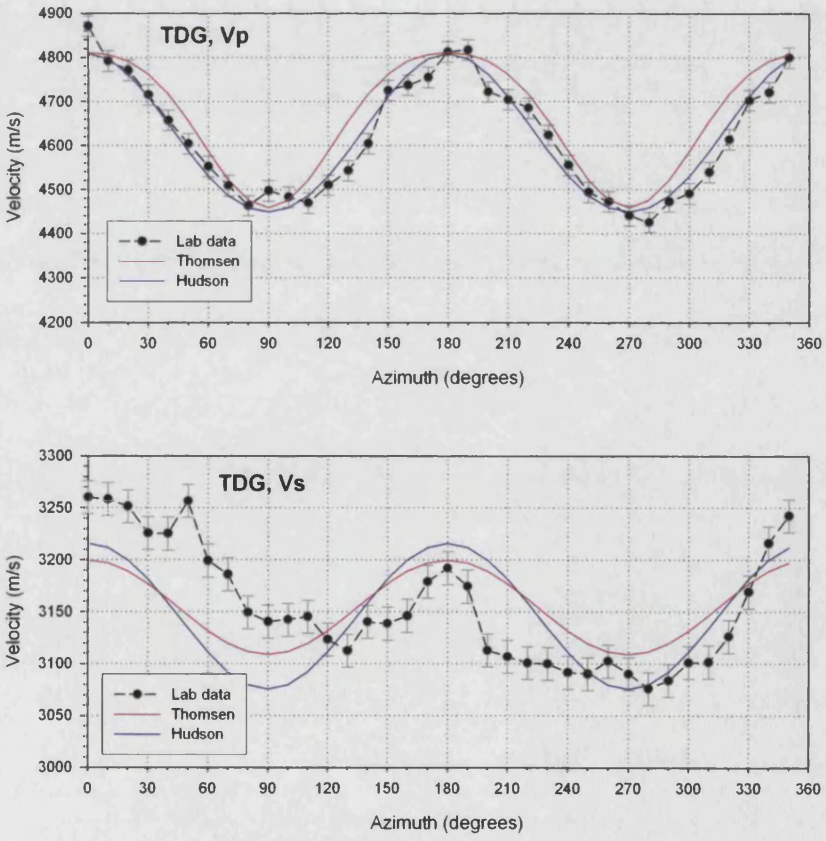

*Figure 6-24. Hudson model fit to Takidani granite azimuthal data (**X direction core axis**, YZ plane), for P-wave (top) and S-wave (bottom), with the Thomsen model fit seem earlier for comparison*

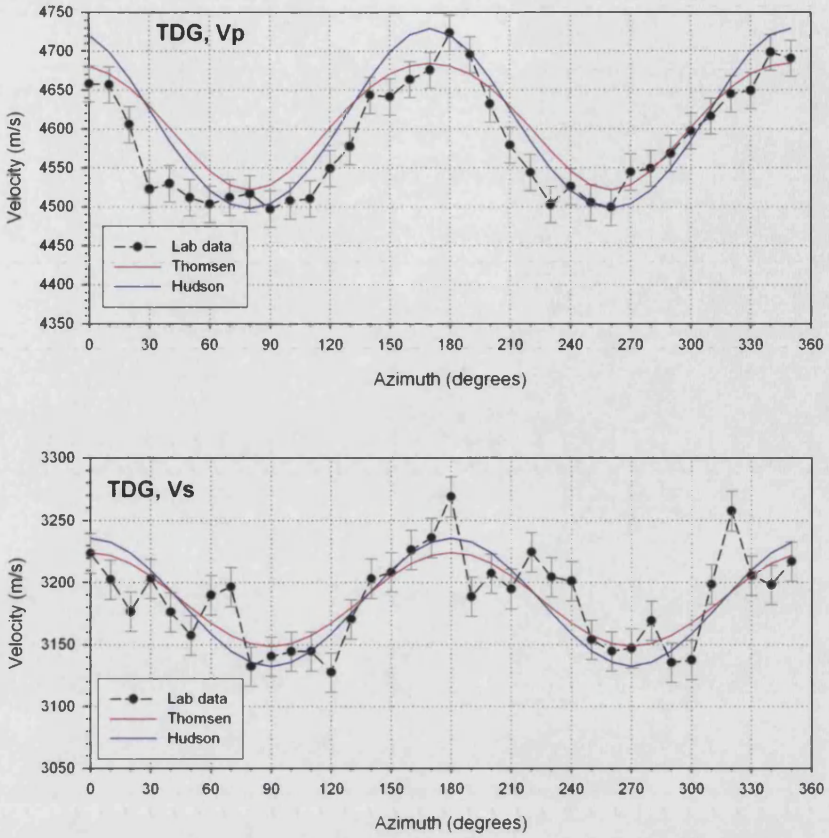

*Figure 6-25. Hudson model fit to Takidani granite azimuthal data (**Z direction core axis**, XY plane), for P-wave (top) and S-wave (bottom), with the Thomsen model fit seem earlier for comparison*

Rock type / direction	Hudson model anisotropy parameters	
	Sigma	Theta (degrees)
BHS, X	0.49	28
BHS, Y	0.50	29
COS, X	0.46	26
COS, Y	0.46	26
TDG, X	0.48	27
TDG, Z	0.50	28

Table 6-5. Hudson crack model: Table of crack 'spread' parameters used for fitting the model to the data. Common properties across all rock types are a crack porosity=0.5% and aspect ratio=0.01.

6.3.3 KACHANOV MODEL FITTING: COMPARISON WITH LAB DATA

The Kachanov crack model predicts changes in crack density as a function of elastic wave velocity, ideally suiting comparison to the elevated pressure tests in a manner similar to the inclusion models. For this model, the assumption of zero crack density at maximum (90 MPa) pressure is not used. The model was applied to Takidani granite only, as the Kachanov model is exclusively an 'aligned crack' model and thus would not be well matched to either BHS or COS (Schubnel, Per. Comm., 2003) as these rocks both contain a significant element of 'quasi-equant' void space. Using the ultrasonic wave velocity data (P-wave and S-wave) for Takidani granite obtained at elevated hydrostatic pressure, a least-squares inversion is performed for crack density as a function of pressure using a novel and state-of-the-art code developed by Schubnel and Hazzard (Per. Comm., 2004).

Crack density for **dry** samples decreases from ~0.28 at 5 MPa to ~0.02 at 90 MPa (figure 6-26 below), a larger range and maximum value than seen for the DEM and K-T models. This crack density evolution is then used to calculate the associated elastic moduli and thus the elastic wave velocity variation with effective pressure (figure 6-27). In general, this exercise produces elastic wave velocities that correlate well with the experimental data. Again, this is not surprising considering that this same velocity variation is used to generate the crack density evolution in the first instance. However, like the K-T and DEM models, this argument is not completely 'circular' as one wave velocity type (P or S) provides a consistency check upon the other.

The P-wave model shows a good fit with laboratory values, in particular the trend and the increase. The Kachanov model code produces a single variation of velocity with pressure in the XZ plane, as this plane is defined as co-incident with the TI symmetry used, whereas two directions in this plane are measured experimentally. Model velocities normal to the TI symmetry plane are therefore coincident with the laboratory Y axis direction, and the velocity data here also shows a high degree of correlation. A small offset between model and laboratory values is noted. S-wave model variation also compares favourably with the laboratory values. However, a larger offset is seen than in the P-wave data. In addition, the code used does not obtain a different velocity-pressure variation with measurement direction, returning a variation with pressure separately for the polarisation end-members of Vs_v and Vs_h (rather than for Vs_v with azimuth to the symmetry axis, for example). The polarisation of laboratory S-wave data is Vs_h, based upon the known transducer and core alignments within the pressure vessel.

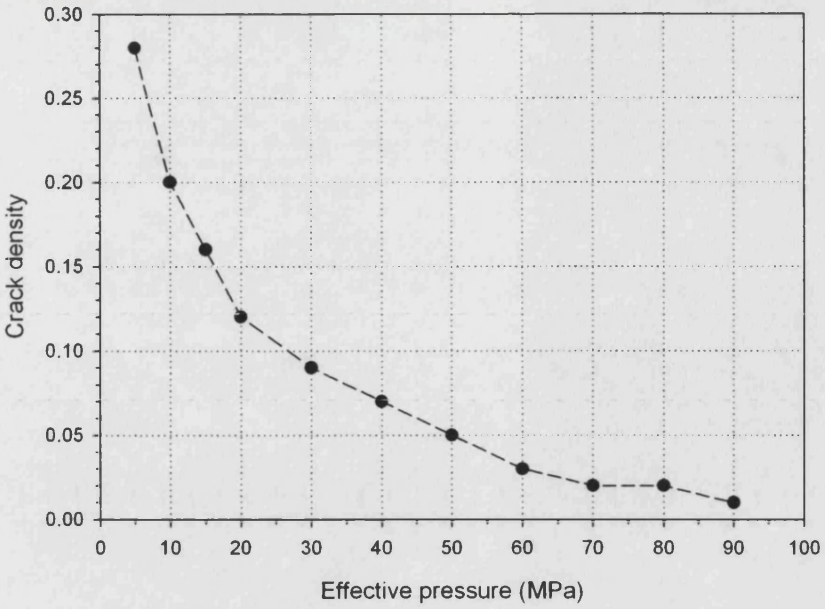

Figure 6-26. Kachanov crack model: crack density variation with effective pressure for ***Takidani granite (dry rock frame)***

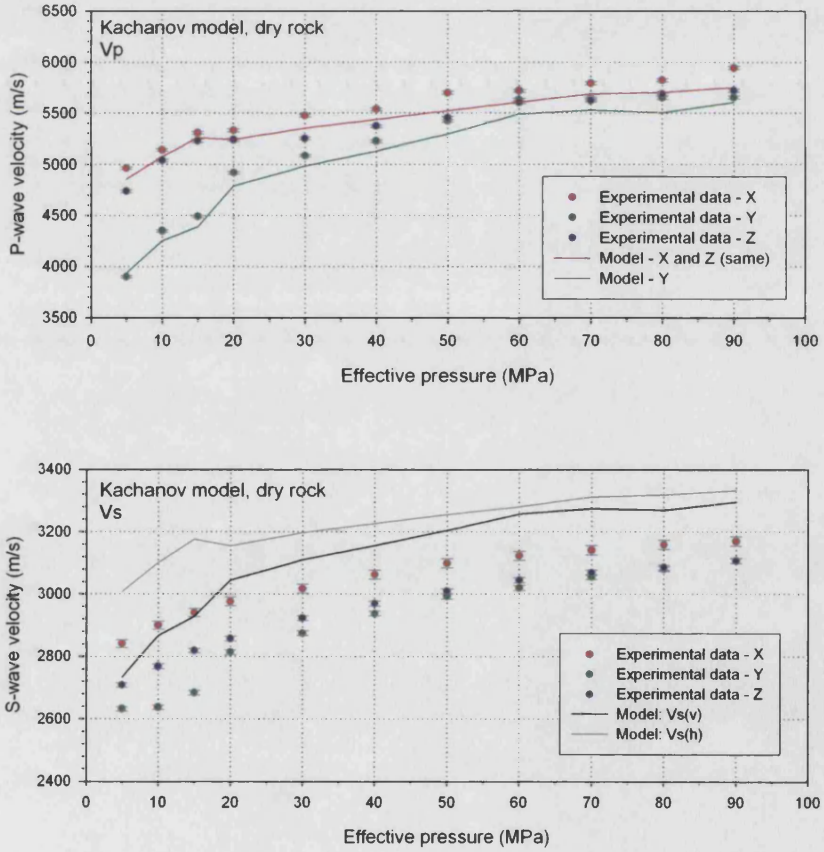

Figure 6-27. Kachanov crack model velocity predictions for ***dry*** *P-wave (top) and S-wave (bottom). Kachanov P-wave model data predicts a 'fast' variation data parallel to the TI plane symmetry (denoted model –X and Z), and a 'slow' variation normal to the TI plane. For S-wave model data, the 'fast' (Vs_h) and 'slow' (Vs_v) shear directions with respect to the TI symmetry are displayed. Laboratory measured P-wave and S-wave (Vs_h) data is shown by the solid symbols and for comparison, as measured in each orthogonal direction (indicated by the key).*

The same procedure is performed for **saturated** samples (figure 6-28). Here, crack density decreases from ~0.34 at 5 MPa to ~0.1 at 90 MPa; a larger range and maximum value than for the inclusion models (although the inclusion models were modelling dry cracks, not saturated, so a direct comparison is less useful). This crack density evolution is used to calculate the associated bulk and shear moduli, and thus the elastic wave velocity with effective pressure (figure 6-29).

The P-wave model produces values which correlate well with experimental values, with the exception of Y-axis model values in the range 10 to 50 MPa. P-wave model values in the X/Z direction lie within the variability seen in the experimental data. Interestingly, the S-wave model shows no dependency with direction or polarisation. However, the model shows an extremely good fit to the experimental Y-axis direction values, within experimental and sample variability up to approximately 80 MPa effective pressure.

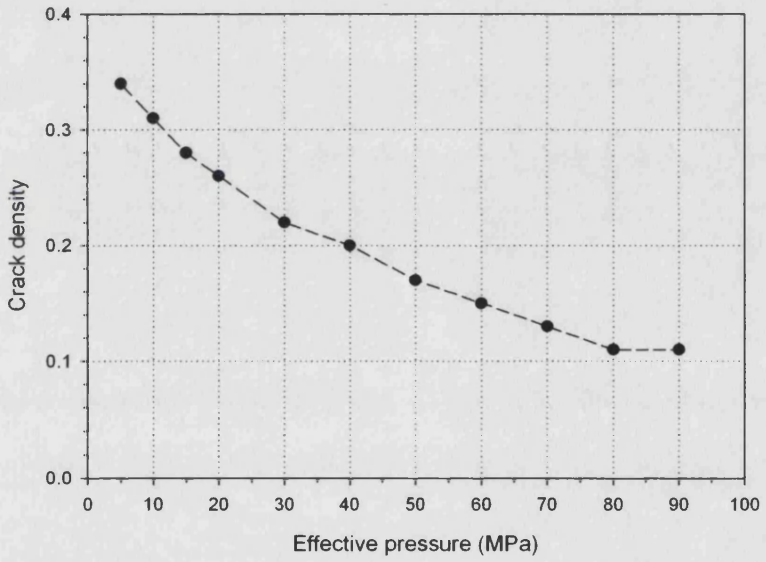

Figure 6-28. Kachanov crack model: crack density variation with effective pressure for ***Takidani granite (saturated rock)***

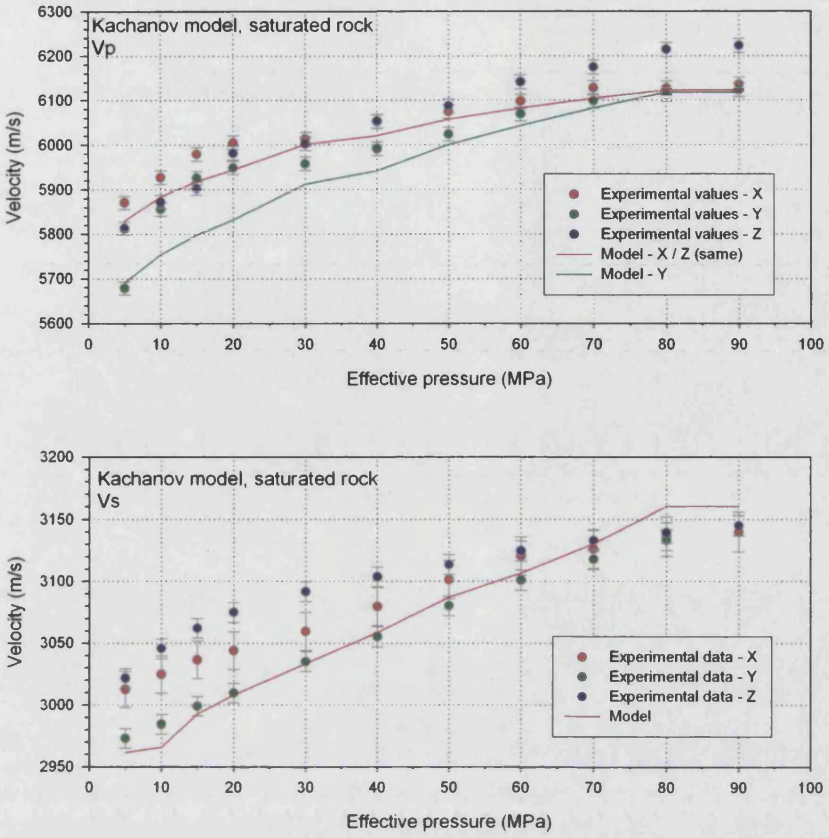

Figure 6-29. Kachanov crack model velocity predictions for ***saturated*** *P-wave (top) and S-wave (bottom). Again, Kachanov P-wave model data predicts a 'fast' variation data parallel to the TI plane symmetry (denoted model –X and –Z), and a 'slow' variation normal to the TI plane (-Y). S-wave model prediction shows only a single velocity variation. Laboratory measured P-wave and S-wave (Vs_h) data is shown by the solid symbols and for comparison, as measured in each orthogonal direction (indicated by the key).*

In addition to basic velocity prediction with effective pressure, it is also possible to combine the modelled P-wave and S-wave velocity predictions made in different directions in order to determine the changing elastic anisotropy evolution with pressure. This is done by calculating the percent change in model velocity between the X/Z (average) and Y directions stepwise with pressure. This is then compared directly with the same data obtained from experimental tests (figure 6-30). The initial anisotropy decrease observed in the P-wave experimental anisotropy data between 0 and 10 MPa is not predicted by the Kachanov model, and the comparison between P-wave model and laboratory anisotropy remains poor up to approximately 40 MPa. However, after this point the P-wave model and experimental anisotropy data agree well up to the maximum pressure attained. For S-wave data there is little correlation over the pressure range, and only a single model velocity variation with pressure is produced with respect to spatial orientation, as previously noted. This leads to a mis-match between the model P-wave and S-wave anisotropy, in contrast to the experimental data.

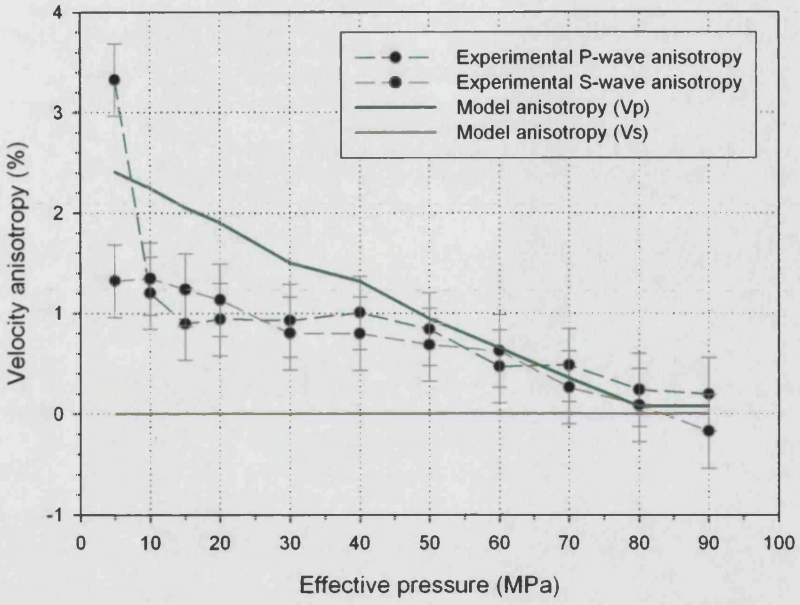

Figure 6-30. Kachanov crack model elastic anisotropy prediction with effective pressure (using saturated model data, so as to compare with experiment). Solid lines show the variation of fast and slow P-wave and S-wave velocity relative to each other at each pressure step, using the data in figures 6-28 and 6-29 (although the S-wave data is a 'null' result as no fast and slow data is available). Solid symbols display the experimental elastic velocity anisotropy for comparison.

6.4 PERMEABILITY

6.4.1 INTRODUCTION

Permeability is one of the most important properties of porous rock, but is also one of the most difficult to examine theoretically. Although a trend is frequently observed between the bulk porosity and permeability of sandstones (for example) there exists, in general, no simple relationship between permeability and commonly measured petrophysical parameters of porous media, such as porosity and elastic wave velocity (Guéguen and Palciauskas, 1994). Where such relationships are investigated, they are often specific to the rock under test, and over a limited range of environmental conditions (e.g. Dullien, 1979; Bourbie and Zinzner, 1985; Klimentos, 1991; Bernabe et al., 2003), due to the seemingly infinite way in which pore space connectivity can be arranged. Despite these problems, a number of models have been proposed which can produce reasonable predictions of permeability based upon simplified rock physical properties such as porosity. Three permeability models are used here, one for each rock type examined. As the pore fabric of each rock type in this investigation is very different, different models using different assumptions about pore fabric connectivity must be used.

6.4.1.1 KOZENY-CARMAN RELATION

One of the oldest and simplest attempts at deriving an expression linking bulk porosity to permeability is based upon hydraulic radius approximations, and gives rise to the Kozeny-Carman relation (e.g. Carman, 1961; Scheidegger, 1974; Guéguen and Palciauskas, 1994). An estimate of the permeability is made based upon simplified key parameters of porosity, internal pore space surface area, and using an idealised pore fabric geometry represented by cylindrical pipes:

$$k \propto \frac{\phi^3}{S^2}$$

Where: k is permeability

ϕ is porosity

S is the internal pore space relative surface area, given by $S = \frac{S_{pore}}{V_{solid}} = \frac{3}{2}\frac{(1-\phi)}{d}$, where d is the average grain diameter, S_{pore} is the internal pore surface area and V_{solid} is the volume of the solid sample, using a spherical packing of grains (Mavko et al., 1998).

Substituting for S gives:

$$k \propto \frac{\phi^3}{(1-\phi)^2} d^2$$

However, no flow is possible below a lower 'critical' porosity, also known as the percolation threshold, which is denoted ϕ_c (Mavko and Nur, 1997). This notion is also consistent

with many crack models (Brace et al., 1968). Mavko and Nur (1997) show how this assumption modifies the basic Kozeny-Carman relation above to:

$$k \propto \frac{(\phi - \phi_c)^3}{\left[1-(\phi - \phi_c)\right]^2} d^2 \qquad \textit{Equation 6-13}$$

Finally, the constant of proportionality which equates permeability to porosity is evaluated using the simple derivation of Walsh and Brace (1984), which, when combined with equation 6-13 above, gives:

$$k = \frac{c}{b} \frac{(\phi - \phi_c)^3}{\tau^2} \frac{d^2}{\left[1-(\phi - \phi_c)\right]^2} \qquad \textit{Equation 6-14}$$

Where c is a constant which depends upon the pore geometry (for spherical grains, c=9/4), and b is a crack parameter which varies between 2 for circular tubes to 3 for pure penny-shaped cracks (Walsh and Brace, 1984). In this work, b = 2.5 is used, as a mixture of tube-like pores and cracks is assumed to exist for the rock type that this model will be applied to – Crab Orchard sandstone. Tortuosity (τ) is defined as the ratio of total fluid flow path length to the sample length. Equation 6-14 can now be applied directly to the data obtained under elevated hydrostatic conditions, using the measured rock porosity and the known average grain size from image analysis. Tortuosity and crack porosity ϕ_c are then varied in order to obtain a fit to the measured permeability.

6.4.1.2 LATTICE BOLTZMAN GAS APPROXIMATION

The lattice Boltzman (LB) method is a numerical and statistical technique which works by approximating the pore fluid as a 'gas' of imaginary particles. These particles obey well defined collision rules, equivalent to the Navier-Stokes equation, whenever they encounter the solid matrix representing the rock fabric (Keehm et al., 2001). Although these imaginary particles are physically larger than the fluid molecules, at macroscopic scale the simulated flow accurately reflects the real fluid flow (Bosl et al., 1998) and thus can be used to estimate permeability.

The specific model used in this study is that of Bosl et al. (1998), and proceeds in the following manner (Ayako Kameda, Per. Comm., 2004). Initial input for the model is a thin section image in which the porosity can be clearly identified (figure 4-27, 4-28). The image is first digitised into a 100x100 pixel black-and-white image, with black pixels representing pore space, and then smoothed with a 3x3 pixel rolling 2-D window to remove isolated pore space (fig 6-31, far left; centre left). A Fourier transform is then used to calculate a porosity. This porosity is then extrapolated in order to give a 3-D volume (fig 6-31, centre right; far right) using the geostatistical method of Deutsch and Journal (1992). This 3-D volume is directly used as input into the Lattice-

Boltzman method, which simulates permeability through the representative 3-D volume using a new and novel code (Ayako Kameda, Per. Comm., 2004).

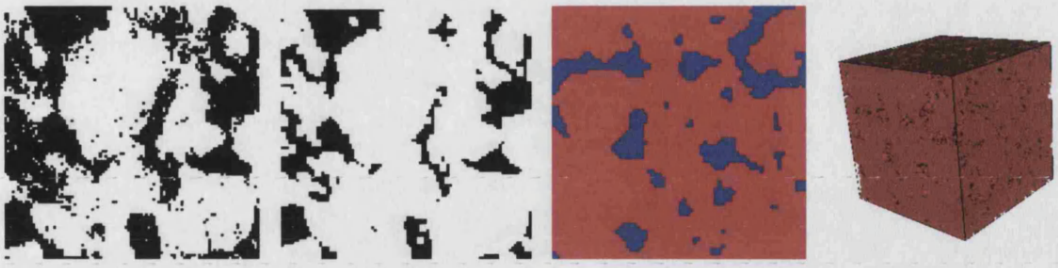

Figure 6-31. building up the 3-D solid matrix from a 2-D thin section image to a 3-D representative volume (left to right). Courtesy Ayako Kameda, Stanford University. See text for detail.

In previous work, the LB method has shown to provide highly accurate results on higher porosity rock types and glass-bead rock analogues (Qian et al., 1992; Ladd, 1994; Ferreol and Rothman, 1995). Therefore, in this study it is only applied to the Bentheim sandstone in order to avoid any complications in attempting to apply this method to low porosity rocks such as Crab Orchard sandstone or Takidani granite. Additionally, the model assumes an isotropic pore fabric, and its application would therefore be wholly inappropriate for COS or TDG.

6.4.1.3 Guéguen & Dienes

In the Kachanov crack model introduced earlier (section 6.3.1.3), the concept of the crack aperture was briefly discussed. Obviously, a crack represents a void space of non-zero size, the aperture being defined as the maximum width of such a crack. This will therefore allow, if the cracks intersect each other, a 'crack permeability' based upon the fluid movement through the network of linked crack elements. Guéguen and Dienes (1989) took this further in order to quantify the effect of penny shaped cracks upon the permeability of an impermeable host matrix and found the following relation:

$$k = \frac{2}{15}\Gamma f \overline{\omega}^2 \overline{\alpha} \qquad \textit{Equation 6-15}$$

Where: Γ is the crack density

$\overline{\alpha}$ is the average aspect ratio

$\overline{\omega}$ is the average crack aperture

The parameter 'f' is the percolation factor (Guéguen and Dienes, 1989) defined through the relation: $f \approx \frac{9}{4}\left(\frac{\pi^2}{4}\Gamma - \frac{1}{3}\right)^2$, and valid for $1/3 < \Gamma\pi^2/4 < 1$. In essence, this factor describes the probability of two cracks intersecting ($\Gamma\pi^2/4$), in which case the volume element created by the intersecting cracks is discounted in the method (an excluded volume). In all cases, $0 \leq f \leq 1$.

Using equation 6-15, the evolution of permeability with increasing effective pressure is evaluated using the P_{eff}-Γ relationship as determined from the Kachanov model for saturated Takidani granite (i.e. figs. 6-28, 6-29). As this rock type is likely to possess a pore fabric composed mostly of cracks, then the application of this model is consistent with Guéguen and Dienes' theory. In order to construct the permeability evolution, a constant value of crack aperture and aspect ratio is assigned to the rock. For Takidani granite, an average aspect ratio of 0.01 is used, based upon information from DEM and K-T models, as well as previous work suggesting that aspect ratios of less than 0.01 are indistinguishable (non-unique) as obtained from P-wave and S-wave elastic data (Roy White, Per. Comm., 2003). For a given crack aperture, equation 6-15 may then be evaluated at each effective pressure used for laboratory permeability measurement. Conversely, equation 6-15 may also be used to calculate the changing crack aperture, by equating the expression to the known experimental permeability.

6.4.2 PERMEABILITY MODEL FITTING: COMPARISON WITH LAB DATA

Bentheim sandstone permeability was modelled using the Lattice-Boltzman approach. As this permeability estimate uses a thin section image for the initial input data, then (obviously) the resulting permeability represents a room pressure (0 MPa effective pressure) value; whereas the lowest pressure used in the pressure vessel for permeability measurement was at 5 MPa. However, this is not an issue as the permeability of Bentheim sandstone has already been seen to vary little with either effective pressure or flow direction. Results of the model predict a porosity of 20% (based on the 2-D image), and a permeability of 0.89 x 10^{-12} m^2. This compares extremely well with the experimental data (figure 6-32), especially between effective pressures of 0-30 MPa, where the room pressure estimate lies within experimental permeability variation.

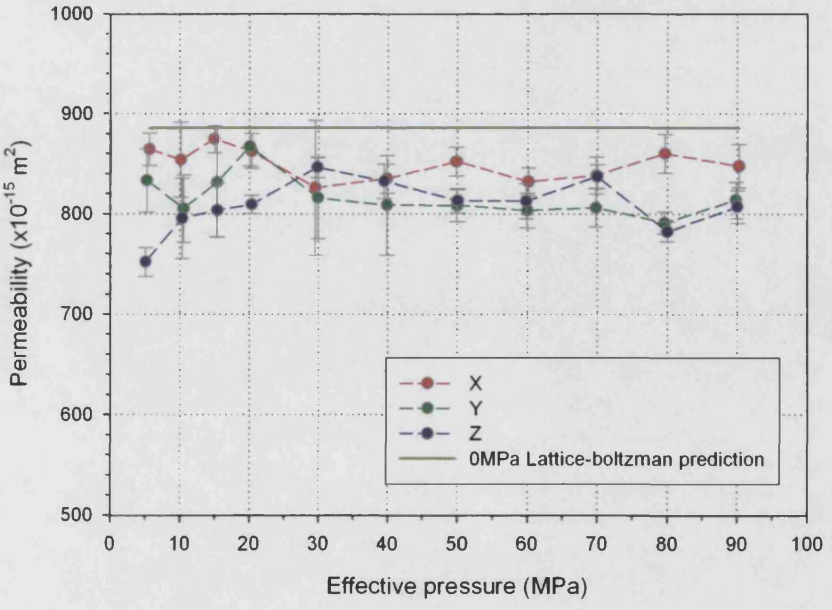

Figure 6-32. Lattice-Boltzman permeability prediction for Bentheim sandstone (dark yellow line), with experimental values at elevated pressures and orthogonal directions for comparison

Crab Orchard sandstone permeability is modelled using the Kozeny-Carman method (figures 6-33, 6-34 and 6-35), which uses porosity as the primary input for calculation. However, as the experimental equipment uses effective pressure as the primary control, this means that, at every point the sample porosity is determined, the effective pressure is also known. Using these experimental pressure/porosity values it is possible to assign an equivalent effective pressure at each point on the Carman-Kozeny model curve where an experimental porosity also exists. For example, if at 5 MPa the experimental porosity is 4.7% and the Carman-Kozeny model is also 4.7%, then the pressure of 5 MPa is assigned to this point on the model curve as well. This allows a relation between effective pressure and permeability to be determined for the Kozeny-Carman approach, even though the original method does not explicitly allow for this.

In general, the modelled data are an extremely good fit to the experimental values, both as a function of porosity and effective pressure, and in each of the X, Y and Z directions. Tortuosity is highest for the Z direction, which is the direction lying normal to the visual cross-bedding in the rock, and is therefore consistent with the data as this direction also shows the lowest fluid permeability. Conversely, the X direction shows the lowest tortuosity, and possesses the highest fluid permeability. The X axis is also observed to lie approximately coincident with the crossbedding strike direction on the sample scale. Interestingly, a high tortuosity is also determined in the Y direction. However, as this direction coincides approximately with the direction of the crossbedding dip as observed in hand specimen, then it might reasonably be assumed that the fluid flow path may have to partly cross the crossbedding plane when measured in the pressure vessel; resulting in a relatively high tortuosity compared to the X axis measurement. In addition, the Y direction possesses a permeability which, whilst higher than the Z axis permeability value, is still slightly lower than that measured in the X direction. This is also consistent with the Y direction tortuosity being slightly lower than determined in the Z direction but higher than that obtained in the X direction.

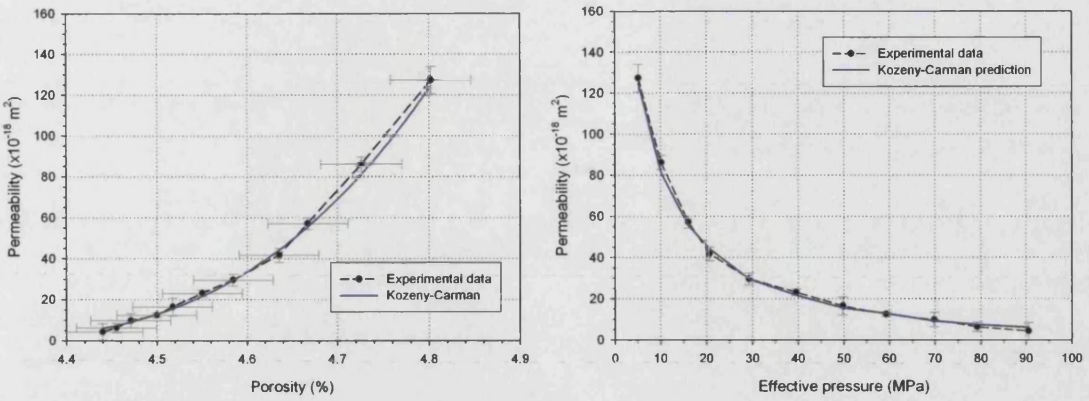

Figure 6-33. Kozeny-Carman model for COS: permeability-porosity prediction (left hand figure) in the X direction is shown by the blue line, with experimental data points shown by solid symbols, with errors. This model fit requires a critical porosity of 0.0423 and tortuosity of 9. Right hand figure shows the permeability variation with the equivalent experimental effective pressure, see text for details

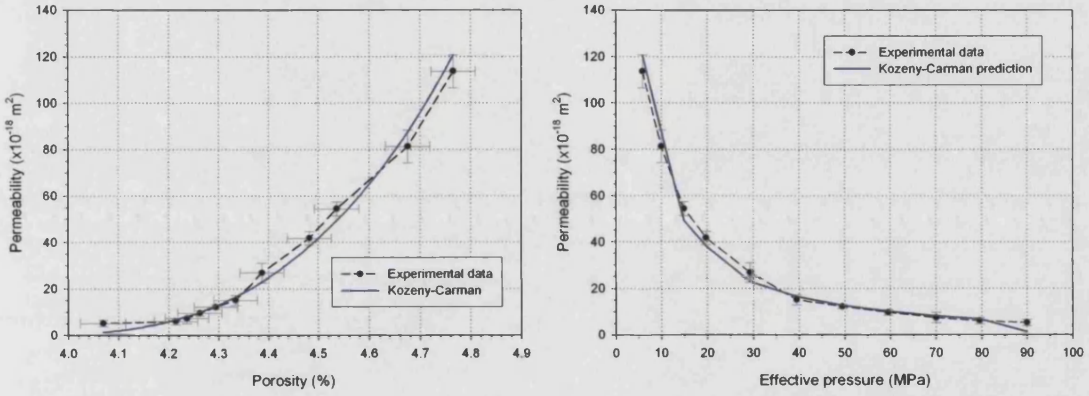

Figure 6-34. Kozeny-Carman model for COS: permeability-porosity prediction (left hand figure) in the Y direction is shown by the blue line, with experimental data points shown by solid symbols, with errors. This model fit requires a critical porosity of 0.0391 and tortuosity of 16.5. Right hand figure shows the permeability variation with the equivalent experimental effective pressure, see text for details

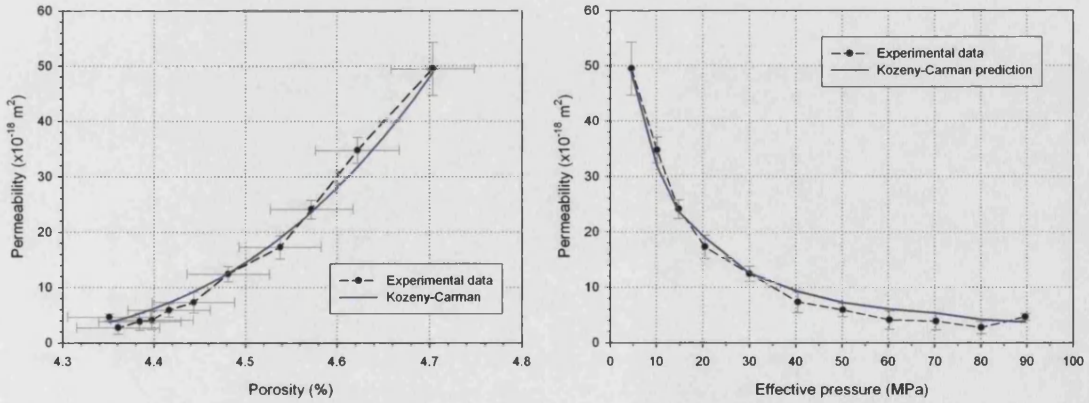

Figure 6-35. Kozeny-Carman model for COS: permeability-porosity prediction (left hand figure) in the Z direction is shown by the blue line, with experimental data points shown by solid symbols, with errors. This model fit requires a critical porosity of 0.04065 and tortuosity of 17.5. Right hand figure shows the permeability variation with the equivalent experimental effective pressure, see text for details

Takidani granite permeability is modelled using the Kachanov crack aperture method together with the Guéguen and Dienes (1989) theory. Figure 6-36 shows the fit between the model permeability for two crack apertures of 0.6 microns (upper bound) and 0.25 microns (lower bound), and the experimentally obtained measurements. Despite the higher variability in experimental permeability with pressure the fit is good, in particular for the lower permeability direction (Y). Figure 6-37 shows the reverse calculation, whereby the measured permeability values are used in order to calculate the associated crack apertures, in each of the three orthogonal directions. This information is useful as it shows that the crack aperture in the 'Y' direction is the lowest of the three, and that it does not change significantly with pressure. Secondly, it shows that the 'upper' aperture bounds, for 'X' and 'Z' directions, should not be fixed, as their values decrease slightly with pressure. However, both 'X' and 'Z' aperture values are similar throughout the pressure range.

Finally, the model permeability values can be used to calculate permeability anisotropy, by taking the percent difference between the average 'Z' and 'X' model permeability and the 'Y' permeability stepwise with pressure (figure 6-38). As the model is based upon the experimental results, the model permeability anisotropy agrees well with the experimental data. However, unlike the laboratory observations the predicted anisotropy as a function of effective pressure is constant as a consequence of the mathematics, at approximately 140%.

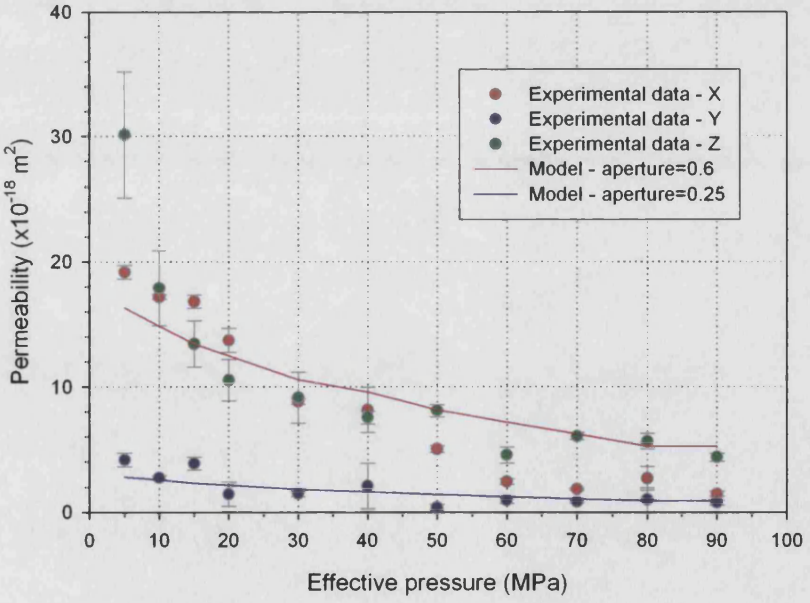

Figure 6-36. Modelled permeability variation with effective pressure using the Guéguen and Dienes (1989) crack aperture model, using crack density data from the Kachanov model. Upper and lower bounds of 0.6 and 0.25 microns effectively constrain the experimental values (solid symbols, see key for direction of measurement), with the model variation matching the experimental variation closely

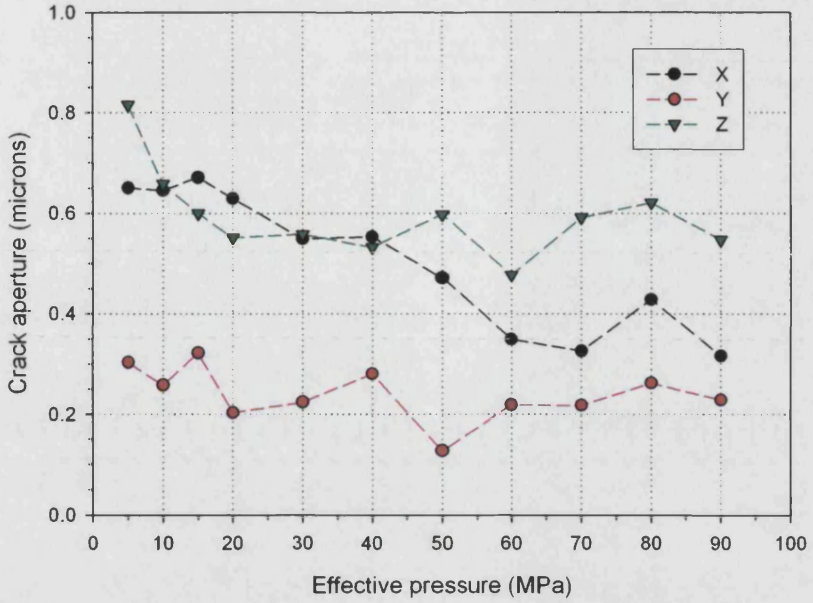

Figure 6-37. Inverse solution for the Guéguen and Dienes model: Calculating the equivalent crack aperture variation with pressure and direction of measurement (see key) using the experimentally measured values of permeability. See text for details

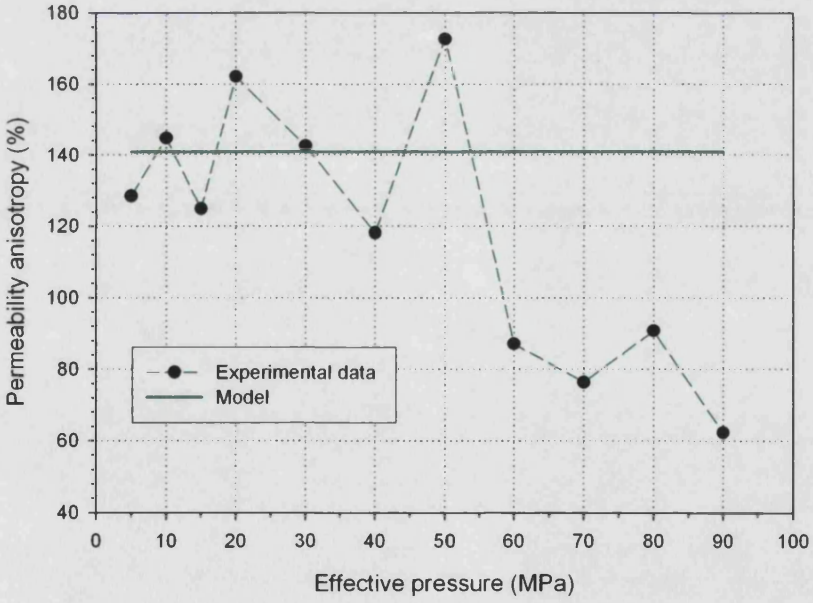

Figure 6-38. Comparison between experimental permeability anisotropy variation with pressure (dashed line) and the Guéguen and Dienes prediction (solid line); using the upper and lower bounds of 0.6 and 0.25 microns and plotting the stepwise percent difference in model permeability with pressure. Average experimental data percent error is approximately ±2.5%, however, this is not plotted as the variability of permeability anisotropy with successive pressure is higher than this mathematical error

7 DISCUSSION

7.1 INITIAL OBSERVATIONS AND COMPARISONS

7.1.1 TRENDS BETWEEN AMS AND ELASTIC VELOCITY PRINCIPAL DIRECTIONS FOR POROUS SANDSTONES (BHS AND COS)

When comparing pAMS with wave velocity data, it must be stressed that the two techniques measure very different petrophysical properties. In this work, void space anisotropy derived from pAMS data is used as a proxy for global average void space geometry and alignment (Hrouda et al., 2000). By contrast, velocities are elastic measurements influenced not only by the shape and alignment of void spaces, but also by the crystallographic and geometrical arrangement of mineral grains in the matrix along each wavepath (Hudson et al., 1995; Berge et al., 1992). By combining velocity measurements along many different wavepaths, an anisotropy ellipsoid can be determined (Benson et al., 2003; Louis et al., 2003) which combines elastic contributions from both the void space and the mineral grain anisotropy. In analysing the velocity data I approximate the spatial variation of the received pulse to an ellipsoidal surface in 3-D. This is only true for a second order symmetric tensor (Stoner, 1945), whereas elastic anisotropy is strictly only fully described by a fourth rank tensor.

However, when deriving the principal anisotropy directions in 3-D, the residual velocities from the ellipsoidal approximation are less than or equal to the measurement accuracy (figure 4-19). Hence, there is essentially no loss of accuracy or information in adopting this second rank approximation. This discussion can also be further extended by considering the symmetry of the appropriate tensors. By examining data presented in Chapter 5, together with reference to the theoretical analyses presented in Chapter 2, we find that we are dealing with rocks exhibiting planar transverse isotropy. Theoretically, this form of anisotropy possesses five independent elastic constants, and so its approximation by a second order ellipsoid (with three independent elastic constants) requires caution, as transverse isotropy can often be highly non-elliptical. However, as the method is only used to extract principal anisotropy length and direction axes, rather than the full shape of the wavefront, then the use of the ellipsoidal approximation to the PTI data is a good first order approximation. In addition, as the velocity anisotropy agrees well to this ellipsoidal fit suggests that we are dealing with rocks in which the three primary parameters used may accurately describe the five constants which are, strictly, needed.

Both the AMS and wave velocity anisotropy techniques used here are capable of characterising the pore fabric anisotropy of rocks in 3-D without prior knowledge of the principal anisotropy directions. However, each method has its limitations. The pAMS method measures bulk void space susceptibility anisotropy, which averages the pore shape and orientation over the sampled volume. For elastic anisotropy measurement, the protocol described requires a minimum of three orthogonal cores, and considers the combination of pore and matrix elasticity. There has been some criticism in the past that the use of multiple cores may lead to measurement of heterogeneity rather

than anisotropy (Rasolofosaon and Zinszner, 2002), as small scale velocity measurement in a single direction on one core, as compared with another directional measurement on another core, may not be representative of anisotropy but simply reflect differences in material properties with position (heterogeneity). This problem has been addressed in this study by making multiple measurements on multiple cores taken in each of the three orthogonal directions from a single block of sandstone. This allows for comparison of data both between samples cored in the same orientation, and also between measurements made in common directions on cores taken in orthogonal directions. Since we found close agreement between measurements made in the same orientation on different cores, and good clustering of principal anisotropy axes, the issue of heterogeneity is unlikely to be a problem in this work. There are, however, very small differences in elastic wave velocity when comparing the velocities made in the same direction but on different cores (< 0.5%). To account for these small differences, the data is 'levelled' in such a way as to effectively treat all data as made upon the same sample (Benson et al., 2003, 2004). This method is similar to that employed previously by Louis et al. (2003).

Results of measurements made under ambient conditions show that COS is highly anisotropic, with a P-wave anisotropy of 19.1% and S-wave anisotropy of 7.6%. By comparison, BHS exhibits a significantly lower anisotropy of 4.7% and 3.0% for P-wave and S-wave velocity, respectively. Measurements of the pore fabrics, using pAMS, are consistent with these observations. The void space of COS shows a volume averaged (pAMS) '**A**' anisotropy of 3.8%, compared with 1.5% for BHS. Both ultrasonic wave velocity and pAMS techniques have been used to determine principal anisotropy axes through fitting the directional data to ellipsoids. Ultrasonic P-wave velocity results provide the most highly clustered data. Generally, directional data for V_p and V_s principal orientations lie within the same stereonet quadrant as each other, but commonly outside their reported statistical errors. In addition, the velocity principal directions lie in the same quadrant as the pAMS derived principal void space directions. Strictly, the pAMS directions are not co-incident with the velocity principal orientations within the calculated 95% confidence cones. However, as they lie within approximately 10° of the velocity derived principal directions, then it is likely that the additional error is as a result of sample variability not taken into account by the confidence ellipsoids, and that pAMS and velocity ellipsoids are essentially describing the same void space fabric in 3-D.

7.1.2 INFLUENCE OF DEPOSITIONAL ENVIRONMENT UPON AMS AND VELOCITY DATA

Bentheim sandstone comes from the Lower Saxony basin, NW Germany. The rock is of Lower Cretaceous age, was deposited in a largely open marine environment, and shows bedding on a massive scale (Kemper, 1976; Wonham et al., 1997). This deposition, as alluded to in section 2.1.1, has implications for the void space shape and alignment which is directly measured with the pAMS method. For this rock type the pAMS minimum principal direction lies approximately co-incident with the normal to the large scale bedding seen in outcrop. Maximum and intermediate principal

pAMS directions are distributed approximately sub-parallel to the plane of bedding. It is likely, therefore, that the deposition influences the measured pAMS data through its influence upon the forming rock, with the flow creating a maximum pore space fabric along the flow direction, which is probably co-incident with the pAMS maximum principal direction.

For Crab Orchard sandstone a clear sedimentary fabric is seen on the millimetre scale, reflecting the hydrodynamics of the environment in which it was deposited. Previous work has described this environment as aqueous, shallow sea or lagoon (Stearns, 1954), which is likely to have been of low energy. This has resulted in the observed high quality grain sorting and relative lack of unstable minerals in the rock. The depositional setting has resulted in a massively bedded sandstone with a clearly visible crossbedding (Stearns, 1954), giving rise to an aligned grain fabric, and hence an aligned pore fabric. With reference to figure 2-1 earlier, the grain fabric has an average geometry with the long axis aligned along the flow direction, and with the short axis aligned along the gravity vector. The intermediate axis, orthogonal to both these directions as previously demonstrated, is therefore approximately aligned along the bedding plane, but normal to the fluid flow direction.

From the mAMS and pAMS techniques, it can be demonstrated that the visible grain fabric (i.e. the crossbedding) of COS posseses a symmetry which is representative of the internal pore fabric. More importantly, for rocks which do not have an obviously crossbedded fabric in hand specimen, such as BHS, the pAMS method is also able to determine the principal anisotropy void space orientations, illustrating the power of the pAMS technique. This is its ability to quickly detect and identify void space anisotropy in rocks either with or without any obvious fabric, where the axes of core samples may not lie along principal anisotropy directions, and using a single sample only. In comparison, to recover principal directions in 3-D using elastic wave velocity, multiple samples must be used. However, despite the more complicated processing required, elastic wave anisotropy principal directions are also in excellent agreement to the visible matrix fabric and to the observed pore fabric. This is an important factor when investigating a rock type which is not easily measured with the pAMS method, due either to low bulk porosity (making ferrofluid saturation difficult) or high matrix susceptibility values (which tend to mask the signal from the ferrofluid impregnated porosity), or a combination of both of these problems.

7.1.3 TAKIDANI GRANITE

The Takidani Granitoid is a pluton located along the major axis of the Japanese Alps, one of the active volcanic belts in Japan, and is reportedly one of the youngest exposed pluton on Earth at 1.2 Ma (Harayama, 1994). The pluton intruded Mesozoic sandstone and mudstone basement rocks, Tertiary granitic rocks and Hotaka Andesites, and was subsequently covered by the quaternary Yakedake volcanics. The existence of major quaternary faulting together with the WNW movement of the Pacific plate during the last 2 Ma, suggests that the compressive tectonic stress field in the

region is also aligned in the W-NW to E-SE orientation, which has produced preferred directions in the mechanical (micro-crack) damage of the rock (Kano and Tsuchiya, 2002).

Due to the different manner of formation for granite compared with sandstones, the Takidani granite exhibits anisotropy primarily due to microcracking as a result of the cooling effects and the local stress field during uplift, or to petrogenetic processes generally (Kano and Tsuchiya, 2002). These processes have produced a micro-crack fabric within the rock, which in turn has resulted in elastic anisotropy. Previous work has shown that this microcracking produces laboratory P-wave anisotropy of approximately 10%, and whose symmetry is co-incident with larger scale faulting seen in outcrop (Kano and Tsuchiya, 2002). When attempting to use the pAMS method on the Takidani granite, a strong magnetic signal from the matrix fabric must be subtracted from the tAMS signal on a measurement-by-measurement basis before the ellipsoid can be fitted, in order to describe the pore fabric (pAMS) alone. However, subtracting such a large signal can pose problems. This results in a large scatter to the pAMS direction data (figure 4-8). Despite this, a subtle trend in the minimum pAMS orientation can nevertheless be distinguished, which approximately correlates to the elastic wave anisotropy principal directions. However, as the ultrasonic anisotropy is likely to be governed, or at least heavily influenced, by the aligned crack fabric it is therefore probable that the pAMS signal, although weak, is also being created by the aligned crack fabric.

7.2 PORE FABRIC ANISOTROPY AND ALIGNMENT

7.2.1 COMPARISON BETWEEN AMS AND ELASTIC VELOCITY DERIVED FABRICS

As seen in section 4.1.3, a representation of the pore fabric geometry useful for comparing results is the Flinn diagram (Flinn, 1962), which plots the length ratio of major to intermediate axes (representing linear fabric contribution) against the length ratio of the intermediate to minor axes (representing planar fabric contribution) of the calculated ellipsoid. The Flinn diagram is a commonly used tool in structural geology to visualise the relative dominance of either the linear or planar fabric contribution compared to the overall fabric shape (whether grain or pore). When considering the Bentheim and Crab Orchard sandstones, pAMS data indicates that the pore fabric is oblate (figure 4-3 and 4-5), as would reasonably be expected for sedimentary rock, especially in the light of their depositional history. However, for Takidani granite the situation is slightly more complicated. Due to the low porosity of this rock type, the void space is only approximately 1/3rd saturated with ferrofluid. This, combined with a high matrix susceptibility, results in the pAMS principal orientations showing a larger degree of variation as compared to the pAMS data obtained from the sandstones. Despite these issues, a measurable pAMS signal is obtained (figure 4-11). However, this signal does not reveal either an oblate or prolate fabric within the reported error, and is thus only able to extract principal directions (figure 4-8), rather than provide the additional fabric information which the Flinn method provides for the sandstones.

Fitting ultrasonic velocity data to an ellipsoid allows the determination of principal axes in 3-D (length and direction), in a manner essentially identical to that used for the pAMS data. The adoption of this powerful technique allows for simple and direct comparison between the principal anisotropy axes derived from pAMS with those obtained with the velocities, regardless of the initial orientation of the orthogonal core-set to the anisotropy symmetry during core preparation. In addition, this method permits the analysis of the Takidani principal axes in a manner analogous to that used to create Flinn diagrams. As stated above, determination of lineation and foliation using pAMS data for the granite produced an inconclusive result. However, the use of an ellipsoidal fit to the velocity data allows a 'velocity' pseudo-Flinn diagram to be derived in preference (for this rock type) to the AMS Flinn diagram.

Velocity pseudo-Flinn plots are shown in figures 7-1, 7-2 and 7-3 for Bentheim sandstone, Crab Orchard sandstone and Takidani granite respectively. These data show that, for P-wave measurements, both BHS and COS have an oblate fabric, which is in agreement with the pAMS fabric. S-wave measurements are less tightly clustered, but show the same general trend of an oblate fabric. For Takidani granite P-wave data, the velocity pseudo-Flinn diagram (figure 7-3) indicates a weakly prolate fabric. This fabric suggests that the rock may exhibit cylindrical transverse isotropy (CTI). Such long, thin cracks with normals aligned in a plane orthogonal to the long axis of the cracks would produce a long, thin average void space orientation in 3-D which is described as prolate in structural geology. This is consistent with the UV thin section images (figures 3-16 and 3-17) which show that the cracks are not aligned along any single direction, but show an obvious angular distribution. In addition, a CTI fabric would also be consistent with theoretical analyses showing that during brittle deformation, cracks tend to align with their normals in a plane perpendicular to the maximum principal stress (Paterson, 1978), but commonly with random orientations within this plane.

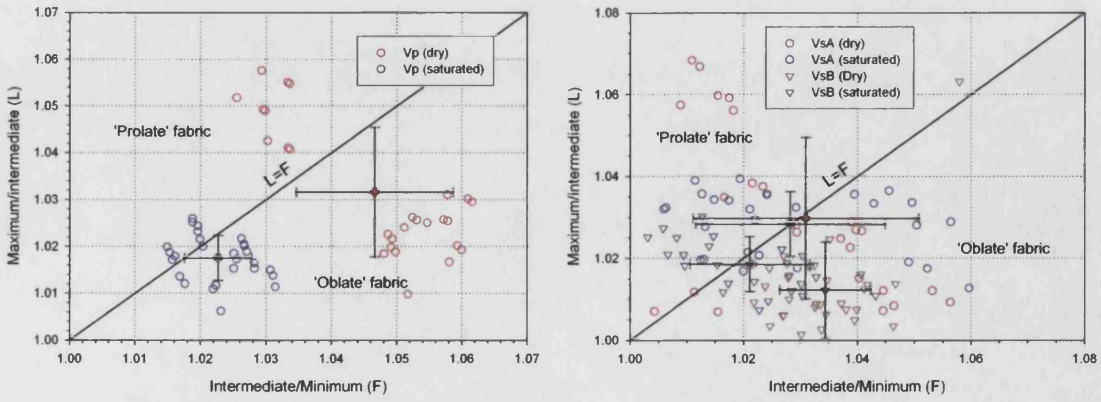

Figure 7-1. Bentheim sandstone elastic wave velocity 'pseudo Flinn' diagrams for P-wave (left) and S-wave (right), for dry and saturated samples. Vs_A and Vs_B refer to the two distinct S-wave polarisations described in Chapter 3

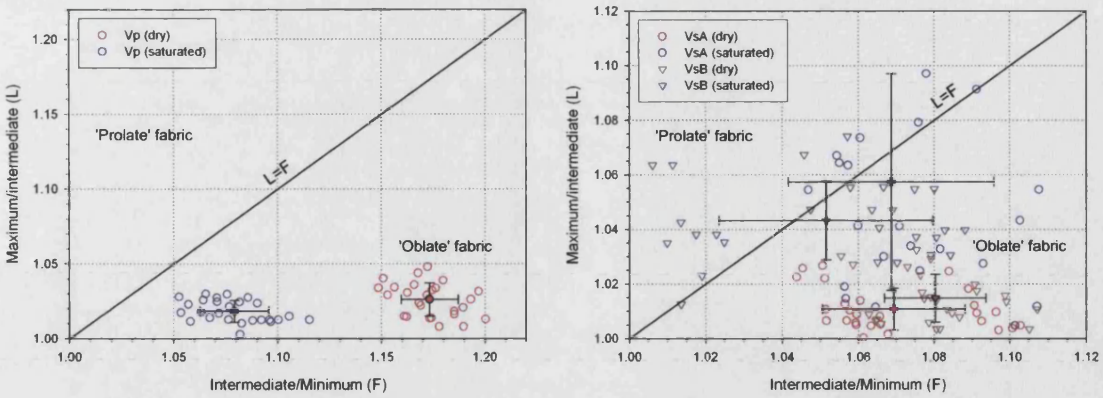

Figure 7-2. Crab Orchard sandstone elastic wave velocity 'pseudo Flinn' diagrams for P-wave (left) and S-wave (right)), for dry and saturated samples. Vs_A and Vs_B refer to the two distinct S-wave polarisations described in Chapter 3

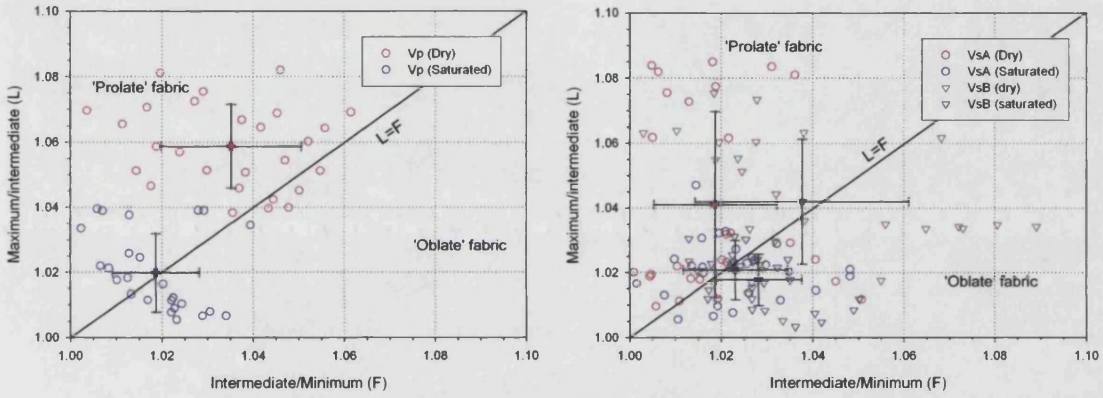

Figure 7-3. Takidani granite elastic wave velocity 'pseudo Flinn' diagrams for P-wave (left) and S-wave (right)), for dry and saturated samples. Vs_A and Vs_B refer to the two distinct S-wave polarisations described in Chapter 3

Finally, it should be noted that the velocity pseudo-Flinn plots show a much stronger and clearer fabric when using velocity data from dry rock. This is potentially important, as measurements of anisotropy made in the field are usually made upon saturated rock, as pore fluids cannot be avoided in the natural Earth environment. Therefore, the interpretation of this data must take this effect into account. This is due to the lower velocity contrast between water (pore fluid) and the rock matrix.

7.2.2 EQUIVALENT PORE GEOMETRY

Clearly, the Flinn diagrams discussed up to this point, whether derived from magnetic fabric or from the velocity fabrics, do not represent the actual **physical** pore shape geometry, as previously discussed in Chapter 2. However, for the case of AMS data, the ferrofluid filled pore space produces a magnetic susceptibility that is related to the average physical void space shape in 3-D, rather than its actual shape, via the demagnetising factor. The Equivalent Pore concept of Hrouda et

al. (2000) attempts to quantify this relationship by linking the physical shape to the AMS signal in a mathematically predictable way. Specifically, the theoretical approach (section 2.3.4) attempts to relate the measured values of lineation and foliation from pAMS to the equivalent physical pore ellipsoid which would produce those same values (Hrouda et al., 2000). If this can be done, then a direct comparison between the average physical pore space ellipsoid and the pAMS data will be possible. First, the relative dimensions of a family of magnetically susceptible ellipsoids of principal length axes $a_i>b_i>c_i$ are specified. The relative dimensions of a_i/b_i and b_i/c_i are then used to calculate the relative demagnetisation factors, and hence the susceptibility ratios $L=k_1/k_2$ and $F=k_2/k_3$ via equations 2-8, 2-9, 2-10, and 2-11. The end result is an 'equivalent pore' which produces the same lineation and foliation as the measured sample by taking into account the demagnetising factor of the average ellipsoid produced by the saturating ferrofluid.

Examples of equivalent pore fabrics are shown in figures 7-4, 7-5 and 7-6 for BHS, COS and TDG, respectively. Superimposed upon the axes is a grid with lines of constant physical ellipsoid length ratio (the families of a_i/b_i and b_i/c_i) representing the physical pore fabric, which would produce those same values of lineation and foliation shown via the axes. Experimental values of lineation and foliation for pAMS samples are plotted directly, with a red star denoting the mean. By taking the average experimental data and interpolating between the equivalent pore fabric families, we can show the average physical pore fabric of each rock type is as follows (table 7-1). Each plot (BHS, COS, TDG) is calculated separately to account for the different ferro-fluid concentration and hence the different intrinsic susceptibilities of the fluid.

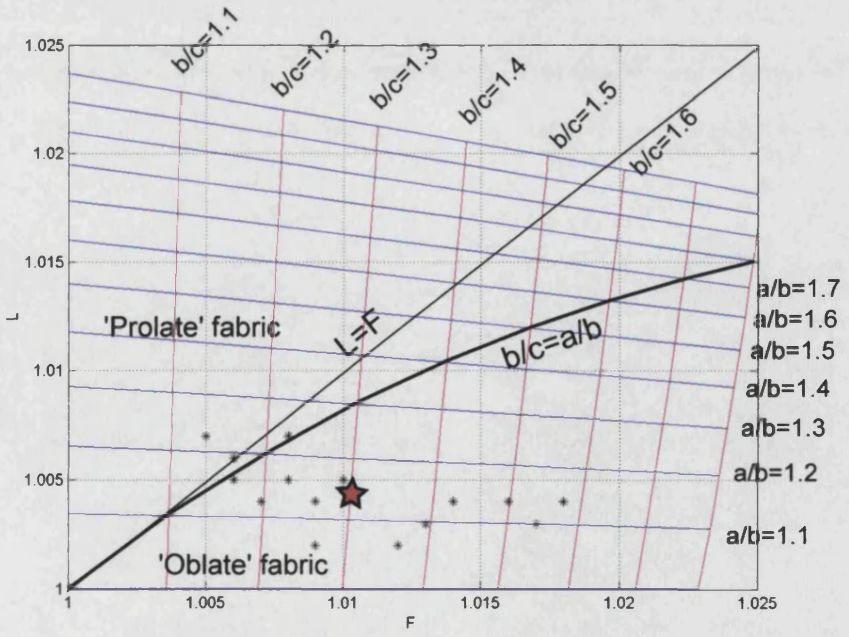

Figure 7-4. Equivalent pore treatment as applied to Bentheim sandstone, for an intrinsic susceptibility (Ki) of 0.09

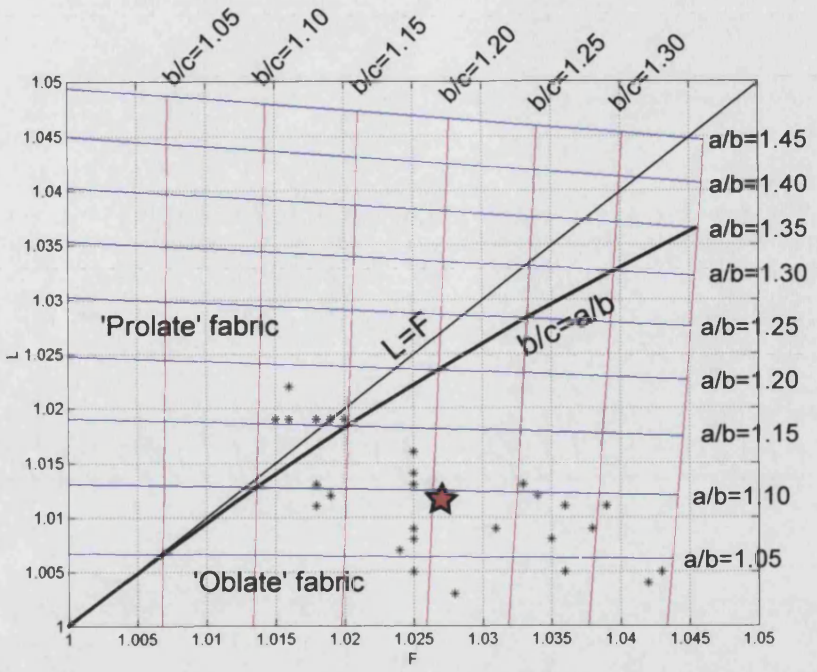

Figure 7-5. Equivalent pore treatment as applied to Crab Orchard sandstone, for an intrinsic susceptibility (Ki) of 0.38

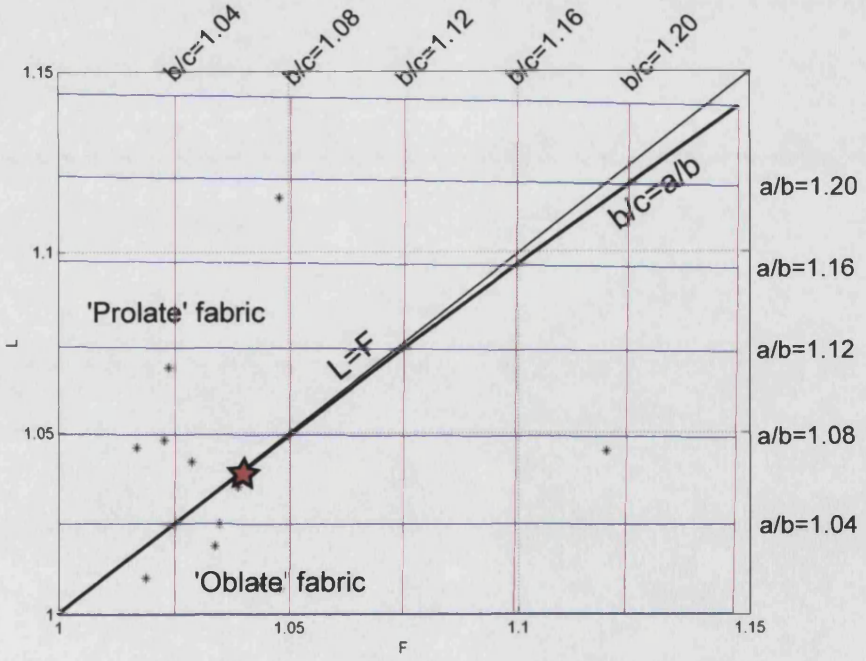

Figure 7-6. Equivalent pore treatment as applied to Takidani granite, for an intrinsic susceptibility (Ki) of 3.34

However, applying the equivalent pore method throws up some serious questions. From the plots above, summarised in table 7-1 below, we can derive a value for the pore fabric bulk anisotropy, analogous to the AMS 'P' parameter via $a/c = \frac{a}{b}\frac{b}{c}$. This gives a/c=1.48 for Bentheim sandstone, a/c=1.32 for Crab Orchard sandstone, and a/c=1.13 for Takidani granite. This compares to a pAMS anisotropy (P) values of 1.015, 1.039, and 1.081 respectively. This is not consistent, as the equivalent pore method appears to shown the void fabric becoming less highly oblate as we move from BHS to COS to TDG. Velocity anisotropy shows the same serious inconsistencies, with a P-wave velocity anisotropy (A) of 1.076, 1.18, and 1.092 (BHS, COS and TDG), and S-wave anisotropy (A) of 1.059, 1.091, and 1.078 (summarised in table 7-2).

Velocity anisotropy is known to overestimate the pore fabric anisotropy, due to the high contrast in velocity between empty void space (for example air, with P-wave velocity of ~340 m/s), and the rock matrix (for example 3000 m/s). pAMS, on the other hand, underestimates the physical void space anisotropy due to the demagnetisation factor. Therefore, the real average physical void anisotropy should lie between these two bounds. This is not the case. For example, Bentheim sandstone possesses an equivalent pore anisotropy of 1.48 (48%), which is totally at odds with the evidence presented thus far from image analysis, pAMS data, and the elastic anisotropy.

Equivalent pore fabric comparison	Bentheim sandstone		Crab Orchard sandstone		Takidani granite	
	L	F	L	F	L	F
pAMS	1.004±0.002	1.010±0.004	1.012±0.005	1.027±0.009	1.039±0.031	1.0409±0.027
	a/b	b/c	a/b	b/c	a/b	b/c
Equivalent pore	1.14	1.30	1.095	1.205	1.065	1.065

Table 7-1. Flinn plot data for pAMS and equivalent pore geometry. L denotes lineation and F denotes foliation, as derived from AMS. The equivalent pore has axes a>b>c, the relative length of which will create the observed L and F.

Equivalent pore fabric comparison	Bentheim sandstone	Crab Orchard sandstone	Takidani granite
pAMS	1.015	1.038	1.077
P-wave velocity	1.076	1.180	1.092
S-wave velocity	1.059	1.091	1.078
Equivalent pore	1.480	1.320	1.130

Table 7-2. Summary of bulk anisotropy as obtained from pAMS, velocity, and the equivalent pore geometry. pAMS anisotropy for Takidani is a known issue, but the equivalent pore geometry figures are inconsistent with both pAMS and velocity anisotropy for unknown reasons

In summary, elastic velocity information seems consistent with the pAMS anisotropy information. However, both the elastic velocity and pAMS data are not consistent with the a/c values derived using the equivalent pore approach, with these a/c values appearing to be reversed with what might be intuitively expected. At this point it appears that the equivalent pore method over-estimates the anisotropy due to void space, especially for equant porosity.

To investigate where the problem may arise, the demagnetisation factors based on input ratios of a/b and b/c were calculated. This gives the demagnetising factors, N_a, N_b, and N_c, summarised in table 7-3, which agree exactly with Stoner (1945) to 4 decimal places and are therefore unlikely to be a source of error. Following this, a closer look at the relation between measured ferrofluid susceptibility and intrinsic ferrofluid susceptibility was made. This calculation uses the relation $K_m = K_i / (1+[K_i/3])$, as given by Hrouda et al. (2000) and Uyeda et al. (1963). Figure 7-7 shows the relationship between measured and intrinsic susceptibility. This relationship appears to be highly non-linear. Since three different ferro-fluid strengths were used for the three different rock types to avoid measurement problems, then this is likely to be the source of the problem.

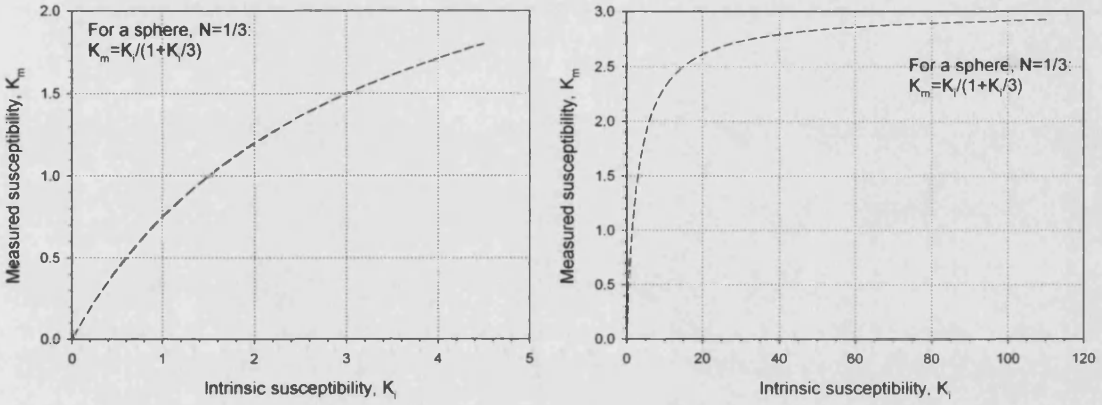

Figure 7-7. Relationship between measured susceptibility (Km) and the intrinsic susceptibility (Ki) of a sphere for Ki up to 5 (left). Extending the calculation for Ki up to 110 (right), shows that the relationship converges rapidly to Km~3 for very high values of Ki

By using this intrinsic vs. measured ferrofluid susceptibility data, I can demonstrate, as an example, the effect that the ferrofluid strength has upon the measured values of lineation (figure 7-8) via the relation $L=(1+K_iN_b)/(1+K_iN_a)$, where K_i is related to K_m via the relation stated above. Three different pore fabrics (a/b and b/c, shown on the figure) are used to calculate the lineation factor for a range of intrinsic susceptibility from 0 to 5. Lineation appears to be strongly related to the intrinsic ferrofluid susceptibility, and hence the measured ferrofluid susceptibility. Therefore, the method produces a non-linear and changing equivalent pore geometry depending on the fluid strength used. For this reason, and through comparison with the data presented in this thesis, the Hrouda et al. (2000) model cannot be considered robust and would require significant amendment before it could be applied with confidence to the data presented in this study.

Ferro-fluid filled pore principal axes (a>b>c): aspect ratio.	Demagnetising factors		
	Na	Nb	Nc
a/b=1.1; b/c=1.1	0.2958	0.3323	0.3719
a/b=1.2; b/c=1.2	0.2630	0.3296	0.4075
a/b=1.3; b/c=1.3	0.2343	0.3256	0.4401

Table 7-3. Equivalent pore geometry demagnetising factors: example

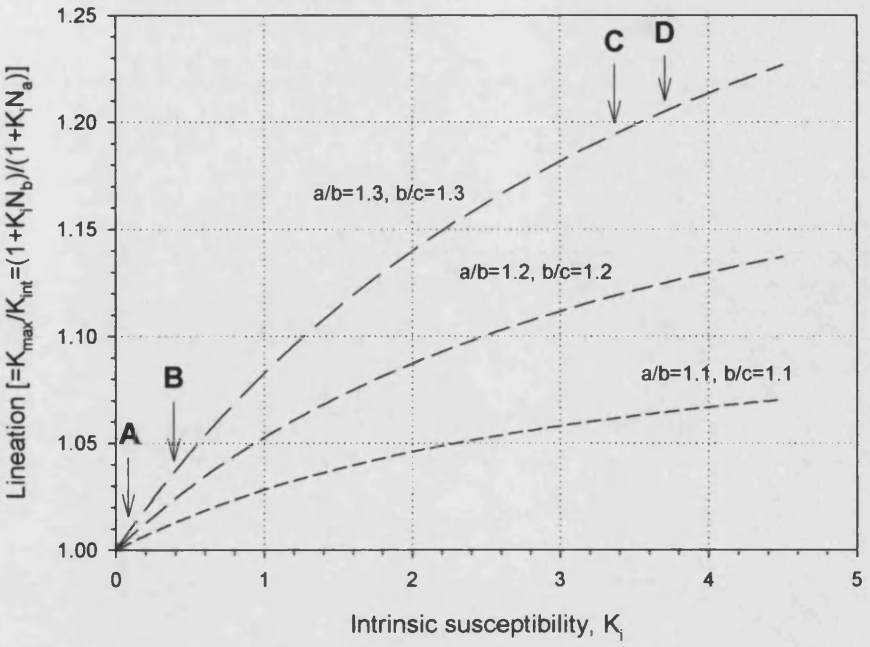

Figure 7-8. Relationship between Lineation (L) and intrinsic susceptibility (Ki) for three different pore geometries (a>b>c). A strong dependence of L upon Ki is noted in all cases. Marker A denotes ferrofluid strength as used for BHS, marker B for COS, marker C for TDG (undiluted), and D is the ferrofluid strength used by Hrouda et al. (2000). See text for additional detail

7.3 TRANSPORT PROPERTIES: COMPARISONS WITH PRINCIPAL AMS AND ELASTIC VELOCITY DIRECTIONS

For Bentheim and Crab Orchard sandstones, principal pAMS orientations show a high degree of correlation with the principal velocity anisotropy directions, supporting the deduction that the internal pore fabric is the dominant factor controlling the elastic anisotropy. However, as the pAMS method measures the average connected void space, it is likely to be a more accurate predictor of fluid flow anisotropy (Benson et al., 2003; Pfleiderer and Halls, 1990, 1994), as compared to the velocity anisotropy. This is because pAMS measures only the connected average void space alignment and geometry in space, which is crucial to the movement of fluids. In contrast, velocity anisotropy is sensitive to factors other than simply the pore space crossed by the propagating wave (or 'linear porosity'), as the elasticity of materials is dependent upon matrix properties such as crystallographic alignments and lattice preferred orientations to which pAMS is not sensitive.

The general correlation between pAMS and permeability anisotropy has been experimentally verified in this study, where a strong correlation is seen between the pAMS minimum principal direction and the direction of lowest permeability. In the case of the Bentheim sandstone, however, this permeability dependency upon flow direction is very weak (figure 5-19), which is consistent with a rock with such a porous, open structure. For Crab Orchard sandstone, the maximum pAMS

principal direction is approximately aligned to the maximum permeability direction (figure 5-21), and that the intermediate pAMS direction is approximately aligned with the 'Y' axis, although strictly, the permeability in the COS 'X' and 'Y' directions are within experimental error, with these directions corresponding to fluid flow within the bedding (XY) plane.

The mean initial permeability of Bentheim sandstone under a hydrostatic pressure of 5 MPa is 0.86×10^{-12} m^2; and this value remains essentially the same both with increasing effective pressure and with measurement orientation. This is in spite of the fact that both wave velocity and pAMS measurements indicate a low, but significant, anisotropy. This suggests that the pore space anisotropy is not sufficiently high compared with the porosity to influence fluid flow, and that the pore connectivity is not greatly altered by elevated pressure. The SEM micrographs in figure 3-5 and 3-6 support this interpretation, since we observe a highly connected set of relatively equant pores with little evidence of any microcracks or cement. The thin section images do show a small number of intergranular microcracks, and it is likely that the closure of these cracks is directly responsible for the small changes in permeability, and its anisotropy, that are seen in the first 30 MPa of increasing effective pressure (figure 5-18). The equant pore structure of BHS and its lack of permeability anisotropy is also consistent with the results of Jones and Meredith (1998), who reported no significant change in permeability with increasing effective pressure for a tuff with predominantly equant porosity. It is also consistent with theoretical approaches (Guéguen and Palciauskas, 1994; Mavko et al., 1998), which often quote the pressure range 30-40 MPa as the pressure over which most 'cracks' are closed in sandstones.

The observations for BHS are in stark contrast with those for Crab Orchard sandstone, where permeability changes markedly, both as a function of pressure and measurement direction. Overall, the permeability of COS is far lower than for BHS (by a factor of $\sim 10^4$). The initial permeability parallel to crossbedding (figure 5-21, X and Y directions) is $\sim 120 \times 10^{-18}$ m^2, more than twice that normal to crossbedding, $\sim 50 \times 10^{-18}$ m^2. This is far higher than either COS pAMS or velocity anisotropy. Also, while the permeability decreases by more than an order of magnitude as effective pressure is increased from 5 to 90 MPa, the permeability anisotropy remains approximately constant throughout, suggesting that the mechanism responsible for the reduction in permeability is acting to reduce fluid flow magnitude by the same relative amount independently of measurement direction. In general, permeability and its anisotropy are highly dependent on effective pressure and the shape of individual voids (Bernabe et al., 2003), and the data presented here is in general agreement with previously reported results for a rock microstructure comprising a mixture of microcracks and open pores. However, these results are in marked contrast to permeability data for rocks with a predominantly planar fabric, e.g. shales. For such materials, the increasing effective pressure reduces the fluid flow parallel to the fabric much more than that normal to it, thus reducing the anisotropy to approximately zero (Jones and Meredith, 1998). Evidence from SEM micrographs and thin sections (figures 3-7 and 3-8) supports my conclusion of COS containing both 'pores' and 'cracks' as both are seen in the images, entirely consistent with the experimental observations.

Takidani granite shows a marked decrease in permeability as the effective pressure is increased, and, as for COS, this occurs both as a function of pressure and measurement direction (figure 5-24). At 5 MPa, the initial permeability parallel to the microcracking (as seen in the image analysis in figure 3-9 and 3-10), is in the range 20 to 30 x 10^{-18} m^2; whereas normal to this plane it is about 10 x 10^{-18} m^2 (figure 5-28). This time, though, comparison with pAMS is inconclusive, for the reasons already discussed. However, comparison to the elastic velocity can be made, especially as we have already observed that a close relationship exists between the pore fabric and the elastic wave anisotropy. This reveals that the direction of velocity minimum approximately coincides with the direction of lowest measured permeability. In a similar manner to Crab Orchard sandstone, we observe that while the permeability decreases by more than an order of magnitude as effective pressure is increased from 5 to 90 MPa, the permeability anisotropy remains approximately constant over this pressure range. The reduction in porosity over this interval, which shows an almost identical trend to the permeability reduction, suggests that the closure of crack related porosity is the dominant mechanism for permeability reduction. This is consistent with SEM micrographs and thin sections (figures 3-9 and 3-10) illustrating the predominantly 'cracked' fabric.

7.3.1 THE RELATIONSHIP BETWEEN POROSITY AND PERMEABILITY

In this study, results from hydrostatic pressure tests on Bentheim sandstone show very little variation in permeability with pressure or with porosity with pressure (figure 7-9). To further investigate the void space in terms of porosity distributions and pore throat connectivity, a number of mercury porosimetry tests were conducted. Figure 7-10 shows data from an example mercury injection experiment. Figure 7-10[A] displays a 'classic' single mode cumulative porosity increase with injection pressure. This data suggests that this rock type is likely to exhibit a pore connectivity which is intergranular, and this suggestion is confirmed by images from thin section analysis and SEM. Using equation 2-2 (section 2.1.2), the pore throat distribution can be calculated as a function of the change in injected mercury volume (figure 7-10[D]). The pore throat radius population peaks at a pore radius of 16.7 microns, entirely consistent with image analysis, and consistent with the high permeability of this rock. In addition, the peak itself is well described, with a sharp full-width half-maximum (FWHM) value of ~7 microns.

As BHS possesses a relatively equant pore fabric, it is entirely plausible that this fabric gives the rock a resistance to the application of mechanical stress. As hydrostatic stress is applied, intergranular cracks between grains begin to close. This is seen as a small reduction in porosity (figure 7-9). However, the hydrostatic stress in insufficient to influence the larger pores and pore throats connecting the majority of porosity. Hence, this results in essentially no permeability change as effective pressure is increased, as the closing intergranular cracks have little influence upon the pore space connectivity (permeability) as compared to the primary conduits formed via the pore throats themselves.

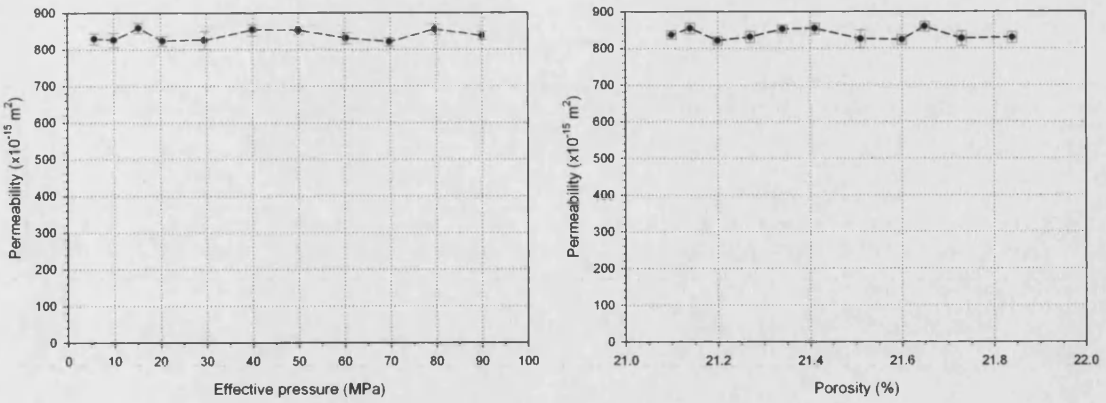

Figure 7-9. Bentheim sandstone permeability variation with pressure (left) and porosity (right)

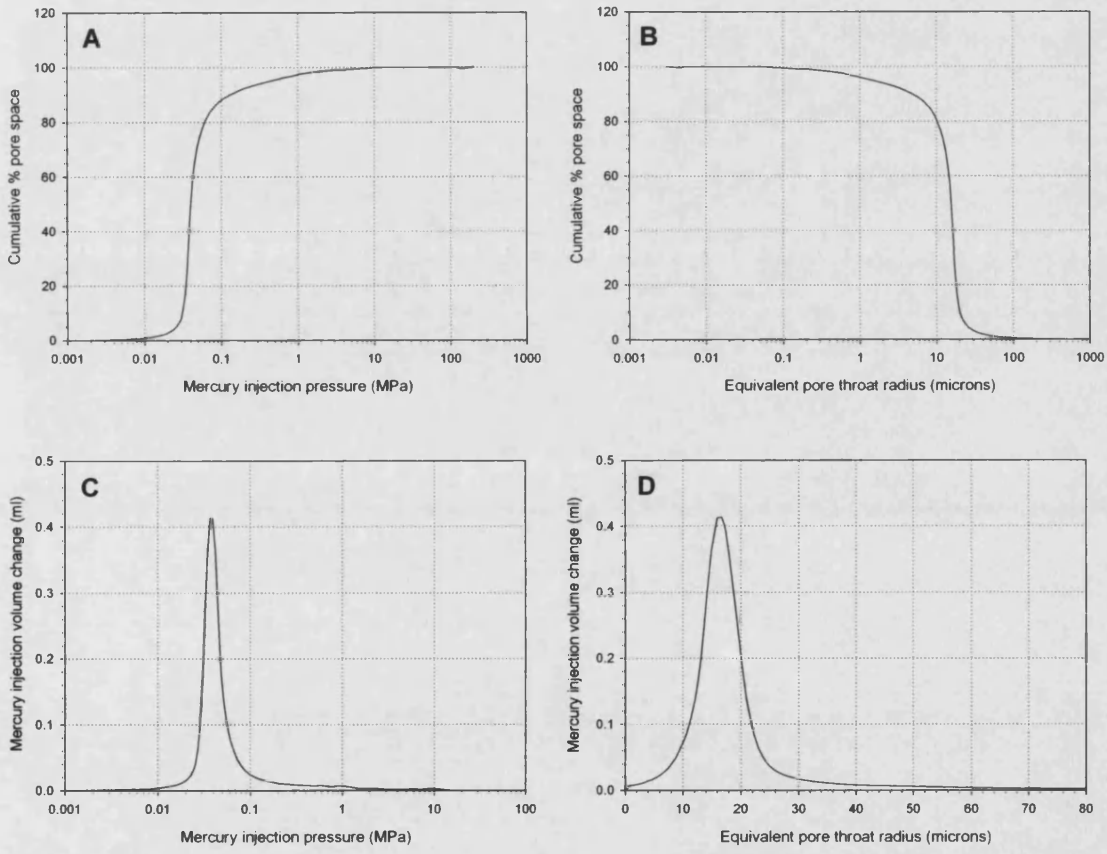

Figure 7-10. Bentheim sandstone mercury injection porosimetry results. A – Mercury injection phase, B – Equivalent pore throat radius variation with cumulative porosity, C – Mercury intrusion volume change / Pressure relationship, D – Pore throat diameter distribution derived from those pressures

For Crab Orchard sandstone, figure 7-11 illustrates how $\log_{10}$(permeability) changes with pressure, plotted as a function of both effective pressure and porosity. A clear break of slope is observed at an effective pressure of 20MPa, occurring at a porosity of approximately 4.64%.

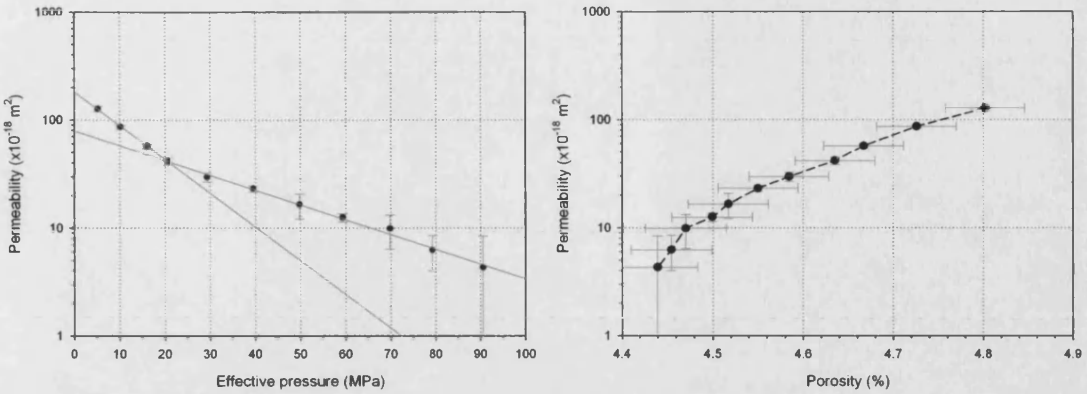

Figure 7-11. Crab Orchard sandstone permeability variation with pressure (left) and porosity (right)

This permeability vs. pressure information is supported by mercury injection porosity data (figure 7-12[A]), which shows a clear break of slope at injection pressures of ~2 MPa and (tenuously) at 20 MPa. When this is analysed as mercury injection volume change (figure 7-12[C] and figure 7-12[D]), a distinct peak at 2 MPa is seen, equivalent to a pore throat radius of 0.16 microns. The second break of slope at ~20 MPa can be seen as a 'shoulder' (arrowed), equivalent to a pore throat radius of ~0.04 microns. However, it should be stated that the invasion (capillary) pressure used during mercury porosimetry is not the same as the confining pressure used and quoted during permeability measurement under hydrostatic stress. Despite this limitation, a direct comparison between the two measures still provides additional insight into the changing pore fabric with pressure.

The 'shoulder' occurs exactly at the pressure at which the experimental permeability data shows a break of slope (figure 7-11). It is therefore likely that the pressure of ~20 MPa separates two populations of total porosity in COS which possess different values of connectivity, and therefore permeability. Below this threshold pressure, permeability is controlled by the larger 'quasi-equant' pore space of ~0.16 microns, resulting in relatively high values of permeability. Above this threshold pressure, the pore space is predominantly controlled by the smaller 'crack' like pore space of ~0.04 microns. This is consistent with previous work (e.g. Dullien, 1979; Bear, 1988; Guéguen and Palciauskas, 1994).

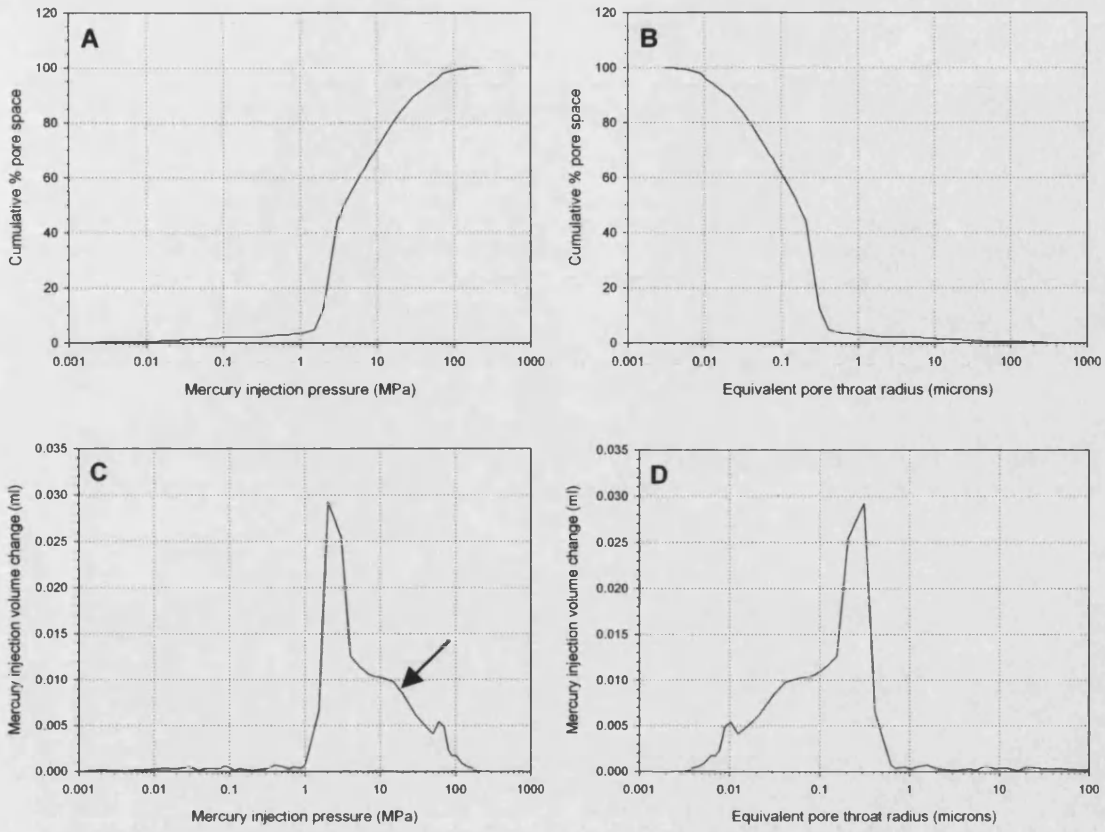

Figure 7-12. Crab Orchard sandstone mercury injection porosimetry results. A – Mercury injection phase, B – Equivalent pore throat radius variation with cumulative porosity, C – Mercury intrusion volume change / Pressure relationship, D – Pore throat diameter distribution derived from those pressures

Finally, permeability vs. effective pressure data for Takidani granite also shows a break of slope, at an effective pressure of ~20 MPa (figure 7-13). This corresponds to a porosity of approximately 0.86%. Unlike the Crab Orchard sandstone, however, the image analysis shows a pore space consisting exclusively of microcracks.

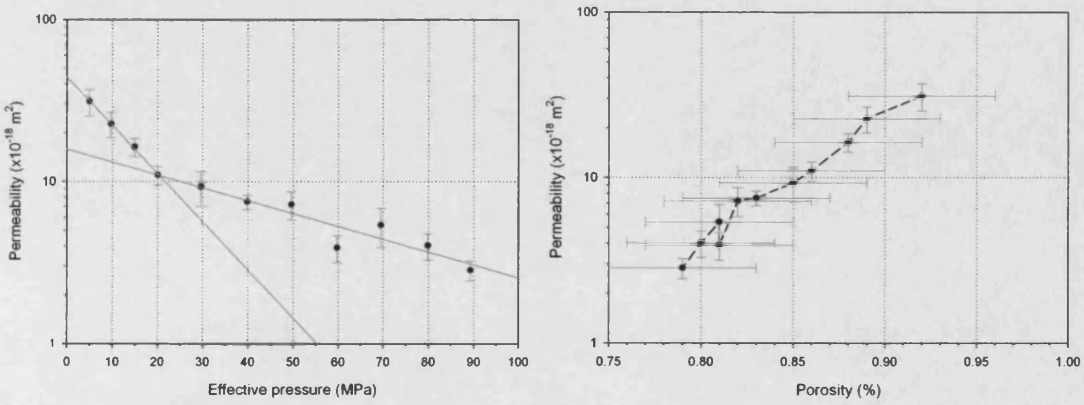

Figure 7-13. Takidani granite permeability variation with pressure (left) and porosity (right)

Using mercury injection porosimetry, some similar observations can be made as for COS. For Takidani granite, however, it has already been established that the porosity is predominantly crack-like, and therefore the pore throat radii derived from mercury porosimetry actually corresponds to average crack apertures. Porosimetry data (figure 7-14[A] and 7-14[B]), shows that mercury injection first commences at pressures of ~3 MPa (~0.2 microns), and is complete at ~60 MPa (~0.015 microns). No change in porosity is seen above a pressure of ~60MPa. This compares favourably with measurements of elastic anisotropy with pressure (figure 5-16), which shows that the elastic anisotropy has reduced to 0% at approximately 60 MPa, suggesting that the reduction in acoustic anisotropy is due to the reduction in crack aperture.

The porosimetry data also provides a useful insight into the mean crack aperture within the sample. Plots of injection volume change (Figures 7-14[C] and 7-14[D]) show an obvious peak at approximately 25 MPa (0.03 microns). This is close to the pressure where the break of slope is seen in the permeabilty vs. pressure data (figure 7-13). In addition, this aperture width is very similar to the mean diameter of the magnetite particles in the ferrofluid (0.01 microns). Therefore, the fact that difficulty in achieving ferrofluid saturation was encountered for this rock type is entirely consistent with this information.

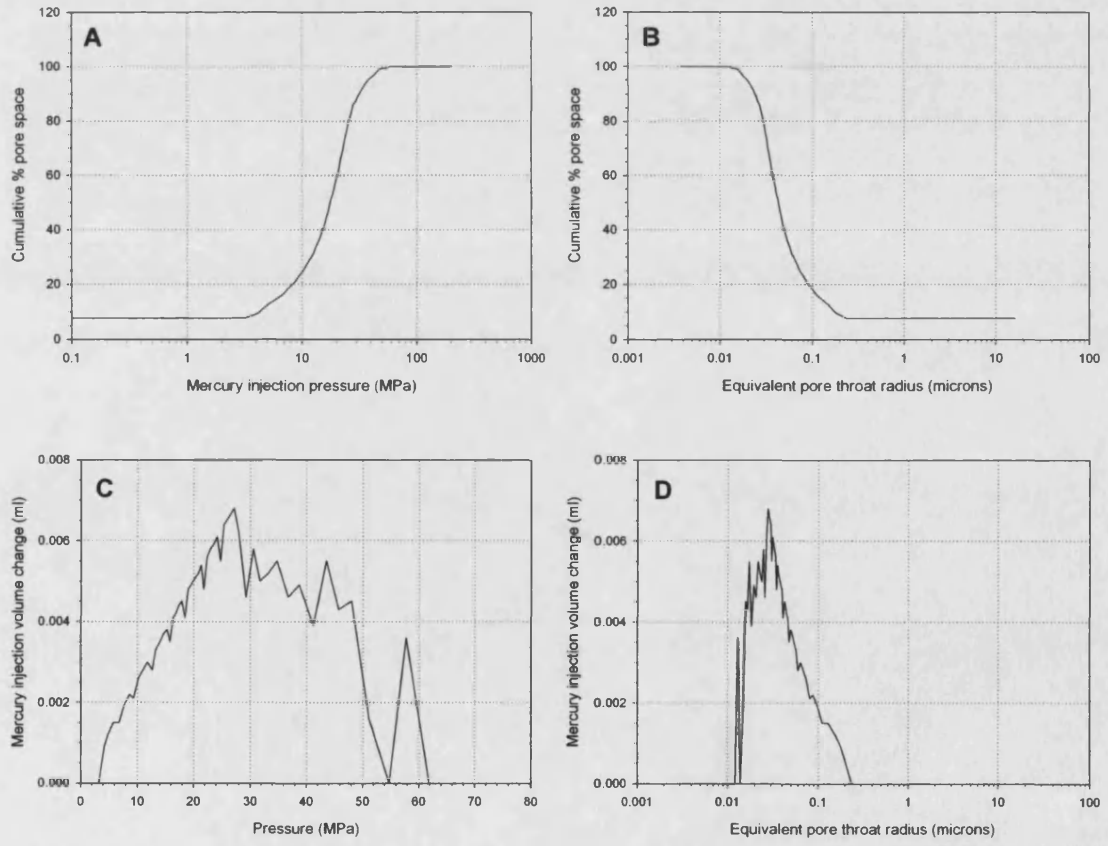

Figure 7-14. Takidani granite mercury injection porosimetry results. A – Mercury injection phase, B – Equivalent pore throat radius variation with cumulative porosity, C – Mercury intrusion volume change / Pressure relationship, D – Pore throat diameter distribution derived from those pressures

7.4 MODELLING: INSIGHTS, ISSUES AND COMPARISIONS

7.4.1 THOMSEN AND EBERHART-PHILLIPS MODELS

As expected, the Thomsen model fits the experimental data very well. The model can be used to estimate the mean P-wave and S-wave velocities α and β, and also the anisotropy parameters ε and γ, representing P-wave anisotropy and S-wave anisotropy respectively. Results are summarised in tables 6-3 and 6-4, and are in close agreement with the experimental data seen earlier in table 6-2. For BHS and COS in particular, the fact that a good match is seen to the data is further evidence that these rocks exhibit planar transverse isotropy. For Takidani granite, the situation is more complex as the plane of symmetry is not aligned exactly with the XY plane, as seen from the elastic anisotropy determination of principal directions (figure 4-22). As a result, the predicted anisotropy parameters from the Thomsen model are slightly lower than those determined using the ellipsoidal velocity model. This is because the Thomsen fit is applied to the 2-D azimuthal anisotropy data only, whereas the EVM model is applied to a 3-D velocity dataset which is able to extract the principal length and orientation in 3-D, and hence the maximum anisotropy. In addition it is likely that TDG is exhibiting cylindrical transverse isotropy (CTI). Therefore, the fact that the transversely isotropic Thomsen model fit to these data is poor provides further support for the conclusion that, in reality, Takidani granite possesses a more complex form of anisotropy than reported previously (Kano et al., 2002).

The Eberhart-Phillip relation is an empirical method which models the P-wave and S-wave velocity variation with pressure. In this study, the general method is further simplified (see section 6.1.1.2), and applied to each rock type and in each of the three principal directions with a simple least squares fit (figures 6-7, 6-8, and 6-9). The modelled trends fit the observed data extremely well. The real strength of the method lies in its ability to predict the velocities where such measurements are difficult or impossible, thus potentially extending the limits of the investigation to deeper crustal environments, for example. This could be done by extrapolating the Eberhart-Phillips data to higher pressures than measured in the laboratory. However, such extrapolations require considerable caution in their application and are not attempted in this work.

7.4.2 INCLUSION MODELS

Ultimately, the Self-Consistent inclusion model was not used to model experimental data due to the shortcomings of the method, such as the scheme counting the effect of the inclusions twice. This problem is well published in the literature (Zimmerman, 1991). Both the Kuster-Toksoz (KT) and Differential Effective Medium (DEM) models were used successfully to model P-wave and S-wave data as a function of effective pressure, and for all three rocks used in this study. As is well known, the method used – of calculating the crack density from a normalised velocity (V_p or V_s), which is then used to calculate the other elastic velocity (V_s or V_p) – can be said to rely in part upon a circular argument. However, this is not necessarily a problem, as the robustness of the model

in predicting crack density should be the same whether the P-wave or S-wave data is used as input. Therefore, the measured P-wave and S-wave data should yield the same crack density, unless some factor other than the crack density is acting to change the velocity. So, the use of this model is essentially a measure of the degree to which cracks alone are responsible for the change in velocity observed experimentally; a good fit between P-wave and S-wave data indicating that cracks dominate.

For Bentheim sandstone this case is met, with S-wave velocity data predicted from the P-wave crack density agreeing extremely well with the measured values (figure 6-11). The P-wave velocity data as predicted from the S-wave crack density is likewise an excellent fit. This provides support for the velocity variation for BHS being provided by intergranular cracks which close quickly up to pressures of 30 to 40 MPa, with any velocity variations after this point most likely occurring as a result of elastic changes. In contrast, model data from Crab Orchard sandstone do not fit so well between S-wave and P-wave data (figure 6-12). In this case, the predicted crack density calculated from S-wave data is higher than that calculated from P-wave data. Therefore the resulting prediction of P-wave velocity from S-wave crack density (and vice-versa) is not as good than for BHS. For the case of COS, the high degree of anisotropy is likely to play a role in the poor fit between the model data and the measured velocity as both the DEM and KT schemes inherently assume an isotropic medium and are therefore less appropriate for this material.

For Takidani granite, although the fit between modelled and measured velocities is better than for COS, it is still not as good as for BHS. However, this may be due to the limitations of the model itself. Initially, both the DEM and KT models rely on a dilute population of non-interacting cracks within the host medium for the starting calculation. Whilst this may be true for the Bentheim case of small intergranular cracks, it is almost certainly not true for Takidani granite, where larger cracks spanning multiple grain dimensions are clearly seen in thin section and scanning electron micrograph images. Crucially, these crack sets can also be seen to intersect. The interaction between intersecting cracks will act to further reduce the elastic velocity, which is not accounted for in the inclusion models.

7.4.3 CRACK MODELS

The Kachanov and Hudson crack models are fundamentally very similar, as both use low aspect ratio 'cracks' to compute the resultant scattered wave field in terms of either the stiffness correction matrix (Hudson) or the crack compliance tensor (Kachanov), where a constant stress and strain at infinite distance is assumed. In this study, Hudson's model has been applied to the elastic anisotropy data obtained as a function of azimuth, and Kachanov's model has been used to investigate the data obtained at elevated pressures, including crack density variation with pressure and mean crack aperture (which will be discussed in section 7.4.4). Both models are used in their respective transverse isotropy cases, as this appears to be the most appropriate scheme for the

sedimentary rocks. The aligned cracks seen in the image analysis and interpreted from elastic wave principal velocity directions would suggest that this is also a good approximation for Takidani granite.

For planar transverse isotropy (PTI) applied to the Hudson model, Mavko et al. (1998) give expressions for crack density relative to the normal of a set of aligned cracks. However, perfect alignment of the crack set is unrealistic, and in this work a crack distribution obeying a Fisher distribution is therefore used. This allows crack density and hence elastic wave velocity to be evaluated as a function of azimuth relative to this crack set distribution. In theory, the highest anisotropy will be derived from a 'zero angle' distribution (i.e. perfect alignment), with wider angular distributions yielding lower anisotropy. By fitting Hudson's model to the experimental data using a simple heuristic method, an indication of the angular distribution of the cracks within the rock frame can be obtained, and this is summarised in table 6-5. This exercise shows that all three rock types in this study require a similar angular distribution in order for the modelled anisotropy to fit that observed in the laboratory. COS requires the smallest angular spread at 26°, while TDG requires 27.5° and BHS requires 28.5°. Intuitively, it might be expected for the rock with the strongest anisotropy to exhibit the smallest angular crack distribution, as this would then give rise to a high crack related anisotropy. As this is not seen, then it is likely that for the rock types which do not possess a high proportion of crack related pores (i.e. the sandstones), that the effect of other rock constituents has a profound effect upon their anisotropy, such as cementation and depositional layering.

For the Kachanov model, the modelled data agrees very well with the experimentally measured data, with the exception of the dry rock model data, which predicts a higher S-wave velocity than that measured by 150 m/s, or approximately 4.5%. For saturated rock, the model is a closer fit. However, no dependency on measurement direction is predicted, in contrast with the experimental data. For the P-wave model, the directional model fit can be used to predict the elastic anisotropy variation with pressure (figure 6-30), which agrees closely with the experimentally measured.

7.4.4 PERMEABILITY MODELS

The three models used in this study were chosen specifically so that the input parameters and assumptions of each were matched as closely as possible to the observed physical characteristics of the three rock types used. Firstly, for high porosity rock the Lattice Boltzman (LB) simulation is appropriate, as the simulated fluid flow relies upon movement and in particular the collisions between the imaginary model particles and the matrix wall to compute the flow (Ladd, 1994). For high porosity Bentheim sandstone, this is therefore a suitable model (Ayako Kameda, Stanford University, per. comm., 2003). A possible drawback with this approach, as used here, is that it depends on data measured on a thin section prepared at room pressure, and the calculated

permeability will therefore reflect the '0 MPa' case. Fortunately this is not a problem, as it has been established (Benson et al., 2004) that the permeability of Bentheim sandstone essentially does not change with pressure up to 90 MPa. The Lattice Boltzmann simulation predicts a permeability of 0.89×10^{-12} m^2, which matches exceptionally well with the measured range of 0.7×10^{-12} to 0.9×10^{-12} m^2 (figure 6-32).

Secondly, the classic approach of Kozeny-Carman has been applied to the low porosity Crab Orchard sandstone. As introduced in section 6.4.1.1, the model uses a simple connected network of tubes and pipes modelled as an single equivalent channel (pore), together with percolation theory (Guéguen and Palciauskas, 1994) to express the permeability as a function of porosity and grain size. In this study, this is modified (Mavko and Nur, 1997) to take into account the non-zero 'threshold' porosity below which no flow is possible. Due to the internal fabric of Crab Orchard sandstone consisting of a mixture of cracks and pores with an abundant cement, it is likely that the internal pore fabric resembles such a tube-like structure as modelled by Kozeny-Carman. For all three measurement directions (X, Y and Z), the calculated permeability values (130×10^{-15} m^2, 120×10^{-15} m^2, and 50×10^{-15} m^2 respectively) fit the trend seen in the experimental data within experimental variability (figures 6-33, 6-34, 6-35). It should be noted, however, that these fits are specific to both the rock type and also to the sample measured, i.e. this is a heuristic approach.

When predicting the permeability-porosity variation, the Kozeny-Carman method uses the concept of tortuosity, defined as the ratio of total flow path length to sample length. For COS, Kozeny-Carman model data in the X direction requires a tortuosity of 9. This direction is co-incident with the crossbedding strike at sample scale. The Y tortuosity is much higher (16.5), and this direction is co-incident with the crossbedding dip direction. Finally, the Z tortuosity is 17.5, which is the direction normal to the crossbedding. This is logical, as fluid flow in the Y and Z direction will have to pass through the crossbedding whilst the fluid movement in the X direction will not, resulting in a far less tortuous fluid flow path. In addition, flow in the Z direction will have to traverse more crossbedding planes than the Y direction, resulting in a still higher tortuosity.

Finally, the permeability model used for Takidani granite is that of the statistical method of Guéguen and Dienes (1989). This makes use of the crack density data as a function of effective pressure, as derived from the Kachanov model. This allows the permeability to be calculated as a function of effective pressure (crack density), for any desired crack aperture. In figure 6-36, the two chosen crack apertures (0.6 microns and 0.25 microns) represent the upper and lower bounds to the experimentally obtained permeability data. Analysis of SEM images quantitatively confirms that these crack apertures are realistic, despite lack of any equivalent information from mercury injection porosimetry, which shows a peak intrusion diameter at only 0.03 microns equivalent capillary pressure. However, as already discussed, this data relates to the pore neck size, rather than the crack itself, and this apparent discrepancy is therefore mitigated through the image analysis. The trend calculated from the model fits well to the trend seen in the experimental data, which is significant as

the crack density was computed from the velocity change; and this is now being related to the fluid flow properties of the rock. This suggests that the crack fabric within Takidani granite is acting as the main conduit for fluid transport.

7.5 PORE FABRIC CHANGES DUE TO INCREASING HYDROSTATIC PRESURE

7.5.1 RELATIVE RESPONSES OF POROSITY, VELOCITY AND PERMEABILITY

During each hydrostatic pressure experiment, simultaneous changes in P-wave and S-wave velocities and porosity were monitored as a function of effective pressure. For each rock type, it is interesting to note the *relative* changes which this change in pressure has upon the measured physical quantities in each case, as this may provide further insights into how the changing pore fabric alters these parameters. For instance, Bentheim sandstone has a high initial porosity of 22.9% which decreases to 21.6% at 90MPa effective pressure (figure 5-19). This equates to a fall of only 3.5% in relative terms. However, this decrease in porosity is associated with a contemporaneous increase in elastic velocities of 10% and 8% (P-wave and S-wave respectively), and with no change in permeability. Taken together, these data suggest a microstructure comprising a clean, well sorted matrix with a well-connected network of relatively equant pores and a low density of microcracks. Due to the relative changes, it is also clear that even the small changes in intergranular crack closure has a significant effect upon the elastic wave velocity, but no effect upon the transport properties.

In contrast, for Crab Orchard sandstone the changes in relative terms are greater. A porosity decrease of 11% (4.8% to 4.3%) over the pressure range 5 to 90 MPa results in increases in elastic wave velocities of between 17% and 19% (P-wave and S-wave respectively). Compared to the BHS case, the porosity change is higher even though the initial porosity is lower. At the same time, permeability decreases markedly, falling by an order of magnitude both normal and parallel to the crossbedding direction. These observations further support the implication that the rock fabric contains a cracked element. However, this proportion is likely to be higher than for BHS due to the greater decrease in the elastic wave velocity. In addition, the reduction in porosity (which has a mean bulk value of only 4.5%) means that the pressure increase has a large effect on the permeability, as the closing cracks would result in the remaining pore space being significantly less well connected.

Finally, Takidani granite provides another example. In this rock, the porosity falls by 16% from an initial, low value of 0.92% to 0.79% at 90 MPa. The resulting increase in P-wave and S-wave velocities of 7% and 6% respectively are likely to be purely due to the closure of cracks, and these changes are similar to the BHS velocity changes noted earlier. Unlike BHS, however, the permeability decrease is very high, by nearly an order of magnitude, as a direct result of the connectivity reduction through the crack network that controls fluid flow.

7.5.2 COMPARISONS TO AN EXAMPLE ISOTROPIC ROCK

So far, a planar transversely isotropic (PTI) scenario has been used in describing the experimental and modelled data, and, as discussed, provides a good match for Bentheim and Crab Orchard sandstone. Takidani granite, although appearing to be transversely isotropic in the first instance, is more likely to be showing cylindrical transverse isotropy (CTI), which would act to further reduce the anisotropy as compared to perfect PTI symmetry. Using the crack density as calculated from the models, with an angular crack distribution in Hudson's model needed to provide a fit to the experimental data and evidence from the image analysis, it is clear that crack alignment is not planar. Together with knowledge regarding the stress environment on the placement of this pluton, it is likely that a cylindrical transverse isotropy (CTI) is applicable in this rock.

At this point, it is useful to compare these results for anisotropic rocks with a simple example case of an isotropic rock. In the example shown in figure 7-15 below, P-wave data as a function of azimuth is presented for two basalts. Seljadur basalt (SB) is a columnar basalt from Iceland, which possesses a very low porosity of <1%, and an ultra-low permeability of 21 x 10^{-21} m^2 (Clint et al., 2001). Etnean basalt (EB) is a lava flow basalt from Etna, Italy, and has a low, but significant, porosity of approximately 2% (Vinciguerra et al., 2004). Both rocks show no discernable elastic wave anisotropy, with the average P-wave velocity of EB being approximately 3400 m/s and that for SB being 5400 m/s. Both rocks were then thermally stressed by slowly heating them at 1°C/s to 900°C to induce thermal crack damage. After this process, and after cooling back to room temperature at the same rate, the velocity of IB decreased significantly to a similar value to EB, and also exhibits no discernable anisotropy (Vinciguerra et al., 2004). In contrast, EB shows no change in mean velocity or velocity anisotropy after thermal treatment. Due to the lack of anisotropy, it is a good assumption that the pre-existing cracks (for EB) or those cracks introduced (in the case of SB), are thus randomly orientated, isotropic crack damage.

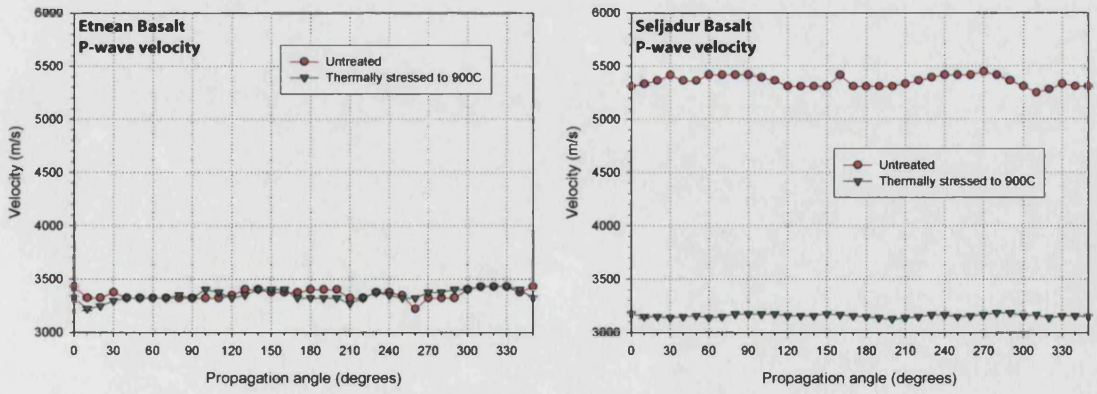

Figure 7-15. Effect of thermal stressing upon Etnean basalt (left) and Icelandic basalt (right), as a function of propagation angle. Neither rock shows significant anisotropy, but the Iceland basalt is significantly affected by thermal treatment

The lack of anisotropy in this example experiment is a good qualitative comparison to the obvious anisotropy which has been seen for all rock types presented in this study so far. Extending this example further, the transport properties can also be considered. Figure 7-16 illustrates the 'untreated' samples once again, comparing the permeability decrease with a concomitant velocity increase with increasing effective pressure. Here, it can be seen that EB possesses a significant permeability. In addition, the P-wave velocity for untreated EB is far lower than that commonly expected for basalts, which are frequently in the range 5 – 6 km/s (Guéguen and Palciauskas, 1994). As effective pressure is increased, the P-wave velocity and permeability changes significantly, showing an increase and decrease respectively. This is in stark contrast to the high velocity (5.5 – 6 km/s) and ultra-low permeability (~21 $x10^{-21}$ m^2) which the untreated SB exhibits. The velocity does not significantly increase after 10 MPa, and no measurable permeability change can be seen over the pressure range applied.

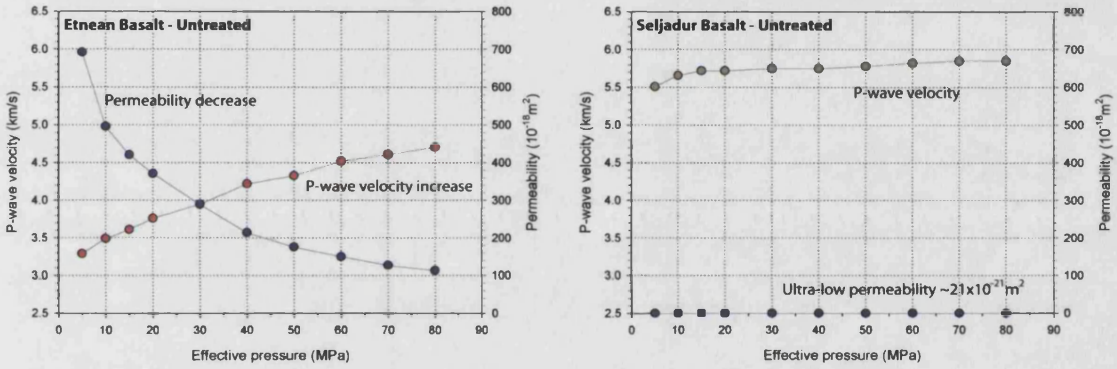

Figure 7-16. Effect of increasing effective pressure upon Etnean basalt (left) and Icelandic basalt (right), as received from the field

For Etnean basalt, after thermal stressing to 900°C, P-wave velocity and permeability changes with pressure are virtually the same as for the untreated rock (figure 7-17). However, performing the same thermal stressing exercise for Seljadur basalt results in significant changes for both P-wave velocity and permeability over the pressure range. For SB, P-wave velocity is far lower compared to the untreated sample, and the velocity increase trend with increasing pressure is significant. Unlike the untreated SB, the P-wave velocity continues to increase even at the highest pressure attained, and does not level off at ~10 MPa as before. Permeability exhibits the greatest change as a result of the thermal stressing, with the permeability of thermally stressed IB some five orders of magnitude higher than for untreated SB. This thermal stressing experiment as applied to the pair of basalts provides a good illustration as to the effect of microcracking in rocks, and its effect upon their elastic wave and transport properties. This illustration also provides a good qualitative comparison to the largely anisotropic rocks studied in detail in this work, in particular the Takidani granite.

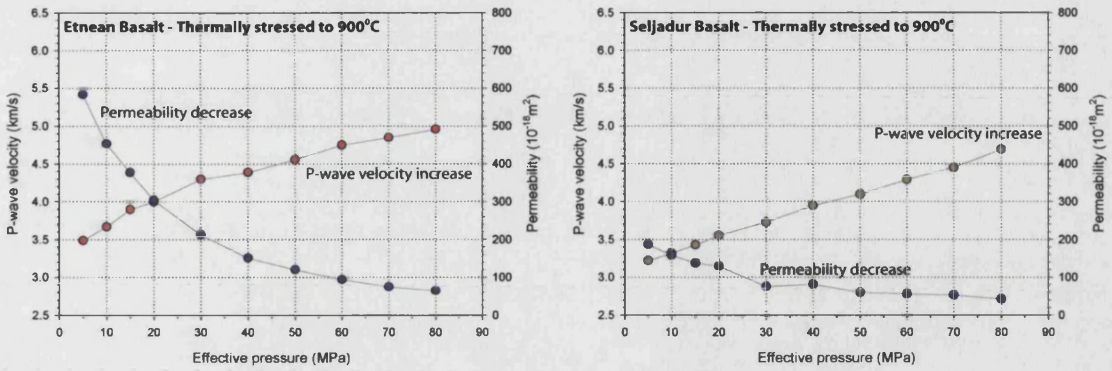

Figure 7-17. Effect of increasing effective pressure upon Etnean basalt (left) and Icelandic Seljadur basalt (right), after thermal stressing. Etnean basalt is largely unaffected compared to the field sample, whilst the Icelandic basalt shows significant changes, both overall and as a function of pressure

7.5.3 ROCK PHYSICS INTERPRETATIONS

By now it is clear that each rock investigated in this study contains a distribution of pore sizes, shapes and alignments, which in past work has often been referred to as the porosity end-members of 'pores' and 'cracks', where a pore reflects equant pore space and a crack reflects a penny-shaped crack with an aspect ratio of typically less than 0.01. The proportion of these constituents are different for each rock, and are crucial in determining the elastic and transport properties of the porous medium, together with the interplay between these two key parameters. In addition, the connectivity of such void space constituents may have significant effects upon the level and anisotropy of permeability.

For Bentheim and Crab Orchard sandstone, these effects can be related to the physical average void space geometry and alignment using pAMS, and with reference to visual analyses (SEM and thin section), and through comparison to the pore throat diameters as measured using mercury injection methods. For relatively 'hard' or micro-cracked rock, the elastic wave velocity is a key parameter, and here the void space is easy to quantify but difficult to interpret in terms of a physical representative ellipsoid. In this case, velocity anisotropy principal directions are more useful as compared to pAMS, as microcracks have a disproportionate effect upon elastic wave velocities. Once again, this data is verified through the more traditional method of mercury injection porosimetry.

However, all of these measurements are made upon laboratory scale samples. The issue of scaling has been widely discussed in such circumstances, where small scale measurements attempt to draw general conclusions using ultrasonic wave velocities, for example. In nature, scales are far greater, and changes in physical processes occur over long time frames. For example, during experimental deformation tests strain rates of 10^{-7} s^{-1} are considered low, whereas in nature rates for tectonic deformation typically range from 10^{-14} s^{-1} to 10^{-16} s^{-1}. Likewise, crustal fluid movement in nature may be much slower than that measured in the laboratory. The problems associated with

scaling, however, whilst acknowledged to exist, have been well reviewed by others (e.g. Main et al., 1990, 1999; Cowie et al., 1996; Bonnet et al., 2001), and lie outside the scope and remit of this particular work. Importantly, the small scales used in this study can be justified as all the measurements have been made contemporaneously upon the same scale, and on the same sample, and under the same conditions. Thus, these data permit the detailed investigation of related and dependent petrophysical parameters under the same accurately known conditions, with application to model testing and verification.

8 SUMMARY AND CONCLUSIONS

This study has investigated the interplay between void space anisotropy, elastic wave velocity (both P-wave and S-wave) and permeability anisotropy. To measure these properties, a new experimental apparatus was developed which is capable of measuring all these properties, together with porosity, contemporaneously at elevated hydrostatic pressures to 100MPa. This state-of-the art apparatus combines a servo controlled steady-state-flow permeability measurement system, capable of measuring fluid flow to nano-Darcy range (10^{-21} m^2), with a hydrostatic pressure vessel capable of up to 375 MPa. A novel design to embed ultrasonic PZT P-wave and S-wave transducer crystals *inside* the internal steel components has been developed as a pre-requisite to this study, in order to achieve the contemporaneous measurement of elastic wave velocities with permeability measurement. In addition, through the use of advanced experimental protocols, methods have been designed which permit the sample porosity to be evaluated contemporaneously with increasing confining pressure.

This equipment was used to conduct a comprehensive study in which the internal pore fabric of three crustal rocks was analysed and compared to seismic and transport properties under representative crustal conditions equivalent to depths up to approximately 4km within the Earth's Crust. First, a new method was employed to independently measure the connected void space (pAMS) of three rock types with contrasting visual properties. These rock types were a high porosity sandstone, a low porosity 'tight' sandstone, and a fractured granite. Using the new equipment, contemporaneous measurements of Vp, Vs, porosity and permeability were made for comparison and contrast with the rock void space principal anisotropy axes using pAMS and room pressure 3-D elastic wave velocity measurement. These data are analysed with respect to the void space anisotropy, and through the application of a small number of geophysical models.

The two sandstones that were chosen (Bentheim and Crab Orchard), show very different porosity and visible structure. Both the pAMS and wave velocity measurements confirm that, for Crab Orchard sandstone, the visible crossbedded fabric in hand specimen is representative of the anisotropy of the internal pore fabric (of 3.8%). In contrast, Bentheim sandstone does not exhibit a visible fabric in hand specimen. However, despite the lack of an obvious visible fabric, the pAMS measurement reveals a clear anisotropy in its void space (of 1.5%). For these rocks, the background matrix susceptibility, mAMS, is low (by three orders of magnitude), so that the total signal due to the matrix and pore AMS (tAMS) may be taken as essentially representing the pore fabric (pAMS) directly, with no additional processing. The third rock type investigated (Takidani granite), requires more treatment as, in this case, the mAMS is of the same overall magnitude as the total magnetic signal (tAMS). In this case, the background matrix AMS must first be subtracted in order to recover the pore fabric AMS alone, pAMS. The resulting principal directions, and the size and shape of the pore fabric (7.7%), exhibit much more scatter as a result of this process and the high natural AMS of

the granite. Therefore the pore fabric is much more difficult to accurately measure using this method. Information from image analysis shows that Takidani granite has an extensively cracked structure. This structure is likely to contribute to the difficulty in using the pAMS method to recover principal pore space directions and anisotropy, as ferrofluid impregnation is difficult, again due to the narrow microcracks that constitute the void space in this case and the finite size of the ferro-fluid suspension. Fortunately, this same issue, which represents a problem for the pAMS method, acts as an advantage when dealing with the complimentary technique of elastic anisotropy, as an aligned crack fabric greatly influences P-wave and S-wave velocity.

Overall, the pAMS technique is a relatively simple, quick and effective at determining the principal pore fabric orientation and shows a high degree of correlation with other, more traditional methods such as velocity anisotropy. This is particularly useful when no aligned fabric can be seen at the sample scale especially as pAMS can produce a true 3D measurement from only a single core taken in any random direction. In this work, I employ a simple ellipsoidal velocity model in order to extract 3-D principal elastic anisotropy axes from the multiple 2-D laboratory measurements. Both pAMS and velocity anisotropy methods can be used to characterise pore space anisotropy in rock without prior assumptions about principal directions. However, the elastic velocity model requires more processing in order to arrive at a 3-D result compared to pAMS. For all three rock types, the principal directions derived using pAMS closely correlates with the principal directions derived using elastic wave velocity measurements, however, S-wave data shows a noticeably higher scatter and variability as compared to the P-wave derived directions. For P-wave data, Bentheim sandstone exhibits a velocity anisotropy of 8%, Crab Orchard sandstone, 18%, and Takidani granite, 9%. For S-wave data the corresponding values are 6%, 9% and 6% respectively. For the sandstones, the relative levels of bulk elastic anisotropy compare well with the void space anisotropy values obtained using pAMS. In addition, it is highly probable that the principal directions measured using pAMS closely correlate to the connected pore space and thus the pAMS method is likely to be a highly accurate permeability anisotropy indicator is than velocity anisotropy, which is sensitive to matrix elasticity which pAMS is not.

Results at elevated pressures, measuring contemporaneous P-wave velocity, S-wave velocity, porosity and permeability, provide an insight into how the characterised pore fabric reacts to the increasing pressure environment. Fluid permeability exhibited particularly high values of percent anisotropy, ranging from zero percent in the case of BHS, to nearly an order of magnitude (80%) in the case of COS and TDG, and did not change significantly over the pressure range for any rock type. In contrast, elastic velocity anisotropy markedly decreased over the same range (for example, for COS V_p; from room pressure anisotropy values of ~18%, to ~7% at 5 MPa, and then to ~0% at 90 MPa). However, permeability and permeability anisotropy is highly dependent on effective pressure and the shape of individual voids. For Crab Orchard sandstone and Takidani granite this fabric exerts a strong influence on fluid flow and its anisotropy. However, for Bentheim sandstone, although the pore fabric anisotropy has a small, but non-zero, shape, this void fabric does not appear

to influence the fluid flow characteristics relative to direction or the increasing pressure environment. It is widely accepted that low aspect ratio cracks close more easily than high aspect ratio pores. Therefore, the significant effect of pressure upon the elastic wave velocity anisotropy of Crab Orchard sandstone and Takidani granite suggests that their microstructures contains a significant crack element which effectively 'closes' at 20 to 30 MPa. These conclusions are further supported through the inspection of mercury injection porosimetry data, which reveals peak in pore neck size distribution at 20 MPa mercury injection pressure. It is therefore reasonable to conclude that the cracks acting in both these rocks affect the transport properties in a similar way, and is therefore likely to be similar in size and alignment. These findings are in contrast to the results for Bentheim sandstone, which are consistent with a microstructure dominated by equant pores, as qualitatively seen during image analysis.

The interpretation of the experimental data is aided through the use of chosen models. The empirical Eberhart-Phillips (1989) model fits extremely well to velocity data from all rock types, even the granite which this model is not explicitly designed for. The effective medium models of Kuster-Toksoz (1974) and Zimmerman (1991) both illustrate that the crack density variation of the rocks may be derived from either the P-wave or S-wave velocity. However, as these models do not take anisotropy and crack communication into account, their crack density predictions when comparing P-wave data to S-wave data for Crab Orchard sandstone and Takidani granite are poor. The crack models of Hudson (1980, 1981) and Kachanov (1994), are used to illustrate the importance of an aligned crack fabric upon the azimuthal seismic velocity, and of the seismic velocity dependence with hydrostatic pressure respectively. The suitability of permeability models is particularly dependent upon rock type. For Bentheim sandstone, the Lattice Boltzman method works well, accurately calculating the permeability over the entire pressure range measured, and confirming that the visible equant pore fabric is the key control on the permeability of the sandstone. The Kozeny-Carman relation is used with Crab Orchard sandstone, and produces a good qualitative fit to the measured data; suggesting that the rock type, due to diagenesis, may have an internal pore structure which is well modelled by a network of tubes. For Takidani granite, the Kachanov derived crack density is used with the statistical/percolation theory of Guéguen and Dienes (1989) to recover the permeability variation with pressure. This approach suggests that crack aperture is the dominant control on the permeabilty of the rock.

In general, studies of the physical properties of rocks often focus on the measurement of a single parameter, and often under fixed conditions. In this study, this specialisation has been expanded to investigate multiple rock properties simultaneously at ambient and elevated pressures through the development of novel equipment and experimental techniques. Using the initial knowledge of void space orientation measured using the pAMS and velocity anisotropy methods, we are able to better understand the subsequent measurements conducted under hydrostatic pressure. For the rocks tested in this study, the velocity anisotropy was dominated by void space anisotropy, whether this be as a result of a well sorted grain matrix; a mature cemented and altered matrix; or

predominantly fractured composition. It should be reiterated that significant differences in the orientations of principal axes are not seen when comparing pAMS to the velocity anisotropy, despite the fact that elastic velocity is sensitive to a range of matrix fabric components which pAMS is not, such as lattice preferential orientation, mineralogical layering or spatial distribution, and grain shape fabric.

9 FUTURE WORK

Through the course of the investigation, a number of issues have been encountered which, due to the constraints of time, were not investigated fully, yet would considerably enhance the state-of-the-art in rock physics knowledge and the interplay between porosity, permeability and elastic wave velocity in porous media. One of the more important questions raised deals with the complex issue of hysteresis in the transport properties of porous media. Figure 9-1 below illustrates, in principle, the problem. This data is taken from a long term pilot experiment carried out to assess the scale and feasibility of addressing this phenomenon. During the experiment, carried out over the course of 14 days, the permeability was measured for a sample of Crab Orchard sandstone with successive cycles of effective pressure, each cycle consisting of increasing and then decreasing the effective pressure.

During the first cycle, permeability decreases, as expected, but does not recover to its original value. The sample was then depressurised and left at this depressurised state for 4 days. Cycle 2 starts from where the end of cycle 1 had left off (~60 x $10^{-18}m^2$), and ends at a lower permeability (~40 x $10^{-18}m^2$). However, when the sample depressurised and left for another period of time under no confining pressure (7 days), the rock pore fabric connectivity appears to recover. This results in the third cycle starting at an initial permeability which is higher than where the previous cycle ended at by 15 x $10^{-18}m^2$ (~39% rise). However, the decreasing pressure part of cycle 3 follows the path of cycle 2.

The 'permeability hysteresis' generated due to this permeability cycling represents an superposition of many inter-related time-dependent elastic effects. These effects range in scope from short term elasticity, in which rock deformation may be full recoverable; to mid-term aneleastic deformation, whereby a deformation may recover through extended periods of time (days to weeks, say); to inelastic deformations, where the damage to the rock is permanent, and is never recovered in any length of time. Thus, a rock retrieved from its natural environment (and under test in the laboratory, for example) has already been 'damaged' to an extent, due to the removal from its *in-situ* pressure conditions. A follow-up study to investigate the extent of such a problem, by using the approach illustrated in figure 9-1 below, would provide some insight into this issue. Although it is impossible to relate the properties of a rock sample recovered at depth and tested in the lab under different conditions, it is possible to monitor and measure how rock properties depend upon well controlled cyclical hydrostatic stresses in an effort to investigate how the rock core recovery process influences the rock physical and transport mechanisms.

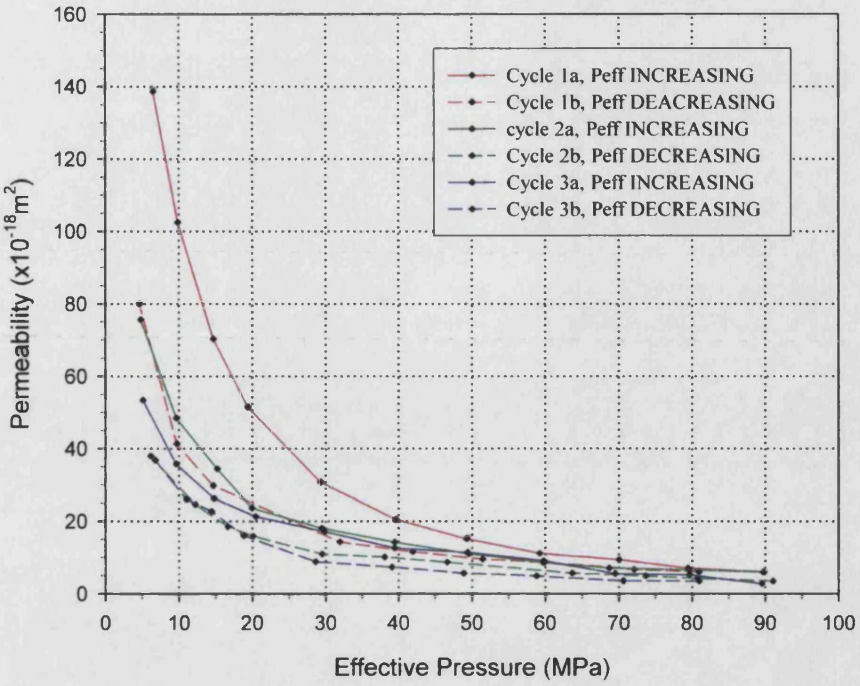

Figure 9-1. Permeability hysteresis pilot test. During this experiment, three separate cycles of increasing and decreasing effective pressure were made, to test the ability of the rock (Crab Orchard) to recover it's permeability over each generation of pressure change

An obvious extension to the work reported in this study is the response of the rock physical and transport properties to deformation under non-hydrostatic stresses, with comparison to the pore fabric both pre-test and post-test using the pAMS method. Although the hydrostatic confining pressure work shown so far is vital to understanding the first order effects of compaction, burial and other pressure related processes upon the pore fabric of crustal rock, it is obviously only part of the larger scale problem. In reality, of course, stresses are anisotropic, and thus an expansion of the work here to replicate such conditions would form a interesting extension to the work presented in this thesis. In addition, when attempting to link such laboratory scale measurements and mechanisms to that found in the field scale, the issue of data scaling is always an inherent problem. This is likely to be even more important when dealing with deviatoric stress than the simple hydrostatic cases presented in this study.

Finally, the equivalent pore concept requires a rigorous test and evaluation, as the results when using ferro-fluid of different dilutions (and hence concentrations) appears to contradict the elastic velocity and permeability data collected in this work, as well as the images from SEM and thin section analysis in a qualitative sense. In addition, the equivalent pore dimensions appears to contradict the logical progression of anisotropic void space at low intrinsic susceptibilities. Therefore, considerable caution should be used when employing this concept in explaining the physical geometry of void space in porous media.

10 REFERENCES

Al-Wardy, W., and Zimmerman, R.W., 2004, Effective stress law for the permeability of clay-rich sandstones. J. Geophys. Res., 109, B04203, doi:10.1029/2003JB002836

Archie, G.E., 1942, The electrical resistivity log as an aid in determining some reservoir characteristics. Trans. Am. Inst. Min. Metal. And Petr. Eng., 146, 54-62

Backus, G.E., 1962, Long-Wave elastic anisotropy produced by horizontal layering. J. Geophys. Res., 67, 4427-4440

Baud, P., Schubnel, A., and Wong, T-f., 2000, Dilatancy, compaction, and failure mode in Solnhofen limestone. J. Geophys. Res., 105(B8), 19289-19303

Bear, J., 1988, Dynamics of Fluids in porous media. American Elsevier. New York, pp764

Benson, P.M., Meredith, P.G., and Platzman, E.S., 2003, Relating pore fabric geometry to elastic and permeability geometry in Crab Orchard Sandstone: A Laboratory study using magnetic ferrofluid. Geophys. Res. Lett., 30(19), 1976, doi:10.1029/2003GL017929

Benson, P.M., Meredith, P.G., Platzman, E.S., White, R.E., 2004, Pore Fabric shape Anisotropy in Porous Sandstone and its Relation to Elastic and Permeability Anisotropy under Hydrostatic Pressure. *Int. Journal. Rock. Mech.* In press.

Berge, P. A., Fryer, G., J., and Wilkens, R., H., 1992, Velocity-Porosity Relationships in the upper Oceanic Crust: Theoretical Considerations. J. Geophys. Res., 97, 15239-15254.

Bernabe, Y., 1987, The effective pressure law for permeability during pore pressure and confining pressure cycling of several crystalline rocks. J. Geophys. Res., 92(B1), 649-657

Bernabe, Y., 1992, On the measurement of permeability in anisotropic rocks, in *Fault mechanics and transport properties of rocks*, Wong, T-f., and Evans, B. (Eds.). Academic Press, 147-167

Bernabe, Y., Mok, U., and Evans, B., 2003, Permeability-porosity relationships in rocks subjected to various evolution processes. Pure and applied Geophysics, 160, 937-960

Bhathal, R.S., 1971, Magnetic anisotropy in rocks. Earth-Science Reviews, 7, 227-253

Bingham, C., 1974, An antipodally symmetric distribution on the sphere. Annals of statistics, 2, 1201-1225.

Birch, F., 1960, The velocity of compressional waves in rocks to 10 kilobars, part 1. J. Geophys. Res., 65, 1083-1102

Bless, S.J. and Ahrens, T.J., 1977, Measurements of the longitudinal modulus of Pierre Clay shale at varying strain rates, Geophysics, 42, 34-40.

Boitnott, G.N., and Scholz, C.H., 1990, Direct measurement of the effective stress law: Deformation of joints subject to pore and confining pressures. J. Geophys. Res., 95, 19,279-19,298

Bonnet, E., O. Bour, N.E. Odling, P. Davy, I. Main , P. Cowie and B. Berkowitz, 2001, Scaling of fracture systems in geological media, Rev. Geophys. 39 , 347-383.

Bosl, W.J., Dvorkin, J., and Nur, A., 1998, A study of porosity and permeability using a lattice Boltzmann simulation. Geophys. Res. Lett., 25, 1475-1478

Bourbie, T., and Zinszner, B., 1985, Hydraulic and elastic properties as a function of porosity in Fontainebleau Sandstone. J. Geophys. Res. 90, 11524-11532

Brace, W. F., Walsh, J. B., and Frangos, W. T., 1968, Permeability of Granite under high pressure. J. Geophys. Res., 73, 2225-2236

Bruner W.M., 1976, Comment on 'Seismic velocities in dry and saturated cracked solids' by R.J. O'Connell and B. Budiansky. J. Geophys. Res., 81, 2573-2576

Budiansky, B., 1965, On the elastic moduli of some heterogeneous materials. J. Mech. Phys. Solids, 13(4): 223-227

Carman, P.C., 1961. L'écoulement des Gas á Travers les Milieux Poreux, Bibliothéque des Sciences et Techniques Nucléaires, Presses Universitaires de France, Paris, pp198

Christensen, N. I., 1965, Compressional wave velocities in Metamorphic rocks at pressures to 10 Kilobars. J. Geophys. Res. 70, 6147-6164

Christensen, N., I., and Wang, H., F., 1985, The influence of pore pressure and confining pressure on dynamic elastic properties of Berea sandstone. Geophysics, 50, 207-213

Clint, O.C., Electric potential changes and elastic emissions generated by fracture and fluid flow during triaxial rock deformation, 1999, PhD thesis, University of London.

Clint, O.C., Meredith, P.G., and Main, I.G, 2001, Porosity-permeability relationships around the percolation threshold in a near-perfect crystalline rock under hydrostatic and deviatoric stress, EOS Trans. AGU, 82 (47), Fall Meet. Suppl.

Collinson, D. W., 1983, Methods in Rock Magnetism and palaeomagnetism. Chapman and Hall, London, pp503

Cowie, P., R. Knipe & I.G. Main, 1996, Scaling laws for fault and fracture populations - analyses and applications, J. Struct. Geol., Vol. 18 .

Deutsch, C.V., and Journal, A.G., 1992, Geostatistical software and library and users guide. Oxford University press. pp340

Dullien, F., 1979, Porous media: Fluid transport and pore structure. Academic Press. pp396

Durrast, H., Rasolofosaon, P.N.J., and Seigesmund, S., 2002, P-wave velocity and permeability distribution of sandstones from a fractured tight gas reservoir. Geophysics, 67, 241-253

Eberhart-Phillips, Han, D.H., and Zoback, M.D., 1989, Empirical relationships among seismic velocity, effective pressure, porosity, and clay content in sandstone. Geophysics, 54, 82-89

Ferreol, B., and Rothman, D.H., 1995, Lattice Boltzmann Fontainebleau sandstone. Transport in Porous media, 20(1), 3

Fischer, George J., 1992, The determination of permeability and storage capacity: Pore pressure oscillation method. In: *Fault mechanics and Transport Properties of Rocks*, Academic Press Ltd, pp. 187-211

Fisher, R., 1952, Dispersion of a sphere. Proc. Roy. Soc., 217, A, 295-305.

Flinn, D., 1962. On folding during 3-D progressive deformation. Quarterly Journal of the Geological Society of London, 118, 385-428.

Gilrane, R., 2000, Anisotropy in Bentheim and Tennessee Sandstones: A comparison using Elastic, Magnetic and Permeability methods. Unpublished MSci thesis, University of London.

Glover, P.W.J., Gomez, J.B., Meredith, P.G., Boon, S.A., Sammonds, P.R. and Murrell, S.A.F., 1996, Modeling the stress-strain behaviour of saturated rocks undergoing triaxial deformation using complex electrical conductivity measurements. Surveys in Geophysics. 17, 307-330

Glover, Paul W.J., Meredith, P.G., Sammonds, P.R. and Murrell, S.A.F., 1994, Measurements of complex electrical conductivity and fluid permeability in porous rocks at raised confining pressures. Eurock '94, expanded abstracts.

Gottschalk, R.R., Kronenberg, A.K., Russell, J.E., and Handin, J., 1990, Mechanical anisotropy of gneiss: Failure criterion and textural sources of directional behaviour. J. Geophys. Res., 95, 21613-21634

Graham, J.W., 1953, Changes of ferromagnetic minerals and their bearing on magnetic properties of rocks, J. Geophys. Res., 58, 243-260

Griffith, A.A., 1924, The theory of rupture. *In: Proc. 1st Int. Cong. Appl. Mech.* (eds. Biezeno, C. B. and Burgers, J. M.). Delft: Tec. Boelhandel en Drukkerji. 56 - 63

Guéguen, Y., and Dienes, J., 1989, Transport properties of rocks from statistics and percolation. Mathematical Geology, 21, 1-13

Guéguen, Y., and Palciauskas, V., 1994, Introduction to the Physics of Rocks. Princeton University press. New Jersey. pp292

Gupta. I.N., 1973, Seismic velocities in rocks subjected to axial loading up to shear fracture. J. Geophys. Res., 78, 6936-6942

Han, D., Nur, A. and Morgan, D., 1986, Effects of porosity and clay content on wave velocities in sandstones. Geophysics, 51, 2093-2107

Harayama, S., 1994, Cooling history of the youngest pluton in the world – The Plio-Pleistocene Takidani Granodiorite (Japan Alps, central Japan). Mem. Geol. Soc. Japan, 43, 87-97

Hashin, Z., and Shtrikman, S., 1963, A variational approach to the elastic behaviour of multiphase materials J. Mech. Phys. Solids, 11 127-140

Haskell, N.A., 1941, The relation between depth lithology and seismic wave velocity in Tertiary sandstones and shales. Geophysics, 6, 318-326.

Heilbronner, R.P., 1992, The autocorrelation function: an image processing tool for fabric analysis. Tectonophysics. 212, 351-370

Hill, R., 1952, The elastic behaviour of crystalline aggregate. Proc. Physical Soc., London, A65, 349-354

Hill, R., 1965, A self-consistent mechanics of composite materials. J. Mech. Phys. Solids and Structures, 13(4): 213-222

Hornby, Brian E., 1998, Experimental laboratory determination of the dynamic elastic properties of wet, drained shales. J. Geophys. Res. 103, 29945-29964

Hornby, Brian E., Schwartz, Larry M., Hudson, John A., 1994, Anisotropic effective-medium Modeling of the elastic properties of shales. Geophysics. 59, 1570-1583

Hrouda, F., 1981. On the superposition of regional slaty cleavage on folded strata and its reflection in magnetic anisotropy. cas. miner. geol., 26, 341-348.

Hrouda, F., 1982, Magnetic anisotropy of rocks and its applications in geology and geophysics. Geophysical surveys, 5, 37-82

Hrouda, F., Hanak, J., and Terzijski, I., 2000, The magnetic and pore fabrics of extruded and pressed ceramic models. Geophysical Journal International. 142, 941-947

Hsieh, P.A., Tracy, J.V., Neuzil, C.E., Bredehoeft, J.D., and Silliman, S.E., 1981, A transient laboratory method for determining the hydraulic properties of 'tight' rocks – 1. Theory. Int. J. Rock. Mech. Min. Sci. and Geomech. Abs. 18, 245-252

Hudson, J.A., 1980, Overall properties of a cracked solid. Math. Proc. Camb. Phil. Soc. 88, 371-384

Hudson, J.A., 1981, Wave speeds and attenuation of elastic waves in material containing cracks. Geophys. J. Royal Astronom. Soc., 64, 133-150

Hudson, J.A., 1990, Overall elastic properties of isotropic materials with arbitrary distribution of circular cracks, Geophys. J. Int., 102, 465-469

Hudson, J.A., Liu, E. and Crampin, S., 1995, The mechanical properties of materials with interconnected cracks and pores. Geophys. J. Int. 124, 105-112

Hudson, J.A., Pointer, T. and Liu, E., 2001, Effective-medium theories for fluid-saturated materials with aligned cracks. Geophys. Prosp. 49, 509-522

Hughes, D.S., and Maurette, C., 1957, Variation of elastic wave velocities in basic igneous rocks with pressure and temperature. Geophysics, 22, 23-31

Johnston, Joel E. and Christensen, Nikolas I., 1995, Seismic anisotropy of shales. J. Geophys. Res. 100, 5991-6003

Jelinek, V., 1973. Precision A.C. bridge set for measuring magnetic susceptibility of rocks and its anisotropy. Studia geophys. geod., 17, 36-48.

Jelinek, V., 1977. The statistical theory of measuring anisotropy of magnetic susceptibility of rocks and its application. Geofyzika, s.p. Brno.

Jelinek, V., 1978. Statistical processing of anisotropy of magnetic susceptibility measured on groups of specimens. Studia geoph. geod., 22, 50-62.

Jelinek, V. & Pokorny, J., 1997. Some new concepts in technology of transformer bridges for measuring susceptibility anisotropy of rocks. Phys. Chem. Earth, 22, 179-181.

Jones, C., and Meredith, P., 1998, An experimental study of elastic wave propagation anisotropy and permeability anisotropy in an illitic shale. Presented at Eurock 98.

Kachanov, M., 1980, Continuum model of medium with cracks. J. Eng. Mech. Div., 106, 1039-1051

Kachanov, M., 1994, Elastic solids with many cracks and related problems, Adv. Appl. Mech., 30, 259-445

Kano, S., and Tsuchiya, N., 2002, Parallelepiped cooling joint and anisotropy of P-wave velocity in the Takidani granitoid, Japan Alps. J. Volcanology and Geothermal Res., 114, 465-477

Kern, H., 1992, P- and S-wave anisotropy and shear-wave splitting at pressure and temperature in possible mantle rocks and their relation to the rock fabric. Physics of the Earth and Planetary Int., 78, 245-256

Keehm, Y., Mukerji, T., Nur, A., 2001, Computational rock physics at the pore scale: Transport properties and diagenesis in realistic pore geometries. The Leading edge, 17, 180-183.

Kemper, E., 1976, Geologischer Führer die Grafschaft Bentheim und die angrenzenden Gebiete mit einem Abriß der emsländischen Unterkreide, Nordhorn, pp206

King, M.S., 1966, Wave velocities in rocks as a function of changes in overburden pressure and pore fluid saturants. Geophysics, 31, 50-73

Klein, E., Baud, P., Reuschlé, T., and Wong, T-f., 2001, Mechanical behaviour and Failure mode of Bentheim sandstone under triaxial compression. Phys. Chem. Earth(A)., 26, 21-25

Klimentos, T., 1991, The effects of porosity-permeability-clay content on the velocity of compressional waves. Geophysics, 56, 1930-1939

Klinkenberg, L. J., 1941, , The permeability of porous media to liquids and gases, *in* Drilling and production practices: American Petroleum Institute, p200, 213

Kranz, R.L., Saltzman, J.S., and Blacic, J.D., 1990, hydraulic diffusivity measurements on laboratory rock samples using an oscillating pore pressure method. Int. J. Rock. Mech. Min. Sci and Geomech. Abstr., 27(5), 345-352

Krief, M., Garat, J., Stellingwerff, J., and Ventre, J., 1990, A petrophysical interpretation using the velocities of P and S waves (full-waveform sonic). The Log Analyst, 31, November, 355-369

Kuster, K. T. and Toksoz, M. N., 1974, Velocity and attenuation of seismic waves in two-Phase media: Part 1. Theoretical formulations. Geophysics, 39, 587-606

Ladd, A.J.C., 1994, Numerical simulations of particulate suspensions via a discretized Boltzmann equation. J. Fluid Mech., 271, 285-309

Leeder, M.R., 1982, Sedimentology: process and product. Allen and Ulwin, London. pp344

Lo, Tien-when, Coyner, Karl B. and Toksoz, M. Nafi, 1986, Experimental determination of elastic anisotropy of Berea sandstone, Chicopee shale, and Chelmsford granite. Geophysics. 51, 164-171

Louis, C.D., David, C., Robion, P., 2003, Comparison of the behaviour of undeformed sandstones under dry and wet conditions. Tectonophysics, 370, 193-212

Main, I.G. , P.G. Meredith, P.R. Sammonds and C. Jones, 1990, Influence of fractal flaw distributions on rock deformation in the brittle field, in Knipe, R.J. & E.H. Rutter (eds.) Deformation Mechanisms, Rheology and Tectonics , Geol. Soc. London Special Publication No 54 , 81-96.

Main, I.G., Smart, B.G.D., Shimmield, G.B., Elphick, S.C., Crawford, B.R., and Ngwenya, B.T., 1994, The effects of combined changes in pore fluid chemistry and stress state on permeability in reservoir rocks: preliminary results from analogue materials. North Sea Oil and Gas Reservoirs – III, pp. 357-370

Main, I.G., T. Leonard, O. Papasouliotis, C.G. Hatton and P.G. Meredith, 1999, One slope or two? Detecting statistically-significant breaks of slope in geophysical data, with application to fracture scaling relationships, Geophys. Res. Lett., 26, 2801-2804.

Mavko, G., and Nur, A., 1997, The effect of a percolation threshold in the Kozeny-Carman relation. Geophysics, 62, 1480-1482

Mavko, G., Mukerji, T., and Dvorkin, J., 1998, The rock physics handbook: tools for seismic analysis in porous media. Cambridge University Press, pp329

Meredith, P. G., I. G. Main, and C. Jones, 1990, Temporal variations in seismicity during quasi-static and dynamic rock failure, Tectonophysics, 175, 249-268

McDonal, F. J., Angona, F. A., Mills, R. L., Sengbush, R. L., van Nostrand, R. G. and White, J. E., 1958, Attenuation of shear and compressional waves in Pierre Shale: Geophysics, 23, 421-439.

Modry, S., Svata, M., and Jindra, J., 1972, Bibliography on mercury porosimetry. House of Technology, Prague. pp451

Nur, A., Marion, D., and Yin, H., 1991, Wave velocities in sediments, in Shear waves in marine sediments, J.M. Hovem, M.D., Richardson. And R.D. Stoll, eds. Kluwer Academic publishers, Dordrecht, Netherlands, 131-140

Nur, A., Mavko, G., Dvorkin, J., and Gal, D., 1995, Critical porosity: The key to relating physical properties to porosity in rocks, in Proc, 65th Ann. Int. Meeting, Soc. Expl. Geophys., 878

Odedra, Anita, Ohnaka, Mitiyasu, Mochizuki, Hiromine and Sammonds, Peter, 2001, Temperature and pore pressure effects on the shear strength of granite in the brittle-plastic transition regime. Geophys. Res. Lett. 28, 3011-3014

Osborn, J.A., 1945, Demagnetising factors of the general ellipsoid. Physical review, 67, 345-357

Palmer, D., 1986, Refraction seismic: the lateral resolution of structure and seismic velocity. Handbook of Geophysical Exploration, 13, Geophysical press. Bilthoven. pp269

Parasnis, D., S., 1997, Principles of applied Geophysics (Fifth Edition). Chapman and Hall.

Paterson, M.S., 1978, Experimental rock deformation – brittle field. Springer-Verlag, Berlin. pp254

Peacock, S., McCann, C., Sothcott, J., and Astin, T. R., 1994, Seismic velocities in fractured rocks: an experimental verification of Hudson's theory. Geophys. Prosp., 42, 27-80

Pfleiderer, S., and Halls, H., C., 1990, Magnetic susceptibility anisotropy of rocks saturated with ferrofluid: a new method to study pore fabric? Phys. Of the Earth and planetary Int. 65, 158-164

Pfleiderer, S., and Halls, H.C., 1993, Magnetic Pore Fabric Analysis: Verification through image autocorrelation. J. Geophys. Res. 98, 4311-4316

Pfleiderer, S., and Halls, H.C., 1994, Magnetic pore fabric analysis: a rapid method for estimating permeability anisotropy. Geophys. J. Int. 116, 39-45

Pfleiderer, S., and Kissel, C., 1994, Variation of pore fabric across a fold-thrust structure. Geophys. Res. Lett., 21, 2147-2150.

Phillips, M., Permeability of the tightest rocks, 2002, PhD thesis, University of London.

Pittman, E.D., 1984, The pore geometries of reservoir rocks, in *Physics and Chemistry of Porous media* [Schlumberger-Doll Research, 1983, AIP Conference Proceedings, 107, Johnson, D.L. and P.N. Sen (Eds.), N.Y.]

Porath, H., Stacey, F.D., and Cheam, A.S., 1966. The choice of specimen shape for magnetic anisotropy measurements on rocks. Earth Planet. Sci. Lett., 21, 2147-2150

Potter, P.E., and Pettijohn, F.J., 1963, Palaeocurrents and basin analysis. Springer, Berlin. pp296

Prasad, M. and Manghnani, Murli H., 1997, Effects of pore and differential pressure on compressional wave velocity and quality factor in Berea and Michigan sandstones. Geophysics. 62, 1163-1176

Qian, Y.H., d'Humieres, D., and Lallemand, P., 1992, Lattice BGK models for Navier-Stokes equation. Europhys. Lett., 17(6), 479-484

Rasolofosaon, P.N.J. and Zinszner, B.E, 2002, Comparison between permeability anisotropy and elastic anisotropy of reservoir rocks. Geophysics, 67, 230-240

Rathore, J.S., Fjaer, E., Holt, R.M. and Renlie, L., 1995, P- and S-wave anisotropy of a synthetic sandstone with controlled crack geometry. Geophys. Prosp. 43, 711-728

Rawling, G.C., Baud, P., and Wong, T.-f., 2002, Dilatancy, brittle strength and anisotropy of foliated rocks: Experimental deformation and micromechanical modeling. J. Geophys. Res., 107(B10), 2234, doi:10.1029/2001JB000472

Raymer, L.L., Hunt, E.R., and Gardner, J.S., 1980, An improved sonic transit time-to-porosity transform, Trans. Soc. Prof. Well Log Analysts, 21st Annual Logging Symposium, Paper P.

Rees, A.I., 1966, the effect of depositional slopes on the anisotropy of magnetic susceptibility of laboratory deposited sands. J. Geol., 74, 856-867

Reinecker, J., O. Heidbach, M. Tingay, P. Connolly, and B. Müller, 2004, The 2004 release of the World Stress Map (available online at www.world-stress-map.org)

Reuss, A., 1929, Berechnung der Fliessgrenzen von Mischkristallen auf Grund der Plastizitätsbedingung für Einkristalle, Zeitschrift für Angewandte Mathematik und Mechanik, 9, 49-58

Rice, P.A., Foutugne, D.J., Latini, R.J., and Barduhn, A.J., 1970, In "Flow Through Porous Media" (R. Nunge, Eds.), p.47. American Chemical Society, Washington D.C.

Rosensweig, R.E., 1985, Ferrohydro-dynamics. Cambridge University Press, Cambridge. pp344.

Sammonds, P.R., Ayling, M. R., Meredith, P.G., Murrell, S.A.F., and Jones, C., 1989, A laboratory investigation of elastic emissions and elastic wave velocity changes during rock failure under triaxial stresses. In *Rock at Great Depth – Rock Mechanics and Rock Physics at Great Depth*, Maury and Fourmaintraux (eds), Balkema, Rotterdam, 1, 233 - 240

Sano, O., Kudo, Y., and Mizuta, Y., 1992, Experimental determination of elastic constants of Oshima granite, Barre granite and Chelmsford Granite. J. Geophys. Res., 97, 3367-3379

Sayers, C.M., 1994, The elastic anisotropy of shales. J. Geophys. Res., 99, 767-774

Sayers, C.M., 1999, Stress dependent seismic anisotropy of shales. Geophysics. 64, 93-98

Sayers, C.M, and Kachanov, M., 1995, Microcrack-induced elastic anisotropy of brittle rocks. J. Geophys. Res., 100(B3), 4149-4156

Sayers, C.M., van Munster, J.G., and King, M.S., 1990, Stress-induced ultrasonic anisotropy in Berea sandstone. Int. J. Rock Mech., 27, 429-436

Scheidegger, A.E., 1974, The Physics of Flow Through Porous Media, 3rd Ed. Univ. Toronto Press, Toronto pp353

Schubnel, A., and Guéguen, Y., 2003, Dispersion and anisotropy of elastic waves in cracked rocks. J. Geophys. Res., 108(B2), 2101, doi:10.1029/2002JB001824

Sheriff, R.E, and Geldart, L.P., 1995 (2nd Ed.). Exploration seismology. Cambridge University Press, Cambridge. pp592

Sokolnikoff, I.S., 1956, Mathematical Theory of Elasticity, 2nd Ed. McGraw-Hill, New York, pp476

Stacey, F.D., 1960, Magnetic anisotropy in rocks. J. Geophys. Res., 65, 2429-2442

Stearns, R.G., 1954, The Cumberland Plateau Overthrust and Geology of the Crab Orchard Mountains area, Tennessee. Tennessee Division of Geology Bulletin 60, pp47

Stoner, E.C., 1945, The demagnetizing factors for ellipsoids. Philos. Mag. Ser., 7, 36, 803-821

Tarling, D.H., and Hrouda, F., 1993, The magnetic Anisotropy of Rocks. Chapman and Hall, pp217

Thomsen, Leon., 1986, Weak elastic Anisotropy. Geophysics. 51, 1954-1966

Terzaghi, K., 1936, The shearing resistance of saturated soils and the angle between the planes of shear. In: Proceedings of the international conference on soil mechanics and foundation engineering, vol 1. Harvard University press, Cambridge, Mass., pp. 54-56

Tosaya, C., and Nur, A., 1982, Effects of diagenesis and clays on compressional velocities in rocks. Geophys. Res. Lett., 9, 5-8

Toksoz, D.H., Johnston, D.,H., and Timur, A., 1979, Attenuation of seismic waves in dry and saturated rocks: 1. Laboratory measurements. Geophysics. 44, 681-690

Toksoz, M.N., Cheng, C.,H., and Timur, A., 1976, Velocities of seismic waves in porous rocks. Geophysics, 41, 621-645

Trimmer, D.A., 1981, Design criteria for laboratory measurements of low permeability rocks. Geophys. Res. Lett. 8(9), 973-975

Uyeda, S., Fuller, M.D., Belshe, J.C., and Girdler, R.W., 1963, Anisotropy of magnetic susceptibility of rocks and minerals, J., Geophys. Res., 68, 279-291

Vernik, L. and Liu, Xingzhou, 1997, Velocity anisotropy in shales: A petrophysical study. Geophysics. 62, 521-532

Vernik, L. and Nur, A., 1992, Ultrasonic velocity and anisotropy of hydrocarbon source rocks. Geophysics. 57, 727-735

Vernik, L., 1997, Predicting porosity from elastic velocities in siliciclastics: A new look. Geophysics. 62, 118-128

Vernik, Lev, 1993, Microcrack-induced versus intrinsic elastic anisotropy in mature HC-source shales. Geophysics. 58, 1703-1706

Vinciguerra, S., Trovato, C., Meredith, P. and Benson, P., 2004, Relating seismic velocities, thermal cracking and permeability in Mt. Etna and Iceland basalts. Int. Journal. Rock. Mech. In press.

Walsh, J.B., 1965, The effect of Cracks on the compressibility of rock. J. Geophys. Res., 70, 381-389

Walsh, J.B., and Brace, W.F., 1984, The effect of pressure on porosity and the transport properties of rock. J. Geophys. Res., 89(B11), 9425-9431

Wendt, A.S., Bayuk, I.O., Covey-Crump, S.J., Wirth, R., and Lloyd, G.E., 2003, An experimental and numerical study of the microstructural parameters contributing to the seismic anisotropy of rocks. J. Geophys. Res., 108(B8), 2365, doi:10.1029/2002JB001915

Winterstein, D. F., 1990, Velocity anisotropy terminology for geophysicists. Geophysics, 55, 1070-1088

Wonham, J.P., Johnson, H.D., Mutterlose, J., Stadtler, A., and Ruffell, A.H., 1997, Characterisation of a shallow marine sandstone reservoir in a syn-rift setting: the Bentheim sandstone formation (Valanginian) of the RŸhlermoor field, Lower Saxony basin NW Germany. In: Shallow marine and Non-marine reservoirs: sequence stratigraphy, reservoir architecture and production characteristics, 18th annual GCSSEPM foundation research conference. Shanley, K.W., and Perkins, B.F., (Eds.), 460, 427-448

Wyllie, M.R.J., Gregory, A.R., and Gardner, L.W., 1956, Elastic wave velocities in heterogeneous and porous media. Geophysics, 21, 41-70

Wyllie, M.R.J., Gregory, A.R., and Gardner, L.W., 1958, An experimental investigation of factors affecting elastic wave velocities in porous media. Geophysics, 23, 459-493

Yale, D.P., 1985, Recent advances in Rock Physics, Geophysics, 50, 2480-2491

Zimmerman, R.W., 1986, Compressibility of two-dimensional cavities of various shapes. ASME Journal of Applied Mechanics, 53(3), 500-504.

Zimmerman, R.W., 1991, Compressibility of Sandstones. Developments in Geoscience, 29. Elsevier (New York), pp173

11 APPENDICES

A. LIST OF PROJECT OUTPUTS: PAPERS AND PRESENTATIONS

NOTE: Refer to enclosed CD for full text (.pdf format).

Refereed Papers

Benson, P.M., Meredith, P.G., Platzman, E.S., White, R.E., Pore Fabric shape Anisotropy in Porous Sandstone and its Relation to Elastic and Permeability Anisotropy under Hydrostatic Pressure (2004). *Int. Journal. Rock. Mech.* In press.

Vinciguerra, S., Trovato, C., Meredith, P. and **Benson, P.**, Relating seismic velocities, thermal cracking and permeability in Mt. Etna and Iceland basalts (2004). *Int. Journal. Rock. Mech.* In press.

Vinciguerra, S., Trovato, C., Meredith, P., **Benson, P.**, De Luca, G., Troise, C. and De Natale, G., Understanding the seismic velocity structure of Campi Flegrei caldera (Italy): from the laboratory to the field scale. *Int. Journal. Rock. Mech.* In preparation.

Benson, P.M., Meredith, P., G. and Platzman, E., S., Relating pore fabric geometry to elastic and permeability anisotropy in Crab Orchard Sandstone: A laboratory study using magnetic ferrofluid (2003), *Geophys. Res. Lett.*, **30**, No. 19, 1976, doi:10.1029/2003GL017929. http://www.agu.org/journals/gl/gl0319/2003GL017929/2003GL017929.pdf

Conference presentations

Benson, P., Schubnel, A., Vinciguerra, S., Hazzard, J., Young, R. P., and Meredith, P. Modelling the physical properties of cracked rocks (2): application to transversely anisotropic granite from the Japanese Alps (2004). *Eos Trans. AGU, 85(17), Jt. Assem. Suppl.*, Abstract V21C-02. ***(Winner, Outstanding Student Paper award).***

Vinciguerra, S., Schubnel, A., **Benson, P.**, Trovato, C., Hazzard, J., Young, R. P., and Meredith, P. Modelling the physical properties of cracked rocks (1): application an isotropic basalt from Mount Etna (2004). *Eos Trans. AGU, 85(17), Jt. Assem. Suppl.*, Abstract V21C-02.

Benson, P., Meredith, P., Platzman, E., and White, R. Relating Pore Fabric Geometry to Elastic Wave Velocity, Anisotropy and Fluid Flow in Porous Sandstone: A Laboratory Study Using Magnetic Ferrofluid (2003). *Eos Trans. AGU, 84(46), Fall Meet. Suppl.*, Abstract S21C-08.

Vinciguerra, S., Trovato, C., Meredith, P., and **Benson, P.**, Relating Seismic Velocities, Permeability and Crack Damage in Interpreting the Mechanics of Active Volcanoes (2003), *Eos Trans. AGU, 84(46), Fall Meet. Suppl.*, Abstract S22A-0440.

Philip M Benson, Philip G Meredith and Ellen S Platzman, Relating pore fabric geometry to elastic wave and permeability anisotropy in Crab Orchard Sandstone and Bentheim Sandstone: A laboratory study using magnetic ferrofluid (2003), EURO-Conference on Rock Physics and Geomechanics Micromechanics, Flow and Chemical Reactions, Kijkduin.

Benson, P., Meredith, P and Platzman, E., Relating fluid flow to pore fabric and elastic anisotropy in Crab Orchard sandstone (2003), European Geophysical Society, EGS-AGU-EUG Joint Assembly, Nice, *Geophysical Research Abstracts*, **5**, 06212. http://www.cosis.net/abstracts/EAE03/06212/EAE03-A-06212.pdf

Philip M Benson and Philip G Meredith, Comparative Anisotropy of Sedimentary rock (2002), British Geological Association Postgraduate Research in Progress, Southampton Oceanography Centre, Southampton, UK ***(Prize for best poster).***

B. AMS RAW DATA

Bentheim Sandstone, Block BS1, mAMS

Core	Bulk susceptibility (SI)	Porosity (%)	Maximum (degrees)		Intermediate (degrees)		Minimum (degrees)	
			Trend	Plunge	Trend	Plunge	Trend	Plunge
BS1-a1	24	N/A	201	20	79	56	301	27
BS1-a2	14	N/A	32	26	158	50	287	28
BS1-a4	36	N/A	144	62	303	26	37	9
BS1-a7	20	N/A	191	64	77	11	343	23
BS1-a8	16	N/A	18	21	209	69	109	4
BS1-a9	9	N/A	356	72	210	15	118	9
BS1-a10	9	N/A	41	43	206	46	304	8
BS1-a11	9	N/A	40	57	208	32	301	6

...continued

Core	Principal susceptibilities (normalised to bulk susceptibility)			L	F	P (%)
	Maximum	Intermediate	Minimum			
BS1-a1	1.0103	1.0048	0.9849	1.005	1.020	2.6
BS1-a2	1.0119	1.0014	0.9867	1.011	1.015	2.6
BS1-a4	1.0312	1.0228	0.9460	1.008	1.081	9.0
BS1-a7	1.0227	0.9635	0.9138	1.009	1.020	3.0
BS1-a8	1.0108	1.0053	0.9839	1.006	1.022	2.7
BS1-a9	1.0149	1.0009	0.9842	1.014	1.017	3.1
BS1-a10	1.0169	1.0075	0.9756	1.009	1.033	4.2
BS1-a11	1.0126	1.0084	0.9790	1.004	1.030	3.4

Bentheim Sandstone, Block BS1, tAMS

Core	Bulk susceptibility (SI)	Porosity (%)	Maximum (degrees)		Intermediate (degrees)		Minimum (degrees)	
			Trend	Plunge	Trend	Plunge	Trend	Plunge
BS1-a1	19224	20.2	72	75	206	11	298	11
BS1-a2	19816	20.9	22	9	143	72	290	15
BS1-a3	19568	20.6	16	8	116	54	280	35
BS1-a4	19502	20.5	19	10	132	65	284	22
BS1-a6	19928	20.6	190	3	84	79	281	10
BS1-a7	19809	20.9	21	38	176	49	281	13
BS1-a8	19795	20.8	11	16	160	71	278	9
BS1-a9	19188	20.2	72	75	206	11	298	11
BS1-a10	19888	20.9	63	74	215	15	307	7
BS1-a11	19609	20.6	89	82	209	4	300	7
BS1-a12	19313	20.3	68	72	226	17	318	6

...continued

Core	Principal susceptibilities (normalised to bulk susceptibility)			L	F	P (%)
	Maximum	Intermediate	Minimum			
BS1-a1	1.0075	1.0003	0.9922	1.007	1.008	1.5
BS1-a2	1.0061	1.0006	0.9932	1.006	1.007	1.3
BS1-a3	1.0069	0.9980	0.9951	1.009	1.003	1.2
BS1-a4	1.0069	0.9997	0.9934	1.007	1.006	1.4
BS1-a6	1.0047	1.0032	0.9921	1.002	1.011	1.3
BS1-a7	1.0053	1.0041	0.9907	1.001	1.013	1.5
BS1-a8	1.0060	1.0047	0.9893	1.001	1.016	1.7
BS1-a9	1.0062	1.0012	0.9927	1.005	1.009	1.4
BS1-a10	1.0050	1.0009	0.9941	1.004	1.007	1.1
BS1-a11	1.0038	1.0009	0.9953	1.003	1.006	0.8
BS1-a12	1.0038	1.0010	0.9952	1.003	1.006	0.9

Bentheim Sandstone, Block BS2, tAMS

Core	Bulk susceptibility (SI)	Porosity (%)	Maximum (degrees)		Intermediate (degrees)		Minimum (degrees)	
			Trend	Plunge	Trend	Plunge	Trend	Plunge
BS2-a1	19300	20.3	250	8	160	2	57	82
BS2-a2	18928	19.9	244	12	151	11	22	74
BS2-a3	18586	19.6	250	11	156	20	7	67
BS2-a4	20743	21.8	253	11	160	16	17	71
BS2-a5	19858	23.5	240	12	146	17	3	68
BS2-a6	20178	21.2	250	7	157	25	354	64
BS2-a7	20066	23.8	245	12	154	5	44	77
BS2-a8	19345	20.3	27	8	294	18	142	70
BS2-a9	20081	21.1	7	4	275	28	105	62
BS2-a10	20066	23.8	195	1	286	18	101	72
BS2-a11	19813	23.5	10	11	276	20	127	67
BS2-a12	19538	23.2	219	6	128	2	17	84
BS2-a13	19880	23.6	214	9	124	4	9	80
BS2-a14	19062	20.1	209	12	118	3	12	78
BS2-a15	19880	20.9	255	9	135	0	45	81
BS2-a16	18326	19.3	216	7	126	2	20	83

...continued

Core	Principal susceptibilities (normalised to bulk susceptibility)			L	F	P (%)
	Maximum	Intermediate	Minimum			
BS2-a1	1.0047	1.0032	0.9921	1.004	1.009	1.3
BS2-a2	1.0038	1.0009	0.9953	1.007	1.005	1.2
BS2-a3	1.0060	1.0010	0.9939	1.005	1.008	1.3
BS2-a4	1.0065	1.0019	0.9916	1.004	1.007	1.2
BS2-a5	1.0062	1.0012	0.9927	1.006	1.006	1.2
BS2-a6	1.0069	0.9980	0.9951	1.005	1.006	1.1
BS2-a7	1.0050	1.0009	0.9941	1.002	1.009	1.2
BS2-a8	1.0061	1.0006	0.9932	1.002	1.012	1.4
BS2-a9	1.0076	1.0044	0.9880	1.006	1.006	1.3
BS2-a10	1.0075	1.0003	0.9922	1.005	1.01	1.5
BS2-a11	1.0060	1.0047	0.9893	1.007	1.008	1.5
BS2-a12	1.0053	1.0041	0.9907	1.004	1.018	2.2
BS2-a13	1.0069	0.9997	0.9934	1.003	1.017	2.0
BS2-a14	1.0038	1.0010	0.9952	1.003	1.013	1.7
BS2-a15	1.0048	1.0023	0.9929	1.004	1.014	1.8
BS2-a16	1.0072	1.0006	0.9922	1.004	1.016	2.0

Crab Orchard Sandstone, Block TS1, mAMS

Core	Bulk susceptibility (SI)	Porosity (%)	Maximum (degrees)		Intermediate (degrees)		Minimum (degrees)	
			Trend	Plunge	Trend	Plunge	Trend	Plunge
TS1-a1	127.1	N/A	43	2	134	31	310	59
TS1-a2	20.1	N/A	9	0	99	2	271	88
TS1-a4	35.7	N/A	169	4	79	13	277	77
TS1-a12	20.0	N/A	10	23	129	48	264	32
TS1-a17	23.3	N/A	2	16	109	47	258	39
TS1-a18	63.7	N/A	186	4	83	73	277	17
TS1-a20	60.6	N/A	45	11	144	41	303	47
TS1-a22	21.1	N/A	101	34	195	6	294	55
TS1-a23	58.3	N/A	87	22	236	65	352	12
TS1-a25	53.1	N/A	81	3	171	2	285	86
TS1-a26	33.7	N/A	346	0	76	4	250	86
TS1-a29	50.7	N/A	78	13	180	42	335	45
TS1-a31	20.8	N/A	358	23	180	67	88	1
TS1-a35	52.0	N/A	32	51	163	28	268	25
TS1-a36	52.4	N/A	199	2	108	7	306	83

...continued

Core	Principal susceptibilities (normalised to bulk susceptibility)			L	F	P (%)
	Maximum	Intermediate	Minimum			
TS1-a1	1.0129	1.0013	0.9858	1.012	1.016	2.7
TS1-a2	1.0284	1.0167	0.9549	1.012	1.065	7.7
TS1-a4	1.0189	1.0068	0.9743	1.012	1.033	4.6
TS1-a12	1.0122	1.0030	0.9848	1.009	1.019	2.8
TS1-a17	1.0119	1.0035	0.9845	1.008	1.019	2.8
TS1-a18	1.0510	0.9848	0.9683	1.072	1.013	8.5
TS1-a20	1.0082	1.0062	0.9856	1.012	1.027	3.9
TS1-a22	1.0166	1.0048	0.9785	1.018	1.026	4.4
TS1-a23	1.0204	1.0024	0.9772	1.018	1.053	7.2
TS1-a25	1.0289	1.0111	0.9601	1.011	1.073	8.5
TS1-a26	1.0309	1.0193	0.9498	1.005	1.015	2.0
TS1-a29	1.0081	1.0034	0.9885	1.012	1.058	7.2
TS1-a31	1.0271	1.0144	0.9585	1.01	1.005	1.5
TS1-a35	1.0081	0.9985	0.9934	1.005	1.044	4.9
TS1-a36	1.0174	1.0125	0.9701	1.012	1.016	2.7

Crab Orchard Sandstone, Block TS1, tAMS

Core	Bulk susceptibility (SI)	Porosity (%)	Maximum (degrees)		Intermediate (degrees)		Minimum (degrees)	
			Trend	Plunge	Trend	Plunge	Trend	Plunge
TS1-a2	14570	4.78	36	8	127	9	267	78
TS1-a4	17820	5.85	27	1	117	10	292	80
TS1-a12	20290	3.71	16	7	108	18	266	71
TS1-a18	10840	3.89	42	8	134	13	282	75
TS1-a25	13910	4.57	192	4	101	12	302	77
TS1-a26	13680	4.49	29	7	120	5	246	81
TS1-a27	15710	5.16	72	22	165	9	276	67
TS1-a28	11970	3.93	83	17	179	19	315	64
TS1-a29	14870	4.88	73	4	165	19	330	71
TS1-a30	11602	3.81	19	1	109	3	280	87
TS1-a31	13940	4.58	195	3	104	26	290	64
TS1-a32	11740	3.85	19	1	109	3	280	87
TS1-a35	12930	4.24	190	2	99	14	287	76
TS1-a36	11820	3.88	191	3	101	9	298	80
TS1-a37	10260	3.37	59	15	151	6	263	74
TS1-a38	10950	3.59	60	13	152	8	271	75
TS1-a39	9993	3.28	71	19	164	9	278	69
TS1-a40	15790	5.18	62	15	154	10	277	72
TS1-a41	11800	3.87	10	8	103	25	264	63
TS1-a42	17820	5.85	183	11	89	18	302	69
TS1-a43	11600	3.81	10	8	106	35	269	53
TS1-a44	11630	3.82	8	11	106	35	264	53
TS1-a45	13920	4.57	188	8	96	9	318	78
TS1-a46	11950	3.92	29	2	120	12	291	77
TS1-a47	11210	3.68	190	10	98	6	336	78
TS1-a48	11060	3.63	26	3	117	9	279	80

...continued

Core	Principal susceptibilities (normalised to bulk susceptibility)			L	F	P (%)
	Maximum	Intermediate	Minimum			
TS1-a2	1.0187	1.0081	0.9732	1.011	1.036	4.7
TS1-a4	1.0170	1.0086	0.9744	1.008	1.035	4.4
TS1-a12	1.0173	1.0034	0.9793	1.014	1.025	3.9
TS1-a18	1.0136	1.0054	0.9810	1.008	1.025	3.3
TS1-a25	1.0195	1.0002	0.9803	1.019	1.020	4.0
TS1-a26	1.0197	1.0063	0.9740	1.013	1.033	4.7
TS1-a27	1.0160	1.0069	0.9771	1.009	1.031	4.0
TS1-a28	1.0113	1.0067	0.9820	1.005	1.025	3.0
TS1-a29	1.0114	1.0082	0.9805	1.003	1.028	3.2
TS1-a30	1.0193	1.0068	0.9739	1.012	1.034	4.7
TS1-a31	1.0166	1.0038	0.9796	1.013	1.025	3.8
TS1-a32	1.0177	0.9991	0.9832	1.019	1.016	3.5
TS1-a35	1.0191	0.9997	0.9812	1.019	1.019	3.9
TS1-a36	1.0149	1.0103	0.9748	1.005	1.036	4.1
TS1-a37	1.0136	1.0022	0.9842	1.011	1.018	3.0
TS1-a38	1.0142	1.0025	0.9833	1.012	1.019	3.1
TS1-a39	1.0147	1.0015	0.9838	1.013	1.018	3.1
TS1-a40	1.0141	1.0052	0.9807	1.009	1.025	3.4
TS1-a41	1.0198	0.9978	0.9824	1.022	1.016	3.8
TS1-a42	1.0176	0.9984	0.9840	1.019	1.015	3.4
TS1-a43	1.0183	0.9995	0.9822	1.019	1.018	3.7
TS1-a44	1.0191	1.0028	0.9781	1.016	1.025	4.2
TS1-a45	1.0166	1.0122	0.9713	1.004	1.042	4.7
TS1-a46	1.0171	1.0123	0.9706	1.005	1.043	4.8
TS1-a47	1.0180	1.0094	0.9726	1.009	1.038	4.7
TS1-a48	1.0199	1.0088	0.9713	1.011	1.039	5.0

Takidani Granite, Block TG2, mAMS

Core	Bulk susceptibility (SI)	Porosity (%)	Maximum (degrees)		Intermediate (degrees)		Minimum (degrees)	
			Trend	Plunge	Trend	Plunge	Trend	Plunge
TG2-a1	21230	N/A	315	19	199	52	57	32
TG2-a2	16620	N/A	316	17	185	65	51	17
TG2-a3	23070	N/A	317	22	185	59	55	21
TG2-a4	19050	N/A	294	46	163	33	54	27
TG2-a5	26720	N/A	147	11	255	57	50	31
TG2-a6	26870	N/A	151	17	267	55	51	29
TG2-a7	22130	N/A	315	22	192	53	57	28
TG2-a8	25810	N/A	305	22	188	48	50	33
TG2-a9	26290	N/A	146	4	242	56	54	34
TG2-a10	6670	N/A	328	28	184	57	67	17
TG2-a11	6379	N/A	241	58	146	3	54	31
TG2-a12	17340	N/A	322	11	215	58	58	30
TG2-a13	28260	N/A	165	21	276	44	57	39
TG2-a14	7409	N/A	317	17	205	50	59	35
TG2-a15	27290	N/A	165	15	279	57	67	29
TG2-a16	9986	N/A	268	64	155	11	60	24
TG2-a17	8579	N/A	309	34	177	45	58	26
TG2-a18	9444	N/A	318	22	198	52	61	30
TG2-a19	14880	N/A	249	67	148	5	56	22
TG2-a20	6941	N/A	149	20	295	66	54	12
TG2-a21	12470	N/A	271	63	150	15	54	22
TG2-a23	24890	N/A	159	14	273	59	62	28
TG2-a24	27230	N/A	327	8	222	62	61	26
TG2-a25	26240	N/A	155	16	265	49	52	36
TG2-a26	12110	N/A	214	51	325	16	66	34
TG2-a27	13670	N/A	317	36	181	45	66	23
TG2-a28	19540	N/A	291	46	169	27	61	31
TG2-a29	12490	N/A	297	57	157	26	57	18

...continued

Core	Principal susceptibilities (normalised to bulk susceptibility)			L	F	P (%)
	Maximum	Intermediate	Minimum			
TG2-a1	1.0375	1.0199	0.9426	1.017	1.082	9.6
TG2-a2	1.0383	1.0155	0.9464	1.023	1.073	9.3
TG2-a3	1.0426	1.0219	0.9355	1.020	1.092	10.8
TG2-a4	1.0293	1.0279	0.9428	1.001	1.090	8.8
TG2-a5	1.0390	1.0263	0.9347	1.012	1.098	10.6
TG2-a6	1.0341	1.0287	0.9373	1.005	1.098	9.8
TG2-a7	1.0379	1.0240	0.9382	1.014	1.091	10.1
TG2-a8	1.0397	1.0176	0.9428	1.022	1.079	9.8
TG2-a9	1.0426	1.0220	0.9354	1.020	1.093	10.8
TG2-a10	1.0325	1.0086	0.9589	1.024	1.052	7.4
TG2-a11	1.0449	1.0050	0.9500	1.040	1.058	9.5
TG2-a12	1.0411	1.0188	0.9401	1.022	1.084	10.2
TG2-a13	1.0317	1.0224	0.9458	1.009	1.081	8.7
TG2-a14	1.0350	1.0219	0.9431	1.013	1.084	9.3
TG2-a15	1.0456	1.0199	0.9346	1.025	1.091	11.2
TG2-a16	1.0275	1.0153	0.9572	1.012	1.061	7.1
TG2-a17	1.0361	1.0156	0.9483	1.020	1.071	8.8
TG2-a18	1.0362	1.0178	0.9460	1.018	1.076	9.1
TG2-a19	1.0372	1.0272	0.9361	1.010	1.097	10.2
TG2-a20	1.0215	1.0080	0.9705	1.013	1.039	5.1
TG2-a21	1.0428	1.0263	0.9309	1.016	1.103	11.3
TG2-a23	1.0413	1.0094	0.9493	1.032	1.063	9.2
TG2-a24	1.0367	1.0209	0.9424	1.016	1.083	9.5
TG2-a25	1.0373	1.0186	0.9440	1.018	1.079	9.4
TG2-a26	1.0323	1.0190	0.9487	1.013	1.074	8.4
TG2-a27	1.0401	1.0201	0.9397	1.020	1.086	10.1
TG2-a28	1.0322	1.0212	0.9466	1.011	1.079	8.7

Takidani Granite, Block TG2, tAMS

Core	Bulk susceptibility (SI)	Porosity (%)	Maximum (degrees)		Intermediate (degrees)		Minimum (degrees)	
			Trend	Plunge	Trend	Plunge	Trend	Plunge
TG2-a6	31150	0.29	166	44	300	36	50	25
TG2-a7	25700	0.24	308	33	175	46	55	25
TG2-a8	30900	0.35	299	26	179	46	48	33
TG2-a9	31300	0.34	145	6	244	56	51	33
TG2-a14	12320	0.34	159	26	289	53	56	25
TG2-a15	33060	0.40	170	19	289	54	69	29
TG2-a16	14290	0.29	258	69	154	5	62	21
TG2-a17	12660	0.28	314	39	173	44	62	21
TG2-a18	14860	0.37	324	10	211	66	58	21
TG2-a21	14210	0.12	260	65	145	11	51	22
TG2-a23	28650	0.26	156	16	269	54	55	31
TG2-a24	29800	0.18	327	2	233	59	58	31
TG2-a25	30700	0.31	158	18	268	47	54	37
TG2-a29	16550	0.28	286	75	162	8	70	12

...continued

Core	Principal susceptibilities (normalised to bulk susceptibility)			L	F	P (%)
	Maximum	Intermediate	Minimum			
TG2-a6	1.0297	1.0252	0.9451	1.004	1.085	8.9
TG2-a7	1.0309	1.0225	0.9466	1.008	1.080	8.9
TG2-a8	1.0338	1.0173	0.9489	1.016	1.072	8.9
TG2-a9	1.0361	1.0217	0.9422	1.014	1.084	10.0
TG2-a14	1.0263	1.0152	0.9586	1.011	1.059	7.1
TG2-a15	1.0426	1.0169	0.9405	1.025	1.081	10.9
TG2-a16	1.0217	1.0113	0.9670	1.010	1.046	5.7
TG2-a17	1.0239	1.0161	0.9600	1.008	1.058	6.7
TG2-a18	1.0244	1.0172	0.9585	1.007	1.073	8.0
TG2-a21	1.0429	1.0137	0.9433	1.029	1.075	10.6
TG2-a23	1.0398	1.0057	0.9545	1.034	1.054	8.9
TG2-a24	1.0359	1.0171	0.9470	1.018	1.074	9.4
TG2-a25	1.0357	1.0147	0.9496	1.021	1.069	9.1
TG2-a29	1.0479	0.9999	0.9522	1.048	1.050	10.1

Takidani Granite, Block TG2, tAMS-mAMS

Core	Bulk susceptibility (SI)	Porosity (%)	Maximum (degrees)		Intermediate (degrees)		Minimum (degrees)	
			Trend	Plunge	Trend	Plunge	Trend	Plunge
TG2-a6	4161	0.26	92	75	307	12	215	8
TG2-a7	3564	0.24	109	75	276	15	7	3
TG2-a8	5090	0.35	227	63	111	12	16	24
TG2-a9	5010	0.34	220	60	113	9	18	28
TG2-a14	4919	0.18	147	55	332	35	240	2
TG2-a15	5769	0.34	188	30	329	54	87	19
TG2-a16	4305	0.29	27	90	168	0	258	0
TG2-a17	4080	0.28	160	76	355	14	264	4
TG2-a18	5416	0.37	144	62	327	28	236	1
TG2-a23	3800	0.40	110	27	223	37	254	41
TG2-a24	2571	0.29	278	1	188	22	10	68
TG2-a25	4466	0.31	181	11	279	39	78	49

...continued

Core	Principal susceptibilities (normalised to bulk susceptibility)			L	F	P (%)
	Maximum	Intermediate	Minimum			
TG2-a6	1.0523	0.9855	0.9622	1.068	1.024	9.4
TG2-a7	1.0393	0.9914	0.9692	1.048	1.023	7.2
TG2-a8	1.0238	1.0047	0.9715	1.019	1.034	5.4
TG2-a9	1.0206	1.0131	0.9663	1.007	1.048	5.6
TG2-a14	1.0371	0.9952	0.9676	1.042	1.029	7.2
TG2-a15	1.0360	1.0007	0.9633	1.035	1.039	7.6
TG2-a16	1.0130	1.0027	0.9844	1.010	1.019	2.9
TG2-a17	1.0197	1.0112	0.9690	1.008	1.044	5.2
TG2-a18	1.0280	1.0029	0.9691	1.025	1.035	6.1
TG2-a23	1.0900	0.9776	0.9324	1.115	1.048	16.9
TG2-a24	1.0664	1.0209	0.9127	1.045	1.119	16.8
TG2-a25	1.0360	0.9903	0.9737	1.046	1.017	6.4

C. AZIMUTHAL VELOCITY DATA

C.1. BENTHEIM SANDSTONE

Bentheim Sandstone	Sample radial P-wave velocity, m/s.								
Vp: DRY	Absolute error 1%; relative error 0.5%.								
Angle (degrees)	BS2-1	BS2-2	BS2-3	BS2-4	BS2-5	BS2-6	BS2-7	BS2-9	BS2-10
0	2885.7	2844.0	2894.2	2843.1	2895.7	2890.7	3103.4	3094.8	3071.8
10	2890.1	2863.7	2924.0	2831.7	2910.7	2896.8	3092.6	3097.7	3076.1
20	2910.2	2877.7	2933.8	2876.2	2953.8	2926.3	3102.1	3091.2	3118.3
30	2908.7	2896.3	2957.9	2896.7	2998.9	2934.1	3089.3	3097.1	3124.1
40	2916.2	2910.5	2980.8	2945.8	3087.2	2963.1	3061.5	3098.2	3105.8
50	2945.0	2935.5	3001.0	2981.0	3119.1	2990.4	3047.1	3092.5	3086.2
60	2967.3	2957.7	3025.5	3035.8	3141.2	3013.2	3047.1	3070.3	3084.5
70	2996.2	3000.8	3052.9	3066.6	3167.3	3026.9	3027.2	3063.6	3073.0
80	3030.1	3020.3	3060.4	3099.3	3181.7	3039.7	3024.1	3068.6	3055.8
90	3045.5	3016.9	3062.0	3104.0	3188.6	3042.5	3015.4	3067.4	3041.6
100	3039.2	2987.9	3037.8	3103.1	3182.6	3024.4	3017.1	3055.7	3041.5
110	3000.8	2959.8	3009.3	3095.2	3167.0	2993.3	3018.7	3054.2	3043.2
120	2957.3	2936.4	2992.2	3040.2	3127.9	2980.4	3029.3	3036.3	3044.8
130	2947.6	2898.2	2978.4	2998.5	3103.9	2982.1	3046.5	3026.4	3046.5
140	2922.9	2885.2	2956.4	2938.2	3084.4	2959.1	3053.6	3024.6	3048.2
150	2913.4	2889.2	2937.0	2890.2	3039.2	2913.0	3074.0	3048.2	3054.8
160	2920.7	2882.5	2914.7	2878.2	2963.6	2865.8	3093.5	3082.2	3070.0
170	2933.1	2883.1	2909.6	2852.2	2868.4	2867.7	3100.2	3104.7	3076.4
180	2934.3	2886.6	2910.5	2849.2	2981.1	2901.1	3108.2	3123.2	3101.3
190	2930.2	2871.2	2938.4	2851.2	2997.0	2910.5	3106.0	3126.4	3103.2
200	2949.2	2897.2	2958.8	2862.3	3020.0	2925.9	3092.5	3115.5	3117.8
210	2953.2	2909.6	2964.8	2892.4	3071.1	2941.8	3076.3	3107.2	3122.5
220	2948.4	2930.7	2988.6	2918.8	3089.8	2984.7	3049.5	3095.2	3112.9
230	2969.0	2945.2	3000.6	2954.8	3122.0	3013.8	3031.0	3084.9	3085.2
240	2977.0	2962.7	3022.4	2998.2	3129.1	3025.3	3020.7	3066.5	3078.0
250	3000.5	3012.9	3054.2	3036.9	3146.6	3043.3	3024.8	3060.4	3068.8
260	3040.4	3025.5	3063.2	3085.5	3180.8	3061.5	3024.1	3065.6	3057.5
270	3050.0	3024.7	3057.4	3096.5	3167.2	3069.0	3015.4	3061.5	3039.9
280	3033.8	2996.9	3042.0	3107.8	3158.4	3040.5	3017.1	3055.7	3041.5
290	2987.7	2961.2	3007.2	3086.9	3167.0	3024.4	3018.7	3054.2	3043.2
300	2955.0	2935.9	2987.6	3057.0	3127.9	2992.8	3066.8	3036.3	3044.9
310	2941.5	2912.2	2966.8	3005.0	3103.9	2982.1	3086.6	3031.2	3046.5
320	2922.6	2892.4	2950.0	2954.4	3084.4	2962.8	3095.1	3023.0	3048.2
330	2888.7	2892.3	2941.3	2909.6	3039.1	2929.1	3102.1	3052.1	3057.7
340	2891.5	2885.6	2922.8	2867.8	2963.6	2877.5	3096.0	3073.0	3056.7
350	2894.3	2862.8	2889.7	2854.9	2861.1	2844.7	3091.6	3089.6	3068.4

Bentheim Sandstone	Sample radial S-wave velocity (Mode A), m/s.								
Vs_A: DRY	Absolute error 1%; relative error 0.5%.								
Angle (degrees)	BS2-1	BS2-2	BS2-3	BS2-4	BS2-5	BS2-6	BS2-7	BS2-9	BS2-10
0	1926.7	2058.3	1891.1	1929.8	2006.9	2033.3	2036.1	2041.6	2035.8
10	1945.2	2061.2	1899.1	1933.8	2010.7	2027.2	2043.1	2023.7	2034.4
20	1944.7	2072.3	1910.8	1916.6	2019.6	2024.9	2044.2	2048.6	2025.9
30	1953.4	2072.1	1906.7	1917.1	2015.1	2054.4	2053.4	2057.7	2029.4
40	1956.1	2082.4	1901.0	1917.8	2017.4	2063.4	2066.4	2056.7	2032.9
50	1975.8	2085.5	1917.7	1925.5	2016.4	2076.9	2057.3	2050.1	2028.4
60	1978.5	2098.9	1925.8	1928.1	2011.5	2085.1	2054.3	2046.8	2017.1
70	1990.6	2106.4	1941.9	1946.3	2010.5	2097.7	2035.2	2047.6	2019.5
80	1999.2	2131.0	1952.5	1936.2	2011.5	2113.9	2066.7	2056.5	2010.3
90	2011.7	2140.9	1959.6	1913.0	2003.6	2128.2	2056.3	2052.1	2003.8
100	2018.2	2136.7	1975.1	1903.4	1999.9	2103.7	2026.0	2043.2	2011.0
110	2009.7	2123.4	1968.4	1906.2	1985.2	2094.1	2029.9	2056.2	2025.3
120	2000.7	2131.2	1968.5	1908.3	1967.0	2090.6	2017.8	2042.9	2027.8
130	1997.6	2125.6	1969.1	1902.1	1943.9	2076.6	2045.6	2060.0	2025.5
140	1983.2	2102.3	1961.8	1903.1	1935.8	2030.6	2063.9	2063.0	2021.0
150	1967.2	2078.4	1951.8	1904.1	1921.7	2029.6	2049.7	2076.1	2012.8
160	1960.5	2052.7	1936.5	1914.0	1958.9	2020.8	2062.2	2048.8	2013.4
170	1959.5	2033.4	1927.5	1921.9	1998.2	2023.1	2028.2	2063.9	2007.3
180	1978.9	2036.5	1912.1	1917.8	2003.1	2006.6	2037.4	2041.6	2013.7
190	1962.3	2032.9	1913.0	1923.7	2015.8	2029.1	2025.4	2023.7	2012.1
200	1947.6	2048.0	1926.7	1931.8	2016.5	2004.4	2039.3	2048.6	2018.3
210	1932.4	2055.3	1926.2	1929.6	2022.1	2029.3	2059.0	2057.6	2013.9
220	1933.4	2064.4	1928.9	1939.5	2018.8	2054.7	2075.8	2056.7	2019.2
230	1941.5	2068.3	1937.9	1925.5	2016.5	2057.9	2084.0	2050.1	2022.5
240	1963.9	2073.5	1927.3	1924.5	2017.5	2069.4	2063.0	2046.8	2015.0
250	1969.5	2086.9	1937.0	1920.7	2012.2	2104.8	2084.0	2047.7	2017.6
260	2001.2	2094.1	1946.5	1942.5	2015.0	2123.4	2043.1	2056.4	2013.9
270	2005.3	2117.0	1974.0	1959.5	1999.9	2133.4	2015.2	2052.0	2005.4
280	2012.8	2117.8	1959.3	1944.7	1994.9	2121.0	2003.3	2043.2	2012.8
290	2001.0	2104.0	1953.7	1929.2	1986.4	2113.3	2029.8	2056.2	2010.5
300	2001.2	2105.4	1919.4	1919.3	1983.6	2094.8	2083.5	2044.6	2020.8
310	1997.1	2102.3	1915.3	1911.4	1952.4	2073.6	2046.7	2049.5	2012.6
320	1977.5	2091.0	1906.5	1906.4	1930.6	2058.2	2034.9	2058.8	2019.1
330	1964.4	2062.0	1894.3	1913.1	1935.4	2042.9	2043.2	2052.0	2018.8
340	1945.6	2030.9	1893.4	1914.0	1971.9	2035.6	2031.0	2048.8	2009.5
350	1938.1	2029.7	1902.6	1915.3	1994.2	2022.6	2037.0	2063.9	2006.3

Bentheim Sandstone	Sample radial S-wave velocity (Mode B), m/s.								
V_{SB}: DRY	Absolute error 1%; relative error 0.5%.								
Angle (degrees)	BS2-1	BS2-2	BS2-3	BS2-4	BS2-5	BS2-6	BS2-7	BS2-8	BS2-10
0	1965.7	1965.0	1954.6	1917.2	1971.8	1953.7	2036.1	2055.2	2035.8
10	1969.2	1991.3	1952.7	1916.7	1981.8	1948.5	2043.5	2050.5	2034.9
20	1982.8	2004.9	1965.8	1923.9	1982.1	1940.5	2045.2	2034.9	2026.8
30	2006.0	2020.8	1951.8	1929.8	1989.4	1970.8	2054.8	2026.3	2030.8
40	1995.0	2037.7	1969.8	1937.8	1983.3	1983.9	2068.3	2029.5	2034.8
50	2006.7	2024.7	1988.7	1947.4	1986.4	1995.0	2059.6	2024.1	2030.7
60	2048.2	2038.7	1992.9	1962.9	1995.7	1993.1	2057.1	2020.4	2019.8
70	2034.8	2020.8	2012.5	1974.8	2005.1	2010.1	2038.5	2015.8	2022.8
80	2031.2	2013.9	2021.8	1998.2	2016.0	2019.7	2070.4	2019.1	2014.0
90	2047.5	2025.1	2022.4	2011.2	2032.4	2022.7	2060.6	2026.5	2007.9
100	2074.6	2010.4	2022.9	2023.2	2045.4	2045.6	2029.8	2038.9	2014.8
110	2043.2	2013.5	2027.3	2032.3	2056.7	2031.9	2033.1	2033.3	2028.5
120	2052.5	2021.2	2020.6	1992.1	2041.9	2029.0	2020.6	2041.2	2030.6
130	2043.3	2009.4	2020.9	2009.4	2024.9	2004.8	2048.0	2046.8	2027.8
140	2035.1	1993.1	2003.4	1988.0	2044.8	2001.5	2065.8	2061.8	2022.9
150	2018.3	1977.9	1981.4	1976.9	2013.1	1986.5	2051.1	2054.8	2014.2
160	2008.4	1991.5	1967.2	1960.6	2017.4	1976.3	2063.1	2037.5	2014.4
170	1984.3	1964.4	1974.8	1947.3	2008.0	1970.0	2028.6	2024.0	2007.7
180	1995.0	1956.2	1957.0	1947.9	2000.2	1960.1	2037.4	2029.6	2013.7
190	2007.8	1967.1	1940.0	1940.5	1988.7	1966.6	2025.9	2037.0	2012.6
200	2008.5	1969.7	1948.7	1951.1	1966.1	1953.6	2040.2	2040.4	2019.3
210	2011.2	1986.8	1946.9	1956.4	1980.0	1961.9	2060.4	2034.0	2015.3
220	2024.3	1996.5	1951.8	1962.2	1998.0	1964.8	2077.6	2033.7	2021.0
230	2042.4	2008.1	1962.0	1967.0	2007.3	2002.4	2086.4	2039.0	2024.8
240	2045.0	2022.0	1983.7	1983.0	2005.0	1990.7	2065.8	2040.5	2017.8
250	2063.3	2038.9	2006.3	1995.4	2011.8	2011.3	2087.3	2023.0	2020.8
260	2064.7	2031.6	2014.3	2007.7	2020.8	2022.9	2046.8	2020.5	2017.6
270	2061.6	2023.8	1997.0	2006.0	2031.9	2042.9	2019.3	2016.7	2009.5
280	2080.6	2033.4	2014.9	2024.8	2042.0	2051.2	2007.0	2026.8	2016.5
290	2070.7	2034.6	2010.7	2034.8	2057.5	2022.6	2033.1	2035.4	2013.7
300	2059.1	2021.5	2005.8	2010.6	2038.8	2005.4	2086.4	2025.9	2023.6
310	2056.5	2004.9	2006.3	1984.1	2003.4	2010.1	2049.1	2020.3	2014.9
320	2041.1	1996.1	1997.1	1952.4	1993.1	2005.0	2036.7	2005.3	2021.0
330	2031.9	1983.3	1994.0	1928.9	1988.5	1981.9	2044.6	2012.6	2020.2
340	2001.8	1990.4	2001.8	1927.1	1982.1	1968.0	2032.0	2019.1	2010.4
350	1977.3	1987.1	1991.0	1924.5	1979.0	1962.2	2037.5	2036.3	2006.8

Bentheim Sandstone	Sample radial elastic-wave velocity, m/s.								
Averages:	Absolute error 1%; relative error 0.5%.								
DRY	Vp: Plane			Vs_A: Plane			Vs_B: Plane		
Angle (degrees)	YZ	XZ	XY	YZ	XZ	XY	YZ	XZ	XY
0	2874.6	2876.5	3090.0	1958.7	1990.0	2037.8	1961.7	1947.6	2042.4
10	2892.6	2879.8	3088.8	1968.5	1990.5	2033.7	1971.1	1949.0	2043.0
20	2907.2	2918.8	3103.9	1975.9	1987.0	2039.6	1984.5	1948.8	2035.6
30	2921.0	2943.2	3103.5	1977.4	1995.5	2046.8	1992.8	1963.4	2037.3
40	2935.9	2998.7	3088.5	1979.8	1999.5	2052.0	2000.8	1968.3	2044.2
50	2960.5	3030.2	3075.2	1993.0	2006.3	2045.3	2006.7	1976.3	2038.1
60	2983.5	3063.4	3067.3	2001.1	2008.2	2039.4	2026.6	1983.9	2032.4
70	3016.6	3086.9	3054.6	2012.9	2018.2	2034.1	2022.7	1996.6	2025.7
80	3036.9	3106.9	3049.5	2027.5	2020.5	2044.5	2022.3	2011.3	2034.5
90	3041.5	3111.7	3041.5	2037.4	2014.9	2037.4	2031.7	2022.1	2031.7
100	3021.7	3103.4	3038.1	2043.4	2002.3	2026.8	2035.9	2038.1	2027.8
110	2990.0	3085.2	3038.7	2033.8	1995.2	2037.1	2028.0	2040.3	2031.7
120	2962.0	3049.5	3036.8	2033.5	1988.6	2029.5	2031.5	2021.0	2030.8
130	2941.4	3028.2	3039.8	2030.7	1974.2	2043.7	2024.5	2013.0	2040.9
140	2921.5	2993.9	3042.1	2015.8	1956.5	2049.3	2010.5	2011.4	2050.2
150	2913.2	2947.4	3059.0	1999.1	1951.8	2046.2	1992.5	1992.2	2040.1
160	2905.9	2902.6	3081.9	1983.2	1964.5	2041.5	1989.0	1984.8	2038.3
170	2908.6	2862.8	3093.8	1973.5	1981.1	2033.1	1974.5	1975.1	2020.1
180	2910.5	2910.5	3110.9	1975.8	1975.8	2030.9	1969.4	1969.4	2026.9
190	2913.2	2919.6	3111.9	1969.4	1989.5	2020.4	1971.6	1965.3	2025.2
200	2935.1	2936.1	3108.6	1974.1	1984.2	2035.4	1975.7	1957.0	2033.3
210	2942.5	2968.4	3102.0	1971.3	1993.6	2043.5	1981.6	1966.1	2036.6
220	2955.9	2997.8	3085.9	1975.6	2004.3	2050.6	1990.9	1975.0	2044.1
230	2971.6	3030.2	3067.0	1982.6	1999.9	2052.2	2004.2	1992.2	2050.1
240	2987.4	3050.8	3055.0	1988.2	2003.8	2041.6	2016.9	1992.9	2041.4
250	3022.5	3075.6	3051.3	1997.8	2012.6	2049.8	2036.2	2006.2	2043.7
260	3043.0	3109.3	3049.1	2013.9	2027.0	2037.8	2036.9	2017.1	2028.3
270	3044.0	3110.9	3038.9	2032.1	2030.9	2024.2	2027.5	2026.9	2015.2
280	3024.3	3102.2	3038.1	2030.0	2020.2	2019.7	2043.0	2039.3	2016.8
290	2985.4	3092.8	3038.7	2019.6	2009.7	2032.2	2038.7	2038.3	2027.4
300	2959.5	3059.2	3049.3	2008.7	1999.2	2049.6	2028.8	2018.2	2045.3
310	2940.2	3030.4	3054.8	2004.9	1979.1	2036.3	2022.6	1999.2	2028.1
320	2921.7	3000.5	3055.4	1991.6	1965.1	2037.6	2011.4	1983.5	2021.0
330	2907.4	2959.3	3070.6	1973.6	1963.8	2038.0	2003.1	1966.4	2025.8
340	2900.0	2903.0	3075.2	1956.7	1973.8	2029.8	1998.0	1959.1	2020.5
350	2882.2	2853.6	3083.2	1956.8	1977.4	2035.7	1985.2	1955.2	2026.8

Bentheim Sandstone	Sample radial P-wave velocity, m/s.								
Vp: SATURATED	Absolute error 1%; relative error 0.5%.								
Angle (degrees)	BS2-1	BS2-2	BS2-3	BS2-4	BS2-5	BS2-6	BS2-7	BS2-9	BS2-10
0	3764.8	3797.7	3813.5	3777.1	3791.3	3792.9	3899.6	3925.4	3954.7
10	3753.2	3778.7	3799.7	3780.8	3761.8	3778.9	3880.8	3930.7	3951.9
20	3757.7	3781.4	3805.4	3809.9	3794.7	3818.3	3863.5	3912.2	3940.5
30	3786.4	3759.6	3764.1	3829.4	3810.6	3832.5	3858.8	3921.1	3946.3
40	3793.6	3798.5	3765.6	3855.0	3847.2	3857.7	3860.4	3921.1	3954.1
50	3806.5	3806.9	3797.0	3878.6	3863.6	3899.2	3868.7	3907.9	3937.8
60	3806.5	3825.4	3830.0	3909.3	3880.5	3913.3	3854.1	3871.7	3933.8
70	3821.1	3816.1	3841.7	3929.1	3897.3	3939.7	3838.5	3859.5	3897.9
80	3840.8	3825.7	3853.0	3930.3	3902.9	3949.9	3824.2	3863.9	3872.9
90	3837.7	3852.9	3854.5	3942.2	3901.3	3945.9	3819.9	3840.5	3884.8
100	3849.0	3838.5	3869.1	3928.7	3878.2	3936.8	3834.2	3833.1	3871.7
110	3853.0	3837.3	3871.1	3903.7	3870.7	3919.0	3840.4	3828.1	3871.7
120	3847.5	3826.0	3887.1	3875.8	3832.9	3883.3	3839.2	3818.4	3872.1
130	3809.5	3807.6	3871.6	3814.4	3825.6	3864.8	3841.6	3826.9	3877.6
140	3825.3	3823.0	3857.0	3824.4	3793.5	3829.0	3828.3	3857.9	3890.6
150	3787.8	3795.0	3824.3	3778.2	3759.1	3804.6	3841.5	3884.7	3903.0
160	3778.7	3764.0	3820.8	3770.3	3770.3	3786.8	3862.3	3869.2	3914.6
170	3777.2	3759.9	3787.1	3780.8	3770.7	3771.8	3861.5	3891.0	3923.4
180	3780.3	3765.5	3783.3	3783.8	3782.7	3762.5	3876.0	3934.7	3914.5
190	3800.1	3773.8	3767.4	3804.6	3770.3	3770.3	3878.5	3912.5	3926.3
200	3809.6	3765.9	3788.2	3794.0	3756.9	3800.4	3874.1	3932.4	3933.6
210	3809.6	3795.1	3792.8	3821.7	3794.7	3817.1	3871.4	3939.3	3934.5
220	3801.5	3803.5	3801.2	3852.7	3811.4	3842.9	3861.2	3943.9	3934.1
230	3808.4	3815.0	3814.2	3878.6	3827.8	3870.7	3849.4	3911.1	3915.5
240	3817.6	3812.3	3820.0	3903.3	3841.8	3889.7	3844.0	3890.3	3905.1
250	3837.4	3830.8	3835.8	3914.5	3881.0	3889.7	3828.4	3845.5	3902.3
260	3842.0	3843.6	3856.5	3903.3	3892.1	3911.3	3811.5	3868.2	3911.5
270	3850.6	3849.0	3867.9	3906.2	3906.6	3912.6	3810.7	3858.8	3895.1
280	3853.8	3839.7	3849.0	3908.9	3893.7	3912.9	3809.5	3839.7	3887.9
290	3854.5	3853.4	3847.1	3896.9	3869.1	3906.1	3809.5	3839.3	3886.3
300	3845.1	3838.9	3876.3	3867.5	3858.9	3871.5	3826.1	3847.0	3889.1
310	3856.2	3835.8	3855.8	3825.2	3851.9	3802.6	3840.4	3857.1	3880.3
320	3841.3	3824.5	3876.8	3793.9	3817.9	3791.7	3845.5	3867.3	3894.2
330	3818.8	3798.0	3855.9	3767.7	3787.9	3749.9	3843.9	3896.2	3907.4
340	3811.5	3783.6	3844.5	3773.3	3744.8	3748.8	3861.1	3883.8	3909.0
350	3807.3	3789.3	3824.3	3760.0	3723.6	3741.9	3867.0	3908.5	3920.6

Bentheim Sandstone	Sample radial S-wave velocity (Mode A), m/s.								
Vs_A: SATURATED	Absolute error 1%; relative error 0.5%.								
Angle (degrees)	BS2-1	BS2-2	BS2-3	BS2-4	BS2-5	BS2-6	BS2-7	BS2-9	BS2-10
0	1912.4	1900.8	1915.0	1880.2	1879.2	1866.1	1926.4	2027.5	1939.4
10	1900.5	1901.4	1897.5	1878.9	1895.5	1877.8	1932.9	2033.6	1950.3
20	1892.4	1911.1	1885.6	1866.2	1879.0	1887.4	1945.5	2035.4	1952.1
30	1894.9	1906.7	1887.5	1885.2	1889.3	1885.0	1954.6	2037.3	1972.2
40	1903.3	1969.6	1876.7	1895.5	1899.6	1896.8	1960.0	2047.0	1970.3
50	1936.9	1958.1	1913.1	1887.1	1910.6	1910.4	1961.7	2056.9	1968.4
60	1947.4	1949.2	1952.4	1920.0	1912.9	1913.0	1963.6	2046.8	1962.9
70	1956.3	1977.5	1965.0	1951.9	1923.4	1912.1	1958.0	2044.7	1972.1
80	1955.5	1988.4	1983.7	1966.0	1969.9	1910.2	1941.7	2042.3	1970.2
90	1960.5	2007.6	1988.0	1975.0	1928.1	1927.8	1943.5	2040.6	1972.0
100	1957.5	2016.7	1982.8	1963.1	1937.9	1943.7	1941.8	2030.9	1959.3
110	1944.7	1993.2	1989.8	1928.8	1931.3	1920.5	1925.8	2033.1	1950.4
120	1938.2	2010.3	2007.5	1945.9	1920.9	1910.4	1924.1	2023.4	1941.4
130	1935.1	1979.2	1994.6	1934.3	1925.6	1918.8	1925.8	2013.8	1946.8
140	1879.6	1976.1	1990.9	1921.8	1911.3	1906.9	1917.0	2015.7	1941.3
150	1867.8	1909.5	1969.5	1898.5	1910.5	1928.0	1925.8	2006.2	1928.9
160	1880.8	1908.7	1882.5	1910.7	1907.3	1912.2	1902.9	2000.5	1930.7
170	1883.7	1906.1	1896.2	1913.8	1906.8	1914.9	1908.1	1991.1	1939.6
180	1898.7	1901.4	1907.5	1891.8	1910.9	1904.9	1899.4	2004.4	1927.1
190	1903.3	1909.6	1883.6	1900.3	1925.1	1898.0	1908.1	1998.6	1950.4
200	1909.8	1933.6	1889.5	1885.1	1892.6	1898.9	1924.0	1996.7	1952.2
210	1887.7	1970.2	1878.4	1888.3	1899.3	1900.0	1943.6	2002.3	1972.2
220	1910.1	1969.8	1914.8	1869.6	1896.2	1893.7	1931.1	2008.0	1970.4
230	1937.1	1958.3	1954.2	1901.2	1898.2	1921.8	1950.9	2006.0	1968.5
240	1947.4	1949.3	1966.7	1920.0	1912.9	1913.0	1917.0	2015.6	1963.0
250	1956.5	1977.6	1992.5	1951.9	1923.4	1912.1	1925.7	2044.8	1972.1
260	1955.5	1988.4	1983.7	1966.0	1969.9	1910.2	1934.6	2042.3	1970.2
270	1960.5	2007.6	1988.0	1975.0	1928.1	1927.8	1922.2	2040.7	1972.1
280	1957.5	2016.7	1982.8	1963.1	1937.9	1943.7	1913.5	2031.0	1959.4
290	1944.7	1993.2	1989.8	1928.8	1931.3	1920.5	1904.9	2033.1	1950.4
300	1938.2	2010.3	2007.5	1945.9	1920.9	1910.4	1920.6	2023.4	1941.4
310	1935.1	1979.2	1994.6	1934.3	1877.7	1918.7	1922.3	2013.8	1946.8
320	1922.9	1976.2	1991.0	1874.0	1888.6	1906.8	1906.5	2015.7	1941.3
330	1947.6	1909.8	1969.9	1866.4	1874.9	1914.1	1911.7	1991.0	1928.9
340	1915.3	1917.1	1972.7	1882.7	1869.7	1904.8	1920.4	1993.0	1930.7
350	1899.9	1908.9	1927.2	1882.2	1883.3	1907.4	1922.2	1994.8	1937.9

Bentheim Sandstone	Sample radial S-wave velocity (Mode B), m/s.								
V_{SB}: SATURATED	Absolute error 1%; relative error 0.5%.								
Angle (degrees)	BS2-1	BS2-2	BS2-3	BS2-4	BS2-5	BS2-6	BS2-7	BS2-9	BS2-10
0	1972.6	1938.7	1860.4	1909.6	1931.0	1920.1	1955.5	1979.3	1995.4
10	1980.7	1924.4	1874.5	1898.5	1927.0	1912.6	1952.8	1981.6	1997.6
20	1962.0	1932.1	1864.6	1901.7	1930.1	1898.1	1946.4	1971.0	2006.3
30	1958.6	1932.5	1861.6	1919.0	1940.7	1894.2	1963.8	1973.4	2011.1
40	1966.6	1944.0	1875.7	1925.7	1951.4	1911.3	1973.0	1979.4	2019.0
50	1978.5	1951.9	1879.5	1939.9	1954.6	1903.9	1965.4	1985.8	2021.7
60	1986.7	1959.9	1879.9	1958.0	1954.2	1921.2	1967.5	1975.9	2003.4
70	1990.9	1975.4	1897.8	1961.3	1961.3	1946.4	1978.0	1967.2	2011.4
80	2007.1	1983.6	1908.9	1968.4	1968.3	1943.2	1961.2	1978.1	2001.7
90	2019.4	1995.6	1912.9	1964.2	1964.2	1960.4	1966.5	1955.9	2005.6
100	2014.9	1983.5	1919.7	1968.4	1964.6	1953.4	1976.7	1950.0	2006.9
110	2022.6	1967.8	1912.1	1961.3	1968.7	1950.0	1975.8	1964.0	2009.6
120	2018.2	1971.2	1911.7	1954.2	1961.7	1946.8	1962.7	1976.7	2015.9
130	2005.9	1963.2	1904.2	1947.2	1954.6	1928.9	1948.4	1964.4	2007.7
140	1989.7	1955.2	1886.1	1936.6	1943.9	1933.0	1952.1	1962.2	1992.5
150	1989.3	1951.1	1885.7	1926.1	1929.7	1926.1	1942.6	1965.3	1974.7
160	1973.4	1932.1	1881.9	1923.0	1926.6	1915.8	1946.8	1982.6	1978.3
170	1984.6	1913.4	1881.5	1930.6	1916.2	1919.7	1944.8	1969.0	1964.4
180	1972.6	1924.0	1860.4	1916.6	1931.0	1909.5	1950.8	1962.8	1979.2
190	1980.7	1913.4	1864.2	1909.2	1919.8	1916.2	1949.0	1963.2	1959.9
200	1962.0	1932.1	1871.5	1919.4	1926.6	1919.3	1944.2	1973.2	1965.4
210	1973.9	1936.2	1878.7	1937.0	1937.0	1933.4	1957.0	1964.6	1961.8
220	1978.1	1947.8	1893.2	1940.3	1947.6	1943.9	1953.6	1968.7	1962.8
230	1974.7	1955.6	1890.1	1936.2	1947.2	1947.2	1950.8	1963.8	1975.9
240	1994.5	1963.6	1901.0	1943.1	1950.5	1957.9	1949.6	1953.2	1972.8
250	2006.7	1975.4	1912.1	1953.8	1953.8	1957.5	1946.4	1962.8	1980.9
260	2007.0	1991.3	1923.4	1960.9	1968.3	1972.2	1952.7	1978.1	1978.1
270	2011.4	2007.4	1916.5	1971.8	1975.5	1945.6	1965.7	1955.8	1980.2
280	2019.0	2003.1	1934.3	1975.9	1964.6	1946.0	1950.0	1950.0	1977.2
290	2022.6	1994.8	1926.6	1961.3	1953.8	1935.4	1958.3	1964.0	1981.0
300	2010.1	2002.3	1911.7	1932.2	1939.5	1921.3	1953.3	1976.7	1981.5
310	2001.8	1982.3	1904.2	1911.1	1932.6	1893.4	1952.8	1964.4	1983.5
320	1997.5	1966.6	1886.1	1922.2	1918.5	1890.3	1961.2	1962.2	1978.6
330	1989.3	1954.8	1885.7	1915.4	1908.3	1901.2	1947.9	1965.3	1973.9
340	1973.4	1939.5	1881.9	1898.1	1905.2	1898.1	1952.3	1963.5	1981.2
350	1984.6	1931.7	1881.5	1906.5	1916.2	1905.6	1945.3	1962.6	1979.2

Bentheim Sandstone Averages:	Sample radial elastic-wave velocity, m/s. Absolute error 1%; relative error 0.5%.								
SATURATED	Vp: Plane			Vs_A: Plane			Vs_B: Plane		
Angle (degrees)	YZ	XZ	XY	YZ	XZ	XY	YZ	XZ	XY
0	3792.0	3787.1	3926.6	1909.4	1875.2	1964.4	1923.9	1920.2	1976.7
10	3777.2	3773.8	3921.2	1899.8	1884.1	1972.3	1926.5	1912.7	1977.3
20	3781.5	3807.6	3905.4	1896.4	1877.5	1977.7	1919.6	1910.0	1974.6
30	3770.0	3824.2	3908.7	1896.4	1886.5	1988.0	1917.6	1918.0	1982.8
40	3785.9	3853.3	3911.9	1916.6	1897.3	1992.4	1928.8	1929.5	1990.5
50	3803.5	3880.5	3904.8	1936.1	1902.7	1995.7	1936.6	1932.8	1991.0
60	3820.6	3901.0	3886.5	1949.7	1915.3	1991.1	1942.1	1944.5	1982.3
70	3826.3	3922.0	3865.3	1966.3	1929.1	1991.6	1954.7	1956.3	1985.5
80	3839.8	3927.7	3853.6	1975.9	1948.7	1984.7	1966.5	1960.0	1980.3
90	3848.4	3929.8	3848.4	1985.4	1943.6	1985.4	1976.0	1962.9	1976.0
100	3852.2	3914.6	3846.3	1985.7	1948.2	1977.3	1972.7	1962.1	1977.9
110	3853.8	3897.8	3846.7	1975.9	1926.9	1969.7	1967.5	1960.0	1983.1
120	3853.5	3864.0	3843.2	1985.3	1925.7	1962.9	1967.0	1954.2	1985.1
130	3829.6	3834.9	3848.7	1969.6	1926.2	1962.1	1957.7	1943.6	1973.5
140	3835.1	3815.7	3859.0	1948.8	1913.3	1958.0	1943.7	1937.8	1968.9
150	3802.4	3780.6	3876.4	1915.6	1912.3	1953.6	1942.0	1927.3	1960.9
160	3787.9	3775.8	3882.0	1890.7	1910.1	1944.7	1929.1	1921.8	1969.2
170	3774.8	3774.5	3892.0	1895.3	1911.8	1946.3	1926.5	1922.2	1959.4
180	3776.4	3776.4	3908.4	1902.5	1902.5	1943.6	1919.0	1919.0	1964.3
190	3780.4	3781.8	3905.8	1898.8	1907.8	1952.4	1919.4	1915.0	1957.4
200	3787.9	3783.8	3913.4	1911.0	1892.2	1957.6	1921.9	1921.8	1960.9
210	3799.1	3811.2	3915.1	1912.1	1895.9	1972.7	1929.6	1935.8	1961.1
220	3802.1	3835.7	3913.1	1931.6	1886.5	1969.8	1939.7	1943.9	1961.7
230	3812.5	3859.0	3892.0	1949.9	1907.1	1975.1	1940.1	1943.5	1963.5
240	3816.6	3878.2	3879.8	1954.5	1915.3	1965.2	1953.0	1950.5	1958.5
250	3834.6	3895.1	3858.7	1975.5	1929.1	1980.9	1964.7	1955.0	1963.3
260	3847.4	3902.3	3863.7	1975.9	1948.7	1982.4	1973.9	1967.1	1969.6
270	3855.8	3908.4	3854.9	1985.4	1943.6	1978.3	1978.4	1964.3	1967.2
280	3847.5	3905.2	3845.7	1985.7	1948.2	1968.0	1985.5	1962.2	1959.1
290	3851.7	3890.7	3845.0	1975.9	1926.9	1962.8	1981.3	1950.2	1967.8
300	3853.5	3866.0	3854.1	1985.3	1925.7	1961.8	1974.7	1931.0	1970.5
310	3849.2	3826.6	3859.3	1969.6	1910.2	1960.9	1962.8	1912.4	1966.9
320	3847.5	3801.2	3869.0	1963.4	1889.8	1954.5	1950.1	1910.3	1967.3
330	3824.2	3768.5	3882.5	1942.4	1885.1	1943.9	1943.2	1908.3	1962.4
340	3813.2	3755.6	3884.6	1935.0	1885.8	1948.0	1931.6	1900.5	1965.7
350	3807.0	3741.8	3898.7	1912.0	1891.0	1951.7	1932.6	1909.4	1962.4

C.2. CRAB ORCHARD SANDSTONE

Crab Orchard Sandstone Vp: DRY	Sample radial P-wave velocity, m/s. Absolute error 1%; relative error 0.5%.								
Angle (degrees)	TS1-17	TS1-18	TS1-19	TS1-21	TS1-22	TS1-23	TS1-25	TS1-26	TS1-27
0	3052.8	3085.1	2994.6	2527.0	2564.7	2554.4	2551.2	2526.9	2598.0
10	3013.8	3082.4	2981.8	2535.3	2605.3	2572.0	2555.5	2492.9	2605.9
20	3005.6	3071.8	3000.6	2560.1	2658.7	2612.7	2551.2	2511.2	2575.8
30	3019.7	3059.1	3005.8	2618.6	2735.1	2654.4	2577.2	2554.4	2590.1
40	3031.4	3035.3	2985.2	2668.3	2761.8	2714.3	2626.9	2604.8	2622.1
50	3041.0	3018.6	2994.8	2729.0	2853.0	2795.8	2687.3	2668.7	2677.4
60	3028.9	3021.4	2980.5	2827.2	2918.7	2853.0	2748.9	2715.6	2740.1
70	3016.1	3064.2	2947.7	2867.4	2961.4	2924.3	2819.7	2791.8	2805.5
80	3005.2	3016.7	2924.7	2929.2	3086.6	2971.7	2858.4	2865.8	2946.7
90	2980.3	3032.9	2941.6	3031.1	3069.3	3034.7	2917.9	2990.6	3046.3
100	3001.8	3037.7	2963.5	3105.9	3030.2	3055.4	2962.2	2944.2	3030.0
110	3003.1	3040.0	2954.3	3034.9	2873.0	3010.0	2910.1	2866.0	2940.4
120	3002.1	3063.5	2940.9	2875.0	2823.7	2906.3	2868.1	2817.1	2917.0
130	3025.1	3078.5	2956.8	2767.8	2757.2	2810.9	2816.0	2736.1	2866.1
140	3028.7	3088.8	2979.3	2687.9	2701.7	2745.8	2736.9	2644.6	2822.7
150	3043.6	3110.2	2978.7	2616.3	2666.6	2680.2	2687.0	2597.5	2767.3
160	3036.4	3139.4	2980.1	2576.0	2633.2	2630.4	2642.0	2582.9	2723.0
170	3024.6	3129.5	2992.4	2552.5	2600.3	2589.2	2592.5	2543.5	2658.6
180	3032.5	3107.6	3025.0	2514.1	2596.0	2584.8	2556.7	2536.7	2601.4
190	3037.7	3087.7	3028.0	2529.1	2638.8	2581.0	2540.9	2523.2	2585.8
200	3025.5	3077.0	3029.6	2558.7	2685.1	2592.7	2553.7	2533.4	2578.2
210	3038.0	3057.8	3006.5	2608.9	2722.1	2664.6	2579.7	2565.3	2582.3
220	3023.5	3036.5	3002.9	2655.6	2806.1	2721.2	2618.0	2614.3	2615.1
230	3044.9	3043.4	2990.8	2705.5	2884.0	2791.0	2681.4	2680.5	2680.3
240	3050.0	3035.6	2983.0	2796.7	2953.5	2843.1	2750.2	2752.2	2739.7
250	3044.3	3047.4	2971.1	2868.1	3010.7	2926.9	2813.9	2820.8	2790.6
260	2976.1	3024.1	2959.7	2921.9	3088.2	2963.3	2837.5	2893.3	2910.9
270	2998.1	3022.8	2943.9	2995.0	3117.0	3053.0	2900.0	3028.5	2970.4
280	3014.6	3066.0	2957.7	3093.3	3020.2	3030.7	2956.3	2948.9	3003.5
290	3024.7	3070.1	2965.3	3033.2	2948.1	2989.1	2926.2	2875.5	2950.2
300	3009.9	3085.1	2956.4	2863.5	2855.2	2889.2	2865.0	2853.1	2925.9
310	3032.8	3081.2	2972.1	2770.1	2775.2	2822.8	2812.9	2785.2	2879.8
320	3022.2	3100.9	2986.3	2699.6	2724.4	2745.2	2739.2	2692.1	2829.2
330	3037.0	3116.3	2985.7	2629.5	2676.8	2705.0	2685.0	2634.8	2774.9
340	3027.4	3141.5	2992.1	2564.0	2642.1	2644.8	2621.7	2608.7	2718.7
350	3033.1	3137.0	2995.7	2554.8	2594.3	2599.4	2588.3	2574.1	2659.8

Crab Orchard Sandstone Vs_A: *DRY*	Sample radial S-wave velocity (Mode A), m/s. Absolute error 1%; relative error 0.5%.								
Angle (degrees)	TS1-17	TS1-18	TS1-19	TS1-21	TS1-22	TS1-23	TS1-25	TS1-26	TS1-27
0	1944.9	1905.1	1881.5	1781.5	1803.0	1793.2	1777.0	1756.0	1798.2
10	1945.5	1903.4	1871.7	1771.9	1811.2	1792.4	1764.8	1762.1	1794.8
20	1954.8	1891.2	1864.9	1786.3	1838.5	1801.9	1756.7	1778.9	1780.7
30	1946.5	1884.1	1850.1	1792.8	1860.8	1816.4	1777.4	1794.3	1786.3
40	1947.7	1875.9	1844.6	1813.1	1878.8	1833.3	1799.0	1813.9	1798.0
50	1951.5	1861.7	1841.4	1838.9	1907.8	1849.0	1815.8	1852.4	1820.2
60	1949.1	1860.3	1846.4	1849.3	1938.0	1863.7	1840.5	1872.6	1832.2
70	1958.7	1864.3	1848.3	1867.5	1949.8	1889.0	1861.9	1888.5	1865.5
80	1940.5	1865.4	1850.7	1903.8	1973.3	1899.8	1860.8	1924.4	1902.7
90	1953.3	1883.1	1855.4	1903.1	1951.0	1896.5	1884.2	1915.8	1891.7
100	1955.1	1874.4	1849.1	1903.8	1957.3	1910.5	1902.2	1906.4	1915.4
110	1961.3	1875.5	1855.9	1903.7	1926.7	1880.9	1900.1	1903.4	1922.2
120	1980.4	1870.8	1864.6	1851.4	1896.0	1885.8	1891.0	1888.6	1919.5
130	1983.7	1871.8	1875.3	1832.9	1873.7	1872.7	1866.6	1855.7	1902.1
140	1990.9	1876.4	1892.9	1823.9	1855.0	1834.4	1849.1	1824.2	1889.0
150	1969.3	1880.0	1883.6	1797.1	1838.6	1828.0	1823.7	1807.2	1863.8
160	1981.1	1874.6	1887.3	1789.1	1839.5	1824.1	1812.4	1789.0	1852.6
170	1981.1	1879.7	1882.9	1773.0	1800.6	1801.9	1798.6	1777.4	1814.5
180	1976.0	1888.0	1889.1	1767.4	1803.3	1784.7	1784.6	1757.2	1813.5
190	1989.6	1900.4	1894.9	1774.6	1800.6	1782.2	1775.6	1768.1	1797.6
200	1994.4	1910.9	1896.4	1780.3	1825.3	1797.8	1771.4	1781.2	1784.3
210	1983.4	1898.8	1876.6	1792.5	1837.6	1808.8	1783.0	1789.6	1788.3
220	1996.7	1898.4	1887.4	1809.1	1875.5	1828.8	1798.6	1815.7	1803.4
230	1994.2	1878.1	1877.7	1845.3	1899.7	1847.6	1815.5	1854.3	1816.6
240	1980.0	1869.8	1868.2	1866.2	1925.3	1861.3	1833.0	1871.3	1835.3
250	1976.5	1856.4	1858.8	1856.7	1937.8	1894.6	1861.4	1892.9	1860.6
260	1953.3	1861.4	1848.6	1904.1	1951.9	1898.5	1852.9	1927.2	1884.5
270	1938.8	1851.5	1841.9	1903.4	1943.9	1905.9	1865.8	1923.5	1898.6
280	1949.7	1873.3	1843.6	1904.1	1938.9	1930.9	1892.3	1917.2	1911.9
290	1950.4	1864.9	1847.6	1910.0	1919.9	1896.8	1901.4	1904.7	1915.8
300	1953.9	1870.8	1847.9	1854.6	1888.4	1890.4	1884.3	1894.1	1914.7
310	1945.2	1889.6	1845.8	1833.7	1863.2	1878.1	1869.6	1861.5	1904.8
320	1952.4	1913.1	1845.3	1820.3	1836.9	1840.0	1853.3	1834.5	1884.7
330	1958.8	1909.4	1856.3	1781.7	1817.3	1827.5	1823.5	1804.8	1867.9
340	1950.2	1888.4	1865.5	1786.6	1814.5	1821.2	1806.5	1795.0	1853.3
350	1953.1	1874.9	1870.9	1776.7	1795.5	1803.0	1795.0	1775.4	1826.9

Crab Orchard Sandstone V_{SB}: *DRY*	Sample radial S-wave velocity (Mode B), m/s. Absolute error 1%; relative error 0.5%.								
Angle (degrees)	TS1-17	TS1-18	TS1-19	TS1-21	TS1-22	TS1-23	TS1-25	TS1-26	TS1-27
0	1808.1	1836.5	1786.3	1598.2	1641.8	1678.6	1669.9	1652.7	1668.5
10	1815.0	1827.6	1781.4	1596.8	1638.6	1663.3	1643.1	1645.5	1650.9
20	1809.6	1821.2	1777.4	1607.8	1642.3	1669.1	1652.8	1657.3	1659.3
30	1801.8	1818.4	1781.5	1644.9	1685.2	1693.4	1658.6	1674.2	1660.9
40	1804.2	1807.2	1772.5	1658.4	1710.5	1703.5	1679.7	1694.4	1679.5
50	1811.2	1800.8	1767.1	1688.6	1720.2	1751.0	1731.7	1698.1	1720.4
60	1808.0	1800.8	1771.7	1703.4	1736.6	1776.1	1753.3	1690.6	1730.8
70	1801.6	1793.7	1761.9	1719.2	1769.5	1788.9	1769.4	1714.4	1740.4
80	1796.2	1792.9	1755.4	1739.9	1793.9	1774.4	1769.0	1753.7	1771.6
90	1799.3	1794.4	1759.1	1787.9	1789.1	1795.8	1778.5	1788.2	1786.0
100	1791.6	1804.5	1759.3	1803.3	1808.3	1746.9	1785.6	1747.3	1793.9
110	1795.6	1810.8	1749.0	1772.1	1770.0	1750.4	1785.8	1725.9	1761.4
120	1804.2	1809.3	1755.3	1715.8	1733.2	1738.2	1779.7	1699.0	1751.9
130	1802.6	1828.4	1762.7	1679.7	1720.6	1701.7	1774.8	1678.4	1733.9
140	1805.8	1827.2	1771.0	1654.6	1706.9	1689.0	1743.0	1658.4	1731.5
150	1806.7	1825.1	1776.2	1644.8	1697.3	1682.4	1730.4	1659.8	1719.7
160	1817.3	1831.0	1773.5	1625.8	1662.1	1676.0	1720.6	1645.9	1702.4
170	1811.1	1834.2	1780.3	1628.8	1653.5	1684.0	1684.5	1629.1	1696.6
180	1808.8	1840.7	1784.1	1610.0	1665.3	1692.8	1668.0	1620.4	1679.7
190	1809.5	1833.7	1782.6	1615.5	1682.8	1700.8	1665.7	1627.9	1674.0
200	1813.4	1827.2	1781.8	1620.8	1695.1	1696.3	1672.1	1640.8	1673.2
210	1800.1	1821.7	1784.3	1644.3	1725.4	1732.3	1687.9	1661.9	1680.3
220	1797.8	1810.1	1771.4	1631.7	1733.7	1753.1	1707.1	1666.0	1697.4
230	1803.1	1804.3	1775.1	1655.8	1743.5	1780.6	1733.5	1678.3	1707.9
240	1810.2	1808.1	1776.1	1677.8	1761.0	1775.4	1742.8	1693.0	1729.8
250	1806.3	1805.8	1758.2	1694.1	1776.0	1790.2	1758.0	1710.8	1754.0
260	1795.2	1803.9	1755.6	1745.3	1789.4	1827.2	1764.4	1737.8	1777.7
270	1795.9	1805.4	1757.8	1791.6	1807.9	1834.1	1762.7	1759.6	1795.0
280	1799.2	1804.7	1762.4	1773.0	1802.1	1805.5	1796.7	1731.7	1791.5
290	1809.3	1810.2	1758.8	1751.7	1790.9	1790.9	1774.5	1730.9	1783.1
300	1802.3	1818.3	1757.4	1698.9	1757.8	1775.9	1784.7	1718.1	1779.5
310	1789.3	1816.1	1770.0	1666.3	1725.2	1724.9	1761.5	1711.1	1757.9
320	1801.0	1825.4	1770.6	1651.4	1715.5	1701.7	1740.4	1704.2	1746.3
330	1798.7	1830.9	1772.1	1644.6	1712.9	1702.2	1719.1	1686.6	1731.4
340	1800.3	1826.2	1774.9	1642.3	1707.0	1692.1	1704.6	1665.4	1711.0
350	1801.1	1830.3	1783.8	1619.9	1700.2	1676.3	1683.7	1630.0	1696.4

Crab Orchard Sandstone Averages: DRY	Sample radial elastic-wave velocity, m/s. Absolute error 1%; relative error 0.5%.								
	Vp: Plane			Vs_A: Plane			Vs_B: Plane		
Angle (degrees)	YZ	XZ	XY	YZ	XZ	XY	YZ	XZ	XY
0	2558.7	2548.7	3044.1	1777.1	1792.6	1910.5	1663.7	1639.5	1810.3
10	2551.4	2570.9	3026.0	1773.9	1791.8	1906.9	1646.5	1632.9	1808.0
20	2546.1	2610.5	3026.0	1772.1	1808.9	1903.6	1656.5	1639.7	1802.8
30	2573.9	2669.4	3028.2	1786.0	1823.4	1893.5	1664.6	1674.5	1800.5
40	2617.9	2714.8	3017.3	1803.7	1841.8	1889.4	1684.5	1690.8	1794.6
50	2677.8	2792.6	3018.1	1829.4	1865.2	1884.9	1716.8	1719.9	1793.1
60	2734.9	2866.3	3010.3	1848.4	1883.7	1885.3	1724.9	1738.7	1793.5
70	2805.7	2917.7	3009.3	1872.0	1902.1	1890.4	1741.4	1759.2	1785.7
80	2890.3	2995.9	2982.2	1895.9	1925.6	1885.5	1764.8	1769.4	1781.5
90	2984.9	3045.0	2984.9	1897.2	1916.9	1897.2	1784.2	1790.9	1784.2
100	2978.8	3063.8	3001.0	1908.0	1923.9	1892.8	1775.6	1786.2	1785.1
110	2905.5	2972.6	2999.1	1908.6	1903.8	1897.6	1757.7	1764.2	1785.1
120	2867.4	2868.3	3002.2	1899.7	1877.7	1905.2	1743.6	1729.1	1789.6
130	2806.1	2778.6	3020.1	1874.8	1859.8	1910.3	1729.0	1700.7	1797.9
140	2734.7	2711.8	3032.3	1854.1	1837.8	1920.1	1710.9	1683.5	1801.3
150	2683.9	2654.4	3044.1	1831.6	1821.2	1910.9	1703.3	1674.8	1802.6
160	2649.3	2613.2	3052.0	1818.0	1817.6	1914.3	1689.6	1654.7	1807.3
170	2598.2	2580.7	3048.8	1796.8	1791.8	1914.6	1670.1	1655.4	1808.5
180	2565.0	2565.0	3055.0	1785.1	1785.1	1917.7	1656.0	1656.0	1811.2
190	2550.0	2583.0	3051.1	1780.4	1785.8	1928.3	1655.9	1666.4	1808.6
200	2555.1	2612.2	3044.1	1779.0	1801.1	1933.9	1662.0	1670.8	1807.5
210	2575.8	2665.2	3034.1	1787.0	1812.9	1919.6	1676.7	1700.7	1802.0
220	2615.8	2727.7	3021.0	1805.9	1837.8	1927.5	1690.2	1706.2	1793.1
230	2680.7	2793.5	3026.4	1828.8	1864.2	1916.6	1706.5	1726.6	1794.2
240	2747.4	2864.4	3022.9	1846.5	1884.3	1906.0	1721.9	1738.1	1798.2
250	2808.4	2935.2	3020.9	1871.7	1896.4	1897.3	1740.9	1753.5	1790.1
260	2880.6	2991.1	2986.6	1888.2	1918.2	1887.8	1760.0	1787.3	1784.9
270	2966.3	3055.0	2988.3	1896.0	1917.7	1877.4	1772.5	1811.2	1786.4
280	2969.5	3048.1	3012.8	1907.1	1924.6	1888.9	1773.3	1793.5	1788.8
290	2917.3	2990.2	3020.0	1907.3	1908.9	1887.6	1762.8	1777.8	1792.8
300	2881.3	2869.3	3017.1	1897.7	1877.8	1890.9	1760.8	1744.2	1792.7
310	2826.0	2789.4	3028.7	1878.6	1858.3	1893.5	1743.5	1705.5	1791.8
320	2753.5	2723.1	3036.5	1857.5	1832.4	1903.6	1730.3	1689.5	1799.0
330	2698.3	2670.4	3046.3	1832.1	1808.9	1908.1	1712.3	1686.6	1800.6
340	2649.7	2617.0	3053.7	1818.3	1807.4	1901.4	1693.7	1680.5	1800.5
350	2607.4	2582.8	3055.3	1799.1	1791.7	1899.6	1670.0	1665.5	1805.1

Crab Orchard Sandstone Vp: SATURATED	Sample radial P-wave velocity, m/s. Absolute error 1%; relative error 0.5%.								
Angle (degrees)	TS1-13	TS1-17	TS1-19	TS1-21	TS1-22	TS1-23	TS1-8	TS1-25	TS1-26
0	4581.2	4558.0	4569.0	4015.2	4284.7	4167.0	4078.3	4165.7	4193.2
10	4603.3	4468.7	4523.1	4063.6	4278.9	4166.2	4096.2	4169.0	4248.2
20	4606.4	4447.6	4534.3	4082.1	4318.0	4190.2	4136.7	4200.0	4257.0
30	4598.4	4475.3	4563.6	4123.1	4341.8	4222.6	4158.4	4259.5	4289.9
40	4579.4	4498.0	4549.7	4216.0	4398.9	4273.2	4221.6	4240.3	4348.5
50	4569.9	4516.0	4582.0	4318.1	4464.8	4351.8	4321.5	4254.5	4373.7
60	4569.7	4486.0	4559.8	4389.1	4507.8	4438.0	4340.8	4331.8	4414.3
70	4561.9	4454.8	4558.1	4457.3	4548.8	4469.9	4428.7	4356.8	4465.3
80	4545.9	4427.7	4582.1	4538.4	4595.6	4491.0	4433.7	4390.4	4551.7
90	4572.1	4370.5	4532.2	4594.4	4571.6	4530.1	4449.9	4403.6	4621.4
100	4556.3	4420.5	4531.3	4587.8	4544.9	4515.6	4399.2	4444.3	4507.7
110	4554.8	4426.3	4527.6	4446.8	4451.5	4497.0	4339.5	4383.9	4463.1
120	4546.8	4427.4	4486.6	4323.9	4411.6	4423.0	4270.3	4378.5	4434.2
130	4562.7	4480.8	4513.9	4250.1	4327.4	4382.0	4217.4	4320.5	4380.3
140	4559.1	4492.1	4539.4	4142.1	4279.9	4313.1	4170.1	4230.1	4343.4
150	4603.5	4528.2	4554.3	4123.1	4256.3	4287.2	4158.9	4240.6	4301.2
160	4634.0	4515.4	4572.5	4113.2	4244.8	4248.6	4097.2	4251.2	4279.9
170	4639.9	4492.5	4578.8	4103.4	4229.1	4237.2	4087.8	4227.5	4263.3
180	4565.2	4513.0	4599.0	4080.3	4208.8	4236.2	4076.6	4169.9	4278.8
190	4560.6	4521.4	4574.9	4130.3	4250.6	4250.1	4113.5	4209.4	4268.6
200	4513.2	4491.3	4556.6	4126.7	4259.2	4280.4	4113.4	4190.1	4258.9
210	4524.9	4515.8	4554.8	4164.0	4346.3	4279.4	4185.0	4231.0	4279.0
220	4555.2	4480.4	4556.9	4197.3	4375.0	4340.3	4217.3	4245.6	4302.8
230	4560.5	4524.6	4529.0	4259.7	4442.2	4372.9	4303.5	4268.6	4345.1
240	4530.4	4532.6	4551.1	4319.0	4527.2	4439.6	4366.8	4342.9	4382.1
250	4534.6	4516.8	4523.8	4400.3	4508.2	4509.8	4455.6	4349.6	4387.5
260	4573.9	4364.6	4535.6	4447.7	4524.2	4522.6	4484.9	4409.6	4487.1
270	4586.4	4409.1	4491.0	4566.7	4533.9	4576.6	4471.0	4403.9	4423.2
280	4583.3	4448.5	4458.4	4522.1	4510.2	4577.3	4424.7	4444.7	4438.4
290	4571.3	4473.7	4450.7	4385.0	4465.7	4503.4	4409.8	4419.2	4390.6
300	4595.2	4444.5	4483.4	4279.9	4371.9	4430.7	4300.3	4395.5	4372.4
310	4625.6	4497.8	4470.3	4175.1	4350.8	4350.8	4249.1	4332.0	4348.7
320	4628.6	4477.8	4493.2	4151.2	4282.8	4277.0	4186.5	4311.8	4309.8
330	4635.0	4513.6	4508.8	4141.2	4269.3	4263.0	4177.1	4297.8	4262.5
340	4663.1	4495.6	4540.2	4095.4	4248.1	4218.7	4144.1	4255.1	4265.3
350	4644.4	4511.2	4534.4	4063.6	4258.6	4212.6	4127.6	4227.1	4250.2

Crab Orchard Sandstone Vs_A: *SATURATED*	Sample radial S-wave velocity (Mode A), m/s. Absolute error 1%; relative error 0.5%.								
Angle (degrees)	TS1-13	TS1-17	TS1-19	TS1-21	TS1-22	TS1-23	TS1-8	TS1-25	TS1-26
0	2285.7	2313.7	2163.6	2115.8	2049.0	1887.9	2299.9	2007.5	1997.5
10	2269.8	2327.4	2210.3	2163.7	2047.3	1903.4	2233.1	1996.5	2047.4
20	2238.8	2277.4	2222.7	2294.4	2077.9	1912.1	2244.9	1989.9	2104.4
30	2196.0	2303.2	2259.6	2327.5	2099.6	1891.2	2289.8	2022.0	2115.3
40	2140.4	2283.9	2224.2	2347.3	2108.0	1913.2	2338.2	2055.1	2127.1
50	2169.6	2260.0	2236.9	2386.3	2165.2	1980.5	2340.7	2087.1	2214.9
60	2159.1	2260.8	2202.4	2391.5	2238.6	1979.4	2322.2	2137.2	2303.8
70	2126.9	2237.4	2214.9	2394.0	2176.9	2040.5	2351.6	2189.5	2288.4
80	2117.0	2209.3	2215.7	2381.0	2142.4	2052.7	2463.3	2205.0	2287.9
90	2107.0	2252.1	2265.6	2313.5	2059.6	2065.1	2426.2	2131.4	2318.5
100	2122.9	2192.5	2240.5	2175.2	2016.9	2028.3	2336.2	2163.7	2193.2
110	2154.8	2238.5	2227.9	2202.5	1987.8	1999.0	2323.0	2182.4	2181.4
120	2187.9	2286.7	2275.4	2178.7	1997.6	2004.9	2365.1	2160.5	2087.2
130	2222.1	2273.5	2202.8	2159.8	1999.3	1910.2	2341.0	2053.8	2099.7
140	2269.6	2236.1	2190.5	2146.2	2040.2	1903.2	2275.0	2067.7	2088.9
150	2288.1	2200.1	2201.3	2123.1	2023.6	1900.7	2243.7	2008.0	2120.6
160	2221.3	2187.8	2247.9	2144.1	2007.2	1860.1	2225.0	2061.4	2062.5
170	2185.3	2222.0	2188.2	2188.9	2017.2	1854.2	2254.6	2033.3	2042.8
180	2196.1	2209.5	2163.6	2150.5	2032.4	1885.4	2246.9	1988.9	2059.7
190	2118.8	2175.7	2210.3	2164.3	2066.7	1835.4	2273.5	2003.5	2098.0
200	2186.1	2222.7	2222.7	2193.3	2093.0	1909.5	2266.6	1996.0	2044.2
210	2198.3	2200.1	2259.6	2181.4	2101.1	1882.6	2278.7	2032.0	2068.2
220	2164.9	2248.2	2224.2	2189.4	2163.0	1928.6	2291.8	2025.0	2074.1
230	2165.6	2249.0	2236.9	2279.1	2218.8	1980.5	2330.7	1992.5	2177.0
240	2155.2	2214.2	2202.5	2331.8	2175.5	1979.3	2431.0	2028.3	2252.3
250	2134.0	2262.8	2214.9	2359.6	2203.0	2040.5	2407.7	2137.2	2265.1
260	2225.6	2239.2	2215.6	2345.2	2190.4	2052.7	2449.9	2139.2	2266.9
270	2209.2	2240.0	2265.5	2325.1	2179.0	2065.1	2443.6	2117.2	2337.6
280	2174.0	2263.5	2240.4	2292.5	2164.9	2028.3	2329.4	2172.8	2294.7
290	2162.0	2300.1	2227.8	2329.6	2146.4	1999.0	2242.2	2141.0	2237.9
300	2150.1	2274.3	2275.5	2271.3	2168.0	2005.0	2309.0	2144.0	2204.2
310	2229.7	2273.5	2202.8	2243.2	2125.4	1985.1	2276.0	2037.2	2207.2
320	2253.1	2272.7	2190.4	2216.4	2079.1	1981.8	2249.5	2028.5	2164.2
330	2259.1	2296.9	2201.3	2151.8	2075.8	1953.7	2256.6	2023.1	2142.3
340	2289.8	2271.1	2247.8	2095.4	2040.3	1881.8	2234.5	2025.5	2158.6
350	2252.0	2245.9	2188.2	2136.2	2065.1	1902.2	2251.9	2005.0	2082.6

Crab Orchard Sandstone V_{SB}: *SATURATED*	Sample radial S-wave velocity (Mode B), m/s. Absolute error 1%; relative error 0.5%.								
Angle (degrees)	TS1-13	TS1-17	TS1-19	TS1-21	TS1-22	TS1-23	TS1-16	TS1-25	TS1-26
0	2150.7	2146.9	2194.7	2047.5	2124.1	1979.4	2180.0	1904.9	1889.2
10	2156.9	2138.3	2238.0	2050.5	2099.1	2033.2	2137.7	1906.0	1886.9
20	2145.6	2107.9	2207.0	2053.6	2102.6	2036.4	2183.7	1914.9	1904.4
30	2161.1	2112.3	2191.4	2066.4	2119.3	2013.3	2180.1	1980.2	1915.0
40	2127.7	2129.6	2175.2	2089.4	2089.4	2077.5	2185.3	1994.0	1905.3
50	2129.7	2143.0	2155.4	2100.8	2137.8	2085.0	2206.0	2026.3	1936.8
60	2173.2	2161.4	2160.3	2120.7	2167.1	2100.4	2180.9	2078.2	1965.8
70	2132.5	2194.0	2181.1	2120.5	2197.6	2116.3	2178.7	2085.9	2037.6
80	2117.5	2198.8	2164.9	2137.0	2166.8	2112.0	2212.3	2118.6	2064.8
90	2101.9	2166.1	2131.2	2153.8	2123.2	2128.4	2232.0	2106.1	2061.1
100	2108.7	2273.7	2156.9	2149.7	2099.8	2121.3	2191.5	2106.6	2041.6
110	2146.2	2262.2	2219.7	2141.4	2141.4	2147.6	2194.4	2085.9	2018.0
120	2147.8	2251.6	2202.4	2108.5	2116.7	2125.0	2219.8	2077.1	2033.0
130	2131.6	2241.1	2176.7	2080.9	2092.9	2088.9	2251.4	2064.6	1994.2
140	2170.0	2207.4	2197.0	2061.9	2089.5	2081.5	2216.9	2037.3	1957.4
150	2158.1	2192.8	2162.5	2051.5	2059.1	1981.9	2200.8	2021.6	1924.9
160	2187.9	2178.9	2224.8	2048.1	2055.8	2010.6	2178.9	1987.2	1886.8
170	2136.1	2155.9	2202.9	2051.0	2022.8	1986.3	2123.5	1975.7	1893.3
180	2124.9	2112.1	2191.5	2012.4	2053.6	2008.7	2212.8	1956.0	1905.9
190	2154.0	2155.9	2189.1	2037.4	2067.9	2022.4	2196.8	1956.5	1927.7
200	2161.0	2147.2	2159.6	2070.9	2074.9	2036.4	2194.3	1939.1	1942.8
210	2145.8	2165.3	2161.8	2039.5	2110.1	2058.6	2257.6	1964.3	1960.7
220	2145.3	2179.0	2141.6	2012.6	2146.9	2061.9	2235.8	1983.8	1939.8
230	2134.1	2179.2	2121.6	2053.5	2163.3	2085.1	2240.0	2014.1	1968.9
240	2086.4	2217.1	2163.9	2096.3	2175.8	2100.4	2247.2	2002.9	2002.9
250	2121.6	2208.0	2144.0	2108.2	2215.5	2116.3	2210.1	2026.5	2014.9
260	2089.3	2175.0	2124.2	2107.9	2220.0	2112.0	2178.2	2046.3	2046.3
270	2127.3	2199.2	2131.2	2115.9	2184.2	2128.4	2171.7	2066.5	2054.5
280	2189.8	2238.0	2202.6	2141.2	2188.7	2121.3	2218.4	2085.8	2041.5
290	2172.7	2238.7	2199.5	2120.4	2224.4	2147.5	2206.9	2065.4	2033.7
300	2147.0	2241.7	2186.8	2096.2	2188.9	2124.9	2257.0	2049.0	1994.8
310	2176.6	2231.7	2217.6	2088.8	2129.6	2088.8	2189.8	2014.7	1958.5
320	2120.8	2207.3	2224.0	2050.2	2121.8	2081.4	2214.9	1980.2	1954.3
330	2167.1	2197.5	2211.6	2028.2	2134.7	2058.5	2156.2	1936.7	1936.7
340	2147.0	2134.0	2227.5	2014.1	2127.0	2040.2	2180.9	1918.3	1914.8
350	2157.8	2133.9	2229.4	2037.3	2087.4	2018.6	2151.6	1919.7	1883.4

Crab Orchard Sandstone Averages: SATURATED	Sample radial elastic-wave velocity, m/s. Absolute error 1%; relative error 0.5%.								
	Vp: Plane			Vs_A: Plane			Vs_B: Plane		
Angle (degrees)	YZ	XZ	XY	YZ	XZ	XY	YZ	XZ	XY
0	4145.7	4155.6	4569.4	2101.7	2017.6	2254.3	1991.4	2050.3	2164.1
10	4171.1	4169.6	4531.7	2092.3	2038.1	2269.1	1976.9	2061.0	2177.7
20	4197.9	4196.8	4529.4	2113.1	2094.8	2246.3	2001.0	2064.2	2153.5
30	4235.9	4229.2	4545.8	2142.4	2106.1	2252.9	2025.1	2066.3	2155.0
40	4270.1	4296.0	4542.4	2173.5	2122.8	2216.2	2028.2	2085.4	2144.1
50	4316.6	4378.2	4556.0	2214.2	2177.3	2222.2	2056.4	2107.8	2142.7
60	4362.3	4445.0	4538.5	2254.4	2203.2	2207.4	2075.0	2129.4	2165.0
70	4417.0	4492.0	4524.9	2276.5	2203.8	2193.1	2100.7	2144.8	2169.2
80	4458.6	4541.7	4518.6	2318.7	2192.1	2180.7	2131.9	2138.6	2160.4
90	4491.6	4565.3	4491.6	2292.0	2146.1	2208.2	2133.1	2135.1	2133.1
100	4450.4	4549.5	4502.7	2231.0	2073.5	2185.3	2113.2	2123.6	2179.8
110	4395.5	4465.1	4502.9	2228.9	2063.1	2207.1	2099.4	2143.4	2209.4
120	4361.0	4386.2	4486.9	2204.3	2060.4	2250.0	2109.9	2116.7	2200.6
130	4306.1	4319.8	4519.2	2164.8	2023.1	2232.8	2103.4	2087.6	2183.1
140	4247.9	4245.0	4530.2	2143.9	2029.9	2232.1	2070.5	2077.6	2191.5
150	4233.6	4222.2	4562.0	2124.1	2015.8	2229.8	2049.1	2030.8	2171.1
160	4209.4	4202.2	4574.0	2116.3	2003.8	2219.0	2017.7	2038.2	2197.2
170	4192.9	4189.9	4570.4	2110.2	2020.1	2198.5	1997.5	2020.0	2165.0
180	4175.1	4175.1	4559.0	2098.5	2022.8	2189.7	2024.9	2024.9	2142.9
190	4197.2	4210.3	4552.3	2125.0	2022.1	2168.3	2027.0	2042.6	2166.3
200	4187.5	4222.1	4520.4	2102.3	2065.3	2210.5	2025.4	2060.7	2155.9
210	4231.7	4263.3	4531.8	2126.3	2055.1	2219.4	2060.9	2069.4	2157.6
220	4255.2	4304.2	4530.8	2130.3	2093.7	2212.4	2053.1	2073.8	2155.3
230	4305.7	4358.3	4538.0	2166.7	2159.5	2217.2	2074.3	2100.6	2145.0
240	4363.9	4428.6	4538.0	2237.2	2162.2	2190.6	2084.3	2124.2	2155.8
250	4397.6	4472.8	4525.1	2270.0	2201.0	2203.9	2083.8	2146.7	2157.9
260	4460.5	4498.2	4491.4	2285.3	2196.1	2226.8	2090.3	2146.6	2129.5
270	4432.7	4559.0	4495.5	2299.5	2189.7	2238.2	2097.6	2142.9	2152.6
280	4436.0	4536.5	4496.7	2265.6	2161.9	2226.0	2115.2	2150.4	2210.1
290	4406.6	4451.3	4498.6	2207.0	2158.3	2230.0	2102.0	2164.1	2203.6
300	4356.1	4360.8	4507.7	2219.1	2148.1	2233.3	2100.3	2136.7	2191.8
310	4310.0	4292.2	4531.2	2173.4	2117.9	2235.3	2054.3	2102.4	2208.6
320	4269.4	4237.0	4533.2	2147.4	2092.5	2238.8	2049.8	2084.5	2184.0
330	4245.8	4224.5	4552.5	2140.7	2060.4	2252.4	2009.9	2073.8	2192.1
340	4221.5	4187.4	4566.3	2139.6	2005.8	2269.6	2004.7	2060.4	2169.5
350	4201.6	4178.3	4563.4	2113.1	2034.5	2228.7	1984.9	2047.8	2173.7

C.3. TAKIDANI GRANITE

Takidani Granite	Sample radial P-wave velocity, m/s.								
Vp: DRY	Absolute error 1%; relative error 0.5%.								
Angle (degrees)	TG2-1	TG2-2	TG2-4	TG2-6	TG2-7	TG2-8	TG2-10	TG2-12	TG2-14
0	4874.1	4761.4	4978.0	4620.5	4655.3	4816.9	4784.6	4717.7	4471.8
10	4823.4	4711.7	4840.5	4758.3	4704.7	4892.8	4724.5	4649.1	4596.4
20	4829.9	4641.4	4841.5	4783.5	4728.8	4929.0	4657.7	4597.7	4561.5
30	4763.8	4541.3	4841.8	4780.0	4760.4	4862.3	4599.3	4480.4	4488.2
40	4694.9	4550.1	4727.0	4670.1	4798.9	4866.1	4648.6	4494.4	4445.9
50	4637.4	4537.1	4638.0	4652.9	4797.7	4912.0	4608.2	4485.5	4440.9
60	4677.0	4481.8	4497.8	4725.7	4816.3	4918.2	4671.9	4433.9	4403.9
70	4565.5	4483.8	4476.9	4637.7	4770.7	4859.6	4664.1	4459.5	4411.5
80	4587.5	4414.9	4386.7	4636.8	4726.3	4790.4	4640.8	4492.8	4416.2
90	4749.1	4358.9	4382.7	4576.6	4702.5	4792.5	4609.3	4428.2	4453.2
100	4748.4	4349.8	4350.3	4630.0	4691.4	4751.9	4634.8	4462.7	4425.4
110	4605.6	4368.4	4433.5	4631.3	4701.1	4689.1	4669.2	4452.9	4409.0
120	4683.5	4411.5	4434.2	4539.1	4606.8	4689.1	4716.1	4476.3	4455.0
130	4673.7	4418.1	4535.8	4505.4	4572.2	4666.5	4730.3	4528.4	4473.5
140	4813.9	4436.6	4561.6	4571.5	4581.8	4555.3	4760.4	4601.6	4567.6
150	4966.9	4512.4	4697.0	4605.7	4624.7	4537.7	4743.5	4673.4	4506.7
160	4817.1	4624.0	4771.3	4658.4	4668.4	4620.5	4760.7	4694.1	4535.3
170	4719.3	4658.9	4887.6	4587.6	4726.6	4744.1	4736.8	4762.2	4528.2
180	4783.8	4691.2	4962.3	4789.1	4724.9	4923.4	4813.0	4731.7	4625.5
190	4804.4	4716.7	4928.8	4894.6	4764.6	4968.3	4708.1	4673.5	4704.6
200	4744.4	4584.9	4837.6	4853.3	4817.6	5024.9	4607.0	4622.1	4667.2
210	4766.5	4509.4	4838.5	4812.3	4767.4	4984.2	4662.9	4503.8	4570.5
220	4666.7	4573.0	4816.1	4865.5	4865.5	4907.3	4620.5	4499.1	4511.8
230	4593.5	4530.0	4747.4	4824.6	4816.6	4900.6	4547.7	4528.4	4431.8
240	4552.4	4503.2	4610.0	4696.4	4834.4	4948.2	4558.2	4485.4	4534.0
250	4596.7	4466.5	4418.0	4643.3	4756.5	4915.0	4541.6	4424.8	4549.1
260	4547.5	4452.6	4417.2	4578.5	4726.9	4817.4	4591.3	4407.3	4498.7
270	4552.0	4396.0	4374.0	4589.8	4733.0	4847.5	4625.1	4500.2	4507.6
280	4483.0	4374.5	4418.5	4581.5	4666.4	4812.7	4648.7	4495.0	4503.3
290	4537.2	4407.7	4471.8	4545.7	4586.3	4784.7	4711.9	4547.9	4445.5
300	4597.2	4401.3	4472.4	4520.7	4546.1	4713.1	4736.5	4552.6	4502.5
310	4657.0	4447.5	4512.0	4491.2	4490.6	4628.4	4740.5	4586.5	4521.7
320	4771.8	4481.7	4587.1	4560.6	4533.8	4566.6	4759.2	4622.1	4552.9
330	4863.2	4529.7	4714.0	4572.4	4622.4	4618.1	4724.1	4694.6	4529.1
340	4743.8	4601.4	4816.8	4606.5	4670.4	4684.3	4803.7	4742.3	4548.7
350	4830.2	4647.6	4920.3	4629.5	4727.5	4768.5	4751.5	4726.2	4594.2

Takidani Granite	Sample radial S-wave velocity (Mode A), m/s.								
V_{SA}: DRY	Absolute error 1%; relative error 0.5%.								
Angle (degrees)	TG2-1	TG2-2	TG2-4	TG2-7	TG2-8	TG2-9	TG2-11	TG2-12	TG2-13
0	3291.0	3178.0	3312.0	3157.8	3176.9	3225.4	3369.0	3155.0	3146.9
10	3276.9	3182.0	3316.7	3233.2	3337.5	3216.1	3254.5	3129.7	3223.5
20	3237.9	3189.9	3326.7	3210.1	3352.6	3200.3	3194.1	3118.9	3217.0
30	3222.3	3164.7	3290.4	3224.5	3387.3	3234.7	3257.8	3128.6	3223.0
40	3231.5	3181.3	3262.6	3250.0	3400.3	3264.5	3241.4	3125.9	3161.6
50	3278.7	3200.8	3290.2	3260.2	3447.0	3257.9	3194.5	3133.1	3144.9
60	3234.4	3153.9	3209.1	3189.7	3426.0	3241.7	3223.6	3198.2	3147.8
70	3243.2	3147.4	3167.1	3166.8	3364.1	3205.3	3217.1	3199.8	3172.7
80	3186.1	3110.4	3151.0	3210.5	3384.1	3199.5	3242.2	2958.3	3196.2
90	3204.1	3081.2	3136.0	3216.7	3295.2	3194.2	3282.8	2926.8	3211.7
100	3203.6	3078.2	3145.1	3199.6	3264.3	3157.2	3264.1	2935.3	3233.9
110	3212.4	3067.1	3156.3	3182.9	3147.5	3220.4	3242.1	2955.9	3235.6
120	3176.1	3045.8	3147.6	3192.2	3092.8	3225.7	3115.6	3100.8	3166.4
130	3150.3	3039.9	3147.0	3162.9	3064.0	3206.3	3164.1	3183.8	3163.9
140	3164.4	3072.3	3183.6	3169.4	3150.5	3178.2	3217.2	3194.0	3198.5
150	3166.3	3052.3	3197.1	3213.6	3224.8	3213.4	3224.0	3203.8	3197.1
160	3126.4	3072.0	3240.0	3201.0	3261.5	3160.6	3272.3	3192.3	3214.3
170	3159.3	3103.6	3274.3	3191.1	3169.9	3175.8	3306.3	3157.0	3245.3
180	3196.3	3107.9	3272.1	3180.0	3215.0	3181.3	3260.0	3090.3	3456.4
190	3147.3	3116.2	3259.6	3169.1	3244.5	3166.4	3258.2	3122.3	3185.6
200	3061.0	3040.3	3237.0	3192.7	3315.8	3175.5	3229.3	3133.3	3259.3
210	3086.1	3037.3	3196.8	3213.2	3315.2	3214.3	3216.0	3106.6	3261.7
220	3120.9	3048.3	3132.9	3228.6	3378.5	3189.3	3208.5	3095.7	3369.4
230	3116.9	3062.9	3119.9	3217.4	3382.3	3222.6	3195.8	3129.8	3287.5
240	3120.6	3075.9	3078.0	3210.2	3448.1	3262.4	3229.9	3127.3	3246.2
250	3150.9	3072.7	3047.1	3205.7	3429.5	3216.5	3223.6	2960.1	3278.3
260	3136.6	3092.3	3078.4	3187.8	3372.8	3205.4	3219.1	2901.9	3312.7
270	3162.1	3038.5	3069.9	3203.0	3399.1	3204.6	3210.5	2944.7	3285.5
280	3151.2	2995.2	3081.4	3221.0	3298.9	3205.3	3178.0	3003.1	3326.5
290	3122.2	3021.3	3107.6	3185.8	3188.0	3221.0	3127.4	2980.6	3298.1
300	3126.6	3042.7	3133.4	3133.7	3214.8	3187.4	3136.7	3011.4	3264.3
310	3128.7	3050.8	3125.3	3094.5	3148.0	3212.0	3186.9	3147.3	3261.4
320	3169.9	3062.0	3146.6	3144.1	3164.8	3159.8	3298.8	3230.3	3243.1
330	3222.1	3084.7	3200.3	3184.0	3176.0	3229.0	3243.4	3185.2	3188.4
340	3287.9	3117.6	3242.8	3163.1	3220.4	3195.4	3305.0	3150.1	3139.3
350	3290.0	3138.2	3299.1	3184.6	3235.9	3162.7	3377.1	3132.5	3141.2

Takidani Granite	Sample radial S-wave velocity (Mode B), m/s.								
V_{SB}: DRY	Absolute error 1%; relative error 0.5%.								
Angle (degrees)	TG2-1	TG2-2	TG2-4	TG2-7	TG2-8	TG2-9	TG2-11	TG2-12	TG2-13
0	3322.8	3035.5	3128.6	3019.3	3106.0	3374.8	3200.3	3164.7	3126.8
10	3323.5	3000.5	3122.9	3074.8	3176.8	3332.7	3207.3	3131.1	3165.5
20	3308.1	3064.0	3146.0	3073.3	3186.5	3266.3	3150.2	3082.9	3189.0
30	3268.2	3126.3	3150.2	3034.2	3208.2	3281.8	3118.3	3092.3	3105.4
40	3257.1	3081.5	3097.1	2991.8	3217.8	3338.8	3128.5	3088.6	3087.9
50	3279.9	3022.9	3006.6	3027.0	3210.5	3321.8	3066.1	3070.0	3084.2
60	3300.3	2973.9	2973.1	3024.6	3218.3	3305.5	3040.2	3068.9	3081.4
70	3280.4	2914.8	2924.4	3059.1	3183.3	3293.0	3045.8	3189.7	3087.6
80	3294.0	2947.3	2938.2	3038.0	3203.5	3294.7	3064.3	3131.0	3093.8
90	3247.5	2975.7	2999.4	3006.3	3153.2	3303.2	3017.9	3095.6	3109.1
100	3202.7	2991.0	3030.1	2965.5	3153.0	3292.7	3052.5	3189.4	3062.9
110	3238.7	3036.5	2966.1	2948.4	3124.9	3303.2	2998.4	3125.6	3097.9
120	3264.5	3048.9	2978.0	2930.8	3105.5	3303.8	3041.3	3169.1	3177.3
130	3269.0	3088.3	3016.2	2906.1	3104.1	3377.9	3131.6	3184.0	3114.9
140	3315.6	3144.8	3073.8	2849.8	3069.5	3540.1	3202.4	3197.8	3136.9
150	3325.9	3058.6	3066.7	2834.0	3057.3	3598.0	3240.9	3223.8	3159.9
160	3395.9	3075.1	3116.5	2856.4	3100.0	3578.4	3265.0	3168.3	3139.3
170	3332.7	3068.5	3155.7	2926.2	3166.1	3495.8	3218.1	3133.9	3180.5
180	3367.8	3041.7	3181.0	2974.4	3189.7	3426.4	3163.9	3095.5	3126.8
190	3355.9	3032.9	3152.8	2958.8	3218.8	3369.5	3104.5	3083.4	3165.4
200	3329.3	3097.8	3180.0	2976.1	3235.8	3273.5	3138.8	3105.7	3137.7
210	3369.7	3064.9	3178.6	2944.3	3237.4	3303.0	3079.7	3133.0	3088.0
220	3359.6	3127.3	3064.6	2950.1	3247.2	3302.4	3036.6	3089.9	3089.3
230	3335.9	3144.4	3025.5	3022.3	3287.9	3297.8	3024.4	3123.8	3077.5
240	3325.7	3118.9	3070.4	3036.0	3302.3	3296.9	3003.4	3111.3	3011.7
250	3320.5	3110.0	3024.0	3009.3	3232.6	3332.1	3012.8	3101.6	3004.7
260	3346.7	3116.9	2968.0	2903.7	3162.1	3310.0	2997.2	3066.9	3033.3
270	3327.1	3073.1	2966.0	2915.9	3170.4	3300.1	2980.8	3095.0	3008.0
280	3239.9	3082.2	3020.7	2945.1	3131.1	3282.9	2974.9	3005.1	2927.5
290	3293.4	3071.2	2995.8	2896.0	3071.4	3272.6	2995.2	3143.9	2978.3
300	3325.6	3106.7	3049.7	2943.5	3129.8	3300.4	3011.6	3180.4	3043.9
310	3273.0	3123.9	3066.0	2963.7	3054.8	3352.3	2989.2	3208.1	3055.8
320	3309.9	3073.0	3136.1	3022.0	3033.6	3377.9	3053.2	3236.6	3117.8
330	3301.8	2968.9	3088.8	2986.2	3021.1	3421.1	3074.0	3205.0	3107.9
340	3325.3	3019.3	3054.6	2968.8	3098.3	3393.0	3095.9	3238.3	3079.1
350	3329.1	3050.2	3082.5	2984.9	2974.1	3395.5	3157.8	3180.8	3151.6

Takidani Granite	Sample radial elastic-wave velocity, m/s.								
Averages:	Absolute error 1%; relative error 0.5%.								
DRY	Vp: Plane			Vs_A: Plane			Vs_B: Plane		
Angle (degrees)	YZ	XZ	XY	YZ	XZ	XY	YZ	XZ	XY
0	4871.2	4697.6	4658.0	3260.3	3186.7	3223.7	3162.3	3166.7	3163.9
10	4791.8	4785.3	4656.7	3258.5	3262.2	3202.6	3149.0	3194.7	3168.0
20	4770.9	4813.8	4605.6	3251.5	3254.3	3176.7	3172.7	3175.3	3140.7
30	4715.6	4800.9	4522.6	3225.8	3282.2	3203.1	3181.5	3174.8	3105.3
40	4657.4	4778.4	4529.7	3225.2	3304.9	3176.3	3145.3	3182.8	3101.7
50	4604.2	4787.5	4511.6	3256.6	3321.7	3157.5	3103.1	3186.4	3073.5
60	4552.2	4820.0	4503.2	3199.1	3285.8	3189.9	3082.4	3182.8	3063.5
70	4508.8	4756.0	4511.7	3185.9	3245.4	3196.5	3039.9	3178.5	3107.7
80	4463.0	4717.8	4516.6	3149.1	3264.7	3132.3	3059.8	3178.7	3096.4
90	4496.9	4690.5	4496.9	3140.4	3235.4	3140.4	3074.2	3154.2	3074.2
100	4482.9	4691.1	4507.6	3142.3	3207.0	3144.4	3074.6	3137.1	3101.6
110	4469.2	4673.9	4510.4	3145.2	3183.6	3144.6	3080.4	3125.5	3074.0
120	4509.7	4611.7	4549.1	3123.2	3170.2	3127.6	3097.2	3113.4	3129.2
130	4542.5	4581.4	4577.4	3112.4	3144.4	3170.6	3124.5	3129.3	3143.5
140	4604.0	4569.5	4643.2	3140.1	3166.0	3203.2	3178.1	3153.1	3179.0
150	4725.4	4589.3	4641.2	3138.6	3217.3	3208.3	3150.4	3163.1	3208.2
160	4737.5	4649.1	4663.4	3146.1	3207.7	3226.3	3195.8	3178.3	3190.9
170	4755.2	4686.1	4675.7	3179.0	3178.9	3236.2	3185.6	3196.0	3177.5
180	4812.5	4812.5	4723.4	3192.1	3192.1	3268.9	3196.8	3196.8	3128.8
190	4816.6	4875.8	4695.4	3174.4	3193.4	3188.7	3180.5	3182.3	3117.8
200	4722.3	4898.6	4632.1	3112.8	3228.0	3207.3	3202.4	3161.8	3127.4
210	4704.8	4854.6	4579.1	3106.7	3247.5	3194.8	3204.4	3161.6	3100.2
220	4685.3	4879.4	4543.8	3100.7	3265.5	3224.6	3183.9	3166.6	3071.9
230	4623.6	4847.2	4502.7	3099.9	3274.1	3204.4	3168.6	3202.7	3075.2
240	4555.2	4826.3	4525.8	3091.5	3306.9	3201.1	3171.7	3211.8	3042.2
250	4493.8	4771.6	4505.2	3090.2	3283.9	3154.0	3151.5	3191.3	3039.7
260	4472.4	4707.6	4499.1	3102.4	3255.3	3144.6	3143.9	3125.3	3032.5
270	4440.7	4723.4	4544.3	3090.1	3268.9	3146.9	3122.1	3128.8	3027.9
280	4425.4	4686.9	4549.0	3075.9	3241.7	3169.2	3114.2	3119.7	2969.2
290	4472.2	4638.9	4568.4	3083.7	3198.3	3135.4	3120.1	3080.0	3039.1
300	4490.3	4593.3	4597.2	3100.9	3178.7	3137.5	3160.6	3124.6	3078.6
310	4538.8	4536.7	4616.2	3101.6	3151.5	3198.5	3154.3	3123.6	3084.4
320	4613.5	4553.7	4644.7	3126.2	3156.2	3257.4	3173.0	3144.5	3135.9
330	4702.3	4604.3	4649.3	3169.0	3196.3	3205.7	3119.8	3142.8	3129.0
340	4720.7	4653.7	4698.2	3216.1	3193.0	3198.1	3133.1	3153.4	3137.8
350	4799.4	4708.5	4690.6	3242.4	3194.4	3216.9	3154.0	3118.2	3163.4

Takidani Granite	Sample radial P-wave velocity, m/s.								
Vp: SATURATED	Absolute error 1%; relative error 0.5%.								
Angle (degrees)	TG2-1	TG2-3	TG2-4	TG2-5	TG2-7	TG2-9	TG2-11	TG2-12	TG2-13
0	6040.9	6045.5	6041.8	5836.8	6044.0	6269.6	6016.1	5851.6	6082.4
10	6023.9	6060.4	6020.2	5874.9	6053.8	6259.4	6014.3	5809.8	6077.7
20	6005.3	6058.4	6011.8	5940.3	6066.5	6273.0	5963.7	5814.4	6065.2
30	6003.3	6016.2	5979.4	5935.8	6102.7	6239.1	5963.8	5816.3	6067.3
40	5992.1	5981.1	5954.6	5958.3	6087.2	6211.7	5979.8	5776.8	6082.9
50	5945.4	5945.4	5904.1	5977.2	6057.3	6202.7	5975.3	5775.2	6075.3
60	5943.5	5892.4	5878.2	5931.6	6035.2	6162.6	5985.8	5758.7	6084.2
70	5948.8	5886.9	5886.9	5896.7	6004.8	6135.8	5997.2	5759.7	6066.9
80	5956.8	5944.1	5904.6	5858.6	5983.2	6118.2	5978.5	5727.0	6071.9
90	5943.1	5997.8	5868.1	5866.0	5950.6	6131.2	6025.0	5741.8	6042.2
100	5941.4	6042.5	5866.4	5841.5	5956.0	6138.0	6059.3	5714.1	6042.0
110	5963.3	6057.6	5849.9	5816.3	5936.3	6141.8	6099.9	5738.9	6027.6
120	5978.1	6014.9	5864.1	5803.7	5914.9	6132.7	6031.2	5759.6	6025.5
130	5990.1	6003.0	5896.1	5808.9	5880.0	6109.9	5961.3	5742.1	6063.7
140	6005.9	6009.6	5917.7	5783.1	5921.1	6129.5	5998.7	5756.7	6086.8
150	6051.7	6013.5	5957.5	5777.7	5915.4	6156.1	6045.2	5780.1	6106.2
160	6019.2	5997.9	5995.1	5785.5	5917.1	6242.0	6012.6	5817.1	6104.1
170	5990.7	5987.0	6033.2	5826.2	5946.6	6253.2	6035.3	5838.3	6107.9
180	6016.7	6018.5	6054.9	5856.6	5978.4	6255.1	5997.2	5849.8	6095.0
190	6017.5	6020.2	6041.6	5898.6	6022.1	6223.5	6005.8	5829.4	6064.1
200	6006.2	6042.4	6014.5	5937.5	6041.4	6226.7	5994.6	5814.4	6074.9
210	6004.2	6019.9	5997.8	5960.9	6081.2	6210.5	5945.2	5810.1	6065.4
220	5989.3	5974.7	5931.1	5948.9	6061.9	6191.4	5963.9	5789.1	6106.3
230	5946.3	5940.9	5904.1	5951.9	6050.5	6150.4	5969.7	5775.2	6082.1
240	5948.0	5900.4	5900.4	5900.2	6009.5	6112.0	5932.6	5773.5	6084.2
250	5975.2	5894.9	5914.5	5888.5	5969.9	6100.3	5978.4	5769.3	6085.3
260	5949.5	5909.9	5874.4	5894.1	5957.9	6120.2	6004.0	5753.8	6077.7
270	5937.6	5976.7	5855.7	5876.9	5946.8	6118.3	5991.8	5739.2	6026.9
280	5939.6	6056.6	5846.2	5873.1	5944.8	6124.1	6044.9	5740.8	6045.9
290	5957.9	6054.8	5872.8	5871.2	5939.1	6118.0	6077.6	5738.9	6037.1
300	5965.3	6028.8	5859.7	5840.3	5903.9	6122.8	6034.1	5752.6	6022.7
310	5970.9	6006.7	5882.8	5793.0	5925.9	6109.9	5983.7	5763.8	6077.3
320	6012.4	6008.7	5913.2	5802.6	5920.2	6129.5	6021.4	5768.0	6088.8
330	6054.5	6020.9	5938.5	5791.8	5946.0	6210.5	6054.8	5792.4	6093.5
340	6043.4	6011.8	5983.2	5789.0	5964.5	6234.8	6049.8	5810.0	6091.4
350	6011.0	5999.0	6023.0	5807.5	5989.8	6254.2	6033.4	5827.6	6089.3

Takidani Granite	Sample radial S-wave velocity (Mode A), m/s.								
Vs_A: SATURATED	Absolute error 1%; relative error 0.5%.								
Angle (degrees)	TG2-1	TG2-3	TG2-4	TG2-5	TG2-7	TG2-9	TG2-11	TG2-12	TG2-13
0	3199.9	3233.0	3215.7	3310.6	3316.5	3342.6	3319.7	3227.7	3389.7
10	3211.6	3206.8	3251.6	3312.7	3311.8	3361.6	3286.8	3226.8	3379.1
20	3263.6	3220.2	3242.7	3252.6	3286.9	3348.9	3287.1	3237.3	3374.2
30	3269.0	3244.8	3229.6	3240.4	3329.0	3336.2	3265.9	3219.3	3371.0
40	3301.5	3247.3	3228.3	3255.6	3320.8	3282.6	3252.9	3233.5	3327.6
50	3296.8	3249.7	3205.3	3257.0	3300.0	3347.1	3241.2	3218.8	3332.7
60	3333.2	3246.5	3201.4	3320.9	3317.5	3275.1	3237.7	3197.1	3324.2
70	3343.7	3262.9	3178.7	3285.4	3267.0	3282.9	3243.9	3206.3	3310.3
80	3341.1	3231.4	3141.0	3172.3	3305.4	3242.8	3231.0	3206.5	3304.5
90	3334.5	3215.8	3136.8	3179.3	3276.6	3235.5	3174.7	3197.4	3314.9
100	3286.9	3224.5	3114.4	3202.1	3253.4	3284.0	3101.8	3192.6	3273.8
110	3272.5	3185.8	3090.4	3231.5	3210.8	3305.5	3198.2	3169.4	3265.9
120	3287.3	3372.0	3095.5	3152.4	3255.5	3341.6	3244.8	3192.4	3271.0
130	3355.0	3308.0	3109.5	3091.8	3223.1	3345.1	3264.3	3155.0	3324.0
140	3369.1	3401.5	3141.4	3042.2	3207.0	3435.2	3301.7	3169.5	3316.4
150	3329.1	3383.5	3167.4	3121.2	3233.2	3364.0	3288.2	3160.2	3357.5
160	3344.3	3366.6	3181.4	3184.3	3275.4	3324.7	3277.9	3160.1	3354.1
170	3357.5	3335.1	3190.4	3179.7	3271.2	3340.5	3293.0	3194.6	3370.7
180	3338.9	3325.0	3214.5	3193.7	3270.2	3414.5	3292.7	3160.8	3379.5
190	3363.5	3354.7	3249.9	3171.4	3284.5	3448.2	3270.9	3176.4	3362.0
200	3376.3	3375.7	3241.1	3186.0	3274.5	3357.6	3266.1	3200.1	3355.9
210	3359.5	3352.2	3228.3	3220.7	3300.7	3315.6	3261.6	3185.4	3337.1
220	3350.6	3342.5	3227.3	3255.3	3298.8	3310.3	3248.6	3179.6	3312.0
230	3351.7	3301.3	3204.5	3233.5	3262.1	3196.1	3292.5	3150.8	3322.9
240	3368.5	3286.7	3200.8	3222.8	3309.5	3237.7	3233.0	3140.7	3296.6
250	3350.5	3328.6	3178.1	3210.0	3251.2	3273.8	3220.1	3137.5	3292.5
260	3391.3	3352.3	3148.0	3226.2	3252.3	3330.2	3078.1	3137.5	3296.5
270	3365.2	3287.9	3154.1	3177.7	3266.0	3389.2	3043.0	3126.7	3274.3
280	3376.8	3366.0	3151.8	3263.3	3253.6	3433.8	3051.0	3141.0	3280.5
290	3360.8	3427.0	3149.5	3245.5	3275.0	3363.3	3147.8	3127.6	3307.6
300	3354.7	3401.8	3143.8	3211.3	3244.4	3341.5	3209.4	3086.5	3303.0
310	3362.3	3393.6	3160.5	3238.7	3302.3	3371.6	3255.7	3115.0	3310.4
320	3304.6	3412.7	3141.8	3233.7	3301.2	3365.1	3293.2	3117.9	3292.0
330	3283.0	3367.7	3167.8	3248.1	3318.4	3293.9	3275.6	3117.2	3353.3
340	3243.7	3316.7	3182.3	3219.9	3340.5	3353.5	3307.6	3141.0	3356.2
350	3209.5	3254.1	3191.7	3276.7	3332.8	3306.2	3291.3	3145.9	3373.6

Takidani Granite	Sample radial S-wave velocity (Mode B), m/s.								
V_{SB}: SATURATED	Absolute error 1%; relative error 0.5%.								
Angle (degrees)	TG2-1	TG2-3	TG2-4	TG2-5	TG2-7	TG2-9	TG2-11	TG2-12	TG2-13
0	3294.7	3346.6	3389.0	3465.6	3322.0	3394.3	3336.0	3288.5	3310.5
10	3359.5	3320.3	3298.6	3468.7	3298.3	3388.8	3282.7	3389.7	3207.1
20	3373.1	3308.6	3327.9	3448.9	3286.0	3376.2	3291.4	3374.5	3256.4
30	3359.8	3321.6	3277.6	3433.1	3282.7	3350.6	3266.7	3384.5	3298.0
40	3270.0	3321.8	3318.0	3434.6	3326.2	3350.0	3269.6	3353.0	3260.9
50	3312.5	3338.9	3306.3	3412.0	3324.9	3373.6	3310.5	3327.4	3236.5
60	3334.9	3302.8	3229.5	3440.5	3295.3	3351.2	3280.2	3312.2	3189.8
70	3292.7	3332.7	3303.6	3463.3	3268.5	3331.4	3285.0	3259.7	3234.2
80	3298.6	3296.5	3273.3	3410.1	3235.5	3310.6	3364.1	3256.1	3193.9
90	3320.2	3302.5	3239.1	3385.5	3229.8	3323.4	3379.6	3236.9	3245.3
100	3278.2	3295.9	3220.4	3395.5	3262.9	3313.6	3397.7	3227.7	3214.5
110	3266.0	3424.8	3192.0	3384.6	3224.4	3368.1	3387.6	3280.2	3209.8
120	3250.6	3390.6	3198.1	3405.3	3185.9	3385.9	3379.5	3302.0	3170.0
130	3258.2	3308.7	3250.9	3377.3	3172.8	3400.7	3328.5	3259.9	3279.7
140	3243.8	3425.2	3261.7	3390.0	3223.8	3409.1	3324.5	3306.2	3285.0
150	3347.7	3458.5	3305.7	3392.5	3254.4	3400.3	3417.4	3348.1	3371.3
160	3313.0	3465.8	3360.6	3395.1	3242.8	3399.1	3362.6	3335.8	3350.5
170	3302.1	3419.9	3367.8	3407.6	3285.6	3420.5	3329.7	3294.3	3168.6
180	3294.5	3465.0	3376.9	3431.8	3278.5	3426.1	3232.1	3348.0	3368.7
190	3332.6	3437.7	3372.6	3415.3	3229.9	3375.4	3263.3	3363.1	3341.8
200	3392.0	3477.0	3386.6	3396.3	3249.8	3404.4	3242.5	3345.3	3341.2
210	3334.6	3450.3	3357.2	3388.9	3260.3	3353.8	3273.0	3262.6	3266.8
220	3318.0	3437.0	3360.8	3398.1	3279.4	3359.1	3315.4	3191.0	3101.4
230	3334.1	3419.6	3324.3	3380.2	3256.8	3400.2	3237.7	3161.0	3197.4
240	3343.3	3396.2	3337.6	3419.5	3241.9	3377.4	3212.4	3235.0	3267.0
250	3352.2	3398.8	3326.0	3440.0	3257.2	3340.5	3284.9	3277.2	3266.1
260	3370.0	3383.9	3300.4	3432.7	3266.3	3349.0	3415.0	3217.1	3307.3
270	3379.8	3342.6	3284.9	3383.6	3241.8	3323.4	3358.2	3197.2	3248.6
280	3329.6	3411.2	3234.8	3398.0	3246.4	3313.9	3277.7	3207.5	3208.4
290	3217.3	3428.1	3215.0	3394.9	3227.2	3341.8	3258.2	3217.6	3278.9
300	3263.8	3463.1	3255.4	3401.9	3207.3	3362.1	3352.9	3285.2	3184.0
310	3234.8	3435.1	3191.0	3386.9	3204.5	3385.0	3385.3	3337.8	3427.7
320	3261.3	3502.8	3296.5	3395.4	3255.8	3433.0	3342.5	3381.7	3387.1
330	3303.2	3436.0	3262.3	3423.3	3277.0	3433.5	3300.9	3339.0	3374.4
340	3314.0	3362.7	3344.3	3420.1	3281.5	3443.0	3344.2	3292.0	3284.0
350	3299.2	3372.1	3296.6	3451.5	3305.0	3422.1	3311.8	3324.0	3294.9

Takidani Granite	Sample radial elastic-wave velocity, m/s.								
Averages:	Absolute error 1%; relative error 0.5%.								
SATURATED	Vp: Plane			Vs_A: Plane			Vs_B: Plane		
Angle (degrees)	YZ	XZ	XY	YZ	XZ	XY	YZ	XZ	XY
0	6042.7	6050.1	5983.4	3216.2	3323.2	3312.4	3343.5	3393.9	3311.6
10	6034.9	6062.7	5967.3	3223.3	3328.7	3297.6	3326.1	3385.2	3293.2
20	6025.1	6093.3	5947.8	3242.2	3296.2	3299.5	3336.5	3370.4	3307.4
30	5999.6	6092.5	5949.1	3247.8	3301.9	3285.4	3319.6	3355.4	3316.4
40	5975.9	6085.7	5946.5	3259.0	3286.3	3271.3	3303.3	3370.3	3294.5
50	5931.7	6079.0	5941.9	3250.6	3301.4	3264.2	3319.2	3370.2	3291.4
60	5904.7	6043.1	5942.9	3260.4	3304.5	3253.0	3289.1	3362.3	3260.8
70	5907.5	6012.5	5941.3	3261.8	3278.4	3253.5	3309.7	3354.4	3259.7
80	5935.2	5986.7	5925.8	3237.8	3240.1	3247.3	3289.5	3318.7	3271.4
90	5936.3	5982.6	5936.3	3229.0	3230.5	3229.0	3287.2	3312.9	3287.2
100	5950.1	5978.5	5938.5	3208.6	3246.5	3189.4	3264.8	3324.0	3279.9
110	5956.9	5964.8	5955.5	3182.9	3249.3	3211.2	3294.2	3325.7	3292.5
120	5952.3	5950.4	5938.8	3251.6	3249.8	3236.0	3279.8	3325.7	3283.8
130	5963.1	5932.9	5922.4	3257.5	3220.0	3247.8	3272.6	3317.0	3289.4
140	5977.7	5944.6	5947.4	3304.0	3228.2	3262.6	3310.2	3341.0	3305.3
150	6007.5	5949.8	5977.2	3293.3	3239.5	3268.6	3370.6	3349.1	3378.9
160	6004.1	5981.5	5977.9	3297.4	3261.5	3264.0	3379.8	3345.7	3349.6
170	6003.6	6008.7	5993.8	3294.3	3263.8	3286.1	3363.3	3371.3	3264.2
180	6030.0	6030.0	5980.7	3292.8	3292.8	3277.6	3378.8	3378.8	3316.3
190	6026.4	6048.1	5966.4	3322.7	3301.4	3269.8	3381.0	3340.2	3322.7
200	6021.1	6068.5	5961.3	3331.1	3272.7	3274.0	3418.5	3350.2	3309.7
210	6007.3	6084.2	5940.2	3313.3	3279.0	3261.4	3380.7	3334.3	3267.4
220	5965.1	6067.4	5953.1	3306.8	3288.1	3246.7	3371.9	3345.5	3202.6
230	5930.4	6050.9	5942.3	3285.8	3230.6	3255.4	3359.3	3345.8	3198.7
240	5916.3	6007.2	5930.1	3285.3	3256.7	3223.4	3359.0	3346.3	3238.1
250	5928.2	5986.2	5944.3	3285.7	3245.0	3216.7	3359.0	3345.9	3276.1
260	5911.3	5990.7	5945.1	3297.2	3269.6	3170.7	3351.4	3349.3	3313.1
270	5923.4	5980.7	5919.3	3269.1	3277.6	3148.0	3335.8	3316.3	3268.0
280	5947.5	5980.7	5943.9	3298.2	3316.9	3157.5	3325.2	3319.4	3231.2
290	5961.8	5976.1	5951.2	3312.5	3294.6	3194.3	3286.8	3321.3	3251.6
300	5951.2	5955.7	5936.5	3300.1	3265.7	3199.6	3327.4	3323.7	3274.1
310	5953.4	5942.9	5941.6	3305.5	3304.2	3227.1	3287.0	3325.5	3383.6
320	5978.1	5950.7	5959.4	3286.4	3300.0	3234.4	3353.6	3361.4	3370.4
330	6004.6	5982.8	5980.2	3272.8	3286.8	3248.7	3333.8	3377.9	3338.1
340	6012.8	5996.1	5983.7	3247.6	3304.6	3268.3	3340.3	3381.5	3306.7
350	6011.0	6017.2	5983.4	3218.4	3305.3	3270.3	3322.6	3392.9	3310.2

D. ELEVATED PRESSURE DATA: PERMEABILITY/VELOCITY/POROSITY

Bentheim sandstone *Average, X direction* *Hydrostatic pressure*	Measured parameters							
	Permeability (10^{-18} m^2)		P-wave velocity (m/s)		S-wave velocity (m/s)		Porosity (%)	
Pressure, MPa	Value	Error	Value	Error	Value	Error	Value	Error
5.63	864.59	16.09	3983.67	10.46	2253.91	5.92	22.15	0.01
10.15	854.21	37.51	4037.89	10.60	2278.16	5.98	22.05	0.01
14.98	874.83	13.66	4100.75	10.76	2305.53	6.05	21.97	0.01
20.36	862.64	17.45	4153.53	10.90	2328.22	6.11	21.92	0.01
29.55	826.17	67.18	4187.63	10.99	2353.92	6.18	21.83	0.01
39.91	835.13	14.52	4216.77	11.07	2369.14	6.22	21.73	0.01
49.85	852.20	14.30	4248.44	11.15	2379.52	6.25	21.67	0.01
60.15	832.16	13.95	4262.21	11.19	2388.59	6.27	21.60	0.01
69.85	838.48	18.47	4281.09	11.24	2396.23	6.29	21.54	0.01
79.67	860.20	19.32	4289.14	11.26	2401.99	6.30	21.47	0.01
90.23	847.71	21.52	4299.61	11.29	2405.95	6.31	21.42	0.01
80.67	827.71	35.80	4259.91	11.18	2402.58	6.31	21.47	0.01
70.99	861.95	18.91	4250.73	11.16	2398.41	6.30	21.51	0.01
60.66	847.22	29.72	4234.84	11.12	2392.10	6.28	21.58	0.01
51.28	846.06	24.76	4220.94	11.08	2385.52	6.26	21.64	0.01
40.30	830.74	37.33	4206.86	11.04	2376.18	6.24	21.72	0.01
30.77	832.05	28.19	4195.38	11.01	2362.61	6.20	21.78	0.01
21.30	844.61	24.57	4166.83	10.94	2346.03	6.16	21.87	0.01
15.81	836.31	28.29	4141.33	10.87	2329.31	6.11	21.93	0.01
9.50	869.41	24.35	4085.97	10.72	2303.75	6.05	22.01	0.01
5.11	845.25	26.31	4018.19	10.55	2292.59	6.02	22.13	0.01

Bentheim sandstone *Average, Y direction* *Hydrostatic pressure*	Measured parameters							
	Permeability (10^{-18} m^2)		P-wave velocity (m/s)		S-wave velocity (m/s)		Porosity (%)	
Pressure, MPa	Value	Error	Value	Error	Value	Error	Value	Error
5.25	833.27	31.43	3877.35	10.18	2162.40	5.68	22.96	0.01
10.53	805.19	33.89	3963.81	10.40	2241.00	5.88	22.83	0.01
15.37	831.56	54.35	4004.53	10.51	2258.69	5.93	22.77	0.01
20.11	867.19	19.37	4033.75	10.59	2272.36	5.96	22.71	0.01
29.91	815.87	40.49	4058.17	10.65	2287.08	6.00	22.61	0.01
39.93	808.51	49.44	4086.23	10.73	2295.11	6.02	22.53	0.01
49.94	808.34	15.91	4097.50	10.75	2300.54	6.04	22.47	0.01
59.99	803.47	17.21	4109.05	10.78	2306.68	6.05	22.41	0.01
69.79	806.10	19.04	4130.39	10.84	2314.02	6.07	22.34	0.01
79.60	791.13	11.21	4131.59	10.84	2318.77	6.09	22.28	0.01
89.81	813.81	18.22	4143.98	10.88	2322.48	6.10	22.20	0.01
79.97	803.41	26.89	4131.64	10.84	2319.48	6.09	22.26	0.01
70.00	810.37	25.98	4122.76	10.82	2314.83	6.08	22.32	0.01
59.44	799.92	11.61	4111.49	10.79	2308.84	6.06	22.39	0.01
50.62	802.93	40.52	4084.32	10.72	2302.91	6.04	22.45	0.01
39.59	795.93	26.08	4072.90	10.69	2294.38	6.02	22.51	0.01
30.10	815.10	20.09	4049.83	10.63	2285.23	6.00	22.59	0.01
22.67	805.71	12.02	4044.81	10.62	2274.03	5.97	22.67	0.01
17.68	809.77	16.46	4030.51	10.58	2264.96	5.94	22.72	0.01
11.66	788.44	22.39	3995.30	10.49	2250.33	5.91	22.78	0.01
6.88	822.60	16.32	3936.40	10.33	2233.37	5.86	22.89	0.01
4.11	783.90	62.94	3899.58	10.24	2226.65	5.84	23.02	0.01

Bentheim sandstone *Average, Z direction* *Hydrostatic pressure*	Measured parameters							
	Permeability (10^{-18} m^2)		P-wave velocity (m/s)		S-wave velocity (m/s)		Porosity (%)	
Pressure, MPa	Value	Error	Value	Error	Value	Error	Value	Error
5.10	752.15	14.42	3719.80	9.76	2124.89	5.58	21.81	0.01
10.34	795.52	39.89	3858.35	10.13	2163.77	5.68	21.69	0.01
15.41	803.44	26.93	3906.37	10.25	2194.83	5.76	21.61	0.01
20.34	809.40	9.37	3950.25	10.37	2210.99	5.80	21.54	0.01
29.84	846.49	10.35	3981.02	10.45	2230.51	5.85	21.44	0.01
39.51	832.51	17.35	4008.40	10.52	2248.60	5.90	21.37	0.01
50.03	813.05	12.19	4037.88	10.60	2266.31	5.95	21.28	0.01
59.81	812.61	17.55	4053.06	10.64	2274.15	5.97	21.22	0.01
69.97	837.36	11.82	4061.63	10.66	2280.53	5.99	21.15	0.01
80.01	782.37	9.99	4067.83	10.68	2285.11	6.00	21.08	0.01
90.02	807.19	16.34	4077.23	10.70	2289.22	6.01	21.01	0.01
80.05	785.45	9.68	4069.82	10.68	2283.46	5.99	20.90	0.01
71.37	785.13	11.05	4065.40	10.67	2280.25	5.98	20.96	0.01
59.39	795.92	32.99	4040.80	10.61	2273.43	5.97	21.04	0.01
50.84	808.80	10.09	4030.96	10.58	2266.89	5.95	21.08	0.01
41.30	809.83	8.65	4010.85	10.53	2259.92	5.93	21.15	0.01
30.41	801.87	8.15	3997.70	10.49	2247.67	5.90	21.24	0.01
21.66	810.47	11.13	3969.12	10.42	2218.89	5.82	21.33	0.01
15.26	776.98	7.82	3954.62	10.38	2197.29	5.77	21.40	0.01
9.65	777.81	34.34	3900.71	10.24	2173.67	5.71	21.49	0.01
5.15	798.88	8.86	3849.32	10.10	2143.04	5.62	21.61	0.01

Crab Orchard sandstone *Average, X direction* *Hydrostatic pressure*	Measured parameters							
	Permeability (10^{-18} m^2)		P-wave velocity (m/s)		S-wave velocity (m/s)		Porosity (%)	
Pressure, MPa	Value	Error	Value	Error	Value	Error	Value	Error
5.19	127.47	6.77	4489.26	11.80	2540.74	6.68	4.80	0.04
10.17	86.29	3.52	4567.68	12.01	2642.54	6.95	4.73	0.04
16.06	57.23	2.88	4664.80	12.26	2672.65	7.03	4.67	0.04
20.65	41.78	3.32	4750.89	12.49	2704.93	7.11	4.64	0.04
29.30	29.69	2.86	4841.13	12.73	2727.31	7.17	4.58	0.04
39.56	23.18	1.57	4902.48	12.89	2768.13	7.28	4.55	0.04
49.77	16.55	4.35	4976.20	13.08	2820.41	7.42	4.52	0.04
59.31	12.54	1.07	5018.51	13.20	2861.46	7.53	4.50	0.04
69.78	9.89	3.46	5060.83	13.31	2900.53	7.63	4.47	0.04
79.21	6.26	2.25	5090.30	13.38	2934.99	7.72	4.45	0.04
90.53	4.30	4.11	5136.25	13.51	2965.62	7.80	4.44	0.04
81.48	8.76	0.38	5109.18	13.41	2942.84	7.72	4.42	0.04
72.21	9.39	1.14	5052.49	13.26	2916.91	7.66	4.42	0.04
61.03	10.07	1.11	5011.43	13.15	2882.77	7.57	4.41	0.04
52.21	11.87	0.54	4974.27	13.06	2852.02	7.49	4.41	0.04
41.79	13.45	1.33	4948.82	12.99	2810.24	7.38	4.40	0.04
31.74	17.63	0.89	4867.59	12.78	2771.21	7.27	4.40	0.04
21.79	22.76	0.75	4812.65	12.63	2731.68	7.17	4.40	0.04
17.47	33.97	0.78	4722.13	12.39	2708.09	7.11	4.40	0.04
10.82	43.02	1.68	4629.51	12.15	2673.89	7.02	4.39	0.04
5.82	77.78	1.76	4526.28	11.88	2628.38	6.90	4.37	0.04

Crab Orchard sandstone *Average, Y direction* *Hydrostatic pressure*	Measured parameters							
	Permeability (10^{-18} m^2)		P-wave velocity (m/s)		S-wave velocity (m/s)		Porosity (%)	
Pressure, MPa	Value	Error	Value	Error	Value	Error	Value	Error
5.86	113.61	7.16	4489.17	11.78	2526.47	6.63	4.77	0.04
10.00	81.35	7.08	4578.03	12.02	2594.80	6.81	4.68	0.04
14.90	54.43	3.01	4665.80	12.25	2627.88	6.90	4.54	0.04
19.75	41.78	2.92	4720.97	12.39	2659.34	6.98	4.48	0.04
29.36	26.86	4.20	4842.03	12.71	2695.54	7.07	4.39	0.04
39.46	15.09	2.21	4921.21	12.92	2772.32	7.28	4.33	0.04
49.44	12.19	0.96	4979.99	13.07	2828.83	7.42	4.29	0.04
59.49	9.58	1.18	5041.06	13.23	2873.48	7.54	4.26	0.04
70.00	7.34	2.27	5088.20	13.35	2926.16	7.68	4.24	0.04
79.50	5.97	1.37	5126.31	13.45	2943.80	7.73	4.21	0.04
89.96	5.16	1.33	5150.39	13.54	2967.14	7.71	4.07	0.05
80.25	5.56	1.46	5133.69	13.47	2949.91	7.74	4.17	0.04
71.65	5.91	1.24	5100.97	13.39	2935.80	7.71	4.18	0.04
60.68	6.41	1.16	5059.94	13.28	2909.09	7.64	4.20	0.04
51.52	8.55	0.96	5027.40	13.20	2880.75	7.56	4.22	0.04
42.00	9.48	1.15	4980.67	13.07	2838.97	7.45	4.25	0.04
31.44	12.34	1.30	4910.10	12.89	2780.97	7.30	4.30	0.04
20.81	15.90	1.76	4838.04	12.70	2710.21	7.11	4.39	0.04
14.87	24.50	1.23	4767.46	12.51	2688.12	7.06	4.43	0.04
10.67	33.44	2.38	4684.71	12.30	2643.59	6.94	4.48	0.04
5.47	55.27	3.31	4559.92	11.97	2602.44	6.83	4.64	0.04

Crab Orchard sandstone *Average, Z direction* *Hydrostatic pressure*	Measured parameters							
	Permeability (10^{-18} m^2)		P-wave velocity (m/s)		S-wave velocity (m/s)		Porosity (%)	
Pressure, MPa	Value	Error	Value	Error	Value	Error	Value	Error
4.63	49.49	4.82	4337.27	11.40	2489.71	6.54	4.70	0.05
10.20	34.76	2.33	4451.85	11.70	2539.60	6.68	4.62	0.05
14.81	24.09	1.65	4541.23	11.93	2584.04	6.79	4.57	0.05
20.43	17.27	2.10	4621.27	12.14	2626.48	6.90	4.54	0.05
30.02	12.43	1.39	4715.60	12.39	2671.54	7.02	4.48	0.05
40.46	7.32	1.91	4828.07	12.69	2751.10	7.23	4.44	0.05
50.14	5.91	1.21	4871.62	12.80	2809.89	7.39	4.42	0.05
60.25	4.08	1.68	4947.87	13.00	2852.04	7.50	4.40	0.05
70.29	3.83	1.55	4974.54	13.07	2892.33	7.60	4.38	0.05
80.08	2.72	1.10	5029.58	13.19	2934.20	7.71	4.36	0.05
89.64	4.63	0.61	5061.67	13.29	2962.19	7.79	4.35	0.05
81.41	2.09	0.73	5054.86	13.27	2951.98	7.75	4.40	0.05
71.60	2.94	0.50	5033.36	13.21	2932.35	7.70	4.42	0.05
59.62	3.88	0.52	4979.07	13.07	2895.43	7.60	4.43	0.05
50.27	4.03	0.28	4931.93	12.94	2864.07	7.52	4.45	0.05
41.50	5.00	0.14	4891.78	12.84	2818.35	7.40	4.47	0.05
30.14	7.08	0.63	4806.16	12.61	2749.53	7.22	4.50	0.05
20.37	9.21	0.53	4736.87	12.43	2717.31	7.13	4.53	0.05
15.08	12.34	0.46	4654.48	12.22	2683.96	7.04	4.55	0.05
10.53	15.57	0.42	4560.88	11.97	2657.77	6.98	4.58	0.05
6.66	19.70	0.48	4510.43	11.84	2635.29	6.92	4.61	0.05

Takidani granite *Average, X direction* *Hydrostatic pressure*	Measured parameters							
	Permeability (10^{-18} m^2)		P-wave velocity (m/s)		S-wave velocity (m/s)		Porosity (%)	
Pressure, MPa	Value	Error	Value	Error	Value	Error	Value	Error
4.58	21.05	0.71	5788.03	15.19	3023.73	7.94	0.93	0.02
10.49	16.54	0.49	5829.57	15.30	3042.37	7.99	0.90	0.02
14.76	14.93	0.64	5879.33	15.43	3060.48	8.03	0.88	0.02
21.11	13.66	0.64	5912.12	15.52	3077.03	8.08	0.86	0.02
29.56	9.97	0.27	5940.75	15.59	3101.30	8.14	0.84	0.02
40.33	7.87	0.71	6005.65	15.76	3125.92	8.20	0.83	0.02
50.24	5.52	0.25	6026.65	15.82	3150.59	8.27	0.82	0.02
60.88	5.23	0.22	6052.43	15.89	3172.42	8.33	0.80	0.02
70.14	3.19	0.25	6081.59	15.96	3189.42	8.37	0.79	0.02
80.63	5.03	0.40	6102.12	16.02	3203.95	8.41	0.78	0.02
89.50	4.84	0.17	6109.30	16.03	3207.50	8.41	0.77	0.02
80.82	4.23	0.23	6098.67	16.01	3202.87	8.41	0.77	0.02
70.29	6.18	0.22	6082.42	15.96	3194.32	8.38	0.78	0.02
60.00	8.18	0.49	6068.12	15.93	3186.88	8.36	0.79	0.02
49.86	8.40	0.43	6049.48	15.88	3170.93	8.32	0.81	0.02
40.35	10.38	0.42	6031.17	15.83	3162.53	8.30	0.82	0.02
29.09	10.13	0.58	5980.64	15.70	3142.02	8.25	0.84	0.02
21.48	12.87	0.45	5936.56	15.58	3119.53	8.19	0.86	0.02
15.94	17.26	0.40	5887.73	15.45	3104.71	8.15	0.89	0.02
10.67	21.58	0.25	5846.40	15.34	3080.99	8.09	0.91	0.02
5.14	27.71	0.58	5813.89	15.26	3044.67	7.99	0.94	0.02

Takidani granite *Average, Y direction* *Hydrostatic pressure*	Measured parameters							
	Permeability (10^{-18} m^2)		P-wave velocity (m/s)		S-wave velocity (m/s)		Porosity (%)	
Pressure, MPa	Value	Error	Value	Error	Value	Error	Value	Error
5.07	11.25	0.57	5693.76	14.94	2933.98	7.70	0.90	0.02
9.65	9.00	0.37	5806.15	15.24	2955.47	7.76	0.88	0.02
15.08	6.86	0.33	5858.21	15.38	2971.22	7.80	0.87	0.02
20.25	4.78	0.25	5888.42	15.46	2980.47	7.82	0.86	0.02
30.19	3.80	0.45	5908.71	15.51	3000.99	7.88	0.84	0.02
39.90	3.60	0.76	5935.37	15.58	3019.35	7.92	0.83	0.02
50.04	1.51	0.33	5961.65	15.65	3042.46	7.99	0.82	0.02
59.80	1.84	0.24	5985.85	15.71	3064.53	8.04	0.81	0.02
69.89	1.76	0.15	6045.14	15.87	3088.78	8.11	0.81	0.02
79.87	1.34	0.21	6068.38	15.93	3106.59	8.15	0.80	0.02
90.03	1.54	0.15	6085.57	15.97	3119.12	8.19	0.79	0.02
80.17	1.90	0.20	6080.50	15.96	3116.00	8.18	0.81	0.02
70.71	2.10	0.17	6063.53	15.91	3106.32	8.15	0.81	0.02
61.27	2.16	0.48	6036.60	15.84	3085.85	8.10	0.82	0.02
51.38	1.98	0.17	6017.61	15.79	3051.27	8.01	0.83	0.02
40.95	2.68	0.28	5941.61	15.59	3027.04	7.94	0.85	0.02
31.45	3.93	0.70	5913.79	15.52	3007.71	7.89	0.86	0.02
21.95	6.04	0.67	5883.50	15.44	2985.98	7.84	0.88	0.02
16.12	7.50	0.89	5852.81	15.36	2973.21	7.80	0.89	0.02
9.90	9.49	0.21	5817.36	15.27	2956.81	7.76	0.92	0.02
4.87	11.84	0.22	5743.17	15.07	2941.69	7.72	0.93	0.02

Takidani granite *Average, Z direction* *Hydrostatic pressure*	Measured parameters							
	Permeability (10^{-18} m^2)		P-wave velocity (m/s)		S-wave velocity (m/s)		Porosity (%)	
Pressure, MPa	Value	Error	Value	Error	Value	Error	Value	Error
4.91	31.08	5.79	5787.70	15.19	2963.11	7.78	0.92	0.02
9.70	22.68	4.01	5844.06	15.34	2983.41	7.83	0.90	0.02
14.92	16.33	2.06	5888.73	15.46	3001.15	7.88	0.88	0.02
20.03	10.96	1.43	5936.95	15.58	3015.63	7.92	0.88	0.02
29.61	9.27	2.23	5989.45	15.72	3037.41	7.97	0.86	0.02
39.84	7.50	0.77	6024.61	15.81	3055.43	8.02	0.84	0.02
49.60	7.22	1.44	6064.50	15.92	3069.12	8.06	0.83	0.02
59.74	3.90	0.73	6117.30	16.06	3092.69	8.12	0.82	0.02
69.50	5.38	1.46	6146.74	16.13	3103.93	8.15	0.82	0.02
79.85	4.02	0.73	6171.19	16.20	3114.49	8.17	0.81	0.02
89.22	2.84	0.40	6190.38	16.25	3121.13	8.19	0.81	0.02
79.83	3.62	0.56	6168.39	16.19	3125.71	8.20	0.81	0.02
70.85	4.69	0.89	6146.12	15.75	3113.89	8.01	0.81	0.02
61.26	7.78	0.74	6123.99	16.07	3103.24	8.14	0.86	0.02
50.60	6.46	0.92	6068.93	15.75	3081.98	7.99	0.83	0.02
40.81	4.81	0.27	6057.34	15.90	3063.09	8.04	0.88	0.02
31.04	5.05	0.77	5997.10	15.74	3040.25	7.98	0.89	0.02
20.89	9.24	1.23	5944.66	15.60	3013.88	7.91	0.91	0.02
15.69	10.20	0.80	5912.62	15.52	2999.77	7.87	0.92	0.02
10.07	13.39	1.88	5857.93	15.38	2981.25	7.82	0.95	0.02
4.94	15.58	0.74	5801.35	15.23	2959.76	7.77	0.96	0.02

E. ELEVATED PRESSURE DATA 2: VELOCITY/PERMEABILITY ANISOTROPY

Bentheim sandstone *Anisotropy* *Hydrostatic pressure*	Measured anisotropy parameters						
	Permeability (%)			P-wave velocity (%)		S-wave velocity (%)	
Pressure, MPa	Kx/Kz	Ky/Kz	Error	Value	Error	Value	Error
5.3	13.9	10.2	0.3	4.6	0.4	2.2	0.4
10.0	7.1	1.2	0.5	2.2	0.4	2.4	0.4
15.4	8.5	3.4	0.5	2.7	0.4	2.3	0.4
20.0	6.4	6.9	0.2	2.1	0.4	2.2	0.4
29.9	-2.4	-3.7	0.3	2.0	0.4	1.9	0.4
39.9	0.3	-2.9	0.4	2.2	0.4	1.7	0.4
50.2	4.7	-0.6	0.2	2.1	0.4	1.6	0.4
60.1	2.4	-1.1	0.2	1.7	0.4	1.5	0.4
69.9	0.1	-3.8	0.2	1.8	0.4	1.5	0.4
80.0	9.5	1.1	0.1	1.7	0.4	1.4	0.4
90.0	4.9	0.8	0.2	2.0	0.4	1.4	0.4

Crab Orchard sandstone *Anisotropy* *Hydrostatic pressure*	Measured anisotropy parameters						
	Permeability (%)			P-wave velocity (%)		S-wave velocity (%)	
Pressure, MPa	Kx/Kz	Ky/Kz	Error	Value	Error	Value	Error
5.6	88.1	78.6	0.7	2.9	0.4	6.7	0.4
9.9	85.1	80.3	0.5	1.7	0.4	8.0	0.4
14.7	81.5	77.3	0.6	0.5	0.4	7.4	0.4
19.5	83.0	83.0	1.1	0.5	0.4	3.9	0.4
29.9	81.9	73.4	1.2	0.9	0.4	3.6	0.4
40.2	104.0	69.4	1.4	0.7	0.4	1.4	0.4
49.7	94.7	69.4	4.1	1.2	0.4	1.7	0.4
59.8	101.8	80.5	2.2	0.7	0.4	1.9	0.4
70.5	88.2	62.7	8.1	1.0	0.4	2.8	0.4
79.1	78.8	74.7	8.4	1.2	0.4	0.9	0.4
89.3	86.7	10.8	9.1	1.7	0.4	1.0	0.4

Takidani Granite *Anisotropy* *Hydrostatic pressure*	Measured anisotropy parameters						
	Permeability (%)			P-wave velocity (%)		S-wave velocity (%)	
Pressure, MPa	Kx/Ky	Kz/Ky	Error	Value	Error	Value	Error
5.04	60.71	93.70	2.07	3.33	0.4	1.33	0.4
9.87	59.07	86.41	1.86	1.21	0.4	1.35	0.4
15.04	74.01	81.61	1.25	0.90	0.4	1.24	0.4
20.25	96.35	78.55	1.31	0.94	0.4	1.13	0.4
29.99	89.66	83.72	3.14	0.93	0.4	0.80	0.4
39.84	74.54	70.36	1.71	1.01	0.4	0.80	0.4
49.86	114.10	130.77	3.04	0.84	0.4	0.69	0.4
59.92	96.02	72.02	2.28	0.47	0.4	0.63	0.4
69.74	57.73	101.31	3.82	0.49	0.4	0.26	0.4
79.88	115.67	99.83	2.42	0.24	0.4	0.09	0.4
89.71	103.65	59.72	1.56	0.20	0.4	-0.17	0.4

F. MISCELLANEOUS THEORY AND MODEL FITTING SCRIPTS/CODE

F.1. HUDSON AND KACHANOV CRACK THEORY

Hudsons' Crack model

For perfect transverse isotropy, and defining the crack normals as aligned along the Z axis, the first and second order corrections in this case are given by Mavko et al. (1998) as:

$$c_{11}^1 = -\frac{\lambda^2}{\mu}\varepsilon U_3 \qquad c_{11}^2 = \frac{q}{15}\frac{\lambda^2}{(\lambda+2\mu)}(\varepsilon U_3)^2$$

$$c_{13}^1 = -\frac{\lambda(\lambda+2\mu)}{\mu}\varepsilon U_3 \qquad c_{13}^2 = \frac{q}{15}\lambda(\varepsilon U_3)^2$$

$$c_{33}^1 = -\frac{(\lambda+2\mu)^2}{\mu}\varepsilon U_3, \qquad c_{33}^2 = \frac{q}{15}(\lambda+2\mu)(\varepsilon U_3)^2$$

$$c_{44}^1 = -\mu\varepsilon U_1 \qquad c_{44}^2 = \frac{2}{15}\frac{\mu(3\lambda+8\mu)}{\lambda+2\mu}(\varepsilon U_1)^2$$

$$c_{66}^1 = 0 \qquad c_{66}^2 = 0$$

Where: $q = 15\frac{\lambda^2}{\mu^2} + 28\frac{\lambda}{\mu} + 28$ and: $\varepsilon = \frac{N}{V}a^3$ ('ε' is crack density, and 'a' is the crack aspect ratio when considering a number of cracks 'N' in a representative volume 'V')

And: $U_1 = \frac{16(\lambda+2\mu)}{3(3\lambda+4\mu)}$, $U_3 = \frac{4(\lambda+2\mu)}{3(\lambda+\mu)}$ (DRY medium, after Hudson, 1990)

Hudsons' Crack model: Transverse Isotropy

However, the preceding equations assume perfect crack alignment, which is probably not the case in this study. Hudson (1990) provides a general first order correction for TI materials:

$$C_{ijpq}^1 = -\frac{A}{\mu}U_3\left[\lambda^2\delta_{ij}\delta_{pq} + 2\lambda\mu\left(\delta_{ij}\tilde{\varepsilon}_{pq} + \delta_{pq}\tilde{\varepsilon}_{ij}\right) + 4\mu^2\tilde{\varepsilon}_{ijpq}\right]$$
$$- A\mu U_1\left(\delta_{jq}\tilde{\varepsilon}_{ip} + \delta_{jp}\tilde{\varepsilon}_{iq} + \delta_{iq}\tilde{\varepsilon}_{jp} + \delta_{ip}\tilde{\varepsilon}_{jq} - 4\tilde{\varepsilon}_{ijpq}\right)$$

Where:

$$A = \int_0^{2\pi}\int_0^{\pi/2}\varepsilon(\vartheta,\varphi)\sin\vartheta\, d\vartheta\, d\varphi$$

$$\tilde{\varepsilon}_{ij} = \frac{1}{A}\int_0^{2\pi}\int_0^{\pi/2}\varepsilon(\vartheta,\varphi)n_i n_j \sin\vartheta\, d\vartheta\, d\varphi$$

$$\tilde{\varepsilon}_{ijpq} = \frac{1}{A}\int_0^{2\pi}\int_0^{\pi/2}\varepsilon(\vartheta,\varphi)n_i n_j n_p n_q \sin\vartheta\, d\vartheta\, d\varphi$$

Here, n_i are the components of the unit vector along the crack normal, $\mathbf{n}=(\sin\theta.\cos\phi, \sin\theta.\sin\phi, \cos\theta)$, and $\varepsilon(\theta,\phi)$ is the crack density distribution function so that $\varepsilon(\theta,\phi).\sin\theta d\theta d\phi$ is the density of cracks with normals lying in the solid angle between $(\theta,\theta+d\theta)$ and $(\phi,\phi+d\phi)$.

Substituting the Fisher function, $\Gamma(\theta)=\dfrac{\Gamma_t}{2\pi}\dfrac{e^{(\cos\theta)/\sigma^2}}{\sigma^2\left(e^{1/\sigma^2}-1\right)}$, in Chapter 6 into the generalised first order stiffness correction, we obtain the following expressions:

$$C_{11}^1=-\Gamma_t\frac{U_3}{\mu}\left(\lambda^2+4\lambda\mu\sigma^2+12\mu^2\sigma^4\right)-\Gamma_t U_1\mu\left(4\sigma^2-12\sigma^4\right)$$

$$C_{12}^1=-\Gamma_t\frac{U_3}{\mu}\left(\lambda^2+4\lambda\mu\sigma^2+4\mu^2\sigma^4\right)+\Gamma_t U_1\mu\left(4\sigma^4\right)$$

$$C_{13}^1=-\Gamma_t\frac{U_3}{\mu}\left[\lambda^2+2\lambda\mu\left(1-\sigma^2\right)+4\mu^2\left(\sigma^2-4\sigma^4\right)\right]+4\Gamma_t U_1\mu\left(\sigma^2-4\sigma^4\right)$$

$$C_{33}^1=-\Gamma_t\frac{U_3}{\mu}\left[\lambda^2+4\lambda\mu\left(1-\sigma^2\right)+4\mu^2\left(\sigma^4-2\sigma^2+1\right)\right]-4\Gamma_t U_1\mu\left(\sigma^2-\sigma^4\right)$$

$$C_{44}^1=-\Gamma_t\frac{U_3}{\mu}\left[4\lambda^2\left(\sigma^2-4\sigma^4\right)\right]-\Gamma_t U_1\mu\left[1-\sigma^2-4\left(\sigma^2-4\sigma^4\right)\right]$$

$$C_{66}^1=\left(C_{11}^1-C_{12}^1\right)/2$$

Where, (again) for dry cracks we have: $U_1=\dfrac{16(\lambda+2\mu)}{3(3\lambda+4\mu)}$, and $U_3=\dfrac{4(\lambda+2\mu)}{3(\lambda+\mu)}$

And: C^1_{xy} are the first order stiffness co-efficients

Γ_t is the maximum crack density

μ is the isotropic shear modulus

λ is the Lamé modulus, where $\lambda=K+2\mu$ (K is the bulk modulus)

Kachanov crack model: TI case

For TI variations of elastic compliance due to cracks ΔS_{ijkl}:

$$\Delta S_{ijkl}=\frac{1}{hE_m}\left(\frac{1}{4}\left(\zeta_{ik}\Gamma_{jl}+\zeta_{il}\Gamma_{jk}+\zeta_{jk}\Gamma_{il}+\zeta_{jl}\Gamma_{ik}\right)+\zeta_{ijkl}\right)$$

where: Γ_{ij} is the crack density tensor, $\Gamma_{ij}=\Gamma\langle n_i n_j\rangle$, and $\langle n_i n_j\rangle=\dfrac{1}{N}\sum_N n_i n_j$, and

ζ_{ijkl} is the 'saturation tensor', $\zeta_{ijkl}=\left[\left(1-\dfrac{\upsilon_m}{2}\right)\dfrac{\zeta}{1+\zeta}-1\right]\Gamma\langle n_i n_j n_k n_l\rangle$

Assume a continuous distribution of crack orientations:

$$\langle n_i \rangle = \frac{1}{2\pi} \int_0^{2\pi} d\phi \int_0^{\pi/2} f(\theta,\phi) n_i \sin\theta d\theta$$

with $f(\theta,\phi)$ being the orientation distribution function. The tensors $\langle n_i n_j \rangle$ and $\langle n_i n_j n_k n_l \rangle$ represent the second order and fourth order moment crack orientation distribution functions respectively. These equations can be greatly simplified due to the symmetry which exists in the transverse isotropy case, in which we can make the following modifications (Sayers and Kachanov, 1995; Schubnel and Guéguen, 2003):

$$\begin{aligned} &\langle n_i n_j \rangle = 0 \\ &\langle n_i n_j{}^3 \rangle = 0 \end{aligned} \quad \text{if } i \neq j, \text{ and:}$$

$$\langle n_1{}^2 \rangle = \langle n_2{}^2 \rangle = \frac{1}{2}\left(1 - \langle n_3{}^2 \rangle\right)$$

$$\langle n_1{}^4 \rangle = \langle n_2{}^4 \rangle$$

$$\langle n_1{}^4 \rangle = 3\langle n_1{}^2 n_2{}^2 \rangle$$

To give:

$$S^*_{1111} = S^*_{2222} = S^i_{1111} + \frac{\Gamma}{E_m h}\left(\langle n_1{}^2 \rangle + \left[\left(1 - \frac{\upsilon_m}{2}\right)\frac{\zeta}{1+\zeta} - 1\right]\langle n_1{}^4 \rangle\right)$$

$$S^*_{3333} = S^i_{3333} + \frac{\Gamma}{E_m h}\left(\langle n_3{}^2 \rangle - \left[\left(1 + \frac{\upsilon_m}{2}\right)\frac{\zeta}{1+\zeta} - 1\right]\langle n_3{}^4 \rangle\right)$$

$$S^*_{1212} = S^i_{1212} + \frac{\Gamma}{E_m h}\left(\frac{\langle n_1{}^2 \rangle}{2} + \left[\left(1 - \frac{\upsilon_m}{2}\right)\frac{\zeta}{1+\zeta} - 1\right]\frac{\langle n_1{}^4 \rangle}{3}\right)$$

$$S^*_{1313} = S^*_{2323} = S^i_{1313} + \frac{\Gamma}{E_m h}\left(\frac{1 - \langle n_1{}^2 \rangle}{2} + \left[\left(1 - \frac{\upsilon_m}{2}\right)\frac{\zeta}{1+\zeta} - 1\right]\langle n_1{}^2 n_3{}^2 \rangle\right)$$

$$S^*_{1122} = S^i_{1122} + \frac{\Gamma}{E_m h}\left(\left[\left(1 - \frac{\upsilon_m}{2}\right)\frac{\zeta}{1+\zeta} - 1\right]\frac{\langle n_1{}^4 \rangle}{3}\right)$$

$$S^*_{1133} = S^*_{2233} = S^i_{1133} + \frac{\Gamma}{E_m h}\left(\left[\left(1 - \frac{\upsilon_m}{2}\right)\frac{\zeta}{1+\zeta} - 1\right]\langle n_1{}^2 n_3{}^2 \rangle\right)$$

Where S^* is the modified compliance matrix elements, and S^i is the isotropic background compliance matrix elements (which are known). These modified compliances may now be inverted in order to provide the stiffness matrix of the cracked medium, and used to finally give the elastic wave velocity variation with wave propagation angle to the TI symmetry. See Sayers and Kachanov (1995) for more detail.

F.2. EQUIVALENT PORE GEOMETRY CODE (MATLAB™)

```
%
% Program to calculate Epore lookup charts
% Phil Benson 2004-07-28
%
%
%
Ksus=0.389;
%%bc=1.2;
%loop start
%N=0;
I=0;
ab = 1.0001:0.05:1.46;  lab  =length(ab);
bc = 1.0001:0.05:1.36;   lbc = length(bc);
%%for (N=0:1:4)
%%Counter=0;
%%ab=1.2;
%%bc=bc+(N/10);
Lnew = zeros(lab,lbc); Fnew = zeros(lab,lbc);
figure
%%    while (Counter<100)
for ii = 1:lbc
    for jj = 1:lab
%%    for I = 1:100
%%    I=(N*100)+(Counter+1);
%%    [L F P] = EPore(ab, bc, Ksus);
      [Lnew(jj,ii), Fnew(jj,ii)] = Epore(ab(jj),bc(ii),Ksus);
%%    Lnew(I)=L; Fnew(I)=F; Pnew(I)=P;
%%    abnew(I)=ab; bcnew(I)=bc;
%%    ab=ab+0.01;
%%    [bc];
%%    Counter=Counter+1;
    end
    plot(Fnew(:,ii),Lnew(:,ii),'r-'), hold on
    axis([1 1.05 1 1.05])
%N=N+1;
%bc=bc+0.1
end
for jj = 1:lab
   plot(Fnew(jj,:),Lnew(jj,:),'b-'), hold on
%  axis([1 1.02 1 1.02])
end
[XL]=X(:,1); [XF]=X(:,2);
plot(XF,XL,'k*'), hold on
plot(1.0270,1.0117,'gO'), hold on
%loop end
xlabel('F'), ylabel('L'), grid on
%%LT=Lnew'; FT=Fnew'; PT=Pnew'; abT=abnew'; bcT=bcnew';
%%LM=[bcT abT LT FT PT];
%save L.txt LM -ascii
%
% ------- subroutines
%
% Subroutine to calculate Epore L,F and P
% P.Benson
%
function[L, F, P] = EPore(ab, bc, Ksus)
% set up parameters
% bc=1.1; ab=3.0; Ksus=3.707; %3.34
BA=1/ab; CA=1/(bc/BA);
%CA=0.76604; BA=0.87037;
Ctheta=CA; Cphi=BA;
Stheta=sqrt(1-(CA^2)); Sphi=sqrt(1-(BA^2)); S3theta=(Stheta^3);
Salpha=Sphi/Stheta; S2alpha=(Salpha^2);
```

```
Calpha=sqrt(1-(Salpha^2)); C2alpha=(Calpha^2);
k=Salpha;
theta=acos(CA);
phi=360*(theta/(2*pi));
%[k,m,theta,phi]
[fe,ee]=elit(k,phi);
K=fe; E=ee;
% calculate Na
facA=(Cphi*Ctheta)/(S3theta*S2alpha);
ellipA=(K-E);
Na=facA*ellipA;
% calculate Nb
facB1=(Cphi*Ctheta)/(S3theta*S2alpha*C2alpha);
facB2=C2alpha;
facB3=(S2alpha*Stheta*Ctheta)/Cphi;
Nb=facB1*(E-(facB2*K)-facB3);
% calculate Nc
facC1=(Cphi*Ctheta)/(S3theta*C2alpha);
facC2=(Stheta*Cphi)/Ctheta;
Nc=facC1*(facC2-E);
% output list
%[CA BA]
%[Ctheta Cphi Calpha C2alpha]
%[Stheta S3theta Sphi Salpha S2alpha]
%[Na Nb Nc]
%Na+Nb+Nc
% Calculate ratios L/F/P
L=(1+(Ksus*(Nb)))/(1+(Ksus*(Na)));
F=(1+(Ksus*(Nc)))/(1+(Ksus*(Nb)));
P=(1+(Ksus*(Nc)))/(1+(Ksus*(Na)));
[L F P];
%
% -----------
%
%This program is a direct conversion of the corresponding Fortran
%program in
%S. Zhang & J. Jin "Computation of Special Functions" (Wiley, 1996).
%online: http://iris-lee3.ece.uiuc.edu/~jjin/routines/routines.html
%
%Converted by f2matlab open source project:
%online: https://sourceforge.net/projects/f2matlab/
% written by Ben Barrowes (barrowes@alum.mit.edu)
%
function [fe,ee]=elit(hk,phi);
%
%       ================================================
%       Purpose: Compute complete and incomplete elliptic
%                integrals F(k,phi) and E(k,phi)
%       Input  : HK  --- Modulus k ( 0 Û k Û 1 )
%                Phi --- Argument ( in degrees )
%       Output : FE  --- F(k,phi)
%                EE  --- E(k,phi)
%       ================================================
%
g=0.0d0;
pi=3.14159265358979d0;
a0=1.0d0;
b0=sqrt(1.0d0-hk.*hk);
d0=(pi./180.0d0).*phi;
r=hk.*hk;
if (hk == 1.0d0&phi == 90.0d0);
fe=1.0d+300;
ee=1.0d0;
elseif (hk == 1.0d0);
fe=log((1.0d0+sin(d0))./cos(d0));
```

```
ee=sin(d0);
else;
fac=1.0d0;
for  n=1:40;
a=(a0+b0)./2.0d0;
b=sqrt(a0.*b0);
c=(a0-b0)./2.0d0;
fac=2.0d0.*fac;
r=r+fac.*c.*c;
if (phi ~= 90.0d0);
d=d0+atan((b0./a0).*tan(d0));
g=g+c.*sin(d);
d0=d+pi.*fix(d./pi+.5d0);
end;
a0=a;
b0=b;
if (c < 1.0d-7) break; end;
end;
         ck=pi./(2.0d0.*a);
ce=pi.*(2.0d0-r)./(4.0d0.*a);
if (phi == 90.0d0);
fe=ck;
ee=ce;
else;
fe=d./(fac.*a);
ee=fe.*ce./ck+g;
end;
end;
%
% END OF PROGRAM %
%
```

F.3. ELLIPSOIDAL VELOCITY MODEL CODE (MATLAB™)

```
% VPSP code to fit ellipsoid to velocity data
% Phil Benson
% W is the slowness vector
% Q is the system matrix (Cartesian co-ords)
% both must be pre-loaded
%
TQ=Q';
TQQ=TQ*Q;
ITTQ=inv(TQQ);
TQW=TQ*W;
P=ITTQ*TQW
x=ones(3,3);
x(1,1)=P(1);
x(2,2)=P(2);
x(3,3)=P(3);
x(1,2)=P(4)/2;
x(2,1)=P(4)/2;
x(1,3)=P(5)/2;
x(3,1)=P(5)/2;
x(2,3)=P(6)/2;
x(3,2)=P(6)/2;
[eigvec,eigval]=eig(x)
L=x*eigvec;
R=eigvec*eigval;
L-R
% END
%
```

F.4. EBERHART-PHILLIPS LEAST SQUARE FIT AND MINIMISATION CODE (MATLAB™)

```
% Eberhart phillips relation least suares
% Data is Peff(MPa) and vp velocity (m/s) in two sperate text files
% Relation used is: v = A + D.Peff - E.exp(F.Peff)
% load data
 load bsx_vp.txt;
 load bsx_peff.txt;
 data=bsx_vp;
 peff=bsx_peff;
% 'F'
 F=-0.072;
% set up matricies for least sq + calc
 sysm = [ones(size(peff)), peff, -exp(F.*Peff)];
 sol = sysm\data  % equivalent to sol = inv(conc'*conc)*conc'*data;
%
 res = data - sysm*sol;
 rpwr = (res'*res);
%
% looping data increment for 'f'
% + graph?
F = -0.2:0.001:-0.01;
f=F';
lf = length(f);
figure
for ii = 1:lf
      sysm = [ones(size(peff)), peff, -exp(f(ii).*Peff)];
      sol = sysm\data;
      res = data - sysm*sol;
      rpwr(ii) = (res'*res);
      plot(f(ii),rpwr(ii),'r-'), hold on
end
% deriviative
for jj= 1:lf-1
    drpwr(jj)=abs(rpwr(jj+1)-rpwr(jj));
    plot(f(jj),drpwr(jj),'b-'), hold on
end
xlabel('F'), ylabel('rpwr'), grid on
mat=[f rpwr']; mat2=[drpwr'];
save EPM_FP_BSXVp.txt mat -ascii
save EPM_FPD_BSXVp.txt mat2 -ascii
```

F.5. THOMSEN WEAK ANISOTROPY LEAST SQUARES FIT CODE (MATLAB™)

```
%
% load data
 load angle.txt;
 load TSY_VP_W.txt;
 theta=angle;
 data=TSY_VP_W;
% set up matricies for least sq + calc
 th = theta*pi/180;
 cosq4 = sin(th).*sin(th).*cos(th).*cos(th);
 snsq4 = sin(th).*sin(th).*sin(th).*sin(th);
 sysm = [ones(size(snsq4)), cosq4, snsq4];
 sol = sysm\data;  % equivalent to sol = inv(conc'*conc)*conc'*data;
%
 res = data - sysm*sol;
 rpwr = (res'*res)/(data'*data);
%
% factors
alpha=sol(1);
delta=sol(2)/sol(1);
epsilon=sol(3)/sol(1);
%
% Now for Vs
load TSY_VS_W.txt;
data2=TSY_VS_W;
% set up matricies for least sq + calc
 snsq = sin(th).*sin(th);
 sysm = [ones(size(snsq)), snsq];
 sol = sysm\data2;  % equivalent to sol = inv(conc'*conc)*conc'*data;
%
 res = data - sysm*sol;
 rpwr = (res'*res)/(data'*data);
%
% factors
alpha
beta=sol(1)
epsilon
gamme=sol(2)/sol(1)
delta
```

F.6. HUDSON TI MODEL CODE (MATLAB™)

```
% Hudson's model for cracked media
% Dry cracks only, TI symmetry
phi=0.005;
% phi = input(' Enter fractional porosity (<= aspect ratio): ');
%
alpha=0.01; rho=2.65*1000;
%vpmax=3450; vsmax=2230; mum=rho*vsmax*vsmax; km=rho*vpmax*vpmax -
4*mum/3;
vpmax=3440; vsmax=2215; mum=rho*vsmax*vsmax; km=rho*vpmax*vpmax -
4*mum/3;
lam = km -2*mum/3;
rlm = lam/mum;
Et=(3*phi)/(4*pi*alpha);     %crack density, perfect alignment
%sig=0.53;  aoff=0    %sigma=Sin(angle0)    sig = angle in radians
<-----
sig=0.50;  aoff=-10   %sigma=Sin(angle0)    sig = angle in radians
<-----
%crack density, crack distn, Ctheta
%
% Enter either dry or saturated cracks.....
%U1=(16*(lam+(2*mum)))/(3*((3*lam)+(4*mum))); %parameter (sat cracks)
%U3=0;                                %parameter (sat cracks)
U1=(16*(lam+(2*mum)))/(3*((3*lam)+(4*mum)));  %parameter (dry cracks)
U3=(4*(lam+(2*mum)))/(3*(lam+mum));%parameter (dry cracks)
%---
% 1st order corrections
P1=lam*lam+4*lam*mum*sig*sig+12*mum*mum*(sig^4); P2=4*sig*sig-
12*(sig^4);
c111=-(Et*U3/mum)*P1-Et*mum*U1*P2;
%
P3=lam*lam+4*lam*mum*sig*sig+4+mum*mum*(sig^4);
c112=-(Et*U3/mum)*P3+Et*mum*U1*4*(sig^4);
%
P4=sig*sig-4*(sig^4); P5=lam*lam+2*lam*mum*(1-sig*sig)+4*mum*mum*P4;
% c113=-(Et*U3/mum)*P5+Et*mum*U1*P4;
c113=-(Et*U3/mum)*P5+Et*mum*U1*4*P4;
%
%P6=8*sig*sig+32*(sig^4);
P6=8*sig*sig-32*(sig^4);
P6B = lam^2+4*lam*mum*(1-2*sig^2)+4*mum*mum*(8*sig^4-4*sig^2+1);
%c133=-(Et*U3/mum)*P6;
c133=-(Et*U3/mum)*P6B-Et*mum*U1*P6;
%
P7=sig*sig-4*(sig^4); P8=1-sig*sig-4*P7;
c144=-(Et*U3/mum)*4*mum*mum*P7-Et*mum*U1*P8;
%
c166=0.5*(c111-c112);
%
C1IJ=[c111 c112 c113  0 0 0;...
        c112 c111 c113  0 0 0;...
        c113 c113 c133  0 0 0;...
        0 0 0 c144 0 0;...
        0 0 0 0 c144 0;...
        0 0 0 0 0 c166];
%---
% background matrix
c011=lam+2*mum;
c012=lam;
c044=mum;
C0IJ=[c011 c012 c012  0 0 0;...
        c012 c011 c012  0 0 0;...
        c012 c012 c011  0 0 0;...
        0 0 0 c044 0 0;...
```

```
        0 0 0 0 c044 0;...
        0 0 0 0 0 c044];
Ceff=C0IJ+C1IJ
%---
% Calculate velocities as function of angle to symmetry
theta=0:10:360;  th = (theta/360)*2*pi;
M1=(Ceff(1,1)-Ceff(4,4)).*(sin(th).^2);
M2=(Ceff(3,3)-Ceff(4,4)).*(cos(th).^2);
M3=((Ceff(1,3)+Ceff(4,4))^2).*(sin(2*th).^2);
M=((M1-M2).^2)+M3;
Vp=(sqrt((Ceff(1,1)*(sin(th).^2))+(Ceff(3,3)*(cos(th).^2))+Ceff(4,4)+s
qrt(M)))/(sqrt(2*rho));
Vsv=(sqrt((Ceff(1,1)*(sin(th).^2))+(Ceff(3,3)*(cos(th).^2))+Ceff(4,4)-
sqrt(M)))/(sqrt(2*rho));
Vsh=sqrt(((Ceff(6,6)*(sin(th).^2))+(Ceff(4,4)*(cos(th).^2)))/rho);
%
%theta=theta+aoff;
figure
load Bsy_vp_w.txt
load Bsy_vs_w.txt
plot(theta,Bsy_vp_w,'r*',theta,Bsy_vs_w,'b*'), hold on
plot(theta+aoff,Vsh,'b-'), grid on
xlabel('angle (deg)'), ylabel('velocity (m/s)')
str1 = num2str(Et); txtstr = [' Hudson dry cracks: crack density = ',
str1(:)'];
title(txtstr)
Vp=Vp'; Vsv=Vsv'; Vsh=Vsh'; theta=theta';
hud=[theta Vp Vsv Vsh];
save hudsonD2R_BSy.txt hud -ascii
%
%
```